The Impact of Glaciation and Permafrost on Groundwater Flow

by
Melissa Barnard

A thesis
presented to the University of Waterloo
in the fulfillment of the
thesis requirement for the degree of
Doctor of Philosophy
in
Civil Engineering.

Waterloo, Ontario, Canada, 2016

Author’s Declaration

I hereby declare that I am the sole author of this thesis. This is a true copy of the thesis, including any required final revisions, as accepted by my examiners.

I understand that my thesis may be made electronically available to the public.

Abstract

Current geologic and climatic conditions need to be considered when choosing an appropriate site for a Deep Geologic Repository (DGR). However, given the million-year timeframe for the radioactivity of the used fuel to reduce to that of its natural uranium content and the record of repeated glacial cycles in the Northern hemisphere over the past million years, the impact of glaciation on the DGR also needs to be considered. Simplifying assumptions are often made in such paleo-climate modelling analyses involving permafrost and glaciation and include the assumptions that fluid flow is isothermal and fully-saturated and the phreatic surface in the permafrost is within metres of the topographic surface. Those assumptions were examined using a modelling approach that included thermal transport and flow conditions with an alternate conceptualization of the water table boundary conditions to develop a more detailed representation of the impact and glacial and periglacial conditions on the groundwater flow system. Two computational models, FRAC3DVS-OPG and COMSOL Multiphysics, were used to carry out those investigations. The numerical models of the Greenland Analogue Project (GAP) study site that investigated groundwater flow and permafrost near the edge of the Greenland Ice Sheet (GIS) and a proposed DGR site in Southern Ontario were used to examine the impact of permafrost on the water table for fully-saturated and variably-saturated flow conditions. Those analyses demonstrated that with the presence of permafrost, the use of a prescribed head boundary condition did not allow drainage that may occur when the recharge to permafrost is set to zero. Permafrost will not allow enough recharge to maintain fully-saturated conditions, and the system will drain beneath it.

Acknowledgements

There are many people who supported me in some way over the last “few” years as I have carried out the research presented here and as I wrote this thesis. It is difficult to find the right words to express how grateful I am for all of that support. “Thank-you” does not seem to be enough because I quite simply would not have been able to achieve this without the support I have received. My research and thesis were only possible because of the technical knowledge and information that was shared with me, the financial support that was provided to me, and the words of encouragement that motivated and guided me.

First, I would like to thank Dr. Jon Sykes, my thesis supervisor, for his technical expertise and guidance as I have worked through the complex investigations presented in thesis. I would also like to thank him for his patience and continued support when I decided to pursue my passion for teaching and curriculum design. He never let me give up on the research I had started.

I would like to thank my colleagues Dr. Stefano Normani and Dr. Yong Yin whose knowledge and experience were invaluable to me as I tried to learn to code in python or when the server and software would crash on me. I would also like to thank my thesis committee members Dr. James Craig, Dr. Shawn Matott, and Dr. Ed Sudicky and my external examiner, Dr. Kerry MacQuarrie, for their time and feedback on my work.

My work complemented the investigations being carried out by the Nuclear Waste Management Organization (NWMO), and I am very grateful for the information and datasets made available to me by the NWMO, in particular the data and results for the Greenland Analogue Project (GAP). Again, I would like to thank my colleagues Dr. Stefano Normani and Dr. Yong Yin for allowing me to build on and extend the research they began for the GAP and the Southern Ontario Deep Geologic Repository program.

Next, I would like to acknowledge Dr. Jon Sykes, the University of Waterloo, and the Natural Sciences and Engineering Research Council (NSERC) for the scholarships and research assistantships that they provided me. That financial support allowed me to pursue this degree and conduct this research full-time, and it also gave me the confidence to do so.

Last, but certainly not least, I would like to thank all of my family and friends for their never-ending support and encouragement. I will be forever grateful to them for tolerating and still loving me while I devoted all of my time and energy to my work.

Table of Contents

List of Figures

List of Tables

List of Symbols

α	Dispersivity [L]
β'	Coefficient of vertical compressibility for porous medium [LT^2/M]
β_f	Fluid compressibility [LT^2/M]
Γ_{ex}	Volumetric fluid exchange rate between subsurface domain and all other domains [L^3/L^3T] (FRAC3DVS-OPG)
γ	Ratio of specific heats [-]
ε	Porosity
ζ	One-dimensional loading efficiency [-]
θ	Liquid volume fraction [-]
θ_s	Pore volume fraction [-] or saturated water content [-] assumed to be porosity (FRAC3DVS-OPG)
μ	Dynamic viscosity of fluid [M/LT]
ρ	Density [M/L^3]
ρ_0	Reference density [M/L^3]
ρ_A	Average density between points z_i and z_r [M/L^3]
ρ_{max}	Maximum density [M/L^3]
ρ_r	Relative density [-]
σ_{zz}	Vertical stress [M/LT^2]
τ	Tortuosity [-]
Ω_C	Concentration source or sink term [M/L^3T]
C	Concentration of solution [M/L^3]
C_{max}	Maximum concentration [M/L^3]
C_p	Fluid heat capacity at constant pressure [$ML^2/T\Theta$]
c_c	Coefficient for the increase in fluid density with increasing brine content [-]
c_T	Coefficient of thermal expansion [-]
c_w	Compressibility of water [LT^2/M]
D	Normalized pulse in the phase change from T_0 to T_1; Derivative of H_{lh} with respect to temperature [$1/\Theta$]
D_{Di} or D_{ij}	Hydrodynamic dispersion tensor [L^2/T]
D_{Li}	Single phase diffusion coefficient for species *i* in liquid phase [L^2/T]
D_m	Molecular diffusion coefficient [L^2/T]
∇D	Unit vector in direction over which gravity acts [-]
E	Young's elastic modulus of porous medium [-]
f	Flotation ratio [-]
g	Gravitational acceleration [L/T^2]
H	Hydraulic head [L]
H_i	Ice thickness [L]
H_{lh}	Volume fraction of water within an element [-]
H_p	Pressure head [L]
h	Equivalent freshwater head
h_{Ei}	Environmental head at point *i* [L]
h_{Fi}	Freshwater head at point *i* [L]

K	Hydraulic conductivity of porous medium [L/T]
K’	Drained confined vertical modulus of porous medium [M/LT^2]
k	Permeability of porous medium [L^2]
k_{eq}	Equivalent thermal conductivity [$ML/T^3\Theta$]
P_e	Equivalent pressure [M/LT^2]
P_i	Ice overburden pressure [M/LT^2]
P_w	Pressure of subglacial water [M/LT^2]
p	Fluid pressure [M/LT^2]
Q	Heat source or sink [M/LT^3]
Q_m	Mass source or sink [M/L^3T]
q	Fluid flux [L/T]
S	Storage [LT^2/M]
S_s	Specific storage [1/L]
S_w	Degree of water saturation [-]
T	Temperature [Θ]
u	Darcy or fluid velocity [L/T]
v	Poisson’s ratio [-]
w_m	Volumetric fraction of total porosity occupied by porous medium [-] (FRAC3DVS-OPG)
z	Elevation head [L]
z_i	Elevation of freshwater at point *i* [L]
z_r	Reference elevation of freshwater above point *i* [L]

List of Abbreviations

BMT	BenchMark Tests
COMSOL	COMSOL Multiphysics
DECOVALEX	DEvelopment of COupled THMC models and their VALidation against EXperiments
DGR	Deep Geologic Repository
DGRTP	Deep Geologic Repository Technology Program
ELA	Equilibrium Line Altitude
FRAC3DVS-OPG	FRACtured 3D Variably-Saturated-OPG
FZ	Fracture Zone
GAP	Greenland Analogue Project
GCM	Global Circulation Models
GIS	Greenland Ice Sheet
GPR	Ground-Penetrating Radar
GPS	Global Positioning System
GSM	Glacial Systems Model
IBCAO	International bathymetric Chart of the Arctic Ocean
IPCC	Intergovernmental Panel on Climate Change
LGM	Last Glacial Maximum
LIA	Little Ice Age
L&ILW	Low and Intermediate Level Wastes
LIS	Laurentide Ice Sheet
MFR	Moderately Fractured Rock
MLE	Mean Life Expectancy
NEST	Northern Ecosystem Soil Temperature model
NFWA	Nuclear Fuel Waste Ace
NMR	Nuclear Magnetic Resonance
NWMO	Nuclear Waste Management Organization
OPG	Ontario Power Generation
SFR	Sparsely Fractured Rock
SKB	Swedish Nuclear Fuel and Waste Management Company
TC	Test Cases
TDS	Total Dissolved Solids
THMC	Thermal, Hydrological, Mechanical, and Chemical processes

1.0 Introduction

In Canada in 2009, nuclear energy accounted for nearly 15% of electricity generation; in Ontario, it accounted for approximately 53% [CNA, 2010]. It is valued as a clean energy source because it releases virtually no emissions deemed to cause climate change or acid rain. Still, nuclear energy produces wastes, which are first stored in water-filled bays at nuclear power reactor sites for five to ten years before being safely stored in concrete canisters [CNA, 2009].

Used nuclear fuel contains radioactive nuclides that emit radiation that can damage living tissue at the molecular level, making it harmful to the health of humans and other organisms. Bundles of used fuel do not return to the natural uranium ore radioactivity level for more than one million years after they are discharged from the nuclear reactor [NWMO, 2008].

The Nuclear Waste Management Organization (NWMO) was formed in 2002 under the Nuclear Fuel Waste Act (NFWA) to investigate approaches for managing Canada's used nuclear fuel. In 2007, the NWMO proposed that a deep geologic repository (DGR) be used to safely contain and isolate low and intermediate level wastes (L&ILW) and used fuel over the long term (i.e. one million years or more) [CNA, 2010; NWMO, 2010b]. Appropriate sites for a high level used fuel DGR need to be geologically stable with predictable flow paths and physical and chemical dispersion properties [Savage, 1995]. In Canada, low permeability crystalline rock (e.g., Canadian Shield) and sedimentary rock (e.g., intracratonic basins) are being investigated as possible DGR sites.

While current geologic and climatic conditions need to be considered when choosing an appropriate site for a DGR, investigation of the long-term evolution of these environmental conditions is also essential due to the million-year timeframe for radioactivity of the used fuel to reduce to that of its natural uranium content. In the past million years, repeated glacial cycles have occurred with the last one in the Northern hemisphere ending approximately 11,000 years ago [Marshak, 2001]. Therefore, it is likely that there will be continued glacial advances and retreats over Canada in the next million years, and the impact of glaciation on a DGR will need to be considered.

Throughout a typical 120,000 year glacial cycle, an ice sheet will advance and retreat several times, transporting sediments and rock debris. As an ice sheet advances, it depresses the Earth's surface, which can alter the groundwater flow beneath it, potentially pushing fresh oxygenated water deeper into the rock. As an ice sheet retreats, the Earth's crust will rebound and may lead to increased seismic activity [Marshak, 2001; NWMO, 2010a]. In addition to the ice sheet itself, lower surface temperatures have an impact on the subsurface, which can lead to

the formation of permafrost (frozen ground that has persisted for at least two consecutive years) in advance of the ice sheet [Harris & Murton, 2005; Hughes, 1998; Ritter et al., 2002]. Within the permafrost, there may be zones of unfrozen ground known as taliks [Ritter et al., 2002]. Permafrost has lower hydraulic conductivity than the surrounding or interrupting unfrozen ground, thus creating a flow system in which the taliks can act as hydraulic "windows" or pathways between the deep groundwater system and the surface [Walsh & Avis, 2010].

1.1 Greenland Analogue Project

A DGR, at an approximate depth of 500 m, would potentially be affected by increased stress on the repository due to the weight of an ice sheet, increased frequency of earthquakes during glaciation, and changes to the groundwater flow and chemistry [NWMO, 2010a]. In 2009, the NWMO began collaboration with the Swedish Nuclear Fuel and Waste Management Company (SKB) and Posiva (Finland) for the Greenland Analogue Project (GAP) to improve understanding of the potential impact of cooling and glaciation on the long-term safety of a DGR. Because Greenland is currently glaciated and the continent has similar geological characteristics as the Canadian Shield and the Fennoscandian Shield, a research site was chosen at the Russell Glacier, east of Kangerlussuaq (Figure 1.1). In addition to field investigations at that site, modelling activities were designed to examine the geosphere flow system and the ice sheet as well as an integrated study of ice sheet dynamics and groundwater flow. The primary objective of the modelling component of GAP is to "demonstrate if, and under what conditions, dilute and oxygenated glacial meltwater can recharge to repository depth in fractured crystalline rock over safety assessment time scales" [Vorauer, 2010].

As collaborators for the GAP, Yin et al. [2013] developed a groundwater model for the region in southwest Greenland near Kangerlussuaq where the field research is currently being conducted. Other contributors to the GAP chose a domain beginning 50 km downstream of the ice margin and extending 200 km onto the ice sheet with a width of 60 km and a depth of 5 km [e.g., Jaquet & Namar, 2010]. Yin, et al. [2013] doubled the length of that domain extending it out into Davis Strait to allow for additional future transient simulations and to ensure a more representative boundary condition. Both of the domains and the ice thickness of the Greenland Ice Sheet (GIS) are illustrated in Figure 1.1.

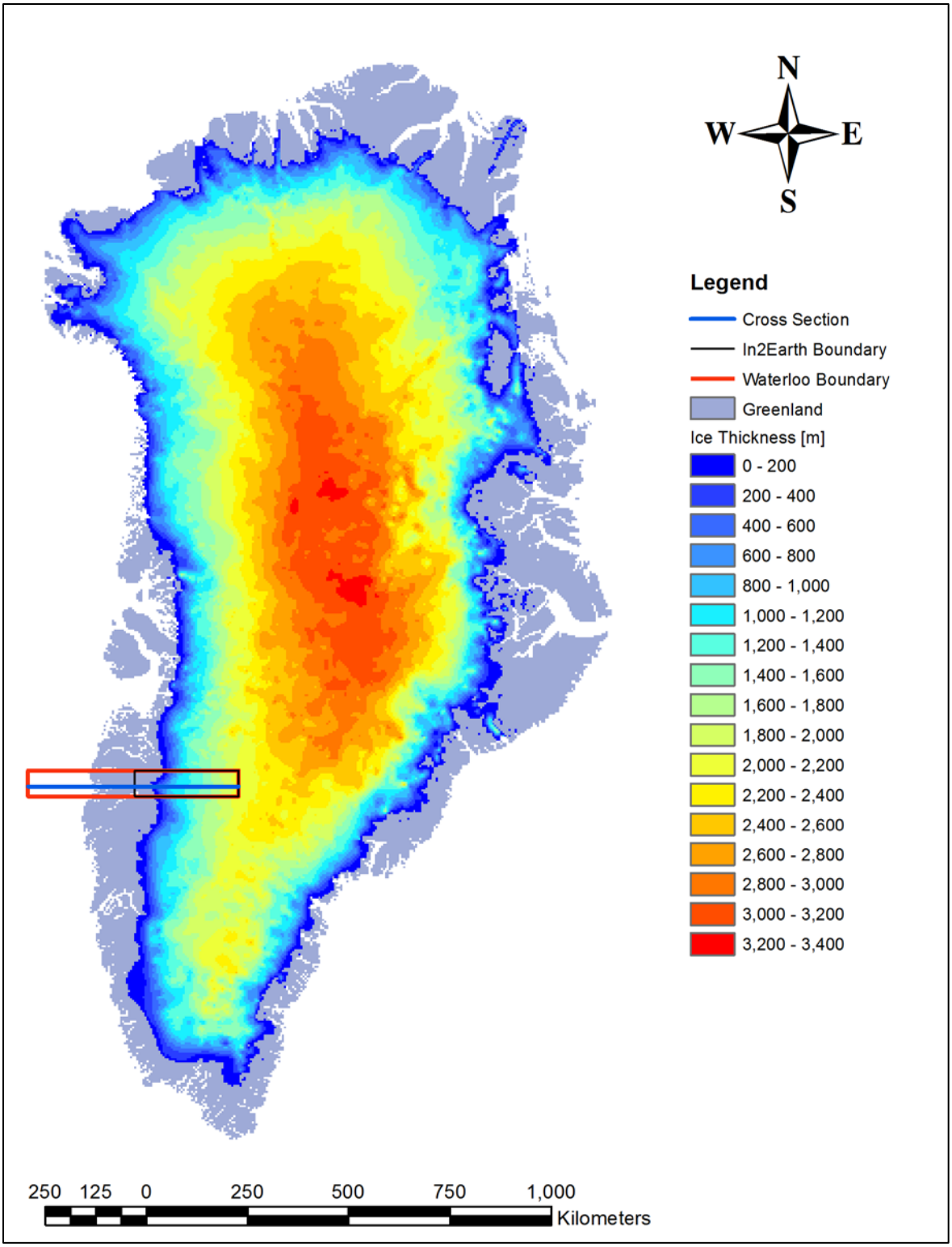

Figure 1.1 Ice sheet thickness in Greenland

Ice sheet thickness in Greenland [Bamber et al., 2001] and model domains for this doctoral research (Cross Section), the In2Earth [Jaquet & Namar, 2010], and the Waterloo [Yin et al., 2013] studies [from Yin et al., 2013]

Using the larger model domain, Yin et al. [2013] investigated the impact of variations in salinity or fluid density profiles and the role of permafrost and talik characterization on the groundwater flow system for glaciation and deglaciation events. It was found that changing the relationships between total dissolved solids (TDS) and density and between TDS and depth had a significant impact on freshwater head distributions beneath the permafrost, but not environmental heads. Additionally, the groundwater flow field and mean life expectancy (MLE) values were not sensitive to changes in those TDS relationships except for near the surface. The horizontally homogeneous and continuous nature of the crystalline rock was the primary reason for this insensitivity.

For the investigations presented in Yin et al. [2013], permafrost was characterized by a reduced hydraulic conductivity (5.0×10^{-11} m/s) compared to that of the unfrozen crystalline rock. It was assumed that the permafrost was located in the entire region between Davis Strait and the ice sheet margin and extended to 10 km beneath the ice sheet except for at discharge zones (e.g., lakes, rivers), which were permafrost-free. Based on observations of the permafrost in the regions surrounding the GIS [Jaquet & Namar, 2010], the permafrost extended to 300 m below the surface [Yin et al., 2013]. Other than an increase in linear velocity magnitudes in regions beneath the ice sheet where permafrost recently degraded, there were no differences observed between the results of scenarios tested with permafrost persisting 10 km and 1 km beneath the edge of the ice margin [Yin et al., 2013]. Open taliks at discharge zones within the permafrost led to an increase in local pore-water velocities, but did not appear to impact flow in the deep groundwater zone beneath a depth of 500 m.

In examining the effects of deglaciation and rates of deglaciation on the groundwater flow system, Yin et al. [2013] found that vertically upward groundwater flow will occur beneath the ice sheet when it melts. That change to the groundwater flow is initially observed near surface, but then propagates deeper into the lower groundwater zone. This same trend was observed for all rates of deglaciation tested (0.5 m/a, 1.0 m/a, 2.0 m/a) with larger deglaciation rates inducing larger gradients and higher vertical pore fluid velocities [Yin et al. 2013].

1.2 Geosynthesis Deep Geologic Repository Program

The NWMO has been involved in carrying out numerous studies with roughly thirty contractors from universities, specialized laboratories, and consulting groups as part of its Geosynthesis DGR program [NWMO, 2011]. This program has investigated a prospective DGR for L&ILW proposed by OPG for the Bruce Nuclear site in the Municipality of Kincardine, Ontario, Canada. There are seven key hypotheses upon which these investigations are built in order to develop a safety case for the proposed DGR site:

1. **Site predictability:** Near horizontally-layered, undeformed sedimentary shale and limestone formations of large lateral extent
2. **Multiple natural barriers:** Multiple low permeability bedrock formations enclose and overlie the DGR
3. **Contaminant transport is diffusion dominated:** Deep groundwater regime is ancient showing no evidence of glacial perturbation or cross-formational flow
4. **Seismically quiet:** Comparable to the stable Canadian Shield setting
5. **Geomechanically stable:** Selected DGR limestone formation will provide stable, virtually dry openings
6. **Natural resource potential is low:** Commercially viable oil and gas reserves are not present
7. **Shallow groundwater resources are isolated:** Near-surface groundwater aquifers are isolated from the deep saline groundwater system [NWMO, 2011].

As contributors to the Geosynthesis program, Sykes et al. [2011] addressed and supported four of those seven hypotheses (1, 2, 3, and 7) with their hydrogeologic modelling and analysis of the proposed DGR site. They developed regional-scale and site-scale conceptual models to examine the characteristics of the flow and transport systems and their sensitivity to paleoclimate perturbations. The model domain for their nearly 18,000 km^2 (2 km deep) regional-scale model of the Michigan Basin, a deep, nearly circular intracratonic basin, is illustrated in Figure 1.2. They also developed a 400 km^2 (2 km deep) site-scale domain to more accurately represent local-scale properties and features; a 677 km (5 km deep) two-dimensional cross-section of the Michigan Basin to explore the hypothesis that at a point in all units/formations a groundwater divide occurs or density-dependent horizontal flow is negligible; and a one-dimensional model to analyze two-phase gas and water flow within the stratigraphic column [Sykes et al., 2011].

Sykes et al. [2011] examined the impact of glaciation on groundwater flow and solute transport to gain an increased understanding of the characteristics of the proposed site and to attempt to find an explanation for abnormal pressures observed in the DGR boreholes. The DGR borehole analyses indicated that the Cambrian is over-pressured relative to the elevation of the surface and the Ordovician shale and limestone units are significantly under-pressured [Sykes et al., 2011]. Their 120,000 year paleohydrogeologic simulations were based on output parameters from models developed by Peltier [2011], another contributor to the Geosynthesis program. Peltier [2011] employed the University of Toronto Glacial Systems Model (GSM), which is described in Section 2.3.1, to develop a description of re-glaciation over North America and examine the impact of that glaciation on DGR performance. Given that the DGR site in Southern Ontario is located near the southern margin of the glacial extent of the last glaciation and a typical glacial cycle involves a series of glacial advances and retreats, Peltier [2011] produced an ensemble of eight models, which cover a range of evolutionary histories for glaciation that are

compatible with available constraints (e.g., relative sea level, precipitation, crustal uplift observations and data).

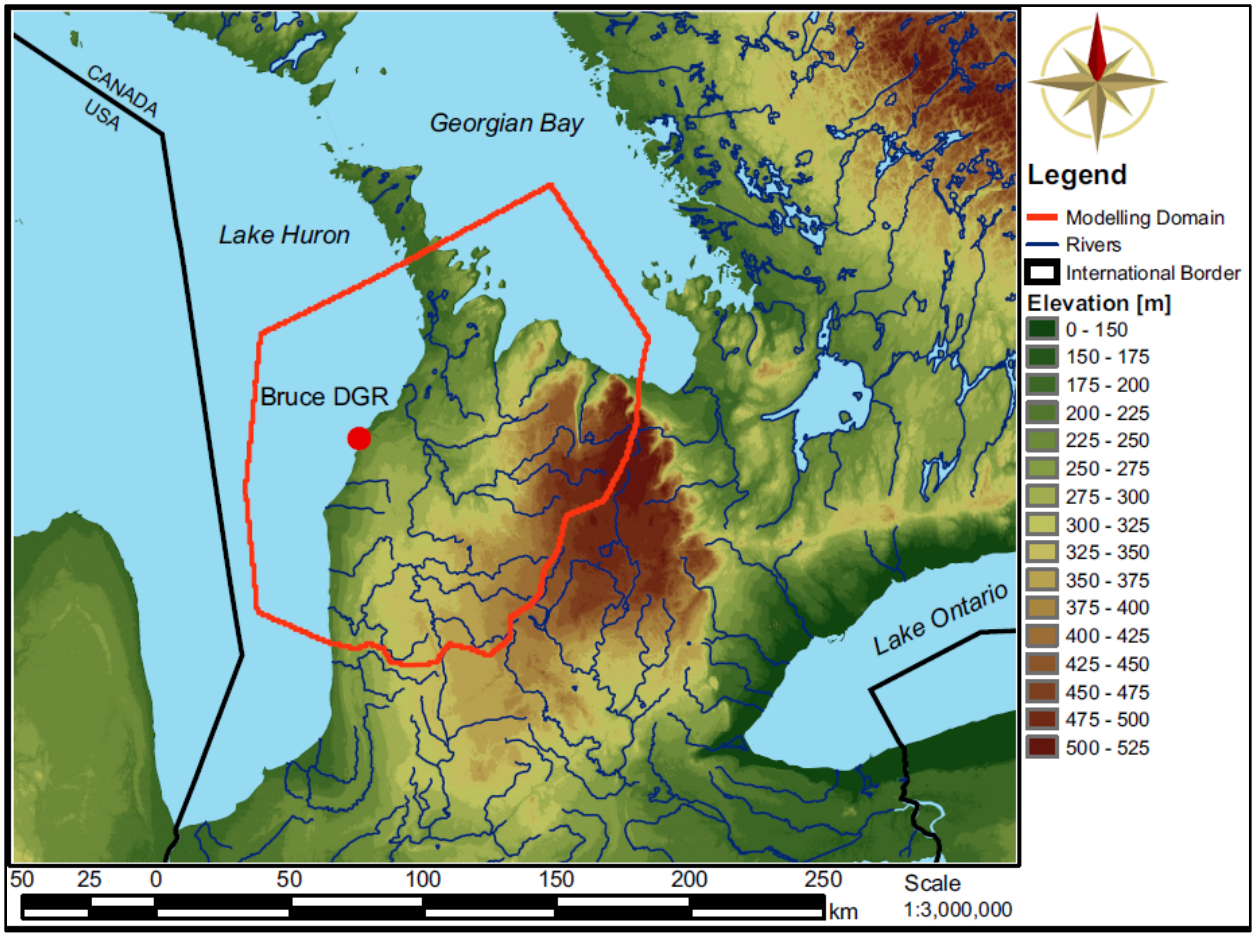

Figure 1.2 Elevation and River Courses, Southern Ontario

Elevation in Southern Ontario and regional-scale modelling domain for OPG's proposed DGR at the Bruce nuclear site in the Municipality of Kincardine, Ontario, Canada [Sykes et al., 2011]

Of Peltier's eight models, Sykes et al. [2011] chose two (nn9921 and nn9930) for their paleohydrogeologic analyses, applying ice thickness, lake depth, and permafrost output from each of those models to the paleohydrogeologic groundwater flow simulations. The two selected models are the best models based on aggregate misfit, and they both include high resolution permafrost development [Sykes et al., 2011].

Sykes et al [2011] determined that glacial loading leads to higher pressures throughout the rock column based on the one-dimensional loading efficiency of the rock mass. The different scenarios examined included different distributions of permafrost and demonstrated that recharge melt water penetrated deeper into the subsurface when less permafrost was present [Sykes et al., 2011]. Permafrost was represented by a reduction in the hydraulic conductivity in the frozen

regions. At each time step, if the extent of permafrost (not expected to be greater than 60 m at this site [Sykes et al., 2011]) extends below the top of a model grid element, that element was assigned the lower hydraulic conductivity (5 x 10-11 m/s). Hydraulic conductivity values were linearly interpolated between time steps to reduce numerical instabilities [Sykes et al., 2011].

Sykes et al. [2011] concluded that the deep groundwater system at the proposed Bruce DGR site is isolated and resilient to surface perturbations due to the multiple barriers provided by the sedimentary sequence, which includes the extremely low permeability Ordovician sediments. Solute transport within the Ordovician layers is diffusion-dominant and the calculated density-dependent fluid velocities are extremely low and vertical. The paleohydrogeologic analyses including several glaciation-deglaciation scenarios could not explain the abnormal pressures that were observed in the DGR boreholes at the site. However, the saturated flow analyses of the Michigan Basin cross-section explained the observed presence of over-pressures in the Cambrian, and the two-phase air-water analyses showed that the presence of a gas phase in the rock could explain the under-pressures observed in the Ordovician limestone and shale [Sykes et al. 2011].

Through their numerous analyses using four different numerical models and borehole data from the Bruce Nuclear site [INTERA, 2011], Sykes et al. [2011] were able to support the hypotheses that the proposed DGR site at the Bruce Nuclear site is predictable with diffusion-dominant contaminant transport. There are multiple natural barriers that isolate the shallow groundwater resources and enclose the DGR.

Further details about the domain, properties, and boundary conditions for the models presented in Yin et al. [2013] and Sykes et al. [2011] are provided in Section 5.0 and Section 6.0 of this thesis respectively.

1.3 Research Objectives

The investigations presented in Yin et al. [2013] and Sykes et al. [2011] and described in the previous sections (Sections 1.1 and 1.2) made the assumptions that fluid flow is fully saturated and isothermal and that the phreatic surface in the permafrost is within metres of the topographic surface. Thus, the main objective of this doctoral research was to examine those assumptions and extend the GAP and Geosynthesis investigations to include thermal transport and flow conditions with an alternate conceptualization of the water table boundary condition. The purpose of this work was to develop a deeper understanding and a more detailed representation of the impact that glacial and periglacial conditions have on groundwater flow. The specific objectives of the doctoral research are to

1. Develop a numerical model representing a two-dimensional cross-section of a generic crystalline rock setting, which will be used to
    a. Examine how permafrost depth and talik size and distribution influence the groundwater flow system during ice sheet advance;
    b. Investigate the distance to and length of time for which permafrost persists beneath the edge of an ice sheet as it advances as a function of the initial depth of the permafrost and the rate at which the ice sheet advances;

2. Extend the numerical model of the study site for the Greenland Analogue Project as presented in Yin et al. [2011] to include the physics for thermal transport including latent heat and to
    a. Investigate the distribution of permafrost between the Greenland Ice Sheet and Davis Strait during the last glacial cycle;
    b. Examine the impact of latent heat transfer on the distribution of permafrost;
    c. Compare the groundwater flow system dynamics of the numerical model without explicit simulation of temperature, the model with temperature but no latent heat transfer, and the model with temperature and latent heat;
    d. Investigate drainage beneath permafrost under fully-saturated and variably-saturated flow conditions.

3. Extend the numerical model of the proposed DGR site presented in Sykes et al. [2011] to include variably-saturated flow conditions and to
    a. Investigate drainage beneath permafrost under fully-saturated and variably-saturated flow conditions.

Two computational models, FRAC3DVS-OPG [Therrien et al., 2007] and COMSOL Multiphysics [COMSOL, 2011], were used to carry out the investigations outlined above. The governing equations and physics represented in each of those models are described in Section 3.0.

1.4 Overview of Thesis Structure

Background information relating to climate change, glaciation, and periglacial conditions including permafrost and taliks is presented in Section 2.0. That section also includes a summary of the approaches and findings of several modelling studies that investigated the key features and processes of past and present glaciations, permafrost development and degradation, and talik formation and closure. Section 3.0 provides an overview of the two numerical models used in this doctoral research, FRAC3DVS-OPG and COMSOL Multiphysics, including the governing equations that represent the physics of fluid flow, solute transport, heat transfer, and one-dimensional mechanical loading.

Sections 4.0 to 6.0 describe the three different conceptual models developed for and used in this thesis, presented in order of increasing complexity. The first, detailed in Section 4.0 is a two-dimensional cross-section of a generic crystalline rock setting with permafrost and taliks. This conceptual model was used to investigate the characteristics and rate of permafrost degradation as a glacier advances over the landscape as well as the impact of glacier advance on groundwater flow and discharge at taliks for a series of scenarios differing in the size, number, and distribution of taliks simulated.

Section 5.0 analyses a two-dimensional west to east cross-section of the three-dimensional model presented in Yin et al. [2013]. This conceptual model was used to investigate the impacts of temperature on permafrost development and degradation at the GAP study site in Greenland. The conceptual model presented in Section 6.0 represents a three-dimensional regional-scale model of the proposed DGR site at the Bruce nuclear site in Southern Ontario. It was used to examine variably-saturated flow and the impact of extensive and persistent permafrost on the water table.

Section 7.0 presents a summary of the key findings from each of the three modelling studies carried out for this doctoral research. It concludes with a discussion of the implications of those findings for future research.

Appendix A summarizes the properties of water as defined in COMSOL's built-in material library. For purposes of this doctoral research, the functions representing those properties were replaced or altered to improve the representation of the properties of water and ice (i.e. liquid and sold properties). See Section 3.2.5 for details about those changes.

The remaining appendices, Appendix B and Appendix C, contain additional figures with results for the GAP analysis of density-dependent flow with heat transport and the GAP analysis of variably-saturated flow and permafrost.

2.0 Background

The following sections present the relevant background information about climate change, glaciation, and periglacial conditions. The focus in each section is on the hydrogeology and, in particular, the impact of glacial and periglacial conditions on the subsurface and the groundwater flow system.

2.1 Climate Change and Glaciation

Climate change, including glacial cycling, is driven by changes in incoming solar radiation, the earth's surface, and atmospheric composition. Changes in the earth's orbital geometry impact the amount, distribution, and timing of incoming solar radiation. Changes in the reflectivity of the ground due to ice and snow cover can enhance those effects. Levels of greenhouse gases, such as carbon dioxide (CO_2), are also influential [Aherns, 2007; Allison, et al., 2009] as those trap heat radiated back by the earth's surface in the atmosphere. Surface air temperature is driven by the combined influences of each of these factors and components.

Compared to present day temperatures, the earth has typically been 8 ^{o}C to 15 ^{o}C warmer with ice-free polar-regions [Ahrens, 2007]. Such conditions have been interrupted by periods of glaciation 700 million years ago, 300 million years ago, and most recently with an "ice age" beginning two million years ago and characterized by repeated ice sheet advance and retreat over the North American landscape. The interglacial period or the time between advances typically lasted around 10,000 years [Ahrens, 2007]. During the last interglacial period, around 120,000 to 125,000 years ago, the summer Arctic temperatures were likely between 2 ^{o}C and 5 ^{o}C warmer than today. Sea levels were between 4 m and 6 m higher than present-day sea levels [Allison et al., 2009; IPCC, 2007].

Following the last glacial maximum between 18,000 and 22,000 years ago [Aherns, 2007; Allison et al., 2009; IPCC, 2007] as ice sheets retreated again, global sea level rose approximately 120 m [IPCC, 2007; Peltier, 1999]. Sea levels stabilized around 2,000 to 3,000 years ago with minimal sea level variation until the late 19th century. Corresponding to a global temperature increase of approximately 0.74 or 0.76 ^{o}C, average sea levels increased 0.17 m during the 20th century [Allison et al., 2009; IPCC, 2007]. Rates of warming have continued to increase over the last 25 years to 0.27 ^{o}C per decade on average for the globe with average rates of warming of 0.33 ^{o}C in the northern hemisphere and 0.13 ^{o}C in the southern hemisphere [IPCC, 2007].

Ice sheets shrink and grow partly in response to surrounding temperatures. As temperatures warm, ice sheets melt and shrink. As temperatures cool, ice sheets can grow.

Typically, ice sheets shrink or retreat at faster rates than those at which they grow because ice sheet retreat is primarily driven by the rising temperatures, while ice sheet growth also depends upon precipitation or snowfall rates [Allison et al., 2009; Bense & Person, 2008].

Snowfall rates are greatly influenced by temperature. Snowfall increases with the water vapour content of the atmosphere, which generally increases with air temperature [Cuffey & Paterson, 2010]. Because the atmosphere above an ice sheet is so cold, the air can only hold a small amount of moisture, making snowfall rates slow [Allison et al., 2009]. Also, air temperatures in the lower atmosphere must be below freezing for precipitation to reach the ground as snow, and where warm air masses cool rapidly, high snowfall rates can occur [Cuffey & Paterson, 2010].

Glacial advance and retreat are determined by the rates of accumulation and ablation. Glaciers, led by the terminus or toe, advance when accumulation rates are greater than ablation rates. Accumulation is primarily from snowfall, although rain and other water freezing on the surface, redistribution by wind, and "freeze on" of meltwater at the glacier base may also contribute to glacier growth and advance. On the other hand, when ablation processes dominate, glacial retreat occurs. Ablation occurs primarily by surface melting, evaporation, or sublimation, but also by basal melting, wind erosion, or calving (breaking off of large ice blocks at the edge of the glacier) [Cuffey & Paterson, 2010; Marshak, 2001; Ritter et al., 2002]. As a glacier rapidly retreats, exposed subglacial basins formed by erosion and isostatic depression can fill with meltwater, forming proglacial lakes [Cuffey & Paterson, 2010; Hughes, 1998].

Currently the East and West Antarctic Ice Sheets are relatively stable due to extremely cold surface temperatures [Parziek & Alley, 2004]. With the warming climate, the Greenland Ice Sheet, on the other hand, is experiencing an increasingly negative mass balance. That is, the ice sheet is thinning with accelerating ice flow along its margins [Chu et al., 2009]. Inland, the glacier moves at a few metres per year due to internal deformation while nearer the coast it moves hundreds to thousands of metres per year due to fast moving streams or outlet glaciers and basal sliding [Allison et al., 2009]. Although poorly understood, a link has been observed between surface warming and meltwater associated with basal sliding [Chu et al., 2009; Parziek & Alley, 2004].

2.1.1 Glaciers

Glaciers are bodies of moving ice formed on land by compaction and recrystallization of snow [Ritter et al., 2002]. Certain conditions must be met in order for a glacier to form. Temperatures must remain cold enough that the winter snow does not entirely melt away in the summers, and there must be a sufficient amount of snowfall for accumulation. The slope of the

surface must be such that accumulated snow and ice will not slide or blow away [Marshak, 2001].

Freshly fallen snowflakes are hexagonal crystals that do not fit together tightly. Over time with melting or sublimation, the tips of the flakes will become blunter. Combined with increased pressure due to the weight of overlying snow as snowfall continues, this process eventually turns the snow into a packed granular material known as firn. Additional weight and pressure transforms the firn into a solid mass of interlocking ice crystals. This whole process can take tens of years to thousands of years depending on the amount of snowfall [Cuffey & Paterson, 2010; Marshak, 2001].

Classification of glaciers can be based on morphology, movement, and temperature. Glaciers can also be classified according to temperature as cold/dry-based or warm/wet-based. Those with a temperature at or greater than the pressure melting point at the bed or base of the glacier are termed warm-based glaciers. Ice is melted at the ice-bed interface due to heat from the earth and basal friction. This allows for basal slip and erosion beneath warm-based glaciers. Cold-based glaciers are those where the temperature is below the pressure melting point at their bases. Essentially frozen to their beds, these glaciers move entirely by internal deformation above the bed with minimal erosion [Locke, 1999; Marshak, 2001].

Glaciers flow due to the effects of gravity such that valley glaciers are pulled downhill, and ice sheets spread out laterally across the landscape. Ice sheets spread laterally as gravity causes the top of the ice sheet to push down on its base until the basal ice is unable to support the weight. At that point the ice sheet begins to deform plastically, “squeezing” the basal ice out the side, carrying the overlying ice with it [Allison, et al., 2009; Cuffey & Paterson, 2010; Hughes, 1998; Marshak, 2001]. This internal deformation of ice is also referred to as glacial creep. The ice may also move by sliding along the base when meltwater accumulates at its base and allows the ice to slide on the layer of water or slurry of water and sediment [Marshak, 2001; Ritter et al., 2002].

An important process enabling sliding of the ice sheet along the irregular ground surface is regelation. In this process, the basal ice melts and refreezes due to the fluctuating pressure conditions caused by the relatively small ground surface irregularities. At the upstream edge of the irregularity the pressure is higher allowing the ice to melt. That meltwater then flows around the irregularity as a thin film before refreezing where pressure is lower on the downstream edge [Ritter et al., 2002].

Glacier velocities are highly variable between different glaciers and between different locations on the same glacier. Glacier velocities vary between seasons and over time. Typically, mid-summer melt velocities are highest due to higher volumes of basal meltwater that facilitate

sliding, and velocities may vary between summer and winter by 20 to 100 % [Menzies, 2002]. Weather conditions, fault slips, and sudden releases of ice that had been blocked by some obstruction can also influence velocities [Ritter et al., 2002]. There are also differences between surface velocities and basal velocities. Typically, basal velocities are around 10 to 20% of the measured surface velocity, although basal velocities are not well documented [Menzies, 2002].

In general, glacier velocities are a function of the mass balance, flow from internal deformation, basal slip or sliding, and sediment motion [Menzies, 2002]. Cold-based glaciers, which are frozen to their beds move only by internal deformation, and are, therefore, slower than warm-based glaciers with beds at the pressure melting point allowing for basal sliding or bed deformation [Benn & Evans, 2010; Menzies 2002]. For example, the cold-based Meserve Glacier in the Dry Valleys of Antarctica reaches velocities of only about 2 m/year [Benn & Evans, 2010], while the warm-based Jacobshavns Isbrae and Kangerdlugsuaq of the Greenland Ice Sheet have velocities upwards of 8 or 12 km/year measured near the calving front [Benn & Evans, 2010; Menzies 2002]. One classification [Benn & Evans, 2010] describes normal glacier velocities as being on the order of 10^1 to 10^2 m/year and fast glacier velocities as 10^2 to 10^3 m/year.

Surging glaciers are ice masses that typically have long periods of quiescent “normal” flow behaviour for years or decades or centuries interrupted by sudden and brief (a few months to a few years) large-scale ice displacements. During these surges, ice can move 10 to 1000 times faster than the normal flow rate for that ice mass [Menzies, 2002; Ritter et al., 2002].

Supraglacial lakes and streams form on the surface of the glacier and behave in similar, although less efficient ways as ordinary ground surface hydrology. Surface melting is usually one to four orders of magnitude larger than basal melting [Arnold & Sharp, 2002; Boulton et al, 1995] Some water flows off the surface of the glacier. Most of the water disappears into the glacier through various cracks and passages. Moulins are deep vertical shafts into which glacial surface streams flow. They initially form where those streams intersect with crevasses or where fractures occur beneath lakes on the ice sheet surface. The water melts the ice walls as it descends through the moulin maintaining the structure and allowing it to grow [Cuffey & Paterson, 2010].

Based on borehole observations, within the glacier there are often many water-filled pockets, fractures and channels [Cuffey & Paterson, 2010]. Crevasses are cracks that form within the upper, brittle zone of the ice sheet and range in size from small fractures to large gaps up to hundreds of metres long and tens of metres deep [Cuffey & Paterson, 2010; Marshak, 2001; Ritter et al. 2002]. Typically crevasses only penetrate up to around 30 m deep [Cuffey & Paterson, 2010], however, water-filled crevasses may penetrate the whole thickness of the ice due to water-driven fracturing. Water-filled crevasses may reach the glacier bed within hours or

days depending on the ice thickness and, most importantly, the availability of water to fill the crevasse. In general, the connection between the surface and glacier bed must be established quick enough so that the water does not refreeze at depth [van der Veen, 2007].

2.1.2 Subglacial Hydrology

Subglacial or basal meltwater is produced under warm-bottomed glaciers at rates of 1 to 100 mm/year due to friction between the ice and bed as well as due to the geothermal heat flux [Boulton et al., 1995; Lemieux et al., 2008a]. Water beneath the ice sheet can include this basal meltwater; surface water that has reached the base via fractures, fissures, crevasses, and moulins; and pore water exfiltrated due to mechanical loading [Clarke, 2005; Zwally et al., 2002]. This water contributes to increased water pressures at the boundary with a corresponding reduction in effective pressure [Clarke, 2005]. Effective pressure is given as $P_e = P_i - P_w$ where P_w is the pressure of the subglacial water and $P_i = \rho_i g H_i$ is the ice overburden pressure in which ρ_i is the ice density, g is the acceleration due to gravity, and H_i is the ice thickness.

Subglacial water pressure varies in time and space and is determined by a balance between the influx and outflux of water, the geometry of the subglacial system, the physical properties of the underlying sediments, the thermodynamic conditions near the ice-bed interface, and the ice overburden pressure [Clarke, 2005]. This pressure buoyantly supports the overlying glacier. This support is represented by the effective pressure and a flotation ratio, $f = P_w/P_i$ [Clarke, 2005]. Water flow is driven by gradients in fluid potential. Generally, flow of subglacial water is driven by the topography of the upper glacier surface and is only weakly influenced by bed topography [Clarke, 2005].

Water may be discharged at the base of the ice sheet via channelized systems, which are relatively efficient pathways allowing for flow through well-connected networks, or distributed systems, which are less efficient as they involve flow along more tortuous routes through or over the bed [Benn & Evans, 2010; Ritter et al., 2002]. Flow through channels, pipes, tunnels, or other conduits (Figure 2.1 3 and 4) are a means to control subglacial water pressure and friction at the ice-bed interface [Boulton et al., 1995]. Rothlisberger- or R-channels cut upwards into the ice while Nye- or N-channels cut downward into the sediment [Benn & Evans, 2010; Cuffey & Paterson, 2010]. Such channels or tunnels may allow meltwater to be discharged to the glacier margins [Boulton et al., 2009]. Within channels with fast flow, the water pressure is drawn down leading to relatively low channel pressures in comparison with the P_i [Boulton et al., 2007a]. Unless $P_w = P_i$, isolated, water-filled voids and channels in a glacier are closed inward by the ice flow. However, if the flowing water dissipates enough energy as heat, thereby melting the ice, englacial or subglacial channels may exist with $P_w < P_i$ [Fountain & Walder, 1998]. Between channels, P_w increases, approaching and sometimes exceeding P_i [Boulton et al., 2007].

Water may also flow as a thin layer or film between the ice and the rock or sediment (Figure 2.1 7), through a linked cavity network between the ice and the rock (Figure 2.1 5), or through a braided canal network between the ice and the sediment (Figure 2.1 6) [Benn & Evans, 2010; Ritter et al., 2002]. Within these distributed systems, P_w increases, approaching P_i as the water flux increases [Boulton et al., 2007].

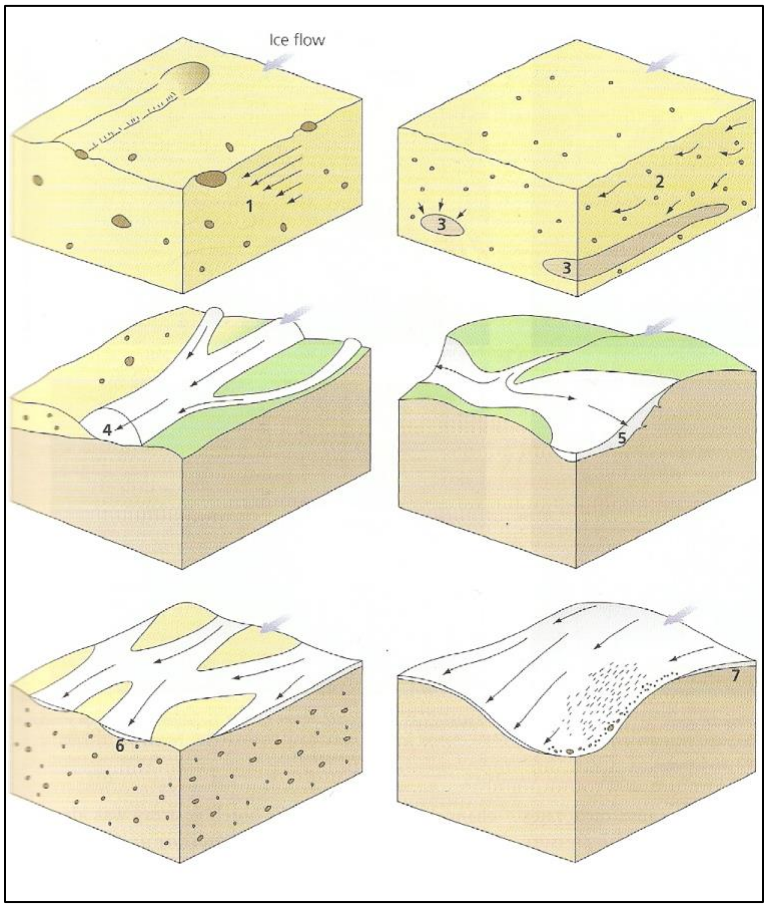

Figure 2.1 Subglacial drainage systems

1) Bulk movement of water within deforming debris 2) Darcian flow through pores in unconsolidated sediment 3) Flow through pipes 4) Flow through discrete channels 5) Flow through a linked cavity system 6) Flow through a braided canal network 7) Thin film at ice-bed interface Channelized systems: 3) and 4) Distributed systems: 1), 2), 5), 6), and 7) [from Benn & Evans, 2010; Ritter et al., 2002]

Efficient subglacial drainage systems only require small water potential gradients for discharge to occur [Boulton et al., 2009]. These systems are made up of large, low pressure channels, which typically collect drainage from smaller, high pressure systems [Benn & Evans, 2010; Fountain & Walder, 1998]. Systems with high potential gradients and water pressures are inefficient drainage systems [Boulton et al., 2009]. High subglacial water pressures can de-couple ice from the underlying geologic substrate, reducing or eliminating friction, and allow for

sliding flow along the ice-bed interface and deformation in underlying glacial sediment [Arnold & Sharp, 2002; Marshall, 2005].

Subglacial water may also be stored in the pore spaces of the sediment or rock or in large subglacial lakes [Clarke, 2005; Cuffey & Paterson, 2010]. Subglacial lakes form when large amounts of water accumulate beneath a temperate ice sheet and in regions on very low hydraulic gradients [Benn & Evans, 2010; Menzies, 2002]. In the Antarctic, Lake Vostok, the largest known subglacial lake, is over 15,000 km^2 in area with an estimated volume of 5,400 km^3 [Cuffey & Paterson, 2010]. Sudden, episodic outbursts of subglacial, supraglacial, or other glacier-dammed lakes may cause significant flooding downstream. These events are known as jokulhlaups ("glacier-leap") or glacial lake outburst floods [Benn & Evans, 2010; Cuffey & Paterson, 2010; Menzies, 2002; Ritter et al., 2002].

2.1.3 Groundwater beneath a Glacier

As an ice sheet advances and covers frozen ground, the subsurface temperature is slowly raised to the pressure melting point and the glacier acts as an insulating blanket from the cold atmospheric temperatures. Thus, permafrost or perennially frozen ground primarily forms around the outside of the ice sheet margins [Peltier, 2002], although limited amounts of permafrost may exist under cold/dry-based ice sheets or at high elevations and close to ice sheet margins [Boulton et al., 1996; Jaquet & Namar, 2010].

The groundwater flow pattern beneath the glacier mimics that of the ice sheet flow lines because it flows from high to low hydraulic head. This flow is primarily driven by two processes in the presence of an ice sheet. First, the load of the ice sheet results in the expulsion of water from sediments, leading to groundwater flow. This is a transient process as the underlying rocks will eventually consolidate to equilibrium if a steady-state ice sheet remained for long enough, and the groundwater flow would cease [Boulton et al., 1995]. The second process leading to groundwater flow is the recharge of subglacial rock by basal meltwater because that will generate a potential gradient. Groundwater flow will continue as long as recharge continues [Boulton et al., 1995]. Section 2.2 will discuss how the groundwater flow systems are further influenced by permafrost and taliks in the regions surrounding the ice sheet.

2.1.4 Geosphere

Present-day groundwater flow systems are driven, in part, by water table topographic gradients. Water density gradients can also impact flow. Precipitation is the primary source for recharge. During glacial periods, subglacial meltwater is the primary or maybe even the only source of groundwater recharge in regions covered with ice. Beneath warm/wet-based ice sheets elevated hydraulic heads influence the groundwater flow regime [Bense & Person, 2008].

Ground conditions including widespread perennially frozen ground (permafrost) with zones or gaps of unfrozen ground (taliks) may also alter the hydraulic conditions beneath the surface.

The lithosphere is elastic and "flexes" as an isostatic adjustment within the mantle in response to the growth and retreat of the ice sheet. The earth's crust deforms causing its surface elevation to be depressed beneath the glacier and raised beyond its margins [Benn & Evans, 2010; Davison et al., 1994; Walcott, 1970]. Figure 2.2 illustrates the isostatic depression beneath the glacier and the forebulge in front of the glacier. Due to the weight of the ice, the underlying bedrock is depressed by up to approximately 30% of the ice thickness [Allison et al., 2009; Bense & Person, 2008]. Complete adjustment to changes in loading may take more than 10,000 years, meaning that during a glacial-interglacial cycle, equilibrium may not be reached. Approximately three-quarters of the rebound, the response to unloading, occurs while the ice is retreating. Because this occurs beneath the thinning ice, it is termed restrained rebound. The rebound rates for the remainder of the rebound, termed post-glacial or unrestrained rebound, decrease exponentially through time [Benn & Evans, 2010; Bense & Person, 2008]. In Canada and in Northwestern Europe, regions that were previously glaciated, ongoing postglacial rebound may exceed 1 cm/year. Around Hudson Bay in Canada, the rate is near 1.1 cm/year [Peltier, 1999].

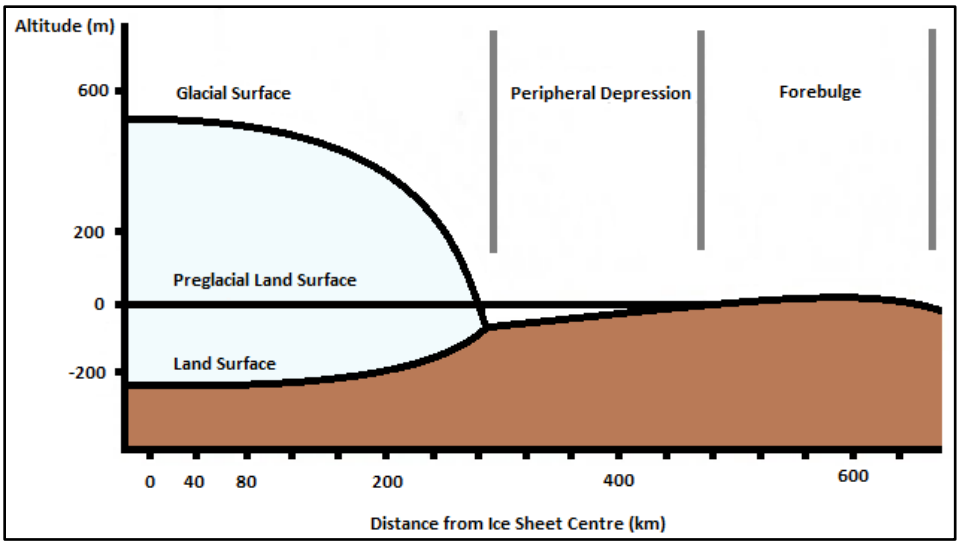

Figure 2.2 Isostatic adjustment of the earth's crust beneath an ice sheet

The earth's crust deforms causing the elevation to be depressed beneath the weight of the overlying ice sheet and raised beyond the ice sheet's margins [based on Benn & Evans, 2010].

The response of the earth's crust to glacial advance and retreat has a large-scale impact on the groundwater flow system. By mechanically loading the surface of a porous medium, the load is transferred to the porous medium and the pore fluid according to their relative compressibilities and to the porosity. Compressibility is a material property describing a change in volume or strain induced in a material under an applied stress [Freeze & Cherry, 1979].

Loading of an ice sheet or glacier mechanically compresses a porous medium because it is somewhat elastic. This causes a reduction in the porosity and hydraulic conductivity as well as an increase in pore water pressure [Bense & Person, 2008; Lemieux, et al., 2008b, 2008c]. Greater compression of the rock matrix can occur if the pore water can escape [Boulton et al., 1995; Cuffey & Paterson, 2010].

Unloading of the glacier or decreasing the stress induced by the glacier allows the compacted material to expand towards its initial state, reversing the flow direction [Bense & Person, 2008; Lemieux et al., 2008b, 2008c]. Thus, glacial advance and retreat may lead to anomalous fluid pressures. Depending on the permeability of the material, these pressure changes may dissipate quickly (high permeability materials) or gradually (low permeability shales, clays, and crystalline rock) [Bense & Person, 2008].

2.2 Periglacial Environments

Periglacial or “near glacial” regions are the extremely cold regions commonly surrounding glaciers or ice sheets, and they are characterized by accelerated freeze-thaw and frost weathering processes as well as the development of subsurface ground ice or permafrost [Ritter et al., 2002]. Permafrost forms as a result of very low (below freezing) surface or air temperatures and propagates downward through the subsurface, developing in front of an ice sheet or as glacial ice retreats. Energy exchange at the surface allows changes in air temperature to influence ground temperature. An increase in air temperature warms the ground leading to permafrost thaw, although it may take from a few years to a few millennia for the thaw to reach the base of the permafrost [Zhang et al., 2008a].

Figure 2.3 illustrates the temperature profile for a layer of permafrost. The upper surface of permafrost is the permafrost table, which tends to reflect surface topography. The lower surface of permafrost is the permafrost base. The region between these positions is perennially frozen while the active layer, a thin (15 cm to 5 m [French & Shur, 2010; Ritter et al., 2002]) layer of material above the permafrost table, thaws and freezes on a seasonal basis. The permeability of the active layer decreases as it freezes in the winter months and increases as it thaws in the summer months [Ge et al., 2011; McKenzie et al., 2007]. In the absence of taliks the water released by thawing of the active layer in the summer cannot flow deeper into the frozen subsurface enhancing the effects of frost action and mass movement [Ritter et al., 2002]. As the active layer refreezes in the winter, beginning from the surface and propagating downwards, some water may become and remain trapped between the advancing freezing front and the permafrost causing increased hydrostatic pressures to develop [Ritter et al., 2002].

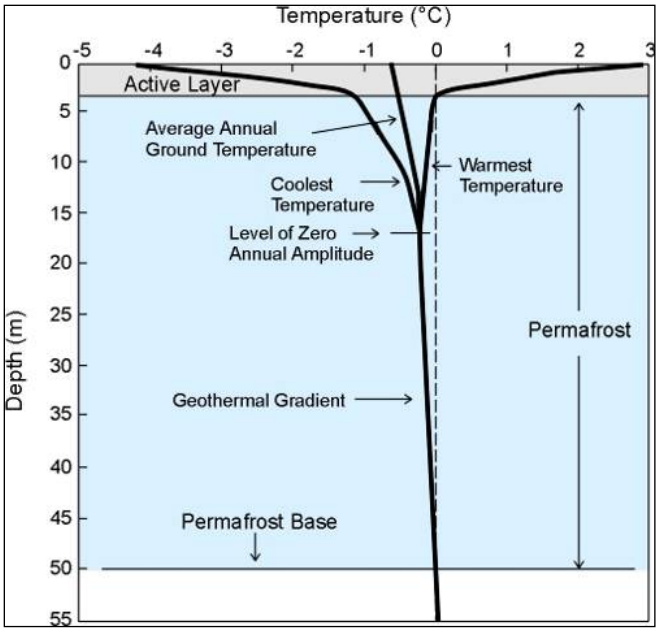

Figure 2.3 Ground temperature change with depth within a layer of permafrost

The permafrost, between the permafrost table and the permafrost base, is perennially frozen while the active layer above the permafrost thaws and freezes on a seasonal basis [GSC, 2007].

In addition to being sensitive to atmospheric conditions, permafrost is also influenced by the geothermal heat flux, which is affected by the thermal conductivity of the material. Thawing may occur downward by expansion of the active layer due to changes in air temperature and climate, laterally due to heat flow from surface and groundwater flow, internally due to groundwater intrusion, and upward due to the geothermal heat flux (Figure 2.4) [Jorgenson et al., 2010]. As the permafrost thaws, permeability increases, and the confining layer that the permafrost formed degrades. This allows for deeper flow paths to develop and causes an increase in groundwater recharge and discharge rates [Bense et al., 2009; Ge et al., 2011].

Continuous permafrost consists of thick layers of permafrost spread evenly under a wide areal surface with average thicknesses in North America ranging between 245 m and 356 m. Slightly thicker permafrost is found in Eurasia, with the thickest permafrost in Siberia [Ritter et al. 2002]. Around the Greenland Ice Sheet, permafrost is up to 300 m thick in the region in front of the ice margin [Jaquet & Namar, 2010]. Where permafrost has formed, the permeability of the soil or rock material can be significantly reduced up to eight orders of magnitude [Bense & Person, 2008] depending on the liquid water and ice content [Ge et al, 2011]. Drainage and recharge are low or impeded by this decrease in hydraulic conductivity [e.g., Bense & Person, 2008; Ge et al, 2011; Jorgenson et al., 2010; Lemieux et al., 2008a; Ritter et al., 2002].

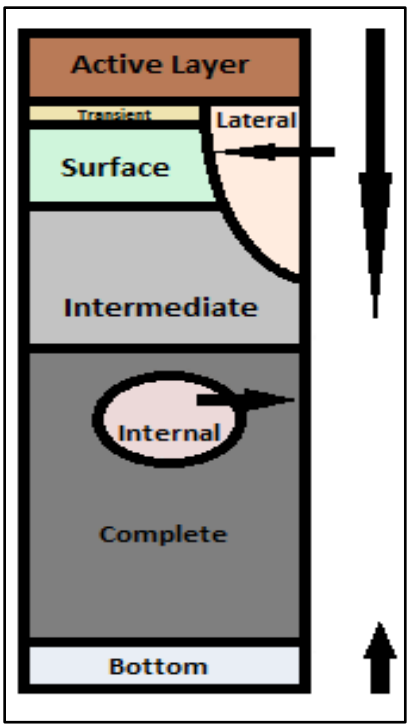

Figure 2.4 Permafrost degradation stages and processes

Permafrost degradation or thaw may occur downward by expansion of the active layer, laterally due to heat flow from surface and groundwater flow, internally due to groundwater intrusion, and upward due to the geothermal heat flux [based on Jorgenson et al., 2010].

Because the permafrost acts as a confining layer, separating shallow groundwater flow from deeper circulation, a perched water table is formed in the active layer above the permafrost table [Fetter, 2001; Scherler et al., 2010] or water may accumulate at the surface [Scherler et al., 2010]. In the presence of permafrost, soil moisture is increased and runoff is enhanced [Woo et al., 2008]. Depending on the hydraulic gradient, groundwater in the active zone can flow laterally [Scherler et al., 2010]. Surficial soils in regions underlain by permafrost typically result in muskeg and marsh vegetation of the tundra [Fetter, 2001]. The potentiometric surface for the water below the permafrost may be in the permafrost layer or above the ground surface [Fetter, 2001].

Because deep subpermafrost aquifers are difficult to access, limited data means that subpermafrost groundwater flow systems are poorly studied [van der Ploeg, et al., 2012]. However, it is known that these systems are strongly controlled by the climate because recharge and discharge can only occur through taliks due to the low hydraulic conductivity and confining nature of the permafrost layer [Booij et al., 1998; Fetter, 2001; Haldorsen et al., 2010; van der Ploeg et al., 2012]. Taliks may occur at the base of a glacier or ice sheet, which acts as an insulating blanket between the cold air temperatures and the subsurface environment, or beneath large lakes or rivers that do not freeze to depth. Artificial taliks have also been developed where

mining activities have led to warming in the subsurface and melting of the permafrost [van der Ploeg et al., 2012]. Taliks are discussed in more detail in Section 2.2.1. There is some evidence that discharge does occur from subpermafrost groundwater systems even in areas with thick, continuous permafrost. Well-defined, high-flow artesian springs and low-flow pingos provide that evidence [van der Ploeg et al., 2012]. Pingos are large, ice-cored, domelike features that form as result of artesian groundwater flow and progressive freezing [Ritter et al., 2002; van der Ploeg et al., 2012].

2.2.1 Taliks

Shallower permafrost with unfrozen zones (taliks) or wide gaps that remain unfrozen characterizes the discontinuous permafrost zone [Ritter et al., 2002]. Taliks are regions of perennially unfrozen ground found within the permafrost zone, below the active layer and above the permafrost base [Ritter et al., 2002; Yershov, 1998; Zhang et al., 2008b]. Closed taliks, or supra-permafrost taliks, are unfrozen zones that do not extend through the entire permafrost layer. Open or through taliks that penetrate the entire permafrost layer can allow surface water and groundwater to interact potentially leading to recharge or discharge of groundwater [Boulton et al., 1995; Boulton et al., 1996; Lemieux et al., 2008b; Yershov, 1998]. Surface water bodies with bottom temperatures above freezing can create discontinuities in the subsurface temperature field and maintain underground flow systems through these open taliks [Grenier et al., 2013; Ling & Zhang, 2003; McKenzie & Voss, 2013; West & Plug, 2008].

Several studies [e.g., Grenier et al., 2013; SKB, 2010; Wellman et al., 2013; West & Plug, 2008] have investigated the formation and closure of taliks beneath lakes and rivers that maintain above-freezing bottom temperatures year-round. These studies have examined the impact of water body depth and area, climate, hydraulic gradient, and latent heat on the rate and depth of talik formation or closure. In general, larger (i.e. deeper and wider) surface water bodies can maintain deeper and wider taliks for longer periods of time because larger water bodies generally have increased thermal buffering against fluctuations in air temperature [Wellman et al., 2013]. Warmer climates lead to greater overall losses of permafrost and therefore faster talik formation and expansion beneath a surface water body [Wellman et al., 2013].

Advection of heat due to the presence of a hydraulic gradient between the surface water body and the subsurface also impacts talik evolution with larger flow velocities having greater impacts [Grenier et al., 2013; McKenzie & Voss, 2013; Rowland et al., 2011; Wellman et al., 2013]. Whether advection of heat slows down or enhances talik development (or closure) depends on the direction of flow along the temperature gradient. In general, the flow of warmer water from the lake or river into the ground will help to maintain the open talik or delay the time to talik closure [Grenier et al., 2013; Wellman et al., 2013]. The absorption or release of latent

heat energy during phase change will further help to maintain the open talik or delay the closure of the system [Grenier et al., 2013].

Where open taliks or unfrozen gaps form in the permafrost surrounding a glacier or ice sheet, strong upward groundwater flow may occur [Boulton et al., 1995; Boulton et al., 1996] as groundwater flows from regions with high hydraulic head beneath the ice sheet to regions with lower hydraulic head beyond the ice and margins [Lemieux et al., 2008a; Vidstrand et al., 2013]. As the ice sheet retreats, groundwater may exfiltrate due to remnant pressure at the subsurface being higher than the basal melt water pressure [Lemieux et al., 2008a]. During deglaciation, the water table can be higher than the surface where proglacial lakes form at the ice margins in isostatic depressions caused by the weight of the overlying ice [Lemieux et al., 2008a].

2.2.2 Latent Heat

Within the frozen soils, the dominant physical processes are thawing and freezing of water, which involves the release or consumption of latent heat (energy required for a change of phase). Depending on the porosity and other properties of the soil, permafrost development and degradation can play a significant role on the subsurface thermal regime. Thus, to understand or reconstruct spatial distributions of past temperatures over a large region (e.g., since the last glaciation), the thermal effects of permafrost must be included. Latent heat effects especially need to be included when high porosities (e.g., 0.30) exist, but those effects may be small or even negligible in crystalline areas with lower porosities [Mottaghy & Rath, 2006]. Where air temperatures fluctuate around the freezing point, latent heat effects may be especially noticeable because as temperatures increase past the melting point, energy is absorbed by the melting pore ice, slowing the rate of temperature increase. As temperatures decrease below the freezing point, latent heat is released, slowing the rate of temperature decrease [e.g., Ge et al., 2011; McKenzie et al., 2007].

2.2.3 Impact of Climate Change on Permafrost

The rate at which global temperatures are warming has increased over the last twenty five years, and it is generally accepted that temperatures will continue to increase over the twenty-first century, although there is not yet certainty about the magnitude of that warming [IPCC, 2007]. If air or surface temperatures increase, thawing of the permafrost may occur due to energy exchanges at the surface. It is important to understand how that thawing occurs and how it impacts groundwater and surface water interactions.

With prolonged atmospheric warming, the active layer may begin to expand, and the permafrost table may be lowered, leading to an increased exchange of groundwater and surface water [Ge et al., 2011]. Eventually, summer thaw depth increases until some of that deeper

thawed soil does not refreeze completely in the winter, forming taliks above the permafrost [Riseborough, 2007; Zhang et al., 2006, 2008a]. Thawing permafrost not only impacts groundwater flow regimes by allowing for deeper circulation, but it also impacts surface hydrology by storing water in subsiding areas and enhancing drainage of upland areas. Thermokarst landforms or depressions may also develop as a result of subsidence of thawing subsurface materials [Jorgenson et al., 2010].

It should be noted that changes in air temperatures do not produce instantaneous changes in permafrost structure. It takes prolonged warming (or cooling) over several years or more before thawing (or freezing) will occur. Riseborough [2007] examined the effects of short term (stationary, inter-annual) variations in air temperatures and snow cover. Results suggest that inter-annual variability does not cause a large change in the multi-year average temperature at the bottom of the active layer. Additionally, temperature changes at depth are smaller than near the surface, so thawing to the bottom of the permafrost may take a few years or even millennia depending on the initial permafrost thickness and aquifer ice content [Bense et al., 2009; Osterkamp & Gosink, 1991; Zhang et al., 2008a].

Permafrost is divided from the atmosphere by a thermal regime mediated by topography, surface water, groundwater, soil properties, vegetation, and snow cover [French & Shur, 2010; Jorgenson et al., 2010]. These ecological properties may also impact the rate at which permafrost responds to warming temperatures. For example, different soils and materials have different thermal conductivities, which dictate the materials ability to conduct heat, and snow cover can act as an insulating blanket, slowing the rate of cooling in the winter [Jorgenson et al., 2010]. Thus, permafrost degradation may continue beyond the twenty-first century even if air temperatures stabilize [Bense et al., 2009; Zhang et al., 2008a].

2.3 Modelling Studies

Many investigations into past and present glaciations, permafrost development and degradation, and talik formation and closure have involved the use of a modelling approach. This section summarizes those modelling approaches and highlighted some of the key results as this doctoral research builds on those methods and findings.

2.3.1 Glaciations

A large body of research has been devoted to modelling the history of glaciation over North America. Work by Lemieux et al. [2008a, b, c] focussed on coupling groundwater flow and glaciation in models to investigate the evolution of the groundwater flow systems under the LIS in Canada (Canadian Shield, sedimentary basins) during the Wisconsinan glaciation. Their three-dimensional simulations included the influence of permafrost development and thawing,

changing topography due to isostasy, sea-level change on coastal margins due to ice sheet formation and thawing, and the presence of high-salinity paleobrines at depth. Bense & Person [2008] centred their two-dimensional cross-section study on a representative sedimentary basin (Williston, Michigan, and Illinois) near the southern limit of the LIS during the last glacial maximum. They investigated the hydrodynamics of these sedimentary basins by considering ice sheet mechanical loading, lithospheric flexure, permafrost development and thawing, and density-dependent flow.

Brevik & Reid [2000] also investigated glaciation during the Wisconsinan, but focussed on estimating ice sheet thickness at the Lake Agassiz basin in North Dakota based on isostatic rebound. Groundwater flow patterns beneath ice sheets have also been investigated using data for European Ice Sheets [Boulton et al., 1995; Boulton et al., 1996; Boulton et al., 2009] and Scandinavian Ice Sheets [Arnold & Sharp, 2002].

The Memorial University of Newfoundland/University of Toronto Glacial Systems Model (GSM) has been developed into a three-dimensional model with six interacting sub-components representing thermomechanically coupled ice-sheet dynamics, basal dynamics, surface mass balance, ice calving, bedrock deflection due to changes in surface loading, and climate forcing [Tarasov & Peltier, 2004, 2005, 2006, 2007 and others]. It has been used in investigations of ice-sheet and permafrost extent and the deglacial history in North America [Tarasov & Peltier, 2004, 2007] and of ocean circulation [Peltier, 2007; Tarasov & Peltier, 2005, 2006]. Glacial reconstructions of the LIS were developed using geological and paleogeological records, the isostatic record of crustal deformation, and an understanding of the behaviour of modern day glaciers and ice sheets [Peltier, 2002].

Looking at the more recent past of present-day glaciers has also been a focus of glacier modelling research. Investigation of present-day processes has been of interest because of mounting evidence of a warming climate. Researchers are examining glacier movement and flow in relation to meltwater and seasonal fluctuations [Alley et al., 2008; Zwally et al., 2002] as well as ice sheet mass balance [Allison et al., 2009]. Analysis of fracture mechanics has aided in the investigation of bottom crevasses [van der Veen, 1998] and ice-sheet fractures as a means for meltwater transport to the base of glaciers [van der Veen, 2007].

Warming in the northern hemisphere in particular has led to a great deal of interest in the Greenland Ice Sheet. Thus, the GAP, discussed in Section 1.1, is not the only project examining the characteristics and processes of the GIS. GIS modelling studies have related to past, present, and future ice sheet processes. Using sea-level, ice core, and isotope observations and data, researchers are piecing together the history of the GIS through previous glaciations, interpreting dynamic response of the GIS to seasonal variations, and making predictions for the future the GIS in a warming world.

Several recent studies have involved characterising the history of the GIS since the Last Glacial Maximum (LGM). Fleming & Lambeck [2004] used observations of relative sea-level change and predictions from glacial-isostatic adjustment models to determine the extent of the GIS during the LGM, the timing of deglaciation, and the evolution of ice thickness. Another study [Simpson et al., 2009] using relative sea-level observations from sea-level index points in sediments preserved in isolation basins, also used past ice extent data discerned from geological and geomorphological features and radiocarbon dating. This investigation combined three methods for reconstructing the deglaciation history of the ice sheet: use of three-dimensional ice sheet models forced by prescribed climate conditions to freely simulate past ice sheet evolution; use of observations from glacial-isostatic adjustment-induced sea-level change to quantitatively infer the ice loading history; and use of field observations to constrain the lateral or height extent of past ice.

Alley et al. [2010] used paleoclimate records to characterize the history of the response of the GIS to changes in temperature. Marine indictors of ice-sheet change include stable isotopic and biotic data indicating times of ice-sheet meltwater release and geophysical data indicating sea-floor erosion or deposition. Terrestrial geomorphic features such as moraines, glacial-isostatic adjustment, and $\delta^{18}O$ from ice cores were also used. Bennike & Bjorck [2002] compiled a list of radiocarbon ages for materials at several locations on Greenland from several previous studies to investigate the extent of ice cover at the end of the last glaciation and compare the behaviour of different regions of the ice sheet.

Studies of the present-day conditions of the GIS have provided clues to how glaciers function. For example, Zwally et al. [2002] gave evidence for seasonal velocity fluctuations near the equilibrium line of the west-central GIS. Using GPS measurements made over several seasons, these researchers demonstrated dramatic speed-ups (25% higher than winter average) in the early summers (early ablation season). They suggested that the speed-ups occur due to increased basal motion in response to surface melting reaching the glacier bed.

An investigation by Parizek & Alley [2004] involved conducting simulations of surface-melt induced flow for the next millennium under various climate scenarios for different amounts of warming over Greenland. Building on the implications of the Zwally et al. [2002] study, they predict that the GIS will be smaller in the future because of a direct link between basal sliding and surface warming.

2.3.1.1 Glaciations and Nuclear Waste Management

The use of glacier models has also extended to research on nuclear waste management and the use of deep geologic repositories to store the waste. Due to the million-year timeframe

for radioactivity of the used fuel to reduce to that of its natural uranium content, it is important to consider the geologic processes that occur on that time scale. Accordingly, the DECOVALEX (**De**velopment of **Co**upled THMC Models and their **Val**idation against **Ex**periments) Project investigated the potential impacts of glaciation on deep geologic repositories for nuclear waste [Chan et al., 2005; Chan & Stanchell, 2009; Tsang, 2009; Tsang et al., 2009]. Initiated by the Swedish Nuclear Power Inspectorate in 1992, this project involved international collaboration between nuclear waste organizations to develop and apply models that simulate the coupled effects of thermal, hydrological, mechanical, and chemical (THMC) processes. Of most direct relevance to this doctoral research are the third and fourth phases of the DECOVALEX Project.

The third phase of the DECOVALEX Project included a series of benchmark tests (BMT) (computer simulations) and test cases (TC) (laboratory and field data). BMT 3 investigated the THM responses of a fractured crystalline rock mass to a glacial cycle [Chan & Stanchell, 2009; Tsang et al., 2009]. That investigation used a generic model based on data from the Whiteshell Research Area (WRA) in Manitoba and transient hydraulic and mechanical glaciated surface boundary conditions generated by the University of Edinburgh's continental scale model of the LIS [Chan & Stanchell, 2009].

In 2004, the fourth phase of the DECOVALEX Project began with a series of tasks to investigate the coupled THMC processes of importance to the design and performance of a deep geologic repository in fractured rock and buffered materials. Task E of this phase of the project addressed the processes associated with long-term climate change (e.g., permafrost, glaciation) and their impact on groundwater system dynamics [Tsang, 2009]. Chan and Stanchell [2009] used time-dependent surface thermal and normal stress boundary conditions in addition to glacial meltwater production rates derived from two of Peltier's University of Toronto GSM scenarios. The model domain and characteristics were derived from the sub-regional modelling work of Sykes et al. [2004]. Finite-element, subsurface, coupled THMC (salinity) simulations were run to address three flow system or geosphere processes: infiltration of glacial meltwater into the subsurface, anomalous hydraulic head, and evolution of states of stress [Chan & Stanchell, 2009; Tsang, 2009].

As introduced in Section 1.2, the impact of glaciation and deglaciation on the groundwater system was investigated for a DGR of L&ILW proposed by OPG for the Bruce Nuclear Power Development site in the Municipality of Kincardine, Ontario, Canada [Normani, 2009; Sykes et al., 2011]. Further information about these studies is presented in Section 6.0. This doctoral research project builds on these investigations by extending the analysis of the impact of permafrost on the flow system to include variably-saturated flow conditions.

2.3.2 Permafrost

Process-based permafrost models use the principles of heat transfer and examine interactions between topography, soil, and vegetation and the climate to determine the thermal state of the ground [Riseborough et al., 2008; Woo et al., 2008]. Simple models are based on a limited number of parameters and provide just one or two indices such as permafrost absence or presence, active layer thickness, or permafrost temperature [Riseborough, 2007]. For example, a simple model may determine that permafrost is present or absent based on the topography (e.g., north facing slope vs. south facing slope, respectively) or the active layer is shallower or deeper because surface temperatures are relatively cooler or warmer, respectively. These simple models are typically then used as input or boundary conditions for more complex spatial models [Riseborough, 2007].

Equilibrium permafrost-climate models assume a stationary temperature and snow cover climate. A stationary temperature or snow-cover climate is typically periodic (e.g., seasonal fluctuations) or quasi-steady state (i.e., minimal inter-annual fluctuations). Riseborough [2007] examined the effects that transient conditions have on an equilibrium model, TTOP, which simulates the temperature at the top of the permafrost. The TTOP model relates mean annual temperatures from the base of the active layer with surface climatology [see Riseborough, 2007; Riseborough et al., 2008; Smith & Riseborough, 2002]. Riseborough [2007] simulated and compared the effects of stationary or short term inter-annual variability and a prolonged air temperature trend. The equilibrium model was not largely affected by inter-annual variability, and it was suggested that such variability will not impact equilibrium models of the permafrost-climate relationship if long-term temperature averages are used. However, large errors were introduced when long-term warming leads to talik development and an overestimation of the rate of permafrost temperature rise, which would have a significant impact on modelling the response of permafrost to climate change [Riseborough, 2007]. Section 3.1.3 further discusses the modelling of talik development.

Alternatively, transient models are used to simulate permafrost conditions from some initial state to a modelled current or future state [Riseborough et al., 2008]. Thus, these models take into account long-term changes in topography, soil, vegetation, and climate. An important aspect of this doctoral research is an investigation of the evolution of permafrost over a glacial cycle. The following sections focus on previous modelling studies of glaciation and permafrost for different time frames: the last glaciation, the little ice age (LIA), and current and future warming conditions.

The INTERFROST Project, a benchmark exercise for addressing subsurface thermal hydrologic processes, was launched in November, 2014. The INTERFROST Project is a collaborative endeavour involving 14 laboratories across Europe and North America. The

objective of the benchmark exercise is to compare numerical codes and approaches to thermos-hydro (TH) coupled heat and water transfer in permafrost regions for evaluation or validation and to optimize those codes or develop new numerical approaches to more accurately simulate three-dimensional systems (Interfrost). Reviews of existing studies as well as preliminary benchmark exercises and results from this project have been published (e.g., Kurylyk & Watanabe, 2013; Kurylyk & MacQuarrie, 2014; Kurylyk, MacQuarrie, & McKenzie, 2014; Ruhaak et al., 2015).

2.3.2.1 The Last Glaciation

The work by Lemieux et al. [2008a, b, c], examined the evolution of groundwater flow systems beneath the LIS in Canada and included the influence of permafrost development and thaw. Permafrost evolution was explicitly was accounted for in their numerical model, HydroGeoSphere, by allowing the hydraulic conductivity of elements affected by permafrost to vary between unfrozen (the material's hydraulic conductivity) and frozen (a reduction in hydraulic conductivity by six orders of magnitude) states and by allowing permeability values to be interpolated between time steps to provide a more realistic transition between those two states.

In their modelling studies, Lemieux et al. [2008a, b, c] made the assumption that the water table elevation is equal to the topographic surface based on the idea that, because the water table is currently typically only a few meters or tens of meters deep in Canada, it would have been that way during a glaciation period as well. Therefore, their models assigned water table values equal to the surface elevation wherever the surface was not covered by glacier ice. They also accounted for the formation of proglacial lakes during deglaciation by setting subsurface pressure head values equal to the surface elevation plus the depth of the surface water body. Where and when sea level rise led to submersion of land surface, hydraulic head was equal to the sea level.

The importance or significance of permafrost in large-scale, long-term glaciation studies was examined by Lemieux et al. [2008a, c] by comparing simulations with permafrost and without permafrost. They found that the absence of permafrost did not significantly change the amount of surface-subsurface water exchange beneath the glacier, likely because subglacial permafrost exists primarily beneath cold-based areas of an ice sheet, which do not produce subglacial melt water [Lemieux et al., 2008a, c]. However, the absence of permafrost in the regions surrounding the glacier (periglacial environment), did result in an increase in surface-subsurface water exchange rates. Additionally, Lemieux et al. [2008c] found that permafrost inhibits the dissipation of hydraulic heads that build at depth due to the weight of the overlying ice and subglacial infiltration because the permafrost acts as a cap trapping the pressure zone beneath it.

Bense & Person [2008] also included permafrost in their study of a sedimentary basin and the LIS (Section 3.1.1). The flow was topographically driven. In this study, permafrost was assigned a permeability value five orders-of-magnitude lower than unfrozen soil under the premise that the permeability of completely frozen soil could be up to eight orders-of-magnitude lower than unfrozen soil, but permeable pathways are created by fracture networks. At the surface in front of the ice sheet, head boundary conditions were set to the surface elevation. This study found that where permafrost existed, the distribution of hydraulic heads and flow patterns were strongly impacted by the lower permeability. It was also noted that permafrost degrades entirely beneath the ice sheet within 1000 years.

Bauder, Mickelson, and Marshall [2005] also studied the southern margin of the LIS by using a three-dimensional thermomechanical ice sheet model and a model for the thermal regime in the upper crust to investigate the thermal evolution at the base of the ice sheet at the last glacial maximum. In relation to permafrost, their study investigated the thickness of permafrost at the ice sheet margins and the rate at which permafrost thawed beneath the ice. They found that permafrost degradation beneath the largely (60-80%) cold-based LIS during the last glacial cycle was slow even under thick ice. However, they noted that ice sheet models tend to over predict ice volumes at the LGM, and their models did not address basal flow dynamics (drainage and storage of water), which could have an impact on energy exchange.

It was concluded by Bauder et al. [2005] that the interactions between the ice sheet and permafrost impact ice dynamics and landform development. This conclusion was in agreement with the study by Winguth et al. [2004], which focussed on the development of the Green Bay Lobe of the LIS at the last glacial maximum and through deglaciation. They used a time-dependent, two-dimensional thermomechanically coupled ice flow model and found that permafrost likely impacted the formation of the ice lobe by reducing basal motion and altering subglacial hydrology.

The Memorial University of Newfoundland/University of Toronto GSM introduced in Section 2.3.1 has also been used in investigations of ice-sheet and permafrost extent and the deglacial history in North America [Tarasov & Peltier, 2007]. With the bed thermal model implicitly coupled to the ice thermodynamics computation, Tarasov & Peltier [2007] determined present-day permafrost depth by linear interpolation between grid cells to the depth of 0 ^{o}C temperature relative to pressure-melting point for ice. They found that there is significant disequilibrium in the lower permafrost boundary in the Arctic in comparison with equilibrium values for present-day climate forcing. This indicates that the system has not completely responded to the removal of the ice sheet from the last glaciation.

Groundwater flow patterns beneath ice sheets have also been investigated using data for European Ice Sheets [Boulton et al., 1995; Boulton et al., 1996; Boulton et al., 2009]. These researchers focussed on the processes related to drainage of melt water as a thin layer at the ice/bed interface; via tunnels, canals, and other conduits; or as groundwater flow beneath European Ice Sheet during the last two glacial cycles (the Saalian and the Weichselian). They used a two-dimensional ice sheet flowline model along a transect through western Sweden to the Netherlands. They also used their model for vertically-integrated flow to examine glacially-driven groundwater flow in a horizontal plane [Boulton et al., 1996]. A no-flow boundary was used in regions of permafrost in proglacial zones. Where there was no permafrost beyond the ice sheet margins or where taliks existed beneath large lakes and rivers, groundwater could discharge and groundwater heads rapidly decreased. Where permafrost was present in the proglacial region, groundwater cannot be discharged and groundwater heads exceed the overburden pressure beneath the ice sheet and up to 50 km within the ice sheet margin [Boulton, et al., 1995]. Such overpressures can lead to hydrofracturing of sediments and rocks at the ice sheet margin, leading to large potential gradients and liquefaction of sediments [Boulton et al., 1996].

Piotrowski [1997] also examined the European Ice Sheet during the last (Weichselian) glaciation, focussing on northwest Germany and using a steady-state two-dimensional model along two vertical transects parallel to the direction of ice movement from the former glacier margin. Because there was little data available for permafrost continuity and properties, Piotrowski [1997] tested the influence that permafrost at the ice sheet margins would have on the groundwater. Not only did the presence of a 50 m thick wedge of permafrost extending 6 km up ice from the margin act as a barrier to recharge from the base of the ice, it also impacted the flow system as far as 30 or 40 km up ice from the glacier terminus by causing recharge areas to be shifted further up ice. It was suggested that if the permafrost extended deeper, likely during early stages of glaciation, and cut off flow through a lower aquifer also, it could lead to hydraulic lifting of the ice sheet by undissipated pressures.

2.3.2.2 The Little Ice Age

Another period of interest for permafrost modelling is the end of the LIA in the mid-1800s. The LIA was termed such because glaciers began to advance in mountainous regions in the thirteenth century [Benn & Evans, 2010]. Because it has been shown that temperatures began to rise again in Canada after the end of the LIA [e.g., Benn & Evans, 2010; IPCC, 2007; Overpeck et al., 1997], some modellers will use this point as an initial condition for permafrost modelling. In a series of papers by Zhang et al. [2006, 2008a, b] and Chen et al. [2003], applications of the Northern Ecosystem Soil Temperature (NEST) model were presented. The evolution of the ground thermal regime was simulated since the end of the LIA to investigate the impact of warming on permafrost distribution and extent in Canada.

The NEST model explicitly considers the effects of different ground conditions (e.g., snow cover, vegetation, forest floor or moss layers, peat layers, mineral soils, bedrock) to simulate soil temperature dynamics using the one-dimensional heat conduction equation with upper surface conditions dictated by the surface energy balance and the lower boundary conditions determined by the geothermal heat flux [Zhang et al., 2003; Zhang et al., 2006, 2008a, 2008b]. Permafrost was characterized using state variables such as permafrost absence/presence, active layer thickness, depth to permafrost table and base, and permafrost thickness, determined each year to account for the annual freeze-thaw cycle. The model accounts for the formation of suprapermafrost taliks when determining active layer thickness based on the depth of winter frost. Infiltration of water into the subsurface is characterized as saturated flow from the top soil layer down, and when a soil layer is frozen, its hydraulic conductivity is set to zero [Zhang et al., 2003].

Warming since the end of the LIA has led to permafrost degradation across most of Canada with a 5.4% reduction in continuous permafrost, expansion of the active layer, and deepening of the permafrost table. Taliks developed and grew above the permafrost table as warming continued [Zhang et al., 2006]. The southern limit of permafrost in Canada was shifted northward around 200 km with a reduction in the area underlain by discontinuous permafrost [Chen et al, 2003]. In the two studies that extended simulations into the future to the year 2100 [Zhang et al., 2008a, b], it was found that ground temperatures at present are not in equilibrium with the present atmospheric conditions. Permafrost thaw from the top can respond quickly to climate warming, but permafrost may persist at depth because of the slow transfer of the surface temperature disturbance.

2.3.2.3 Present Conditions

Naturally, recent field and modelling studies for permafrost research has focused on the regions that have been or will be immediately impacted by permafrost degradation due to climate warming. Currently, 24% of the northern hemisphere is underlain by permafrost [NSIDC, 2012], which has been thawing and disappearing since warming began in the mid-1800s. Over the past 25 years, atmospheric warming in the northern hemisphere has occurred at a rate of 0.33 ^{o}C per decade, and warming is expected to continue [IPCC, 2007]. In North America, observations and analyses have been carried out for Alaska [e.g., Jorgenson et al., 2010; Osterkamp & Gosink, 1991; Williams, 1970] because more than 80% of its land surface is underlain by permafrost [NSIDC, 2012], and the Canadian Arctic [e.g., Pomeroy et al., 2007; Smith & Riseborough, 2002; Woo et al., 2000; Zhang et al., 2003] including the Mackenzie Delta [e.g., Burn & Kokelj, 2009] and the Scotty Creek Watershed [Hayashi et al., 2007].

Permafrost research is also being carried out in Europe and Svalbard relating to melt water infiltration, active layer thickness, and modelling techniques [Hjort et al., 2010; Scherler, et al., 2010; Westermann et al., 2010]. The Qinghai-Tibet plateau in China is of particular interest for its sensitivity to climate change because it has the highest and most extensive high-altitude permafrost on earth [e.g., Cheng & Wu, 2007; Ge et al., 2011]. Monitoring along the Qinghai-Tibet highway over 40 years up to the end of the 1990s, showed that the continuous permafrost zone experienced noticeable degradation with increases in mean annual ground temperatures and active layer thickness as well as talik and thermokarst formation. The ground temperature of the discontinuous permafrost in this region also increased [Cheng & Wu, 2007]. The IPCC summarizes recent data about permafrost depth and changes in permafrost temperature from the last forty years on average (some records are shorter, others longer) for the United States, Canada, Russia, Europe, and China [IPCC, 2007].

In Greenland, the study area for the GAP investigations (Section 1.1) covers a small portion of the ice sheet margin in southwestern Greenland near Kangerlussuq, and borehole investigations have shown the existence of permafrost at the ice sheet margins. Other research that has focused on permafrost in Greenland has examined the active layer thickness including a study by Jorgensen & Andreasen [2007]. They investigated permafrost depth beneath a parking lot near the Kangerlussuaq airport using ground-penetrating radar and found that reduced insulation from snow cover has led to lowering of the permafrost table depressions in the parking lot surface.

Borehole measurements are typically used in field studies for permafrost investigation, however there are increasingly advanced tools that now also being used to determine permafrost distribution and extent [Kneisel et al., 2008]. Ground-penetrating radar (GPR) impulses respond to physical changes in the ground, which allows this method to be used for mapping permafrost distribution and near-surface geological features. GPR profiles clearly show the interface between unfrozen and frozen soil where the boundary between unsaturated and saturated frozen soil is well-developed [Jorgensen & Andreasen, 2007; Westermann et al., 2010]. Nuclear magnetic resonance (NMR) measurements can be used to determine the pore size distribution of water-saturated rock, which can be used to estimate hydraulic permeability. This technology allows one to determine the unfrozen water content in boreholes in regions of permafrost [Kleinberg & Griffin, 2005].

2.3.2.4 Future Predictions

While present concerns relate to the impact of permafrost degradation on ecology, hydrology, and infrastructure, there is also great concern about how and how quickly permafrost will respond to prolonged warming. In particular, future predictions strive to understand the impact of warming on groundwater flow and discharge, permafrost distribution, and active layer

thickness. Some models of permafrost use input from global circulation models (GCMs) of climate. Additionally, of increasing concern is the release of permafrost carbon into the atmosphere, which can lead to further warming and further permafrost degradation.

To investigate the evolution of groundwater flow conditions in response to prolonged warming, Bense et al. [2009] modelled an idealized aquifer with topographically-driven flow with discharge focused at a central topographic low, like a valley. They used models in FlexPDE software to calculate transient fluid and heat flow. Three scenarios, each with different initial surface temperatures and permafrost thicknesses, were simulated. For each simulation, the average seasonal surface temperature was increased 3 ^{o}C over 100 years after which the temperature was held constant for another 1100 years. Permeability was a function of the water-saturation state such that the permeability approached zero where all of the pore fluids were frozen. This study demonstrated how warming of that magnitude will lead to permafrost reduction. As permafrost degrades from the surface downward, a shallow aquifer forms above the permafrost table. That aquifer will double in size after 300 years and lead to the development or re-enactment of regional scale flow paths after 500 years. Rates of groundwater discharge are positively correlated with initial permafrost thickness and ice content.

Ge et al. [2011] also imposed a temperature increase of 3^{o}C over 100 years in the study of seasonal and long term changes in active layer thickness. They also found that with prolonged warming, there will be an increase in groundwater flow in the active layer (i.e. above the permafrost table) and consequently increased groundwater discharge to rivers. If there is not enough water to replenish the shallow groundwater system as it discharges, there will be an overall lowering of the water table in that region. Scherler et al. [2010] examined the process of infiltration of melt water (from snow cover) into the active layer. Infiltration may occur when the surface water level reaches a critical pressure head. Scherler et al. [2010] found that infiltration into a frozen active layer depends on initial temperatures, ice content, and the availability of melt water. While infiltration is important for recharge of shallow groundwater systems that may exist, infiltration may also have a significant thermal effect on the permafrost itself, causing sudden temperature shifts towards the melting point in the shallow subsurface.

To predict the future distribution of permafrost in the Northern hemisphere, Anisimov et al. [1997] have used air temperature and precipitation data from global circulation models (GCMs) as input for their permafrost models. GCMs can provide estimates of these parameters based on atmospheric CO_2 concentrations, which provide the initial radiative forcing to the climate system [Anisimov & Nelson, 1996]. As an alternative to GCMs, paleoreconstructions of temperature and precipitation for previous warm periods (interglacials) based on paleobotanical and paleogeological data. Anisimov & Nelson [1996] used data from three GCMs and one paleoreconstruction with the frost index method to map potential zones of permafrost distribution in the northern hemisphere. The frost index is a dimensionless number based on a ratio of annual

degree day sums above and below 0 ^{o}C and can be modified to incorporate the conductive effects of snow cover and other parameters. Anisimov et al. [1997] then used a periodic function to describe the annual variations in air temperature and determine active layer thickness accounting for the effects of snow cover, vegetation, soil moisture, and soil thermal properties.

Another consequence of thawing permafrost and an increase in active layer thickness is the decomposition of previously frozen organic carbon. Estimates of the amount of carbon in permafrost are highly variable and depend on a complete understanding of permafrost extent and depth, but it is generally agreed that there may be enough carbon in the permafrost that, if released the atmosphere as CO_2, a greenhouse gas, could impact air temperatures by leading to further warming [e.g., Anisimov & Nelson, 1997; Schuur et al., 2008]. Further atmospheric warming, in turn, can lead to additional permafrost thaw, and so on.

2.3.3 Taliks

Water bodies such as lakes and rivers that are deeper than the maximum thickness of ice that forms at the surface of the water body during winter months, which is typically 2 m to 2.5 m [Yershov, 1998], will remain unfrozen year round. While the critical depth for a water body to remain unfrozen is ultimately determined by climatic characteristics such as air temperature and snow cover thickness [Yershov, 1998], the Swedish Nuclear Fuel and Waste Management Company (SKB) used a one-dimensional permafrost model to simulate permafrost development near circular lakes with constant, positive bottom temperature (0.1 ^{o}C) and a constant, negative bedrock temperature (-8 ^{o}C) to determine that an open talik, which completely penetrates the permafrost, can develop beneath a lake under either of the following conditions:

- The radius of a shallow lake (if the surface area is interpreted as a circle) exceeds the thickness of the surrounding permafrost. A shallow lake is a defined as a lake with a mean depth between 0.5 m and 4 m and a bottom temperature greater than 0 ^{o}C.
- The radius of a deep lake is greater than or equal to 0.6 times the thickness of the surrounding permafrost. A deep lake is defined as a lake with a mean depth greater than 4 m and a bottom temperature greater than 4 ^{o}C [SKB, 2006, 2010].

It was indicated that these results seem to be independent of the site simulated and can be applied to different lake bottom level subsurface temperatures [SKB, 2006].

SKB's one-dimensional permafrost model was based on present-day reference data (i.e. geologic and thermal properties of the rock) from their study sites in Forsmark and Laxemar. A series of transient simulations representing a glacial cycle of 120,000 years with constant mean annual ground surface temperatures ranging from -2 ^{o}C to -20 ^{o}C was applied to the subsurface model to investigate the impact of surface temperature on permafrost depth.

Wellman et al. [2013] examined a range of hydrologic gradients, climate scenarios, and lake depths (sizes) to determine the impact of those conditions on the development of sub-lake taliks following lake formation in watersheds in the Yukon Flats region of Alaska. They concluded that all three of those factors are equally important in controlling permafrost thaw and talik formation. They described an exponential increase in the time required for an open talik to form with decreasing lake size defined by the depth of the lake but also found that the shallower lakes (less than 3 m deep) may still form sub-lake taliks after an exceptionally long time period. Those shallower lakes would need to maintain mean lake bottom temperatures greater than 0 ^{o}C though for a talik to form [Ling & Zhang, 2003; Rowland et al., 2011; West & Plug, 2008]. Shallow lakes that do not maintain a bottom temperature above freezing may still increase the temperature of the underlying permafrost over time, depending on that lake bottom temperature [Ling & Zhang, 2003].

To investigate the impact of glaciation on groundwater flow and the development of taliks below surface water bodies, Grenier et al. [2013] simulated coupled fluid flow and thermal transport for a generic two-dimensional cross-section of a valley-plateau river system in the Paris sedimentary basin in France (porosity of 0.1). In particular, they examined the conditions and time required for river talik closure using an east-west profile of two rivers separated by a plain with initial unfrozen conditions (4 ^{o}C for the rivers and 1 ^{o}C for the plain). After imposing a negative temperature (-8 ^{o}C) on the plain at time zero, they examined the cold front as it propagated at depth with time leading to the development of permafrost beneath the plain. Grenier et al. [2013] found that for rivers with widths less than 100 m, taliks would close within decades or some centuries based solely on conduction, while rivers with widths greater than 150 m would require several thousand years for their underlying taliks to close. The depths of these rivers were not indicated in the study. Additionally, groundwater flow or advection of heat influenced closure times such that where flow was from the plain to the river, heat advection led to reduced closure times and where flow was from the (warmer) river to the plain, closure times were delayed and occurred at greater depths.

Instead of examining talik closure under imposed negative temperatures, McKenzie & Voss [2013] simulated the impacts of surface water bodies on talik formation in a two-dimensional ‘Tothian Hills’ (sinusoidal hills of uniform frequency and amplitude superimposed on a sloping surface) hydrogeologic system with a porosity of 0.1. In this system, surface water bodies with constant bottom temperatures of 2 ^{o}C are located in one or more of the valleys. Flow enters the water bodies at higher elevation and travels downhill below the permafrost, discharging to water bodies at lower elevations. Initially, a continuous layer of permafrost was applied from the ground surface to a depth of 220 m below the valleys and 300 m below the hills. McKenzie & Voss [2013] determined that the total thaw time for the system was reduced depending on the number of lakes in the system with a system containing just one lake thawing in a similar manner to a system with no lakes until another open talik forms to allow for regional

flow to occur. That is, in systems with no surface water bodies, when permafrost thaw occurs, the taliks preferentially form beneath the hilltops or recharge areas of this system.

3.0 Computational Models

To meet the objectives of this doctoral research (Section 1.3), a modelling approach was chosen, and two computational models, FRAC3DVS-OPG [Therrien et al., 2007] and COMSOL Multiphysics (COMSOL) [COMSOL, 2011] were used. The three-dimensional, control volume, finite element numerical code, FRAC3DVS-OPG, solves the variably saturated density-dependent groundwater flow and solute transport equations in non-fractured or discretely fractured media. It was adapted for use with Ontario Power Generation's (OPG) Deep Geologic Repository Technology Program (DGRTP). For the purposes of this doctoral research, the greatest limitation of FRAC3DVS-OPG is that systems are assumed to be under isothermal conditions because the physics for temperature are not included. Additional assumptions include the assumption that the fluid is incompressible, the porous medium and fractures are non-deformable, and the air phase is infinitely mobile [Therrien et al, 2007].

COMSOL is a finite-element, numerical modelling platform for simulating a wide range of physics-based problems from many disciplines. It allows for coupled or "multiphysics" phenomena to be represented using physics interfaces or equation-based modelling. COMSOL allows models to be developed in one, two, and three dimensions, although there are limitations in three dimensions for transient simulations. In particular, COMSOL does not allow for simulation of a property that varies in three dimensions as well as in time, which poses a challenge when trying to simulate glacier movement and the impacts that glacier has on properties such as head or pressure, stress or mechanical load, and temperature at the top boundary (ground surface).

Drawing on the strengths of each of these numerical models, COMSOL was selected to examine the impacts of temperature on permafrost development and degradation for two-dimensional models of the study site in Greenland and a generic periglacial/glacial system. Additionally, FRAC3DVS-OPG was used to investigate the impact of permafrost on the water table and the groundwater flow system for three-dimensional models of the study sites in Greenland and Southern Ontario.

3.1 FRAC3DVS-OPG

The following sections describe how the physical processes involved in this study are represented in FRAC3DVS-OPG: Richards' equation for fluid flow, an equation for solute transport, isothermal conditions for temperature, a one-dimensional loading efficiency term for hydromechanical coupling, and functions representing fluid properties.

3.1.1 Fluid Flow

FRAC3DVS-OPG uses a modified form of Richards' equation to describe three-dimensional transient subsurface flow in variably-saturated porous media [Therrien et al., 2007]:

$$-\boldsymbol{\nabla} \cdot (\boldsymbol{w_m q}) + \sum \boldsymbol{\Gamma_{ex}} \pm \boldsymbol{Q} = \boldsymbol{w_m} \frac{\boldsymbol{\partial}}{\boldsymbol{\partial t}} (\boldsymbol{\theta_s S_w}) \qquad \textbf{3.1}$$

where w_m represents the volumetric fraction of the total porosity occupied by the porous medium [-] and is always equal to 1.0 unless a second porous continuum is considered. The fluid flux, q [L/T], is given by

$$\boldsymbol{q} = -\boldsymbol{K} \cdot \boldsymbol{k_r} \boldsymbol{\nabla} (\boldsymbol{\psi} + \boldsymbol{z}) \qquad \textbf{3.2}$$

where $k_r = k_r(S_w)$ is the relative permeability of the medium [-] with respect to the degree of water saturation, S_w [-]; ψ is the pressure head [L]; z is the elevation head [L]; and θ_s is the saturated water content [-], which is assumed to be equal to the porosity. Q [L^3/L^3T] is the volumetric fluid flux per unit volume representing a source (positive) or sink (negative) to the porous medium system [Therrien et al., 2007]. The hydraulic conductivity tensor, K [L/T], is given by

$$\boldsymbol{K} = \frac{\boldsymbol{\rho g}}{\boldsymbol{\mu}} \boldsymbol{k} \qquad \textbf{3.3}$$

where ρ is the density of water [M/L^3], which can be a function of the concentration, C [M/L^3], of any given solute; g is the gravitational acceleration [L/T^2]; μ is the viscosity of water [M/LT]; and k is the porous media permeability tensor [L^2] [Therrien et al., 2007].

Water saturation is related to the water content, θ [-], as

$$\boldsymbol{S_w} = \frac{\boldsymbol{\theta}}{\boldsymbol{\theta_s}} \qquad \textbf{3.4}$$

In Equation 3.1, Γ_{ex} is the volumetric fluid exchange rate between the subsurface domain and all other domains [L^3/L^3T]. It is expressed per unit volume of other domain types. A positive value represents flow into the porous medium, and a negative value represents flow out of the porous medium [Therrien et al., 2007].

3.1.2 Solute Transport

The general equation representing solute transport for saturated porous media is [Bear, 1988]

$$\frac{\partial}{\partial x_i}\left(\varepsilon D_{ij}\frac{\partial C}{\partial x_j}\right) - \frac{\partial}{\partial x_i}(q_i C) \pm \Omega_C = \frac{\partial}{\partial t}(\varepsilon C) \quad i,j = 1,2,3 \qquad \textbf{3.5}$$

where C is concentration [M/L^3], Ω_C is concentration source/sink term [M/L^{3}T], ε is the porosity [-], and D_{ij} is the hydrodynamic dispersion tensor [L^2/T] defined by Burnett & Frind [1987] as

$$\varepsilon D_{11} = \alpha_L \frac{q_1^2}{|q|} + \alpha_{TH}\frac{q_2^2}{|q|} + \alpha_{TV}\frac{q_3^2}{|q|} + \varepsilon\tau D_m$$

$$\varepsilon D_{22} = \alpha_L \frac{q_1^2}{|q|} + \alpha_{TH}\frac{q_2^2}{|q|} + \alpha_{TV}\frac{q_3^2}{|q|} + \varepsilon\tau D_m$$

$$\varepsilon D_{33} = \alpha_L \frac{q_1^2}{|q|} + \alpha_{TH}\frac{q_2^2}{|q|} + \alpha_{TV}\frac{q_3^2}{|q|} + \varepsilon\tau D_m$$

$$\varepsilon D_{21} = \varepsilon D_{12} = (\alpha_L - \alpha_{TH})\frac{q_1 q_2}{|q|} \qquad \textbf{3.6 (a-f)}$$

$$\varepsilon D_{31} = \varepsilon D_{13} = (\alpha_L - \alpha_{TV})\frac{q_1 q_3}{|q|}$$

$$\varepsilon D_{32} = \varepsilon D_{23} = (\alpha_L - \alpha_{TV})\frac{q_2 q_3}{|q|}$$

where α_L is the longitudinal dispersivity [L], α_{TH} is the horizontal transverse dispersivity [L], α_{TV} is the vertical transverse dispersivity [L], $|q|$ is the magnitude of the Darcy flux [L/T], τ is the tortuosity of the porous medium [-], and D_m is the molecular diffusion coefficient [L^2/T].

The pore water diffusion coefficient is also referred to as the diffusion coefficient of the porous medium [Bear, 1988]. For variably dense fluids, fluid density depends on the pore fluid concentration:

$$\rho_r = \gamma\frac{C}{C_{max}}, \quad \gamma = \frac{\rho_{max}}{\rho} - 1 \qquad \textbf{3.7}$$

where C_{max} is the maximum concentration [M/L^3], ρ_{max} is the maximum density [M/L^3], and γ is the maximum relative density [-]. These relationships are typically used to represent heavy brines with concentrations of 300 g/L or higher.

3.1.3 Freshwater and Environmental Head

Typically, groundwater studies involve freshwater systems with a constant density for water. In making this simplification for density, gradients and flow velocities can be directly calculated by knowing the difference in "head." The piezometric head represents the free surface elevation, which can be determined in the field [Oberlander, 1989]. Variable density fluids have a non-linear pressure profile with depth because the density affects the pore water pressure. Environmental-water heads define hydraulic gradients of constant or variable density along a vertical, making them comparable along a vertical [Lusczynski, 1961].

Most groundwater flow models that can simulate variable density flow use freshwater head as a state variable for flow. Environmental head is then calculated from the freshwater head and brine concentration output from the model [Sykes et al., 2011]. Environmental head is calculated as

$$\boldsymbol{h_{Ei} = h_{Fi} - \frac{(\rho_F - \rho_A)(z_i - z_r)}{\rho_F}, \quad \rho_A = \frac{1}{z_r - z_i}\int_{z_i}^{z_r} \rho(z)\,dz} \qquad \textbf{3.8}$$

where h_{Ei} is the environmental-water head at point i [L] and h_{Fi} is the freshwater head at a point i. ρ_A, is the average density of fluid between z_i and z_r [M/L^3] where z_r is the reference elevation of freshwater above point i [L], and $\rho(z)$ is the fluid density as a function of z [M/L^3].

3.1.4 Mechanics – One-dimensional Loading Efficiency

In hydromechanical coupling, it is common to simplify the impact of the glacier as one-dimensional vertical loading and unloading [Neuzil, 2003; Jaeger et al., 2007]. The assumption of purely vertical strain is appropriate because lateral gradients in fluid pressures and pressure changes tend to be small in comparison with vertical gradients. Because ice loads can be considered aerially homogeneous and laterally extensive, the change in vertical stress is also spatially homogeneous [Neuzil, 2003]. Thus, the groundwater flow equation can be written as follows:

$$\boldsymbol{\nabla \cdot \rho \left[-\frac{k}{\mu}(\nabla p + \rho g \nabla D) \right] + Q_m = \rho S \frac{\partial p}{\partial t} - \rho_0 S \zeta \frac{\partial \sigma_{zz}}{\partial t}} \qquad \textbf{3.9}$$

where S is the storage term [LT^2/M], ζ is the one-dimensional loading efficiency [-], and σ_{zz} is the vertical stress [M/LT^3]. The loading efficiency term represents how much of the vertical loading rate is associated with a change in pore pressure with values nearer zero resulting from stiff porous media allowing little load to be transferred to the pore fluid. A loading efficiency

near one represents a situation where the porous medium is more compressible than the pore fluid, and the pore fluid supports most of the applied load.

The hydromechanical term, $\rho_0 S\zeta \frac{\partial \sigma_{zz}}{\partial t}$, from Equation 3.12 represents a fluid source or sink term to increase or decrease the fluid pore pressure. By assuming incompressible grains ($K_s = \infty$), the storage, S, and loading efficiency, ζ, become

$$\boldsymbol{S = \beta' + \varepsilon\beta_f} \quad \textbf{3.10}$$

$$\boldsymbol{\zeta = \frac{\beta'}{\beta' + \varepsilon\beta_f}} \quad \textbf{3.11}$$

where β' is the coefficient of vertical compressibility for the porous medium [LT^2/M] and β_f is the fluid compressibility [LT^2/T]. Using rock mechanics properties, β' can be calculated as follows:

$$\boldsymbol{K = \frac{E}{3(1-2v)}} \quad \textbf{3.12}$$

$$\boldsymbol{K' = K\frac{3(1-v)}{1+v}} \quad \textbf{3.13}$$

$$\boldsymbol{\beta' = \frac{1}{K'}} \quad \textbf{3.14}$$

where E is the Young's elastic modulus of the porous medium [M/LT^2], v is Poisson's ratio [-], and K' is the drained confined vertical modulus of the porous medium [M/LT^2].

3.2 COMSOL Multiphysics

The physics that were involved in this study were represented by the physics interfaces available in COMSOL: Darcy's Law for fluid flow, Species Transport in Porous Media for solute transport, and Heat Transfer in Porous Media for temperature. Additional variables, parameters, and functions were added to represent latent heat, mechanical coupling (one-dimensional loading efficiency), and the properties of water. It should be noted that some terms differ between the FRAC3DVS-OPG and COMSOL Multiphysics numerical models.

3.2.1 Fluid Flow – Darcy's Law

The Darcy's Law interface within COMSOL Multiphysics uses Darcy's law to describe flow in porous media, solving for pressure, p [M/LT^2]:

$$\boldsymbol{u = -\frac{k}{\mu}(\nabla p + \rho g \nabla D)} \qquad \textbf{3.15}$$

In this equation, u represents the Darcy velocity [L/T], k represents the permeability of the porous medium [L^2], μ represents the fluid's dynamic viscosity [M/LT], p represents the fluid's pressure [M/LT^2], ρ represents the density [M/L^3], g represents the magnitude of gravitational acceleration [L/T^2], and ∇D is a unit vector in the direction over which gravity acts [COMSOL, 2011].

In COMSOL, density-dependent flow is included by turning on the "gravity effects" feature so that the hydraulic head, H, is equal to the sum of the pressure head, H_p, and the elevation head, z:

$$\boldsymbol{H = H_p + z} \qquad \textbf{3.16}$$

where

$$\boldsymbol{H_p = \frac{p}{\rho g}} \qquad \textbf{3.17}$$

In COMSOL, the density of water is defined as a function of temperature only, so to represent elastic fluids, that function was replaced so that the density of the fluid was defined as a function of the fluid pressure, p, solution concentration, C, and temperature, T:

$$\boldsymbol{\rho = \rho_0(1 + c_w p - c_T(T - 273.15) + c_c C)} \qquad \textbf{3.18}$$

Here, ρ_0 is the reference density [kg/m^3], c_w is the compressibility of water (4.4×10^{-10} Pa^{-1}), c_T is the coefficient of thermal expansion (5×10^{-4}), and c_C is the coefficient for the increase in fluid density with increasing brine content (3.9×10^{-5}) [HSI GeoTrans, 2000]. Section 3.2.5 further describes how material properties (e.g., the properties of water) are defined in COMSOL.

The Darcy's Law Interface in COMSOL combines Darcy's law equation with the continuity equation producing

$$\boldsymbol{\frac{\partial}{\partial t}(\rho \varepsilon) + \nabla \cdot \rho\left[-\frac{k}{\mu}(\nabla p + \rho g \nabla D)\right] = Q_m} \qquad \textbf{3.19}$$

where ε is the porosity and Q_m is the mass source or sink term (M/L^{3}T) [COMSOL, 2011].

3.2.2 Solute Transport – Species Transport in Porous Media

For saturated porous media, the governing equation for solute transport without adsorption or reactions is

$$\boldsymbol{\theta_s \frac{\partial c_i}{\partial t} + c_i \frac{\partial \theta_s}{\partial t} + \nabla \cdot (c_i u) = \nabla \cdot \left[\left(D_{D,i} + \theta \tau_{L,i} D_{L,i} \right) \nabla c_i \right] + S_i} \quad \textbf{3.20}$$

where *ci* is the concentration of species *i* and θ_s and θ represent the pore volume fraction [-] and the liquid volume fraction [-] respectively. The dispersion tensor for species *i*, $D_{D,i}$, is the mechanical mixing caused by local variations in pore fluid velocity. Directional dispersivities or user defined values can be entered for the dispersion tensor. The effective diffusion, which depends on the structure of the porous material and the phases (solid or solid and gas), is represented by $\theta\tau_L D_{L,i}$ for a mobile liquid and immobile solid where τ_L is the tortuosity factor [-] and D_{Li} is the single phase diffusion coefficient for species i in the liquid phase [L^2/T] [COMSOL, 2011].

3.2.3 Temperature – Heat Transfer in Porous Media

The heat equation used by COMSOL [2011] is as follows:

$$\boldsymbol{(\rho C_p)_{eq} \frac{\partial T}{\partial t} + \rho C_p u \cdot \nabla T = \nabla \cdot \left(k_{eq} \nabla T \right) + Q} \quad \textbf{3.21}$$

Here, ρ represents the fluid density [kg/m^3], C_p represents the fluid heat capacity at constant pressure [J/kg·K], and $(\rho C_p)_{eq}$ represents the equivalent volumetric heat capacity at constant pressure [J/m·K]. k_{eq} is the equivalent thermal conductivity [W/m/K], *u* is the fluid velocity field or the Darcy velocity [m/s], and *Q* is a heat source or sink [W/m^3] [COMSOL, 2011].

Both k_{eq} and $(\rho C_p)_{eq}$ are dependent on the volume fractions of the solid material (matrix) and the fluid (porosity):

$$\boldsymbol{k_{eq} = \Theta_p k_p + \Theta_L k} \quad \textbf{3.22}$$

$$\boldsymbol{\left(\rho C_p \right)_{eq} = \Theta_p \rho_p C_{p,p} + \Theta_L \rho C_p} \quad \textbf{3.23}$$

Here the subscript *p* denotes conductivity, density, and heat capacity values for the solid while the subscript *L* denotes those values for the fluid [COMSOL, 2011].

3.2.3.1 Latent Heat

Additional variables and functions had to be added to a COMSOL model to account for the release or consumption of latent heat involved in the freezing and thawing of water in frozen soils. First, a variable, H_{lh}, was created to represent the volume fraction of water in an element with a value of unity for water and zero for ice. A step function with a transition zone size of dT was used to represent the switch between liquid and solid (Figure 3.1):

$$\int_{T_0}^{T_1} \frac{dH_{lh}}{dT} dT = 1 \qquad \textbf{3.24}$$

Next, the derivative of this variable, H_{lh}, was taken with respect to temperature and defined in COMSOL as an analytic function, D, where D is a normalized pulse in the phase change temperature range T_0 to T_1. Finally, latent heat was incorporated in the model as a modification to the effective specific heat capacity in Equation 3.21:

$$C_p = C_p + D(T) l_m \qquad 3.25$$

where l_m is the latent heat of fusion [J/kg] [COMSOL, 2012].

For this doctoral research, the transition between liquid water and solid ice occurred at 273.15 K with a transition zone size, dT, of 1 K, meaning that the phase change occurred over a one degree interval at the freezing/melting point as illustrated in Figure 3.1.

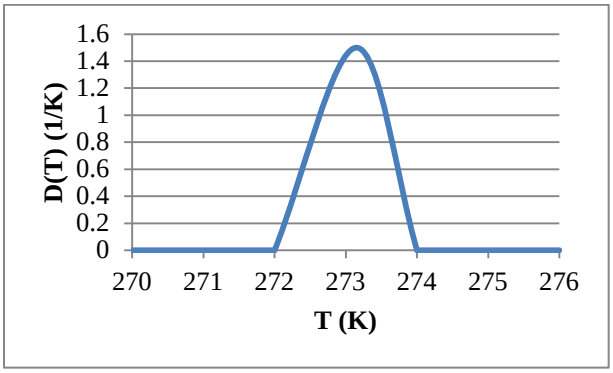

Figure 3.1 Step function H_{lh} (left) and analytic function D (right)
H_{lh} represents the volume of fraction of water within a model element. D is a normalized pulse in the phase change temperature range T_0 to T_1 and represents the derivative of H_{lh} with respect to temperature [Graphs adapted from COMSOL, 2012].

Modifying the effective heat capacity in this manner means that both the conduction and advection terms are impacted by latent heat. For the purposes of this doctoral research, this is

acceptable because the low porosity and low permeability of the rock mean that heat transfer is dominated by conduction. Thus, the advection component is negligible.

3.2.4 Mechanics – One-dimensional Loading Efficiency

One-dimensional hydromechanical coupling was implemented in COMSOL based on the governing equations presented in Section 3.1.4 (Equation 3.10 to Equation 3.15).

3.2.5 Material Properties – Temperature-Dependent Properties of Water

COMSOL includes a built-in database of properties for commonly used materials. Instead of entering in values and functions for all of the properties of a common material, the user can select the material from the library and apply it to the parts of the model domain that are composed of that material, and the properties of that material (e.g., density, viscosity, thermal conductivity) are all applied to that domain. Users can also create their own materials or modify the properties of the existing materials. For this research, the material water was chosen from the built-in database, and the functions given in COMSOL to define the properties of that material are outlined in Appendix A. This section outlines how several thermal properties were modified to include the properties of ice.

3.2.5.1 Density

For this doctoral research, the function for the density of water provided in the built-in database was completely replaced with the analytic function represented by Equation 3.19, which defined the density as a function of the fluid pressure, solution concentration, and temperature (Figure 3.2).

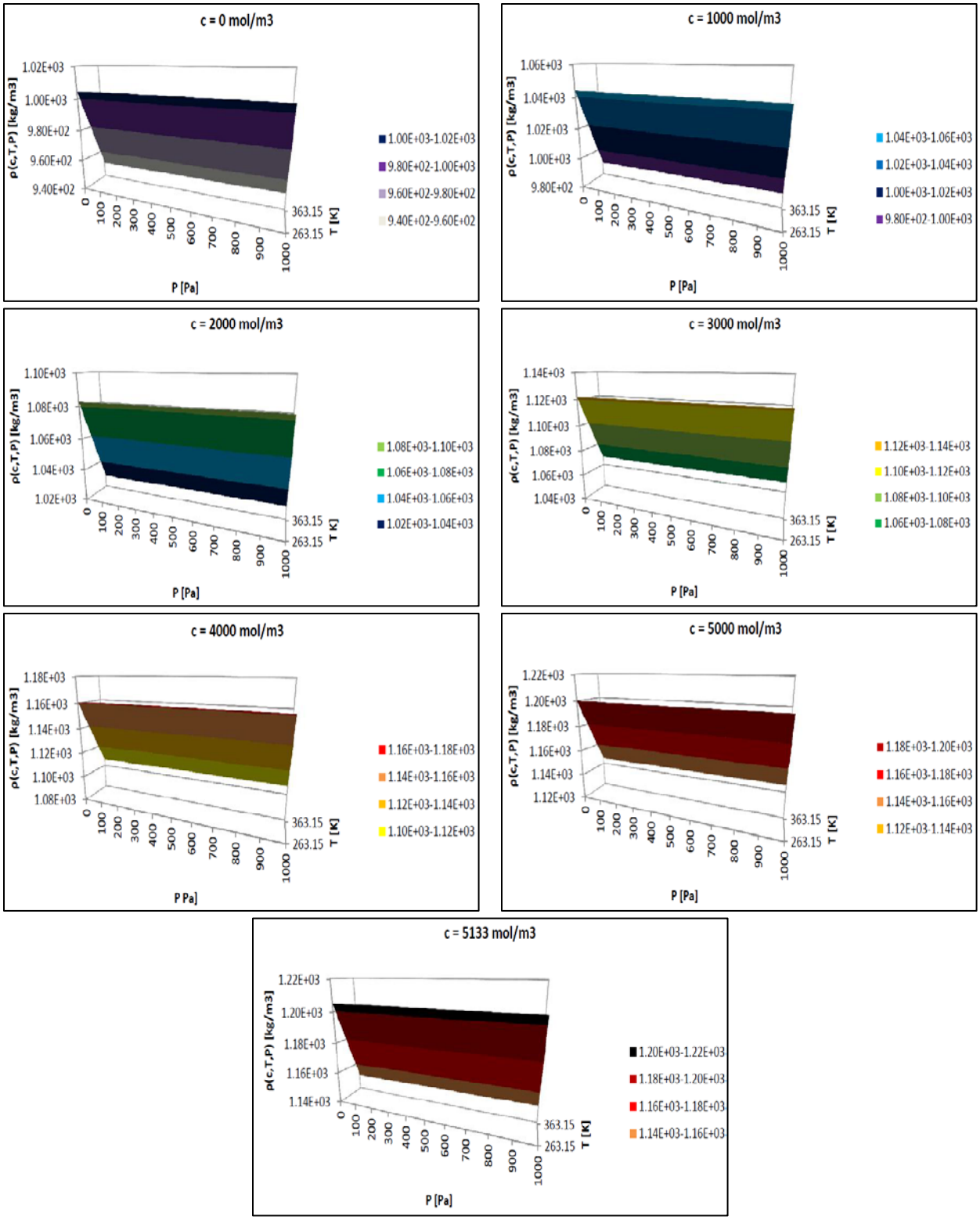

Figure 3.2 Density of water as a function of fluid pressure, solution concentration, and temperature

3.2.5.2 Dynamic Viscosity

The function for the dynamic viscosity of water provided in COMSOL's built-in database was also replaced with a function that defines the dynamic viscosity of water as a function of temperature for temperatures below and above freezing [Tan et al., 2011] (Figure 3.3):

$$\mu_{water} = 661.2 \times (T - 229)^{-1.562} \times 10^{-3} \quad \textbf{3.26}$$

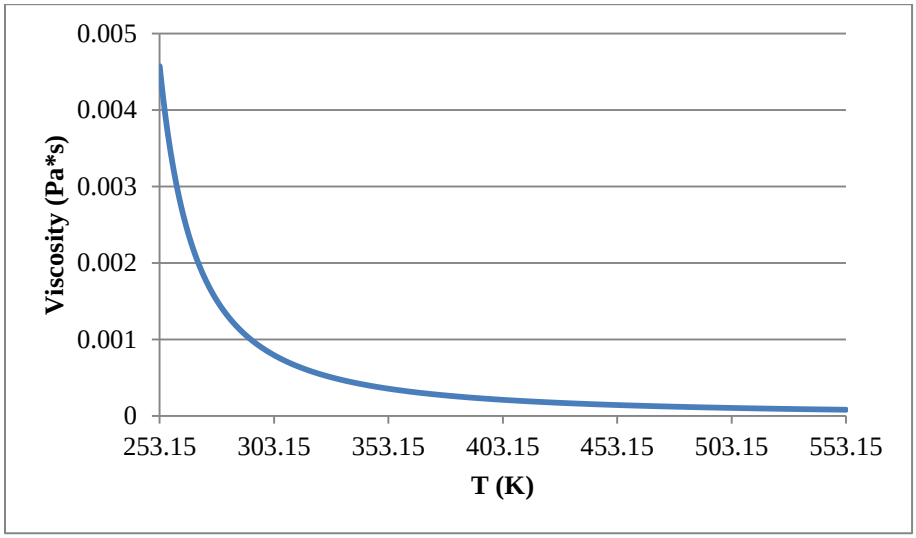

Figure 3.3 Viscosity of water as a function of temperature
[based on Equation 3.26 from Tan et al., 2011]

3.2.5.3 Thermal Conductivity

Studies have indicated that the thermal conductivity of ice varies linearly with temperature [e.g., Mottaghy & Rath, 2006; Ratcliffe, 1962]. Thus, a linear function was developed based on the values for the thermal conductivity of ice for temperatures from -100 ^{o}C to 0 ^{o}C from the Chemical Rubber Company's (CRC) Handbook of Chemistry and Physics [CRC, 2013] (Figure 3.4):

$$k_{eq,water} = -0.0151 * (T - 273.15) + 2.0785 \quad \textbf{3.27}$$

The temperature conversion from degrees Celsius to Kelvins (T - 273.15) was required because this equation is based on data with temperature values in degrees Celsius and COMSOL measures temperature in Kelvins.

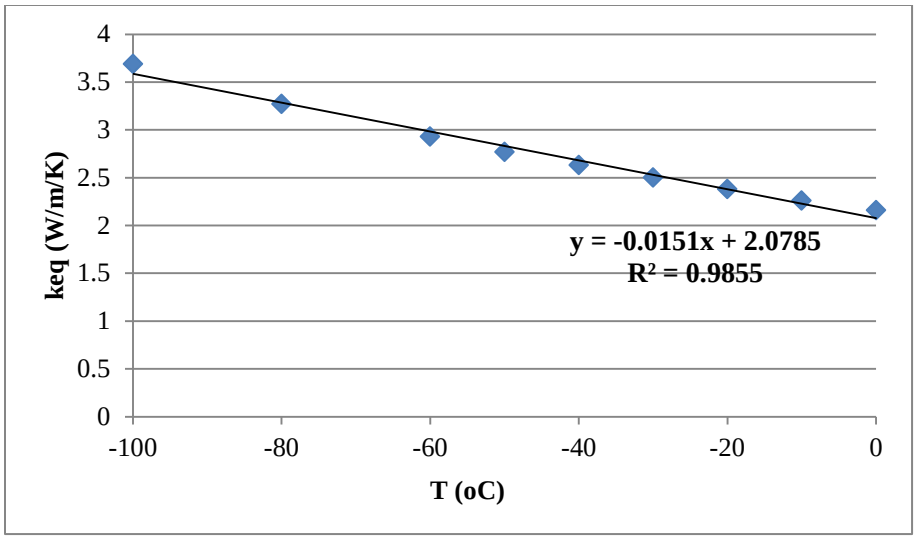

Figure 3.4 Thermal conductivity of ice

A linear function for the relationship between the thermal conductivity of ice and its temperature was developed based on data from the CRC Handbook of Chemistry and Physics [CRC, 2013].

3.2.5.4 Heat Capacity

To account for temperatures below freezing (173.15 K to 273.15 K), the heat capacity of water was defined based on the molar heat capacity of ice as a function of temperature [Murphy & Koop, 2005]:

$$C_{p,water} = -2.0572 + 0.14644T + 0.06163T^{\left(-\left(\frac{T}{125.1}\right)^2\right)} \quad \textbf{3.28}$$

This function is valid for temperatures greater than 20 K. Because this function represents the molar heat capacity of ice (J/mol·K), it was multiplied by a conversion factor (1000 g/18.01528 g) to obtain the units required in COMSOL (J/kg·K) (Figure 3.5).

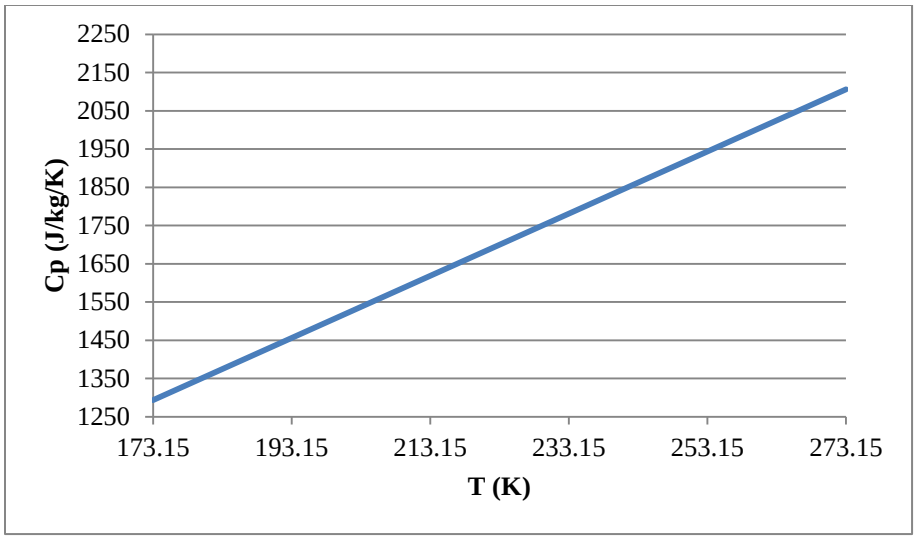

Figure 3.5 Heat capacity of ice

The heat capacity of ice is plotted as a function of temperature [based on the function from Murphy & Koop, 2005].

3.2.6 Verification

To represent all of the physics involved in the analyses presented in the following chapters, additional functions and variables had to be developed in COMSOL. This section describes how those functions and variables were implemented to represent temperature-dependent permeability, latent heat, and a one-dimensional loading efficiency, and it explains the verification processes used to ensure that those functions and variables were implemented correctly.

3.2.6.1 Temperature-Dependent Permeability

For this doctoral research, the permeability of the permafrost or frozen ground was six orders-of-magnitude smaller than that of the surrounding unfrozen ground and freezing occurs over a one degree interval from -0.5 ^{o}C to 0.5 ^{o}C. Additional variables and functions were created in COMSOL to represent that change in permeability with changing temperature over this freezing/melting point. The permeability was multiplied by a relative permeability, k_r,

$$\boldsymbol{k_r = 10^{a(T)}} \qquad \textbf{3.29}$$

where a is a linear interpolation function representing a one degree interval over which the temperature change (freezing/melting) would occur with $a = -6$ at -0.5 ^{o}C (completely frozen) and $a = 0$ at 0.5 ^{o}C (completely thawed).

To verify that these functions and variables worked as expected, they were tested on a simple rectangular domain with predefined permeability of 10^{-16} m^2 and a temperature profile imposed by fixed temperatures at the left and right boundaries of -0.5 ^oC and 0.5 ^oC, respectively. Flow was forced from left to right by fixing the pressure at each end of the domain. Figure 3.6 illustrates the final permeability distribution with temperature contours. These results confirm that between -0.5 ^oC and 0.5 ^oC, the permeability varies over six orders of magnitude.

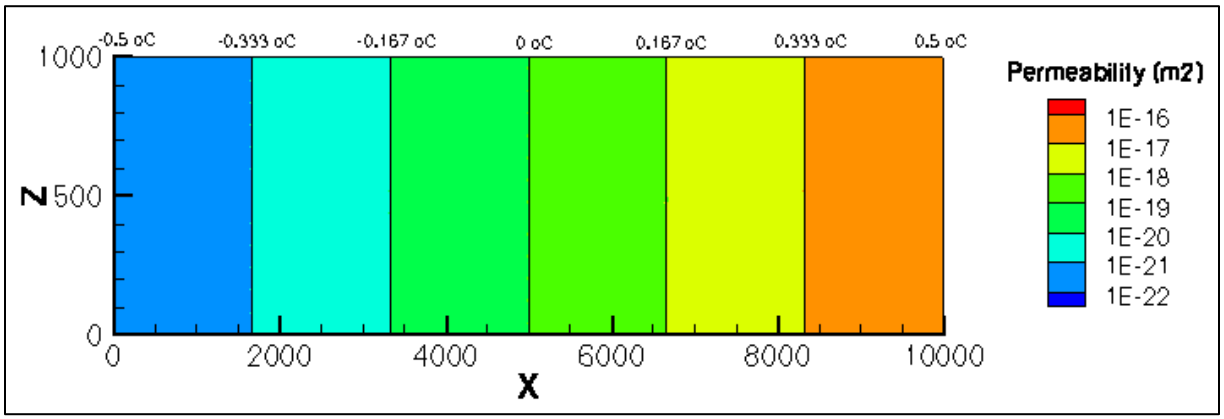

Figure 3.6 Permeability distribution with temperature contours

3.2.6.2 Latent Heat

The release or consumption of latent heat involved in freezing and thawing of water in frozen soils was accounted for using the method described in Section 3.2.3.1. This method was verified by COMSOL with a one-dimensional model from the software's model library [COMSOL, 2012; Model Library path: Heat_Transfer_Module/Tutorial_Models/phase_change].

A second one-dimensional model was also used to verify the latent heat formulation used in this doctoral research. This second model was presented as Case T1 for the INTERFROST Project, which was described in Section 2.3.2. Case T1 follows from McKenzie, Voss, and Siegel [2007] who used the one-dimensional heat conduction case with phase change leading to an analytic expression that was developed by Lunardini [1988].

The Lunardini solution to this problem takes a range of temperatures over which the phase change occurs (T_f, 0 ^oC, to T_m, -1 ^oC). This range of temperatures for phase change results in three zones: a frozen zone, a mushy zone, and a thawed zone. The one-dimensional domain with a length of 7.5 m had an initial constant temperature of 4 ^oC (T_0) before a temperature of -6 ^oC was imposed (T_s) at one end of the domain and the progression of the freezing front over time was observed. Table 3.1 outlines the parameters used for to calculate the analytic solution. These parameters were adapted from the documentation shared by the INTERFROST Project [Interfrost].

Table 3.2 outlines the parameters used in COMSOL. Plots of the temperature profiles from both the analytical and numerical solutions were compared for three days of simulation. The close match between the two solutions further verifies the latent heat formulation that was used in this doctoral research.

Table 3.1 Parameters for the Lunardini analytic solution for the one-dimensional heat conduction case with phase change [adapted from the INTERFROST Project].

* The Heat Transfer in Porous Media module in COMSOL does not include the physics for simulating residual saturation.

Parameter	Symbol	Value	Units
Equivalent thermal conductivity of the frozen zone	k1	2.64	J/sm^oC
Equivalent thermal conductivity of the mushy one	k2	2.38	J/sm^oC
Equivalent thermal conductivity of the thawed zone	k3	2.12	J/sm^oC
Thermal diffusivity of the frozen zone	$\alpha 1$	1.28×10^{-6}	m^2/s
Thermal diffusivity of the mushy zone	$\alpha 2$	7.52×10^{-7}	m^2/s
Thermal diffusivity of the thawed zone	$\alpha 3$	2.07×10^{-8}	m^2/s
Equivalent volumetric heat capacity of the frozen zone	C1	2.06×10^6	$J/m^{3o}C$
Equivalent volumetric heat capacity of the mushy zone	C2	2.44×10^6	$J/m^{3o}C$
Equivalent volumetric heat capacity of the thawed zone	C3	2.82×10^6	$J/m^{3o}C$
Unfrozen water content when there is no freezing	ξ_0	0.2	kg_l/kg_s
Unfrozen water content when temperature is freezing temperature	ξ_f	0*	kg_l/kg_s
Maximum variation of unfrozen content	$\Delta\xi$	0.2	kg_l/kg_s
Global density	γd	1680	kg/m^3

Table 3.2 Parameters for the COMSOL numerical solution for the one-dimensional heat conduction case with phase change

Parameter	Symbol	Value	Units
Density of water	ρ_w	1000	kg/m^3
Density of ice	ρ_i	920	kg/m^3
Density of soil	ρ_s	2530.1	kg/m^3
Thermal conductivity of water	k_w	0.58	$J/m^{3o}C$
Thermal conductivity of ice	k_i	2.14	$J/m^{3o}C$
Thermal conductivity of soil	k_s	2.9	$J/m^{3o}C$
Specific heat capacity of water	C_{pw}	4187	J/kg^oC
Specific heat capacity of ice	C_{pi}	2108	J/kg^oC
Specific heat capacity of soil	C_{ps}	840	J/kg^oC
Porosity	ε	0.336	
Water residual saturation	S_{wres}	0	

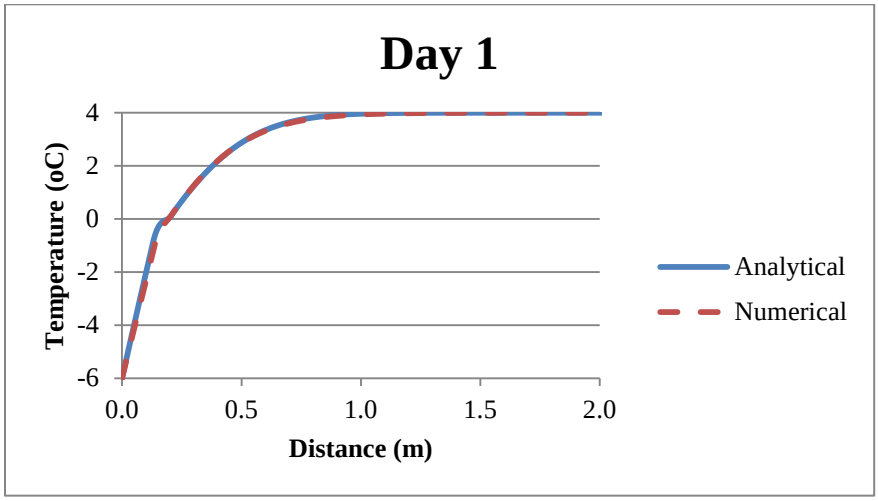

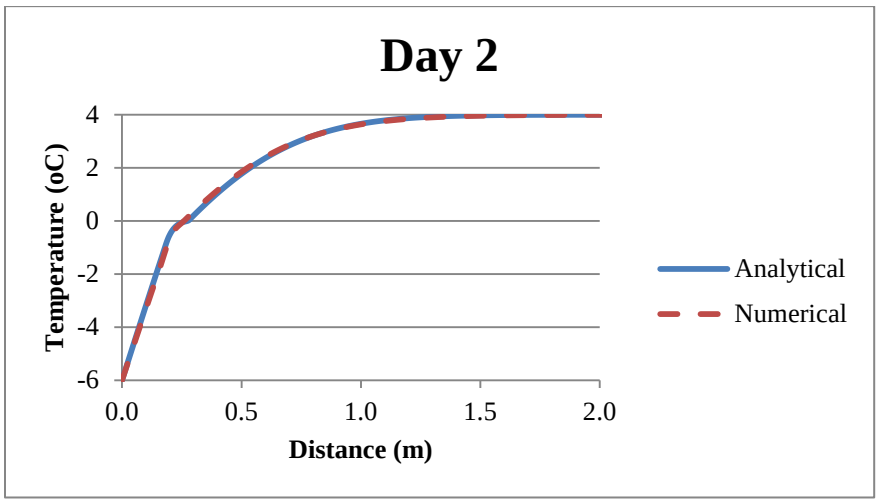

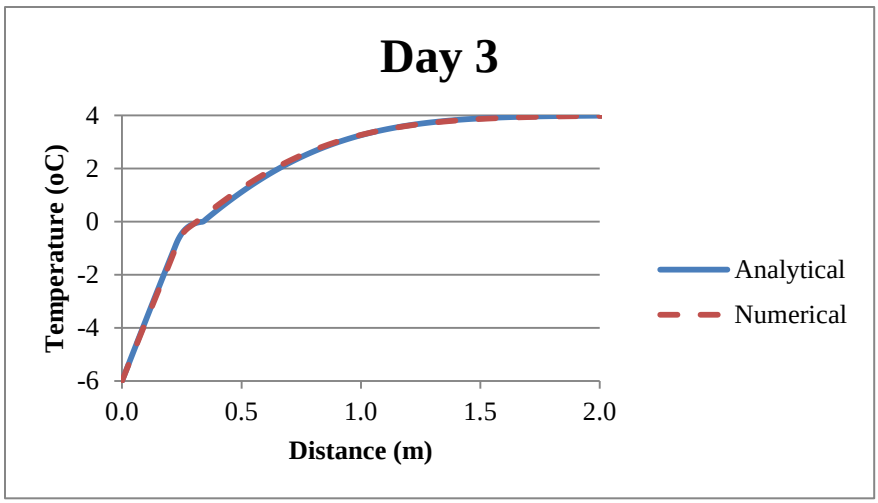

Figure 3.7 Temperature profiles from both the analytical and numerical solutions to the one-dimensional heat conduction case with phase change.

3.2.6.3 One-Dimensional Hydromechanical Coupling

The parameters, variables, and functions defined in Section 3.1.4 were added to COMSOL to represent one-dimensional hydromechanical coupling. In particular, the porosity (ε), the compressibility of water (β_f), Young's elastic modulus of the porous medium (E), one-dimensional loading efficiency (ζ), and Poisson's ratio (v) were defined as parameters with values as defined for the analyses in Section 4.0 and Section 5.0. The variables – coefficient of vertical compressibility for the porous medium (β'), and the drained confined vertical modulus of the porous medium (K') – were calculated based on those parameters. The stress term (σ_{zz}) was defined by an interpolation function (Section 4.3.3 and Section 5.3.4) to apply the load of the ice sheet across the domain and in time. Finally, the storage term (S) and a mass source term (Q_m) were assigned within the Darcy's Law interface.

To verify that this formulation of the one-dimensional hydromechanical coupling is correct, an analytical solution was used for comparison. The analytical solution for a one-dimensional vertical column model was presented in Lemieux [2006] with the solution for the hydraulic head along the column represented as follows:

$$\boldsymbol{h(z,t) = \frac{\zeta}{\rho g}\frac{\partial \sigma_{zz}}{\partial t}\left[t - \left(t + \frac{z^2}{2D}\right) erfc\left(\frac{z}{2\sqrt{Dt}}\right) + z\sqrt{\frac{t}{\pi D}}\exp\left(-\frac{z^2}{4Dt}\right)\right]} \qquad \textbf{3.30}$$

where D is the hydraulic diffusivity ($D = K_{zz}/S_s$).

The column is fully saturated and has a semi-infinite length, which was represented in the numerical model as a domain 10,000 m in length. The boundary condition at the top of the domain was a specified head of 0 m to represent the top of the column as being drained. The bottom of the domain was a no flow boundary. The initial head in the column was 0 m. The remaining properties are listed in Table 3.3 and are based a generic crystalline rock setting. The mechanical load is applied as an ice sheet that grows in thickness at a rate of 0.32 m/year (equivalent to 0.3 m of water/year) for 10,000 years.

Table 3.3 Fluid and matrix properties

Property	Value
Porosity, ε	0.2
Permeability, k	3.24×10^{-18} m^2
Compressibility of water, β_f	4.4×10^{-10} 1/Pa
Young's modulus, E	6.32×10^{10} Pa
Poisson's ratio, v	0.2

Figure 3.8 illustrates the hydraulic head versus depth over time (t = 100 years, 500 years, 1,000 years, 5,000 years, and 10,000 years) both the numerical and analytical solutions. In that figure, the numerical solution is represented by the symbols and the analytical solution is represented by the solid lines. The numerical solution fits the analytical solution well, with both showing that the head increases along the column with depth. This agreement verifies that the method used to represent one-dimensional hydromechanical coupling in COMSOL was appropriate.

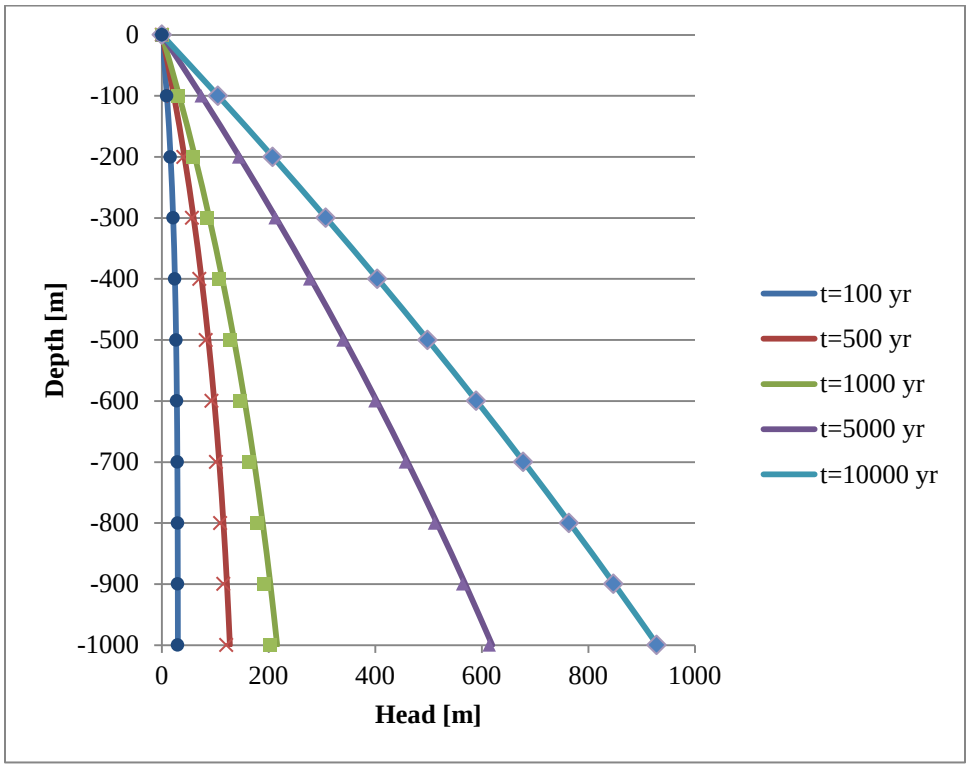

Figure 3.8 Hydraulic head versus depth at different points in time for the numerical (symbols) and analytical (solid lines) solutions.

4.0 Hypothetical Crystalline Rock Setting

Permafrost will form in advance of an ice sheet and degrade or melt as that glacier advances across the landscape, covering and insulating the ground beneath it. Because permafrost has lower hydraulic conductivity than the unfrozen ground, both the existence of the permafrost and its degradation beneath an advancing ice sheet will alter the groundwater flow system. Although it has been observed that some permafrost will exist beneath the edge of an advancing ice sheet, there is little presented in the literature to quantify the distance to which or length of time for which permafrost will persist beneath a blanket of ice.

One of the objectives of this doctoral research was to examine the impact of the initial depth of the permafrost and the rate at which the ice sheet advances on the rate of permafrost degradation beneath the ice sheet. A two-dimensional cross-section of a hypothetical crystalline rock setting was developed to carry out this investigation, chosen as such to provide a direct comparison with the GAP model presented in Section 5.0. The same two-dimensional cross-section was also used to examine how permafrost depth and talik size and distribution influence the groundwater flow system during glacial advance.

4.1 Equilibrium Ice Sheet Profiles

In the absence of data that represent the ice sheet profile or ice thickness, analytic solutions can be used to estimate the profile of an ice sheet. Those analytic solutions are based on assumptions made about the properties of the ice and the bed elevation.

Ice deformation will only occur if basal shear stress is equal to the yield stress. If the basal shear stress is less than the yield stress, the ice will not move. Rather, it will thicken or steepen until the yield stress is reached. Then the ice will flow at the rate required to prevent the basal shear stress from exceeding the yield stress [Benn & Evans, 2010]. Basal shear stress can be calculated as

$$\boldsymbol{\tau_b = \tau_{yield} = \rho_i g H_i \frac{\partial h}{\partial x}} \qquad \textbf{4.1}$$

where $\frac{\partial h}{\partial x}$ is the ice surface gradient, H_i is the ice thickness, and ρ_i is the ice density, which is assumed constant [Benn & Evans, 2010; Cuffey & Paterson, 2010]. For land terminating glaciers, the yield stress or basal shear stress is typically within a range of 50 to 100 kPa [Cuffey & Paterson, 2010]. Smaller values for yield stress imply that the ice sheet surface is lower and flatter [Benn & Evans, 2010; Cuffey & Paterson, 2010; van der Veen, 1999].

Based on the assumptions that the ice sheet is perfectly plastic and is symmetrical and that the profile of the bed is flat, the ice sheet thickness can be calculated as follows [Benn & Evans, 2010; Cuffey & Paterson, 2010; van der Veen, 1999]:

$$H = \left[\frac{2\tau_b(x-L)}{\rho g}\right]^{1/2} \qquad 4.2$$

where x is the distance from the ice sheet terminus and L is the location of the ice sheet terminus. Figure 4.1 illustrates the solution to Equation 4.2 for three basal shear stress values representing the typical range for land terminating glaciers.

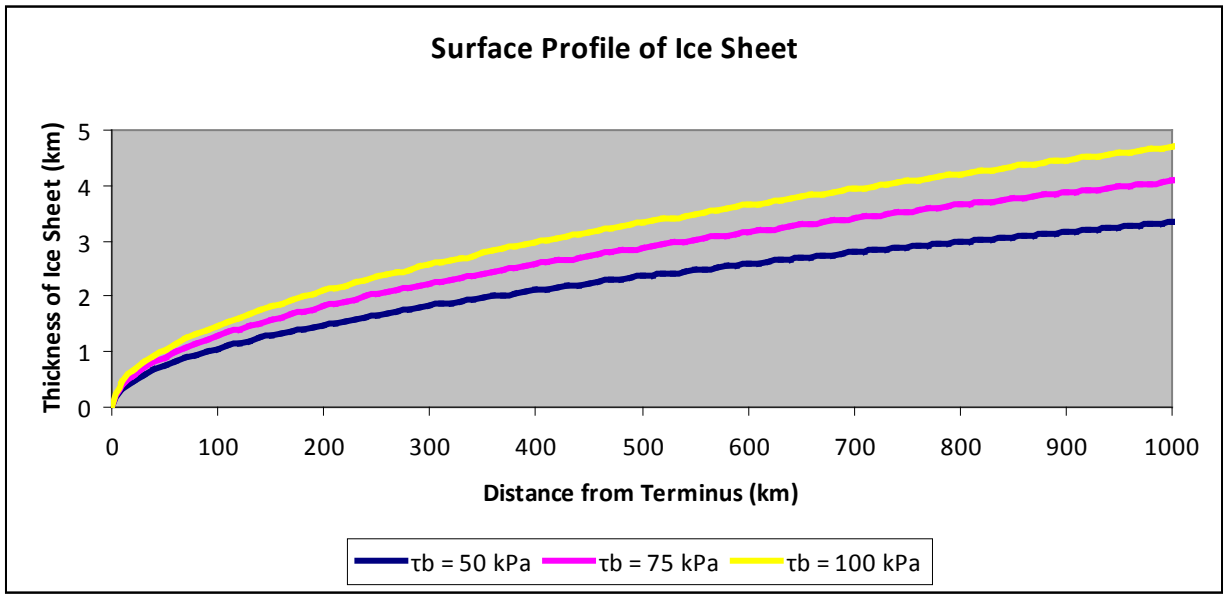

Figure 4.1 Equilibrium ice sheet profile.
Ice sheet thickness is calculated for three basal shear stress values representing the typical range for land terminating glaciers.

Although this analytic approach yields a good approximation, it should not be used if the bed elevation or yield stress varies along the flow line. To account for those variations, numerical methods must be used to define the ice surface elevation in a step-wise fashion from the ice sheet terminus up glacier. van der Veen [1999] proposes a method for calculating the equilibrium profile of an ice sheet using a function that defines the ice surface elevation at the point h_{i+1}:

$$h_{i+1}^2 - h_{i+1}(z_{bi} + z_{bi+1}) + h_i(z_{bi+1} - H_i) - \frac{2\Delta x\overline{\tau_b}}{\rho_i g} = 0 \qquad 4.3$$

where the bar over the yield stress indicates that the average value of the yield stress over the grid interval is used.

4.2 Model Domain

The groundwater model domain for this study, illustrated in Figure 4.2 covers a two-dimensional cross section of a generic crystalline rock setting. The model domain is 6 km wide. The top surface rises from sea level in the west to 300 m elevation in the east such that the model domain is 1500 m to 1800 m deep in the west and east, respectively. The domain is discretized into 9,902 free or unstructured triangular elements with an element size of 50 m.

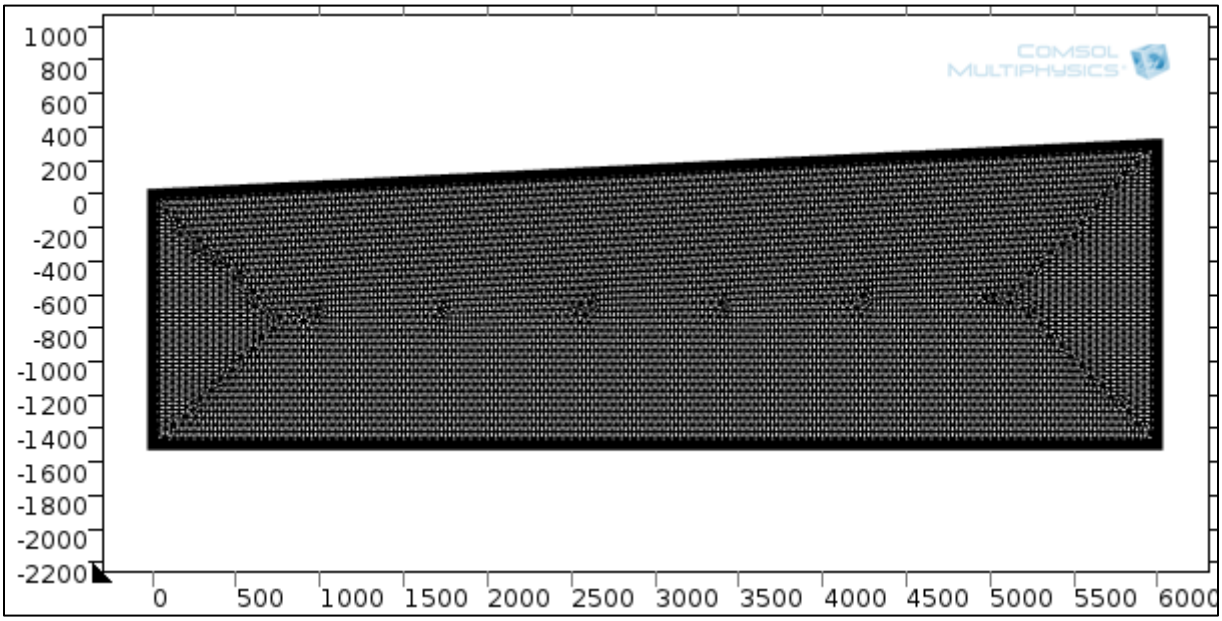

Figure 4.2 Discretization of the two-dimensional cross-section of the model domain for a generic crystalline rock setting

The model was discretized into 9902 free triangular elements.

4.3 Properties and Boundary Conditions

The following sections summarize the properties and boundary conditions used to develop the base-case conceptual model.

4.3.1 Boundary Conditions

The following sections describe the boundary conditions that were used for the fluid flow, solute transport, and temperature physics.

4.3.1.1 Fluid Flow

In regions without ice sheet cover, head values were assigned based on the assumption that the water table is 3 m below ground surface. The ice sheet was applied as a freshwater head equal to pressure applied at the base of the ice sheet and as a mechanical load for hydromechanical coupling. The domain bottom and sides were no flow boundaries.

Both head and vertical stress were applied to the top boundary as an interpolation function with head and stress values set every 1 m and every 1 year. Head values were linearly interpolated to maintain computational stability. A nearest neighbour interpolation function was used to represent the vertical stress as a change in vertical stress with a change in time (See Equation 3.10 in Section 3.1.4).

4.3.1.2 Total Dissolved Solids (TDS) and Solute Transport

Total dissolved solid (TDS) concentrations are based on characteristics derived from studies of the Canadian Shield to be consistent with the other models examined for this thesis research. In general, salinity (dissolved salt content) increases with depth due to either recharge from episodes of marine intrusion or geochemical interactions between the fluid and the rock. At depths greater than 1 km, the salinity can be greater than that of sea water [Bense & Person, 2008; Oberlander, 1989] (3.5% or 35 g/L).

Salinity plays an important role in fluid flow within the Canadian Shield in the context of a deep geologic repository. An increase in the TDS will result in an increase in fluid density. The increase in fluid density of the deeper fluids will act as an inhibitor of active flow at depth [Park et al., 2008]. Data for the Canadian Shield from Frape and Fritz [1987 (Figure 2b)] was used in the preliminary study by Yin et al. [2013]. Equation 4.4 represents an upper bound for total dissolved solids (TDS) as a function of depth. TDS is in units of g/L.

$$\boldsymbol{TDS} = \begin{cases} \mathbf{10^{0.001981697d}}, & \boldsymbol{d \leq 1250m} \\ \mathbf{300}, & \boldsymbol{d > 1250m} \end{cases} \qquad \textbf{4.4}$$

COMSOL Multiphysics requires that concentrations be entered in terms of mol/m^3. For consistency with other GAP studies and Southern Ontario studies [Yin et al., 2013; Sykes et al., 2011], a brine of sodium chloride (NaCl) was chosen for the base case scenario. Thus, the maximum TDS concentration for depths greater than 1250 m was 5133 mol/m^3.

4.3.1.3 Temperature

The top surface boundary was assigned a temperature representing the atmospheric temperature. Surface water bodies within the domain were assigned a temperature of 2 ^{o}C. For regions not covered in ice, the surface temperature was set to -3 ^{o}C to achieve an initial maximum permafrost depth of approximately 100 m for the base case scenario. To achieve the shallow permafrost depth (approximately 50 m) and the deep permafrost depth (approximately 300 m), top surface temperatures of -2 ^{o}C and -8 ^{o}C were assigned, respectively. These depths correspond to permafrost depths used in the analyses presented in Chapter 5 (Greenland Analogue Project; approximately 300 m) and Chapter 6 (Southern Ontario Deep Geologic Repository; approximately 50 m) as well as an intermediate depth in between the two.

The domain sides were insulated while a geothermal heat flux of 55 mW/m^2, similar to values and averages used in other studies [Benn & Evans, 2010 (40 – 90 mW/m^2 with average of 60 mW/m^2); Greve, 2005 (42 – 65 mW/m^2); SKB, Posiva, Terrasolve, personal communication, August 2011 (53.3 mW/m^2); van der Veen et al, 2007 (42 mW/m^2 for Precambrian Shields and 57 mW/m^{2}continental average)], was applied to the bottom of the domain.

4.3.2 Matrix Properties

To account for variations in hydraulic conductivity due to changes in density, permeabilities were used. These values were based on characteristics derived from studies of the Canadian Shield. Horizontal and vertical permeabilities as a function of depth are expressed as follows [Normani, 2009]:

$$\boldsymbol{k_H = 10^{-14.5-4.5(1-e^{-0.002469d})}} \qquad \textbf{4.5}$$

$$\boldsymbol{k_V = \begin{cases} 10k_H, & d \leq 300m \\ [0.09(400-d)+1]k_H, & 300 < d \leq 400m \\ k_H, & d > 400m \end{cases}} \qquad \textbf{4.6}$$

where $\boldsymbol{k_H}$ is the horizontal permeability [$\boldsymbol{L}^2$], $\boldsymbol{k_V}$ is the vertical permeability [$\boldsymbol{L}^2$], and $\boldsymbol{d}$ is the depth below ground surface [$\boldsymbol{L}$]. Matrix permeabilities (k_H and k_V) decrease exponentially with increasing depth.

To represent a crystalline rock matrix, the matrix porosity was constant at 0.5% or 0.005 and the matrix density was set to that of granite (2700 kg/m^3 [average of range given by CRC, 2013]). Storage values are calculated by COMSOL based on the loading efficiency (ζ), Young's Modulus (E), and Poisson's ratio (v). Poisson's ratio was 0.25.

Table 4.1 summarizes the loading efficiency and Young's Modulus values for different depths within the domain:

Table 4.1 Loading efficiency and Young's Modulus values as a function of depth for generic crystalline rock cross-section.

Loading efficiency and Young's Modulus are used to calculate storage values [based on Chan and Stanchell, 2008].

Depth (below ground surface)	Young's Modulus (E) [GPa]	Loading Efficiency (ζ) [-]
To 150 m	20	0.795
150 m to 350 m	30	0.782
350 m and deeper	60	0.744

For heat transport, the matrix properties include a thermal conductivity of 2.1 W/m·K and a specific heat capacity of 0.79 J/kg·K; these values are also consistent with a granitic material.

4.3.3 Ice Sheet Profile

Equation 4.3 was used to define the ice sheet profile used in the analyses described in this chapter. The ice sheet was initially located at the eastern end of the domain with the terminus at 5000 m (Figure 4.3). The average basal shear stress was set to 75 kPa, the middle value in the range of typically basal shear stress values given by Cuffey & Paterson, 2010, and the ice sheet was advanced from east to west across the top surface of the domain at 1 m/year.

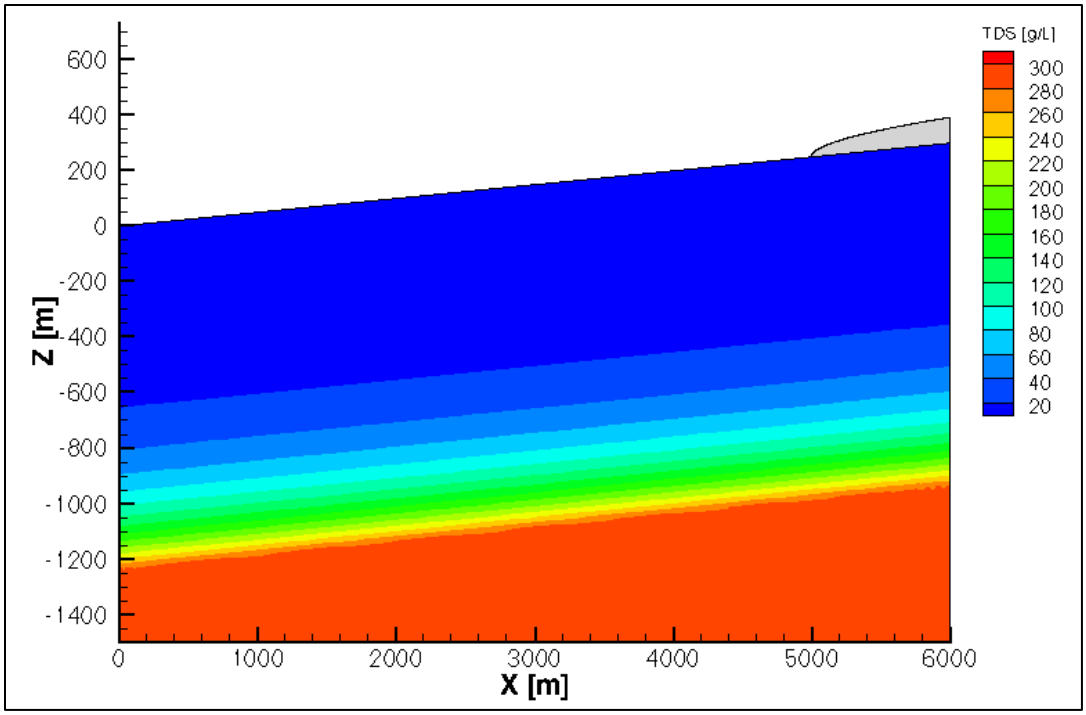

Figure 4.3 West-east cross-section of the steady-state depth-dependent total dissolved solids distribution and ice sheet profile for a generic crystalline rock setting

4.3.4 Permafrost and Taliks

To simulate the occurrence of permafrost within the model, permeability is dependent on temperature as well as depth such that the permeability of frozen elements (i.e. elements with permafrost) is reduced by six orders-of-magnitude. This freezing occurs over a range of 1 ^{o}C such that the permeability is reduced gradually between 0.5 ^{o}C and -0.5 ^{o}C. Taliks, therefore, will form wherever temperatures remain above freezing (e.g., beneath surface water bodies). While an unfrozen water phase would still exist within the frozen permafrost as adsorbed water on the solid grains, the volume of unfrozen water content would be very small.

For the base-case scenario, the initial maximum permafrost depth was approximately 100 m. This was achieved by setting the top surface temperature in regions without the ice sheet or a surface water body to -3 ^{o}C as described in Section 4.3.1.3 for a steady-state simulation. For the base case scenario, no taliks were included.

4.4 Analyses

The following sections detail the analyses carried out to examine the impact of initial permafrost depth and talik size and distribution on the permafrost distribution and groundwater

flow system during ice sheet. Table 4.2 and Table 4.3 outline the scenarios that were investigated. Plots illustrating the initial conditions and select transient simulation results for these analyses are presented in following sections.

Table 4.2 Scenarios investigated to examine the impact of initial permafrost depth and rate of ice sheet advance on permafrost distribution during ice sheet advance

	1	2	3	4	5	6
Initial Permafrost Extent						
40 m (Shallow)	x	x				
100 m (Intermediate)			x	x		
200 m (Deep)					x	x
Rate of Ice Sheet Advance						
1 m/year	x		x		x	
2 m/year		x		x		x
Number of Taliks						
None	x	x	x	x	x	x

Table 4.3 Scenarios investigated to examine the impact of the number, distribution, and size of taliks on the groundwater flow system during ice sheet advance

	1	2	4	5	6	7	8	9
Initial Permafrost Extent								
100 m (Intermediate)	x	x	x	x	x	x	x	x
Rate of Ice Sheet Advance								
2 m/year	x	x	x	x	x	x	x	x
Number of Taliks								
1	x	x						
2			x	x	x			
3						x	x	x
Size of Taliks (Diameter/Width)								
50 m	x		x	x	x			
100 m		x				x	x	x
Distance between Taliks								
N/A	x	x						
50 m			x			x		
100 m				x			x	
500 m					x			x

4.4.1 Initial Depth of Permafrost

To develop the initial pressure and temperature conditions for the transient analyses, steady-state simulations were run first using the properties and boundary conditions detailed in

Section 4.3. The first steady-state simulation to be run involved only the Darcy's Law physics (Section 3.2.1) with a constant depth-dependent TDS distribution, which is illustrated in Figure 4.3. This simulation established the regional flow system yielding the pressure distribution and velocity field as input for the next steady-state simulation, which included both the Darcy's Law and Heat Transfer in Porous Media physics (Section 3.2.3). Figure 4.4, Figure 4.5, Figure 4.6, and Figure 4.7 illustrate the results of this steady-state simulation, which are the initial conditions (pressure, hydraulic head, temperature, and velocity magnitude respectively) for the transient analyses.

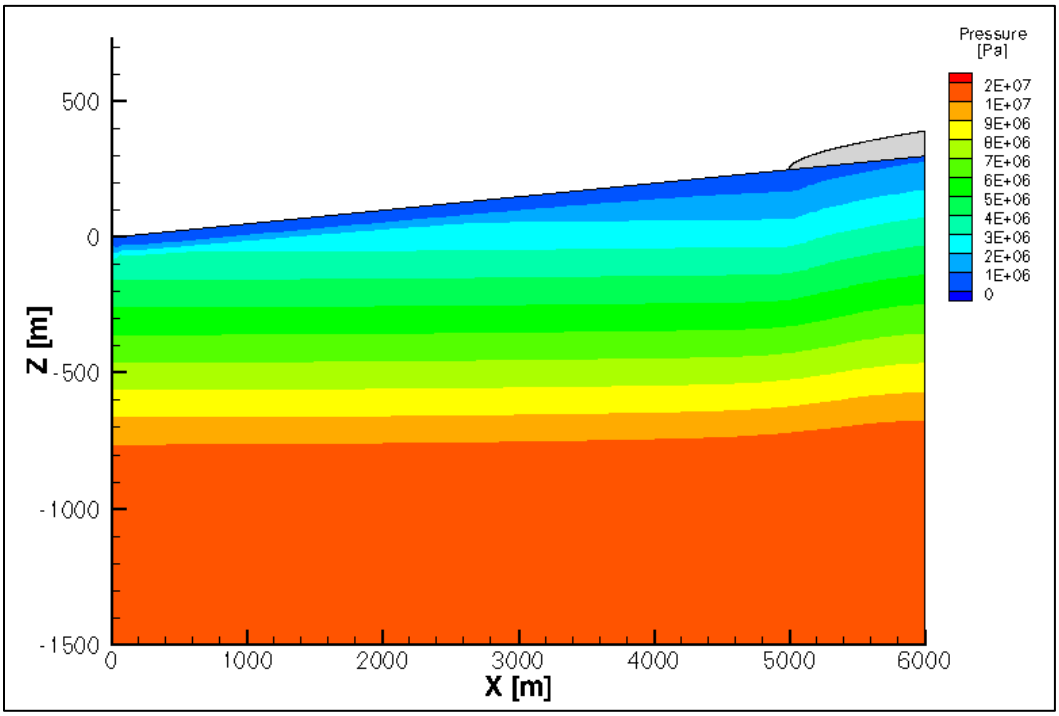

Figure 4.4 West-East cross-section of steady-state density-dependent pressure for density-dependent flow with heat transport for an intermediate permafrost depth

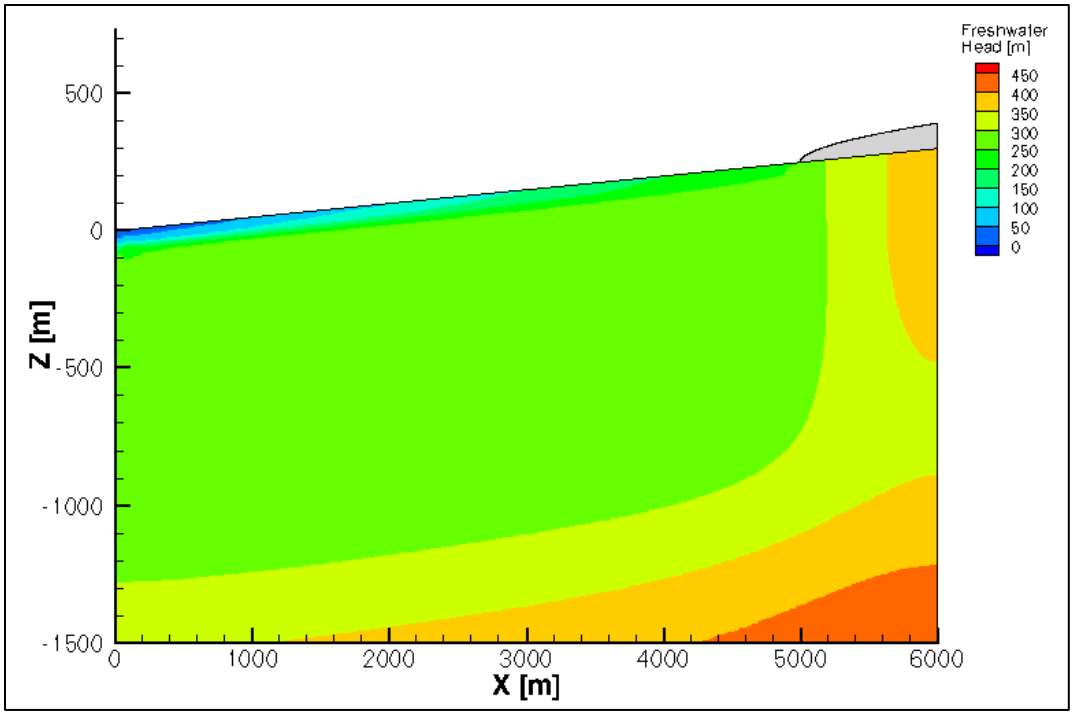

Figure 4.5 West-East cross-section of steady-state density-dependent freshwater head for density-dependent flow with heat transport for an intermediate permafrost depth

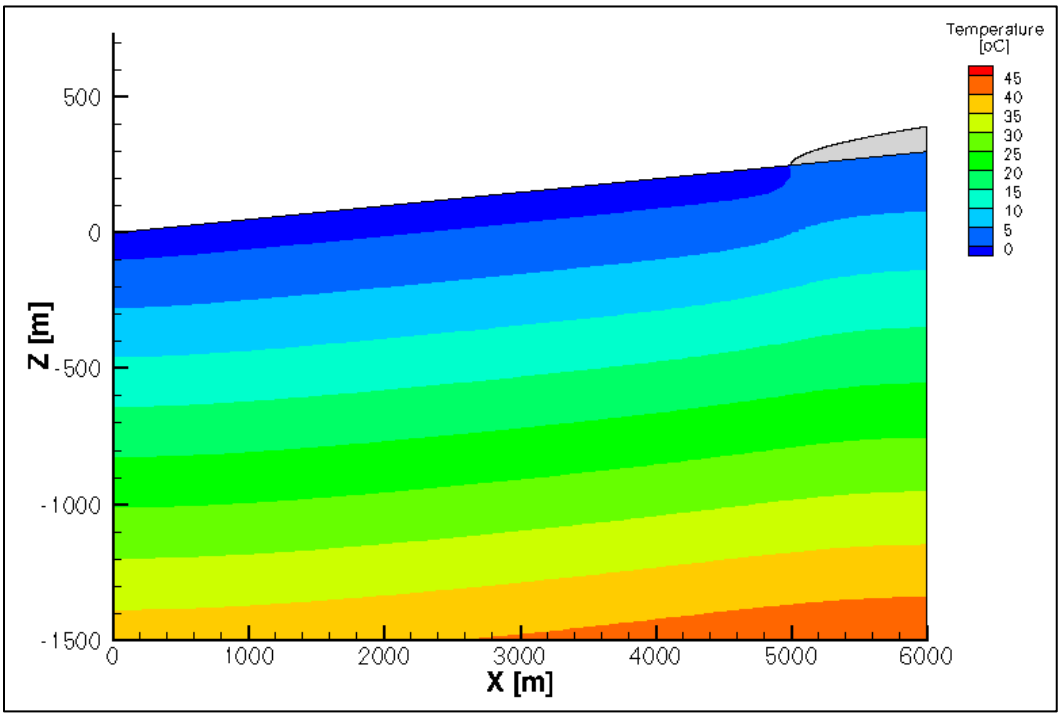

Figure 4.6 West-East cross-section of steady-state temperature for density-dependent flow with heat transport for an intermediate permafrost depth

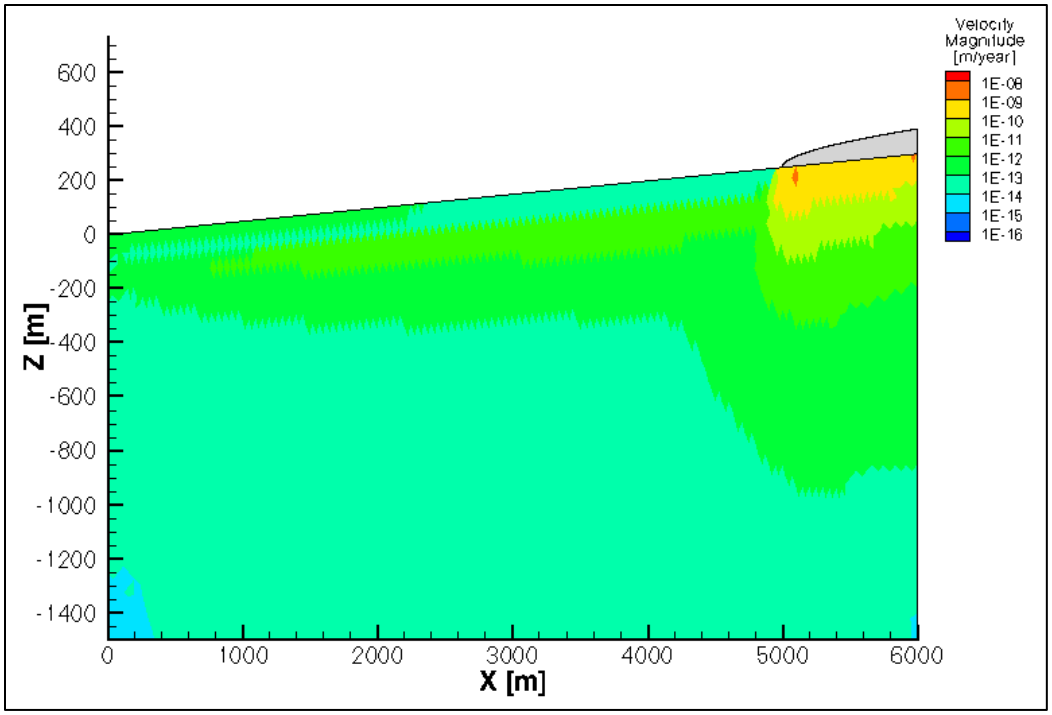

Figure 4.7 West-East cross-section of steady-state velocity magnitude for density-dependent flow with heat transport for an intermediate permafrost depth

As illustrated in Figure 4.4 and Figure 4.5, pressure and hydraulic head values are elevated beneath the ice sheet due to the weight of the ice. In general, temperature increases linearly with depth (Figure 4.6). Figure 4.6 also shows the initial depth of permafrost at approximately 100 m. Velocity magnitudes (Figure 4.7) are greater in the shallow subsurface and decrease with increasing depth as expected given the depth-dependent permeability profile used (Section 4.3.2). However, the velocity magnitude distribution is also affected by both the temperature and pressure distributions. Subsurface temperatures below freezing indicate the presence of permafrost, which has a much lower permeability than the surrounding unfrozen subsurface as described in Section 4.3.4. Thus, in regions with permafrost (indicated by below freezing temperatures in Figure 4.6), the velocity magnitude is reduced by up to four orders-of-magnitudes with magnitudes on the order of 10^{-14} m/year.

To examine the impact of the initial permafrost depth on permafrost distribution during subsequent ice sheet advance, a shallow maximum permafrost depth (approximately 40 m) and a deep maximum permafrost depth (approximately 300 m) were used in addition to the maximum permafrost depth for the base-case scenario (approximately 100 m). These permafrost depths were obtained by adjusting the top surface boundary condition for temperature as described in Section 4.3.1.3 and Section 4.3.4. Figure 4.8 and Figure 4.9 illustrate the subsurface temperature profiles with shallow permafrost and deep permafrost, respectively.

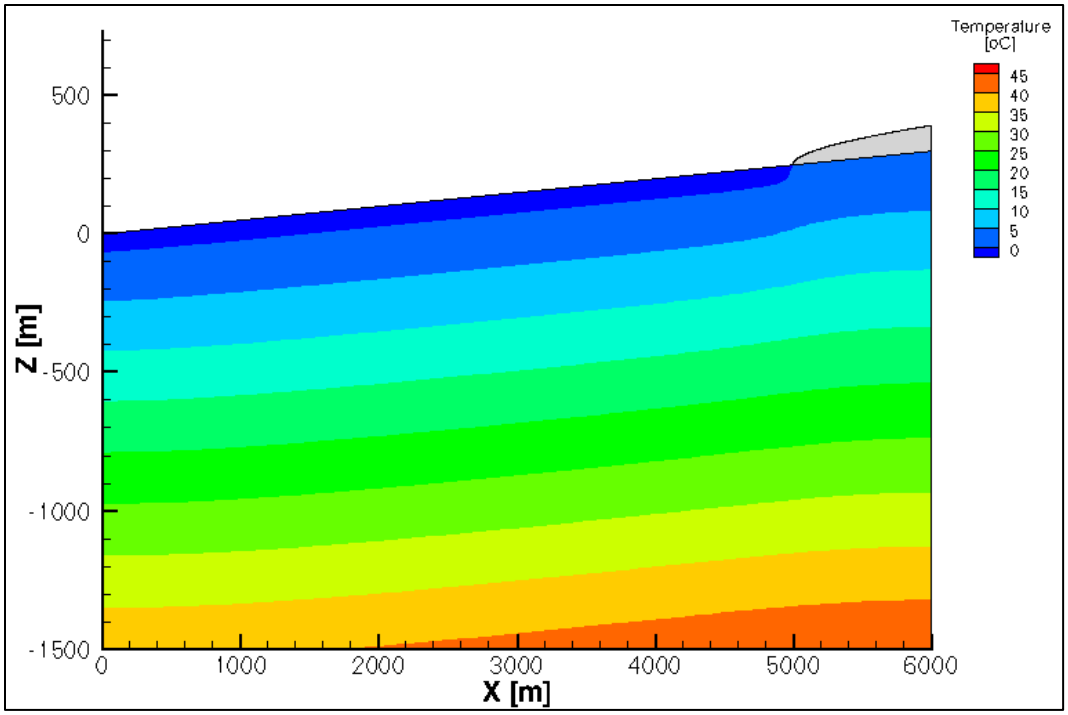

Figure 4.8 West-East cross-section of steady-state temperature distribution for density-dependent flow with heat transport for shallow permafrost

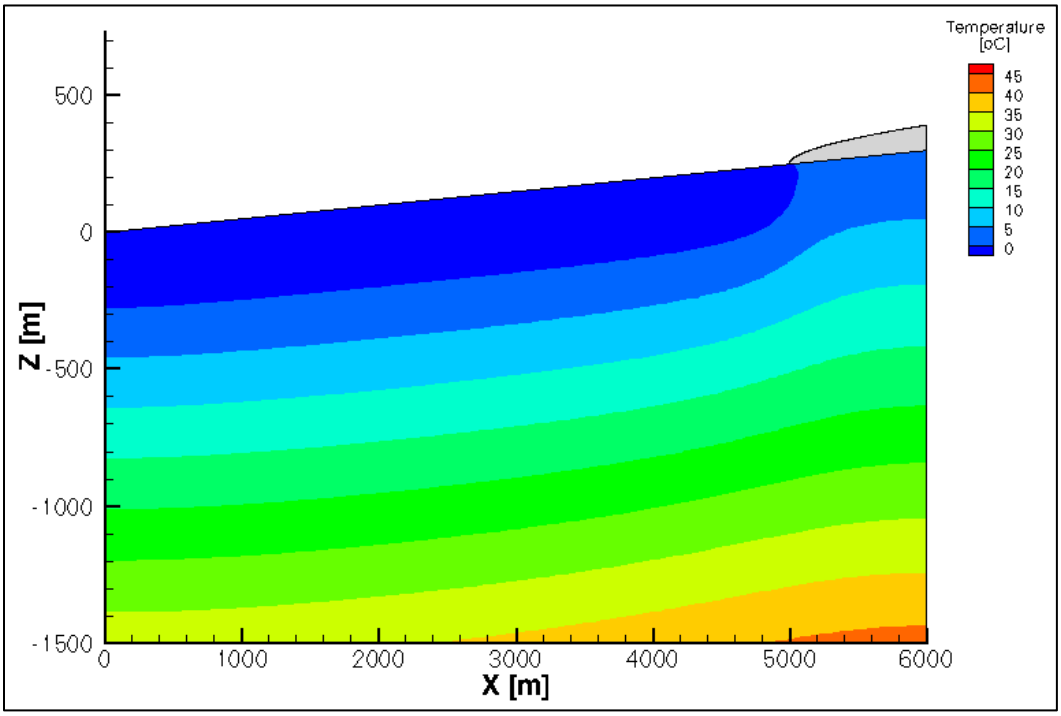

Figure 4.9 West-East cross-section of steady-state temperature distribution for density-dependent flow with heat transport for deep permafrost

The changes to the temperature and permafrost depth resulted in differences in the pressure, head, and velocity magnitude distributions surrounding the permafrost. In the shallow permafrost scenario, the pressure and head distributions resemble those of a system without permafrost. In general, with deeper permafrost, lower pressure and head values extend deeper into the subsurface. Figure 4.10 and Figure 4.11 illustrate the pressure and head distributions with shallow permafrost; Figure 4.12 and Figure 4.13 illustrate the pressure and head distributions with deep permafrost.

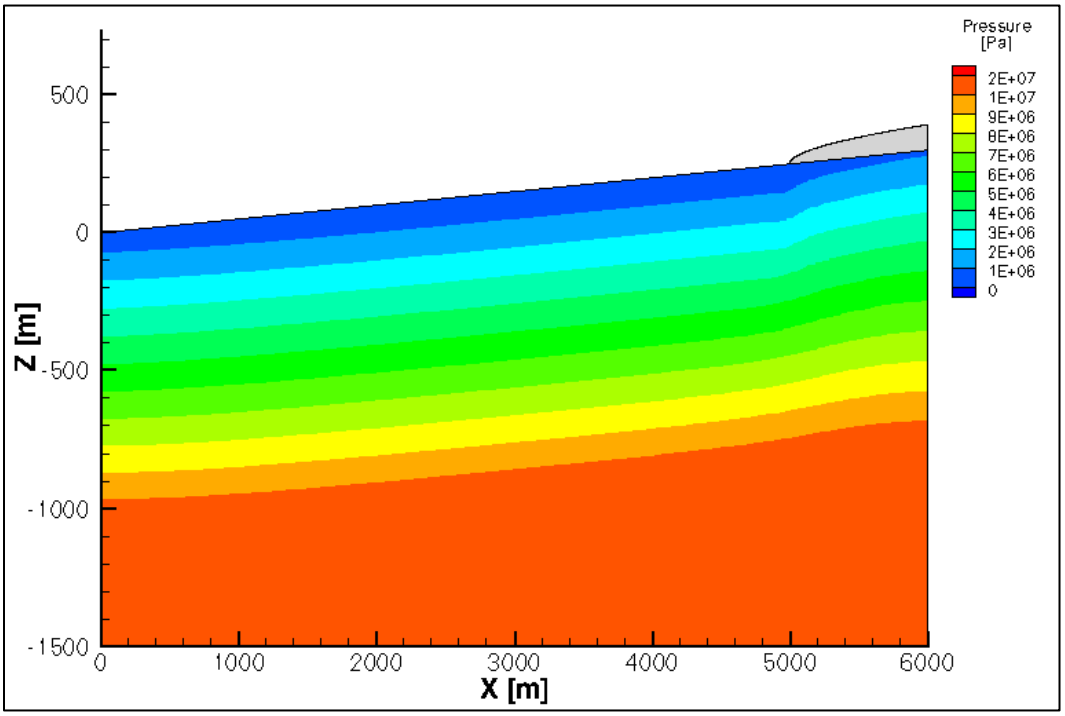

Figure 4.10 West-East cross-section of steady-state density-dependent pressure for density-dependent flow with heat transport for shallow permafrost

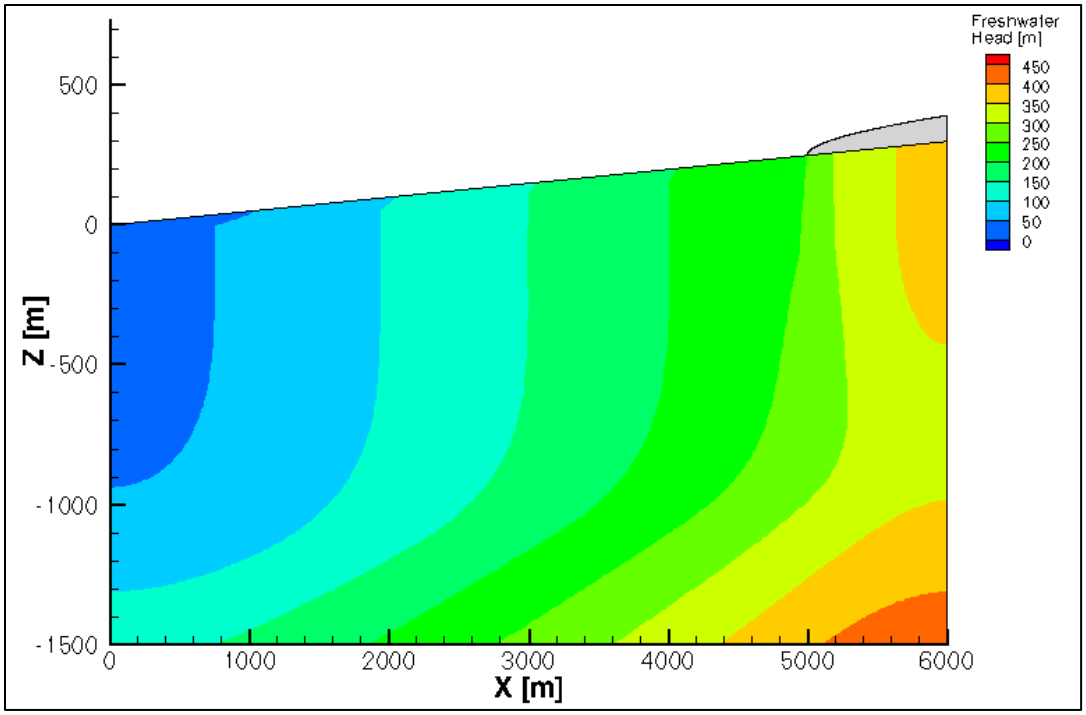

Figure 4.11 West-East cross-section of steady-state density-dependent head distribution for density-dependent flow with heat transport for shallow permafrost

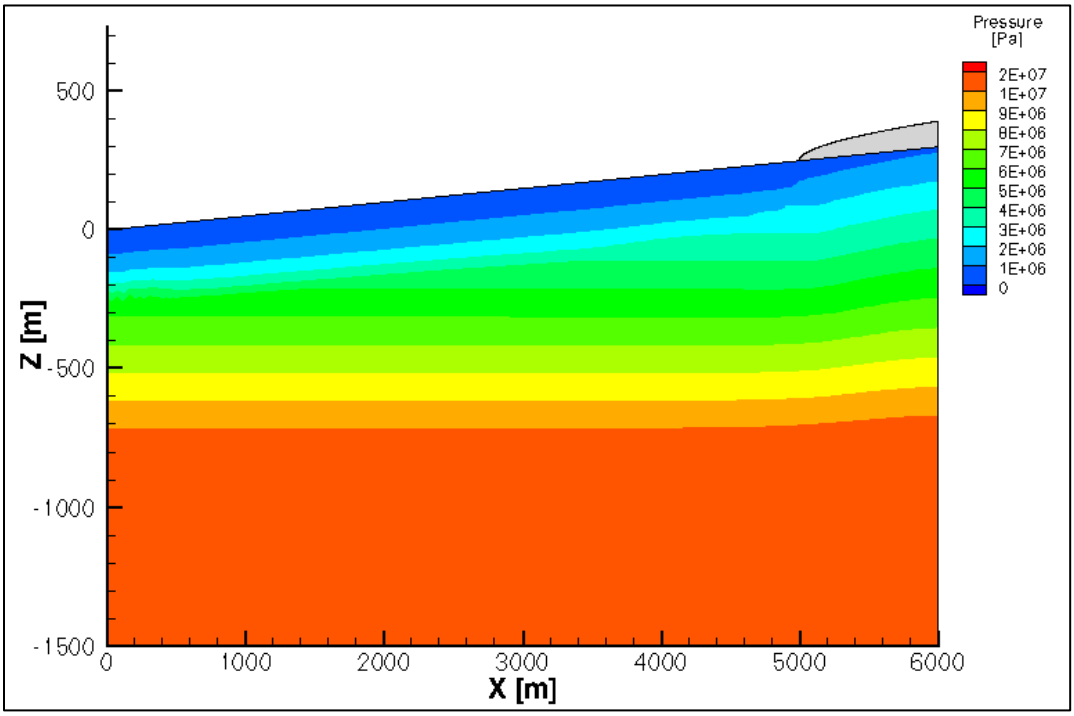

Figure 4.12 West-East cross-section of steady-state density-dependent pressure for density-dependent flow with heat transport for deep permafrost

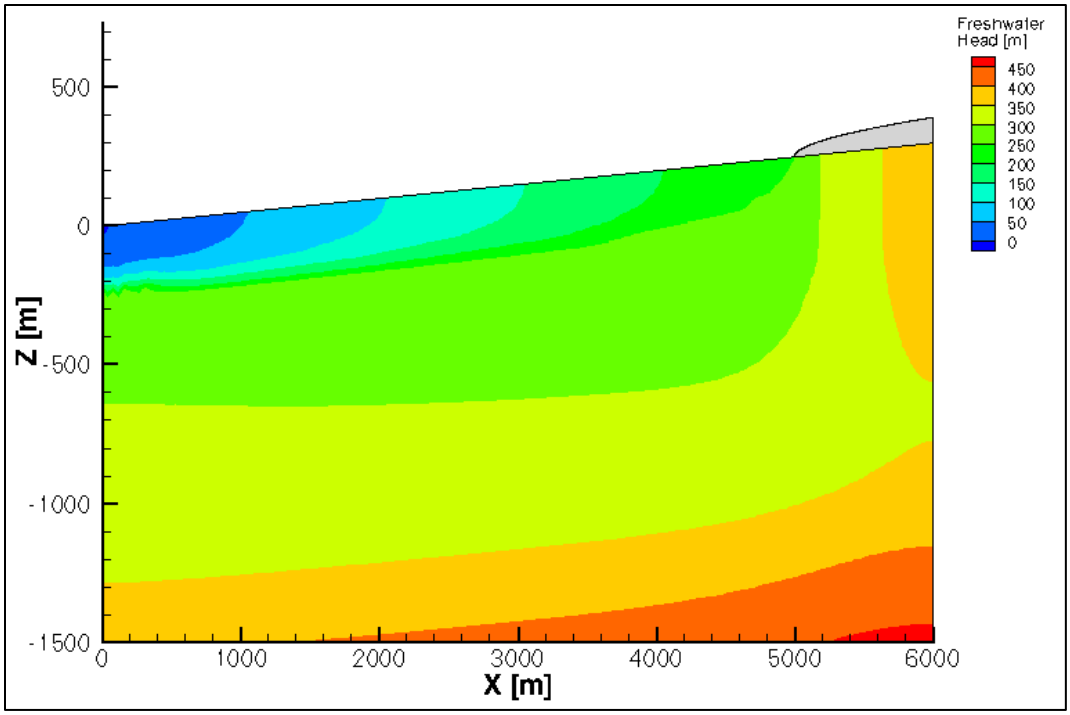

Figure 4.13 West-East cross-section of steady-state density-dependent head distribution for density-dependent flow with heat transport for deep permafrost

Figure 4.14 illustrates the velocity magnitude distribution with shallow permafrost. It appears that the permafrost does not have an effect on the velocity magnitude, which only varies with depth in this scenario because the depth of the permafrost is too shallow (approximately 40 m) in relation to the element or mesh size (50 m). Figure 4.15 illustrates the velocity magnitude distribution with deep permafrost and shows that the velocity magnitude is reduced by up to five orders of magnitude within the permafrost region. The velocity magnitude remains at least four orders of magnitude lower beneath the permafrost than beneath the ice sheet, unlike in the original scenario (intermediate permafrost depth; Figure 4.7) where the velocity magnitude beneath the permafrost was the same as the velocity magnitude beneath the ice sheet at a similar depth.

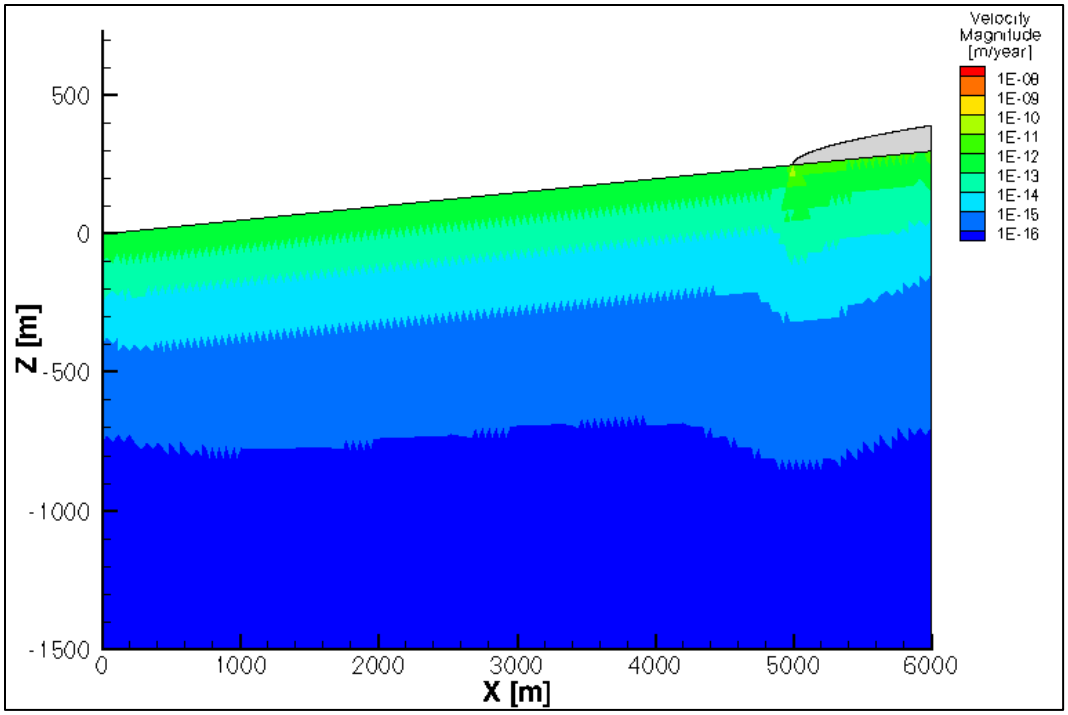

Figure 4.14 West-East cross-section of steady-state velocity magnitude distribution for density-dependent flow with heat transport for shallow permafrost

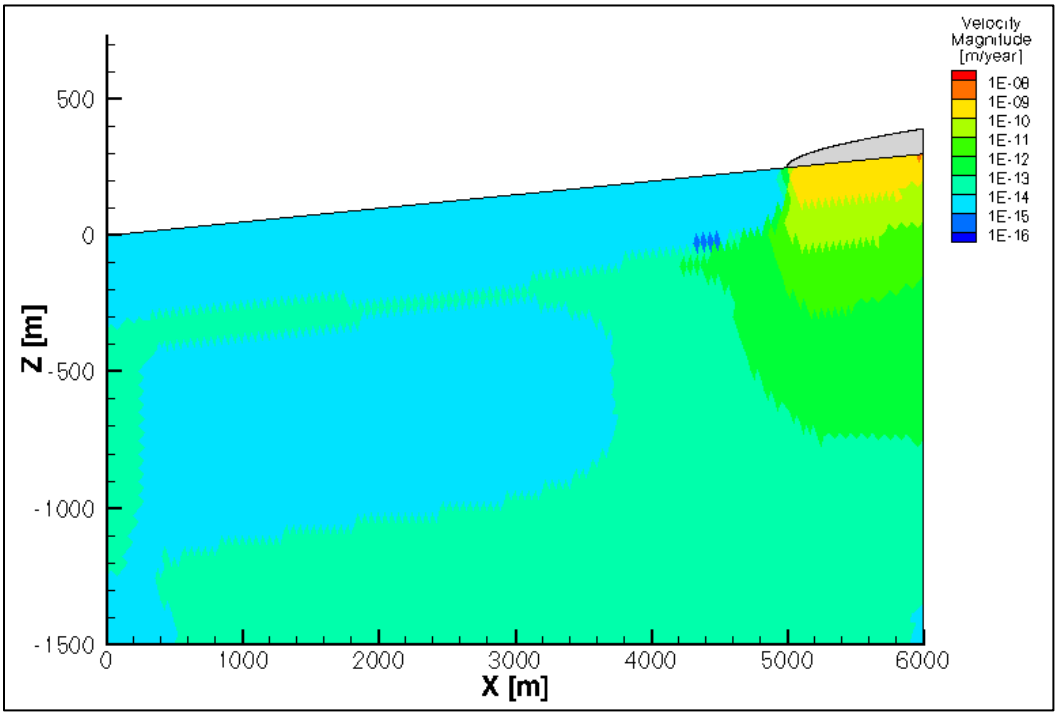

Figure 4.15 West-East cross-section of steady-state velocity magnitude distribution for density-dependent flow with heat transport for deep permafrost

The transient simulation included fluid flow (Darcy's Law), temperature (Heat Transport in Porous Media), and one-dimensional hydromechanical coupling (Section 3.2.4). Over the course of 500 years, which was enough time to observe the impact of the ice sheet and initial permafrost depth on the permafrost distribution, the ice sheet advanced over the surface. As the ice sheet advanced, pressures beneath it were raised. The velocity magnitude distribution also followed the same trends as described above for the steady-state distribution with the exact distribution shifting as the ice sheet advanced and the permafrost melted.

The intermediate permafrost depth scenario was examined first with one-year time steps. As the ice sheet advanced at 1 m/year, the permafrost remained frozen beneath the ice sheet for approximately 50 years. At 50 years after the ice sheet began to advance, the permafrost started to melt and continued to do so over the next three years until there was no more permafrost beneath the ice sheet (Figure 4.16). This pattern continued every 50 years for the remainder of the simulation. At most, the permafrost remained beneath the ice sheet up to approximately 45 m in from the edge of the ice sheet.

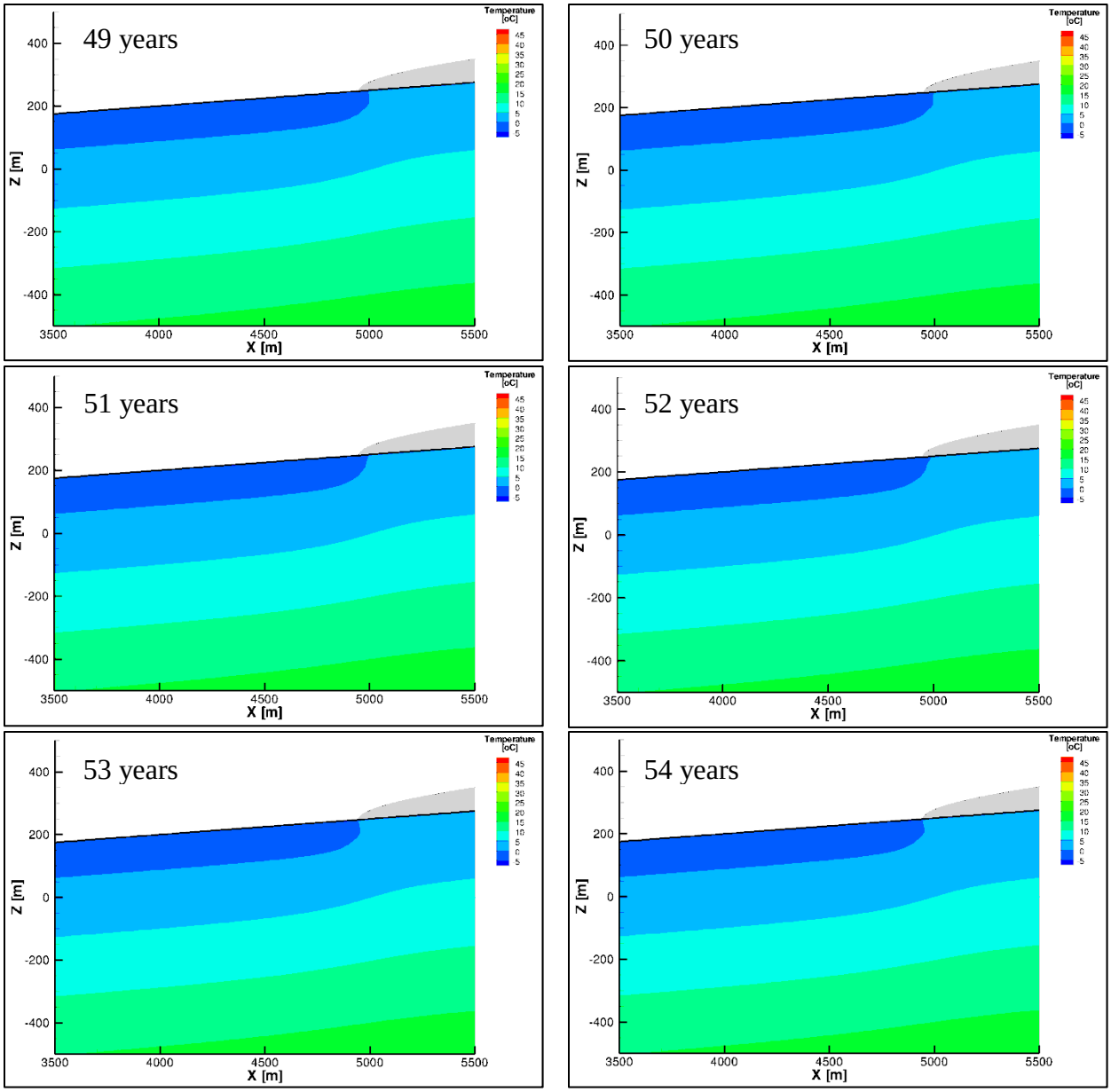

Figure 4.16 West-east cross-sections of temperature distribution for density-dependent flow with heat transport for an intermediate permafrost depth from 49 to 54 years after the start of ice sheet advance

In all three scenarios (shallow, intermediate, and deep permafrost), the permafrost remained beneath the ice sheet to varying degrees as the ice sheet advanced. In the shallow permafrost scenario, the permafrost remained to its initial depth beneath the advancing ice sheet for approximately 30 years before beginning to melt. At that time, the permafrost reached approximately 20 m in from the edge of the ice sheet. As it thawed, it thawed more from the bottom of the permafrost up than from the side such that the depth of permafrost beneath the ice sheet decreased further in from the edge of the ice sheet as illustrated Figure 4.17. Melting also

occurred much more gradually than in the scenario with the intermediate permafrost depth. Around 52 years, when no permafrost remained beneath the ice sheet, melting ceased again. Also unlike the scenario with intermediate permafrost depth, the shallow scenario did not repeat this pattern of thawing at regular intervals. For most of the simulation, thawing was continuous, and some permafrost remained beneath the ice sheet between approximately 10 and 20 m in from the edge of the ice sheet although often at reduced depths.

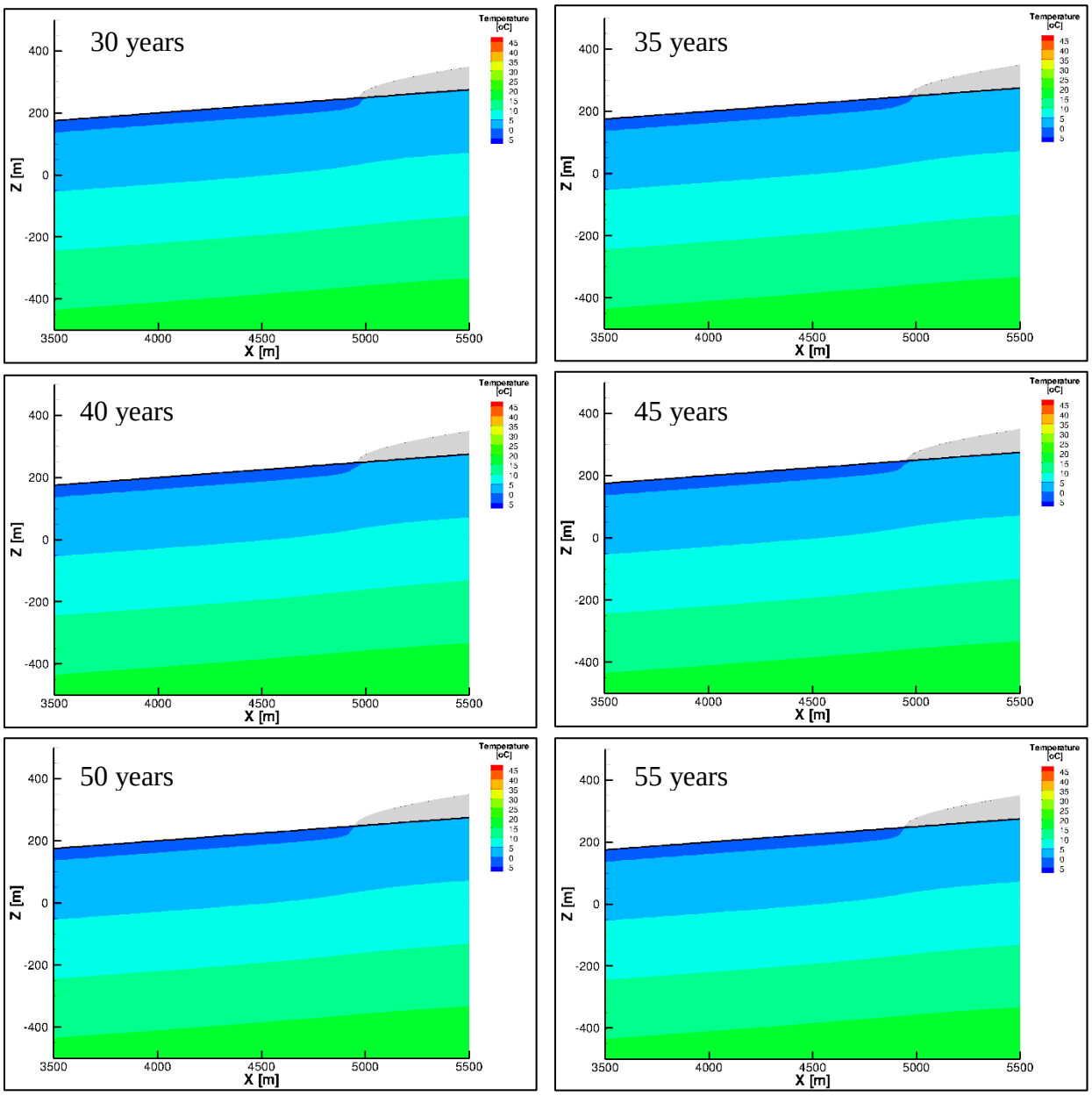

Figure 4.17 West-east cross-sections of temperature distribution for density-dependent flow with heat transport for shallow permafrost from 30 to 55 years after the start of ice sheet advance (5-year intervals)

In the deep permafrost scenario, the permafrost already extended beneath the ice sheet to approximately 50 m from the ice sheet's edge at the start of the simulation. Because the atmospheric temperature needed to be much colder (-8 ^{o}C) to maintain permafrost to a depth of approximately 300 m, the temperature of the permafrost was also colder than with the shallow and intermediate permafrost depths. Thus, Figure 4.18 shows two temperature intervals below freezing (0 ^{o}C to -5 ^{o}C in light blue and less than -5 ^{o}C in dark blue) with the permafrost that is beneath the ice sheet ranging in temperature from 0 ^{o}C to -5 ^{o}C. Additionally, there is a great enough difference between the permafrost temperature and the basal temperature of 0.1 ^{o}C that the permafrost is shown to melt from the top as well as the bottom.

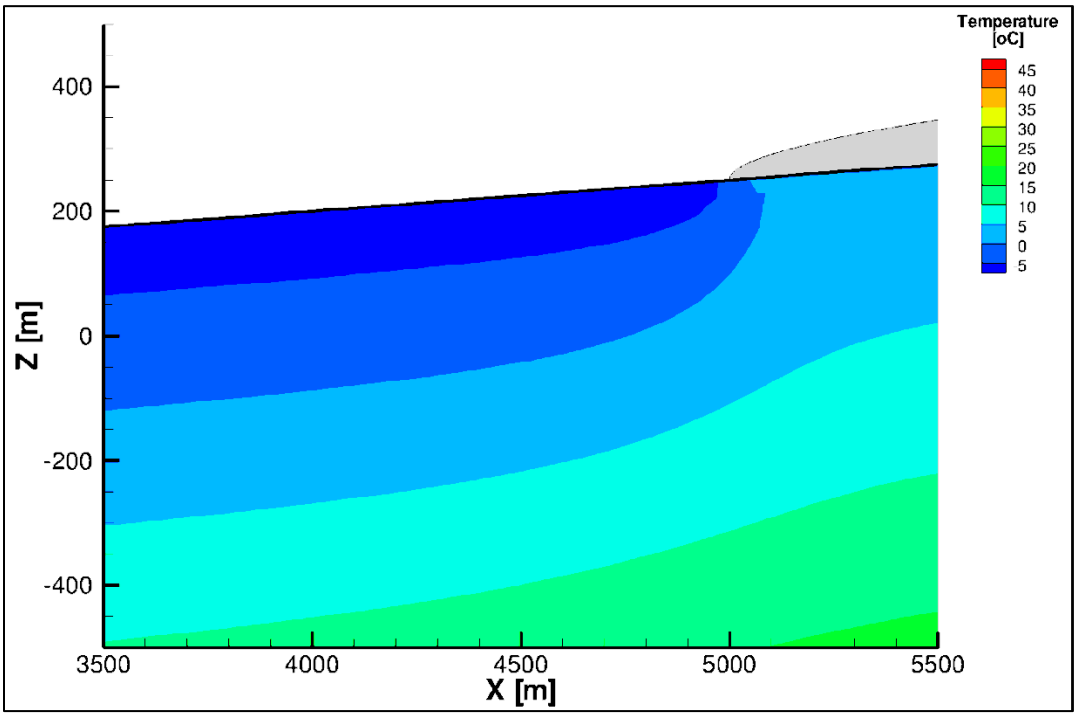

Figure 4.18 West-east cross-section of temperature distribution for density-dependent flow with heat transport for deep permafrost 1 year after the start of ice sheet advance

In the deep permafrost scenario, the permafrost distribution that existed at 1 year remained for approximately 50 years at which time the permafrost began to melt. That was also the time at which the edge of the ice sheet had reached the region of colder permafrost (-5 ^{o}C or less). Melting ceased six years later (Figure 4.19). This pattern continued every 50 years for the remainder of the simulation. At most, the permafrost remained beneath the ice sheet up to approximately 100 m in from the edge of the ice sheet.

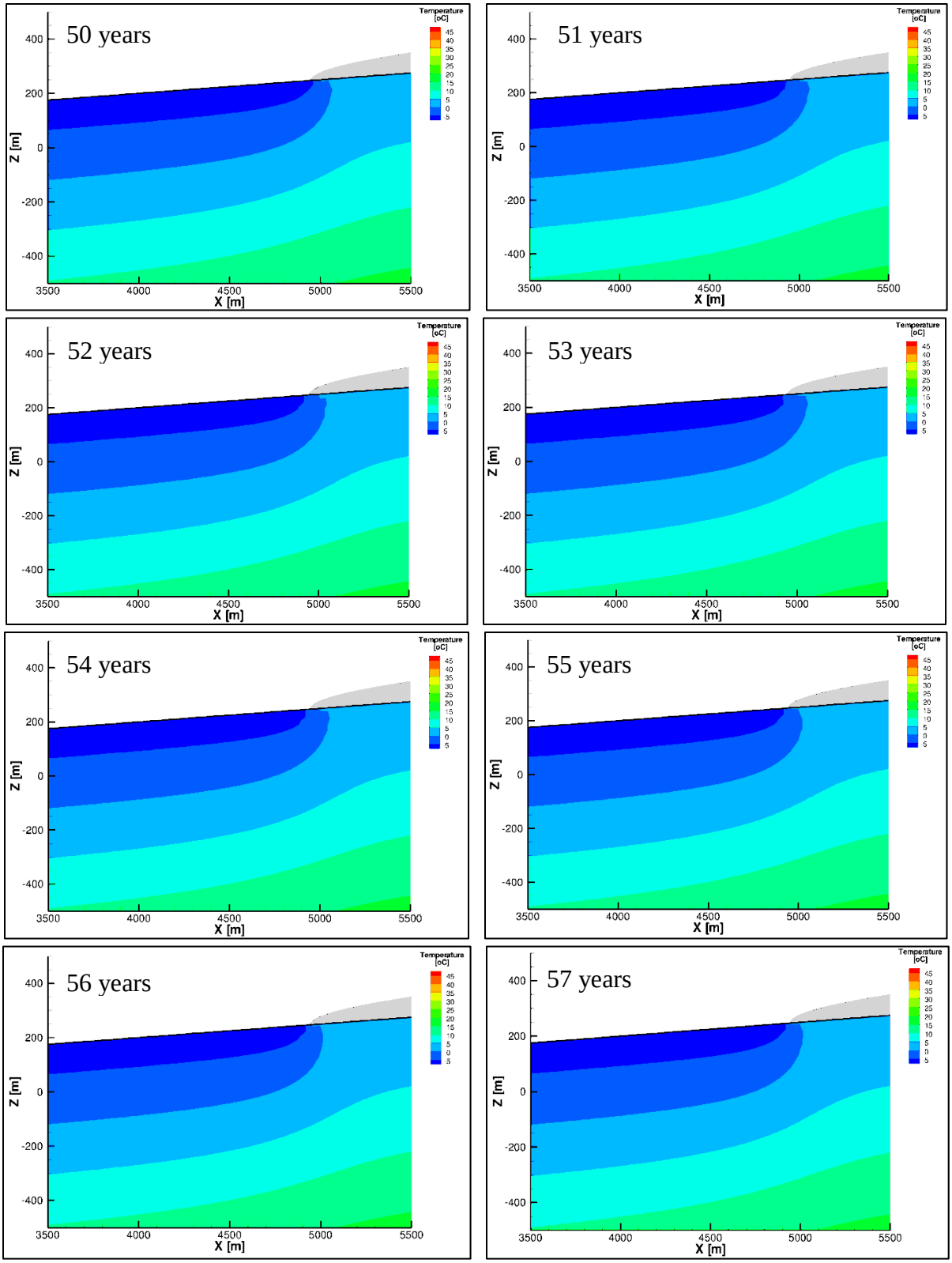

Figure 4.19 West-east cross-sections of temperature distribution for density-dependent flow with heat transport for deep permafrost from 50 to 57 years after the start of ice sheet advance

4.4.2 Rate of Ice Sheet Advance and Retreat

To examine the impact of the rate of ice sheet advance on the permafrost distribution, the shallow, intermediate, and deep permafrost scenarios were each re-run with a rate of ice sheet advance of 2 m/year. The doubling of the rate of ice sheet advance did not change the maximum distance from the edge of the ice sheet to which the permafrost existed beneath the ice sheet, but it did decrease by half the length of time before the permafrost began to melt. For example, for the base-case or intermediate permafrost depth scenario, the permafrost began to melt around 25 years after the start of ice sheet advance with a rate of 2 m/year instead of around 50 years after the start of ice sheet advance with a rate of 1 m/year with the permafrost reaching 45 m in from the edge of the ice sheet in both scenarios.

4.4.3 Talik Size

Subsequent scenarios included one to three taliks of two different sizes (diameter/width): 50 m and 100 m. As with the previous simulations, the initial pressure and temperature conditions were developed for the transient analyses by first running steady-state simulations using the properties and boundary conditions detailed in Section 4.3 with the addition of one talik. Within the talik, the water table was set at the ground surface and a surface temperature of 2 ^{o}C was applied.

The first steady-state simulation to be run involved only the Darcy's Law physics (Section 3.2.1) with a constant depth-dependent TDS distribution, which is illustrated in Figure 4.3. This simulation established the regional flow system yielding the pressure distribution and velocity field as input for the next steady-state simulation, which included both the Darcy's Law and Heat Transfer in Porous Media physics (Section 3.2.3). Figure 4.20, Figure 4.21, Figure 4.22, and Figure 4.23 illustrate the results of this steady-state simulation, which were the initial conditions (pressure, hydraulic head, temperature, and velocity magnitude respectively) for the transient analyses.

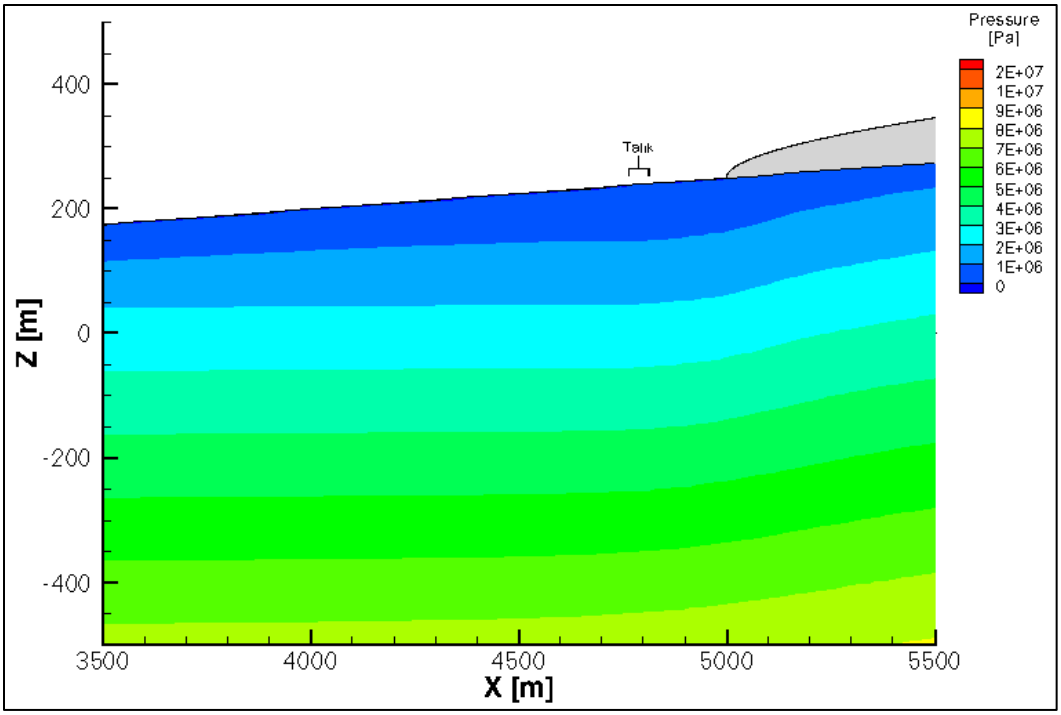

Figure 4.20 West-east cross-section of steady-state density-dependent pressure distribution for density-dependent flow with heat transport for an intermediate permafrost depth and one 50 m-wide talik

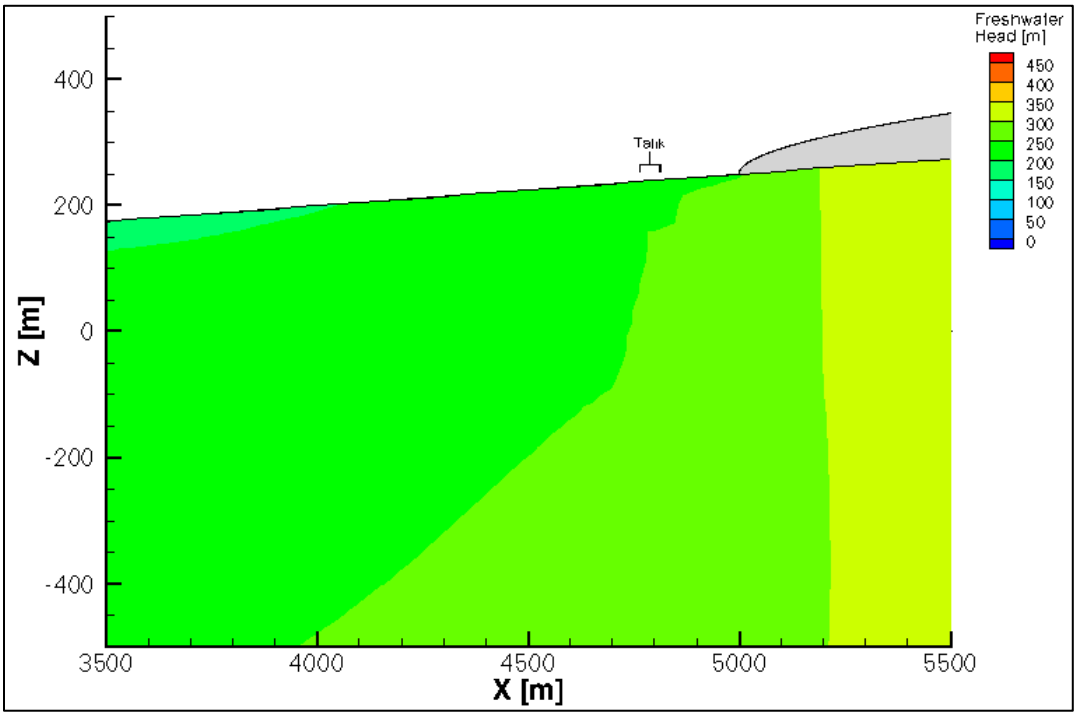

Figure 4.21 West-east cross-section of steady-state density-dependent freshwater head distribution for density-dependent flow with heat transport for an intermediate permafrost depth and one 50 m-wide talik

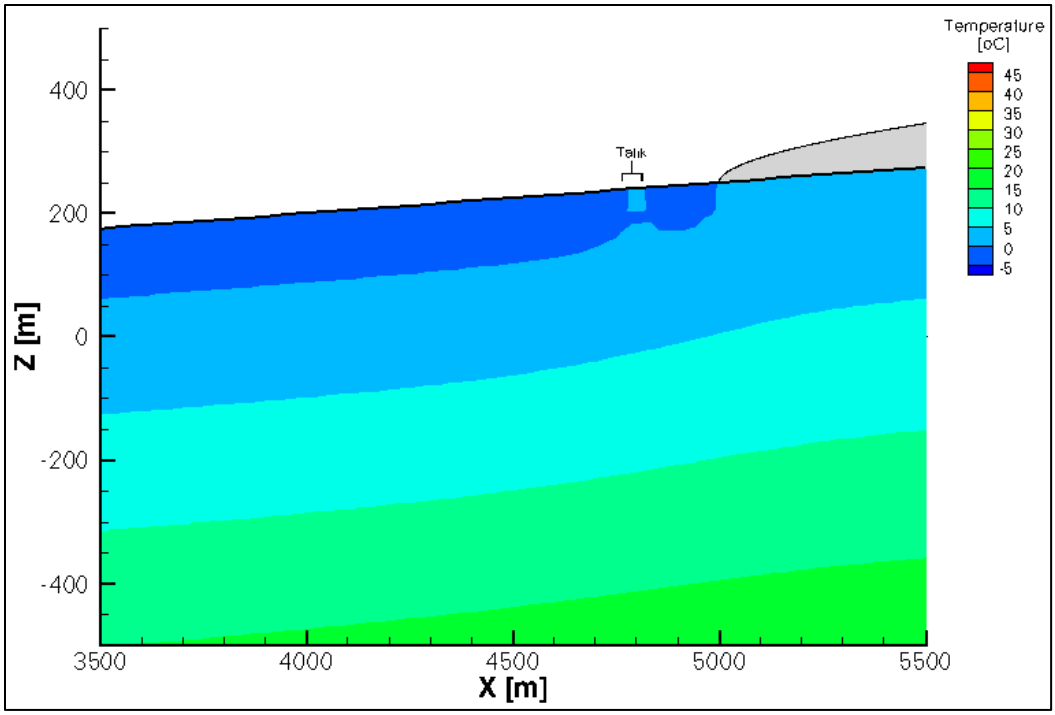

Figure 4.22 West-east cross-section of steady-state temperature distribution for density-dependent flow with heat transport for an intermediate permafrost depth and one 50 m-wide talik

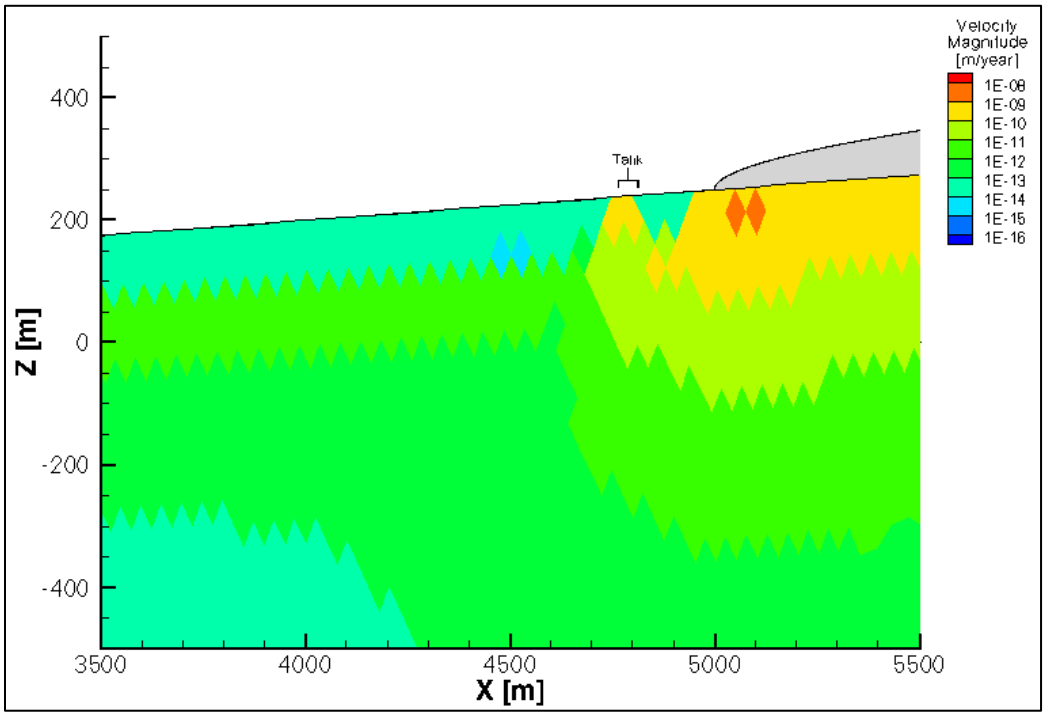

Figure 4.23 West-east cross-section of steady-state velocity magnitude distribution for density-dependent flow with heat transport for an intermediate permafrost depth and one 50 m-wide talik

As with the previous simulations without any taliks, Figure 4.20 and Figure 4.21 show that pressure and hydraulic head values were elevated beneath the ice sheet due to the weight of the ice. The impact of the talik on the pressure distribution is minimal, only slightly lowering the pressure at the location of the talik. The head distribution illustrated the impact of the talik more clearly with the region of 200 m to 250 m head values expanded from the location of the talik beneath the permafrost to a depth of approximately 1000 m. The temperature increased linearly with depth (Figure 4.22).

Figure 4.22 also shows the initial depth of permafrost at approximately 100 m except where a 2 ^{o}C surface temperature representing a surface water body located between 4750 m and 4800 m led to the formation of a talik. The talik formed by this 50 m-wide surface water body did not extend through the entire layer of permafrost. This unfrozen zone extended to a depth of approximately 35 m, leaving an approximately 20 m layer of permafrost beneath the talik and raising the base of the permafrost layer beneath the talik to a depth of approximately 55 m. The base of the permafrost layer in the region between the talik and ice sheet was also raised so that the permafrost was between 55 m (closer to the edge of the ice sheet) and 70 m (further from the edge of the ice sheet) thick in that region.

Figure 4.23 illustrates the velocity magnitude distribution with one 50 m-wide talik. Within the talik itself, above and below the permafrost layer in that region, the velocity magnitudes were elevated by three to four orders of magnitude, matching the velocity magnitude beneath the edge of the ice sheet at similar depths. This velocity magnitude distribution does not show as significant a reduction in velocity magnitude within the layer of permafrost directly beneath the talik as in the previous simulations that did not include a talik (two orders of magnitude instead of four orders of magnitude; on the order of 10^{-12} m/year). This difference in the velocity magnitude is a result of the temperature of the permafrost in that region and the manner in which the permeability was reduced as a function of temperature. Temperatures in the layer of permafrost beneath the talik were below freezing, but they were only as cold as approximately -0.26 ^{o}C. As described in Section 4.3.4, the permeability is reduced by six orders-of-magnitude as a function of temperature between 0.5 ^{o}C and -0.5 ^{o}C.).

To examine the impact of the talik size on the permafrost distribution and flow system during subsequent ice sheet advance, a 100 m-wide talik between 4700 m and 4800 m was included. Figure 4.24 illustrates the subsurface temperature profile for this wider talik, which extends through the entire layer of permafrost. Figure 4.25, Figure 4.26, and Figure 4.27 illustrate the pressure, freshwater head, and velocity magnitude distributions for this simulation and show that the same pattern of alteration from the case without taliks as the 50 m-wide talik did, but to a greater extent or over a larger area.

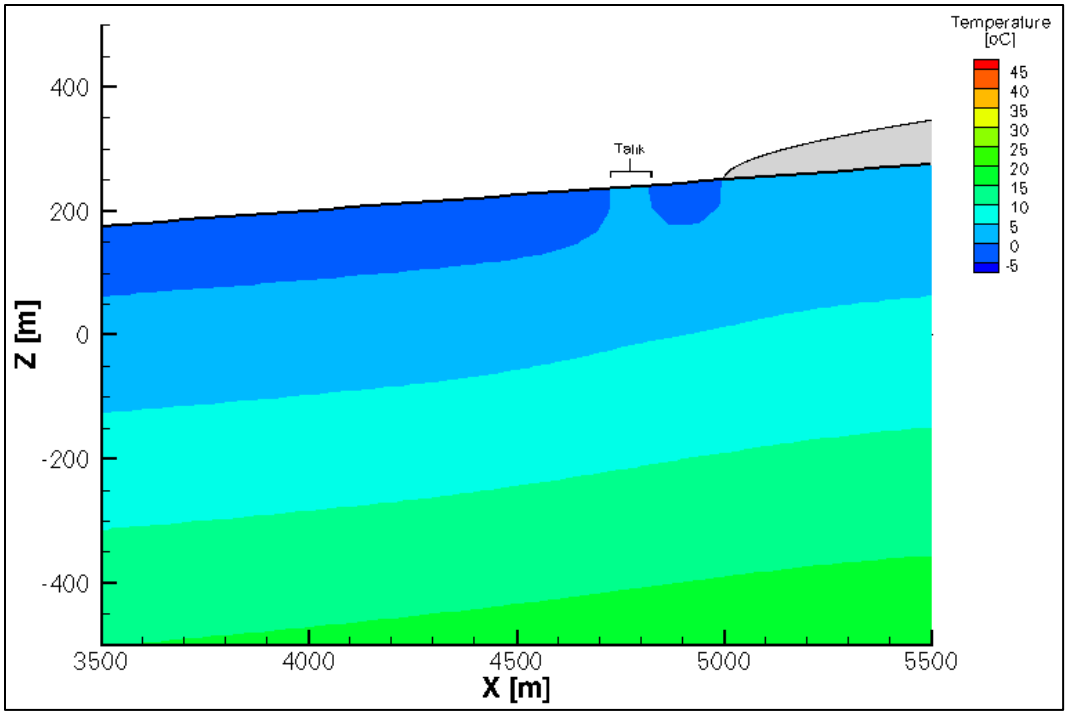

Figure 4.24 West-east cross-section of steady-state temperature distribution for density-dependent flow with heat transport for an intermediate permafrost depth and one 100 m-wide talik

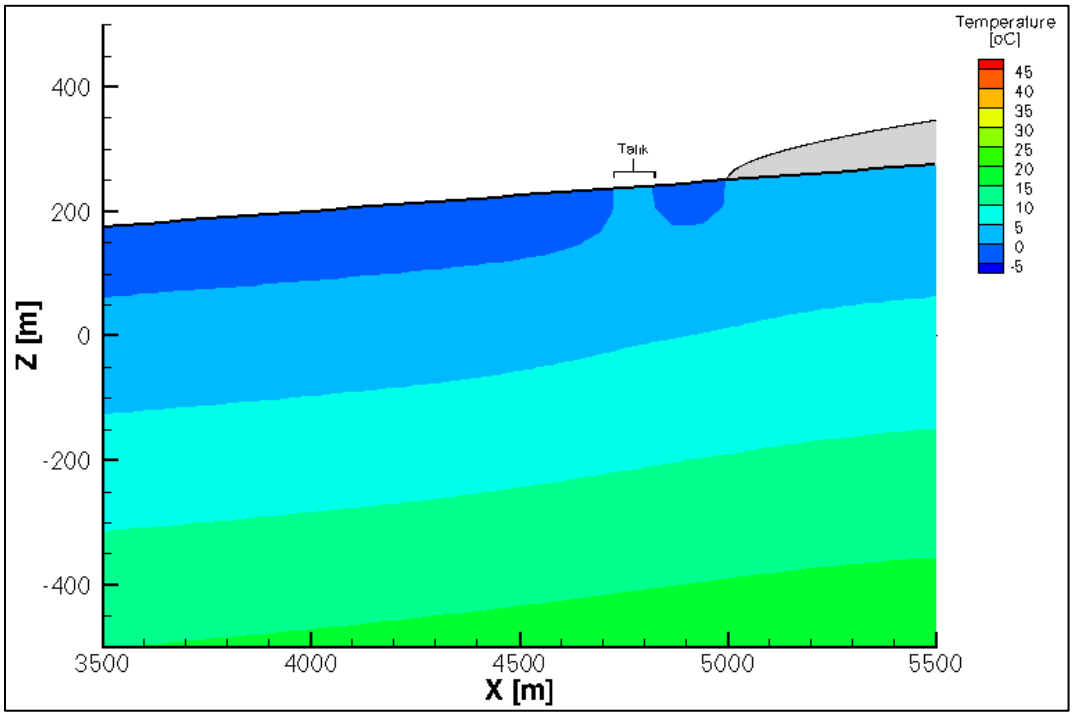

Figure 4.25 West-east cross-section of steady-state density-dependent pressure distribution for density-dependent flow with heat transport for an intermediate permafrost depth and one 100 m-wide talik

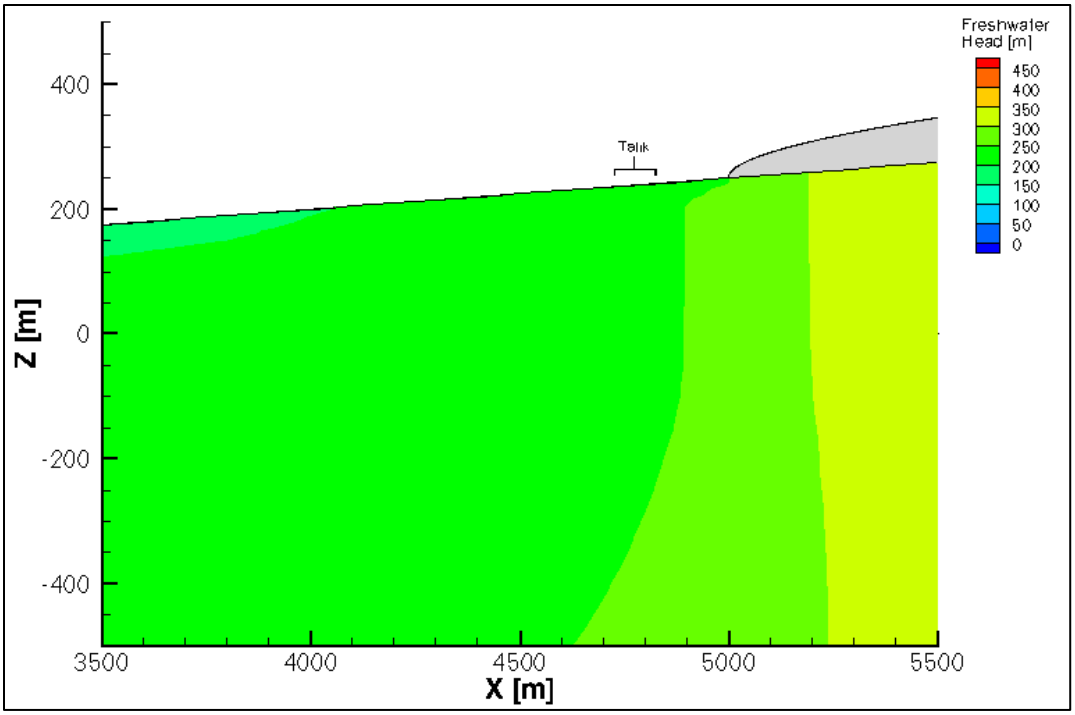

Figure 4.26 West-east cross-section of steady-state density-dependent freshwater head distribution for density-dependent flow with heat transport for an intermediate permafrost depth and one 100 m-wide talik

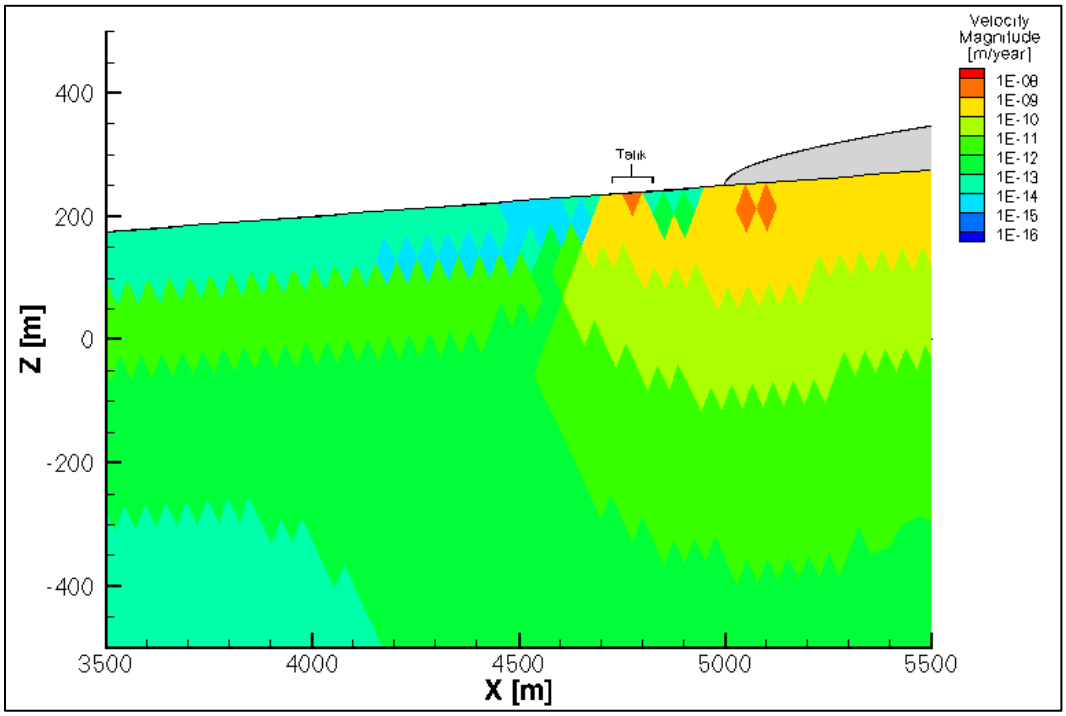

Figure 4.27 West-east cross-section of steady-state velocity magnitude distribution for density-dependent flow with heat transport for an intermediate permafrost depth and one 100 m-wide talik

A scenario with a 100 m-wide talik located between 3500 m and 3600 m (1400 m from the edge of the ice sheet) (Figure 4.28) was also examined and showed that the velocity magnitude remained elevated beneath the entire 1400 m of permafrost between the talik and the edge of the ice sheet (Figure 4.29).

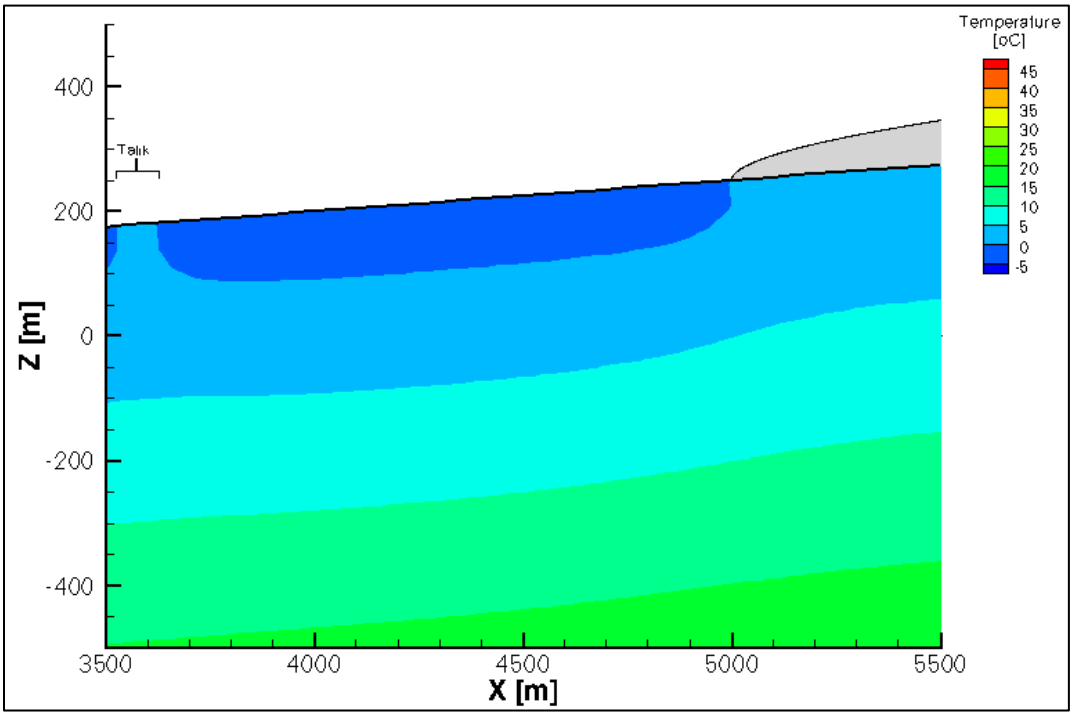

Figure 4.28 West-east cross-section of steady-state temperature distribution for density-dependent flow with heat transport for an intermediate permafrost depth and one 100 m-wide talik 1400 m west of the ice sheet

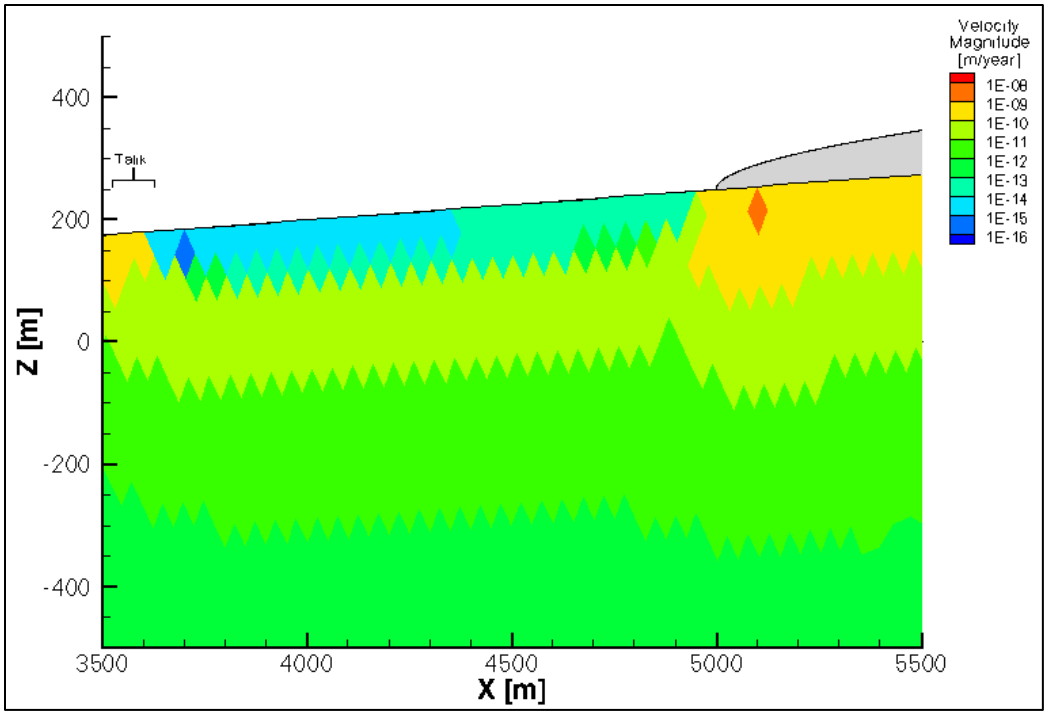

Figure 4.29 West-east cross-section of steady-state velocity magnitude distribution for density-dependent flow with heat transport for an intermediate permafrost depth and one 100 m-wide talik 1400 m west of the ice sheet

The initial 100 m-wide talik scenario with the taliks located between 4700 m and 4800 m was re-run without the ice sheet to investigate the impact of the ice sheet on the velocity magnitude distribution in the presence of an open talik. Figure 4.30 illustrates the temperature distribution without the ice sheet, showing permafrost on both sides of the talik and extending to both sides of the domain. Figure 4.31 shows the velocity magnitude distribution. Without the ice sheet, the only elevated velocity magnitudes are as a result of the open talik.

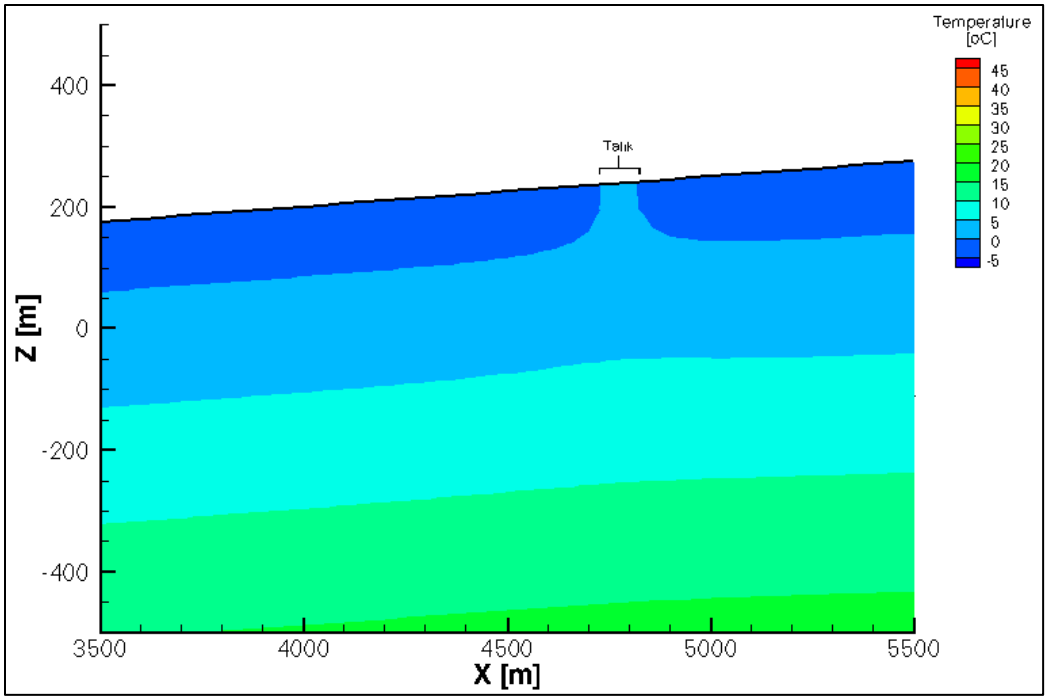

Figure 4.30 West-east cross-section of steady-state temperature distribution for density-dependent flow with heat transport for an intermediate permafrost depth and one 100 m-wide talik without an ice sheet

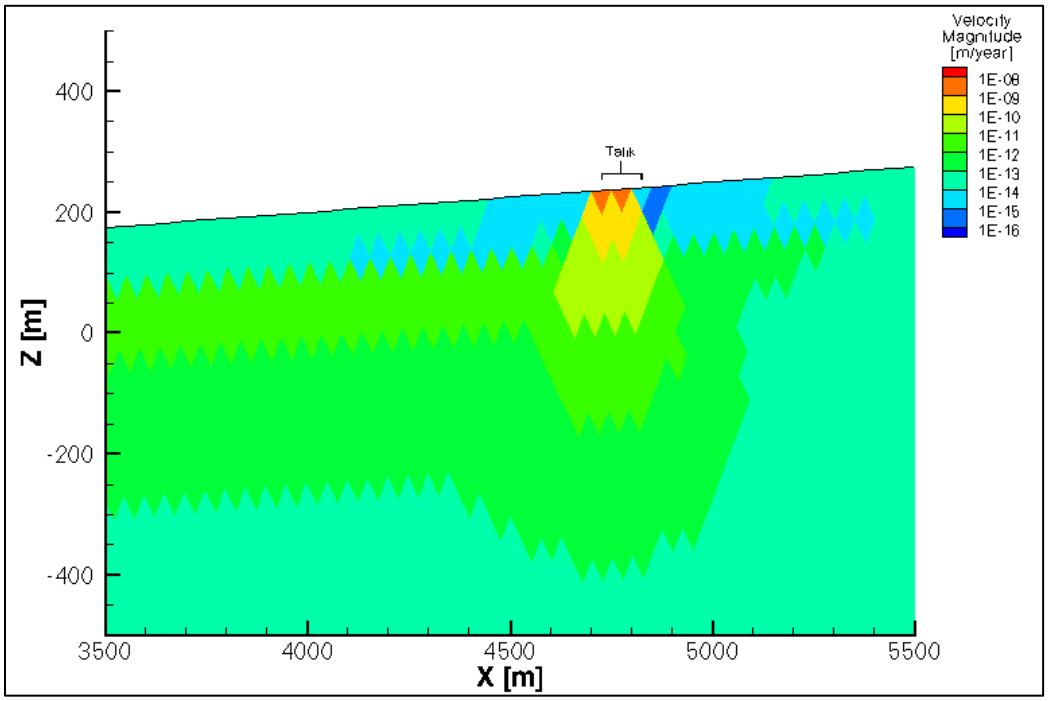

Figure 4.31 West-east cross-section of steady-state velocity magnitude distribution for density-dependent flow with heat transport for an intermediate permafrost depth and one 100 m-wide talik without an ice sheet

The transient simulation included fluid flow (Darcy's Law), temperature (Heat Transport in Porous Media), and one-dimensional hydromechanical coupling (Section 3.2.4). As with the previous simulations without taliks, a 500-year scenario with ice sheet advance was examined. The ice sheet advanced at a rate of 2 m/year. The impact of the ice sheet on the pressure, head, temperature, and velocity magnitude distributions was also the same. For both scenarios with the taliks, the permafrost began to melt at the same time as in the scenarios without any taliks. The permafrost beneath the ice sheet, although thinner, persisted beneath the ice sheet to the same distance.

The scenario with the 50 m-wide talik was examined first. As the ice sheet advanced at 2 m/year, the permafrost remained frozen beneath the ice sheet for approximately 25 years. At 25 years after the ice sheet began to advance, the permafrost started to melt and continued to do so over the next five years until there was no more permafrost beneath the ice sheet (Figure 4.32). At around 45 years, the permafrost beneath the talik began to thin, and at 50 years, the permafrost beneath the ice sheet began to melt. By 52 years, the talik became a through talik. Figure 4.33 illustrates a portion of the time when the permafrost beneath the talik was melting. The permafrost that remained in the region between the talik and the edge of the ice sheet had melted to become less than half as thick (approximately 40 m) as the permafrost on the side of the talik opposite the ice sheet (approximately 110 m) (Figure 4.33). That remaining patch of permafrost between the talik and the edge of the ice sheet remained as such beneath the ice sheet as it advanced until approximately 75 years when it began to melt from the base upward before disappearing completely approximately 5 years later.

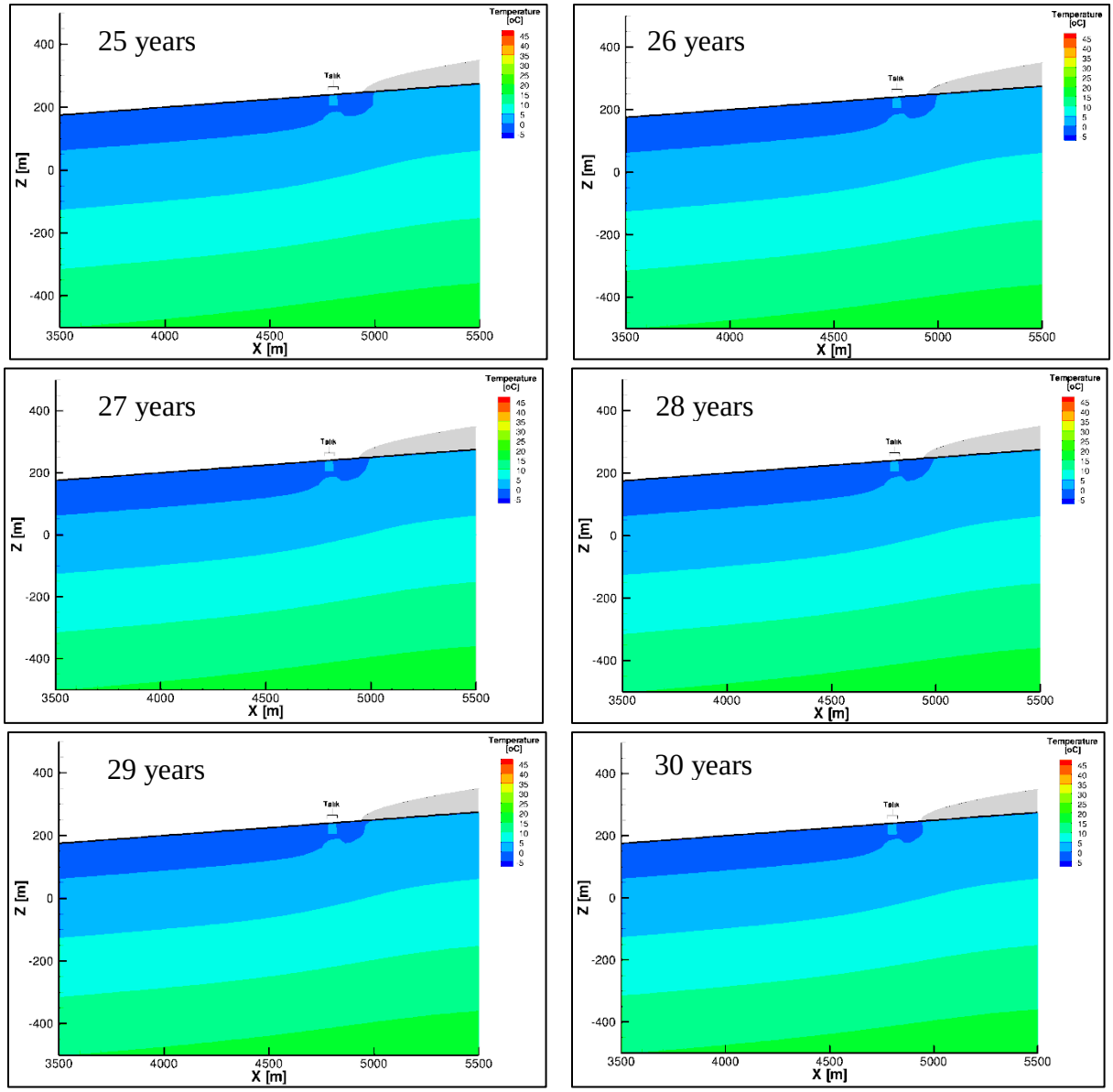

Figure 4.32 West-east cross-sections of temperature distribution for density-dependent flow with heat transport for an intermediate permafrost depth and one 50 m-wide talik from 25 to 30 years after the start of ice sheet advance

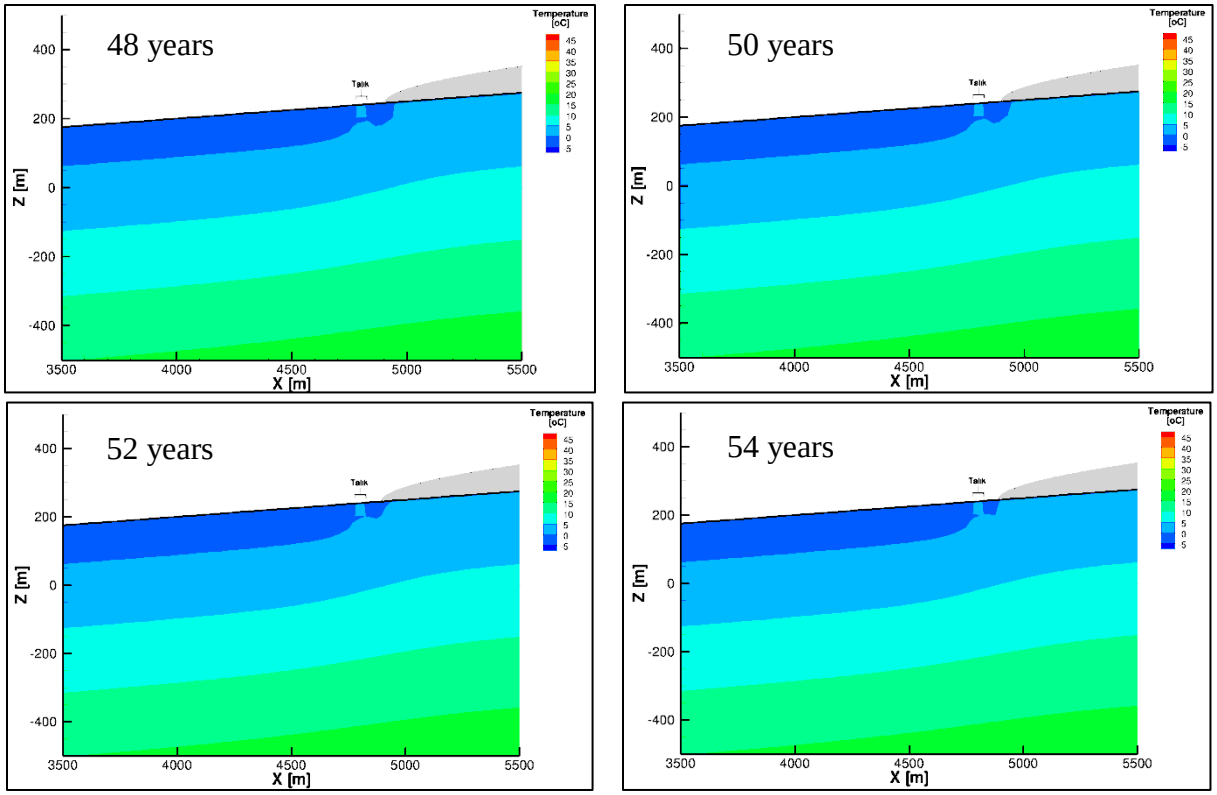

Figure 4.33 West-east cross-sections of temperature distribution for density-dependent flow with heat transport for an intermediate permafrost depth and one 50 m-wide talik from 48 to 54 years after the start of ice sheet advance (2-year intervals)

As shown in Figure 4.34, as the ice sheet passed over the talik region, the permafrost region extended slightly (approximately 20 m) to the east near the base of the permafrost. Once the ice sheet reached the edge of the permafrost at around 105 years, the remainder of the simulation showed the same pattern of permafrost melting as observed in the simulations without taliks. Figure 4.35 shows the velocity magnitude distributions for these same points in time. The velocity magnitude is greatest in and around the talik when it is located directly beside the edge of the ice sheet (around 81 years). The velocity magnitude remained elevated directly beneath the edge of the ice sheet after the talik had been completely covered over by the ice sheet (105 years), but it had returned to a similar distribution as was observed beneath the ice sheet before it began to advance.

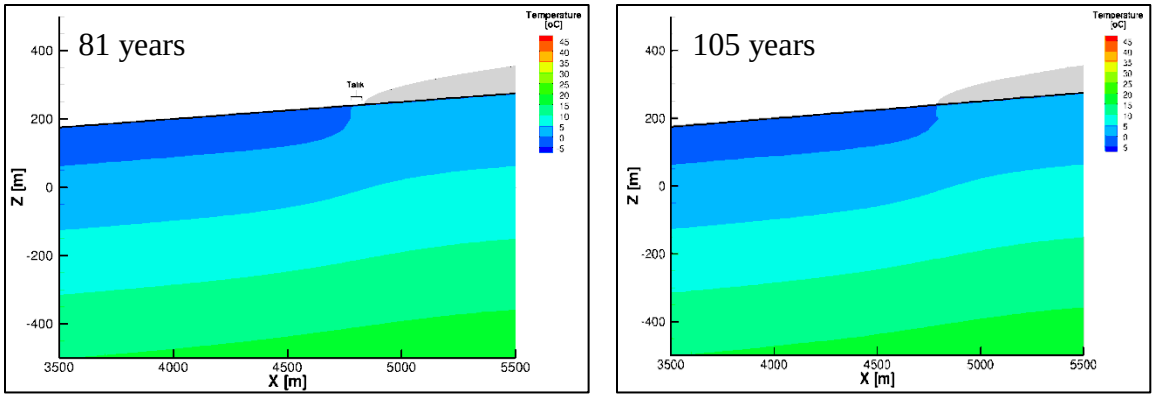

Figure 4.34 West-east cross-sections of temperature distribution for density-dependent flow with heat transport for an intermediate permafrost depth and one 50 m-wide talik at 81 and 105 years after the start of ice sheet advance

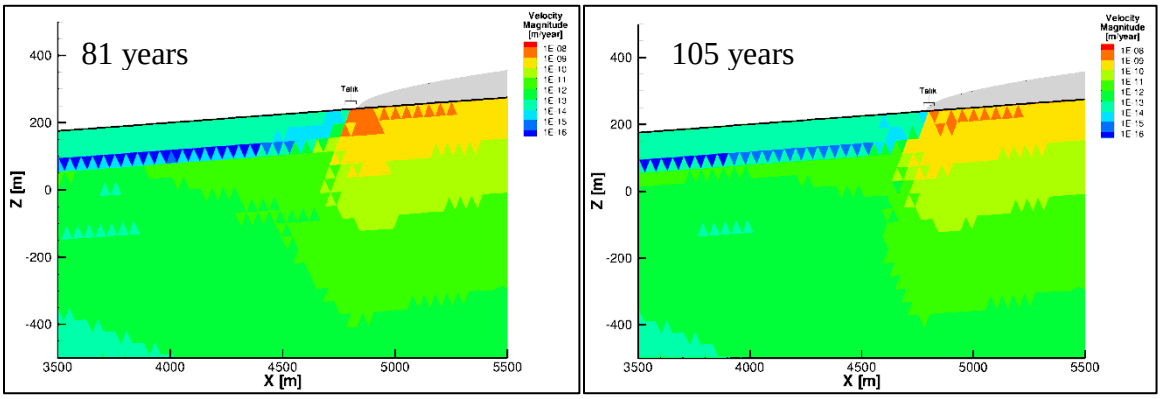

Figure 4.35 West-east cross-sections of velocity magnitude distribution for density-dependent flow with heat transport for an intermediate permafrost depth and one 50 m-wide talik at 81 and 105 years after the start of ice sheet advance

A scenario with a 100 m-wide talik was also examined. Again, the ice sheet advanced at a rate of 2 m/year. As with the previous simulation, the permafrost remained frozen beneath the ice sheet for approximately 25 years at which time it began to melt. By 33 years after the ice sheet began to advance, there was no more permafrost beneath the ice sheet (Figure 4.36). Between 35 years and 49 years after the ice sheet began to advance, the next region of permafrost being covered by the ice sheet expanded to the east and upward from the base of the ice sheet (Figure 4.37). Figure 4.38 shows the velocity magnitude distribution for this same time period and illustrates how the velocity magnitude increased within the talik and beneath the permafrost that remained between the talik and the ice sheet as the ice sheet advanced closer to the talik.

At 50 years, the next approximately 45 m of permafrost that had been covered by the ice sheet began to melt from the bottom up until it too had disappeared from beneath the ice sheet around 52 years. The remaining permafrost between the talik and the edge of the ice sheet, now only around 40 m thick, melted as the ice sheet advanced over it. That permafrost was

completely gone around 83 years. The ice sheet reached the opposite side of the talik around 133 years, and the remainder of the simulation showed the same pattern of permafrost melting as observed in the simulations without taliks. Again, as the ice sheet passed over the talik region, the permafrost region extended approximately 20 m to the east near the base of the permafrost.

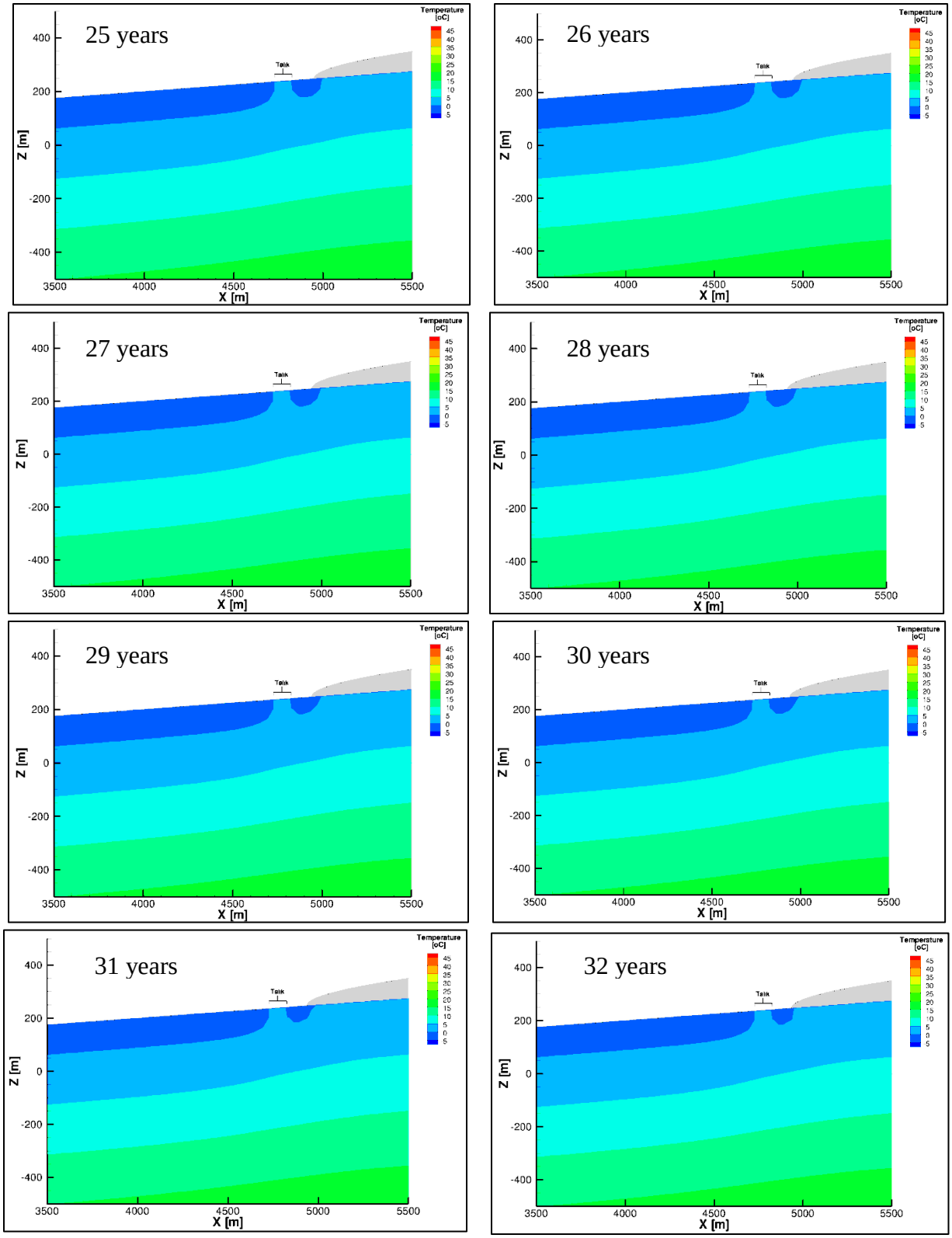

Figure 4.36 West-east cross-sections of temperature distribution for density-dependent flow with heat transport for an intermediate permafrost depth and one 100 m-wide talik from 25 to 32 years after the start of ice sheet advance

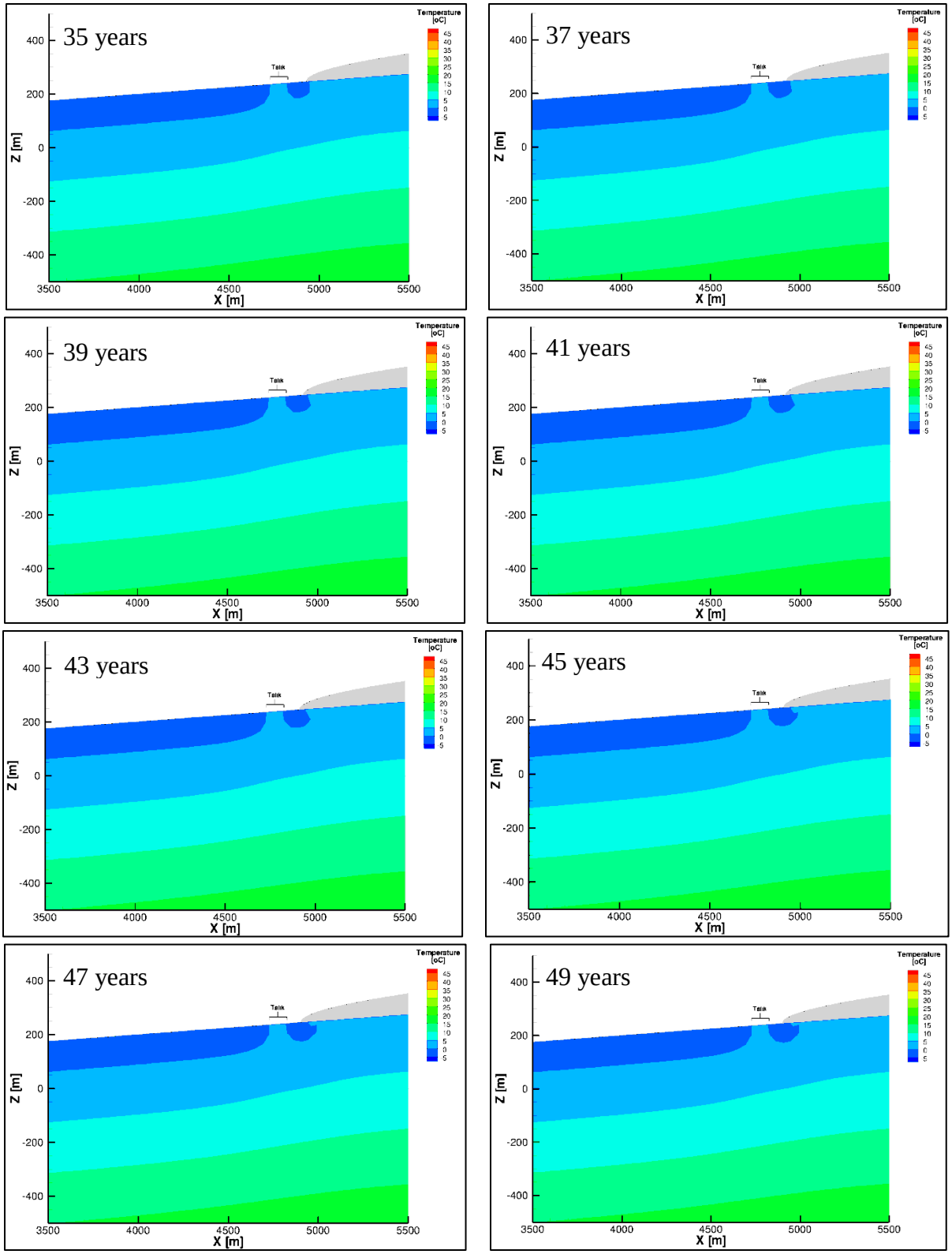

Figure 4.37 West-east cross-sections of temperature distribution for density-dependent flow with heat transport for an intermediate permafrost depth and one 100 m-wide talik from 35 to 49 years after the start of ice sheet advance (2 year intervals)

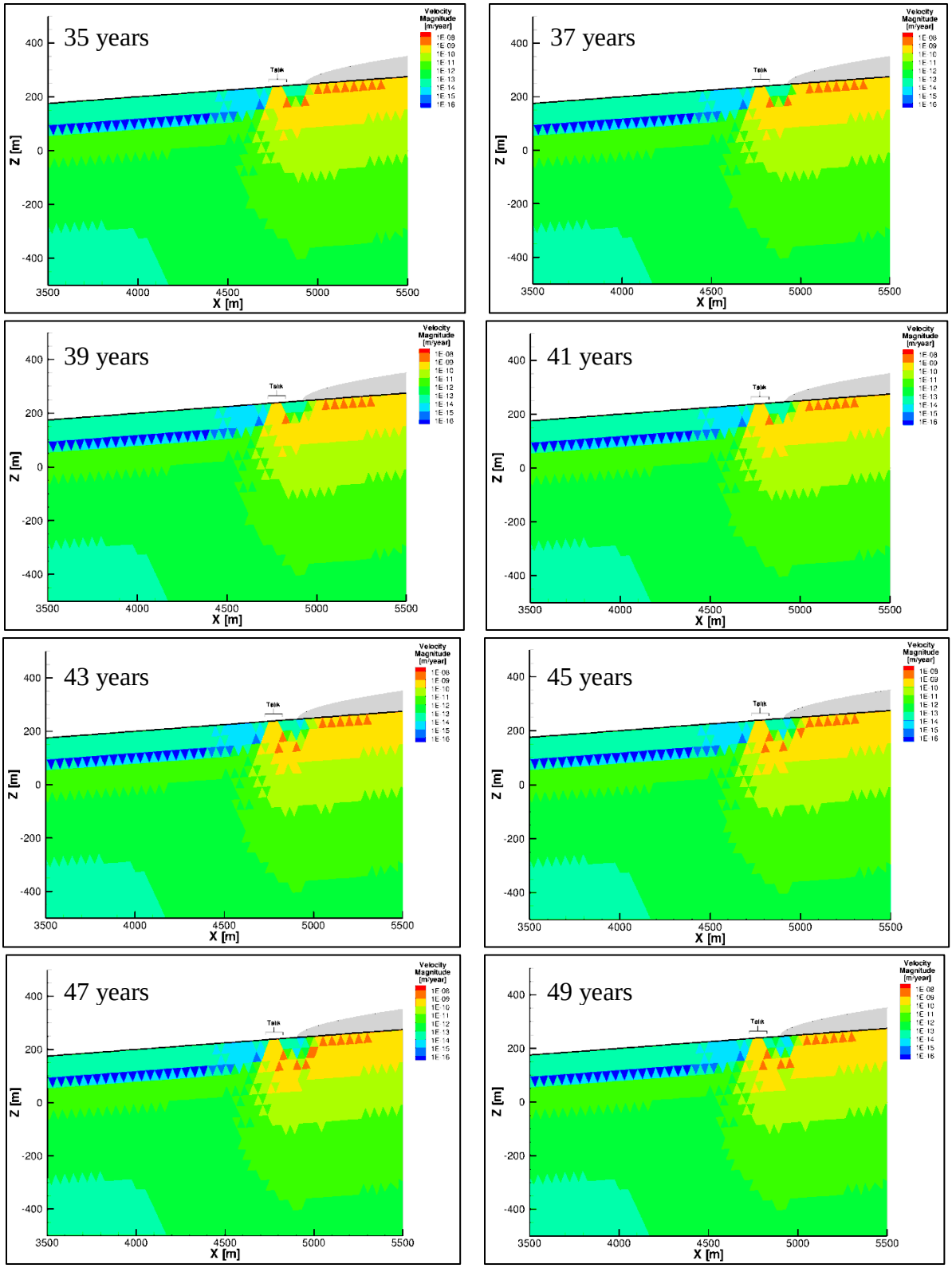

Figure 4.38 West-east cross-sections of velocity magnitude distribution for density-dependent flow with heat transport for an intermediate permafrost depth and one 100 m-wide talik from 35 to 49 years after the start of ice sheet advance (2 year intervals)

4.4.4 Talik Distribution

In addition to varying the number (2, 3) of taliks included in the simulation and their size/width (50 m, 100 m), the distance between those taliks (50 m, 100 m, 500 m) was also varied. A steady-state simulation with the 50 m-wide taliks was examined first. When only one 50 m-wide talik was included in the simulation, the talik did not extend through the entire layer of permafrost. When two or three 50 m-wide taliks were located 50 m apart from each other, each of the taliks did extend through the entire layer of permafrost as shown in Figure 4.39. Figure 4.39 also shows that the permafrost between three taliks was only 40 m wide and 35 m to 40 m deep with the deeper permafrost being further away from the ice sheet. The depth of the permafrost between the edge of the ice sheet and the talik closest to it was reduced to 65 m at its deepest point.

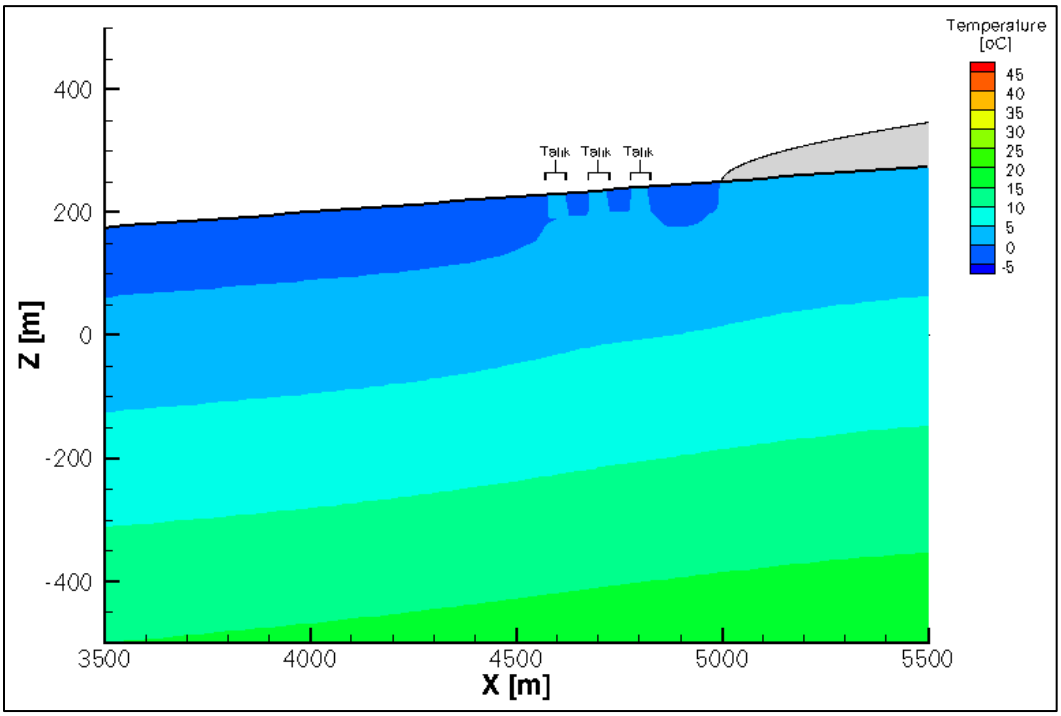

Figure 4.39 West-east cross-section of steady-state temperature distribution for density-dependent flow with heat transport for an intermediate permafrost depth and three 50 m-wide taliks 50 m apart

When three 50-m wide taliks were located 100 m apart from each other, they did not extend through the entire layer of permafrost, but the layer of permafrost beneath the two taliks closest to the ice sheet was only between 5 m and 10 m thick (as compared to the simulation with only one 50 m-wide talik in which that layer of permafrost was approximately 20 m thick). The permafrost beneath the talik furthest was the ice sheet was up to 20 m thick (Figure 4.40).

Spacing the 50 m-wide taliks even further apart (500 m) also led to the formation of closed taliks. The talik furthest from the ice sheet extended 32 m into the permafrost with an approximately 38 m thick layer of permafrost beneath it. The base of the permafrost was raised from approximately 110 m to approximately 70 m below ground surface. The middle talik extended 30 m into the permafrost with an approximately 32 m thick layer of permafrost beneath it. The base of the permafrost was raised to 62 m below the ground surface. The talik closest to the ice sheet extended 40 m into the permafrost with 10 m of permafrost beneath it (Figure 4.41).

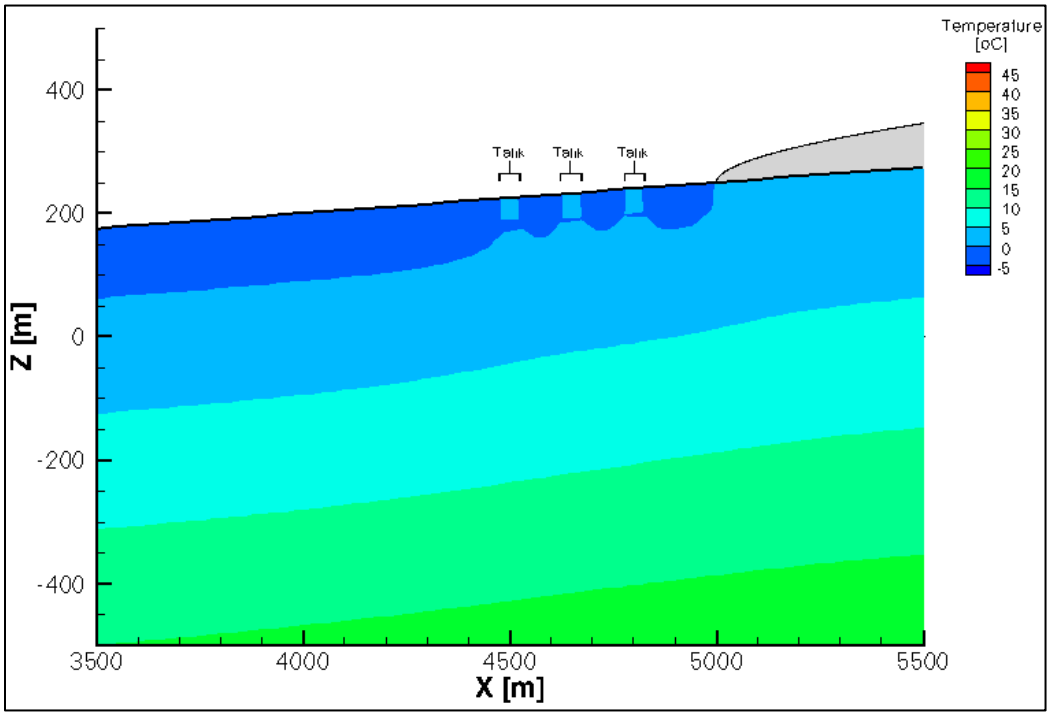

Figure 4.40 West-east cross-section of steady-state temperature distribution for density-dependent flow with heat transport for an intermediate permafrost depth and three 50 m-wide taliks 100 m apart

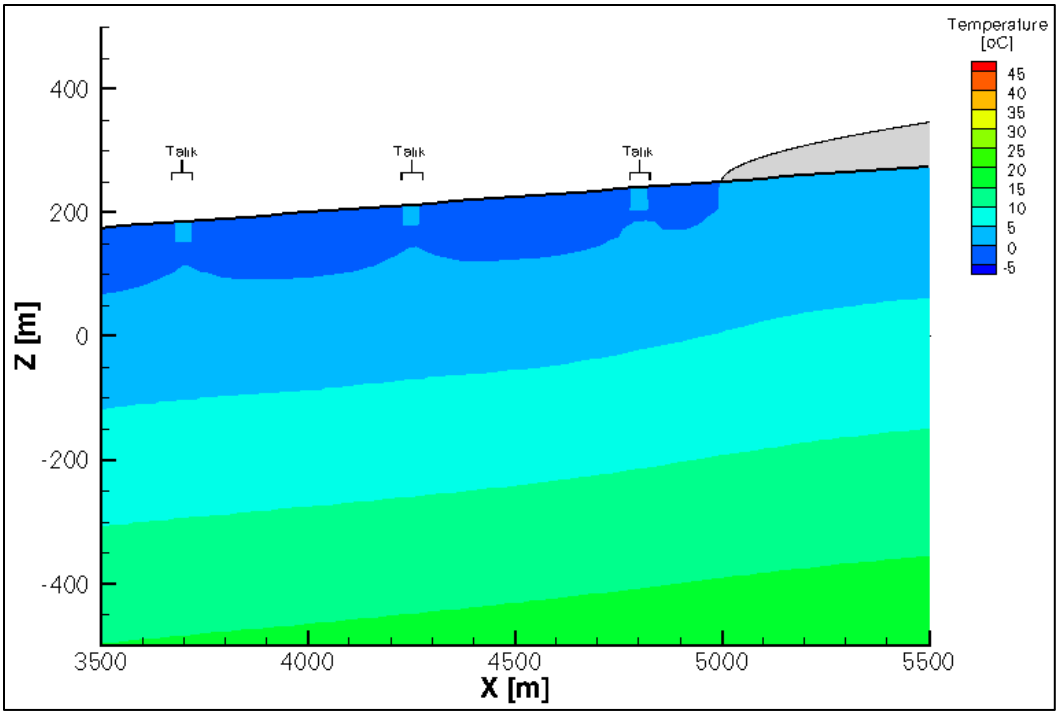

Figure 4.41 West-east cross-section of steady-state temperature distribution for density-dependent flow with heat transport for an intermediate permafrost depth and three 50 m-wide taliks 500 m apart

When two or three 100 m-wide taliks were located any distance apart from each other, they extended through the entire layer of permafrost as shown in Figure 4.42, Figure 4.43, and Figure 4.44. In general, the closer the taliks were together, the shallower the permafrost was between them.

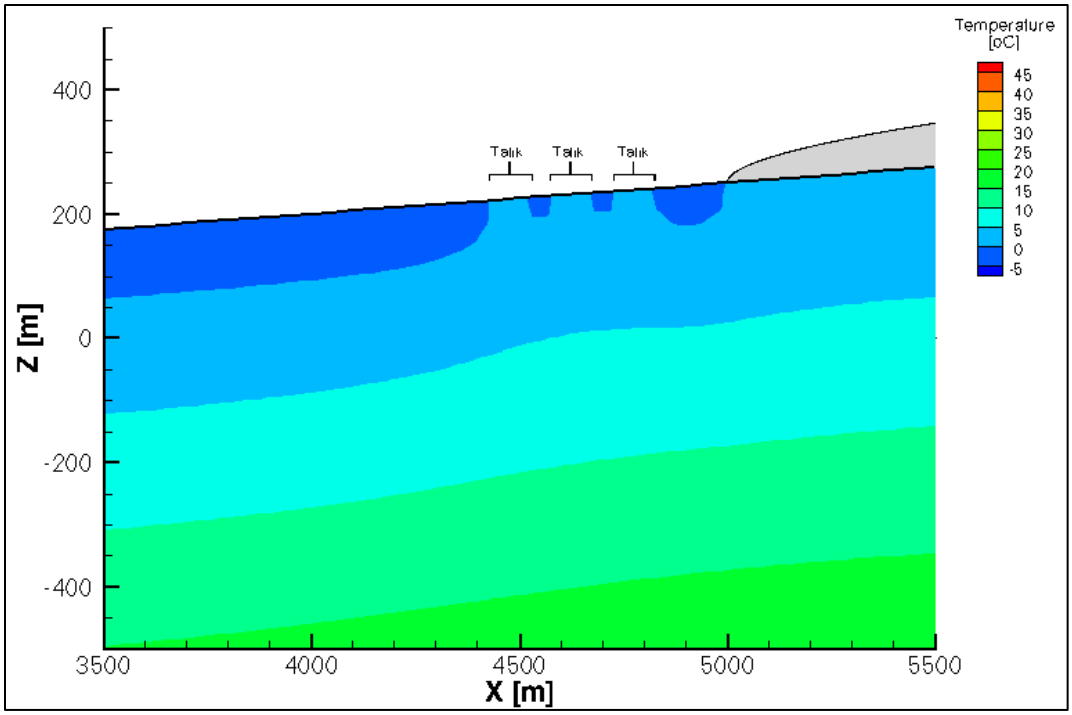

Figure 4.42 West-east cross-section of steady-state temperature distribution for density-dependent flow with heat transport for an intermediate permafrost depth and three 100 m-wide taliks 50 m apart

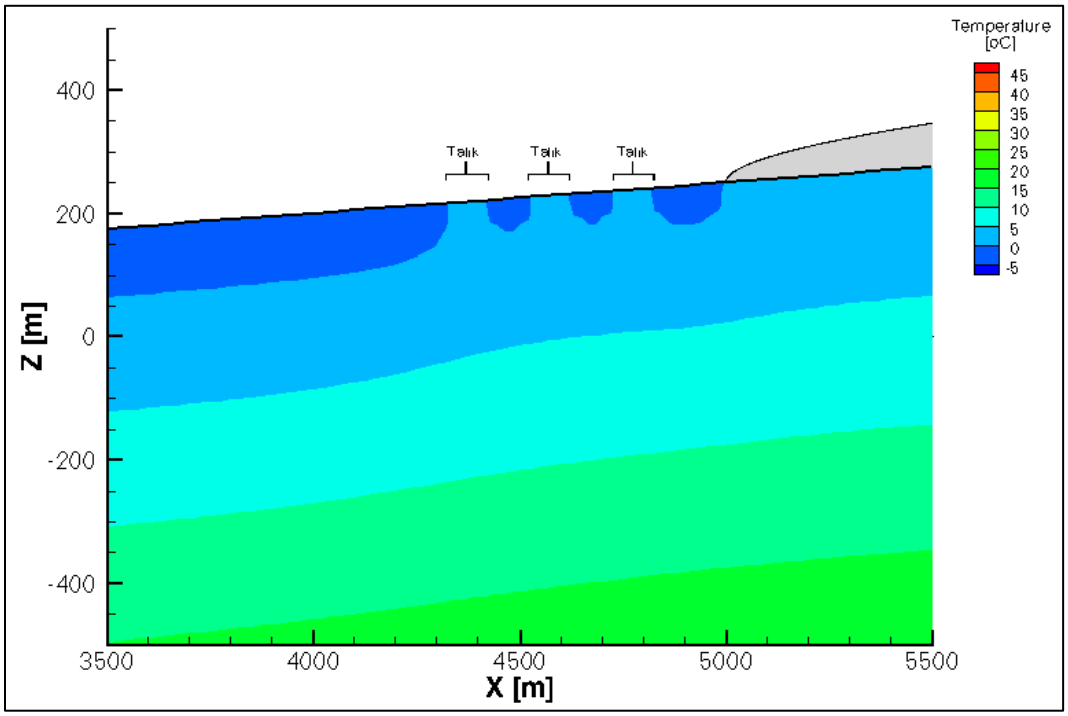

Figure 4.43 West-east cross-section of steady-state temperature distribution for density-dependent flow with heat transport for an intermediate permafrost depth and three 100 m-wide taliks 100 m apart

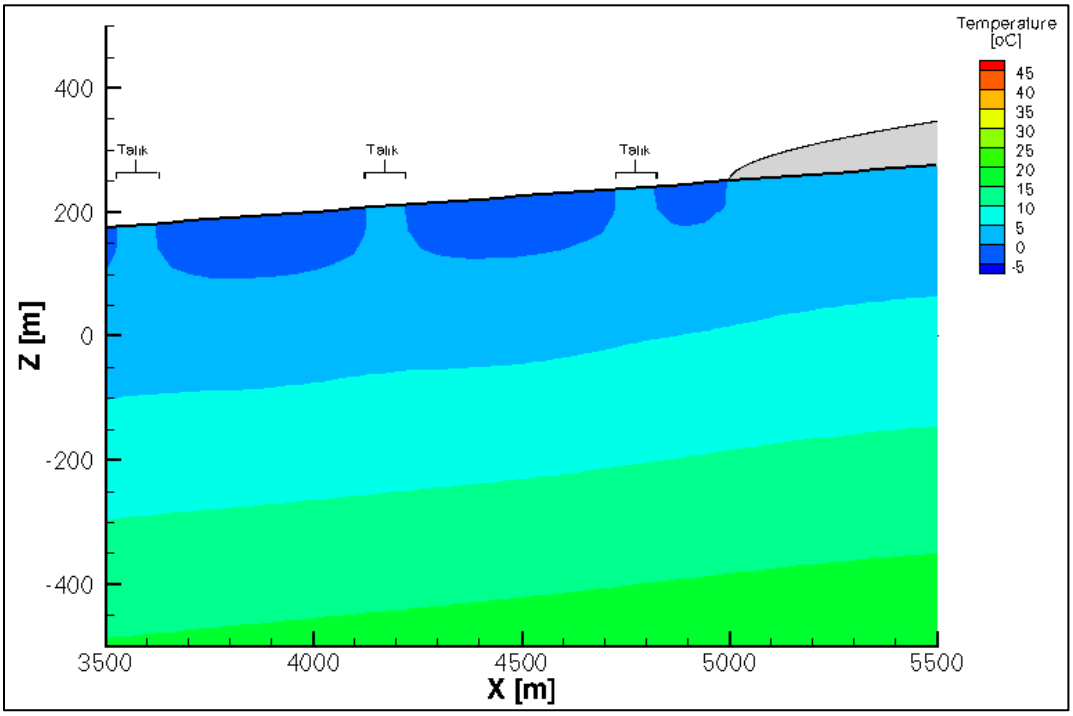

Figure 4.44 West-east cross-section of steady-state temperature distribution for density-dependent flow with heat transport for an intermediate permafrost depth and three 100 m-wide taliks 500 m apart

Figure 4.45 illustrates the steady-state velocity magnitude distribution for the scenario with three 100 m (open) taliks located 500 m apart from each other. It shows that the velocity magnitude is elevated (on the order of 10^{-11} m/year) beneath all of the permafrost and even greater (on the order of 10^{-10} m/year or 10^{-9} m/year) within the taliks and beneath the ice sheet. Figure 4.7, which illustrates the scenario without any taliks, shows the maximum velocity magnitude beneath the ice sheet to be on the order of 10^{-12} m/year.

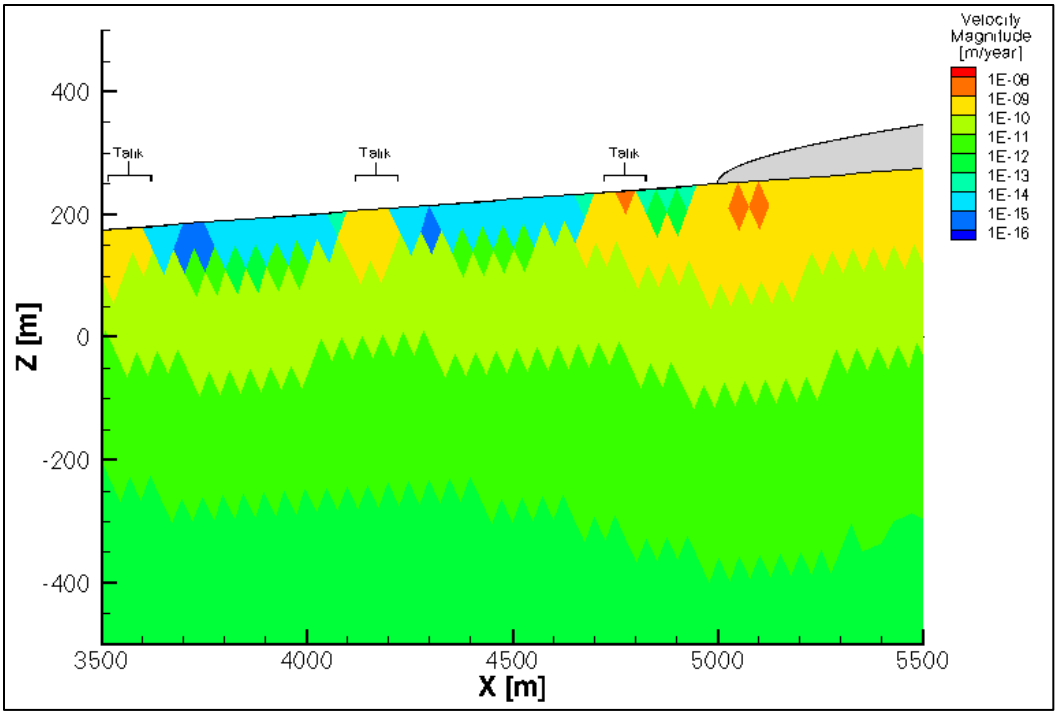

Figure 4.45 West-east cross-section of steady-state velocity magnitude distribution for density-dependent flow with heat transport for an intermediate permafrost depth and three 100 m-wide taliks 500 m apart

As with the previous simulations in this chapter, the transient simulation included fluid flow (Darcy's Law), temperature (Heat Transport in Porous Media), and one-dimensional hydromechanical coupling (Section 3.2.4). The ice sheet advanced at a rate of 2 m/year, and a 500-year scenario with ice sheet advance was examined. The ice sheet had the same impact on the pressure, head, temperature, and velocity magnitude distributions as it did in the previous simulations. Additionally, the permafrost degradation in the simulations with multiple taliks followed the same pattern or trends as observed in the simulations with only one talik.

4.5 Summary

Using a two-dimensional cross-section of a hypothetical crystalline rock setting and the COMSOL Multiphysics computational model, the analyses presented in this chapter were carried out to examine the impact of the initial depth of permafrost and the rate at which the ice sheet advances on the spatial distribution of permafrost beneath and in front of the ice sheet. The cross-section and model were also used to investigate the impact of the talik size and distribution on the groundwater flow system during glacial advance.

The temporal patterns of permafrost thaw presented in Section 4.4 and summarized below influenced by the discretization of the model. The ice advances in discrete steps to the

next node with the interval for advance being greater than the time to thaw the permafrost at a node. The elements used in the model were 50 m across, and the ice sheet advanced at 1 m/year or 2 m/year, depending on the scenario. Thus, the permafrost distribution was not altered until the ice sheet reached the next node 50 m away in 50 year or 25 years depending on the rate or advance. When the ice sheet did reach the next node, the permafrost beneath it thawed rapidly within a few years.

4.5.1 Impact of Permafrost Depth on the Flow System and the Rate of Permafrost Degradation beneath an Advancing Ice Sheet

Three initial permafrost depths were used in this examination of their impact on the rate of permafrost degradation beneath an advancing ice sheet: approximately 40 m (shallow), 100 m (intermediate), and 300 m (deep). With all three initial permafrost depths, the permafrost remained beneath the ice sheet to varying degrees as the ice sheet advanced at a rate of 1 m/year for the first set of simulations. In general, when the permafrost was deeper (and colder), it remained beneath the ice sheet for a longer time and to a greater distance from the ice sheet edge than when the permafrost was shallower.

4.5.2 Impact of the Rate of Ice Sheet Advance on the Rate of Permafrost Degradation beneath an Advancing Ice Sheet

Two rates of ice sheet advance were examined: 1 m/year and 2 m/year. Doubling the rate of ice sheet advance reduced the length of time for which the permafrost persisted beneath the edge of the advancing sheet by half, but did not impact the distance to which the permafrost remained from the edge of the ice sheet. For example, with an initial permafrost depth of approximately 100 m, the permafrost begins to melt approximately 50 years after the start of ice sheet advance when the ice sheet advances at a rate of 1 m/year; the permafrost begins to melt approximately 25 years after the start of ice sheet advance when the ice sheet advances at a rate of 2 m/year. In both scenarios, the permafrost remains beneath the ice sheet approximately 45 m in from its advancing edge.

4.5.3 Impact of Talik Size and Distribution on the Groundwater Flow System during Glacial Advance

An initial permafrost depth of 100 m was used for all simulations that included taliks, which formed as the result of setting the surface temperature to 2 ^{o}C to represent an unfrozen surface water body. A series of simulations with different combinations of the number of surface water bodies (1, 2, or 3), the width of the surface water bodies (50 m or less than the thickness of

the permafrost and 100 m or the same as the thickness of the permafrost), and the distance between them (50 m, 100 m, or 500 m).

When only one surface water body was included in the simulation, a closed talik formed when a width of 50 m was used, and a through talik formed when a width of 100 m was used. In both cases, the base of the permafrost was raised beneath the closed talik and in the region of permafrost between the talik and the advancing ice sheet. When multiple surface water bodies or taliks were included, the closer they were to each other, the shallower the permafrost was beneath and directly beside them. Thus, when multiple 50 m-wide surface water bodies were located 50 m apart from each other, open or through taliks formed beneath them, and the base of the permafrost was raised to a shallower depth than when only one 50 m talik was included.

5.0 The Greenland Analogue Project

Simplifying assumptions are often made with the thermal conditions in permafrost models. Some studies ignore temperature and the effects of latent heat because of computational constraints [e.g., Jaquet & Namar, 2010; Sykes et al., 2011; Yin et al., 2013]. However, because thawing and freezing are such important and prevalent processes in periglacial environments, the energy associated with those phase changes should be accounted for, especially because the release and absorption of latent heat can slow the rate of temperature increase or decrease, respectively [Ge et al., 2011; McKenzie et al., 2007]. Additionally, the transfer of heat by convection has been omitted in some studies, which focus on heat transfer by conduction only [e.g., Chen et al., 2003; Hayashi et al., 2007; Mottaghy & Rath, 2006; Zhang et al., 2003; Zhang et al., 2006, 2008a, b]. Although the low hydraulic conductivity of permafrost does limit or prevent flow, secondary pathways such as fractures and taliks may allow groundwater flow and, thus, heat transfer by convection.

As discussed in Section 1.1 and 1.3, this doctoral research builds on the GAP modelling study presented in Yin et al. [2013]. In particular, this research examines the impacts of temperature including the effects of latent heat on permafrost development and degradation and talik formation and closure for the GAP study site in Greenland. Because COMSOL does not allow the simulation of a property that varies in three dimensions as well as in time, a two-dimensional slice of the three-dimensional model presented in Yin et al. [2013] was used to investigate the impact of temperature on the subsurface model. The FRAC3DVS-OPG model simulates fluid flow, heat transport, and one-dimensional mechanical loading of the ice sheet.

Some glaciation studies that include permafrost [Bense et al., 2009; Lemieux et al., 2008a, b, c] used a fixed prescribed head equal to the topographic head for the top surface flow domain boundary condition for regions not covered with ice. While this simplifies the simulation, it is based on the assumption that there will always be enough precipitation excess to maintain the water table at this level. The assumption also neglects the effect that the low hydraulic conductivity of the permafrost has on the underlying groundwater flow. Permafrost acts as a confining layer, restricting or eliminating deep circulation and forming a perched water table in the active layer [Fetter, 2001; Scherler et al., 2010] or causing an accumulation of water at the surface [Scherler et al., 2010]. Therefore, this doctoral research also modified the prescribed head boundary condition (3 m below ground surface) used in Yin et al. [2013] to account for water table adjustment and variably-saturated flow conditions. The variably-saturated flow simulations were carried out using the three-dimensional model presented in Yin et al. [2013] and FRAC3DVS-OPG.

5.1 Greenland Ice Sheet

The Greenland Ice Sheet (GIS) is the largest mass of glacier ice in the northern hemisphere accounting for 10% of the Earth's total freshwater [Benn & Evans, 2010]. The ice sheet is approximately 1.7 million km^2 in area, covering much of the continent of Greenland with approximately 2.9 million km^3 of ice in volume [Alley et al., 2010]. This volume represents around 7 m of sea level rise if spread evenly over the earth's oceans [Alley et al., 2010; Benn & Evans, 2010; Fleming & Lambeck, 2004]. Maximum ice sheet thickness is 3367 m with an average ice sheet thickness of 1600 m [Alley et al., 2010] arranged as two domes, northern (elevation 3200 m) and southern (elevation 2850 m), linked together by a long "saddle" (elevation 2500 m) [Benn & Evans, 2010].

Beneath the central region of the ice sheet, the bed rock is flat and close to sea level, while along the periphery lie coastal mountains through which outlet glaciers drain the interior [Benn & Evans, 2010]. In central regions of the GIS, the ice is frozen to the bed meaning that movement in this region is dominated by internal deformation with velocities around $10^1 – 10^2$ m/year. Around the periphery there is basal sliding and possibly till deformation in thawed bed regions with velocities of $10^2 – 10^4$ m/year for the fast-flowing outlet glaciers [Alley et al., 2010; Benn & Evans, 2010].

During the last interglacial period (120,000 years ago) the GIS was greatly diminished by temperatures warmer than present day temperatures. At the LGM, the GIS had expanded considerably (2 to 3 m of ice-equivalent sea level [Simpson et al., 2009] to the east and west with ice sheet margins close to the continental shelf edge [Cuffey & Paterson, 2010; Roberts et al., 2009]. Following the LGM in West Greenland, ice sheet retreat began with break-up of the marine-based portion of the ice sheet 15,000 and 10,000 years ago before slower retreat of the land-based ice during the early Holocene [Roberts et al., 2009; Simpson et al., 2009].

Recently, temperatures have warmed and there has been increasing snowfall and rapidly increasing meltwater runoff [Alley et al., 2010; Benn & Evans, 2010]. Precipitation over the GIS is mostly snowfall and rates decrease from south to north as temperatures decrease and the distance between the primary oceanic moisture source increases [Cuffey & Paterson, 2010]. Mass loss on the GIS is dominated by melting in low elevations and calving of icebergs. There is some minor loss via sublimation, snowdrift, and melting or freezing at the ice-bed interface [Alley et al., 2010]. The average snowfall rate over the GIS is greater than the average melt rate, so the surface mass balance is positive. This does not account for melt loss at the base of the glacier as well as calving [Benn & Evans, 2010]. Calving and melt at marine margins account for 50 to 60% of the total ablation, and the total ablation is greater than the yearly accumulation. Thus, the GIS has been losing mass [Cuffey & Paterson, 2010].

Permafrost surrounds the ice sheet on the continent of Greenland with continuous permafrost in the northern regions, discontinuous permafrost at the middle latitudes and along the coasts, and sporadic permafrost at the southern tip [Nielson, 2010]. Permafrost may also exist beneath the ice sheet at higher elevations or near the ice margin, however, such permafrost would be of limited extent [Jaquet & Namar, 2010]. Figure 5.1 illustrates the distribution of permafrost around the GIS. Kangerlussuaq marks the location of the GAP study site, which lies within the continuous permafrost zone. It should be noted that the model domain used by Yin et al. [2013] is based at the Kangerlussuaq site but extends past the coast into Davis Strait, so the domain includes a region of discontinuous permafrost as well.

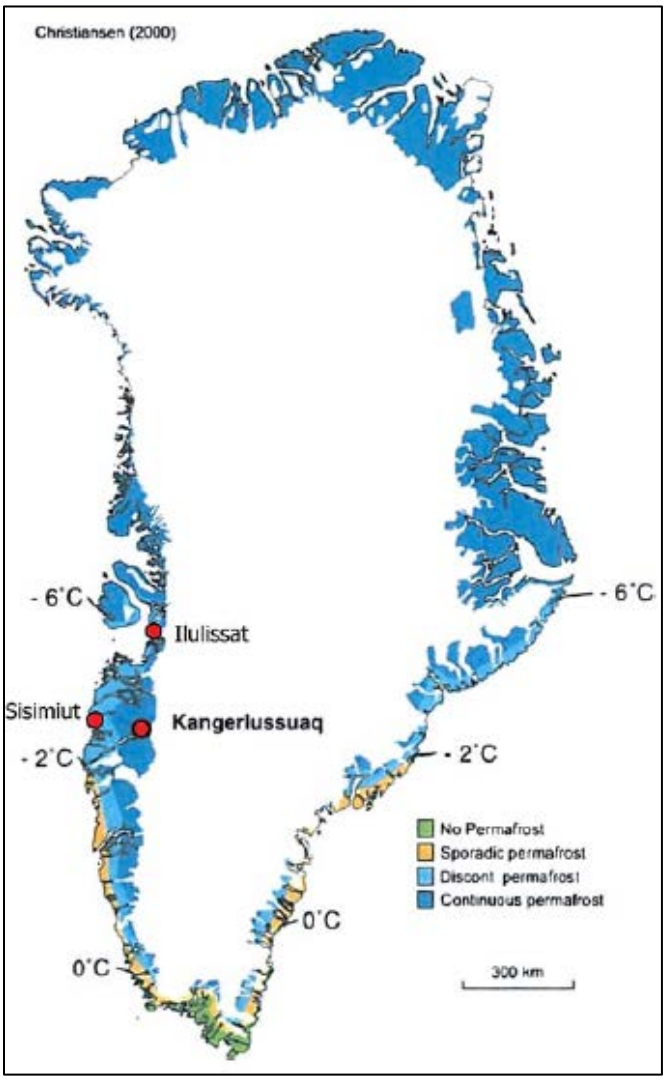

Figure 5.1 Permafrost distribution in Greenland

The distribution of continuous, discontinuous, and sporadic permafrost in Greenland [from Wallroth et al., 2010 based on figure from Christiansen, 2000 and printed in Jorgensen & Andreasen, 2007].

van Tatenhove & Olesen [1994] used surface and ground temperature measurements and assumptions about the thermal properties of the underlying materials to calculate the depth of permafrost in the continuous zone at Kangerlussuaq and in the discontinuous zone further west at the coast at Sisimiut. They indicated that the permafrost was 127 ± 31 m at Kangerlussuaq and 33 ± 9 m at Sisimiut. However, based on preliminary borehole results from the GAP field research program (Borehole DH-GAP03), it is estimated that the permafrost within the continuous permafrost zone around Kangerlussuaq is around 300 m thick [Claesson-Liljedahl and Lehtinen, personal communication, 2009].

In West Greenland between the GIS and the coast between 66 and 67^{o}N, there are around 20,000 lakes including some saline lakes [Anderson et al., 2001, 2002], which occur within an 80 km zone from the edge of the ice sheet [Wallroth et al., 2010]. With mean annual temperatures of -6 ^{o}C [Ryves et al., 2006], these lakes are typically covered in ice for the majority of the year (ice free for approximately three months in a year) with ice thickness of 1 to 2 m [Williams, W. D., 1991]. These lakes range in size from 10^{-2} to 10^{2} km^{2} and less than 2 m to greater than 100 m deep [Ryves et al., 2006]. Thus, some of these lakes are large enough and deep enough to remain unfrozen at depth (See Section 2.3.3) indicating the presence of taliks or connections between the surface water and deeper groundwater system in the region between the edge of the ice sheet and Davis Strait in West Greenland.

5.2 Model Domain

The groundwater model domain for this study covers a two-dimensional cross section through the centre of the 520 km by 64 km rectangular area used in the other GAP investigations by Yin et al. [2013] (Figure 1.1). The model domain extends 200 km onto the ice sheet in the east and into Davis Strait in the west of the ice margin with the east-west orientation being parallel to the primary ice flow direction [Jaquet & Namar, 2010]. The domain reaches a depth of 5 km.

The model domain is discretized into 476,490 free or unstructured triangular elements. Element size ranges from 50 m to 1000 m with the coarser elements at depth. The element size was refined (4 refinements) near the surface to a depth of 1500 m as shown in Figure 5.2. The refinement method used was the regular refinement method in which each element is divided into four regular triangular elements of the same shape [COMSOL, 1998-2011].

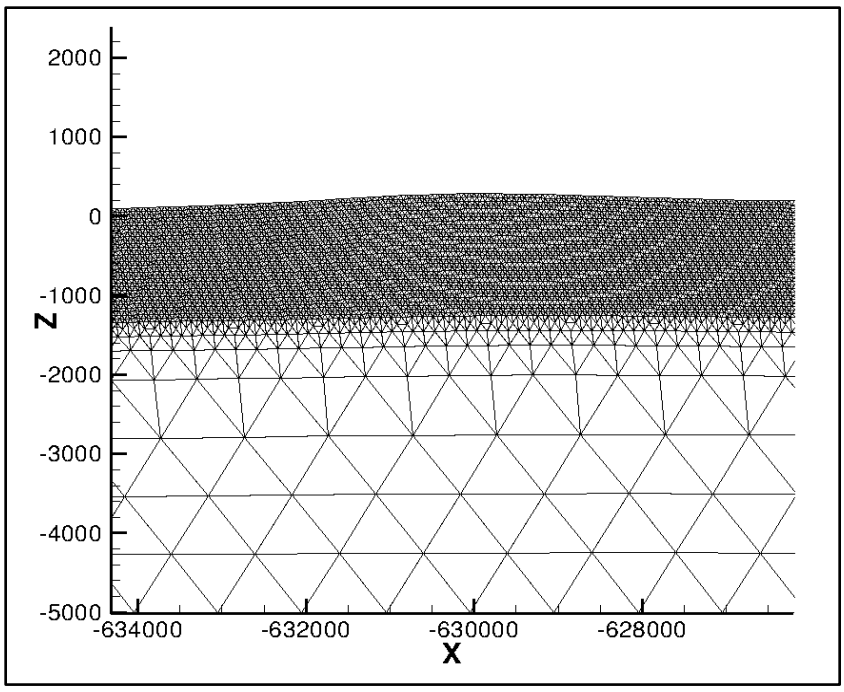

Figure 5.2 Discretization of cross-section domain

The model was discretized into free triangular elements with regular refinement near the surface to a depth of 1500 m.

5.3 Properties and Boundary Conditions

The following sections summarize the properties and boundary conditions used to develop the base-case conceptual model.

5.3.1 Bathymetry and Topography

Bathymetry and topography data are taken from the International Bathymetric Chart of the Arctic Ocean (IBCAO), Version 2.23 [2008] with 1 arc minute of resolution. The Bamber dataset [2001] is used for both bed topography and ice thickness with 5 m resolution for each. The bed topography data is used to set the elevation for the top of the geosphere beneath the ice sheet. Figure 5.3 illustrates bed topography data and ice thickness data for all of Greenland.

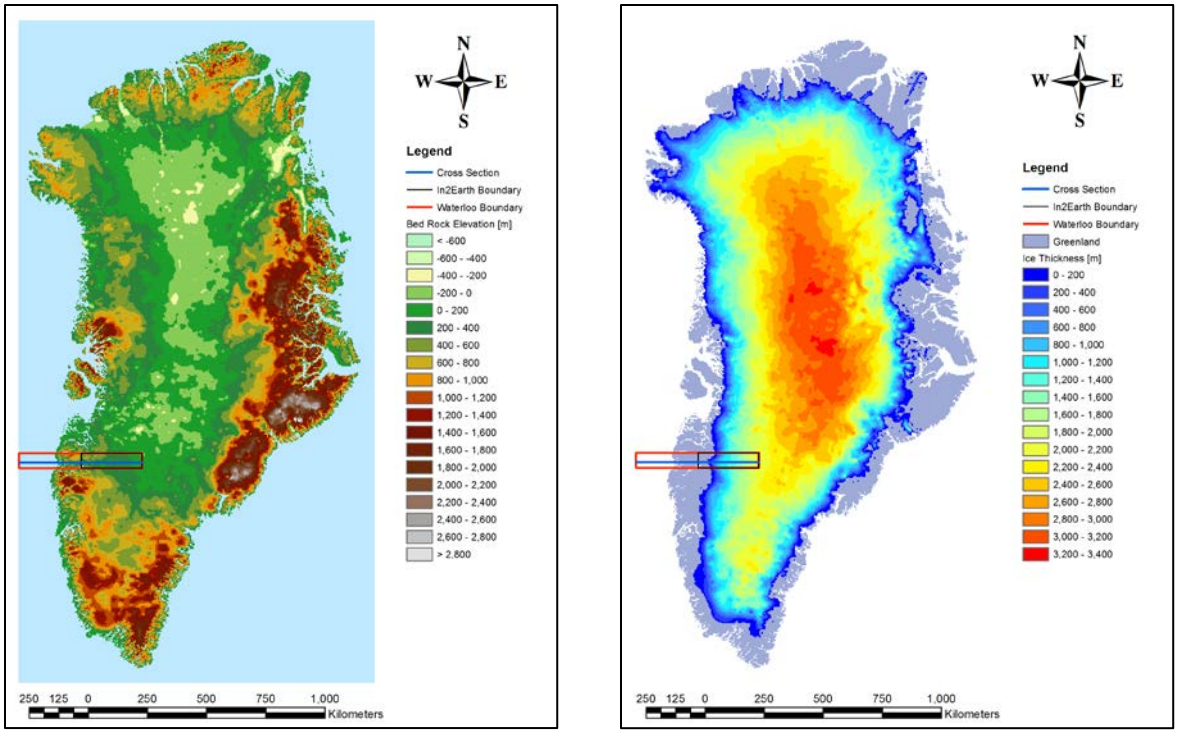

Figure 5.3 Greenland bedrock topography (left) and ice thickness (right)
Greenland bedrock topography and ice thickness were taken from the Bamber dataset [2001]. Model domains for this doctoral research (Cross Section), the In2Earth [Jaquet & Namar, 2010], and the Waterloo [Yin et al., 2013] studies are also shown.

5.3.2 Boundary Conditions

The following sections describe the boundary conditions that were used for the fluid flow, solute transport, and temperature physics.

5.3.2.1 Fluid Flow

In regions without ice sheet cover, head values were assigned based on the assumption that the water table is 3 m below ground surface as defined by the digital elevation model. Surface boundary conditions for Davis Strait are given as sea level. The ice sheet was applied as a freshwater head equal to pressure applied at the base of the ice sheet and as a mechanical load for hydromechanical coupling. The domain bottom and sides are no flow boundaries.

Both head and vertical stress were applied to the top boundary as an interpolation function with head and stress values set every 1,000 m and every 1,000 years to match the spatial and temporal step sizes used in the FRAC3DVS-OPG simulations by Yin et al. [2013]. Head values were linearly interpolated to maintain computational stability. A nearest neighbour

interpolation function was used to represent the vertical stress as a change in vertical stress with a change in time (See Equation 3.10 in Section 3.1.4).

5.3.2.2 Total Dissolved Solids (TDS) and Solute Transport

As in Chapter 4, total dissolved solid (TDS) concentrations are based on characteristics derived from studies of the Canadian Shield because such data are not available for the modelled domain in Greenland. Data for the Canadian Shield from Frape and Fritz [1987 (Figure 2b)] was used in the preliminary study by Yin et al. [2013]. Equation 4.4 in Chapter 4 represents an upper bound for total dissolved solids (TDS) as a function of depth. TDS is in units of g/L.

COMSOL Multiphysics requires that concentrations be entered in terms of mol/m^3. For consistency with other GAP studies and Southern Ontario studies [Yin et al., 2013; Sykes et al., 2011], a brine of sodium chloride (NaCl) was chosen for the base case scenario. Thus, the maximum TDS concentration for depths greater than 1250 m was 5133 mol/m^3.

5.3.2.3 Temperature

The top surface boundary was assigned a temperature representing the atmospheric temperature for each region and time. In particular, for Davis Strait, a temperature of 4 ^oC is applied. For regions not covered in ice, the temperature was -7.5 ^oC, and for regions with ice cover, the temperature was 0.1 ^oC. Other surface water bodies within the domain were assigned a temperature of 2 ^oC. These temperatures were chosen to be consistent with observations made in Greenland for the GAP field studies and with what other modellers for the GAP were using [SKB, Posiva, Terrasolve, personal communication, August 2011]. In COMSOL, temperatures were applied to the top boundary as an interpolation function with the above temperatures set where appropriate every 1000 m and every 1,000 years to match the spatial and temporal step sizes used in the FRAC3DVS-OPG simulations by Yin et al. [2013]. Temperatures were linearly interpolated between those points and times to maintain computational stability.

The domain sides were insulated while a geothermal heat flux of 55 mW/m^2, similar to values and averages used in other studies [Benn & Evans, 2010 (40 – 90 mW/m^2 with average of 60 mW/m^2); Greve, 2005 (42 – 65 mW/m^2); SKB, Posiva, Terrasolve, personal communication, August 2011 (53.3 mW/m^2); van der Veen et al, 2007 (42 mW/m^2 for Precambrian Shields and 57 mW/m^2continental average)] was applied to the bottom of the domain.

5.3.3 Horizontal and Vertical Permeabilities

To account for variations in hydraulic conductivity due to changes in density, permeabilities were used. Because such data were not yet available for the modelled domain in

Greenland, these permeabilities were based on characteristics derived from the Canadian Shield. Horizontal and vertical permeabilities as a function of depth are expressed as presented in Equation 4.4 and Equation 4.5 in Section 4.3.2.

5.3.4 Glaciation and Sea Level Data

Glaciation and sea level data were provided by Dr. Jesse Johnson and his research group at the University of Montana. Dr. Johnson provided a transient ice sheet model of the GIS simulating its advance and retreat and the rise and fall of the sea level over the last 120,000 years. Figure 5.4 illustrates the change in ice volume over that time frame; Figure 5.5 illustrates the change in sea level. This data was used to develop several input files for the COMSOL simulations that represented the surface boundary conditions described in Section 5.3.2. This data was used to develop the input files for head and vertical stress for the COMSOL simulations that represented the surface boundary conditions described in Section 5.3.2.

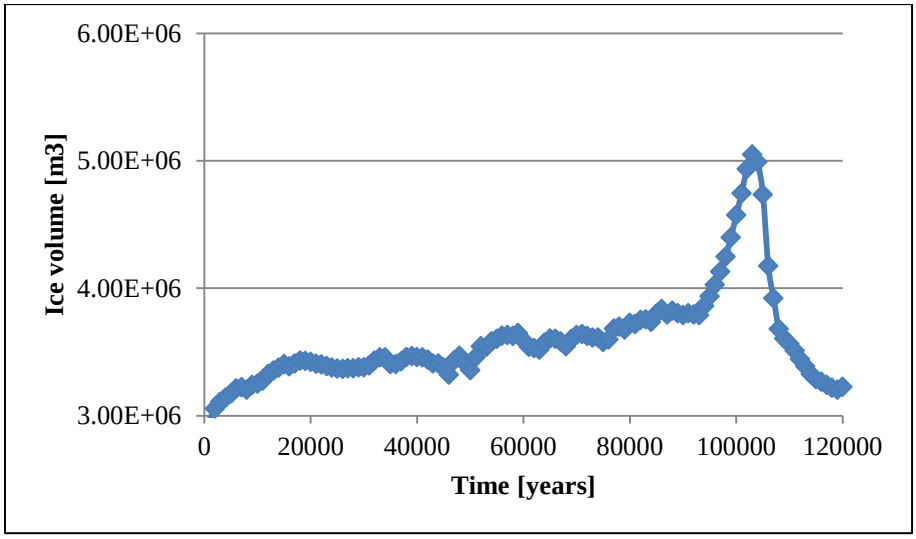

Figure 5.4 Change in ice volume over the last 120,000 years

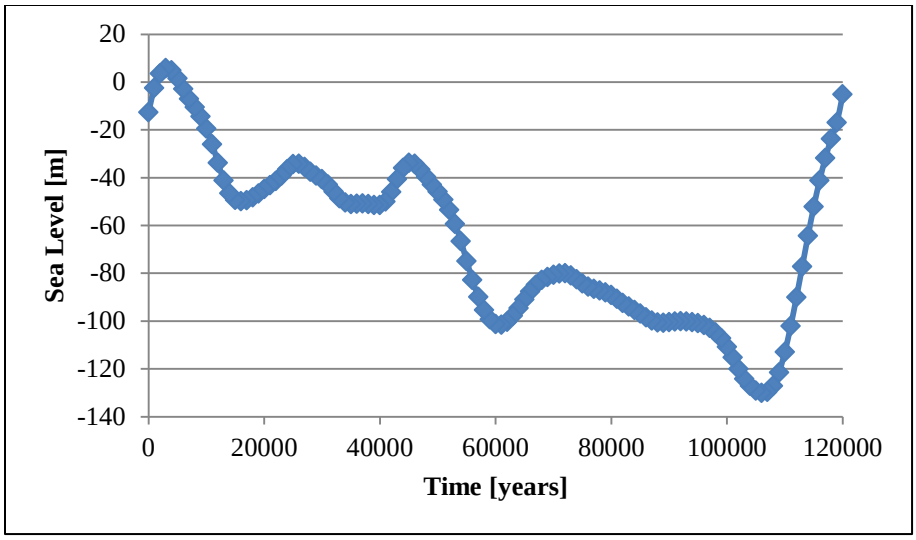

Figure 5.5 Change in sea level over the last 120,000 years

5.3.5 Permafrost and Taliks

To simulate the occurrence of permafrost within the model, permeability is dependent on temperature as well as depth such that the permeability of frozen elements (i.e. elements with permafrost) is reduced by six orders-of-magnitude. This freezing occurs over a range of 1 ^{o}C such that the permeability is reduced gradually between 0.5 ^{o}C and -0.5 ^{o}C. Taliks, therefore, will form wherever temperatures remain above freezing (e.g., beneath surface water bodies). While an unfrozen water phase would still exist within the frozen permafrost as adsorbed water on the solid grains, the volume of unfrozen water content would be very small.

5.3.6 Deformation Zones

Crystalline rock has among the lowest hydraulic conductivity and porosity of all geologic materials with hydraulic conductivities on the order of 10^{-11} to 10^{-13} m/s and porosities rarely larger than 0.02 [Freeze & Cherry, 1979]. Hydraulic conductivity decreases as a function of depth because shallow rocks are more fractured and weathered than deeper more sparsely fractured rock [Davison et al., 1994]. A network of discrete fractures can influence the flow system in these settings, acting as pathways for fluid flow.

Depending on frequency and spacing of fractures, rock can be classified into three domains. Fracture Zones (FZ) are regions of intensely fractured rock. Moderately Fractured Rock (MFR) zones are volumes of rock containing a small number of sets of relatively widely spaced discrete open fractures, and Sparsely Fractured Rock (SFR) zones contain microcracks and very sparsely distributed open fractures that typically are not connected [Davison et al., 1994]. Sparsely distributed fractures that are hydraulically active, but poorly connected, can

cause the local water table to be irregular. At depth, pressure irregularities become smoother and are governed by fracture zones with higher permeabilities [Park et al., 2008; Sykes et al., 2009].

Deformation zones were included in the three-dimensional regional-scale model domain, but not in the simulations using the two-dimensional west to east cross-section domain. Because deformation data were not available when this study was conducted, this study used the 20 deformation zones that were randomly generated in north-south or east-west directions (Figure 5.6) by Yin et al. [2013]. Jaquet & Namar [2010] identified major fault zones orienting in both the Northwest-Southeast and Southwest-Northeast directions for the In2Earth modelling domain at the GAP study site. The In2Earth modelling domain is outlined in Figure 1.1.

The Equilibrium Line Altitude (ELA), which represents the divide between the glacier's ablation and accumulation areas, is shown in Figure 5.6 and was introduced to ensure that the hydraulic boundary condition was similar to that used by other GAP researchers [Jaquet & Namar, 2010]. The deformation zones were of a constant length of 40 km and were assumed to penetrate the entire model vertically. The deformation zone apertures or width were assumed to follow a log-normal probability distribution

$$F_x(x) = \frac{1}{x\sigma\sqrt{2\pi}} e^{-\frac{1}{2}\left(\frac{\ln(x/m)}{\sigma}\right)^2} \qquad \textbf{5.1}$$

where the log-normal parameters σ = 0.48 m and m = 4.6 m were determined by trial and error in order to generate a deformation zone width distribution comparable to that used by other GAP researchers [Jaquet & Namar, 2010]. To account for these deformation zones, Yin et al. [2013] adjusted the hydraulic conductivity of the grid blocks using harmonic and arithmetic averaging.

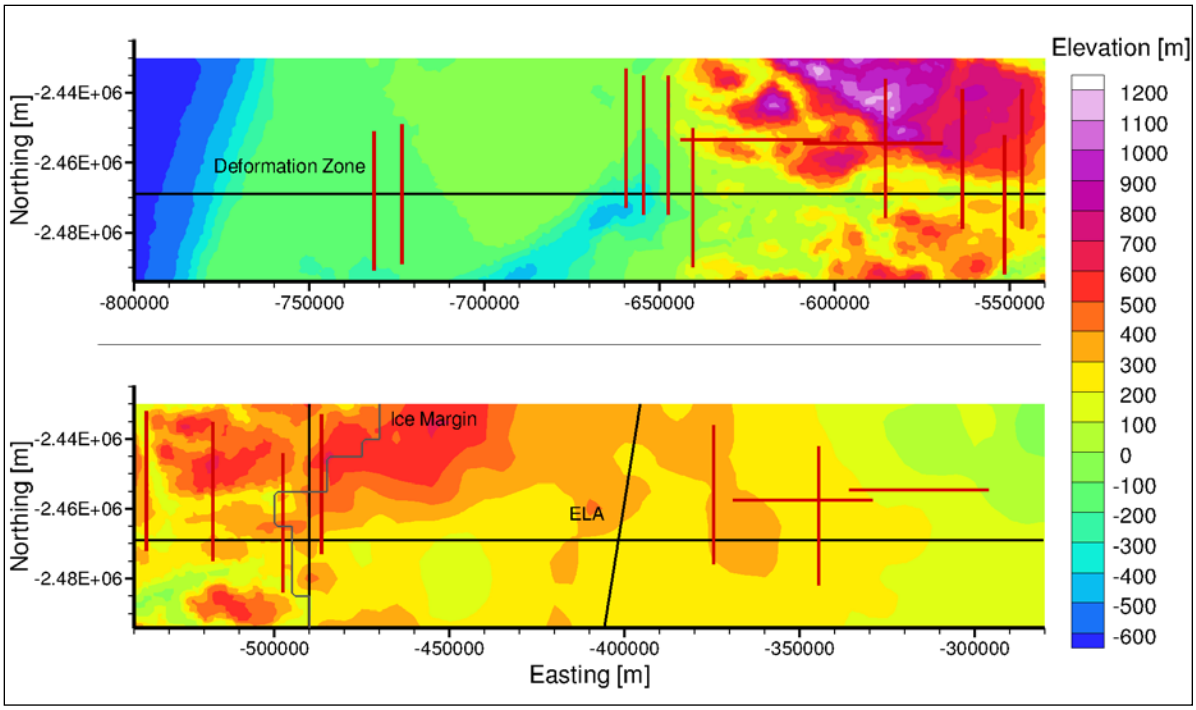

Figure 5.6 Areal view of the GAP model domain with deformation zones

The 20 deformation zones are indicated by the red lines, the location of the ice margin is shown by the grey line, and the ELA conceptualization and the location of the two-dimensional west to east cross-section are indicated with labelled black lines [Yin et al., 2013].

5.3.7 Other Properties

To represent a crystalline rock matrix, the matrix porosity was constant at 0.5% or 0.005 and the matrix density was set to that of granite (2700 kg/m^3 [average of range given by CRC, 2013]). Storage values are calculated by COMSOL based on the loading efficiency (ζ), Young's Modulus (E), and Poisson's ratio (v). Poisson's ratio was 0.25. Table 5.1 summarizes the loading efficiency and Young's Modulus values for different depths within the domain:

Table 5.1 Loading efficiency and Young's Modulus values as a function of depth for Greenland

Loading efficiency and Young's Modulus are used to calculate storage values [based on Chan and Stanchell, 2008].

Depth (below ground surface)	Young's Modulus (E) [GPa]	Loading Efficiency (ζ) [-]
To 150 m	20	0.795
150 m to 350 m	30	0.782
350 m and deeper	60	0.744

For heat transport, the matrix properties include a thermal conductivity of 2.1 W/m·K and a specific heat capacity of 0.79 J/kg·K; these values are consistent with a granitic material.

5.4 Analyses

The following sections detail the analyses carried out to examine the impact of heat transport and latent heat on permafrost distribution and, in turn, the hydrologic flow system as well as the impact of variably-saturated flow conditions and the presence of permafrost on the water table and hydrologic flow system at the Kangerlussuaq site in Greenland.

Plots illustrating the initial conditions and select transient simulation results for the analyses conducted for this doctoral research are presented in the following sections. It should be noted that all simulations begin with present day conditions, and the time elapsed in years represents the number of years before the present date over the last 120,000-year glacial cycle.

5.4.1 Density-dependent Flow with Heat Transport

To develop the initial pressure and temperature conditions for the transient analyses, steady-state simulations were run first using the properties and boundary conditions detailed in Section 5.3. The first steady-state simulation to be run involved only density-dependent flow with a constant depth-dependent TDS distribution, which is illustrated in Figure 5.7 (i.e. it did not include the thermal effects). This simulation established the regional flow system yielding the pressure distribution and velocity field as input for the next steady-state simulation, which included both the Darcy's Law and Heat Transfer in Porous Media (Section 3.2.3) physics. Figure 5.8, Figure 5.9, Figure 5.10 and Figure 5.11 illustrate the results of this steady-state simulation, which are the initial conditions (pressure, hydraulic head, temperature, and velocity magnitude respectively) for the transient analyses. The vertical to horizontal exaggeration in the figure is 50:1.

As illustrated in Figure 5.8 and Figure 5.9, pressure and hydraulic head values are elevated beneath the ice sheet due to the weight of the ice. In general, temperature increases linearly with depth (Figure 5.10). Figure 5.10 also shows the initial distribution of permafrost and taliks with permafrost reaching an approximate depth of 250 m beneath regions exposed to below freezing atmospheric temperatures. In general, velocity magnitudes (Figure 5.11) are greater in the shallow subsurface and decrease with increasing depth as expected given the depth-dependent permeability profile used (Section 5.3.3). However, the velocity magnitude distribution is also affected by both the temperature and pressure distributions. Subsurface temperatures below freezing indicate the presence of permafrost, which has a much lower permeability than the surrounding unfrozen subsurface as described in Section 5.3.5. Thus, in regions with permafrost (indicated by below freezing temperatures in Figure 5.10), the velocity

magnitude is reduced by up to five orders of magnitude with magnitudes on the order of 10^{-6} m/year. Within the taliks or unfrozen gaps within the permafrost and beneath the ice sheet where pressures are elevated, the velocity magnitude is on the order of 10^{-1} m/year to an approximate depth of 150 m and on the order of 10^{-2} m/year beneath that to an approximate depth of 340 m (Figure 5.11).

The transient simulation, which represented a glacial cycle of 120,000 years included fluid flow (Darcy's Law), temperature (Heat Transport in Porous Media), and one-dimensional hydromechanical coupling (Section 3.2.4). Over the course of the 120,000-year glacial cycle, the ice sheet advanced and retreated over the landscape multiple times, and the sea level dropped and rose accordingly as described in Section 5.3.4. As the ice sheet advanced, the pressures beneath it were raised, and as the ice sheet retreated, the pressures were lowered again (Figure B.1 to Figure B.12 in Appendix B). The velocity magnitude distribution also followed the same trends as described above for the steady-state distribution with the exact distribution evolving with the advancing/retreating ice sheet and freezing/melting permafrost (Figure B.13 to Figure B.24).

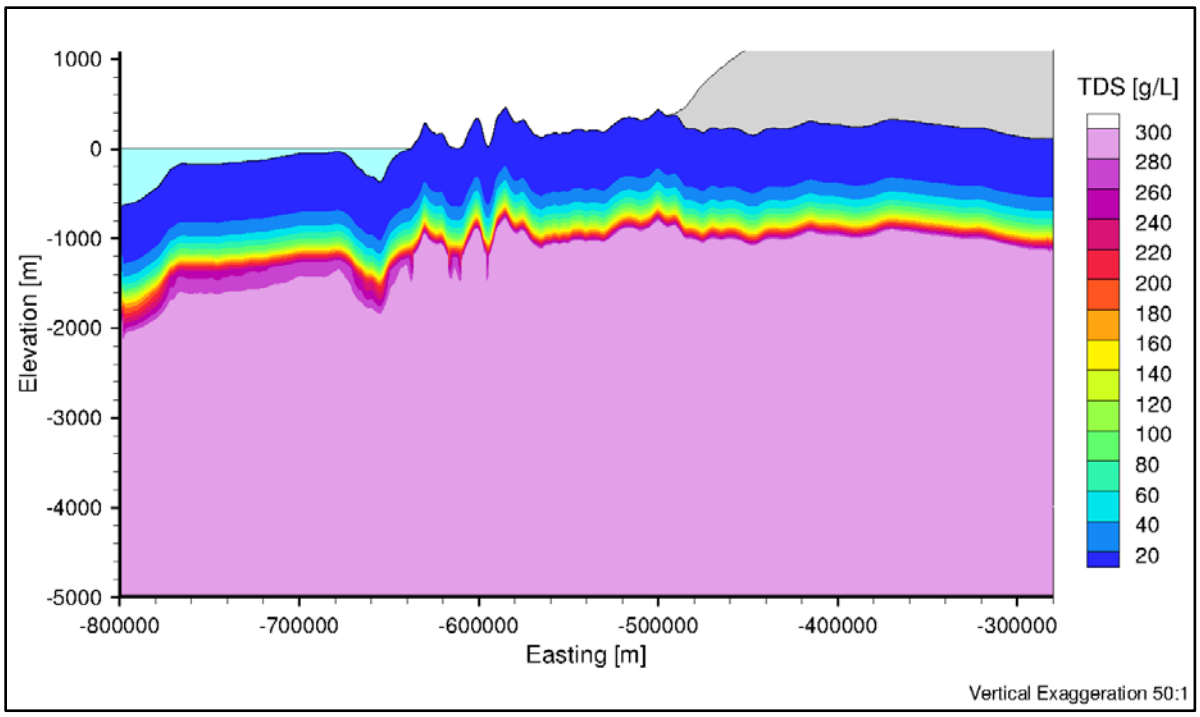

Figure 5.7 West-East cross-section of depth-dependent total dissolved solids distribution for density-dependent flow with heat transport

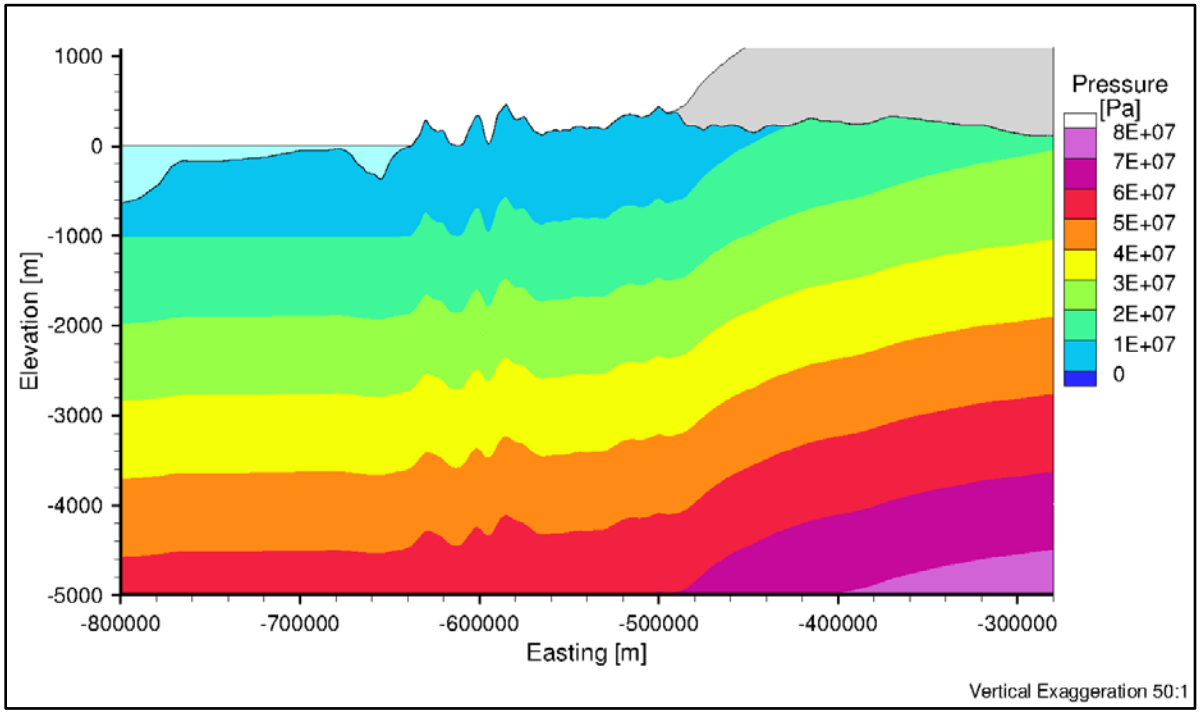

Figure 5.8 West-East cross-section of steady-state density-dependent pressure for density-dependent flow with heat transport

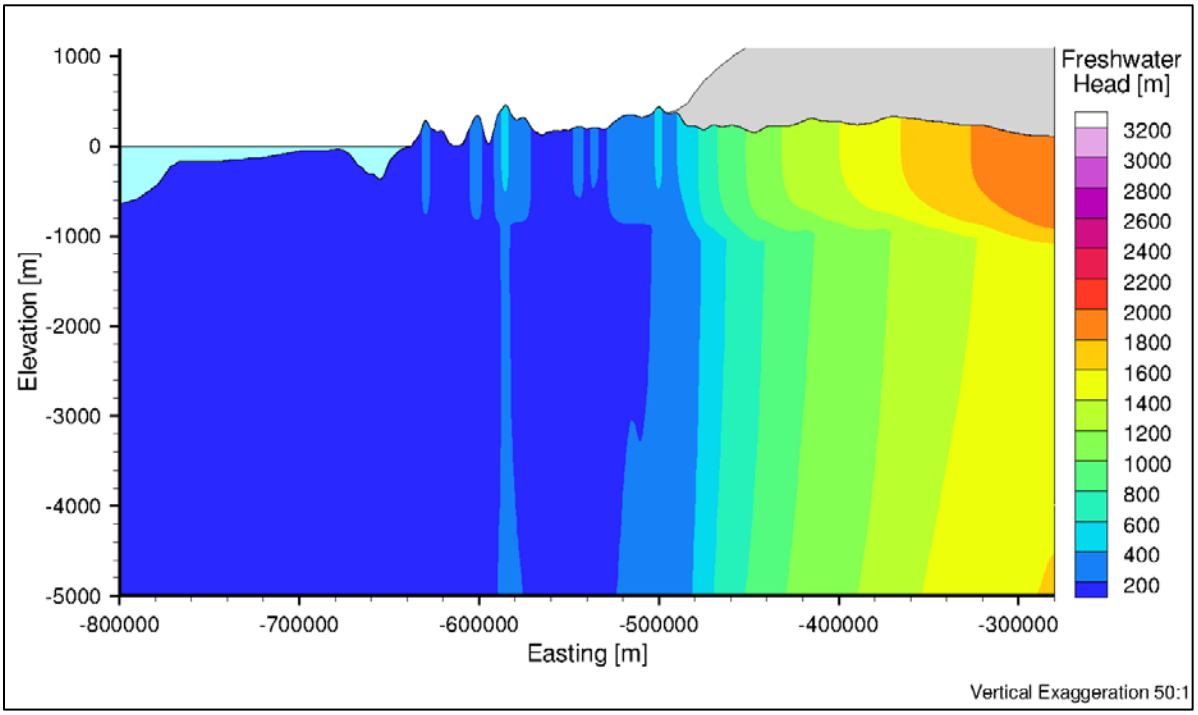

Figure 5.9 West-East cross-section of steady-state density-dependent head distribution for density-dependent flow with heat transport

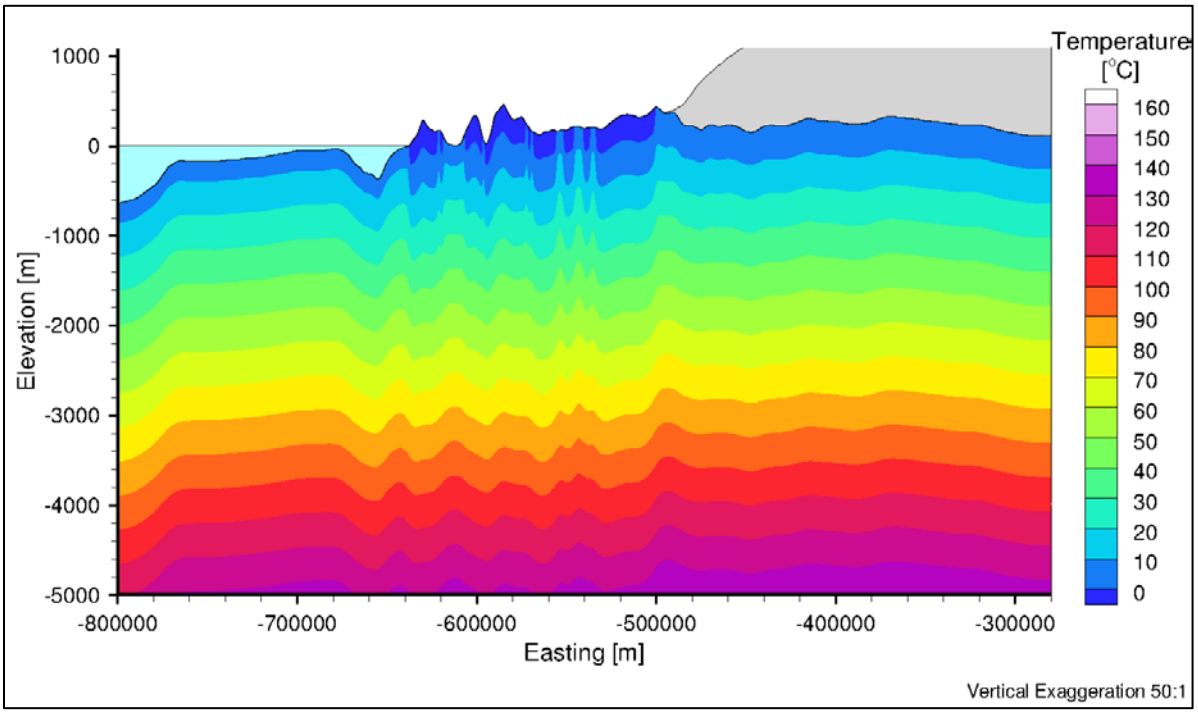

Figure 5.10 West-East cross-section of steady-state temperature distribution for density-dependent flow with heat transport

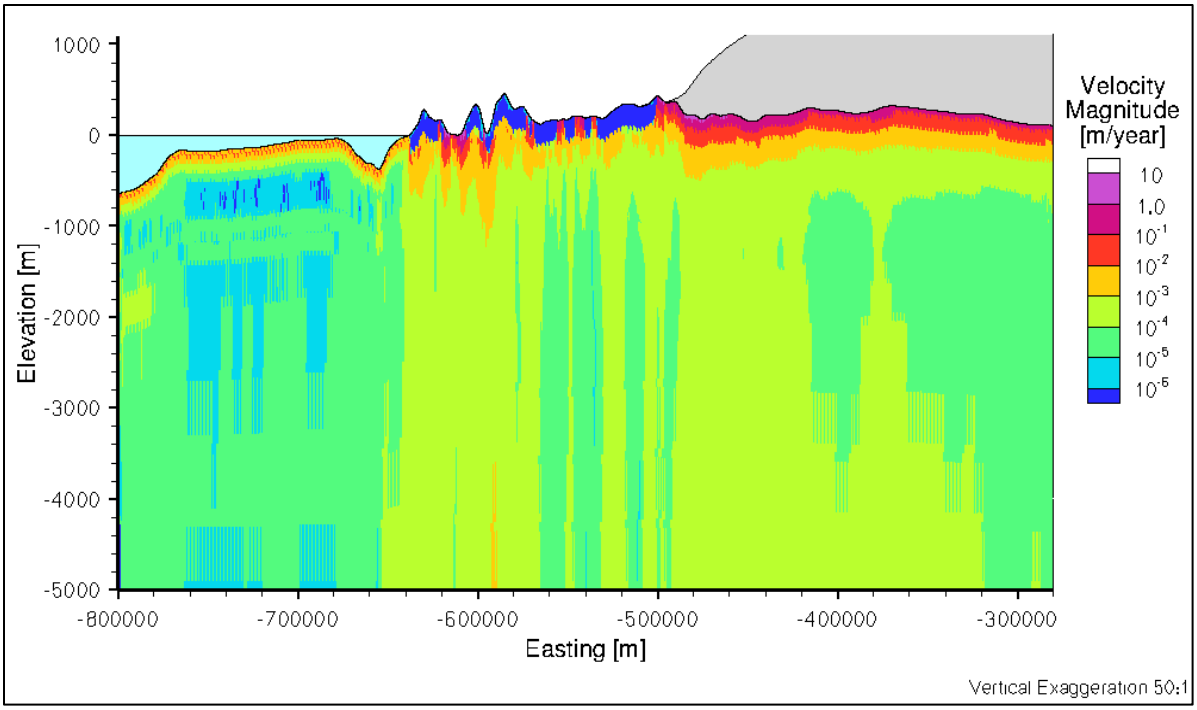

Figure 5.11 West-East cross-section of steady-state velocity magnitude distribution for density-dependent flow with heat transport

The ground surface was only exposed to below freezing atmospheric temperatures in the absence of the ice sheet and bodies of water that do not freeze to depth. Thus, the distribution of subsurface temperatures and, therefore, permafrost, evolves with the advance and retreat of the ice sheet as well as the fall and rise of sea level. By 3,200 years into the glacial cycle, all of the initial permafrost illustrated in Figure 5.10 had melted beneath the advancing ice sheet, and no other regions were exposed to atmospheric temperatures below freezing. By 6,400 years, the sea level in Davis Strait had dropped enough to expose some the underlying ground surface (around Easting -680000 m) to the atmosphere before the ice sheet had advanced that far west. Thus, a new region of permafrost formed there, expanding and shrinking in extent and depth as sea level continued to fluctuate until around 60,000 years when the ice sheet reached and covered that region. Permafrost formed again further west in Davis Strait as the sea level dropped in advance of the ice sheet (around 77,400 years) and later (around 92,100 years) melted as the ice sheet covered that region. While the ice sheet retreated, the sea level rose such that the Davis Strait region remained insulated from the below 0 ^{o}C atmospheric temperatures. Permafrost did begin to form again on the continent around 112,800 years as the ice sheet retreated.

Figure 5.12 illustrates the temperature distribution from 25,000 years to 40,000 years, a period when sea level in the Davis Strait fluctuated allowing permafrost to form where the ground surface was exposed to below 0 ^{o}C atmospheric temperatures in advance of the ice sheet. At 25,000 years, the permafrost extended over an area of approximately 6,250 m and to an approximate depth of 205 m. As sea level continued to drop from -34.41 m to -50.4 m over the

subsequent 9,000 years, as illustrated in Figure 5.5, the region of permafrost expanded to approximately 24,125 m across and approximately 255 m deep. Around that time (34,000 years), the sea level started to rise again, causing the permafrost to melt and degrade to approximately 2,250 m across and approximately 205 m deep by 40,000 years. This figure should be compared with Figure 5.14, which illustrates the temperature distribution for density-dependent flow with heat transport but not including latent heat. A discussion of that comparison is included with that figure in Section 5.4.2.

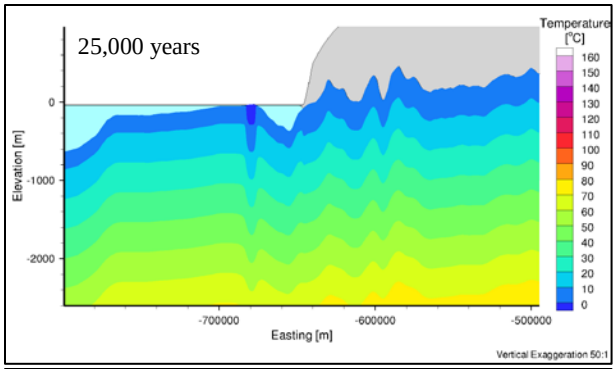
25,000 years
Temperature [°C]
160
150
140
130
120
110
100
90
80
70
60
50
40
30
20
10
0
Elevation [m]
0
-1000
-2000
-700000
-600000
-500000
Easting [m]
Vertical Exaggeration 50:1

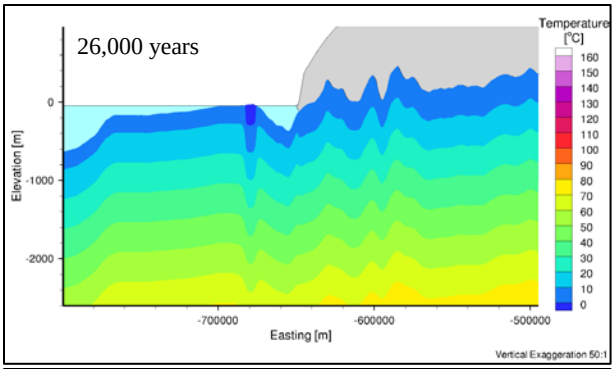
26,000 years
Temperature [°C]
160
150
140
130
120
110
100
90
80
70
60
50
40
30
20
10
0
Elevation [m]
0
-1000
-2000
-700000
-600000
-500000
Easting [m]
Vertical Exaggeration 50:1

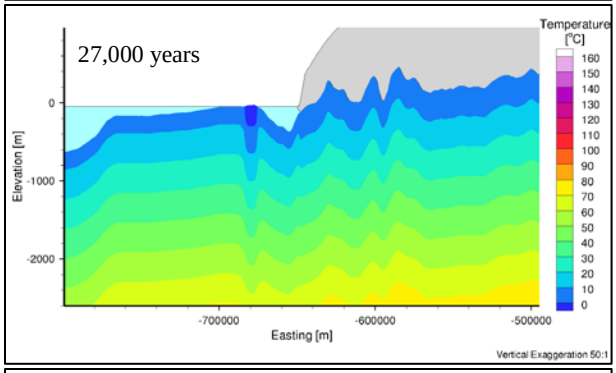
27,000 years
Temperature [°C]
160
150
140
130
120
110
100
90
80
70
60
50
40
30
20
10
0
Elevation [m]
0
-1000
-2000
-700000
-600000
-500000
Easting [m]
Vertical Exaggeration 50:1

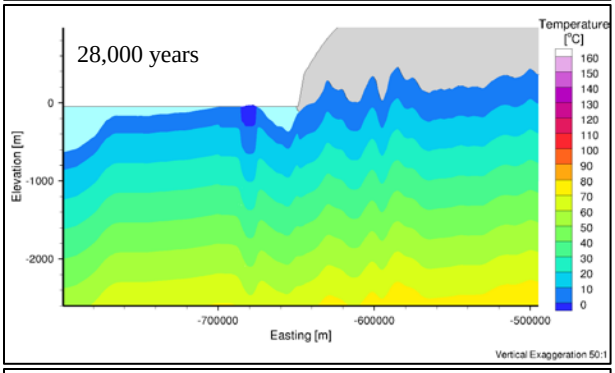
28,000 years
Temperature [°C]
160
150
140
130
120
110
100
90
80
70
60
50
40
30
20
10
0
Elevation [m]
0
-1000
-2000
-700000
-600000
-500000
Easting [m]
Vertical Exaggeration 50:1

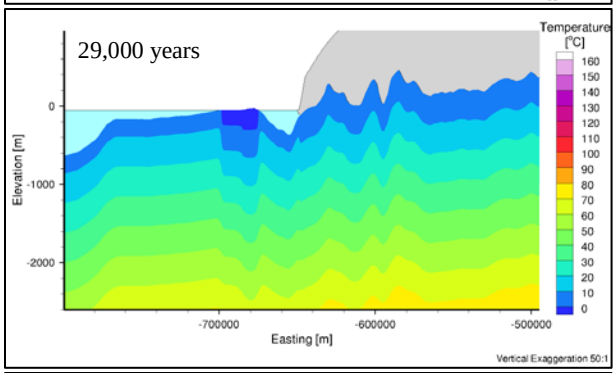
29,000 years
Temperature [°C]
160
150
140
130
120
110
100
90
80
70
60
50
40
30
20
10
0
Elevation [m]
0
-1000
-2000
-700000
-600000
-500000
Easting [m]
Vertical Exaggeration 50:1

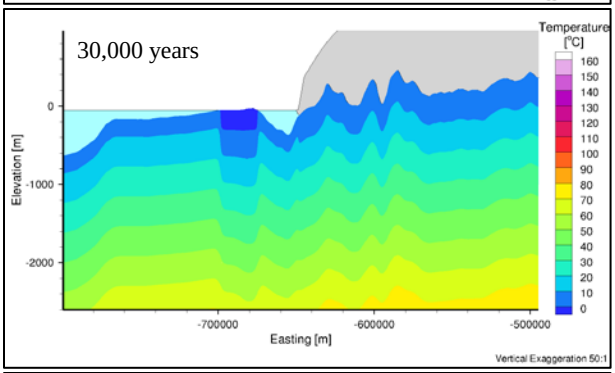
30,000 years
Temperature [°C]
160
150
140
130
120
110
100
90
80
70
60
50
40
30
20
10
0
Elevation [m]
0
-1000
-2000
-700000
-600000
-500000
Easting [m]
Vertical Exaggeration 50:1

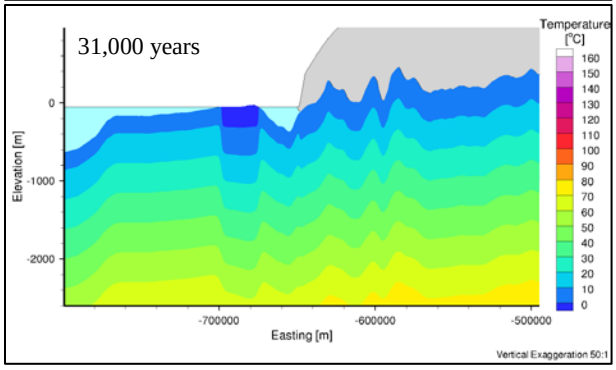
31,000 years
Temperature [°C]
160
150
140
130
120
110
100
90
80
70
60
50
40
30
20
10
0
Elevation [m]
0
-1000
-2000
-700000
-600000
-500000
Easting [m]
Vertical Exaggeration 50:1

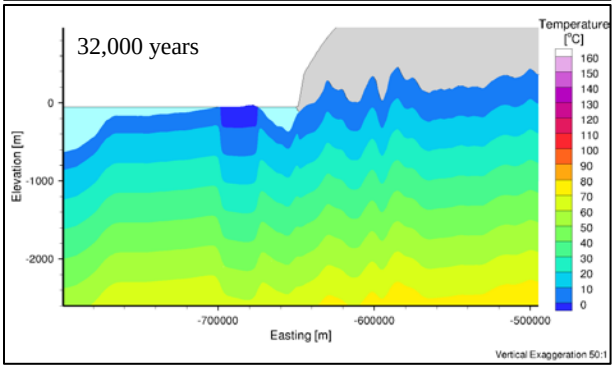
32,000 years
Temperature [°C]
160
150
140
130
120
110
100
90
80
70
60
50
40
30
20
10
0
Elevation [m]
0
-1000
-2000
-700000
-600000
-500000
Easting [m]
Vertical Exaggeration 50:1

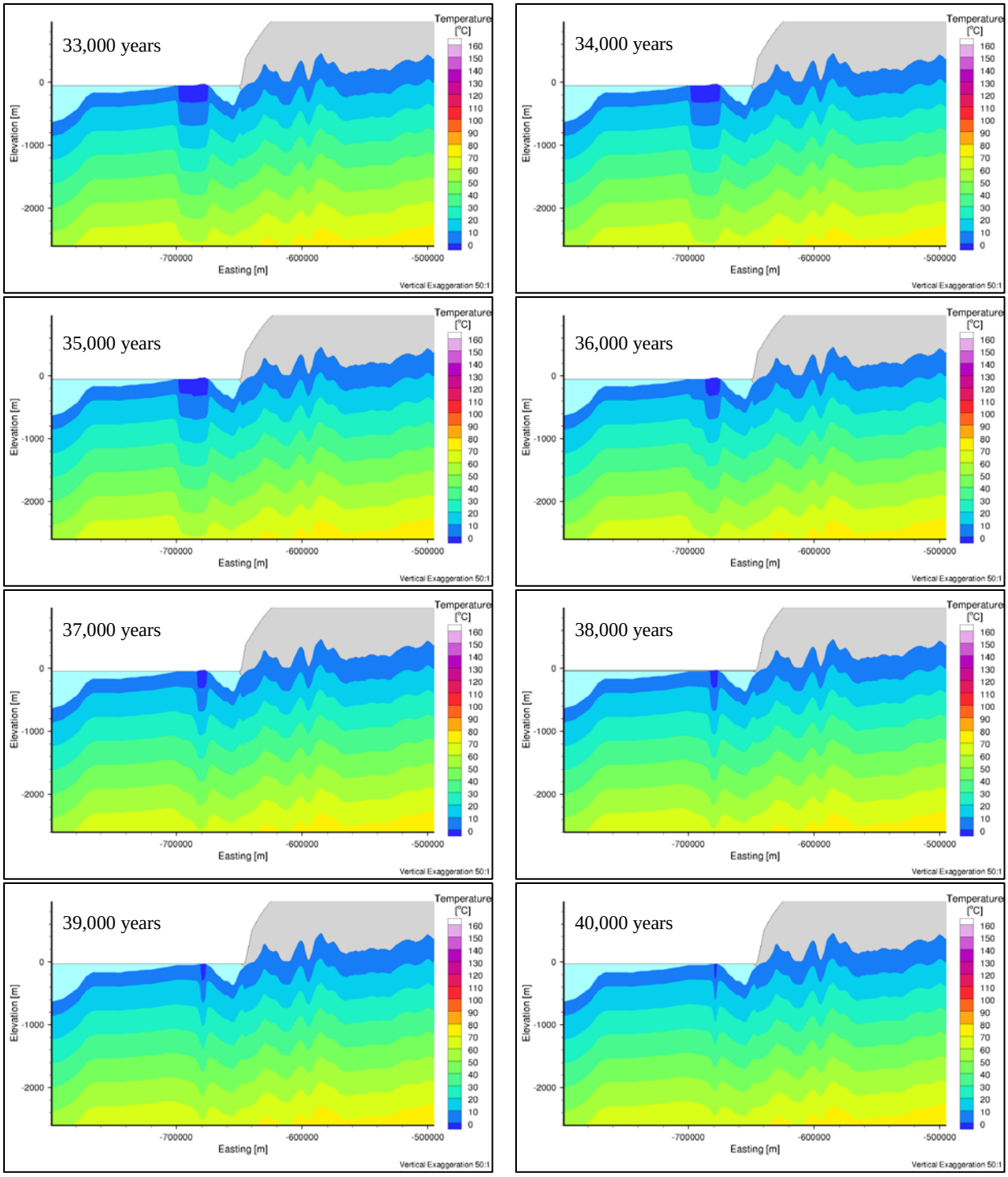

Figure 5.12 West-East cross-section of the temperature distribution for density-dependent flow with heat transport for t = 25,000 years to t = 40,000 years with Δt = 1,000 years.
As sea level dropped in Davis Strait, the ground surface was exposed to freezing atmospheric temperatures, which allowed permafrost to form (froze); as sea level rose again, the permafrost degraded (melted). Compare with Figure 5.14 illustrating the temperature distribution for density-dependent flow with heat transport including latent heat for the same time frame.

5.4.2 Density-dependent Flow with Heat Transport including Latent Heat

The procedure outlined in Section 5.4.1 for developing the initial pressure and temperature conditions for the transient analyses was the same procedure used for the scenarios that included latent heat. Again, a constant depth-dependent TDS distribution was used (Figure 5.7). Figure 5.8, Figure 5.9, Figure 5.10, and Figure 5.11 illustrate the results of the final steady-state simulation, which were the initial conditions (pressure, hydraulic head, temperature, and velocity magnitude) for the transient analyses.

Again, the transient simulation, which represented a glacial cycle of 120,000 years (Section 5.3.4) included fluid flow (Darcy's Law), temperature (Heat Transport in Porous Media), and one-dimensional hydromechanical coupling (Section 3.2.4). For these steady-state and transient simulations, latent heat was represented in the manner described in Section 3.2.3.1. As with the previous analysis (Section 5.4.1), as the ice sheet advanced, pressures beneath it were raised, and as the ice sheet retreated, the pressure was lowered again. The velocity magnitude distribution also followed the same trends as described for the previous analysis with the exact distribution evolving with the advancing/retreating ice sheet and freezing/melting permafrost.

It should be noted here that the transient solver needed to be configured differently for simulations that included the effects of latent heat than for the previous simulations without the effects of latent heat. For the previous simulations that did not include the effects of latent heat, the maximum time-step size the solver was allowed to take was restricted to the difference between the specified output times, in this case 500 years. For simulations that did include the effects of latent heat, that restriction had to be removed in order for the solver to converge to a solution. Additional computational power or resources may allow for that restriction to be made for simulations that include the effects of latent. Because that restriction was removed, however, the solver took some time-steps that were larger than the 500 year interval between output times. In those instances, COMSOL interpolated between the time-steps taken to provide results at the specified output times.

The impact of incorporating the effects of latent heat in the model on the pressure distribution is illustrated in Figure 5.13 showing the change in magnitude of the difference in pressure between the two simulations over 25,000 years. These differences in pressure are a result of the differences in temperature between the two scenarios (without and with latent heat). Pressure differences are most pronounced at depth beneath the edge of the ice sheet with pressure differences up to 10^6 Pa in magnitude. The pressure differences do not appear or disappear immediately, but develop and increase in magnitude when the ice sheet is stationary and dissipate gradually when the ice sheet advances or retreats again.

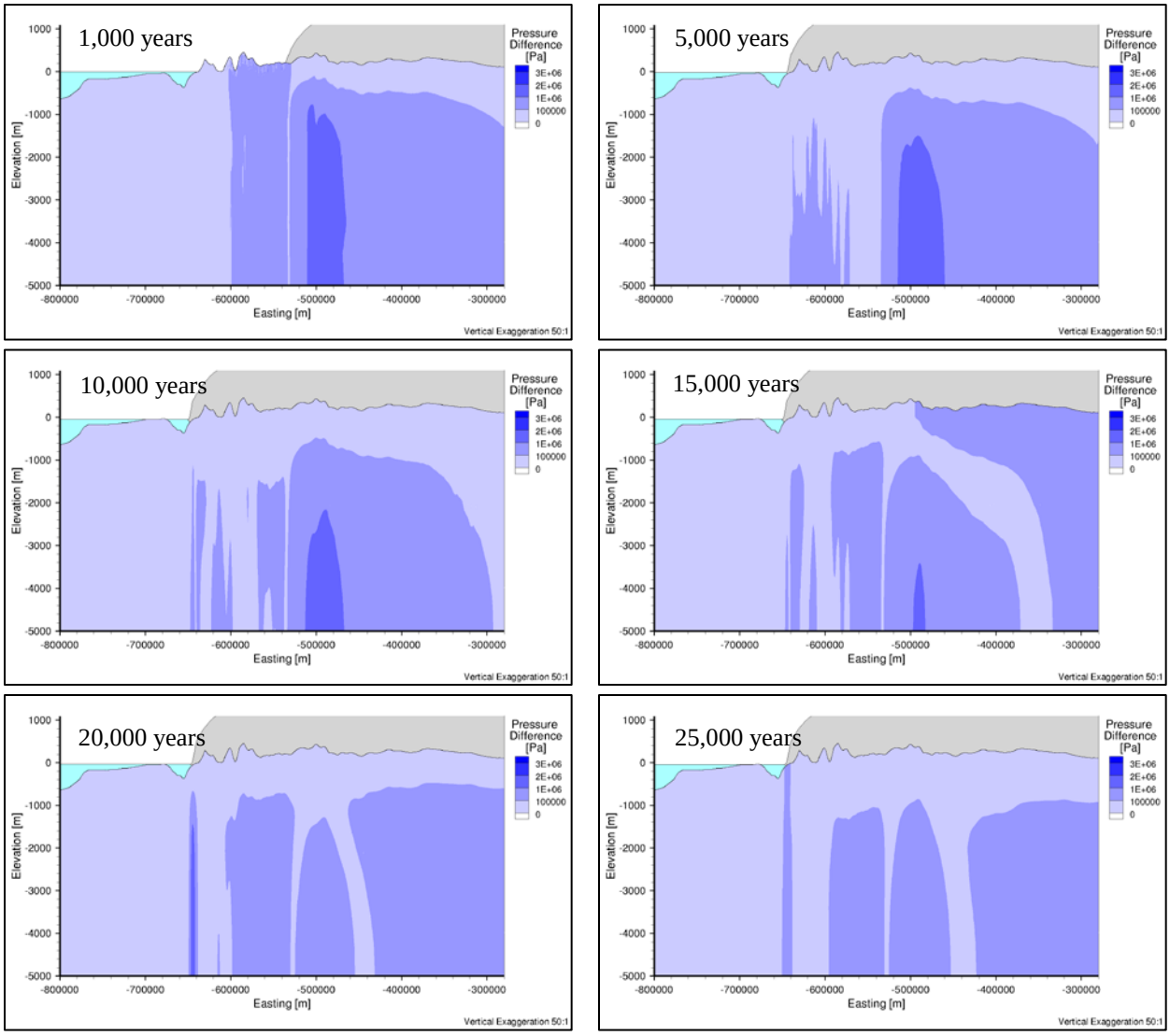

Figure 5.13 West-East cross-section of the difference in pressure between simulations without and with the effects of latent heat.

As with the previous simulation, the distribution of subsurface temperatures and, therefore, permafrost evolved with the advance and retreat of the ice sheet as well as the fall and rise of sea level. Figure 5.14 illustrates the temperature distribution from 25,000 years to 40,000 years, a period when sea level in the Davis Strait fluctuated, allowing permafrost to form where the ground surface was exposed to freezing atmospheric temperatures in advance of the ice sheet. This figure should be compared with Figure 5.12, which illustrates the temperature distribution for density-dependent flow with heat transport but not including latent heat for the same time frame.

At 25,000 years, the permafrost extended over an area of approximately 5,625 m, a narrower region than in the simulation without latent heat, and an approximate depth of 205 m,

the same depth as in the simulation without latent heat. As sea level dropped over the subsequent 9,000 years, the region of permafrost expanded to approximately 24,000 m across and approximately 255 m deep. Around 34,000 years, the sea level started to rise again, and the permafrost melted and degraded to approximately 2,500 m across and approximately 200 m deep by 40,000 years.

The maximum permafrost depths were the same for the simulations with latent heat as they were for the simulations without latent heat. For the simulations without latent heat, the depth of the permafrost was approximately the same across the entire region of permafrost at each time step. For simulations with latent heat, the permafrost developed unevenly across the entire region of permafrost. As shown in Figure 5.14, between 26,000 years and 33,000 years, as the permafrost developed, it reached maximum depths on the eastern side of the permafrost region quicker than in the western side. However, by 34,000 years, the depth of the permafrost was approximately the same across the entire region of permafrost. The same pattern was observed when the permafrost degraded with the permafrost melting more quickly on the western side than on the eastern side.

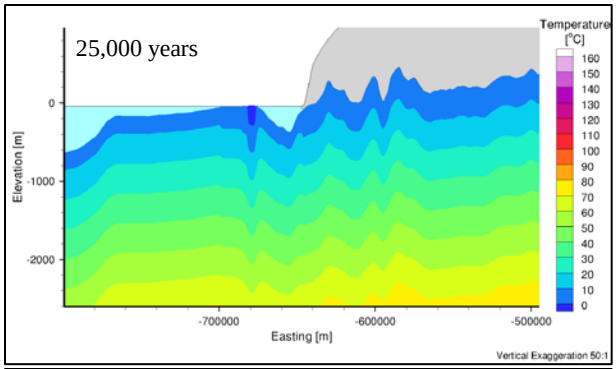
25,000 years
Temperature [°C]
160
150
140
130
120
110
100
90
80
70
60
50
40
30
20
10
0
Elevation [m]
0
-1000
-2000
-700000
-600000
-500000
Easting [m]
Vertical Exaggeration 50:1

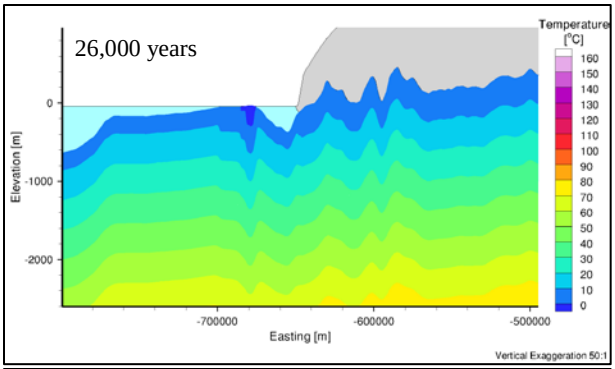
26,000 years
Temperature [°C]
160
150
140
130
120
110
100
90
80
70
60
50
40
30
20
10
0
Elevation [m]
0
-1000
-2000
-700000
-600000
-500000
Easting [m]
Vertical Exaggeration 50:1

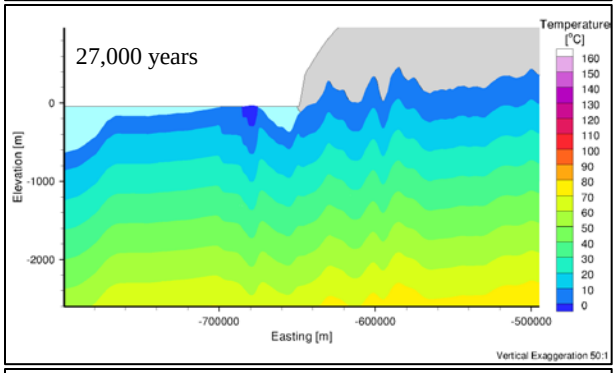
27,000 years
Temperature [°C]
160
150
140
130
120
110
100
90
80
70
60
50
40
30
20
10
0
Elevation [m]
0
-1000
-2000
-700000
-600000
-500000
Easting [m]
Vertical Exaggeration 50:1

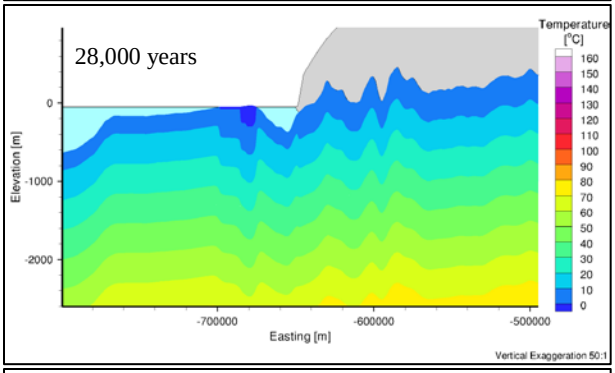
28,000 years
Temperature [°C]
160
150
140
130
120
110
100
90
80
70
60
50
40
30
20
10
0
Elevation [m]
0
-1000
-2000
-700000
-600000
-500000
Easting [m]
Vertical Exaggeration 50:1

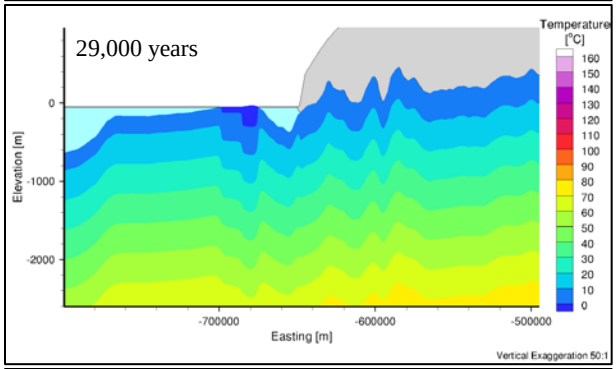
29,000 years
Temperature [°C]
160
150
140
130
120
110
100
90
80
70
60
50
40
30
20
10
0
Elevation [m]
0
-1000
-2000
-700000
-600000
-500000
Easting [m]
Vertical Exaggeration 50:1

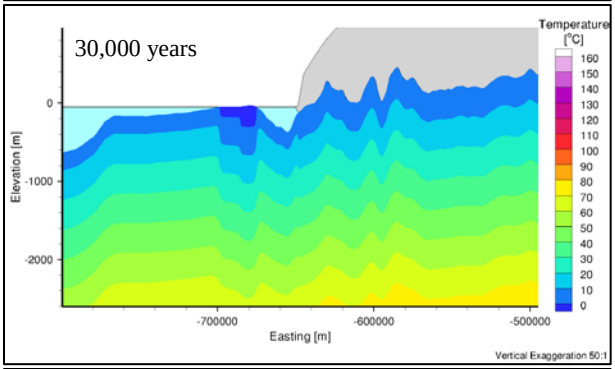
30,000 years
Temperature [°C]
160
150
140
130
120
110
100
90
80
70
60
50
40
30
20
10
0
Elevation [m]
0
-1000
-2000
-700000
-600000
-500000
Easting [m]
Vertical Exaggeration 50:1

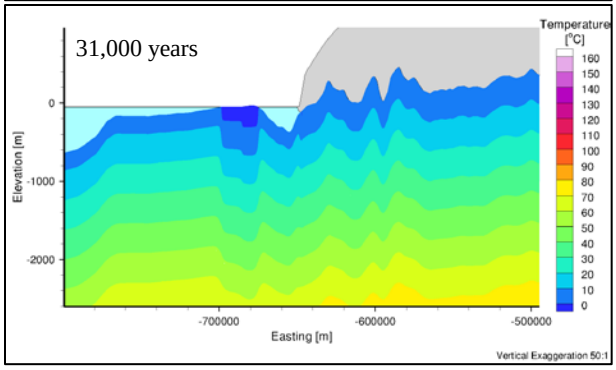
31,000 years
Temperature [°C]
160
150
140
130
120
110
100
90
80
70
60
50
40
30
20
10
0
Elevation [m]
0
-1000
-2000
-700000
-600000
-500000
Easting [m]
Vertical Exaggeration 50:1

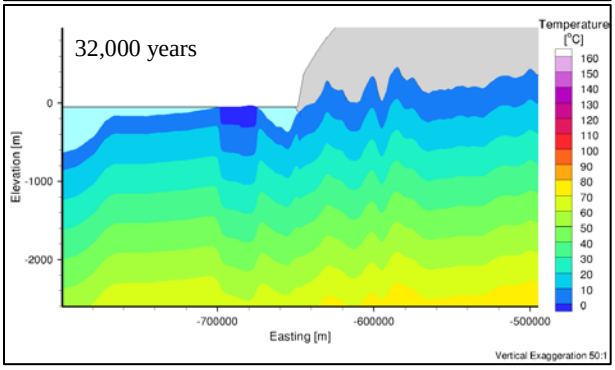
32,000 years
Temperature [°C]
160
150
140
130
120
110
100
90
80
70
60
50
40
30
20
10
0
Elevation [m]
0
-1000
-2000
-700000
-600000
-500000
Easting [m]
Vertical Exaggeration 50:1

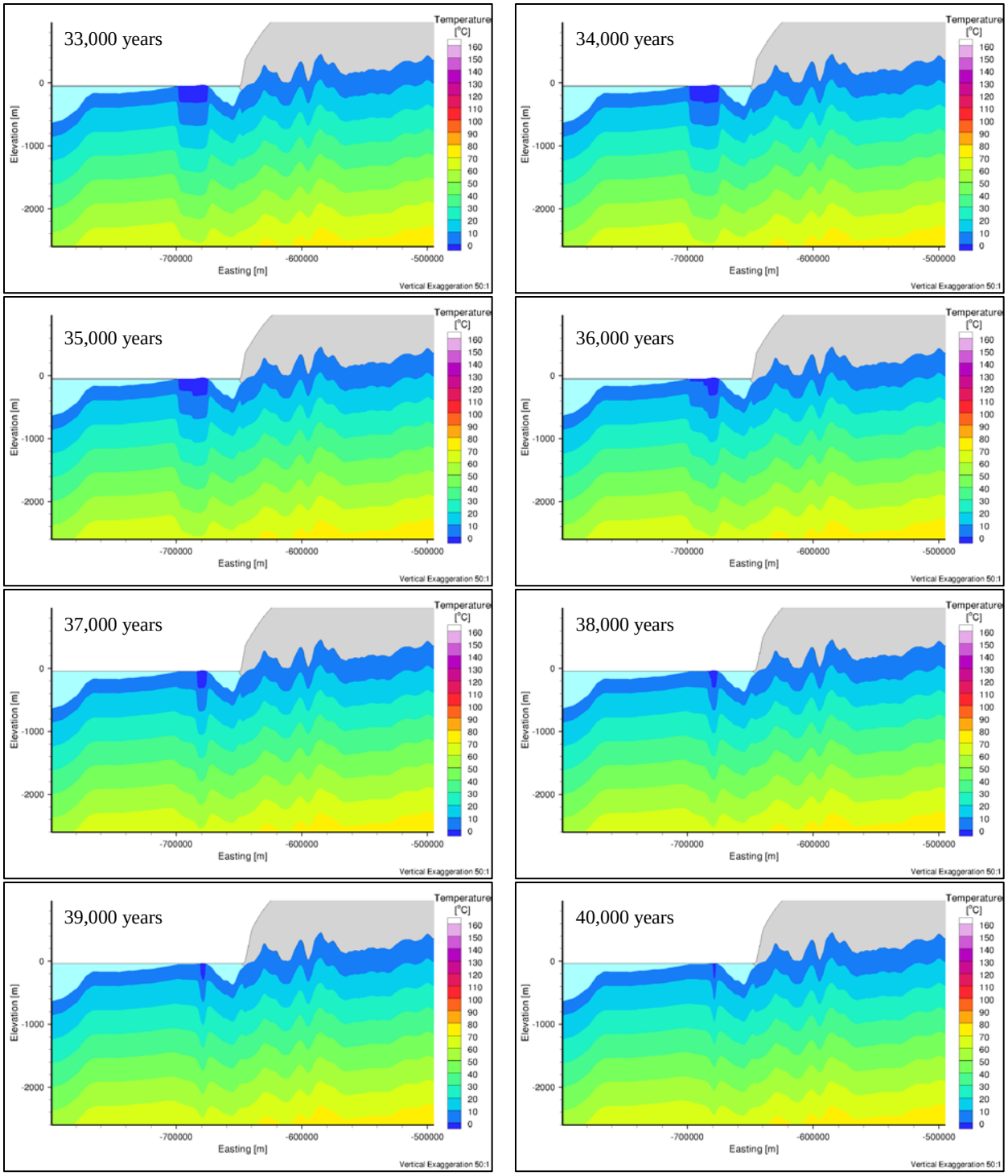

Figure 5.14 West-East cross-section of the temperature distribution for density-dependent flow with heat transport including latent heat for t = 25,000 years to t = 40,000 years with Δt = 1,000 years.

As sea level dropped in Davis Strait, the ground surface was exposed to freezing atmospheric temperatures, which allowed permafrost to form (froze); as sea level rose again, the permafrost degraded (melted). Compare with Figure 5.12 illustrating the temperature distribution for density-dependent flow with heat transport without latent heat for the same time frame.

5.4.3 Variably-saturated Flow and Permafrost

To examine the impact of variably-saturated flow conditions on the water table and the hydrologic flow system, FRAC3DVS-OPG was used to simulate variably-saturated flow and solute transport for the three-dimensional GAP domain. Table 5.6 outlines the scenarios that were investigated. To begin, a steady-state simulation was run for the three-dimensional GAP domain without density-dependent flow or ice sheet dynamics. These simplifications were made to ensure model stability and convergence. For the first simulation, fully-saturated conditions were imposed with the specified head equal to 3 m below the elevation at the top surface and the elevation of the surface water bodies at lakes and rivers. Permafrost was excluded so that the effect of permafrost on the water table and the hydrologic flow system could be examined through comparison. The porosity used in these simulations investigating variably-saturated flow and permafrost is different (0.003) than the porosity used in the simulations presented in Yin et al. [2013] and in Section 5.4.1 and Section 5.4.2 (0.005). This difference occurred because the porosity value was updated to 0.003 to reflect the most recent results from the GAP field investigations during this thesis research.

Table 5.2 Scenarios investigated to examine the impact of variably-saturated flow and the presence of permafrost on the water table

	1	**2**	**3**	**4**	**5**	**6**	**7**	**8**	**9**	**10**	**11**	**12**
Flow												
Steady-State	✓	✓	✓	✓	✓	✓						
Transient							✓	✓	✓	✓	✓	✓
Saturation												
Saturated	✓	✓					✓	✓				
Variably-saturated – Constant *k*			✓	✓					✓	✓		
Variably-saturated – Linear Relationship					✓	✓					✓	✓
Permafrost												
No Permafrost	✓		✓		✓		✓		✓		✓	
Permafrost		✓		✓		✓		✓		✓		✓
Initial Conditions												
N/A	✓	✓	✓	✓	✓	✓						
Head values from previous simulation							1	2	1	2	1	2

Figure 5.15 and Figure 5.16 illustrate the results of this steady-state simulation (freshwater head and velocity magnitude, respectively), which were later used as the initial conditions for the transient simulations. The freshwater head values (Figure 5.15) were elevated beneath the ice sheet with head values increasing further beneath the ice sheet where the ice sheet was thicker. Velocity magnitudes (Figure 5.16) were greatest (on the order of 10^1 to 10^0 m/year at the surface) in the shallow subsurface and decreased with increasing depth as expected given the depth-dependent permeability profile used (Section 5.3.3). The velocity magnitude was approximately one order-of-magnitude greater at the locations of deformation zones (Figure 5.6)

than the surrounding subsurface, which was also to be expected given that the hydraulic conductivity of the deformation zones was greater than that of the surrounding rock matrix (Section 5.3.6).

This steady-state simulation imposed fully-saturated flow conditions. Thus, as expected with the head specified to be 3 m below the elevation of the top surface, the depth to the water table was constant. For fully-saturated conditions, the depth to the water table or the deepest zero potentiometric surface was determined using elevation and hydraulic head (environmental head for density-dependent problems). The deepest zero-potentiometric surface was located at the first instance where the elevation was equal to the hydraulic head or where the pressure was equal to zero when searching up through the domain from the bottom of the domain.

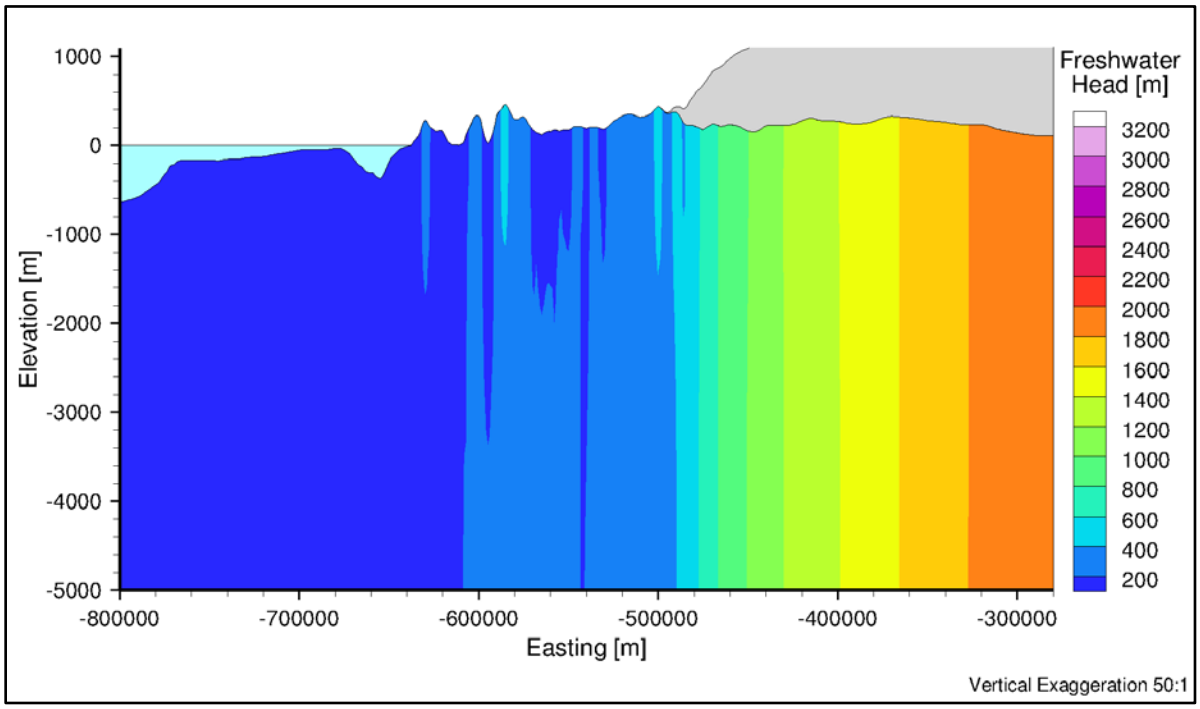

Figure 5.15 West-East cross-section of freshwater head distribution for saturated, density-independent flow without permafrost

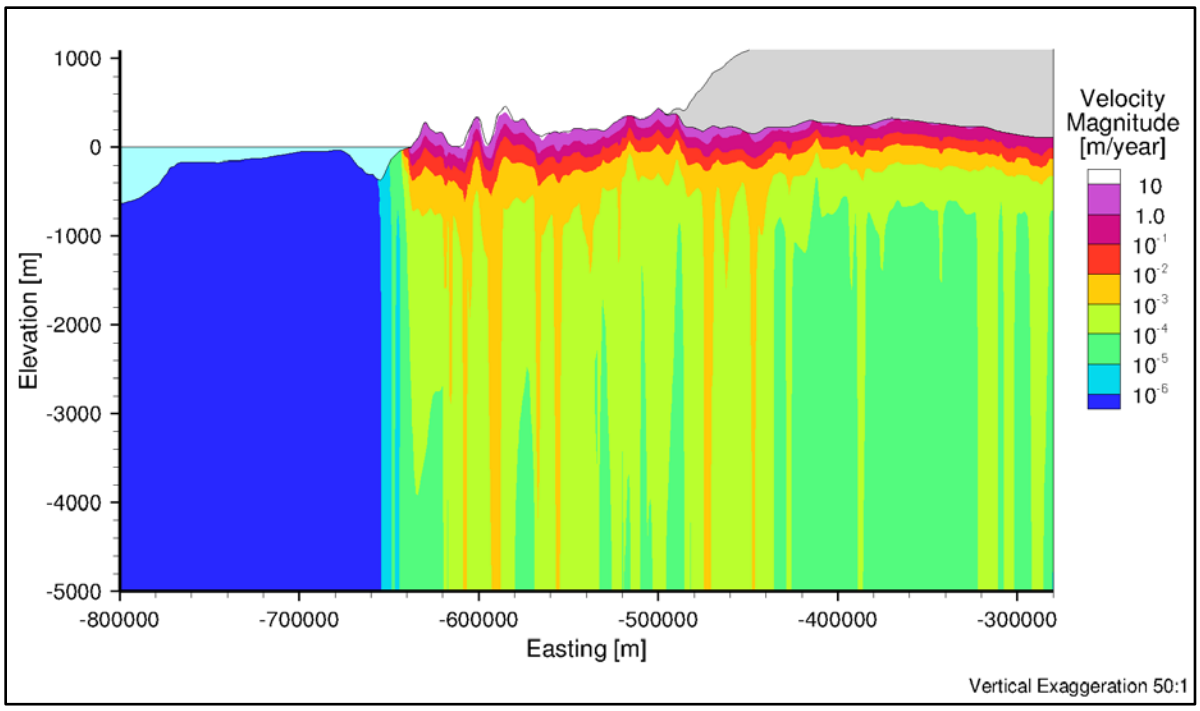

Figure 5.16 West-East cross-section of velocity magnitude distribution for saturated, density-independent flow without permafrost

The next step was to simulate steady-state, variably-saturated flow conditions. First, a simple linear relationship between saturation and relative permeability was implemented in order to obtain preliminary results quickly. However, that simple linear relationship between saturation and relative permeability would not allow the model to converge to a solution. To improve numerical stability, the saturation-relative permeability relationship was first held constant (k_{rw} = 0.5), and then the results of that steady-state simulation were used as initial conditions for variably-saturated flow with a linear relationship between saturation and relative permeability (Table 5.3). Figure 5.17, Figure 5.18, and Figure 5.19 illustrate the results of the steady-state simulation with variably-saturated flow conditions. Figure 5.20 illustrates the depth to the water table for the GAP domain in areal view. For variably-saturated flow conditions, the water table was determined to be where saturation was equal to one (i.e. fully saturated).

Table 5.3 Relationships between pressure, saturation, and relative permeability for variably-saturated flow conditions

Pressure (m)	Saturation
-10.0	0.053
0.0	1.0
Saturation	**Relative Permeability**
0.053	0.5
1.0	1.0

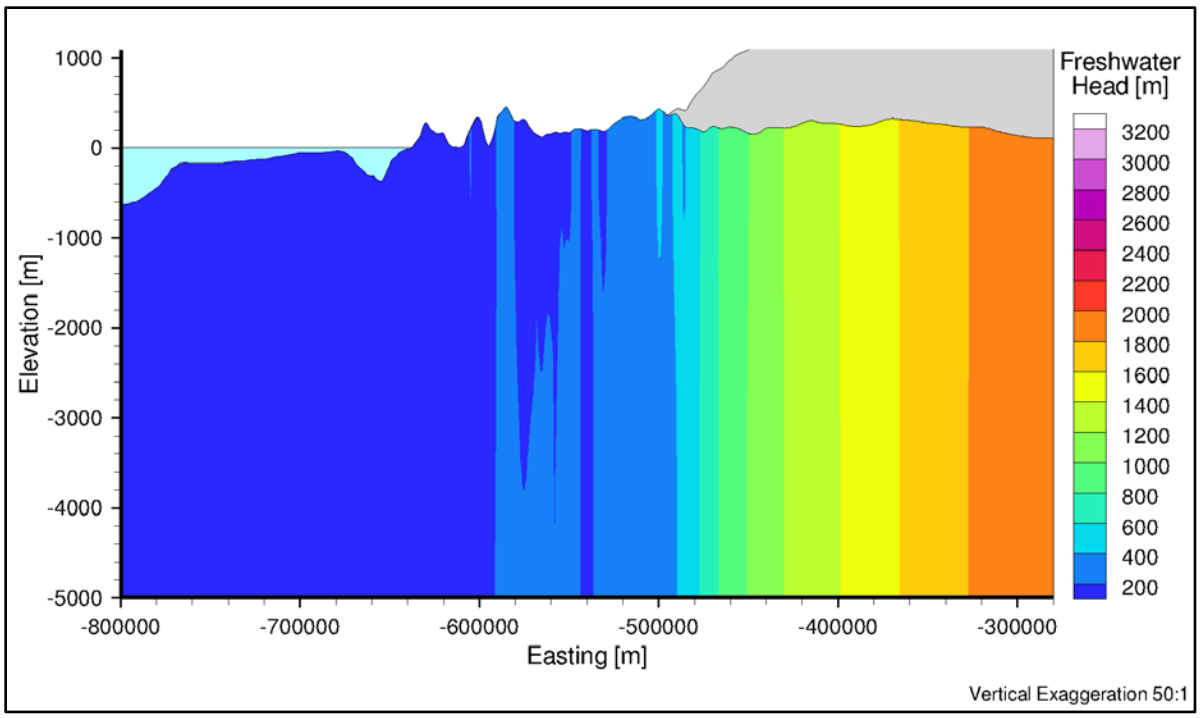

Figure 5.17 West-East cross-section of freshwater head distribution for variably-saturated, density-independent flow without permafrost

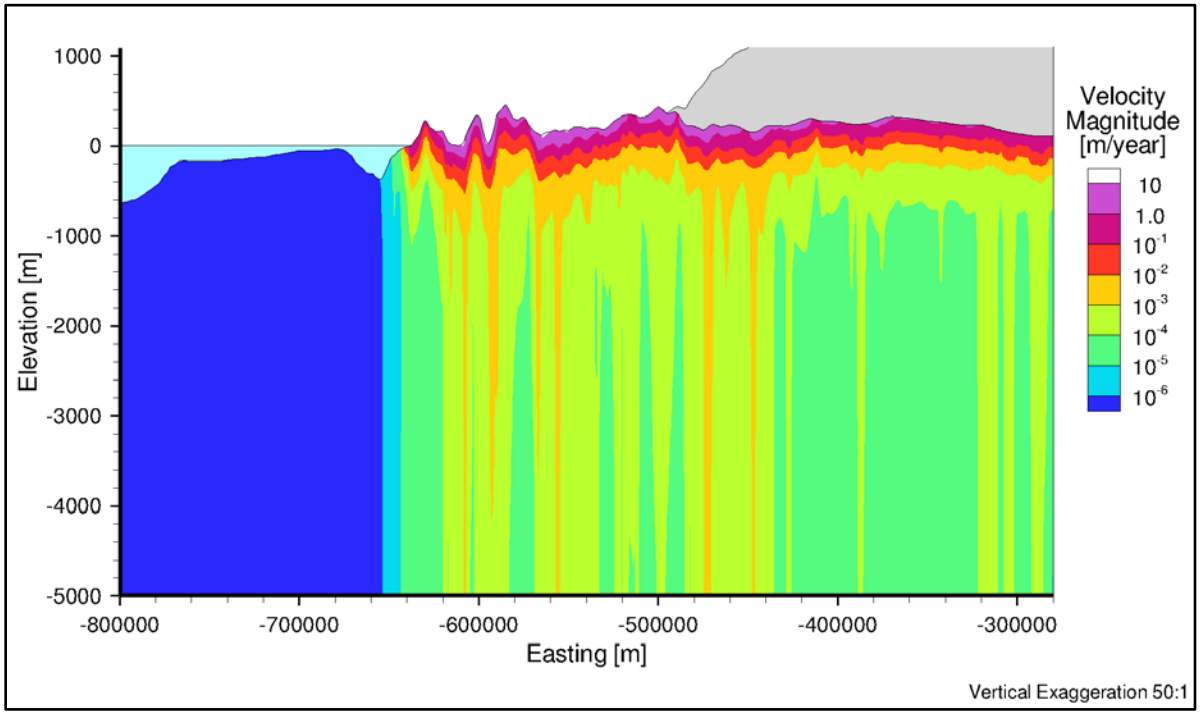

Figure 5.18 West-East cross-section of velocity magnitude distribution for variably-saturated, density-independent flow without permafrost

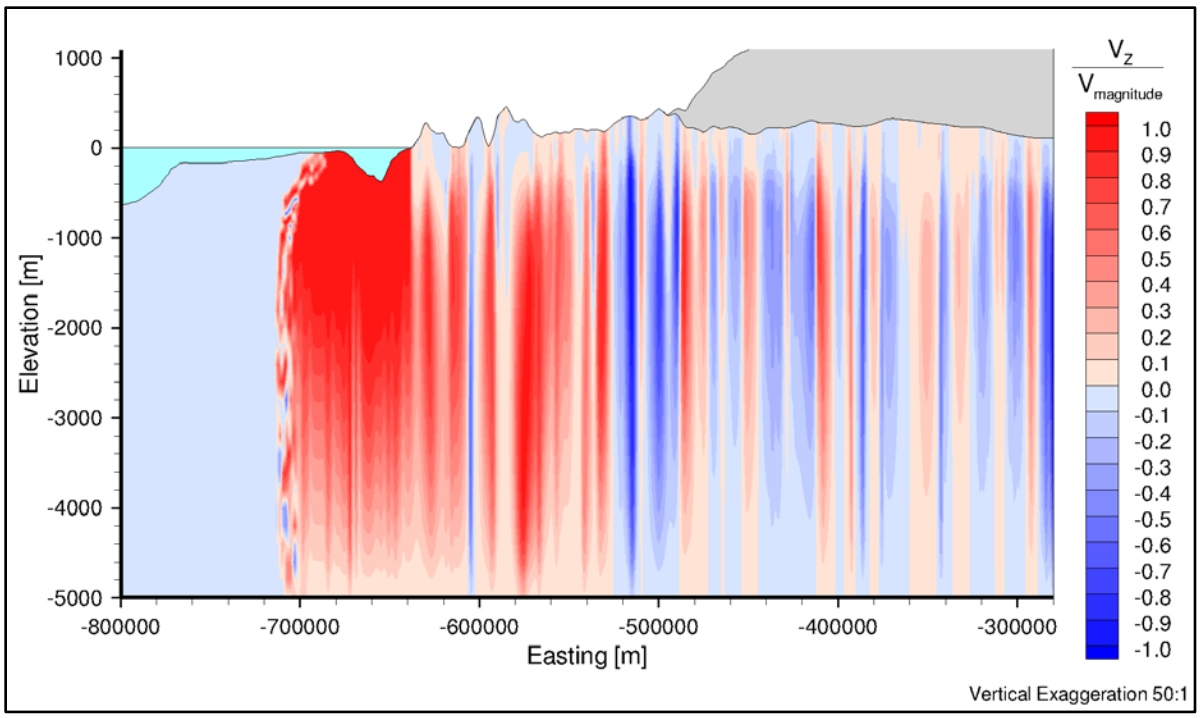

Figure 5.19 West-East cross-section of the ratio of vertical pore water velocity to the pore water velocity magnitude distribution for variably-saturated, density-independent flow without permafrost

The variably-saturated flow conditions resulted in lower head values and an extended water table. As shown in Figure 5.20, the depth to the water table is up to approximately 650 m in regions of higher elevation. As a consequence of this reduction in freshwater heads, the pore water velocities were also reduced up to one order-of-magnitude in the shallow subsurface at higher elevations as observed in a comparison of Figure 5.18, which illustrates the velocity magnitude distribution for variably-saturated flow, with Figure 5.16, which illustrates the velocity magnitude distribution for fully-saturated flow.

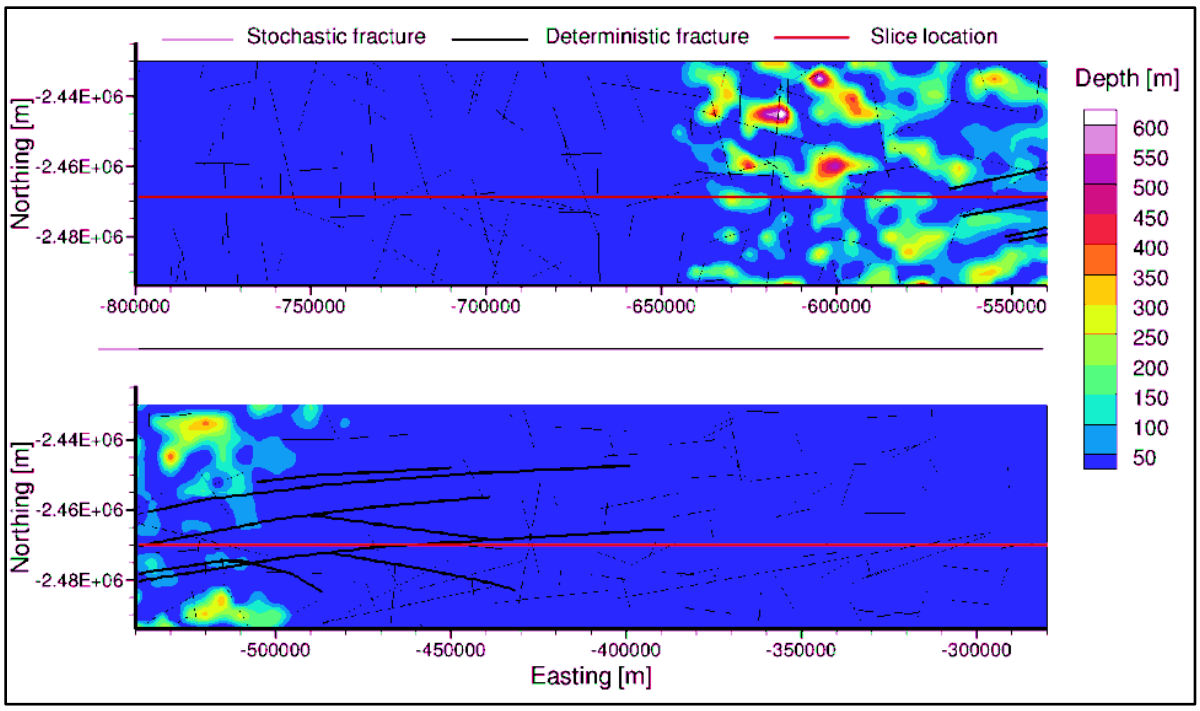

Figure 5.20 Areal view of the depth to the water table for variably-saturated, density-independent flow without permafrost

To examine the effects of permafrost on the water table, the steady-state simulations described in the preceding paragraphs were re-run with the addition of a 300 m layer of permafrost with a hydraulic conductivity of 5×10^{-11} m/s. Boundary conditions remained the same with the specified head equal to 3 m below the elevation at the top surface and the elevation of the surface water bodies at lakes and rivers. There was no recharge. Figure 5.21 shows that the permafrost was absent beneath all water bodies. Figure 5.22 illustrates the depth to the water table for variably-saturated flow conditions. While the impact of permafrost on the water table is more pronounced in the transient simulations, a comparison of Figure 5.20 and Figure 5.22 does show the depth to the water table differs by up to 60 m for the steady-state simulations. Figure 5.23 illustrates the difference between the depths to the water table for the two scenarios (i.e. depth to water table without permafrost - depth to water table with permafrost), with the greatest difference occurring at higher elevations between -650,000 m and -550,000 m (Easting) and -2,460,000 m and – 2,430,000 m (Northing).

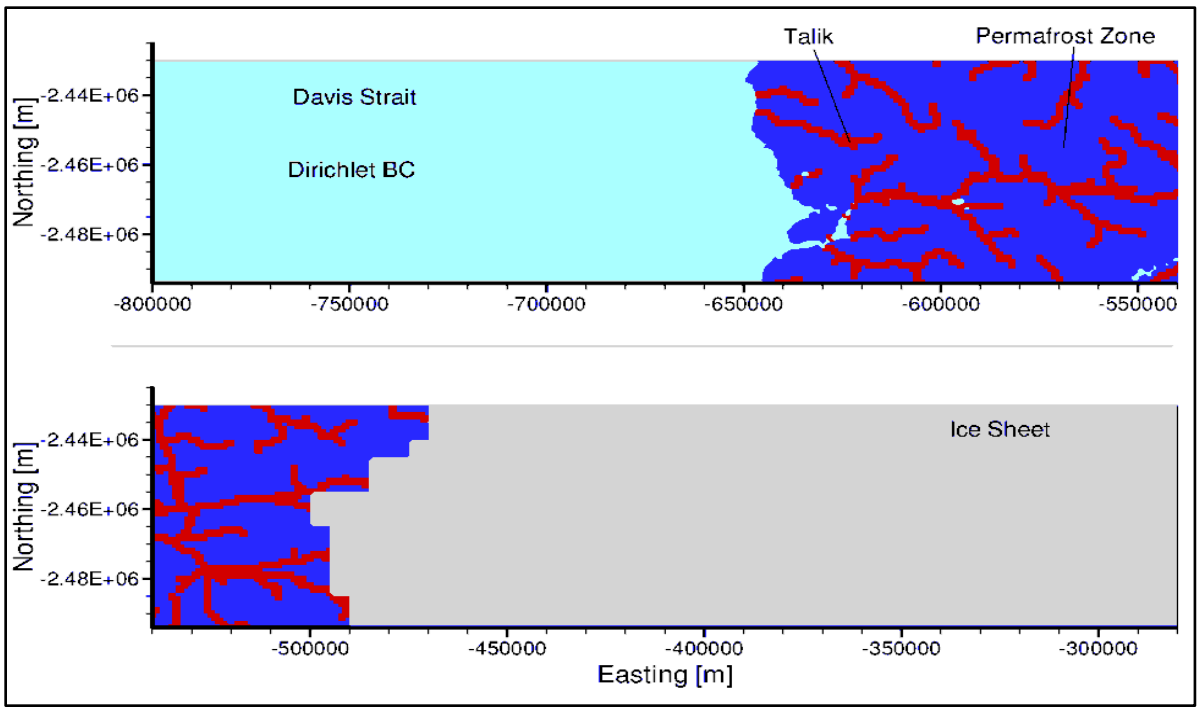

Figure 5.21 Areal view of prescribed permafrost and taliks

Permafrost with a depth of 300 m and a hydraulic conductivity of 5×10^{-11} m/s was prescribed for the GAP domain.

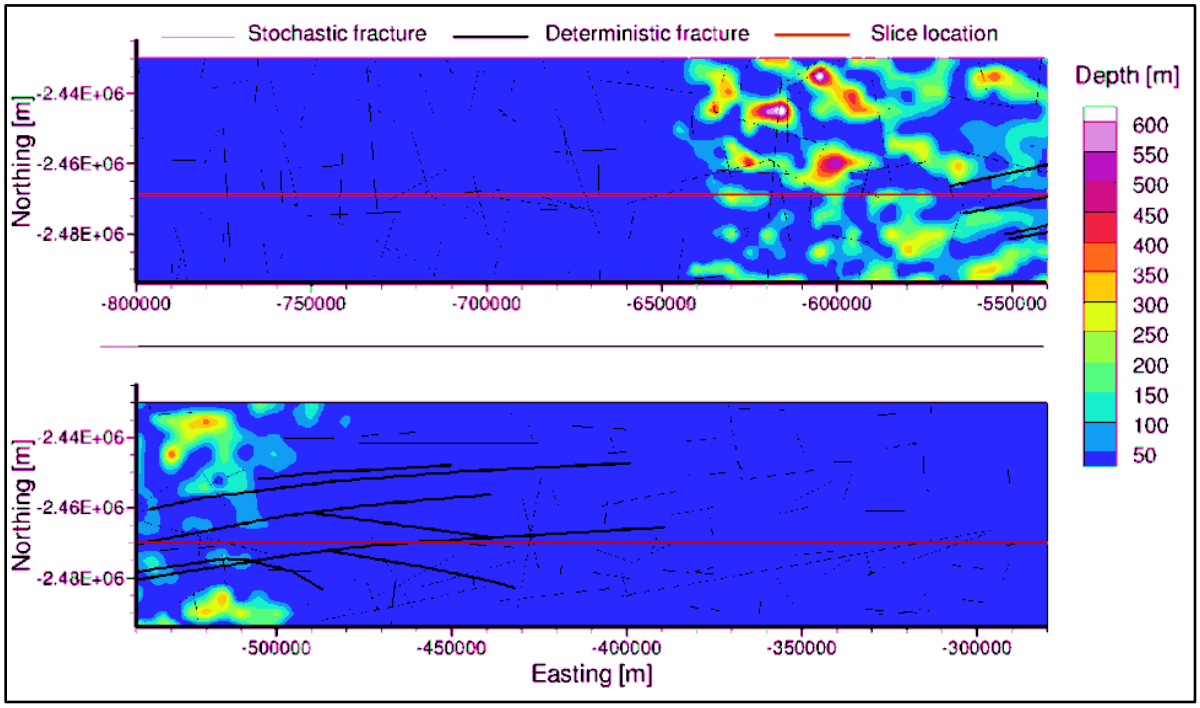

Figure 5.22 Areal view of the depth to the water table for variably-saturated, density-independent flow with permafrost

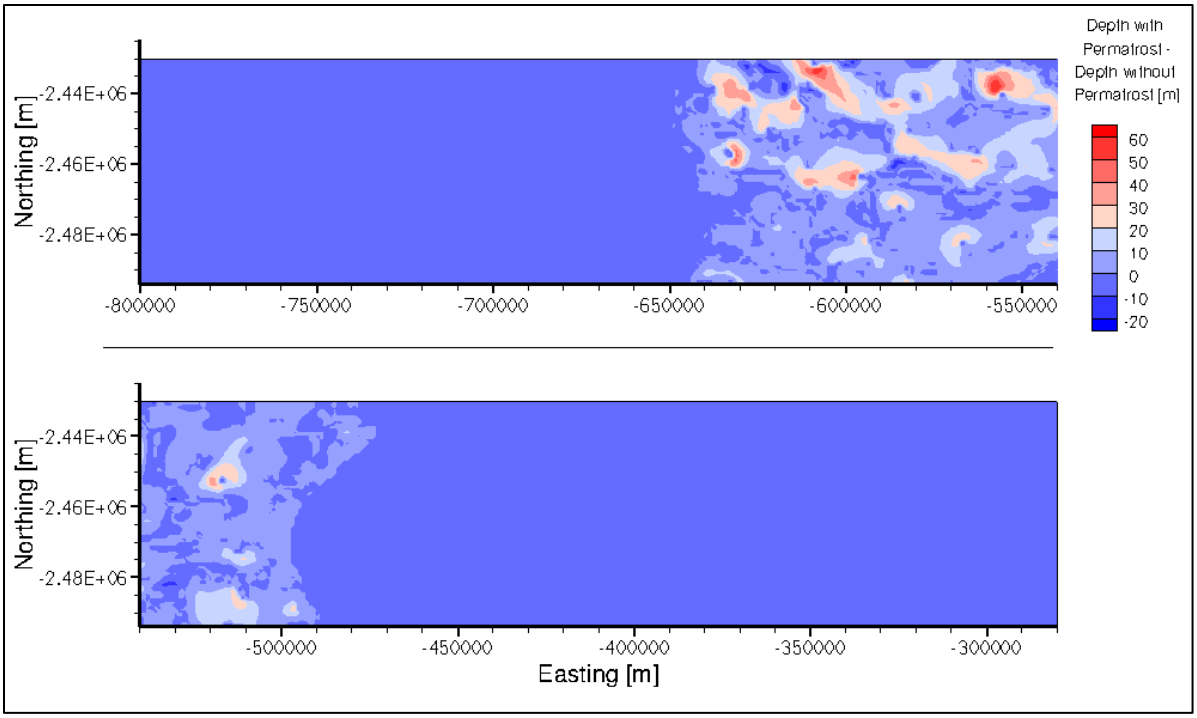

Figure 5.23 Areal view of the difference between the depth to water table for variably-saturated, density-independent flow without and with permafrost

Each transient simulation began with fully-saturated conditions using the results of the steady-state simulations as initial conditions according to Table 5.2. Because ice sheet dynamics were ignored (i.e. the ice sheet was stationary), the transient simulations were run for 100,000 years. This timeframe was long enough to capture the effects of variably-saturated flow and permafrost on the water table. As the flow system evolved with no recharge, the water table dropped and the sub-surface became variably-saturated with saturation being higher beneath valleys and lower at the tops of the mountains. While the majority of the change in head values and saturation occurred within the first 2,000 or 4,000 years for simulations without and with permafrost respectively, it took around 50,000 years before little to no further reduction in saturation occurred for the simulations with permafrost. Figures illustrating this progression are found in Appendix C. Figure C.1 to Figure C.10 and Figure C.11 to Figure C.19 illustrate the freshwater head distributions for simulations representing variably-saturated flow without and with permafrost respectively.

The water table and level of saturation lowered more quickly in simulations without permafrost than those with permafrost because the permafrost acts as a confining layer that restricts deep circulation. In simulations without permafrost, the saturation was reduced from the fully-saturated initial conditions to less than 50% saturated within the first 2,000 years. It took around 50,000 years for the simulations with permafrost to experience the same reduction in saturation to the same depth. Little to no further reduction of saturation occurred after 2,000 years for simulations without permafrost or after 50,000 years for simulations with permafrost.

Figure C.20 to Figure C.29 and Figure C.30 to Figure C.38 illustrate the depth to the water table for simulations representing variably-saturated flow without and with permafrost respectively. Figure C.39 to Figure C.45 illustrate the depth to the water table for simulations representing fully-saturated flow conditions with permafrost.

The presence of permafrost also affected the pore water velocities. Those velocities were approximately two to three orders of magnitude lower when permafrost was present than when it was excluded from the simulation. Figure C.46 to Figure C.55 and Figure C.56 to Figure C.64 illustrate the velocity magnitude distributions for simulations representing variably-saturated flow without and with permafrost respectively.

5.5 Summary

The numerical model of the study site for the Greenland Analogue Project as presented in Yin et al. [2013] was extended to include the physics for temperature including latent heat and for variably-saturated flow. The analyses presented in this section were used to examine the impact of heat transport and latent heat on the permafrost distribution and the hydrologic flow system at the Kangerlussuaq site in Greenland. Additional analyses were used to investigate the impact of that permafrost on the water table and hydrologic flow system between the Greenland Ice Sheet and Davis Strait during the last glacial cycle.

In the following sections, the results of the analyses presented in this chapter are compared with the results of the simulations presented in Yin et al. [2013]. There a number of key differences that should be reviewed: the computational model used, the physics included in the model, dimensionality of the model domain, and the inclusion of discrete fracture zones. As discussed in Section 3.0, the finite element numerical model, FRAC3DVS-OPG was used by Yin et al. [2013] to simulate density-dependent flow and solute transport in a three-dimensional domain with vertical fractures; the finite-element, numerical model, COMSOL Multiphysics, was used in the analyses presented in Section 5.4.1 and Section 5.4.2, which simulated density-dependent flow and heat transport for a two-dimensional cross-section of the three-dimensional domain excluding the fractures and with a constant solute distribution.

For both numerical models, the simulations that were run included density-dependent flow, however the density itself was dependent on different physics in each model. In the simulations presented in Yin et al [2013], the density was dependent on the concentration of the solute; in the analyses presented in Section 5.4.1 and Section 5.4.2, the density was dependent only on pressure, temperature, and solute concentration although the solute distribution was held constant.

Deformation zones were included in the three-dimensional regional-scale model domain (Yin et al. [2013]), but not in the two-dimensional cross-section. The deformation zones influenced the flow within these systems by providing additional pathways for fluid flow. The difference between the simulations with and without deformation zones is most evident when examining the velocity magnitude distributions, which show higher velocities within the deformation zones where the hydraulic conductivity is greater than that of the surrounding rock.

5.5.1 Impact of Thermal Transport and Latent Heat on Permafrost Distribution

To examine the impact of thermal transport and latent heat on the distribution of permafrost and the density-dependent flow system, the analyses presented in this chapter were compared with the prescribed permafrost scenario presented in Yin et al. [2013].

In Yin et al. [2013], permafrost was applied to a constant depth of 300 m anywhere that the top surface was exposed to atmospheric conditions (Figure 5.24). While Yin et al. [2013] did include permafrost in the "paleo" or glacial cycle scenarios they examined, they did not include the presence of taliks in those glacial cycle scenarios. Thus, Figure 5.24 is the steady-state permafrost distribution with the inclusion of taliks or discharge zones. Yin et al. [2013] also assumed that the permafrost would persist beneath the ice sheet 10 km to the east of the ice sheet's edge. The hydraulic conductivity was reduced (5×10^{-11} m/s) for any model elements that were in that permafrost region.

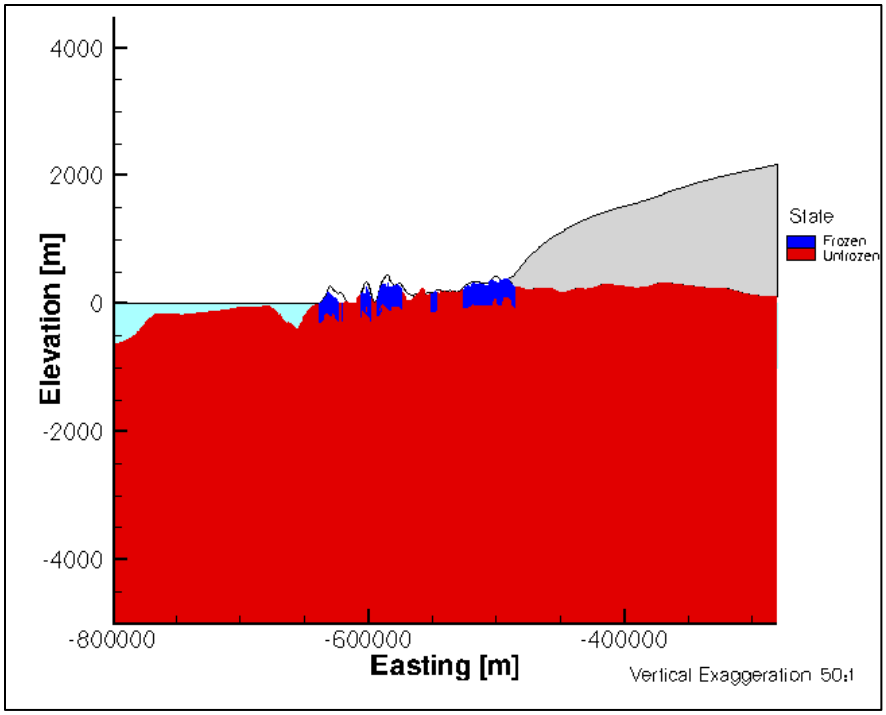

Figure 5.24 West-east cross-section of steady-state permafrost distribution including taliks (discharge zones) from Yin et al. [2013].

For the analyses in this chapter, the temperature was set along the top of the domain based on where and when during the glacial cycle the surface was exposed to atmospheric conditions (-7.5 ^{o}C), buried beneath the ice sheet (0.1 ^{o}C), or covered by a body of water (4 ^{o}C beneath Davis Strait; 2 ^{o}C beneath all other surface water bodies) as described in Section 5.3.2.3. Figure 5.25 shows that the permafrost disappeared completely beneath the ice sheet after the ice sheet reached Davis Strait. In the simulations described in Yin et al. [2013], the permafrost was assumed to have remained beneath the ice sheet for 10 km from the ice sheet edge and to a depth of 300 m.

The warm-based glacier scenario did not prevent permafrost from existing beneath the ice sheet entirely. Over the first 1,000 years of the simulation, the ice sheet advances approximately 38 km to the west, covering a 32 km-wide region of permafrost initially up to approximately 280 m deep. At 1,000 years, that permafrost had melted beneath the ice sheet. Figure 5.26 shows a magnified view of that region of the cross-section to better illustrate the existence of shallow permafrost beneath the ice sheet, although it should be noted that the temperature of that permafrost was between -0.5 ^{o}C and 0 ^{o}C, which is the lower half of the range of temperatures over which the phase change occurs as described in Section 3.2.3. The permafrost remained beneath the ice sheet as it was covered at around 3,000, 55,000 and 120,000 years with temperatures again between -0.5 ^{o}C and 0 ^{o}C.

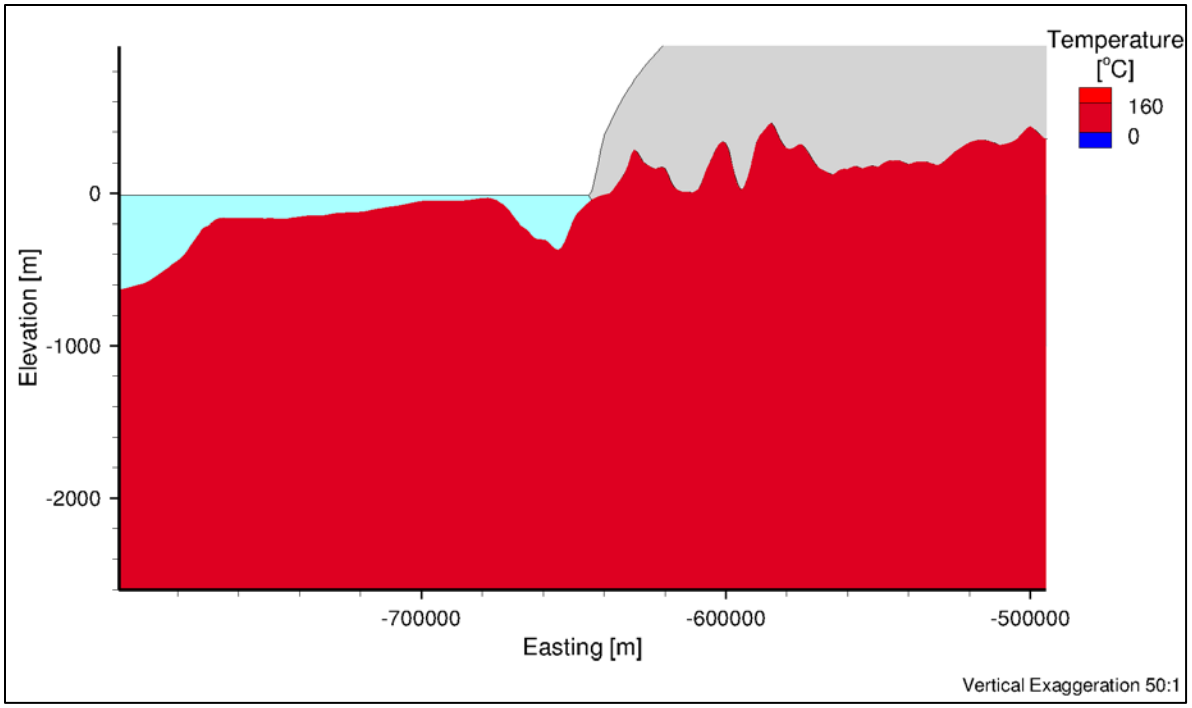

Figure 5.25 West-east cross-section of permafrost distribution at 4,000 years with temperature-dependent permafrost.

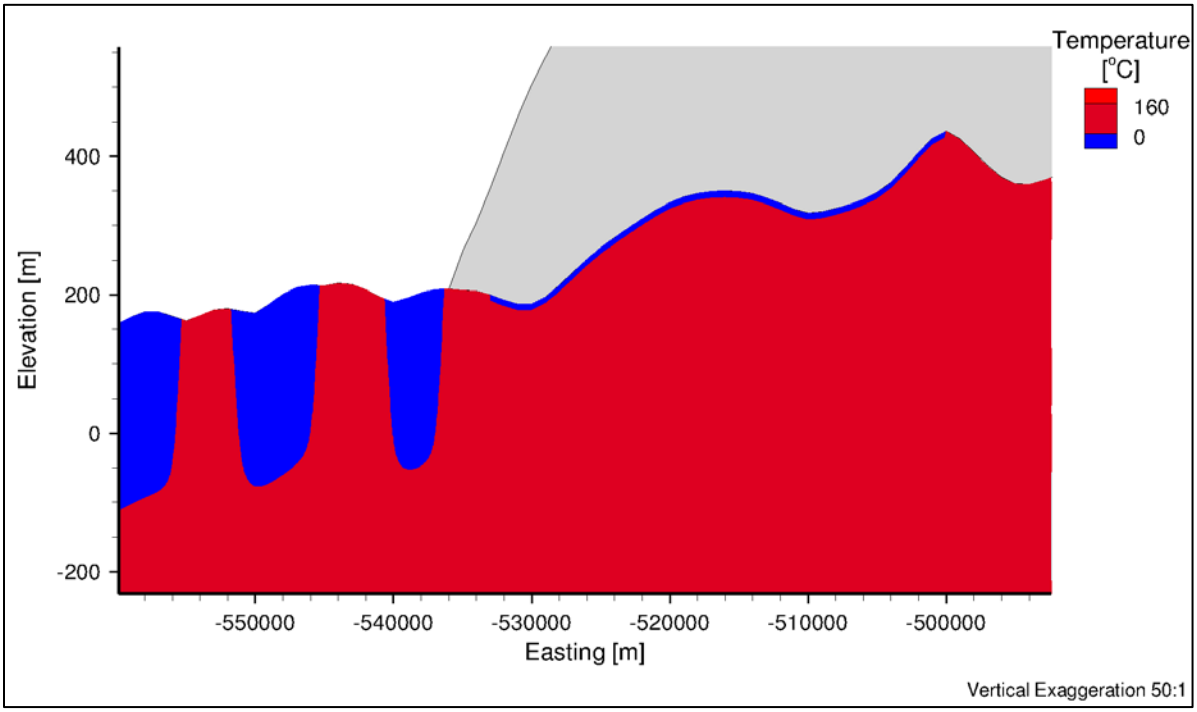

Figure 5.26 Magnified view of west-east cross-section of permafrost distribution at 1,000 years with temperature-dependent permafrost.

Accounting for latent heat did impact the permafrost and pressure distributions in the system as discussed in Section 5.4.2 and illustrated in Figure 5.12, Figure 5.14, and Figure 5.13 respectively, although it did not impact the maximum depth of permafrost for the whole glacial cycle relative to the scenarios with temperature and no latent heat. The key difference in permafrost distribution between the Yin et al. [2013] simulation and the temperature-dependent scenarios (without and with latent heat) is the depth of the permafrost. While the simulations with temperature-dependent permafrost did yield a maximum permafrost depth of approximately 300 m (e.g., around Easting -630000 m at 1,000 years as shown in Figure 5.27), that maximum depth was not constant or uniform throughout the glacial cycle (Figure 5.27). Because that 300 m depth was based on field observations conducted by other GAP researchers [Jaquet and Namar, 2010], this demonstrates that the temperature profile used in these simulations was appropriate for recreating recent permafrost conditions (i.e. approximately 1,000 years ago).

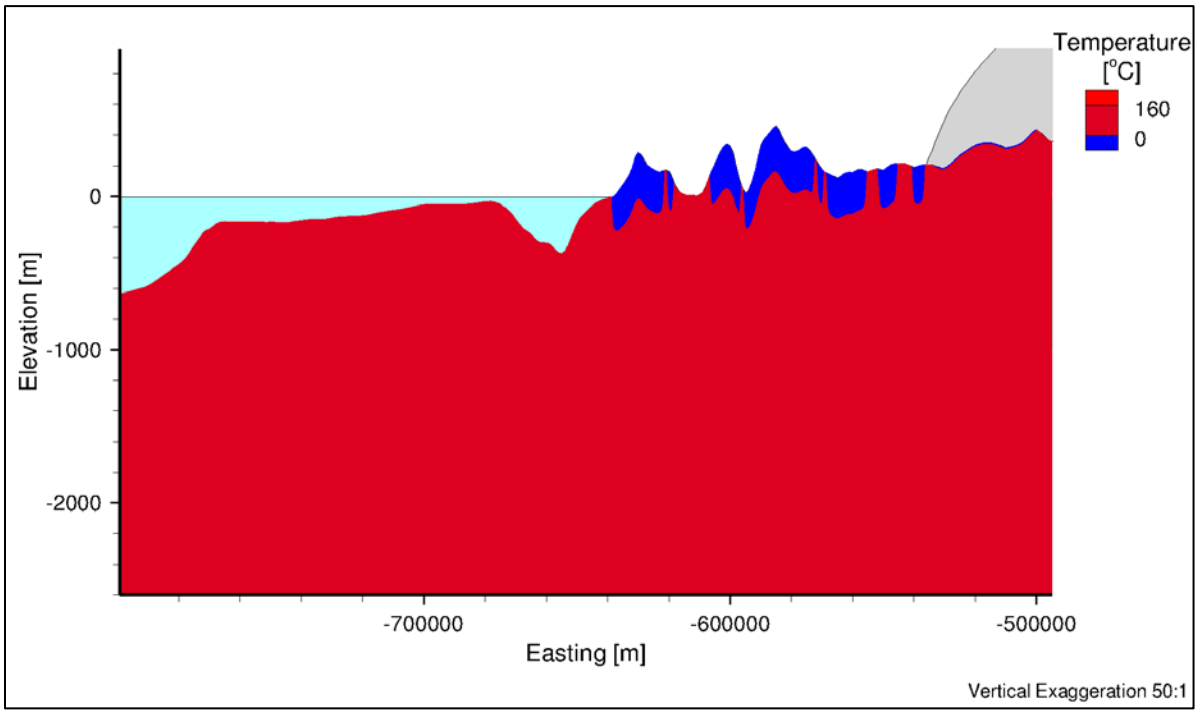

Figure 5.27 West-east cross-section at 1,000 years with temperature-dependent permafrost.

The simulations that included temperature with latent heat showed that the permafrost depth was not constant when the permafrost formed or degraded as illustrated previously in Figure 5.14. This further suggests that Yin et al. [2013] overestimated the depth of permafrost in the Kangerlussuaq region by holding that depth constant at 300 m although the interpolation of hydraulic conductivity values in time would have minimized those effects. At around 7,000 years in the glacial cycle, the sea level dropped and left the ground beneath Davis Strait exposed to freezing atmospheric conditions. In Yin et al. [2013], the constant permafrost depth of 300 m would have been imposed as soon as that happened. The simulations with temperature-dependent flow showed that permafrost that formed at that time was minimal and did not reach its

maximum depth (approximately 265 m) for that location until approximately 4,000 years later while the sea level continued to drop and expose a larger area to the freezing atmospheric conditions (Figure 5.28 and Figure 5.29).

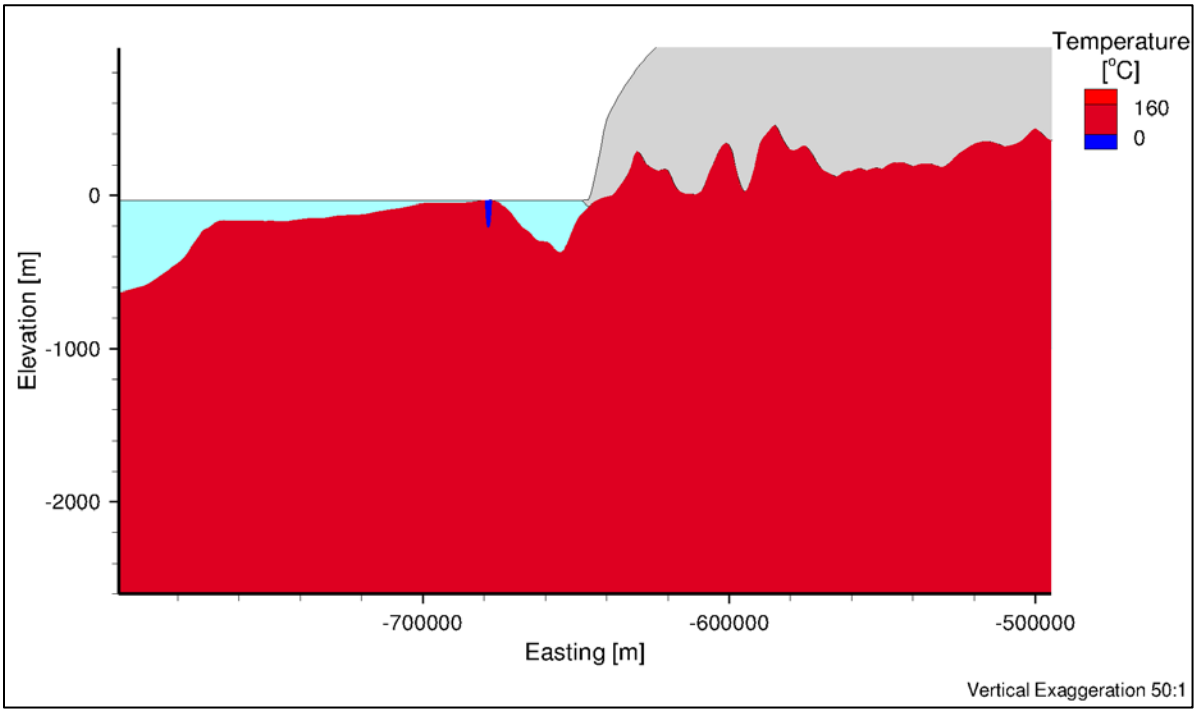

Figure 5.28 West-east cross-section of permafrost distribution at 7,000 years with temperature-dependent permafrost (without latent heat).

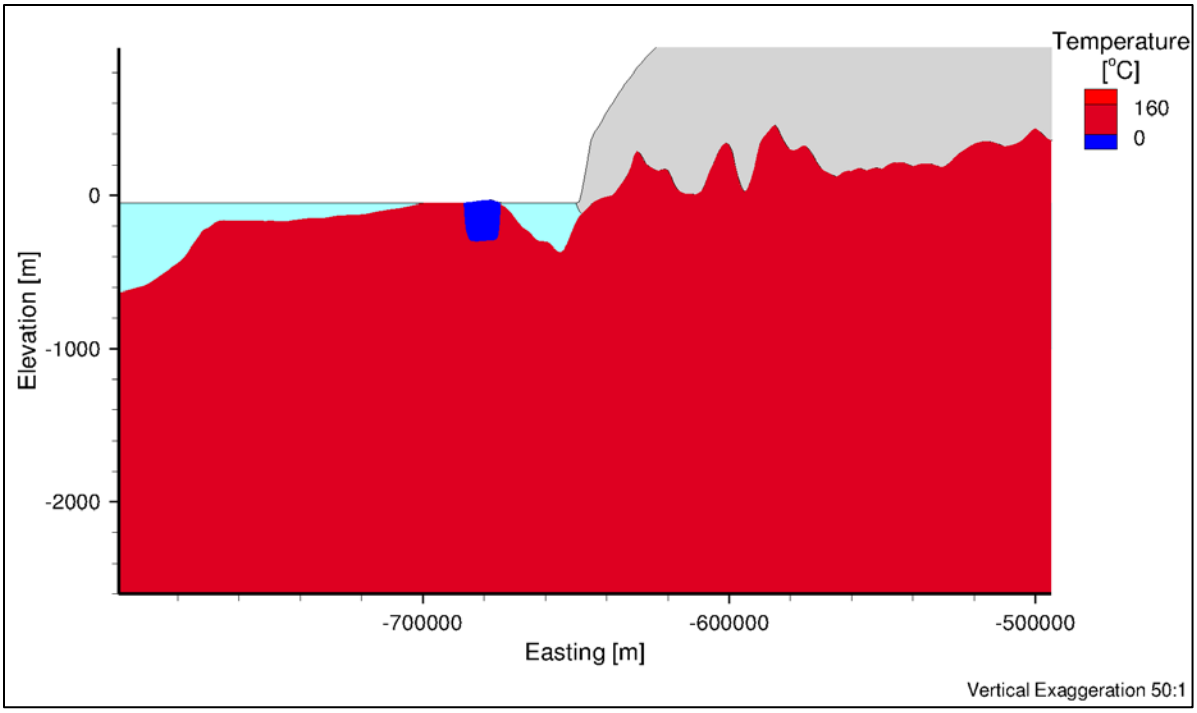

Figure 5.29 West-east cross-section of permafrost distribution at 11,000 years with temperature-dependent permafrost (without latent heat).

5.5.2 Impact of Variably-saturated Flow Conditions and Permafrost on the Water Table and Flow System

Using FRAC3DVS-OPG to simulate variably-saturated flow and solute transport in the three-dimensional regional-scale GAP domain model it was shown that drainage occurred more slowly with variably-saturated flow conditions than with fully-saturated conditions. The water table reached nearly its maximum depth around 600 years with fully-saturated conditions and around 2,000 years with variably-saturated flow conditions.

The impact of permafrost on the water table and flow system was also investigated using FRAC3DVS-OPG to simulate variably-saturated flow and solute transport in the three-dimensional regional-scale GAP domain model. Those simulations showed that drainage occurred more slowly with permafrost than without permafrost because the permafrost acts a confining layer restricting flow to depth. For the three-dimensional GAP domain model, the differences were significant. For simulations without permafrost, the saturation was reduced from the fully-saturated initial conditions to approximately 50% saturation within the first 2,000 years. However, it took approximately 50,000 years for the simulations with permafrost to experience the same reduction in saturation to the same depth. Additionally, pore water velocities were approximately two to three orders-of-magnitude lower when permafrost was present than when it was excluded from the simulation.

A comparison of the transient simulations for fully-saturated and variably-saturated conditions shows that, while both simulations will eventually result in approximately the same depth to water table profiles, the fully-saturated simulations reach the maximum depth to the water table much more quickly than the variably-saturated simulations with and without permafrost. For example, for simulations with permafrost, fully-saturated conditions reach the maximum depth to the water table at approximately 26,000 years, while the variably-saturated conditions required the full 100,000 years to reach a similar depth to the water table.

6.0 Geosynthesis Deep Geologic Repository Program

As discussed in Sections 1.2 and 1.3, this doctoral research in part built on the hydrogeologic modelling investigations presented in Sykes et al. [2011]. To further examine the impact of permafrost on the water table, this research modified the prescribed head boundary condition (3 m below ground surface) used in Sykes et al. [2011] to account for water table adjustment and variably saturated flow conditions. Chapter 5 describes how these modifications to the prescribed boundary conditions were made to examine the assumption made in some glaciation studies that include permafrost [Bense et al., 2009; Lemieux et al., 2008a, b, c] that there will always be enough deep recharge to maintain the water table at (or 3 m below) ground surface. Thus, the analyses outlined in this chapter examine how the three-dimensional regional-scale model of the Michigan basin will drain in the absence of recharge (i.e. with a confining layer of permafrost). Unlike the GAP site presented in Chapter 5, the Bruce Nuclear Site examined in this chapter does not show any potential for taliks in land. The only open talik at the Bruce Nuclear Site is beneath Georgian Bay and Lake Huron. Thus, the system will only refill with oxygenated meteoric water or glacial meltwater after the permafrost has thawed. Due to the coarse discretization required to examine the regional-scale model in FRAC3DVS-OPG, these analyses are screening level investigations developed to approximate what can happen when the system drains during prolonged periods of permafrost cover.

6.1 Laurentide Ice Sheet, Wisconsin Glaciation

The Laurentide Ice Sheet (LIS) covered most of Canada, including Southwestern Ontario, during the last glaciation, known as the Wisconsin Glaciation. Approximately 110,000 years ago, the LIS began to form over Labrador, Quebec, the High Arctic islands, and the western region of Hudson Bay, flowing radially out from the ice centre across the Canadian landscape [Eyles & Miall, 2007]. The LIS reached its maximum extent around 20,000 years ago terminating as far south as the northern United States. At its greatest extent, the LIS attained a thickness of more than 3 km over Hudson Bay and a volume of approximately 33 million km^3 [Eyles & Miall, 2007], depressing the Earth's crust more than 500 m [Peltier, 2011].

At the LGM, between 20% and 40% of the LIS exhibited fast flow processes characteristic of a warm-based ice sheet [Bense & Person, 2008; Peltier, 2011; Tarasov & Peltier, 2004]. During deglaciation that fraction would have been much higher [Peltier, 2011]. Radiocarbon dating of materials in the northern Great Lakes region provides evidence that as the ice sheet advanced, it over-rode permafrost, which developed in advance of the ice sheet due to

climate variations, and that permafrost influenced the dynamics of the ice lobe in several ways [Cutler et al., 2000]. Permafrost or frozen-bed conditions would have altered the sub-glaciation hydraulic conditions, possibly leading to the formation of subglacial lakes, and prevented basal sliding at the edge of the ice sheet. Additionally, the heat budget at the base of the ice sheet would be altered due to the release/absorption of latent heat during phase change [Cutler et al., 2000]. Beneath the Green Bay lobe, permafrost that was initially at least tens of metres deep, thawed beneath the ice sheet at a rate of centuries to a few thousand years [Cutler et al., 2000]. However, thawed bed conditions likely persisted across the Michigan Basin during the LGM due to the presence of the lake [Bense & Person, 2008; Cutler et al., 2000; Tarasov & Peltier, 2004].

Approximately 15,000 years ago, temperatures in the northern hemisphere began to rise, and the LIS began to retreat, marking the start of the current interglacial period, the Holocene. Occasional re-advances interrupted that retreat and produced numerous moraines and other glacial landforms [Eyles & Miall, 2007]. Most of central Canada was ice free by about 12,000 years ago, but there are still remnants of this last ice-sheet on several of the islands in the High Arctic today. Postglacial rebound of the Earth's crust is also still occurring today with regions around Hudson Bay rebounding at a rate of 1.1 cm/year [Peltier, 1999].

6.2 Model Domain

The Michigan Basin is a deep, nearly circular cratonic basin in Southwestern Ontario. It is bounded by the Algonquin and Findlay Arches to the Southeast, the Frontenac Arch in the Northeast, and the Findlay Arch in the Northwest, which acted as structural and topographic controls on the depositional patterns during the Paleozoic Era [NWMO, 2011]. Figure 6.1 illustrates the geology of Southern Ontario, highlighting the Michigan basin in the Southwest. The basement rock for much of Southern Ontario is comprised of metamorphic and crystalline Precambrian material including gneisses, mafic metavolcanics, and marble [NWMO, 2011; OGS, 2013]. Sedimentary deposits from the Upper Cambrian to the Devonian/Mississippian rest unconformably on that basement rock [NWMO, 2011].

A geologic cross-section through the Michigan Basin is presented in Figure 6.2. The vertical exaggeration is approximately 45 times to allow for a clearer view of the relative thicknesses of each of the sedimentary layers from the Cambrian units lying directly on top of the Precambrian basement to the more recently deposited Pennsylvanian sediments and overburden. This cross-section does not show the Mesozoic rocks that overlie the Pennsylvanian sediments as those rocks are too thin and discontinuous to been seen at this scale [NWMO, 2011].

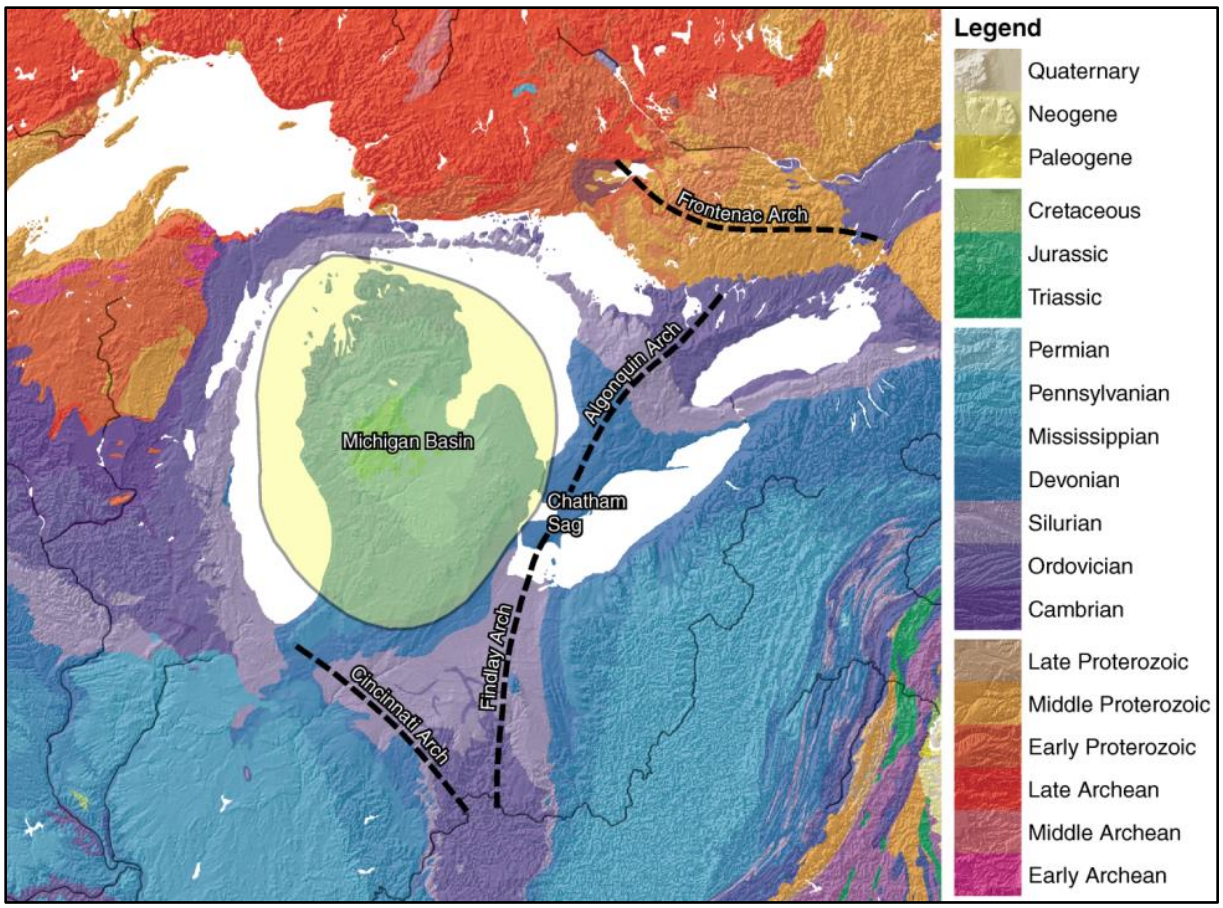

Figure 6.1 Geology of Southern Ontario and spatial extent of the Michigan Basin. Geologic map is coloured by geologic age and was adapted from geologic map courtesy of the United States Geologic Survey [Barton et al., 2003].

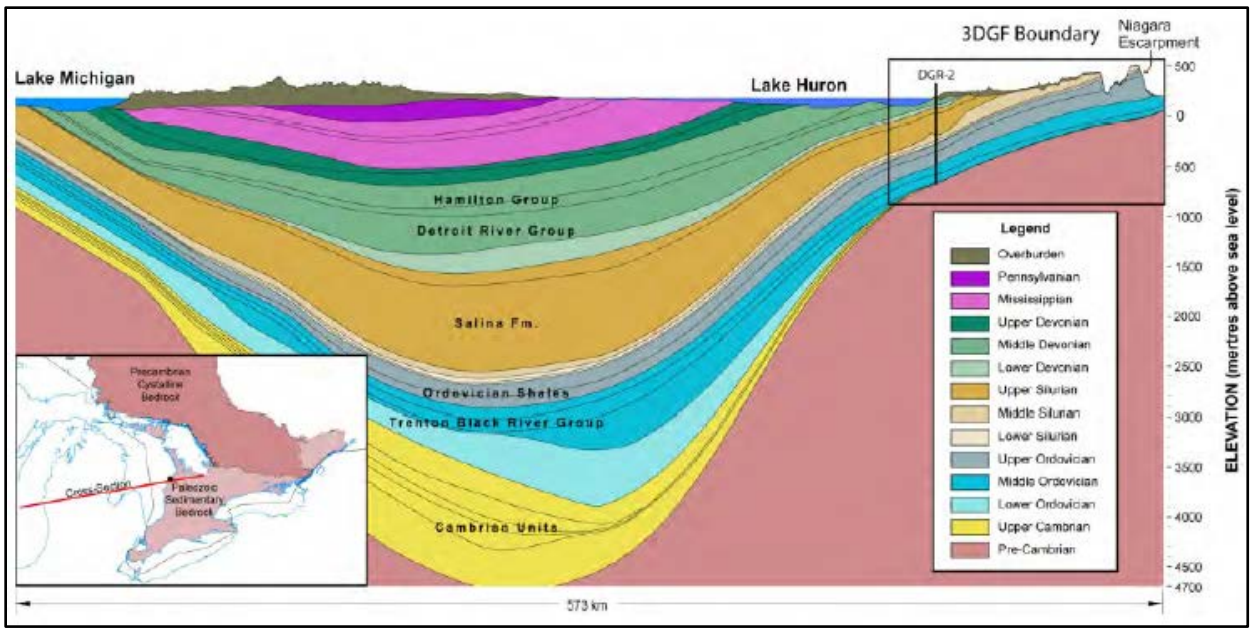

Figure 6.2 Geologic cross-section through the Michigan Basin

The vertical axis represents elevation above sea level, and the vertical exaggeration is 45 times. The location of the DGR borehole at the Bruce nuclear site is projected onto the section, and the boundary of the regional three-dimensional framework is indicated in black in the top right corner of the cross-section [from NWMO, 2011].

The model domain used for this doctoral research is the 18,000 km^2 (2 km deep) regional-scale model of the Michigan basin used by Sykes et al. [2011]. That domain is illustrated in Figure 1.2. The domain is divided into three horizons based on the hydrogeology: a shallow zone, an intermediate zone, and a deep groundwater zone. Figure 6.3 illustrates the stratigraphic column at the Bruce Nuclear Site based on data from two boreholes at the site (DGR-1 and DGR-2). This figure also points out the proposed location of the DGR within the Cobourg Formation in the Middle Ordovician.

The shallow zone is characterized by the dolomite and limestone units of the Devonian and Upper Silurian. The permeability in this zone is higher than in other zones, and groundwater flow pathways are strongly influenced by the topography. The TDS content of the groundwater in this shallow zone is relatively low.

The intermediate zone includes the low permeability carbonates, shales, salt, and evaporate units of the Upper Silurian as well the more permeable units in the Niagaran group (Guelph, Goat Island, Gasport, and Lions Head), and the carbonates and shales of the Lower Silurian. This zone essentially isolates the deep groundwater domain from the influence of local-scale topographic changes.

Finally, the deep zone reaches to the Precambrian and includes the shales and carbonate formations of the Ordovician and the sandstones and dolomites of the Cambrian. The pore waters in this zone are near stagnant and have a high TDS content, which can be greater than 300 g/L.

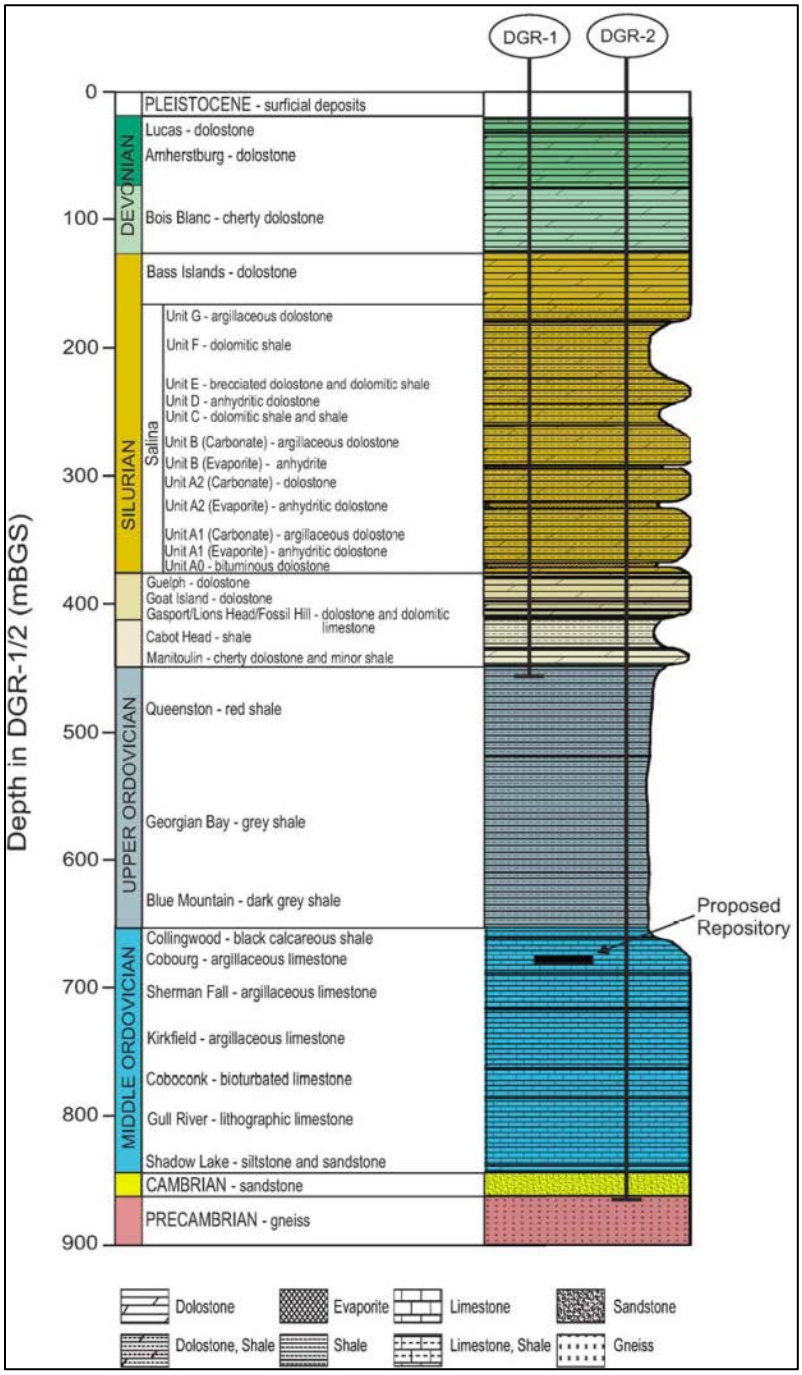

Figure 6.3 Stratigraphic column at the Bruce Nuclear site

The stratigraphic column is based on data from two boreholes at the site (DGR-1 and DGR-2) [Sykes et al., 2011].

The model domain is discretized into a two-dimensional areal grid composed of 27,322 quadrilateral elements measuring 762.794 m by 900.876 m. The grid covers a total area of 18.775 km^2 and acts as a template for developing the three-dimensional grid through interpolation of the vertical position of each node. The process of generating the three-dimensional grid is described in Sykes et al. [2011].

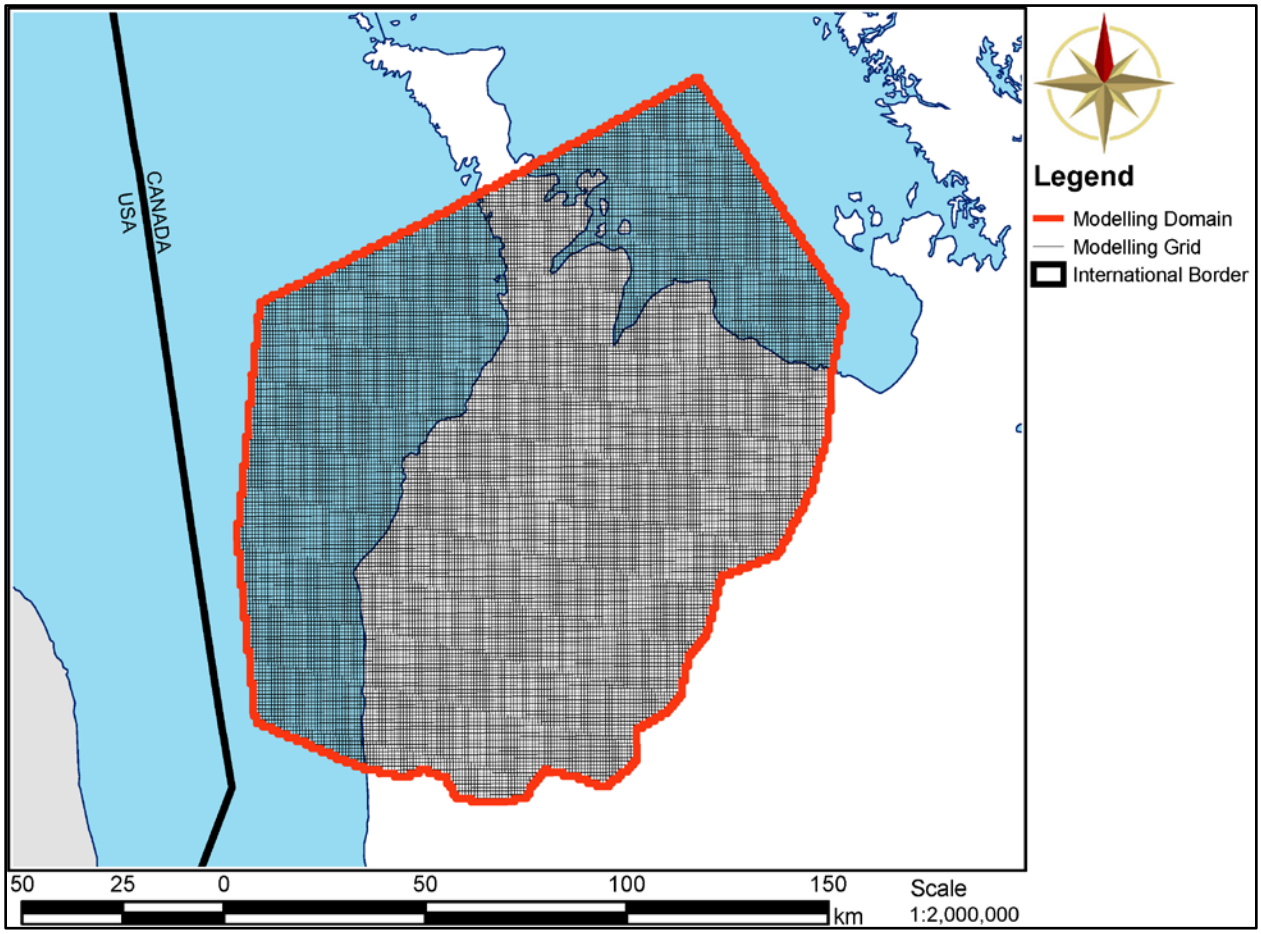

Figure 6.4 Discretization of the regional-scale modelling domain
The modelling grid was developed in FRAC3DVS-OPG [Sykes et al., 2011].

Figure 6.5 and Figure 6.6 provide an areal and a block cut view, respectively, of the geologic units included within this regional-scale modelling domain. Figure 6.5 shows the outcrop limits or extent of the various geologic units, which are coloured by geologic period. Figure 6.6 provides the block cut view of all of the geologic deposits, excluding the Quaternary drift deposits.

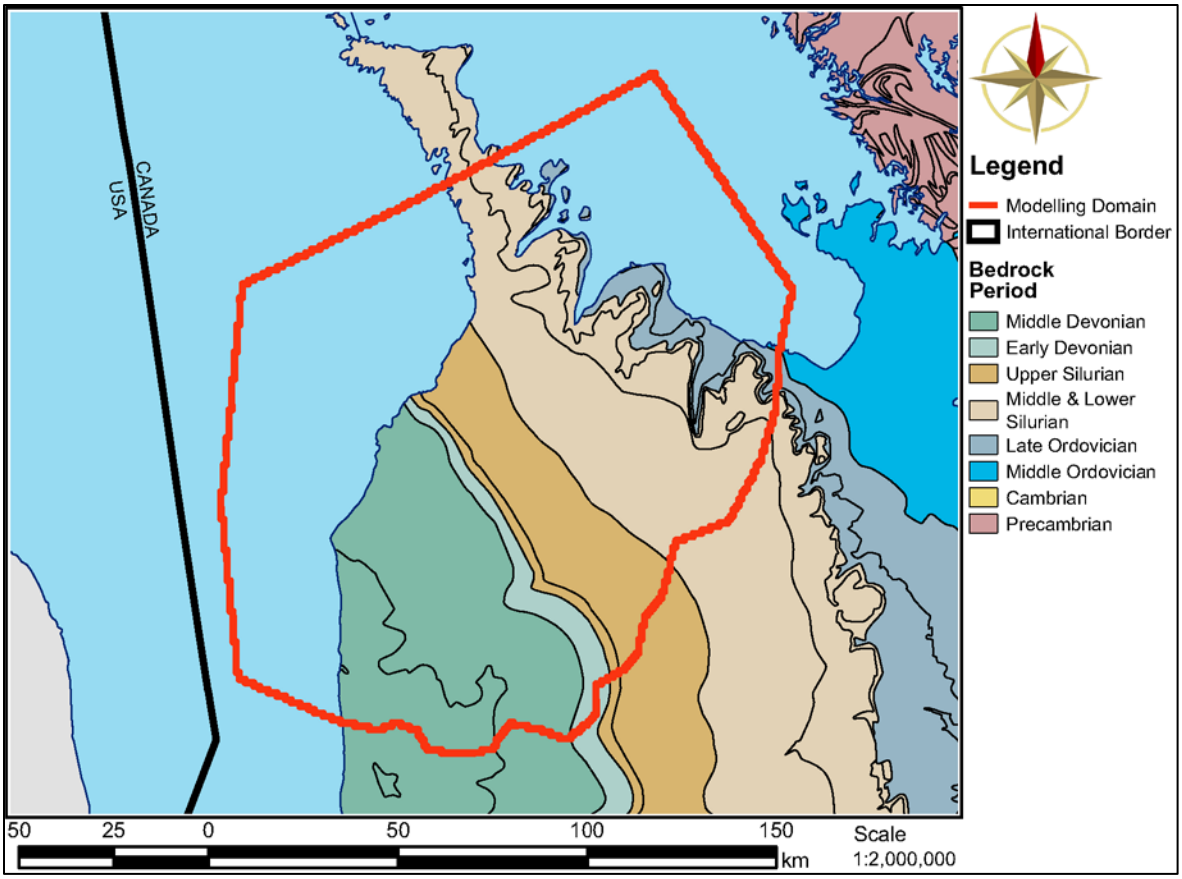

Figure 6.5 Map of bedrock subcrops beneath the Quaternary deposits of Southwestern Ontario [Sykes et al., 2011].

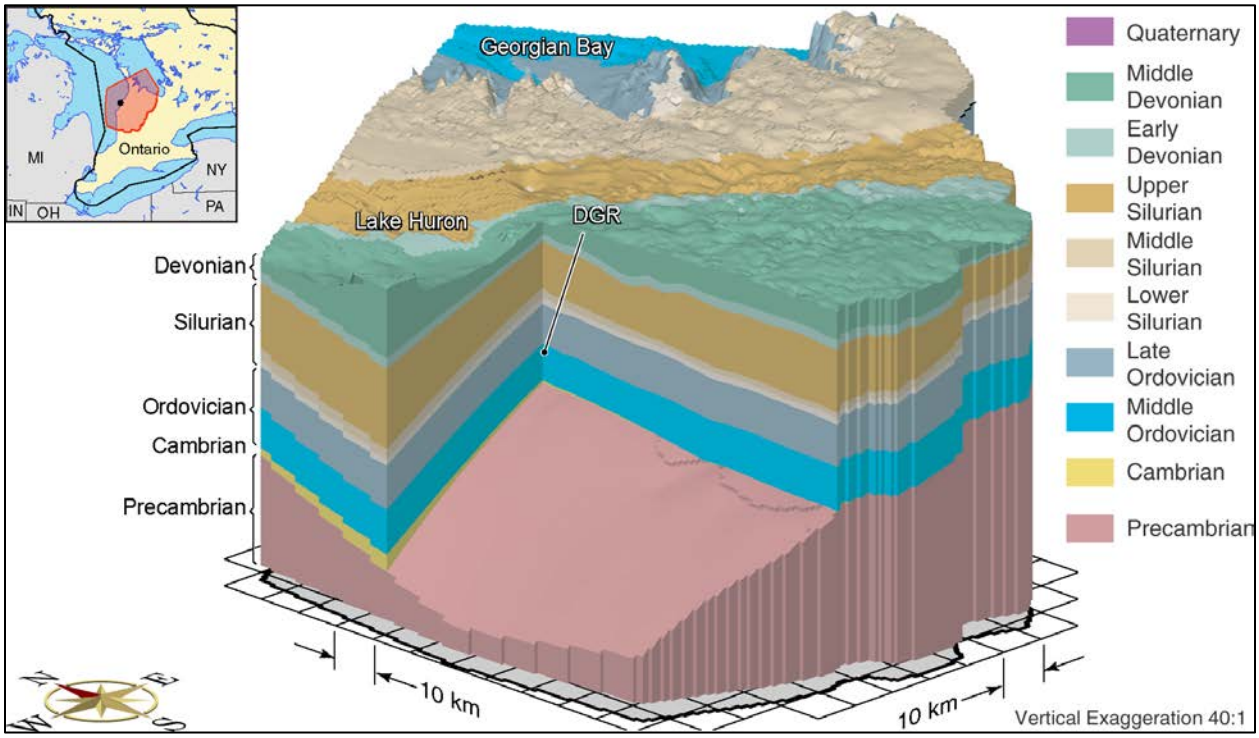

Figure 6.6 Block cut view of the spatial extent of bedrock units excluding the Quaternary deposits for the regional modelling domain [Sykes et al., 2011].

6.3 Properties and Boundary Conditions

The following sections summarize the properties and boundary conditions used in the regional-scale base-case analysis from Sykes et al. [2011], which forms the basis for the investigation of the impact of permafrost on the water table for this doctoral research.

6.3.1 Hydraulic Boundary Conditions

For the base-case analysis presented in Sykes et al. [2011] upon which this doctoral research is based, a Dirichlet or Type 1 boundary condition was applied to the top surface of the model to set the water table to 3 m below ground surface although not less than the elevation of Georgian Bay or Lake Huron (mean elevation of 176 m). No flow or zero-flux boundary conditions were applied to the sides and the bottom of the model domain.

Mechanical loading due to the presence of the ice sheet is implemented as a hydraulic boundary condition in the groundwater flow model according to Equations 6.1 and 6.2. This implementation is based on the assumption that the height of the ice sheet can be replaced by an

equivalent height of freshwater resulting in the same pressure or stress at its base [Sykes et al., 2011].

$$\sigma_{zz} = \begin{cases} \rho_i g h_i & if\ h_w < \frac{\rho_i}{\rho_w} h_i \\ \rho_w g h_w & if\ h_w \geq \frac{\rho_i}{\rho_w} h_i \end{cases} \quad \textbf{6.1}$$

$$\hat{h} = h_w \quad \textbf{6.2}$$

Here ρ and h represent the density and the height respectively of ice (denoted with subscript i) and water (denoted with subscript w), and $\hat{h}$ is the specified head boundary condition. The vertical stress, σ_{zz}, is part of the hydromechanical term presented in Equation 3.9 in Section 3.1.4.

6.3.2 Hydrogeologic Parameters

The hydrogeologic parameters applied to this model are based on the DGR borehole investigations conducted at the Bruce Nuclear Site. Table 6.1 summarizes the groundwater flow parameters for the site formations. The porosity, density, and specific storage parameters for grouped layers were calculated using a weighted average based on the site formation values and thicknesses and are presented in Table 6.2. All values were used in Sykes et al. [2011] for their base-case analysis.

Table 6.1 Summary of formation parameters at the DGR site

Formation parameters were used for the base-case analysis in Sykes et al. [2011].

Period	Formation	kH [m/s]	kV [m/s]	kH:kV	θ	ρ [kg/m3]	TDS [g/L]	E [GPa]	ν	Ks [GPa]	β' [1/Pa]	Ss [1/m]	ζ	Cpp [1/Pa]	τ
Quaternary	Drift	1.0E-08	5.0E-09	2:1	0.200	1000	0.0	—	—	—	1.0E-08	9.9E-05	0.99	5.0E-08	4.0E-01
Devonian	Kettle Point	3.0E-09	3.0E-10	10:1	0.100	1006	9.0	7.7	0.18	∞	—	1.5E-06	0.80	1.2E-09	1.2E-01
	Hamilton Group	2.2E-11	2.2E-12	10:1	0.100	1008	12.0	7.7	0.18	∞	—	1.5E-06	0.80	1.2E-09	1.2E-01
	Dundee	8.4E-08	8.4E-09	10:1	0.100	1005	8.0	7.7	0.18	∞	—	1.5E-06	0.80	1.2E-09	1.2E-01
	Lucas	1.0E-06	1.0E-07	10:1	0.077	1000	0.5	7.7	0.18	∞	—	1.4E-06	0.84	1.6E-09	9.4E-02
	Amherstburg (top 20 m)	1.0E-06	1.0E-07	10:1	0.077	1001	1.0	7.7	0.18	∞	—	1.4E-06	0.84	1.6E-09	9.4E-02
	Amherstburg (lower 25 m)	1.0E-07	1.0E-08	10:1	0.077	1001	2.0	7.7	0.18	∞	—	1.4E-06	0.84	1.6E-09	9.4E-02
	Bois Blanc	1.0E-07	1.0E-08	10:1	0.077	1002	3.2	7.7	0.18	∞	—	1.4E-06	0.84	1.6E-09	9.4E-02
Silurian	Bass Islands (upper 20 m)	1.0E-04	1.0E-05	10:1	0.056	1004	6.0	4.0	0.30	∞	—	2.0E-06	0.92	3.3E-09	2.8E-01
	Bass Islands (lower 25 m)	1.0E-05	1.0E-06	10:1	0.056	1004	6.0	4.0	0.30	∞	—	2.0E-06	0.92	3.3E-09	2.8E-01
	Salina G	1.0E-11	1.0E-12	10:1	0.172	1010	14.8	13.9	0.22	∞	—	1.1E-06	0.55	3.7E-10	3.0E-03
	Salina F	5.0E-14	5.0E-15	10:1	0.100	1040	59.6	13.9	0.22	∞	—	9.5E-07	0.68	6.3E-10	4.9E-02
	Salina E	2.0E-13	2.0E-14	10:1	0.100	1083	124.0	22.6	0.32	∞	—	6.5E-07	0.51	3.1E-10	5.7E-02
	Salina D	2.0E-13	2.0E-14	10:1	0.089	1133	200.0	22.6	0.32	∞	—	6.4E-07	0.53	3.5E-10	6.4E-02
	Salina C	4.0E-13	4.0E-14	10:1	0.205	1166	249.0	22.6	0.32	∞	—	1.1E-06	0.33	1.5E-10	6.5E-02
	Salina B	4.0E-13	4.0E-14	10:1	0.145	1214	321.0	22.6	0.32	∞	—	8.9E-07	0.41	2.1E-10	1.0E-01
	Salina B Evaporite	3.0E-13	3.0E-14	10:1	0.089	1214	321.0	22.6	0.32	∞	—	6.9E-07	0.53	3.5E-10	1.0E-03
	Salina A2 Carbonate	3.0E-10	3.0E-11	10:1	0.120	1091	136.0	22.6	0.32	∞	—	7.2E-07	0.46	2.6E-10	1.2E-02
	Salina A2 Evaporite	3.0E-13	3.0E-14	10:1	0.089	1030	45.6	22.6	0.32	∞	—	5.8E-07	0.53	3.5E-10	1.0E-03
	Salina A1 Upper Carbonate	2.0E-07	2.0E-07	1:1	0.070	1019	28.6	22.6	0.32	∞	—	5.2E-07	0.59	4.4E-10	8.4E-02
	Salina A1 Carbonate	9.0E-12	9.0E-13	10:1	0.019	1128	192.0	22.6	0.32	∞	—	4.1E-07	0.84	1.6E-09	1.1E-02
	Salina A1 Evaporite	3.0E-13	3.0E-14	10:1	0.007	1217	325.0	22.6	0.32	∞	—	3.9E-07	0.94	4.4E-09	5.2E-03
	Salina A0	3.0E-13	3.0E-14	10:1	0.032	1240	360.0	22.6	0.32	∞	—	4.9E-07	0.76	9.7E-10	1.1E-03
	Guelph	3.0E-08	3.0E-08	1:1	0.057	1247	370.0	37.0	0.37	∞	—	4.0E-07	0.47	2.7E-10	6.8E-02
	Goat Island	2.0E-12	2.0E-13	10:1	0.020	1200	300.0	37.0	0.37	∞	—	2.5E-07	0.72	7.6E-10	9.0E-03
	Gasport	2.0E-12	2.0E-13	10:1	0.020	1200	300.0	37.0	0.37	∞	—	2.5E-07	0.72	7.6E-10	9.0E-03
	Lions Head	5.0E-12	5.0E-13	10:1	0.031	1200	300.0	37.0	0.37	∞	—	2.9E-07	0.62	4.9E-10	2.4E-01
	Fossil Hill	5.0E-12	5.0E-13	10:1	0.031	1200	300.0	37.0	0.37	∞	—	2.9E-07	0.62	4.9E-10	6.2E-01
	Cabot Head	9.0E-14	9.0E-15	10:1	0.116	1204	306.0	13.8	0.30	∞	—	1.1E-06	0.60	4.6E-10	3.2E-02
	Manitoulin	9.0E-14	9.0E-15	10:1	0.028	1233	350.0	13.8	0.30	∞	—	7.5E-07	0.86	1.9E-09	6.4E-03
Ordovician	Queenston	2.0E-14	2.0E-15	10:1	0.073	1207	310.0	13.8	0.30	∞	—	9.0E-07	0.71	7.4E-10	1.6E-02
	Georgian Bay	3.0E-14	3.0E-15	10:1	0.071	1205	308.0	13.8	0.30	∞	—	8.9E-07	0.71	7.6E-10	7.3E-03
	Blue Mountain	5.0E-14	5.0E-15	10:1	0.078	1197	295.0	5.2	0.30	∞	—	2.0E-06	0.86	1.8E-09	1.3E-02
	Collingwood	2.0E-14	2.0E-15	10:1	0.012	1150	225.0	31.5	0.25	∞	—	3.4E-07	0.88	2.2E-09	4.9E-02
	Cobourg	2.0E-14	2.0E-15	10:1	0.015	1181	272.0	37.1	0.33	∞	—	2.6E-07	0.80	1.2E-09	3.0E-02
	Sherman Fall	1.0E-14	1.0E-15	10:1	0.016	1180	270.0	23.9	0.21	∞	—	4.9E-07	0.88	2.3E-09	1.7E-02
	Kirkfield	8.0E-15	8.0E-16	10:1	0.021	1156	234.0	23.9	0.21	∞	—	4.9E-07	0.85	1.8E-09	2.4E-02
	Coboconk	4.0E-12	4.0E-15	1000:1	0.009	1170	255.0	23.9	0.21	∞	—	4.6E-07	0.93	4.1E-09	3.6E-02
	Gull River	7.0E-13	7.0E-16	1000:1	0.022	1135	203.0	23.9	0.21	∞	—	4.9E-07	0.85	1.7E-09	1.4E-02
	Shadow Lake	1.0E-09	1.0E-12	1000:1	0.097	1133	200.0	23.9	0.21	∞	—	7.4E-07	0.56	3.8E-10	7.6E-02
Cambrian	Cambrian	3.0E-06	3.0E-06	1:1	0.071	1157	235.0	76.6	0.25	∞	—	3.7E-07	0.34	1.5E-10	1.3E-01
Precambrian	Upper Precambrian	1.0E-10	1.0E-10	1:1	0.038	1200	300.0	76.6	0.25	∞	—	2.6E-07	0.49	2.9E-10	9.5E-03
	Precambrian	1.0E-12	1.0E-12	1:1	0.005	1200	300.0	76.6	0.25	∞	—	1.5E-07	0.88	2.2E-09	7.2E-02

Table 6.2 Summary of formation parameters for the regional and site-scale numerical models

Formation parameters were developed and used for the base-case analysis in Sykes et al. [2011].

Period	Formation	kH [m/s]	kV [m/s]	kH:kV	θ	ρ [kg/m3]	TDS [g/L]	Ss [1/m]	ζ	τ
Quaternary	Drift	1.0E-08	5.0E-09	2:1	0.200	1000	0.0	9.9E-05	0.99	4.0E-01
Devonian	Kettle Point	3.0E-09	3.0E-10	10:1	0.100	1006	9.0	1.5E-06	0.80	1.2E-01
	Hamilton Group	2.2E-11	2.2E-12	10:1	0.100	1008	12.0	1.5E-06	0.80	1.2E-01
	Dundee	8.4E-08	8.4E-09	10:1	0.100	1005	8.0	1.5E-06	0.80	1.2E-01
	Detroit River Group	5.9E-07	2.0E-08	30:1	0.077	1001	1.4	1.4E-06	0.84	9.4E-02
	Bois Blanc	1.0E-07	1.0E-08	10:1	0.077	1002	3.2	1.4E-06	0.84	9.4E-02
Silurian	Bass Islands	5.0E-05	1.7E-06	30:1	0.056	1004	6.0	2.0E-06	0.92	2.8E-01
	Unit G	1.0E-11	1.0E-12	10:1	0.172	1010	14.8	1.1E-06	0.55	3.0E-03
	Unit F	5.0E-14	5.0E-15	10:1	0.100	1040	59.6	9.5E-07	0.68	4.9E-02
	Unit F Salt	5.0E-14	5.0E-15	10:1	0.100	1040	59.6	9.5E-07	0.68	4.9E-02
	Unit E	2.0E-13	2.0E-14	10:1	0.100	1083	124.0	6.5E-07	0.51	5.7E-02
	Unit D	2.0E-13	2.0E-14	10:1	0.089	1133	200.0	6.4E-07	0.53	6.4E-02
	Unit B and C	4.0E-13	4.0E-14	10:1	0.165	1198	296.7	9.5E-07	0.38	8.4E-02
	Unit B Anhydrite	3.0E-13	3.0E-14	10:1	0.089	1214	321.0	6.9E-07	0.53	1.0E-03
	Unit A-2 Carbonate	3.0E-10	3.0E-11	10:1	0.120	1091	136.0	7.2E-07	0.46	1.2E-02
	Unit A-2 Evaporite	3.0E-13	3.0E-14	10:1	0.089	1030	45.6	5.8E-07	0.53	1.0E-03
	Unit A-1 Carbonate	1.4E-08	9.7E-13	14912:1	0.023	1120	180.2	4.1E-07	0.82	1.2E-02
	Unit A-1 Evaporite	3.0E-13	3.0E-14	10:1	0.020	1229	343.7	4.5E-07	0.83	1.8E-03
	Niagaran Group	3.6E-09	2.5E-13	14431:1	0.026	1206	308.4	2.7E-07	0.66	1.2E-02
	Reynales/Fossil Hill	5.0E-12	5.0E-13	10:1	0.031	1200	300.0	2.9E-07	0.62	6.2E-01
	Cabot Head	9.0E-14	9.0E-15	10:1	0.116	1204	306.0	1.1E-06	0.60	3.2E-02
	Manitoulin	9.0E-14	9.0E-15	10:1	0.028	1233	350.0	7.5E-07	0.86	6.4E-03
Ordovician	Queenston	2.0E-14	2.0E-15	10:1	0.073	1207	310.0	9.0E-07	0.71	1.6E-02
	Georgian Bay/Blue Mountain	3.5E-14	3.3E-15	11:1	0.070	1200	299.4	1.2E-06	0.79	8.8E-03
	Cobourg	2.0E-14	2.0E-15	10:1	0.015	1181	272.0	2.6E-07	0.80	3.0E-02
	Sherman Fall	1.0E-14	1.0E-15	10:1	0.016	1180	270.0	4.9E-07	0.88	1.7E-02
	Kirkfield	8.0E-15	8.0E-16	10:1	0.021	1156	234.0	4.9E-07	0.85	2.4E-02
	Coboconk	4.0E-12	4.0E-15	1000:1	0.009	1170	255.0	4.6E-07	0.93	3.6E-02
	Gull River	7.0E-13	7.0E-16	1000:1	0.022	1135	203.0	4.9E-07	0.85	1.4E-02
	Shadow Lake	1.0E-09	1.0E-12	1000:1	0.097	1133	200.0	7.4E-07	0.56	7.6E-02
Cambrian	Cambrian	3.0E-06	3.0E-06	1:1	0.071	1157	235.0	3.7E-07	0.34	1.3E-01
Precambrian	Upper Precambrian	1.0E-10	1.0E-10	1:1	0.038	1200	300.0	2.6E-07	0.49	9.5E-03
	Precambrian	1.0E-12	1.0E-12	1:1	0.005	1200	300.0	1.5E-07	0.88	7.2E-02

6.3.3 Groundwater Transport Parameters

The transport parameters used in this study are summarized in Table 6.3. These parameters describe the movement of the brine within the pore fluids, the movement of the tracer to determine the depth of recharge water penetration, and the calculations for mean life expectancy. Tortuosity varies by layer as described in Table 6.1 and is calculated from the tracer, sodium iodide, effective diffusion coefficient, the porosity, and the free solution diffusion coefficient for sodium iodide at 1.0 mol/L (1.662×10^{-9} m^2/s) and assuming a diffusion accessible porosity of 0.5 for sodium iodide.

Table 6.3 Groundwater transport parameters

Groundwater transport parameters describing brine movement within the pore fluids, tracer movement to determine depth of recharge water penetration, and calculations for mean life expectancy [Sykes et al., 2011]

Parameter	Value
Brine diffusion coefficient (NaCl at 1 mol/L)	1.484×10^{-9} m^2/s
Tracer diffusion coefficient ($H_2{}^{18}O$)	2.66×10^{-9} m^2/s
Longitudinal dispersivity	500 m
Horizontal transverse dispersivity	50 m
Vertical transverse dispersivity	5 m

Values for the Precambrian hydraulic conductivity and TDS were based on characteristics derived from studies of the Canadian Shield. Horizontal and vertical permeabilities as a function of depth are expressed as outlined in Equation 4.4 and Equation 4.5 in Section 4.3.2.

Precambrian hydraulic conductivities were calculated, in part, by using Equations 6.1 and 6.2. Zero depth is set at an elevation of 176 m because these equations were developed using data from sites where the Canadian Shield is exposed. In the case of the Upper Precambrian, if the hydraulic conductivity is greater than that calculated from Equations 4.4 and 4.5, the higher value is applied [Sykes et al., 2011].

Data for the Canadian Shield from Frape & Fritz [1987] was used to develop an initial TDS distribution. Equation 5.1 in Section 5.3.2.2 represents an upper bound for total dissolved solids (TDS) as a function of depth. TDS is in units of g/L. Again, zero depth is set to an elevation of 176 m and the TDS values in the Precambrian below the sedimentary rock are set to the higher value of Equation 5.1 or the TDS value of the overlying unit at a given vertical location [Sykes et al., 2011].

6.3.4 Density-Dependent Flow

Sykes et al. [2011] developed a model of TDS concentration versus density based on DGR site data [INTERA, 2011] and the saline waters elsewhere in the Michigan Basin [Gupta, 1993]:

$$\rho = 0.000667 C_{TDS} - 1.0 \qquad 6.3$$

Due to the absence of a source term for salinity, initial distributions for freshwater heads and TDS concentrations were specified. To begin, a freshwater head distribution was determined using density-dependent steady-state flow. Next, an initial condition for the TDS distribution was assigned. TDS concentrations for each layer are presented in Table 6.1, and the depth-dependent TDS distribution for the Precambrian was determined using Equation 6.5. The density-dependent freshwater heads were allowed to equilibrate to that TDS distribution in a transient solution in which the TDS was not allowed to evolve. Finally, in a 1 Ma transient analysis both the TDS distribution and freshwater heads were allowed to vary to reach pseudo-equilibrium [Sykes et al., 2011].

6.3.5 Glacial Systems Model

The University of Toronto GSM was used to develop a description of glaciation over the North American continent and produce eight models, which cover a range of evolutionary histories for glaciation that are compatible with available constraints including relative sea level, precipitation, and crustal uplift observations and data [Peltier, 2011]. Two of those models, nn9921 and nn9930, were chosen by Sykes et al. [2011] for their paleohydrogeologic analyses because they are two of the best models based on aggregate misfit and they both include high resolution permafrost development. Output parameters for those two models are presented in Figure 6.7 and Figure 6.8 and include data for ice thickness, meltwater production rate, lake depth, permafrost depth, ground elevation, and ice-sheet basal temperature relative to the pressure melting point. Only ice thickness, lake depth, and permafrost depth were applied to the paleohydrogeologic groundwater flow simulations in Sykes et al. [2011].

The following analyses examine drainage beneath the permafrost under fully-saturated and variably-saturated flow conditions. Thus, for simplicity, as well as to maintain computational stability, glaciation was not accounted for and a constant lake depth corresponding to present day conditions (176 m) was assumed. Additionally, the permafrost was applied everywhere except the lakes and to a depth of 50 m, an average between the maximum permafrost depths given in Peltier [2011] for models nn9921 and nn9930 (See Figure 6.7 and Figure 6.8). That permafrost distribution was held constant for 30,000 years to represent a maximum estimate for drainage.

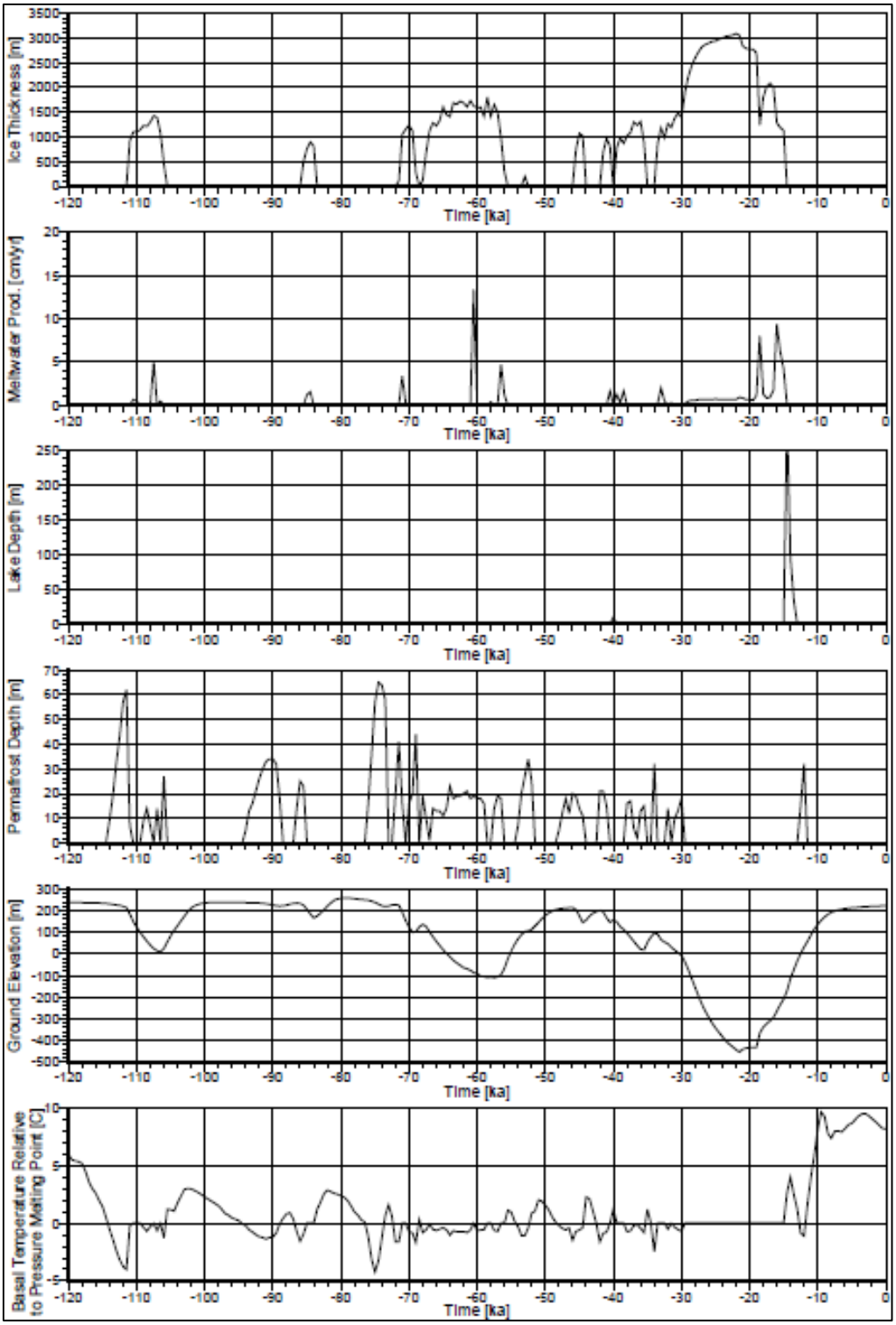

Figure 6.7 Temporal plots for output parameters from the nn9921 GSM grid block at the proposed Bruce DGR site

Temporal plots of ice thickness, meltwater production rate, lake depth, permafrost depth, ground elevation, and ice-sheet basal temperature relative to the pressure melting point [based on data from Peltier, 2011].

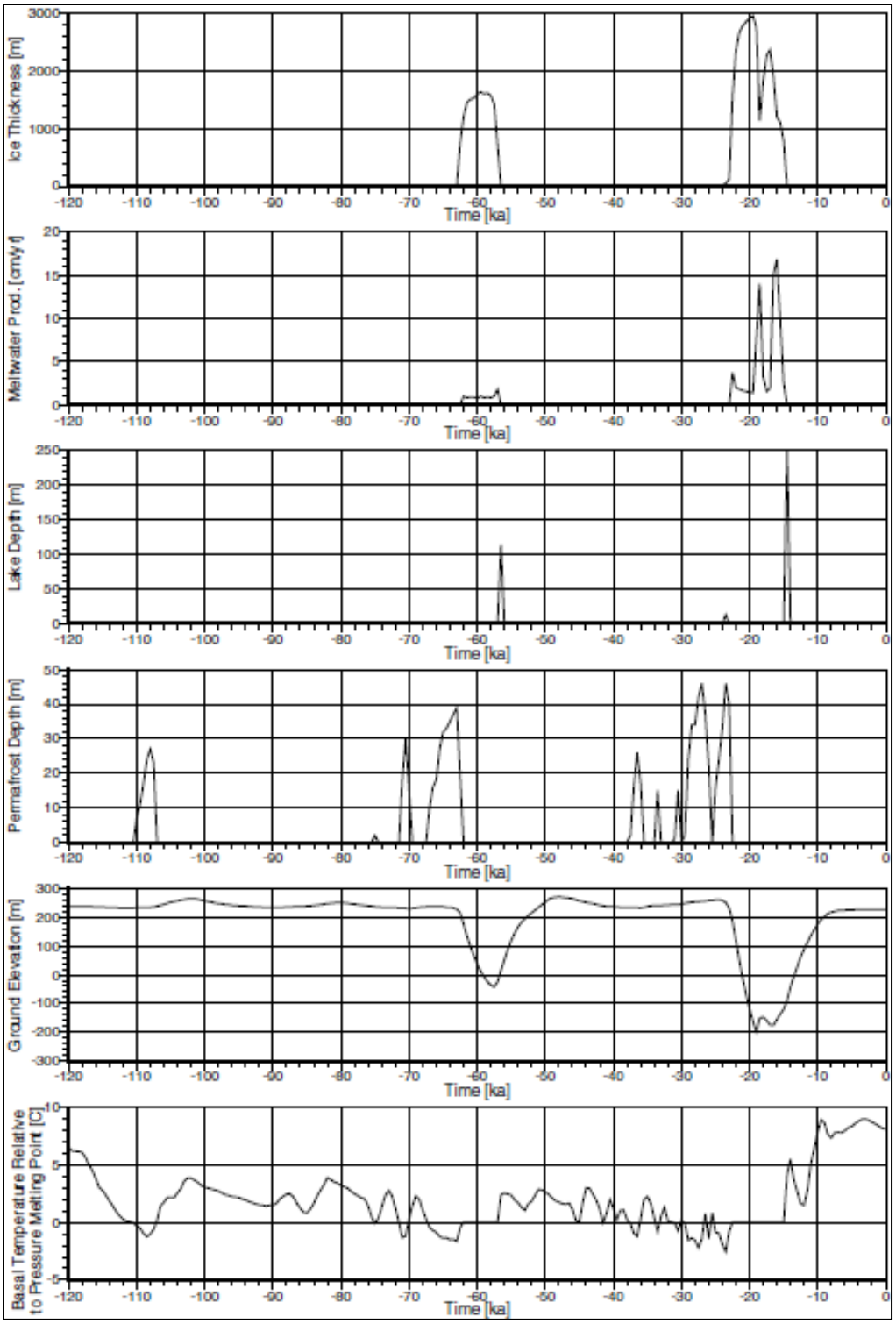

Figure 6.8 Temporal plots for output parameters from the nn9930 GSM grid block at the proposed Bruce DGR site

Temporal plots of ice thickness, meltwater production rate, lake depth, permafrost depth, ground elevation, and ice-sheet basal temperature relative to the pressure melting point [based on data from Peltier, 2011].

6.3.6 Permafrost

In Sykes et al. [2011], permafrost depths were interpolated from the glacial systems model presented in Peltier [2011] for models nn9921 and nn9930 introduced in Section 6.3.5. In the following analyses, the permafrost distribution was held constant at 50 m. The permafrost depth was used to select any FRAC3DVS-OPG grid block or element with a top face within the permafrost zone for each time step. Each element identified as being within the permafrost zone is assigned a hydraulic conductivity of 5×10^{-11} m/s [Sykes et al., 2011].

6.4 Analyses

The following section details the analyses carried out to examine the impact of variably-saturated flow conditions and the presence of permafrost on the hydrologic flow system in Southern Ontario. These analyses are screening level investigations conducted to assess the amount of drainage that will occur during a prolonged period with permafrost cover and determine whether or not variable flow conditions and/or the presence of permafrost should be included or accounted for in subsequent analyses of the Bruce DGR site and other similar scenarios. Plots illustrating the initial conditions and select paleohydrogeologic simulation results for the analyses conducted for this doctoral research are presented in the following sections.

6.4.1 Variably-saturated flow

To examine the impact of variably-saturated flow conditions on the water table and hydrologic flow system, a series of simulations was run to prepare the initial conditions for this analysis. The methodology follows that developed by Sykes et al. [2011]. To begin, the distribution of freshwater head was calculated for regional-scale, density-independent, steady-state flow. Next, a steady-state simulation was conducted to allow the density-independent freshwater heads to equilibrate to the initial salinity distribution (Equation 5.1), which was held constant. Finally, a 1 Ma transient simulation was run that allowed the TDS and freshwater head distributions to evolve together [Sykes et al., 2011].

Figure 6.9, Figure 6.10, Figure 6.11, and Figure 6.12 illustrate the results of this 1 Ma transient simulation, which were to be the initial conditions (freshwater heads and TDS distribution) for the following analyses of the impact of variably-saturated flow conditions and permafrost on the water table and hydrologic flow system.

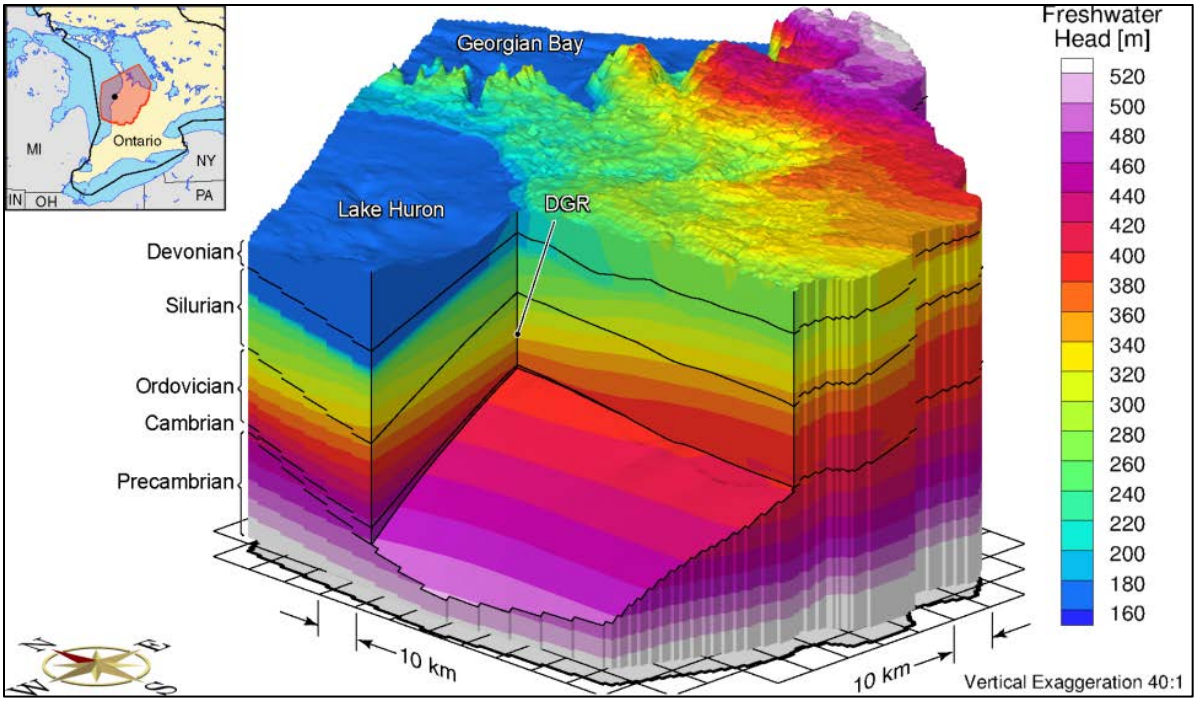

Figure 6.9 Block cut view of freshwater heads at present for the paleohydrogeologic scenario

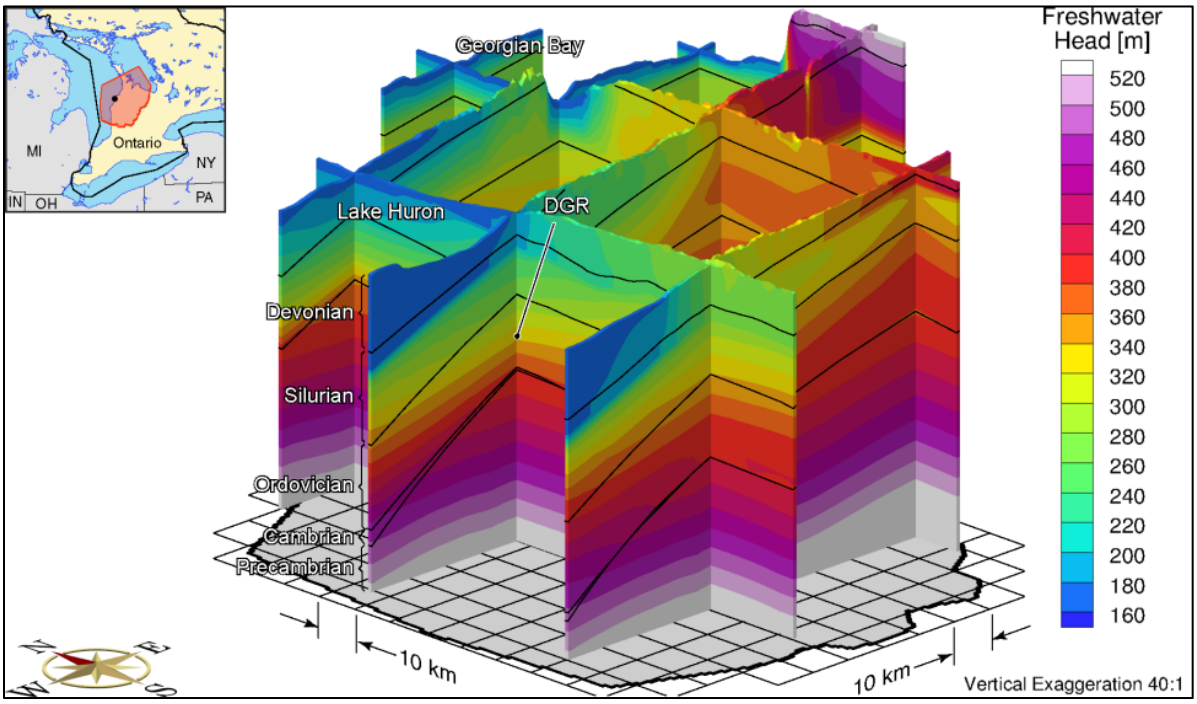

Figure 6.10 Fence view of freshwater heads at present for the paleohydrogeologic scenario

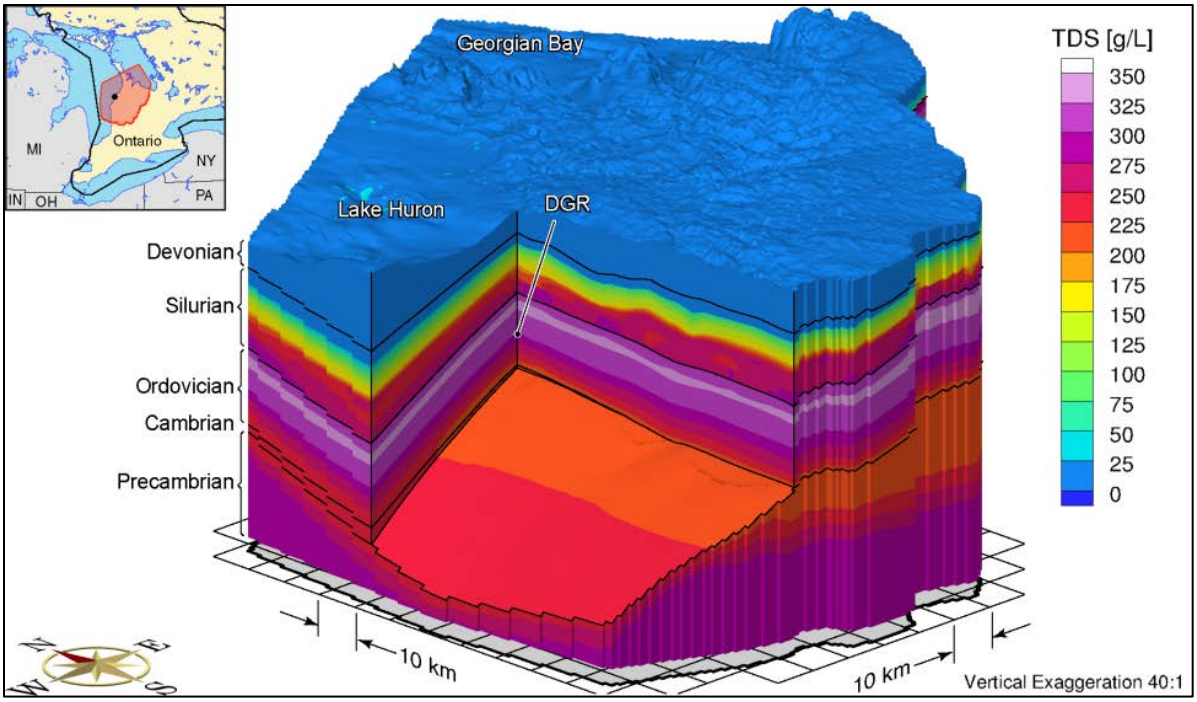

Figure 6.11 Block cut view of total dissolved solids at present for the paleohydrogeologic scenario

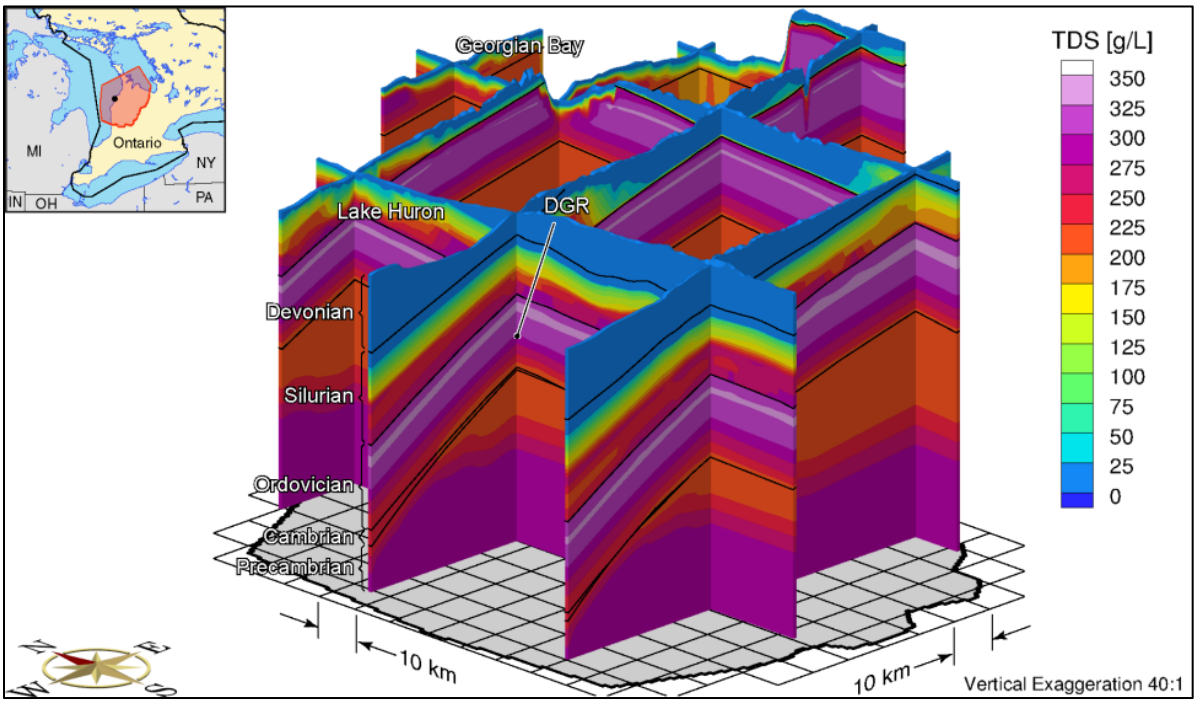

Figure 6.12 Fence view of the total dissolved solids at present for the paleohydrogeologic scenario

The simulations with transient variably-saturated flow conditions with the 1 Ma pseudo-equilibrium results calculated following Sykes et al. [2011] as the initial condition would not converge to a solution. There were a number of factors that contributed to this non-convergence: the coarse mesh, the unstable TDS distribution, and the addition of permafrost. The coarse grid is highly distorted with a high aspect ratio, especially near the surface. Layers of relatively low TDS beneath relatively high TDS layers (Figure 6.11 and Figure 6.12) cause the TDS distribution to be unstable. Because the 1 Ma paleohydrogeologic simulations did not include permafrost, suddenly including permafrost in subsequent simulations caused numerical instabilities (Yin, Y., personal communication, December, 2014).

To maintain numerical stability, the 1 Ma paleohydrogeologic simulations were not used as initial conditions. Instead, the two steady-state simulations, one with fully-saturated flow conditions and the other with variably-saturated flow conditions, were first run with a prescribed head boundary condition 3 m below the elevation of the top surface everywhere except the lakes, which had a prescribed head of 176 m. These simulations as well as the subsequent transient simulations did not include solute transport, but did include permafrost that was evenly distributed with a depth of 50 m. This permafrost distribution, illustrated in Figure 6.13 and Figure 6.14, was held constant for the duration of the simulations. This permafrost distribution was chosen and held constant to maintain computational stability and for simplicity because the purpose of this investigation is to examine the impact of the existence of permafrost on the water table. Essentially, these simulations represent low leakage through the permafrost layer, and, therefore, the results are sensitive to the hydraulic conductivity of the permafrost. A sensitivity analysis examining the impact of the magnitude of the permafrost hydraulic conductivity on the flow system is outside the scope of this thesis.

For the variably-saturated flow conditions, a linear relationship was chosen for the pressure, saturation, and relative permeability in order to maintain computational stability in FRAC3DVS-OPG. The relationships between pressure, saturation, and permeability are presented in Table 6.4. Again, this linear relationship was chosen to maintain numerical stability.

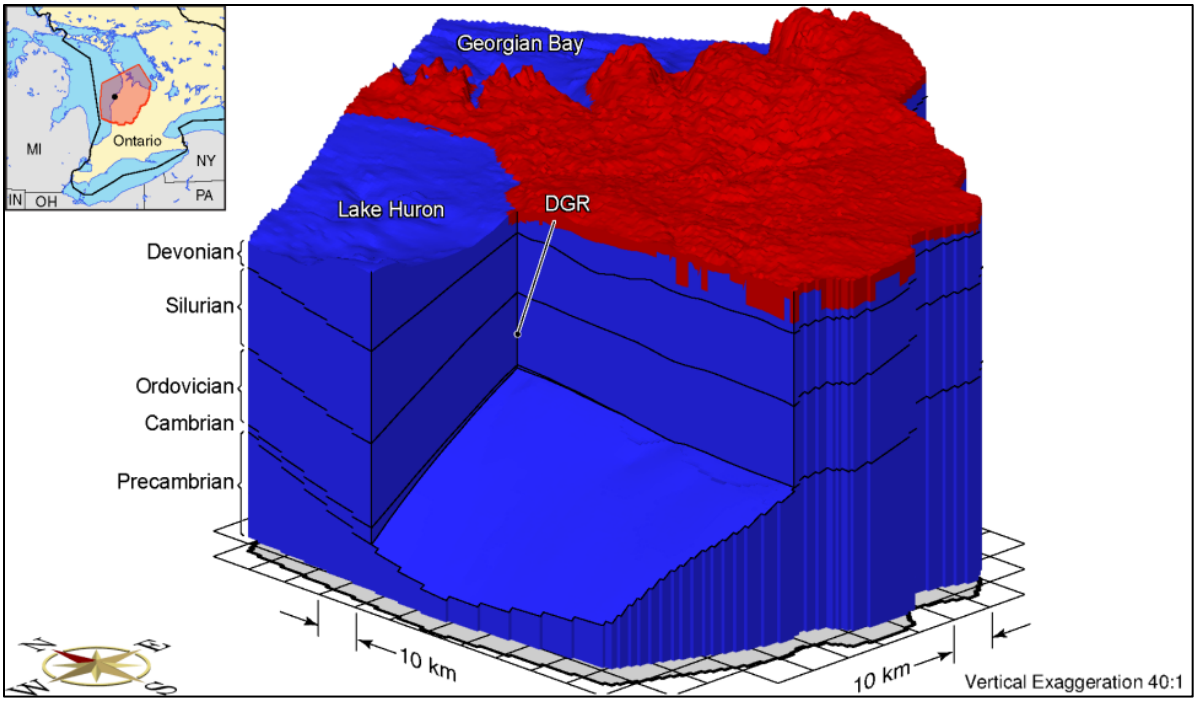

Figure 6.13 Block cut view of the distribution of permafrost

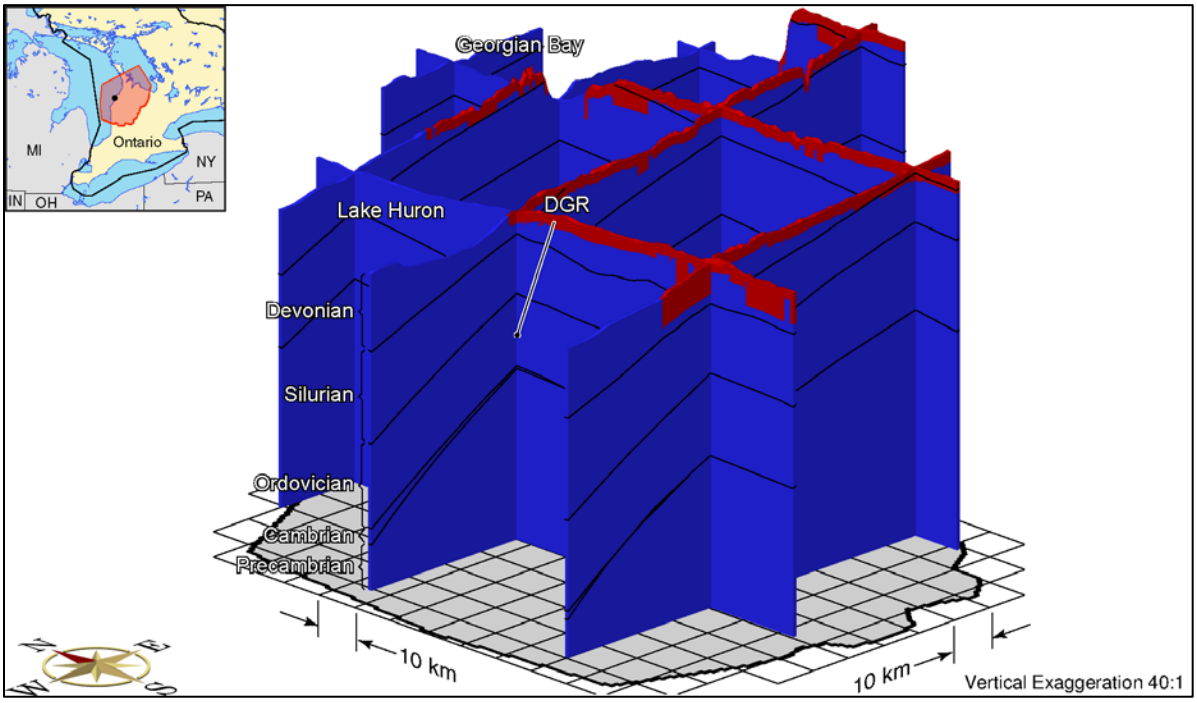

Figure 6.14 Fence view of the distribution of permafrost

Table 6.4 Relationships between pressure, saturation, and relative permeability for variably-saturated flow conditions

Pressure (m)	Saturation
-10.0	0.5
0.0	1.0
Saturation	**Relative Permeability**
0.5	1.0
1.0	1.0

Figure 6.15 and Figure 6.16 illustrate the freshwater head distributions; Figure 6.17 illustrates the depth to the water table for the fully-saturated conditions; Figure 6.18 and Figure 6.19 illustrate the freshwater head distribution; and Figure 6.20 illustrates the depth to the water table for the variably-saturated scenario. For fully-saturated conditions, the depth to the water table was determined using elevation and hydraulic head (environmental head for density-dependent problems). The water table was located where the elevation was equal to the hydraulic head or where the pressure was equal to zero. For variably-saturated conditions, the water table was considered to be at the zero potentiometric surface found by scanning the model domain from the bottom up. The maximum difference in the depths to the water table observed between the steady-state results for fully-saturated and variably-saturated scenarios was on the order of 10^{-4} m in the south-east region of the domain as illustrated in Figure 6.23. Figure 6.21 and Figure 6.22 show the level of saturation for the simulation with variably-saturated flow conditions.

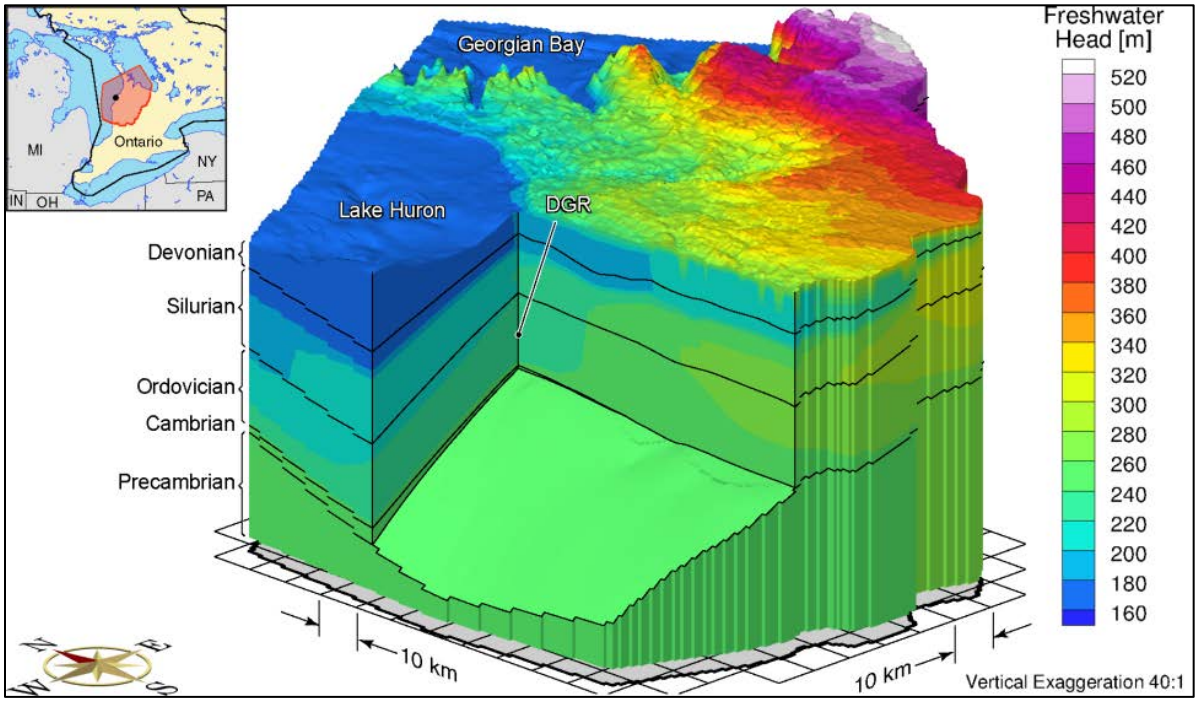

Figure 6.15 Block cut view of freshwater heads for steady-state saturated flow

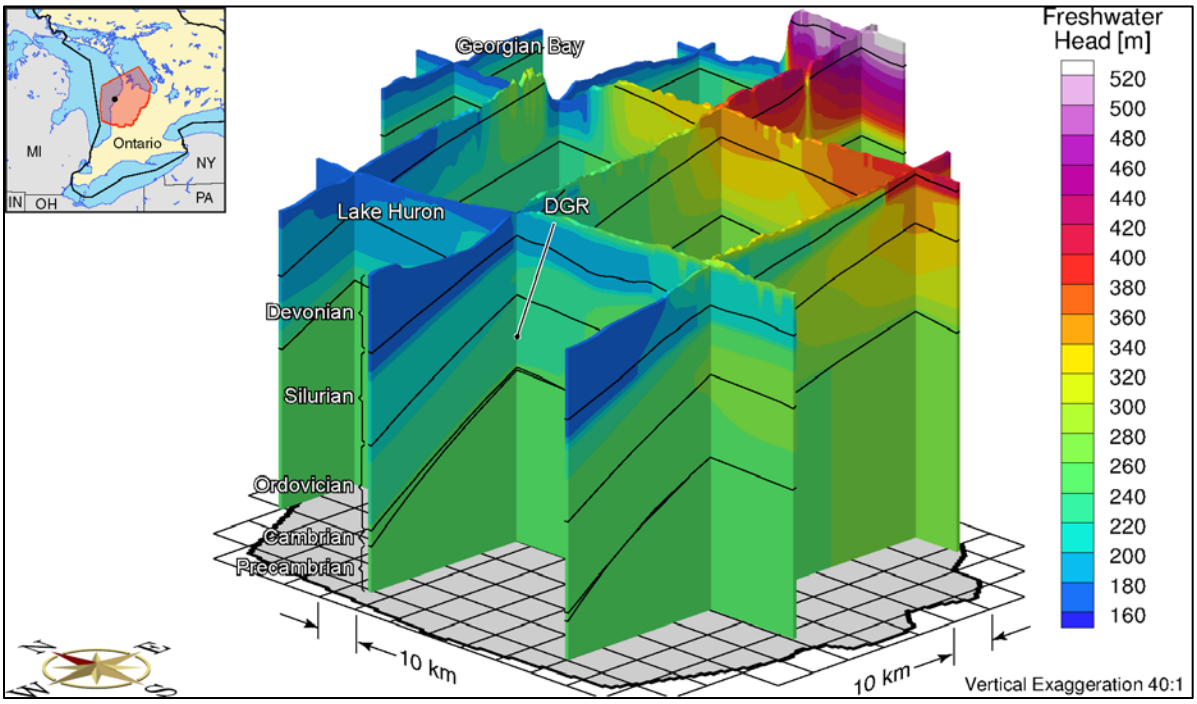

Figure 6.16 Fence view of freshwater heads for steady-state saturated flow

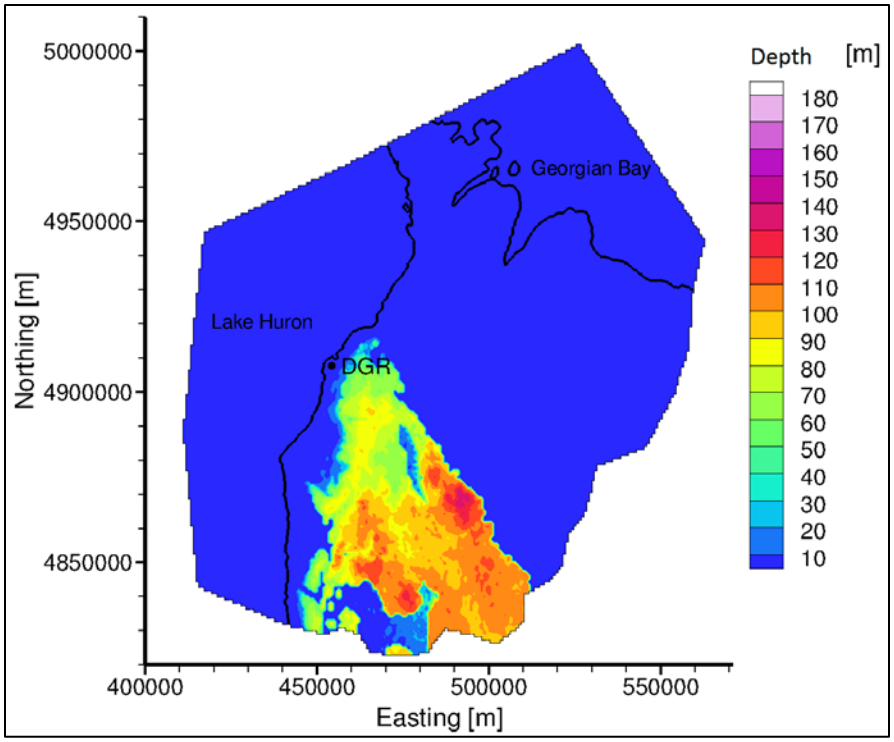

Figure 6.17 Areal view of depth to the water table for steady-state saturated flow

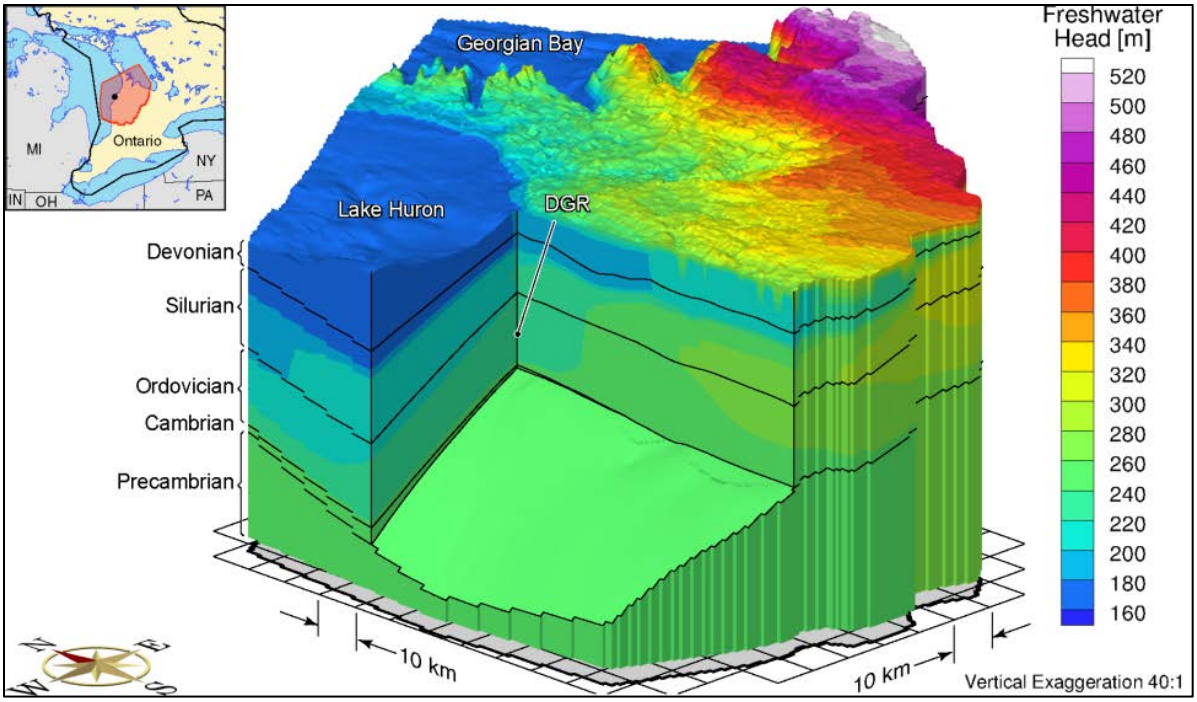

Figure 6.18 Block cut view of freshwater heads for steady-state variably-saturated flow

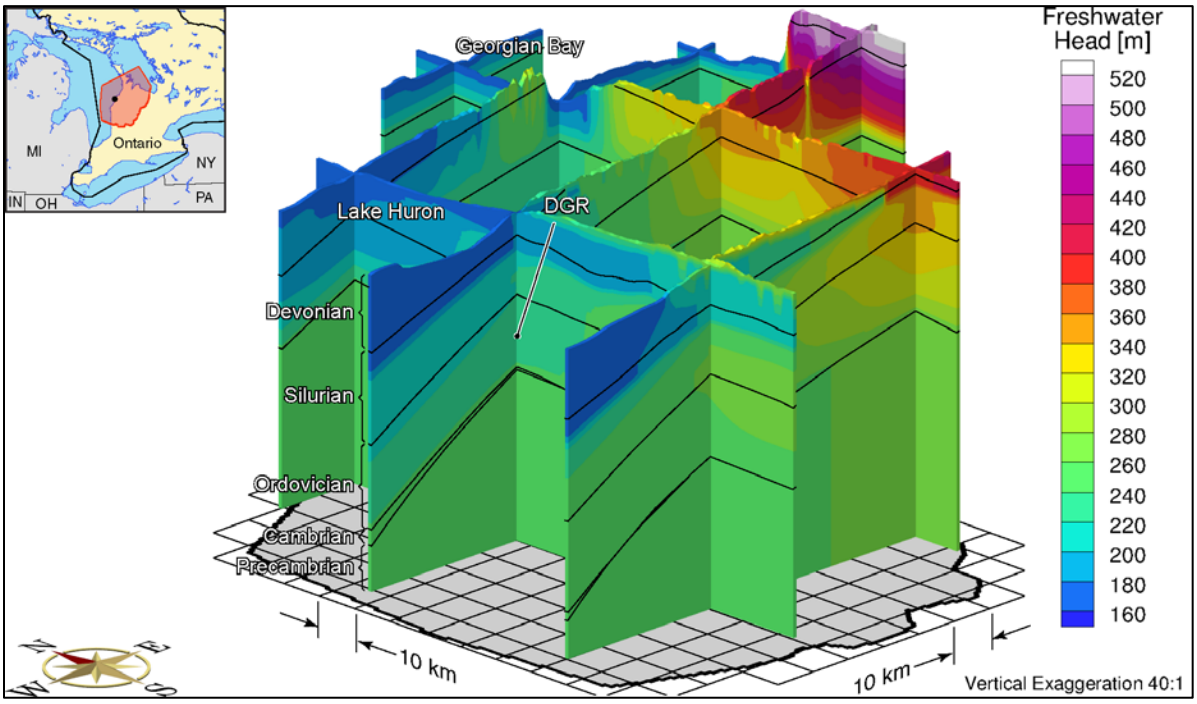

Figure 6.19 Fence view of freshwater heads for steady-state variably-saturated flow

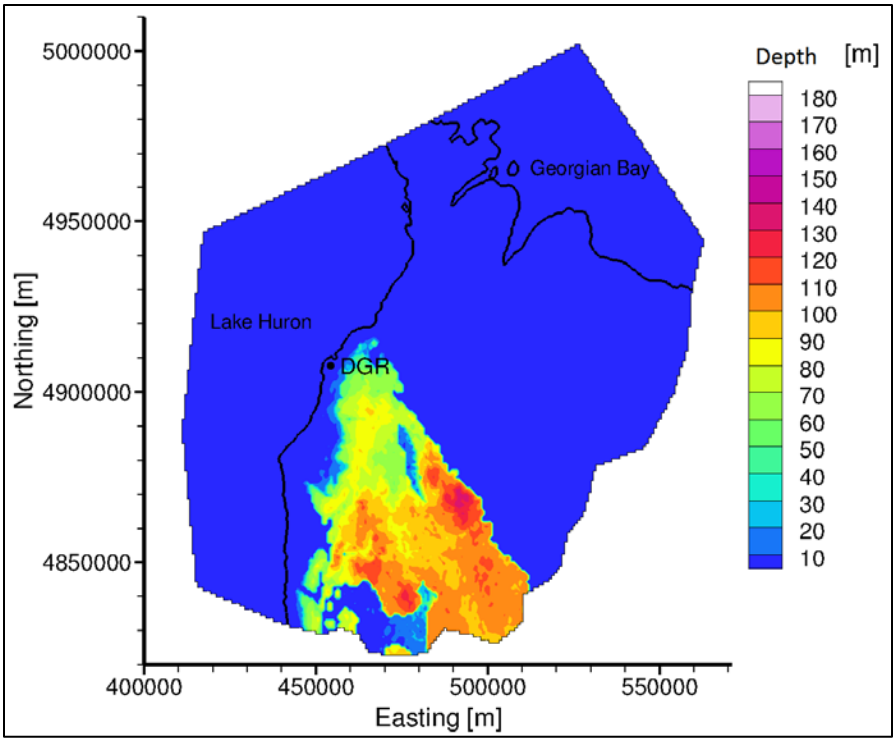

Figure 6.20 Areal view of depth to the water table for steady-state variably-saturated flow

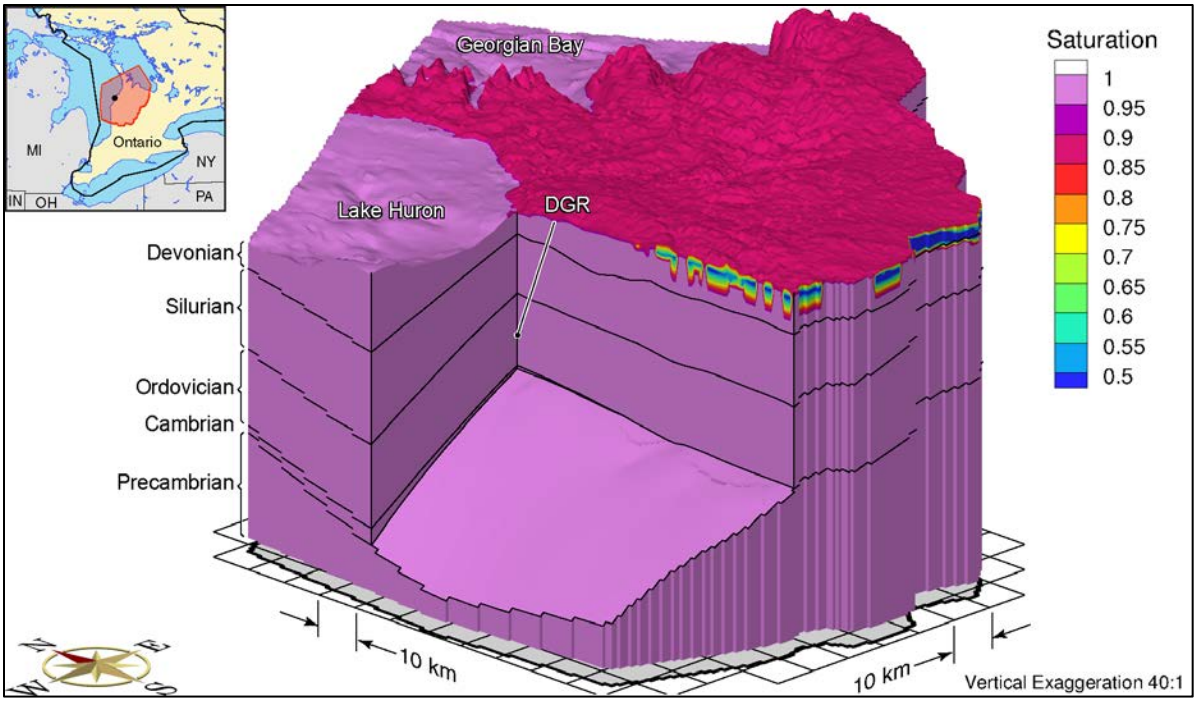

Figure 6.21 Block cut view of saturation for steady-state variably-saturated flow

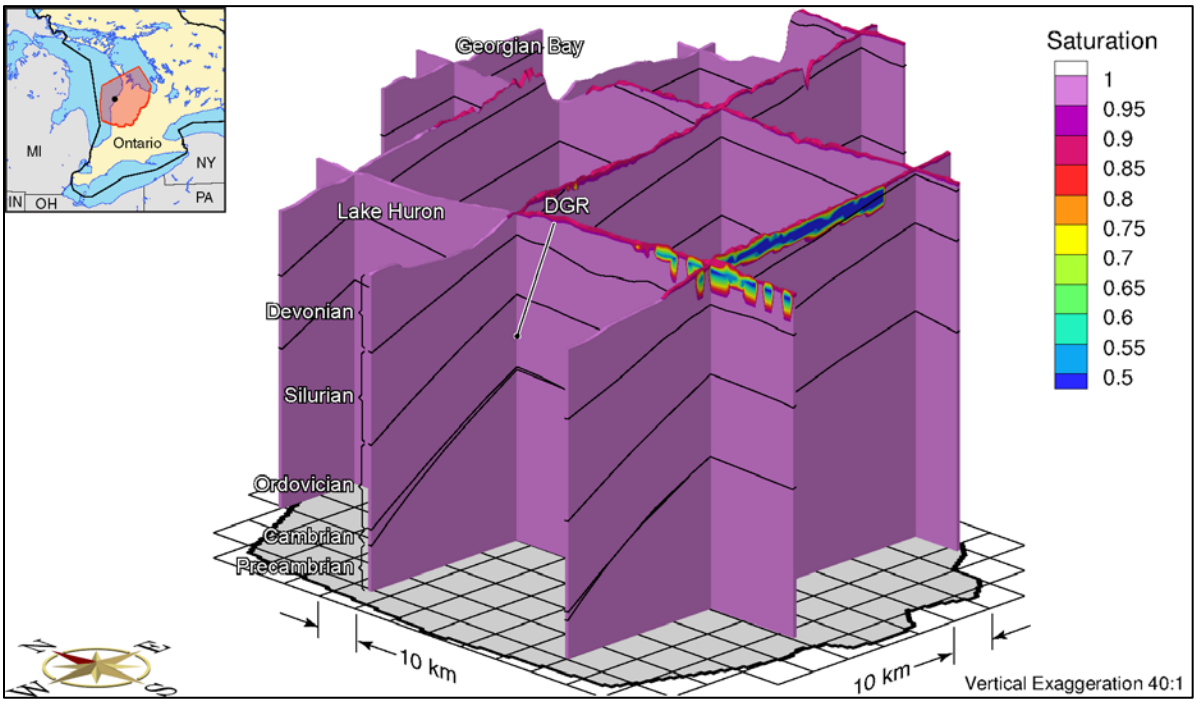

Figure 6.22 Fence view of saturation for steady-state variably-saturated flow

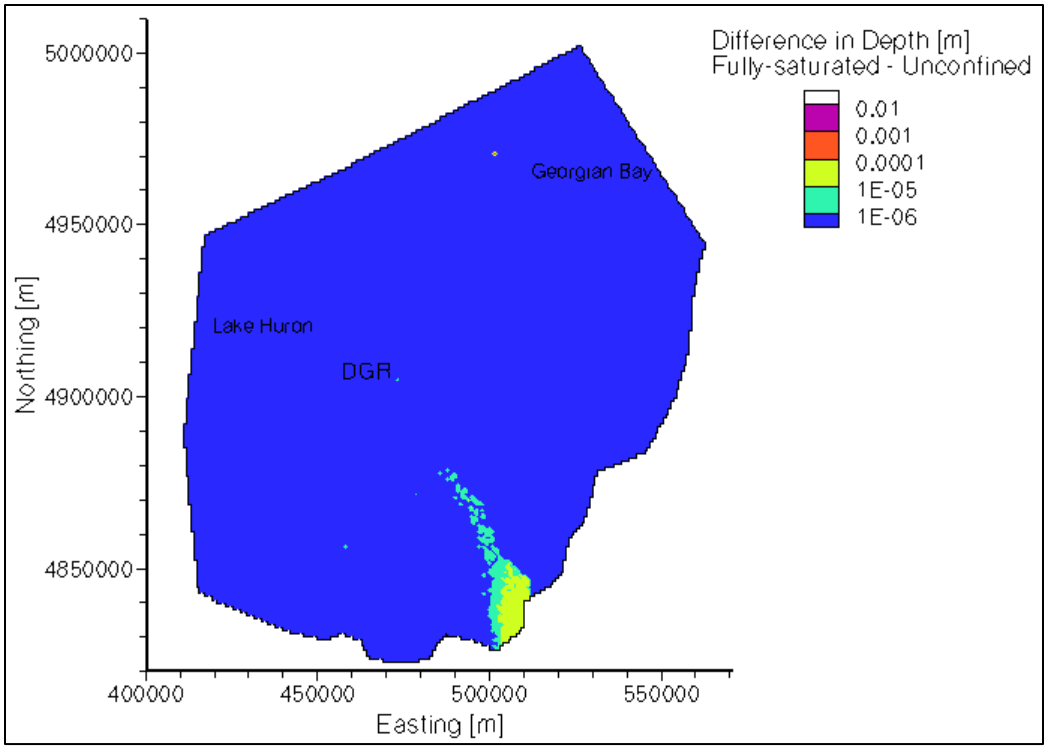

Figure 6.23 Areal view of the difference in depths to water table for fully-saturated and variably-saturated, steady state flow conditions.

Each transient simulation began with fully-saturated conditions using the results of the steady-state simulations as initial conditions so that the patterns and rates of drainage for the two flow conditions could be observed and compared. For these transient simulations, the top boundary conditions included the prescribed head for the Lake Huron and zero recharge everywhere else. Ice sheet dynamics were ignored, and the transient simulations were run for 30,000 years. This timeframe was long enough to capture the effects of variably-saturated flow on the water table.

At the onset of permafrost, the head distribution and the depth to water table were effectively the same for both the fully-saturated (Figure 6.24, Figure 6.25, and Figure 6.26) and the variably saturated flow systems (Figure 6.27, Figure 6.28, and Figure 6.29). Both systems showed extensive drainage (up to approximately 140 m) in the southwestern region of the domain where a high permeability layer (the Devonian) connects with Lake Huron as illustrated in Figure 6.5, a map of the bedrock outcrops. Initially, little or no drainage occurred through the relatively low permeability Ordovician and Silurian layers.

By three years after the onset of permafrost, it was becoming evident that the system with fully-saturated conditions was draining through the Devonian layer more rapidly than the system with variably-saturated flow conditions. After approximately 1,000 years, the fully-saturated system showed little or no further drainage in that southeastern region, but the water table did continue to lower gradually at topographic highs throughout the rest of the domain (the Silurian layers) until the end of simulations at 30,000 years after the onset of permafrost. At 30,000 years, the maximum depth reached within the rest of the domain was around 100 m although the for the most part the water table only dropped between 10 m and 20 m. Figure 6.36 illustrates the depth to the water table at 1,000 years after the onset of permafrost. Figure 6.30, Figure 6.31, and Figure 6.32 illustrate the head distribution (block cut and fence views) and the depth to the water table, respectively, all at 30,000 years after the onset of permafrost.

For the variably-saturated scenario, because the flow system evolved without recharge, the water table dropped and the shallow sub-surface became variably-saturated with higher saturation in regions of lower elevation and lower saturation at higher elevations. The rate at which the water table dropped for the variably-saturated scenario was slower than that of the fully-saturated scenario. Thus, it took much longer (around 30,000 years after the onset of permafrost) for the depth to water table profile for variably-saturated conditions (Figure 6.35) to approach the same amount of drainage as experienced by the fully-saturated scenario about 1,000 years after the onset of permafrost (Figure 6.36). Figure 6.33 and Figure 6.34 illustrate the head distribution at 30,000 years after the onset of permafrost for variably-saturated flow.

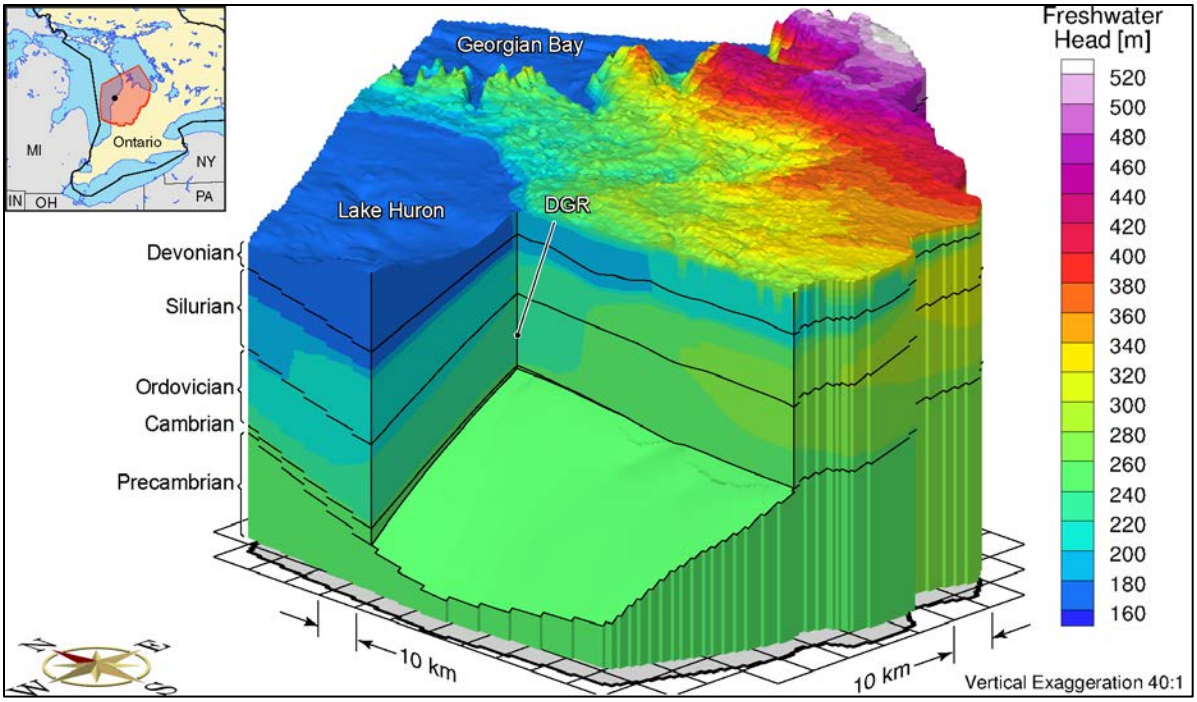

Figure 6.24 Block cut view of freshwater heads at the onset of permafrost for saturated flow

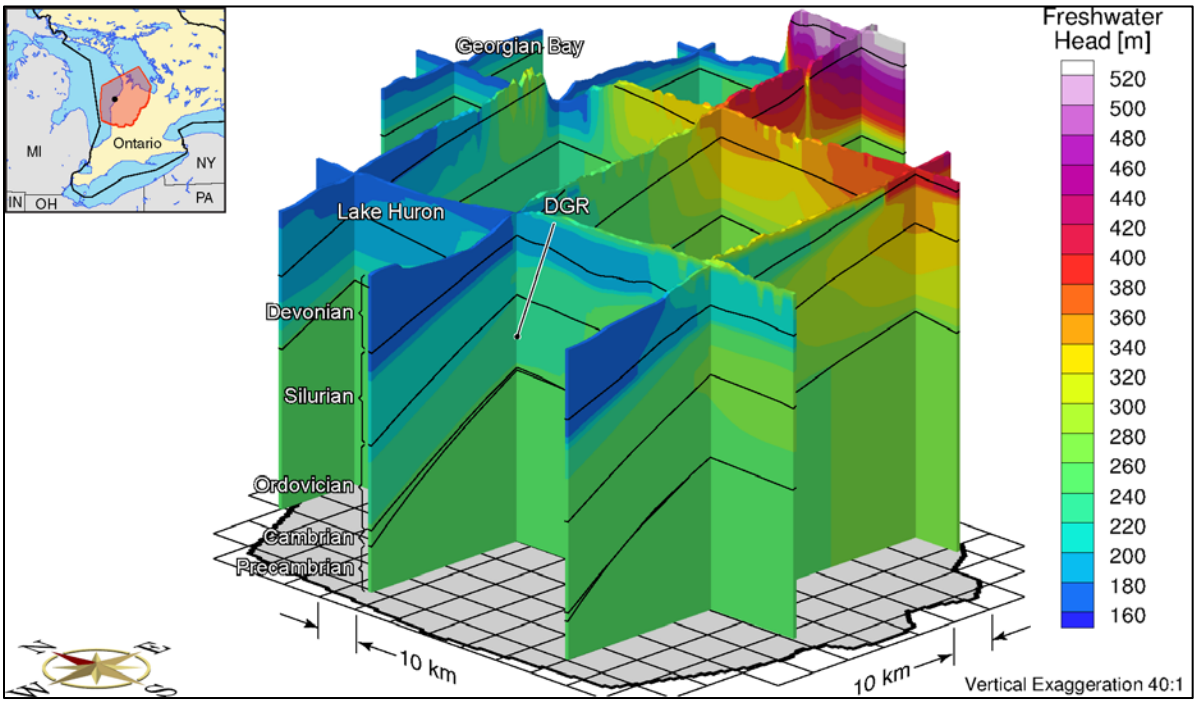

Figure 6.25 Fence view of freshwater heads at the onset of permafrost for saturated flow

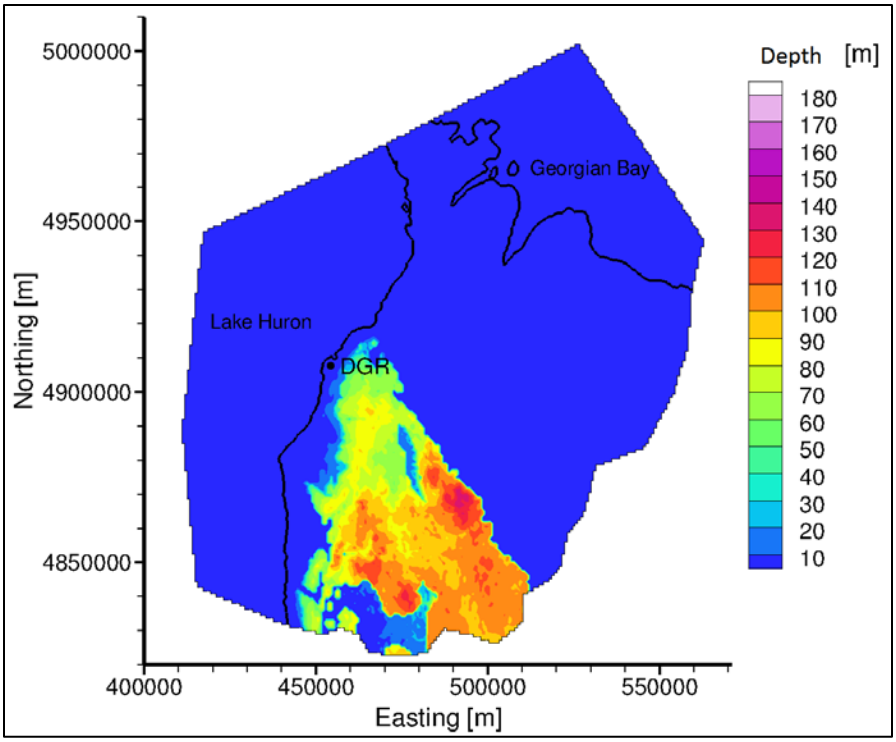

Figure 6.26 Areal view of depth to water table at the onset of permafrost for saturated flow

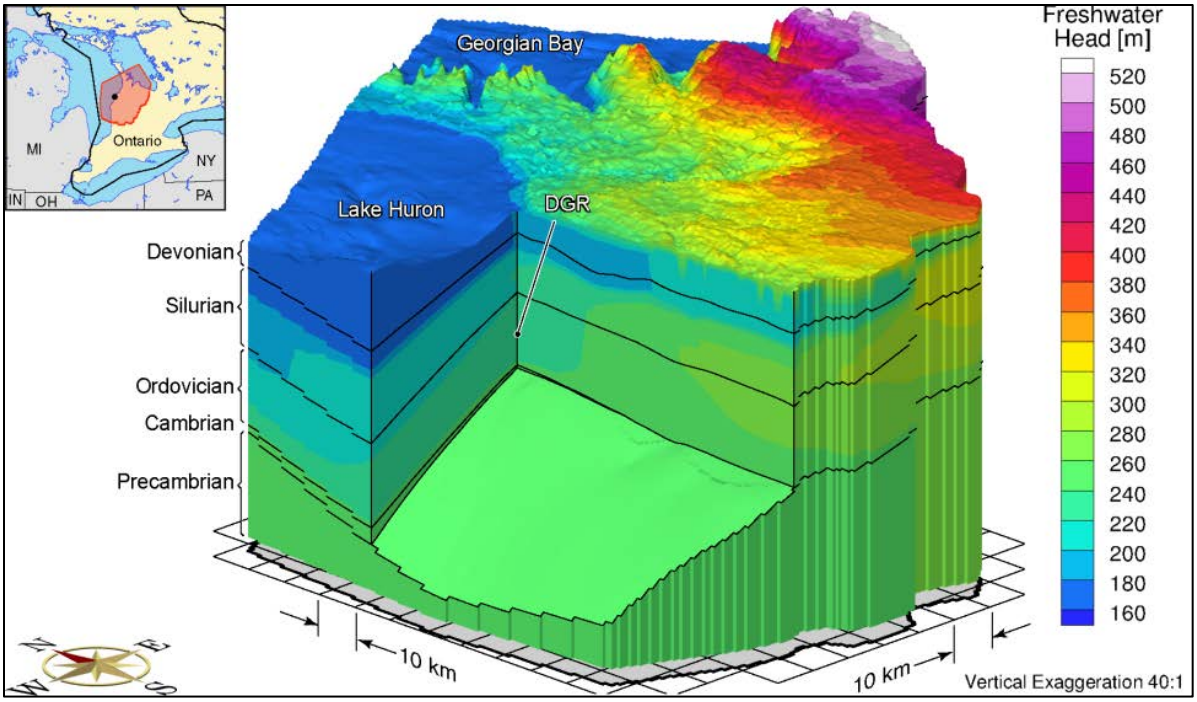

Figure 6.27 Block cut view of freshwater heads at the onset of permafrost for variably-saturated flow

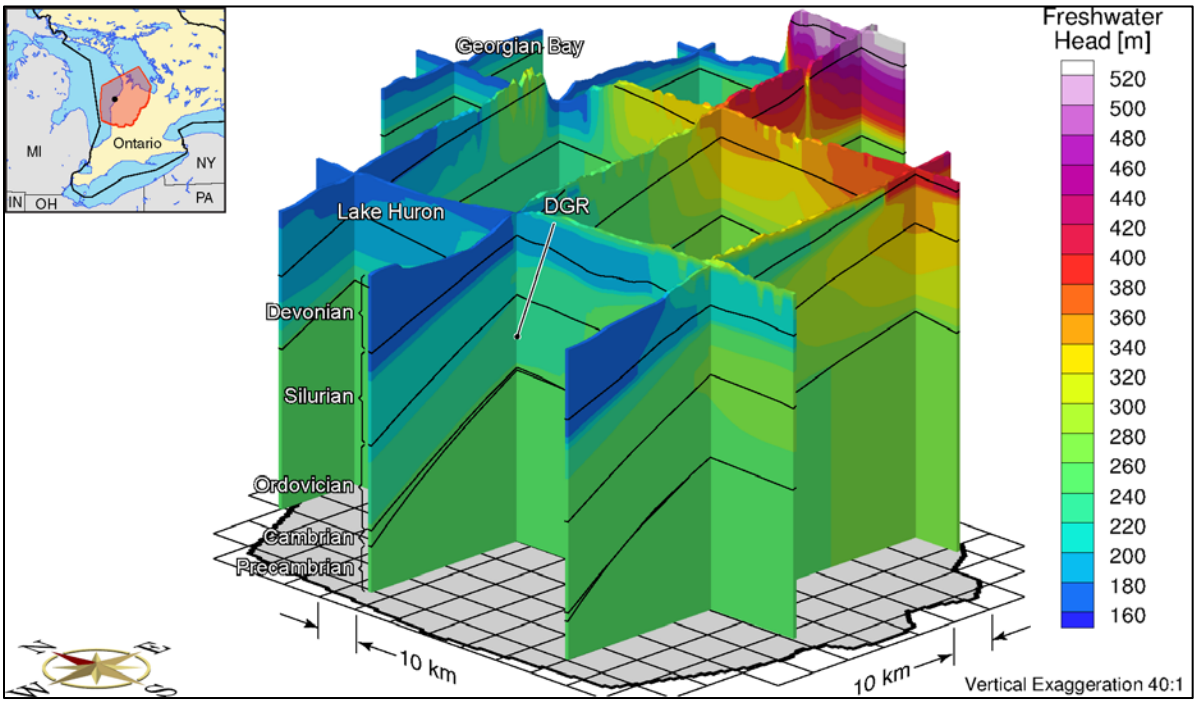

Figure 6.28 Fence view of freshwater heads at the onset of permafrost for variably-saturated flow

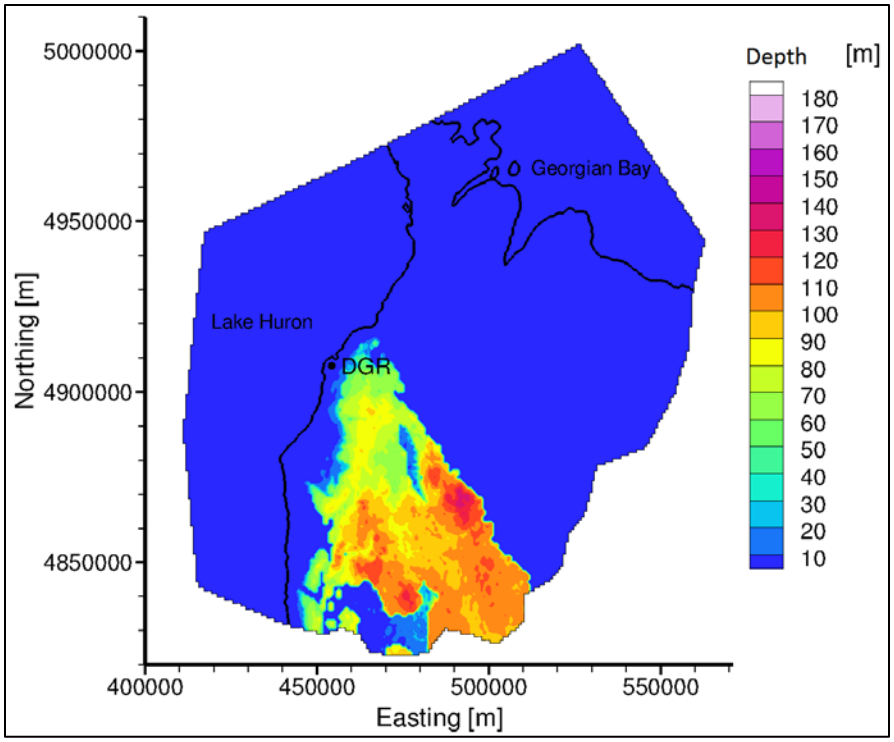

Figure 6.29 Areal view of depth to water table at the onset of permafrost for variably-saturated flow

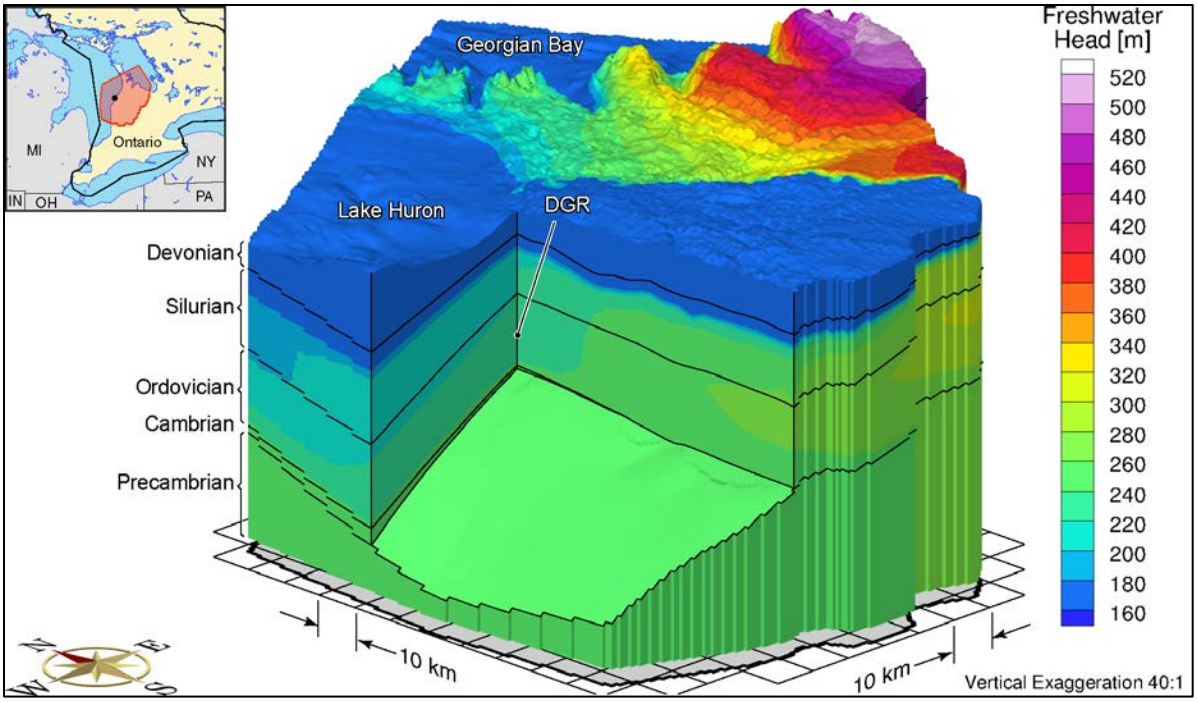

Figure 6.30 Block cut view of freshwater heads 30,000 years after the onset of permafrost for saturated flow

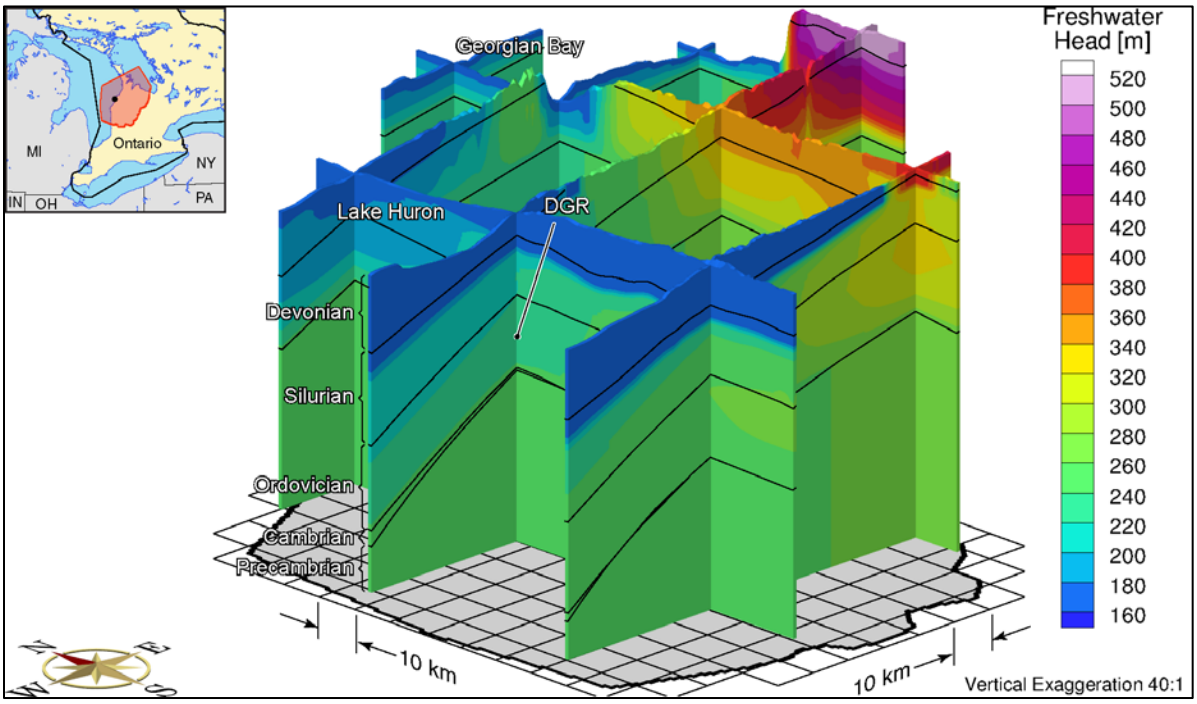

Figure 6.31 Fence view of freshwater heads 30,000 years after the onset of permafrost for saturated flow

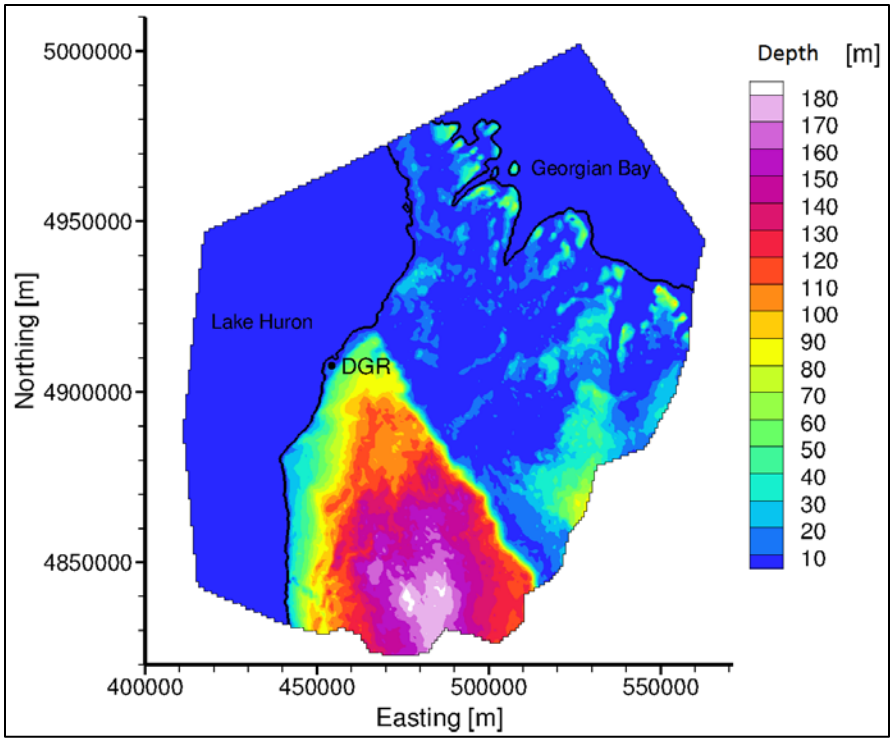

Figure 6.32 Areal view of depth to the water table 30,000 years after the onset of permafrost for saturated flow

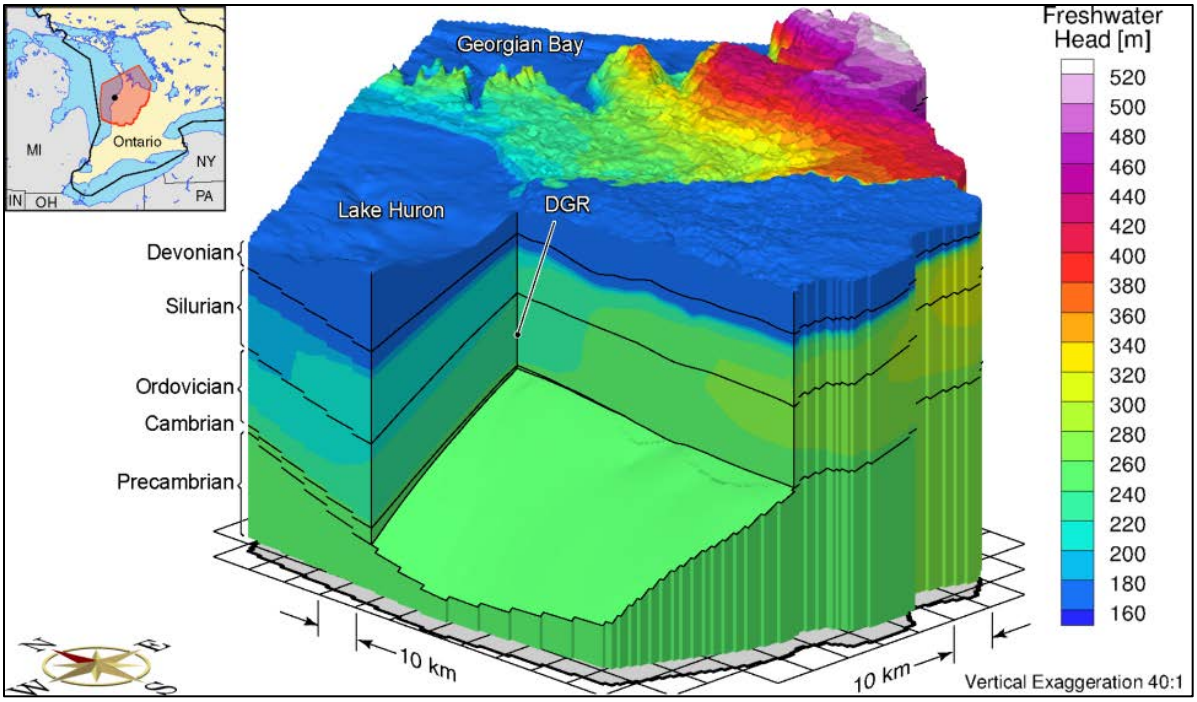

Figure 6.33 Block cut view of freshwater heads 30,000 years after the onset of permafrost for variably-saturated flow

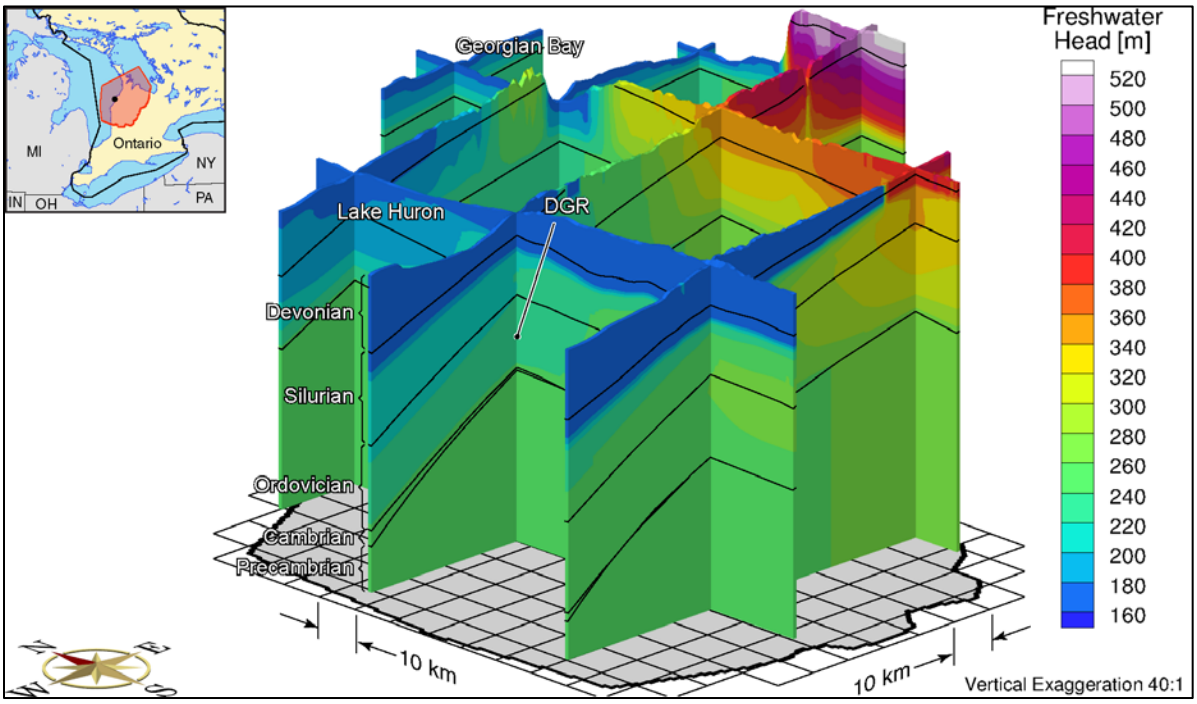

Figure 6.34 Fence view of freshwater heads 30,000 years after the onset of permafrost for variably-saturated flow

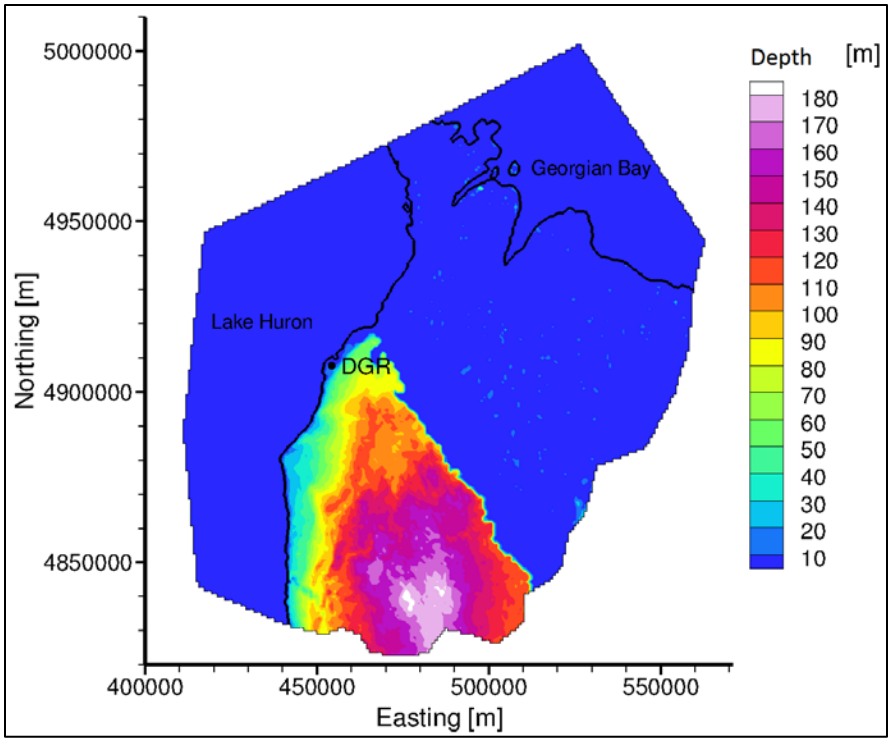

Figure 6.35 Areal view of depth to the water table 30,000 years after the onset of permafrost for variably-saturated flow

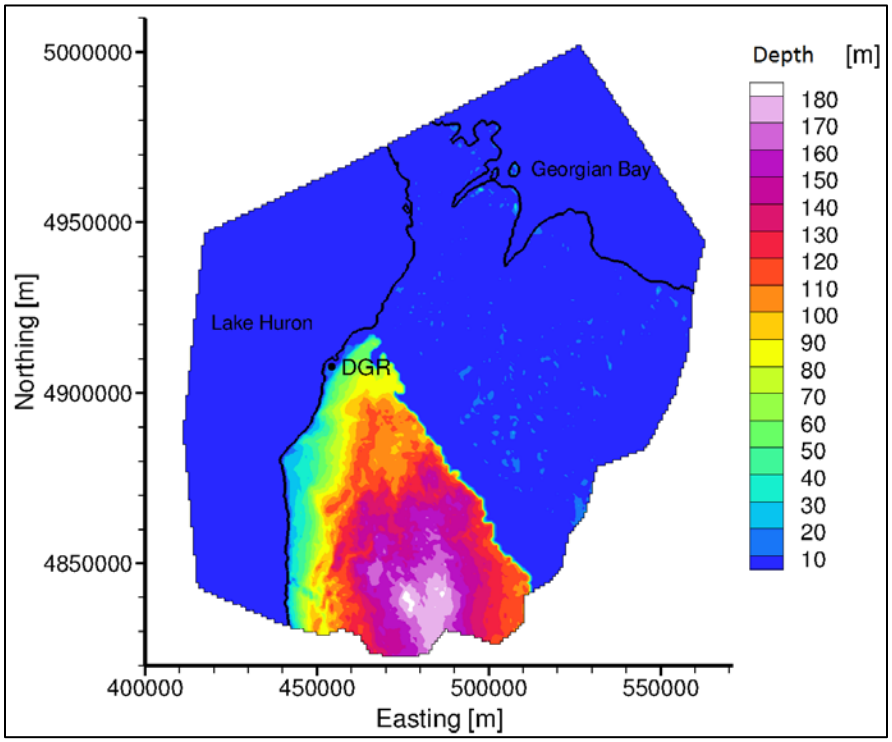

Figure 6.36 Areal view of depth to the water table 1,000 years after the onset of permafrost for saturated flow

6.5 Summary

Some glaciation studies that included permafrost used a fixed prescribed head equal to the topographic head [Bense et al., 2009; Lemieux et al., 2008a, b, c] or to 3 m below ground surface [Sykes et al., 2011]. The analysis presented in Section 6.4.1 demonstrated that with the presence of permafrost, the use of a prescribed head boundary condition did not allow drainage that may occur when the recharge to permafrost is set to zero. Leakage through the permafrost layer was insufficient to support the head values in the layers beneath it, and, in the absence of taliks inland, these layers drained, dropping the water table up to 180 m or more depending on the stratigraphy, hydraulic parameters, and constitutive laws.

Within the proposed DGR site domain model, the most significant level of drainage occurs in the southern region where the Devonian connects to Lake Huron in the west (See Figure 6.5 for a map of the bedrock outcrops for this region.). The permafrost above this layer makes it a confined aquifer. Without recharge and with little leakage through the permafrost layer, all of the water above the elevation of the lake (176 m) in this relatively high permeability layer drains to the lake. After much of the southern region of the domain had drained by around 1,000 years for simulations with fully-saturated conditions, the water table begins and continues to lower gradually at topographic highs throughout the rest of the domain until the end of the simulations (30,000 years after the onset of permafrost).

As discussed in Section 6.4.1, simulations that included variably-saturated flow necessitated further simplifications (e.g., removal of solute transport, constant depth and distribution of permafrost) to maintain numerical stability and converge to a solution. Thus, the fully-saturated flow conditions were used in the analysis presented in Section 6.4.1 primarily as a screening analysis or first approximation because it allowed for numerical expediency in comparison with variably-saturated flow. Nonetheless, a comparison of the transient simulations run with fully-saturated and variably-saturated conditions, demonstrated that the water table and flow system are affected by the flow conditions used. Drainage occurred more slowly with the variably-saturated conditions than with the fully-saturated conditions. It took around 30,000 years after the onset of permafrost before the depth to water table profile for the variably-saturated conditions to result in the same level of drainage as experienced with fully-saturated conditions just approximately 1,000 years after the onset of permafrost.

7.0 Discussion

The purpose of this doctoral research was to examine the common assumptions that fluid flow for paleo-climate analyses is isothermal (e.g., Jaquet & Namar, 2010; Sykes et al., 2011; Yin et al., 2013) or that heat transport is by conduction only (e.g., Chen et al., 2003; Hayashi et al., 2007; Mottaghy & Rath, 2006; Zhang et al., 2003; Zhang et al., 2006, 2008a, b) and that fluid flow is fully-saturated and the phreatic surface in the permafrost is within metres of the topographic surface (e.g., Bense et al., 2009; Lemieux et al., 2008a, b, c; Sykes et al., 2011; Yin et al., 2013). This doctoral research included thermal transport and flow conditions with an alternate conceptualization of the water table boundary conditions in order to develop a deeper understanding and more detailed representation of the impact of glacial and periglacial conditions on the groundwater flow system.

Two computational models, FRAC3DVS-OPG [Therrien et al., 2007] and COMSOL Multiphysics (COMSOL) [COMSOL, 2011] were used for this doctoral research. FRAC3DVS-OPG is a three-dimensional, finite element numerical code that solves variably saturated density-dependent groundwater flow and solute transport equations in non-fracture or discretely fractured media. FRAC3DVS-OPG was used to investigate the impact of permafrost on the water table and the groundwater flow system for three-dimensional models of the study sites in Greenland and Southern Ontario.

For the purposes of this doctoral research, the greatest limitation of FRAC3DVS-OPG is that systems are assumed to be under isothermal conditions because the physics for temperature are not included. Thus, COMSOL, a finite-element, numerical modelling platform for simulating a wide range of physics-based problems from many disciplines, was selected to examine the impacts of temperature (and latent heat) on permafrost development and degradation. COMSOL allows for coupled or “Multiphysics” phenomena to be represented using physics or equation-based modelling. While COMSOL does allow models to be developed in one, two, and three dimensions, it does not allow for simulation of a property that varies in three dimensions as well as time. That limitation hindered the simulation of glacier movement and the impact that glacier has on properties such as head or pressure, stress or mechanical load, and temperature at the top boundary (ground surface).

Thus, while demonstrating the need to eliminate (or at least minimize) assumptions about saturation, boundary conditions, and thermal conditions, this doctoral research also showed that computational challenges continue to limit the ability to use more complex physical relationships. The analyses presented in this thesis were numerically complex and computationally intensive because they included density-dependent flow, thermal transport (with latent heat), solute transport, and hydromechanical coupling for relatively large model domains.

Additionally, the density varied with pressure, temperature and solute concentration, and the permeability of the porous media was dependent on the temperature or physical state of the fluid.

Although all of the physical relationships described above were included and examined in this doctoral research, they could not all be included in the same model. Each analysis required the elimination or simplification of one or more component (e.g., solute distribution held constant) in order to address the key issues: the impact of permafrost and variably saturated flow on the water table, the impact of temperature and latent heat on the permafrost distribution, and the impact of talik size and distribution on the groundwater flow system during glacial advance.

7.1 Impact of Permafrost and Variably-saturated Flow on the Water Table

The numerical model of the Greenland Analogue Project (GAP) study site was used to examine the impact of permafrost on the water table for fully-saturated and variably-saturated conditions. The impact of permafrost on the water table was also investigated by extending the numerical model of the proposed Deep Geologic Repository (DGR) site developed by Sykes et al. [2011]. Comparisons of simulations run with fully-saturated and variably-saturated conditions for both the GAP and proposed DGR models showed that the water table and flow system are affected by the flow conditions and constitutive laws used.

For both fully-saturated and variably-saturated flow conditions, the presence of permafrost restricts deep circulation and slows down drainage. This was demonstrated with the three-dimensional GAP domain model, which showed that for simulations without permafrost, the saturation was reduced from the fully-saturated initial conditions to approximately 50% saturation within the first 2,000 years of the scenario while simulations with permafrost did not reach those same conditions until around 50,000 years. The presence of permafrost also lowered the pore water velocities by two to three orders of magnitude compared to simulations that did not include permafrost. For both the GAP and the DGR site models, drainage occurred more slowly with the variably-saturated conditions than with the fully-saturated conditions although they both eventually resulted in similar profiles of water table depths.

These analyses tested that the assumption that the phreatic surface is at (or a few metres below) the topographic surface throughout a glacial cycle, particularly in the periglacial environment. With the presence of permafrost, the use of a prescribed head boundary condition did not allow drainage that may occur when the recharge to permafrost is set to zero. Permafrost will not allow enough recharge to maintain fully-saturated conditions, and the system will drain beneath it. If the system drains beneath the permafrost while the permafrost exists, it will refill when the permafrost melts as either the atmospheric temperatures increase, which will allow oxygenated meteoric water to refill the system, or the ice sheet covers the permafrost, which will allow glacial meltwater to infiltrate to depth.

7.2 Impact of Thermal Transport and Latent Heat on Permafrost Distribution

The numerical model of the study site for GAP as presented in Yin et al. [2011] was also extended for this doctoral research to include the physics for heat transport including latent heat. This extension provided valuable insight about the impact of accounting for heat transport and latent heat on the distribution of permafrost between the Greenland Ice Sheet (GIS) and Davis Strait during the last glacial cycle. The permafrost distributions for the system presented in Yin et al. [2011], the system with temperature but no latent heat, and the system with temperature and latent heat were compared. The 300 m permafrost depth used by Yin et al. [2013] did match field observations [Jaquet & Namar, 2010] and the maximum permafrost depths that developed in the temperature-dependent simulations. However, holding that permafrost depth constant throughout the glacial cycle resulted in an overestimation of permafrost depths during times of glacial advance and retreat when the permafrost degraded and formed.

In addition to using a constant permafrost depth, Yin et al. [2013] also assumed that the permafrost would persist for 10 km beneath the ice sheet. The temperature-dependent simulations for this doctoral research showed that permafrost could remain beneath the ice sheet, but to much shorter or longer distances from the edge of the ice sheet, depending on the rate of ice sheet advance and the initial depth of permafrost. For example, when the ice sheet advanced to the west around 38 km over approximately 1,000 years and covered a 32 km region of permafrost that reached up to around 280 m deep, the permafrost extended nearly the entire 32 km beneath the ice sheet although it had degraded to around 10 m deep and temperatures ranged between -0.5 ^{o}C and 0 ^{o}C.

Other factors impacting the permafrost depth and distribution during glacial advance were examined using a more detailed model representing a two-dimensional cross-section of a generic crystalline rock setting, which included fluid flow, heat transport, and hydromechanical coupling as well as an analytic profile for the ice sheet. Three initial permafrost depths were chosen: approximately 40 m (shallow), 100 m (intermediate), and 300 m (deep). In all three scenarios, the permafrost remained beneath the warm-bottomed ice sheet to varying distances as the ice sheet advanced with the deeper (and colder) permafrost remaining for a longer time and to a greater distances from the ice sheet edge than when the permafrost was shallower. The temporal patterns of permafrost thaw were influenced by the discretization of the model. The ice advances in discrete steps to the next node with the interval for advance being greater than the time to thaw the permafrost at a node. When the ice sheet did reach the next node, the permafrost beneath it thawed rapidly within a few years.

With deep permafrost as the initial condition, the permafrost remained beneath the ice sheet up to 100 m from the ice sheet edge and for up to 50 years before beginning to melt when

the ice sheet advanced at a rate of 1 m/year. That result varies significantly from the assumptions made in Yin et al. [2013], which used a constant permafrost depth of 300 m and fixed the permafrost beneath the ice sheet for a distance of 10 km from the ice sheet edge. While there are differences in the scale of the generic cross-section and the Yin et al. [2013] model, the results of the generic cross-section analyses combined with those described previously for the GAP site model including heat transport, show that the permafrost depth and distribution beneath an advancing ice sheet will not remain constant. (Section 7.3 will discuss how the presence of taliks will further alter the depth and distribution of the permafrost.)

The model of a generic crystalline rock setting was also used to investigate the impact of the rate of glacial advance on permafrost distribution with 1 m/year and 2 m/year rates of ice sheet advance being considered. The rate of ice sheet advance did not change the distance to which the permafrost remained from the edge of the ice sheet as it advanced. However, doubling the rate of ice sheet advance did reduce the length of time for which the permafrost remained beneath the ice sheet by approximately half.

For the GAP analysis, accounting for latent heat did not impact the maximum depth of permafrost for the glacial cycle relative the scenarios with temperature and no latent heat, but it did further impact the permafrost and pressure distributions. In the simulations without latent heat, the permafrost region expanded relatively uniformly over time, while in the simulations that included latent heat, the depth of permafrost increased unevenly across the region of permafrost, depending on flow direction, until maximum depths were reached. Differences in the pressure distribution were most pronounced at depth beneath the edge of the ice sheet, developing and increasing in magnitude (up to 10^6 Pa difference in magnitude) whenever the ice sheet is stationary and dissipating gradually when the ice sheet advances or retreats again.

Given the scope of this doctoral research, using constant temperatures to represent the ice sheet, the atmospheric conditions, and the presence of a surface water body was appropriate. Because this research has demonstrated that the inclusion of thermal transport will impact the distribution of permafrost and the flow system during a glacial cycle, further investigations should account for variations in surface temperatures as a result of factors such as changes in atmospheric temperatures over time, surface cover (e.g., vegetation, snow) on ground temperatures, or the thermal characteristics of the ice sheet.

7.3 Impact of Talik Size and Distribution on the Groundwater Flow System during Glacial Advance

This doctoral research also investigated the impact of talik size and distribution on the groundwater flow system during glacial advance. The numerical model of the generic crystalline rock setting was used for those analyses. The initial permafrost depth was held constant at

approximately 100 m by setting the surface temperature to -3 ^{o}C. Up to three surface water bodies were created by setting the surface temperature to 2 ^{o}C in their locations. The width of the surface water bodies was either 50 m (less than the thickness of the permafrost) or 100 m (the same as the thickness of the permafrost) and they were positioned 50 m, 100 m, or 500 m apart.

One 50 m surface water body resulted in the formation of a closed talik while a 100 m surface water body led to the development of an open or through talik as was expected based on the analyses of other researchers (e.g., SKB, 2006, 2010). Both surface water bodies caused the base of the permafrost to be raised around or beneath the talik and in the region of permafrost between the talik and the advancing ice sheet. When multiple surface water bodies or taliks were located closer together, the permafrost beneath or directly beside them was made shallower than when the taliks were further apart (or there was only one talik). For example, when multiple 50 m-wide surface water bodies were located 50 m apart from each other, through taliks formed beneath them.

It was shown that the presence (and advance) of the ice sheet led to higher velocity magnitude values upward through the taliks than if the taliks existed without the ice sheet there. Additionally, the presence of the taliks (and the ice sheet) led to higher velocity magnitudes beneath the permafrost than in similar scenarios that did not include any taliks. As the ice sheet advanced closer to the talik, the velocity magnitude values were further increased within the talik and beneath the permafrost located between the talik and the ice sheet.

7.4 Implications for Nuclear Waste Management

When choosing an appropriate site in Canada for a DGR to isolate low and intermediate level wastes and used fuel over the million-year timeframe for radioactivity to reduce to that of its natural uranium content, the impact of glaciation and permafrost must be considered. Thus, this doctoral research has examined how glaciation and permafrost may impact the groundwater flow systems in low permeability crystalline rock and sedimentary rock, which have been proposed as possible sites for DGRs.

Because variably-saturated flow conditions and the presence of permafrost greatly impact drainage rates and patterns and the location of the phreatic surface, they should be accounted for in future modelling studies for DGR analyses. Although neither the simulations with variably-saturated flow conditions nor those with fully-saturated conditions showed drainage occurring to typical repository depths of 500 m or more, other factors such as geologic properties, fractures, and taliks could potentially alter the flow system in such a way that leads to changes in flow rates, temperatures, or chemical composition at those depths.

References

Aherns, C. D. (2007). *Meterology Today: An Introduction to Weather, Climate, and the Environment, 8th Edition.* Belmont, CA, USA: Thomson Brooks/Cole.

Alley, R. B., Andrews, J. T., Brigham-Grette, J., Clarke, G. K. C., Cuffey, K. M., Fitzpatrick, J. J., Funder, S., Marshall, S. J., Miller, G. H., Mitrovica, J. X., Muhs, D. R., Otto-Bliesner, B. L., Polyak, L., & White, J. W. C. (2010). History of the Greenland Ice Sheet: paleoclimatic insights. *Quaternary Science Reviews, 29,* p 1728-1756.

Alley, R. B., Fahnestock, M., & Joughin, I. (2008). Understanding Glacier Flow in Changing Times. *Science, 322,* p 1061-1062.

Allison, I., Alley, R. B., Fricker, H. A., Thomas, R. H., & Warner, R. C. (2009). Review: Ice sheet mass balance and sea level, *Antarctic Science, 21 (5),* p 413-426.

Anderson, N. J., Harriman, R., Ryves, D. B., & Patrick, S. T. (2001). Dominant factors controlling variability in the ionic composition of West Greenland lakes. *Arctic, Antarctic, and Alpine Research, 33(4),* p 418-425.

Anderson, N. J., Fritz, S. C., Gibson, C. E., Hasholt, B., & Leng, M. J. (2002). Lake-catchment interactions with climate in the low Arctic of southern West Greenland. *Geology of Greenland Survey Bulletin, 191,* p 144-149.

Anisimov, O. A. & Nelson, F. E. (1996). Permafrost distribution in the Northern Hemisphere under scenarios of climate change. *Global and Planetary Change,* 14, p 59-72.

Anisimov, O. A. & Nelson, F. E. (1997). Permafrost zonation and climate change in the northern hemisphere: Results from transient general circulation models. *Climate Change,* 35, p 241-258.

Anisimov, O. A., Shiklomanov, N. I., & Nelson, F. E. (1997). Global warming and active layer thickness: Results from transient general circulation models. *Global and Planetary Change,* 15, p 61-77.

Arnold, N. & Sharp, M. (2002). Flow variability in the Scandinavian ice sheet: modelling he coupling between ice sheet flow and hydrology. *Quaternary Science Reviews, 21,* p 485-502.

Bamber, J.L., Layberry, R. L., & Gogenini, S. P. (2001). A new ice thickness and bed data set for the Greenland ice sheet 1: Measurement, data reduction, and errors. *Journal of Geophysical Research* 106 (D24): 33773-33780.

Bamber, J.L., Layberry, R. L., & Gogenini, S. P. (2001). A new ice thickness and bed data set for the Greenland ice sheet 2: Relationship between dynamics and basal topography. *Journal of Geophysical Research* 106 (D24): 33781-33788.

Bauder, A., Mickelson, D. M., & Marshall, S. J. (2005). Numerical modeling investigations of the subglacial conditions of the southern Laurentide Ice Sheet. *Annals of Glaciology, 40,* p 219-224.

Bear, J. (1988). *Dynamics of Fluids in Porous Media.* Dover Publications Inc., New York, USA.

Benn, D. I. & Evans, D. J. A. (2010). *Glaciers and Glaciation, 2nd Edition.* London, UK: Hodder Education.

Bennike, O. & Bjorck, S. (2002). Chronology of the last recession of the Greenland Ice Sheet. *Journal of Quaternary Science, 17 (3),* p 211-219.

Bense, V. F., Ferguson, G., & Kooi, H. (2009). Evolution of shallow groundwater flow systems in areas of degrading permafrost. *Geophysical Research Letters,* Vol. 36.

Bense, V. F. & Person, M. A. (2008). Transient hydrodynamics within intercratonic sedimentary basins during glacial cycles. *Journal of Geophysical Research, Vol. 113.*

Booij, M., Leijnse, A., Haldorsen, S., Heim, M., & Rueslatten, H. (1998). Subpermafrost groundwater modelling in Ny-Alesund, Svalbard. *Nordic Hydrology, 29 (4/5),* p 385-396.

Boulton, G. S., Caban, P. E., & van Gijssel, K. (1995). Groundwater flow beneath ice sheets: Part 1 – Large scale patterns. *Quaternary Science Reviews, 14 (6),* p 545-562.

Boulton, G. S., Caban, P. E., van Gijssel, K., Leijnse, A., Punkari, M, & van Weert, F. H. A. (1996). The impact of glaciation on the groundwater regime of northwest Europe. *Global and Planetary Change, 12,* p 397-413.

Boulton, G. S., Lunn, R., Vidstrand, P., & Zatsepin, S. (2007). Subglacial drainage by groundwater-channel coupling, and the origin of the origin of esker systems: Part 1 – Glaciological observations. *Quaternary Science Reviews, 26 (7-8),* p 1067-1090.

Boulton, G. S., Hagdorn, M., Maillot, P. B., & Zatsepin, S. (2009). Drainage beneath ice sheets: groundwater-channel coupling, and the origin of esker systems from former ice sheets. *Quaternary Science Reviews, 28,* p 621-638.

Brevik, E. C. & Reid, J. R. (2000). Uplift-based limits to the thickness of ice in the Lake Agassiz basin of North Dakota during the late Wisconsinan. *Geomorphology, 32,* p 161-169.

Burn, C. R. & Kokelj, S. V. (2009). The environment and permafrost of the Mackenzie Delta area. *Permafrost and Periglacial Processes,* 20, p 83-105.

Burnett, R. D. & Frind, E. O. (1987). Simulation of contaminant transport in three dimensions 2. Dimensionality effects. *Water Resources Research, 23(4),* p 695-705.

Canadian Nuclear Association (CNA). (2009). *Presentation: Nuclear Energy 101*. [Online]. Retrieved November 1st, 2010 from http://www.cna.ca.

Canadian Nuclear Association (CNA). (2010). *Celebrating 50 Years: Seizing Opportunities for Growth – CNA 2010 Factbook Anniversary Edition.* [Online]. Retrieved November 1st, 2010 from http://www.cna.ca.

Chan, T., Christiansson, R., Boulton, G. S., Erisson, L. O., Hartikainen, J., Jensen, M.R., Mas Ivars, D., Stanchell, F. W., Vistrand, P., & Wallroth, T. (2005). DECOVALEX III BMT3/BENCHPAR WP4: The thermo-hydromechanical responses to a glacial cycle and their potential implications for deep geological disposal of nuclear fuel waste in a fractured crystalline rock mass. *International Journal of Rock Mechanics and Mining Sciences, 42,* p 805-827.

Chan, T. & Stanchell, F. W. (2008). DECOVALEX THMC Task E – Implications of glaciation and coupled thermohydromechanical processes on Shield flow system evolution and performance assessment. *NWMO Report TR-2008-03.* Toronto, Ontario: Nuclear Waste Management Organization.

Chan, T. & Stanchell, F. W. (2009). Implications of subsurface thermal-hydraulic-mechanical processes associated with glaciation on Shield flow system evolution and performance assessment. *Environmental Geology, 57,* p 1371-1389.

Chemical Rubber Company (CRC). (2013). *CRC Handbook of Chemistry and Physics, 94th Edition, 2013-2014.* Cleveland, Ohio: CRC Press.

Chen, W., Zhang, Y., Cihlar, J, Smith, S. L., & Riseborough, D. W. (2003). Changes in soil temperature and active layer thickness during the twentieth century in a region in western Canada. *Journal of Geophysical Research,* 108, No. D22, 4696.

Cheng, G. & Wu, T. (2007). Responses of permafrost to climate change and their environmental significance, Qinghai-Tibet Plateau. *Journal of Geophysical Research,* 112.

Chu, V. W., Smith, L. C., Rennermalm, A. K., Forster, R. R., Box, J. E., & Reeh, N. (2009). Sediment plume response to surface melting and supraglacial lake drainages on the Greenland ice sheet. *Journal of Glaciology, Vol. 55, No. 194.*

Clarke, G. K. C. (2005). Subglacial Processes. *Annual Reviews of Earth Planetary Sciences, 33,* p 247-276.

COMSOL. (2011). Subsurface Flow Module User's Guide. Version 4.2a.

COMSOL. (2012). Phase Change.

Cuffey, K. M. & Paterson, W. S. B. (2010). *The Physics of Glaciers, 4th Edition.* Burlington, MA, USA: Elsevier, Inc.

Cutler, P. M., MacAyeal, D. R., Mickelson, D. M., Parizek, B. R., & Colgan, P. M. (2000). A numerical investigation of the ice-lobe-permafrost interaction around the southern Laurentide ice sheet. *Journal of Glaciology, 46, 153,* p 311-325.

Davison, C. C., Chan, T., Brown, A., Gascoyne, M., Kamineni, D. C., Lodha. G. S., Melnyk, T. W., Nakka, B. W., O'Connor, P.A., Ophori, D. U., Scheier, N. W., Soonawala, N. M., Stanchell, F. W., Stevenson, D. R., Thorne, G. A., Vandergraaf, T. T., Vilks, P., & Whitaker, S. H. (1994). The Disposal of Canada's Nuclear Fuel Waste: The Geosphere Model for Postclosure Assessment. *Technical Report AECL-10719, COG-93-9, AECL Research, Whiteshell Laboratories, Pinawa, Manitoba, Canada.*

Evans, D. J. A. (Ed). (2003). *Glacial Landsystems.* London, UK: Arnold Publishers.

Eyles, N. & Miall, A. (2007). *Canada Rocks: The Geologic Journey*. Markham, Ontario: Fitzhenry and Whiteside, Limited.

Fetter, C. W. (2001). *Applied Hydrogeology, 4th Edition*. Upper Saddle River, New Jersey, USA: Prentice Hall, Inc.

Fleming, K. & Lambeck, K. (2004). Constraints on the Greenland Ice Sheet since the Last Glacial Maximum from sea-level observations and glacial-rebound models. *Quaternary Science Reviews, 23,* p 1053-1077.

Fountain, A. G. & Walder, J. S. (1998). Water flow through temperate glaciers. *Reviews of Geophysics, 36, 3,* p 299-328.

Frape, S.K. & Fritz, P. (Eds). (1987). Saline Water and Gases in Crystalline Rocks. *Geological Association of Canada Special Paper, 33,* p 19–38.

Freeze, R. A. & Cherry J. A. (1979). *Groundwater.* Englewood Cliffs, NJ, USA: Prentice Hall.

French, H. & Shur, Y. (2010). The principles of cryostratigraphy. *Earth-Science Reviews, 101,* p 190-206.

Frind, E. O. (1982). Simulation of long-term transient density-dependent transport in groundwater. *Advances in Water Resources, 5,* p 73-88.

Fritz, P. & Frape, S. K. (1982). Saline groundwaters in the Canadian Shield – A first overview. *Chemical Geology, 36,* p 179-190.

Ge, S., McKenzie, J., Voss, C., & Wu, Q. (2011). Exchange of groundwater and surface-water mediated by permafrost response to seasonal and long term air temperature variation. *Geophysical Research Letters,* 38.

Geological Survey of Canada (GSC). (2007). *Permafrost*. [Online Resource]. Retrieved September 5th, 2010 from http://gsc.nrcan.gc.ca/permafrost/index_e.php.

Grenier, C., Regnier, D., Mouche, E., Benabderrahmane, H, Costard, F., & Davy P. (2013). Impact of permafrost development on groundwater flow patterns: A numerical study considering freezing cycles on a two-dimensional vertical cut through a generic river-plain system. *Hydrogeology Journal, 21,* p 257-270.

Greve, R. (2005). Relation of measured basal temperatures and the spatial distribution of the geothermal heat flux for the Greenland ice sheet. *Annals of Glaciology, 42,* p 424-432.

Gupta, N. (1993). Geologic and fluid-density controls on the hydrodynamics of the Mt. Simon sandstone and overlying geologic units in Ohio and the surrounding states. PhD dissertation, Ohio State University, Columbus, Ohio.

Guvanasen, V. (2007). FRAC3DVS-OPG Enhancements: Subgridding, Hydromechanical Deformation, and Anisotropic Molecular Diffusion. *NWMO Report TR-2007-05*. Toronto, Ontario: Nuclear Waste Management Organization.

Haldorsen, S., Heim, M., Dale, B., Landvik, J. Y., van der Ploeg, M., Leijnse, A., Salvigsen, O., Hagen, J. O., & Banks, D. (2010). Sensitivity to long-term climate change of subpermafrost groundwater systems in Svalbard. *Quaternary Research, 73,* p 393-402.

Harris, C. & Murton, J. B. (Eds). (2005). *Cryospheric Systems: Glaciers and Permafrost*. Geological Society, London, UK, Special Publications, 242.

Hayashi, M., Goeller, N., Quinton, W. L., Wright, N. (2007). A simple heat-conduction method for simulating the frost-table depth in hydrological models. *Hydrological Processes,* 21, p 2610-2622.

Hjort, J., Etzelmuller, B., & Tolgensbakk, J. (2010). Effects of scale and data source in periglacial distribution modelling in a high Arctic environment, western Svalbard. *Permafrost and Periglacial Processes,* 21, p 345-354.

HSI GeoTrans. (2000). *Theory and Implementation for SWIFT for Windows: The Sandia Waste-Isolation Flow and Transport Model for Fractured Media.* Sterling, Virginia.

Hughes, T. J. (1998). *Ice Sheets*. Oxford, UK: Oxford University Press.

INTERA. (2011). Descriptive geosphere site model. INTERA Engineering Ltd. Nuclear Waste Management Organization (NWMO) DGR-TR-2011-24R000.

Interfrost. (n.d.). Interforst: Intercomparison project for TH (Thermo-Hydro) coupled heat and water transfers in permafrost regions. [Online]. Retrieved January 30th, 2016 from https://wiki.lsce.ipsl.fr/interfrost/doku.php.

Intergovernmental Panel on Climate Change (IPCC). (2007). *Climate Change 2007: The Physical Science Basis.* Contribution of Working Group I to the Fourth Assessment Report of the Intergovernmental Panel on Climate Change [Solomon, S., Qin, D., Manning, M., Chen, Z., Marquis, M., Averyt, K.B., Tignor, M., & Miller, H. L. (Eds).] Cambridge, UK; New York, NY, USA: Cambridge University Press.

Jaeger, J. C., Cook, N. G. W. & Zimmerman, R. W. (2007). *Fundamentals of Rock Mechanics, 4th Edition*. Blackwell Publishing Ltd.

Jaquet, O. & Namar, R. (2010). *Groundwater Flow Modelling under Ice Sheet Conditions.* Basel, Switzerland: In2Earth Modelling Ltd.

Jennings, A. E., Hald, M., Smith, M., & Andrews, J. T. (2006). Freshwater forcing from the Greenland Ice Sheet during the Younger Dryas: evidence from southeastern Greenland ice cores. *Quaternary Science Reviews, 25,* p 282-298.

Jorgensen, A. S. & Andreasen, F. (2007). Mapping of permafrost surface using ground-penetrating radar at Kangerlussuaq Airport, western Greenland. *Cold Regions Science and Technology, 48,* p 64-72.

Jorgenson, M. T., Romanovsky, V., Harden, J., Shur, Y., O'Donnell, J., Schuur, E. A. G., Kanevskiy, M., & Marchenko, S. (2010). Resilience and vulnerability of permafrost to climate change, *Canadian Journal of Forestry Research, Vol. 40,* p 1219-1236.

Kleinberg, R. L. & Griffin, D. D. (2005). NMR measurements of permafrost: unfrozen water assay, pore-scale distribution of ice, and hydraulic permeability of sediments. *Cold Regions Science and Technology,* 42, p 63-77.

Kneisel, C., Hauck, C., Fortier, R., & Moorman, B. (2008). Advances in Geophysical Methods for Permafrost Investigations. *Permafrost and Periglacial Processes, 19,* p 157-178.

Kurylyk, B. L. & Watanabe, K. (2013). Review: The mathematical representation of freezing and thawing processes in variably-saturated, non-deformable soils. *Advances in Water Resources, 60,* p 160-177.

Kurylyk, B. L., MacQuarrie, K. T. B. (2014). A new analytical solution for assessing climate change impacts on subsurface temperature. *Hydrological Processes, 28,* p 3161-3172.

Kurylyk, B. L., MacQuarrie, K. T. B., & McKenzie, J. M. (2014). Climate change impacts on groundwater and soil temperatures in cold and temperate regions: Implications, mathematical theory, and emerging simulation tools. *Earth-Science Reviews, 138,* p 313-334.

Lemieux, J.-M. (2006). *Impact of the Wisconsinian Glaciation on Canadian Continental Groundwater Flow*. PhD Dissertation, Department of Earth and Environmental Sciences, University of Waterloo, Waterloo, Ontario, Canada.

Lemieux, J.-M., Sudicky, E. A., Peltier, W. R., & Tarasov, L. (2008a). Dynamics of groundwater recharge and seepage over the Canadian landscape during the Wisconsinian glaciation, *Journal of Geophysical Research, Vol. 113.*

Lemieux, J.-M., Sudicky, E. A., Peltier, W. R., & Tarasov, L. (2008b). Simulating the impact of glaciations on continental groundwater flow systems: 1. Relevant processes and model formulation, *Journal of Geophysical Research, Vol. 113.*

Lemieux, J.-M., Sudicky, E. A., Peltier, W. R., & Tarasov, L. (2008c). Simulating the impact of glaciations on continental groundwater flow systems: 2. Model application to the Wisconsinian glaciation over the Canadian landscape, *Journal of Geophysical Research, Vol. 113.*

Ling, F. & Zhang, T. (2003). Numerical simulation of permafrost thermal regime and talik development under shallow thaw lakes on the Alaskan Arctic Coastal Plain. *Journal of Geophysical Research, Vol. 108.*

Locke, W. W. (1999). *Glacier Morphology: Classification by Shape and Temperature.* [Online Resource] Retrieved November 15th, 2010 from http://www.homepage.montana.edu/~geol445/hyperglac/morphology1/.

Lunardini, V. J. (1988). Freezing of soil with an unfrozen water content and variable thermal properties. *U.S. Army Cold Regions Research and Engineering Laboratory (CRREL) Report 88-2.*

Lusczynski, N. J. (1961). Head and low of groundwater of variable density. *Journal of Geophysical Research, 66 (12),* p 4247-4256.

Marshak, S. (2001). *Earth: Portrait of a Planet.* New York: W. W. Norton & Company, Inc.

McKenzie, J. M., Voss, C. I., & Siegel, D. I. (2007). Groundwater flow with energy transport and water-ice phase change: Numerical simulations, benchmarks, and application to freezing peat bogs. *Advances in Water Resources,* 30, p 966-983.

McKenzie, J. M & Voss, C. I. (2013). Permafrost thaw in a nested groundwater-flow system. *Hydrogeology Journal, 21,* p 299-316.

Menzies, J. (Ed.). (2002). *Modern and Past Glacial Environments.* Oxford, UK, Woburn, Massachusetts, USA: Butterworth-Heinemann.

Mottaghy, D. & Rath, V. (2006). Latent heat effects in subsurface heat transport modelling and their impact on paleotemperature reconstructions. *Geophysical Journal International, 164,* p 236-245.

Murphy, D. M. & Koop, T. (2005). Review of the vapour pressures of ice and supercooled water for atmospheric applications. *Quaternary Journal of the Royal Meteorological Society, 131,* p 1539-1565.

National Snow and Ice Data Center. (2012). *All About Frozen Ground.* [Online]. Retrieved May 1st, 2012 from http://nsidc.org.

Natural Resources Canada. (2008). *From Impacts to Adaptation: Canada in a Changing Climate 2007*. Natural Resources Canada. [Online]. Retrieved November 1st, 2010 from http://adaptation.nrcan.gc.ca/assess/2007/index_e.php.

Neuzil, C. E. (2003). Hydromechanical coupling in geologic processes, *Hydrogeology Journal, Vol. 11,* p 41-83.

Nielson, A. B. (2010). Present conditions in Greenland and the Kangerlussuaq area. *Working Report 2010-7*. Posiva Oy: Eurajoki, Finland.

Normani, S. D. (2009). *Paleoevolution of Pore Fluids in Glaciated Geologic Settings.* PhD Dissertation, Department of Civil and Environmental Engineering, University of Waterloo, Waterloo, Ontario, Canada.

Nuclear Waste Management Organization (NWMO). (2008). *Backgrounder: Nature of the Hazard.* [Online]. Retrieved November 1st, 2010 from http://www.nwmo.ca.

NWMO. (2010a). *Backgrounder: Planning for Climate Change.*. [Online]. Retrieved November 1st, 2010 from http://www.nwmo.ca.

NWMO. (2010b). *Backgrounder: Project Description.* [Online]. Retrieved November 1st, 2010 from http://www.nwmo.ca.

NWMO. 2011. *Geosynthesis.* NWMO, Technical Report, DGR-TR-2011-11 R000, Toronto, Canada.

Oberlander, P. L. (1989). Fluid Density and Gravitational Variations in Deep Boreholes and Their Effect on Fluid Potential, *Groundwater, Vol. 27, No. 3.*

Ontario Geological Survey (OGS). (2013). Geology and Selected Mineral Deposits of Ontario. Map. Queen's Primer for Ontario, Ontario, Canada.

Osterkamp, T. E. & Gosink, J. P. (1991). Variations in permafrost thickness in response to changes in paleoclimate. *Journal of Geophysical Research,* Vol. 96, No. B3, p 4423-4434.

Overpeck, J., Hughen, K., Hardy, D., Bradley, R., Case, R., Douglas, M., Finney, B., Gajewski, K., Jacoby, G., Jennings, A., Lamoureux, S., Lasca, A., MacDonald, G., Moore, J., Retelle, M., Smith, S., Wolfe, A., & Zielinski, G. (1997). Arctic Environmental Change of the Last for Centuries. *Science,* 278, p 1251-1256.

Park, Y.-J., Cornaton, F. J., Normani, S. D., Sykes, J, F., Sudicky, E. A. (2008). Use of groundwater lifetime expectancy for the performance assessment of a deep geologic radioactive waste repository: 2. Application to a Canadian Shield environment. *Water Resources Research, 44, W04407.*

Parziek, B. R. & Alley, R. B. (2004). Implications of increased Greenland surface melt under global-warming scenarios: ice-sheet simulations. *Quaternary Science Reviews, 23,* p 1013-1027.

Peltier, W. R. (1999). Global sea level rise and glacial isostatic adjustment. *Global and Planetary Change, 20,* p 93-123.

Peltier, W. R. (2002). A Design Basis Glacier Scenario. *Ontario Power Generation, Technical Report 06819-REP-01200-10069-R00,* Toronto, Canada.

Peltier, W. R. (2007). Rapid climate change and Arctic Ocean freshening. *Geology, 35 (12),* p 1147-1148.

Peltier, W. R. (2011). Long-term climate change. *Nuclear Waste Management Organization, Technical Report NWMO DGR-TR-2011-14 R000,* Toronto, Canada.

Pidwirny, M. (2006). Periglacial Processes and Landforms. *Fundamentals of Physical Geography, 2nd Edition.* [Online Resource]. Retrieved October 30th, 2010 from http://www.physicalgeography.net/fundamentals/10ag.html.

Piotrowski, J. A. (1997). Subglacial groundwater flow during the last glaciation in northwestern Germany. *Sedimentary Geology, 111,* p 217-224.

Pomeroy, J. W., Gray, D. M., Brown, T., Hedstrom, N. R., Quinton, W. L., Granger, R. J., & Carey, S. K. (2007). The cold regions hydrological model: A platform for basing process representation and model structure on physical evidence. *Hydrological Processes,* 21, p 2650-2667.

Ratcliffe, E. H. (1962). The thermal conductivity of ice new data on the temperature coefficient. *Philosophical Magazine, 7:79,* p 1197-1203.

Riseborough, D. (2007). The Effect of Transient Conditions on an Equilibrium Permafrost-climate Model. *Permafrost and Periglacial Processes,* 18, p 21-32.

Riseborough, D., Shiklomanov, N., Etzelmuller, B., Gruber, S., & Marchenko, S. (2008). Recent Advances in Permafrost Modelling. *Permafrost and Periglacial Processes,* 19, p 137-156.

Ritter, D. F., Kochel, R. C., & Miller, J. R. (2002). *Process Geomorphology, 4th Ed.* New York: McGraw-Hill Higher Education.

Roberts, D. H., Long, A. J., Schnabel, C., Davies, B. J., Xu, S., Simpson, M. J. R., & Huybrechts, P. (2009). Ice sheet extent and early deglacial history of the southwestern sector of the Greenland Ice Sheet. *Quaternary Science Reviews, 28,* p 2760-2773.

Rowland, J. C., Travis, B. J., & Wilson, C. J. (2011). The role of advective heat transport in talik development beneath lakes and ponds in discontinuous permafrost. *Geophysical Research Letters, Vol. 38.*

Ruhaak, W., Anbergen, H., Grenier, C., McKenzie, J., Kurylyk, B. L., Molson, J., Roux, N., & Sass, I. (2015). Benchmarking numerical freeze/thaw models. *Energy Procedia, 76,* p 301-310.

Ryves, D. B., Batterbee, R. W., Juggins, S., Fritz, S. C., & Anderson, N. J. (2006). Physical and Chemical Predictors of Diatom Dissolution in Freshwater and Saline Lake Sediments in North America and West Greenland. *Limnology and Oceanography, Vol. 51, No.3,* p 1355-1368.

Savage, D. (1995). *The Scientific and Regulatory Basis for the Geological Disposal of Radioactive Waste.* Chichester; New York: John Wiley.

Scherler, M., Hauck, C., Hoelzle, M., Stahli, M., & Volksch, I. (2010). Meltwater Infiltration into the Frozen Active Layer at an Alpine Permafrost Site. *Permafrost and Periglacial Processes,* 21, p 325-334.

Schuur, E. A. G., Bockheim, J., Canadell, J. G., Euskirchen, E., Field, C. B., Goryachkin, S. V., Hagemann, S., Kuhry, P., Lafleur, P. M., Lee, H., Mazhitova, G., Nelson, F. E., Rinke, A., Romanovsky, V. E., Shiklomanov, N., Tarnocai, C., Venevsky, S., Vogel, J., & Zimov, S. A. (2008). Vulnerability of Permafrost Carbon to Climate Change: Implications for the Global Climate Cycle, *BioScience, Vol. 58, No. 8,* p 701-714.

Simpson, M. J. R., Milne, G. A., Huybrechts, P., & Long, A. J. (2009). Calibrating a glaciological model of the Greenland ice sheet from the Last Glacial Maximum to present-day using field observations of relative sea level and ice extent. *Quaternary Science Reviews, 28,* p 1631-1657.

Smith, M. W. & Riseborough, D. W. (2002). Climate and the Limits of Permafrost: A Zonal Analysis. *Permafrost and Periglacial Processes,* 13, p 1-15.

Srivastava, R. M. (2002). The discrete fracture network model in the local scale flow system for the Third Case Study. *Technical Report 06819-REP-01300-10061-R00, Ontario Power Generation, Nuclear Waste Management Division, Toronto, Canada.*

Statsna, M. & Peltier, W. R. (2007). On box models of the North Atlantic thermohaline circulation: Intrinsic and extrinsic millennial timescale variability in response to deterministic and stochastic forcing. *Journal of Geophysical Research, 112.*

Stouffer, R. J., Yin, J., Gregory, J. M., Dixon, W., Spelman, M. J., Hurlin, W., Weaver, A. J., Eby, M., Flato, M., Hasumi, H., Hu, A., Jungclaus, J. H., Kamenkovich, I. V., Levermann, A., Montoya, M., Murakami, S., Nawrath, S., Oka, A., Peltier, W. R., Robitaille, D. Y., Sokolov, A., Vettoretti, G., & Weber, S. L. (2006). Investigating the Causes of the Response of the Thermohaline Circulation to Past and Future Climate Changes. *Journal of Climate, 19,* p 1365-1387.

Kärnbränslehantering AB, S. (2006). Climate and climate-related issues for safety assessment SR-Can. TR-06-23. Swedish Nuclear Fuel and Waste Management Company (SKB), Stockholm.

Kärnbränslehantering AB, S. (2010). Climate and climate-related issues for the safety assessment SR-Site. TR-10-49. Svensk Karnbranslehantering. SKB, Stockholm.

Sykes, J. F., Normani, S. D., Jensen, M. R., & Sudicky, E. A. (2009). Regional-scale groundwater flow in a Canadian Shield setting. *Canadian Geotechnology Journal, 46,* p 813-827.

Sykes, J. F., Normani, S. D., Sudicky, E. A., & McLaren, R. G. (2004). Sub-regional scale groundwater flow within an irregular discretely fractured Canadian Shield setting. *Ontario Power Generation, Nuclear Waste Management Division Report 06819-REP-01200-10133-R00,* Toronto, Canada.

Sykes, J. F., Normani, S. D., & Yin, Y. (2011). Hydrogeologic Modelling. *Deep Geologic Repository for OPG's Low and Intermediate Level Waste.* Nuclear Waste Management Organization (NWMO) DGR-TR-2011-16.

Tan, X., Chen, W., Tian, H., & Cao, J. (2011). Water flow and heat transport including ice/water phase change in porous media: Numerical simulation and application. *Cold Regions Science and Technology, 68,* p 74-84.

Tarasov, L. & Peltier, W. R. (2004). A geophysically constrained large ensemble analysis of the deglacial history of the North American ice sheet complex. *Quaternary Science Reviews, 23,* p 359-388.

Tarasov, L. & Peltier, W. R. (2005). Arctic freshwater forcing of the Younger Dryas cold reversal. *Nature, 435,* p 662-665.

Tarasov, L. & Peltier, W. R. (2006). A calibrated deglacial drainage chronology for the North American continent: evidence of an Arctic trigger for the Younger Dryas. *Quaternary Science Reviews, 25,* p 659-688.

Tarasov, L. & Peltier, W. R. (2007). Coevolution of continental ice cover and permafrost extent over the last glacial-interglacial cycle in North America. *Journal of Geophysical Research, 112.*

Tarbuck, E. J., Lutgens, F. K., & Tsujita, C. J. (2005). *Earth: An Introduction to Physical Geology, Canadian Edition.* Toronto, Ontario, Canada: Pearson Education Canada, Inc.

Therrien, R., McLaren, R. G., Sudicky, E. A., Panday, S. M., Guvanasen, V. (2007). *FRAC3DVS_OPG: A Three-Dimensional Numerical Model Describing Subsurface Flow and Solute Transport.* Groundwater Simulations Group, University of Waterloo, Waterloo.

Tsang, C-F. (2009). Introductory editorial to the special issue on the DECOVALEX-THMC project. *Environmental Geology, 57,* p 1217-1219.

Tsang, C-F., Stephansson, O., Jing, L., & Kautsky, F. (2009). DECOVALEX Project: from 1992 to 2007. *Environmental Geology, 57,* p 1221-1237.

van der Ploeg, M. J., Haldorsen, S., Leijnse, A., & Heim, M. (2012). Subpermafrost groundwater systems: Dealing with virtual reality while having virtually no data. *Journal of Hydrology, 475,* p 42-52.

van der Veen, C. J. (1998). Fracture mechanics approach to penetration of bottom crevasses on glaciers. *Cold Regions Science and Technology, 27,* p 213-223.

van der Veen, C. J. (1999). *Fundamentals of Glacier Dynamics.* Rotterdam, Brookfield, VT: Balkema.

van der Veen, C. J. (2007). Fracture propagation as means of rapidly transferring surface meltwater to the base of glaciers. *Geophysical Research Letters, Vol. 34.*

van der Veen, C. J., Leftwich, T., von Frese, R., Csatho, B. M., & Li, J. (2007). Subglacial topography and geothermal heat flux: Potential interactions with drainage of the Greenland ice sheet. *Geophysical Research Letters, 34, L12501.*

van Tatenhove, F. G. M. and Olesen, O. B. (1994). Ground temperature and related permafrost characteristics in West Greenland. *Permafrost and Periglacial Processes, 5,* p 199-215.

Vidstrand, P., Follin, S., Selroos, J-O., Naslund, J-O., & Rhen, I. (2013). Modelling of groundwater flow at depth in crystalline rock beneath a moving ice-sheet margin, exemplified by the Fennoscandian Shield, Sweden. *Hydrogeology Journal, Vol. 21.*

Vorauer, A. (2010). Greenland Analogue Project – Modelling Plan, Version 1.0. *Nuclear Waste Management Organization.*

Walcott, R. I. (1970). Isostatic response to loading of the crust in Canada. *Canadian Journal of Earth Sciences, 7,* p 716-727.

Wallroth, T., Lokrantz, H, & Rimsa, A. (2010). The Greenland Analogue Project (GAP): Literature of hydrogeology/hydrogeochemistry. *SKB R-10-34.* Stockholm, Sweden: Swedish Nuclear Fuel and Waste Management Co.

Walsh, R. & Avis, J. (2010). Glaciation Scenario: Groundwater and Radionuclide Transport Studies, *NWMO Report TR-2010-09.* Toronto, Ontario: Nuclear Waste Management Organization.

Wellman, T. P., Voss, C. I., & Walvoord, M. A. (2013). Impacts of climate, lake size, and supra- and sub-permafrost groundwater flow on lake-talik evolution, Yukon Flats, USA. *Hydrogeology Journal, 21*, p 281-298.

West, J. J. & Plug, L. J. (2008). Time-dependent morphology of thaw lakes and taliks in deep and shallow ground ice. *Journal of Geophysical Research, Vol. 113.*

Westermann, S., Wollschlager, U., & Boike, J. (2010). Monitoring of active layer dynamics at a permafrost site on Svalbard using multi-channel ground-penetrating radar. *The Cryosphere,* 4, p 475-487.

Williams, J. R. (1970). Ground Water in Permafrost Regions of Alaska. *U.S. Government Printing Office.*

Winguth, C., Mickelson, D. M., Colgan, P. M., & Laabs, B. J. C. (2004). Modeling the deglaciation of the Green Bay Lobe of the southern Laurentide Ice Sheet. *Boreas,* Vol. 33, p 34-47.

Woo, M-K., Kane, D. L., Carey, S. K., & Yang, D. (2008). Progress in Permafrost Hydrology in the New Millennium. *Permafrost and Periglacial Processes,* 19, p 237-254.

Woo, M-K., Marsh, P., & Pomeroy, J. W. (2000). Snow, frozen soils, and permafrost hydrology in Canada, 1995-1998. *Hydrological Processes,* 14, p 1591-1611.

Yershov, E. D. (1998). *General Geocryology.* Cambridge: Cmabridge University Press.

Yin, Y., Normani, S. D., Sykes, J. F., & Barnard, M. (2013). Hydrogeologic modelling of a crystalline rock setting in Western Greenland. *Technical Report TR-2013-20.* Nuclear Waste Management Organization, Toronto, Canada.

Zhang, Y., Chen, W., & Cihlar, J. (2003). A process-based model for quantifying the impact of climate change on permafrost thermal regimes. *Journal of Geophysical Research,* 108, No. D22, 4695.

Zhang, Y., Chen, W., & Riseborough, D. W. (2006). Temporal and spatial changes of permafrost in Canada since the end of the Little Ice Age, *Geophysical Research Letters, Vol. 111.*

Zhang, Y., Chen, W., & Riseborough, D. W. (2008a). Disequilibrium response of permafrost thaw to climate warming in Canada over 1850-2100, *Geophysical Research Letters, Vol. 35.*

Zhang, Y., Chen, W., & Riseborough, D. W. (2008b). Transient projections of permafrost distribution in Canada during the 21st century under scenarios of climate change, *Global and Planetary Change, Vol. 60,* p 443-456.

Zwally, H., Abdalati, W., Herring, T., Larson, K., Saba, J., & Steffan, K. (2002). Surface-melt induced acceleration of Greenland ice-sheet flow, *Science, 297,* p 218–222.

Appendix A – Properties of Water in COMSOL

Table of Figures

COMSOL's built-in material database [COMSOL v. 4.2] defines the properties of water using the following functions.

A.1 Density

The density of water, ρ [kg/m^3], is defined as a piecewise function of temperature for the temperature range 273.15 K to 553.75 K with constant extrapolation (Figure A.1):

$$\rho = 838.466135 + 1.40050603T - 0.0030112376T^2 + 3.71822313e^{-7}T^3 \quad \text{A.1}$$

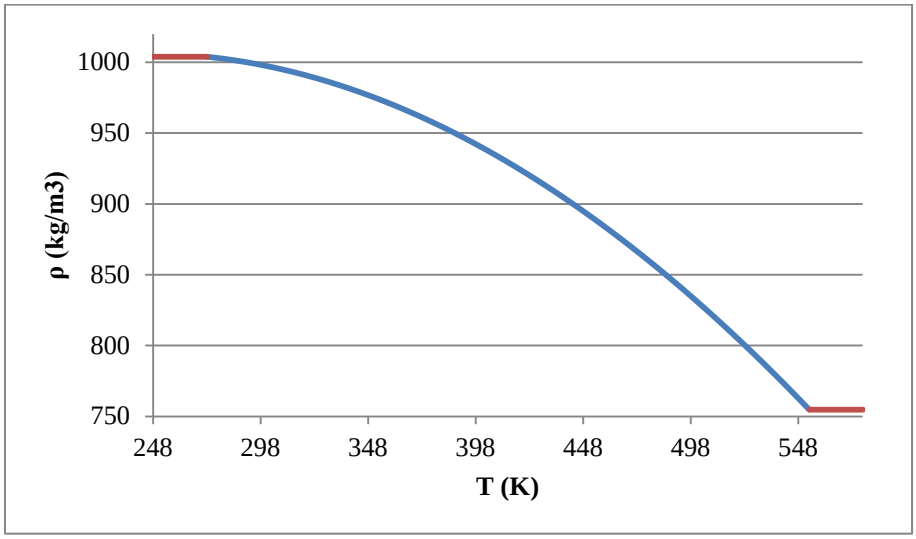

Figure A.1 Density of water as a function of temperature as defined in COMSOL

A.2 Viscosity

The viscosity of water, μ [Pa·s] as a piecewise function of temperature with constant extrapolation (Figure A.2):

$$\mu = 1.3799566804 - 0.021224019151T + 1.3604562827e^{-4}T^2 - 4.6454090319e^{-7}T^3 + 8.9042735735e^{-10}T^4 - 9.0790692686e^{-13}T^5 + 3.8457331488e^{-16}T^6 \quad \text{A.2}$$

for 273.15 K ≤ T > 413.15 K

$$\mu = 0.00401235783 - 2.10746715e^{-5}T + 3.85772275e^{-8}T^2 - 2.39730284e^{-11}T^3 \quad \text{A.3}$$

for 413.15 K ≤ T > 553.75 K

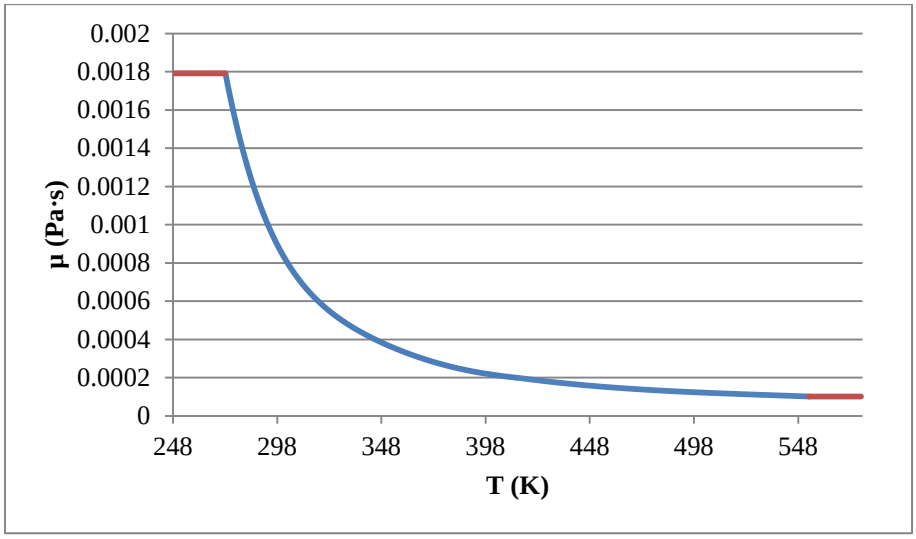

Figure A.2 Viscosity of water as a function of temperature as defined in COMSOL

A.3 Thermal Conductivity

Thermal conductivity, k_{eq} [W/m/K], is defined as a piecewise function of temperature for the temperature range 273.15 K to 553.75 K (Figure A.3):

$$k_{eq} = -0.869083936 + 0.00894880345T - 1.58366345e^{-5}T^2 + 7.97543259e^{-9}T^3 \quad \text{A.4}$$

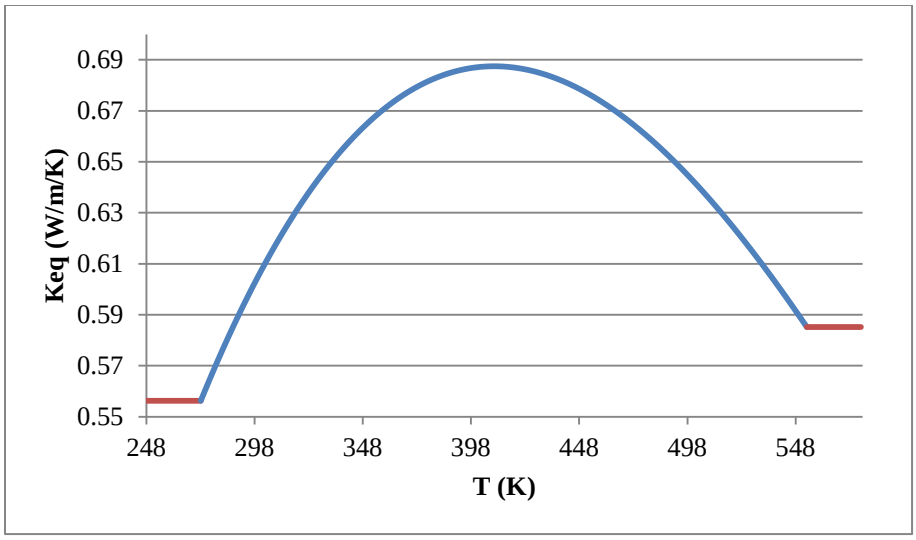

Figure A.3 Thermal conductivity of water as a function of temperature as defined in COMSOL

A.4 Heat Capacity at Constant Pressure

The heat capacity of water, C_p [J/kg·K], is defined as a piecewise function of temperature for the temperature range 273.15 K to 553.75 K (Figure A.4):

$$C_p = 12010.1471 - 80.4072879T + 0.309866854T^2 - 5.38186884e^{-4}T^3 + 3.62536437e^{-7}T^4 \quad \text{A.5}$$

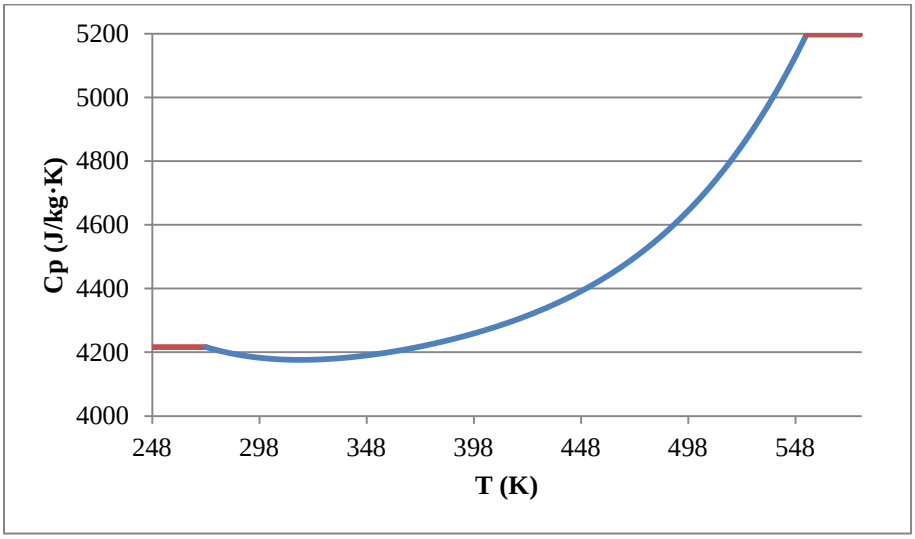

Figure A.4 Heat capacity of water as a function of temperature as defined in COMSOL

A.5 Ratio of Specific Heats

The ratio of specific heats, γ [-], was set to 1.0.

Appendix B – Greenland Analogue Project Analysis of Density-Dependent Flow with Heat Transport

Table of Figures

B.1 Pressure Distribution for Density-Dependent Flow with Heat Transport

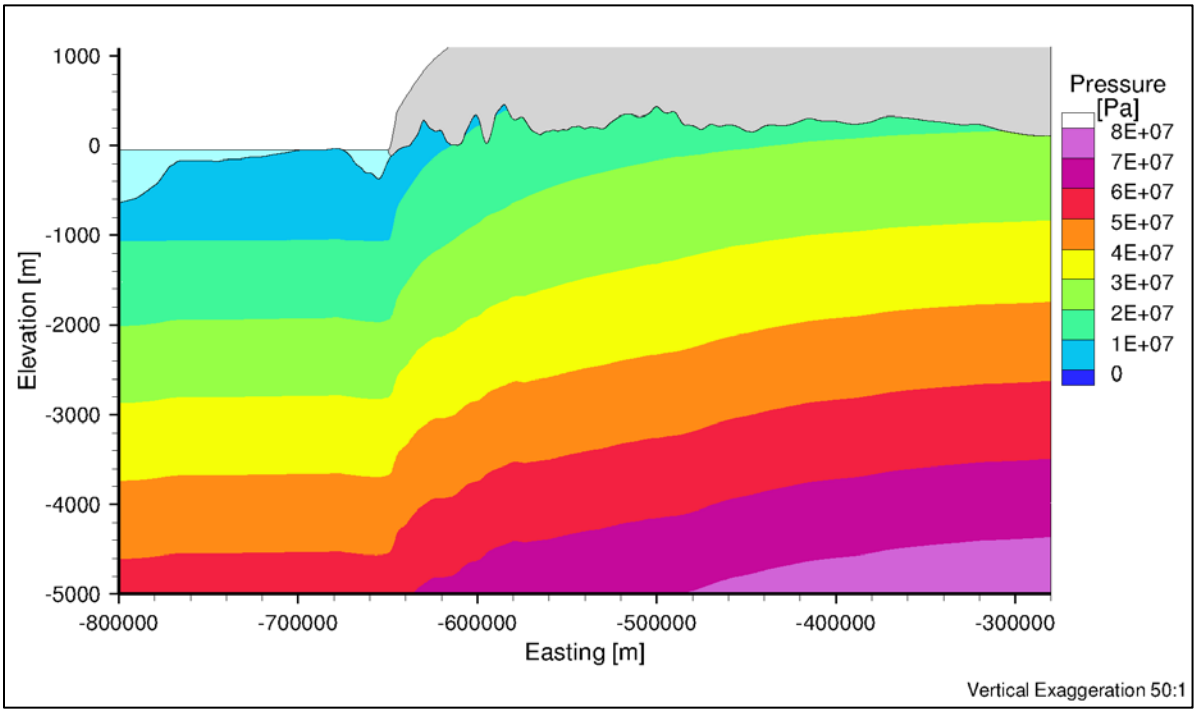

Figure B.1 West-East cross-section of pressure distribution for density-dependent flow with heat transport after 10,000 years

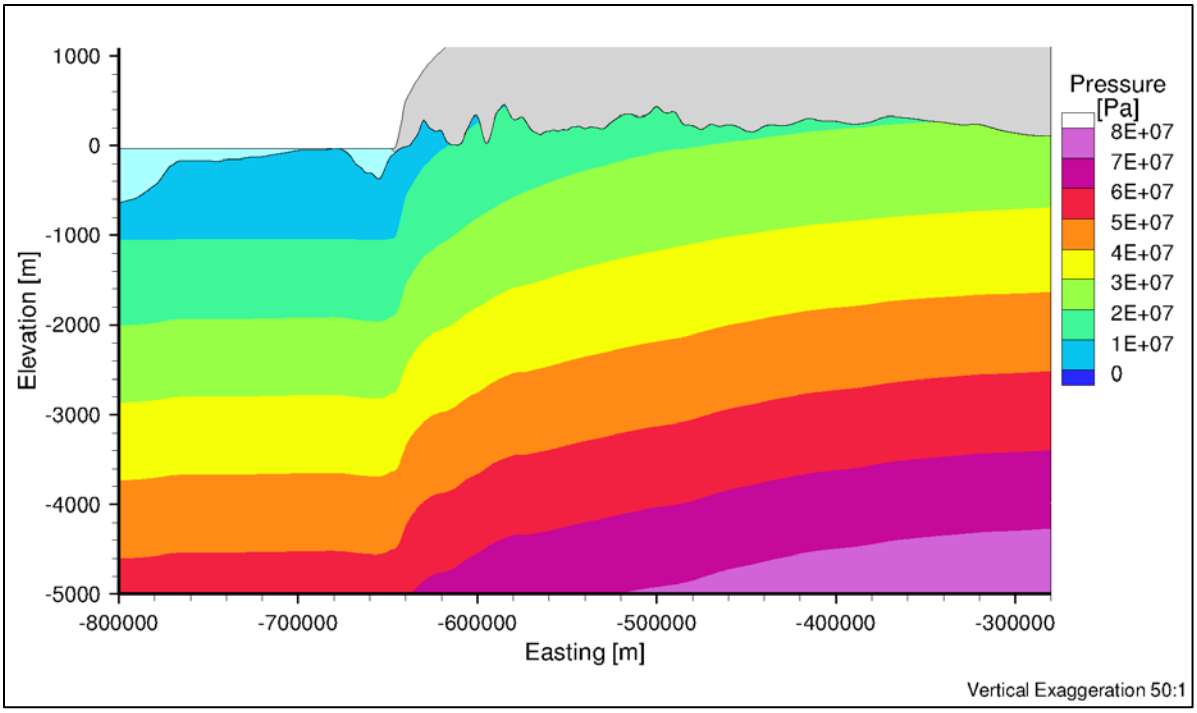

Figure B.2 West-East cross-section of pressure distribution for density-dependent flow with heat transport after 20,000 years

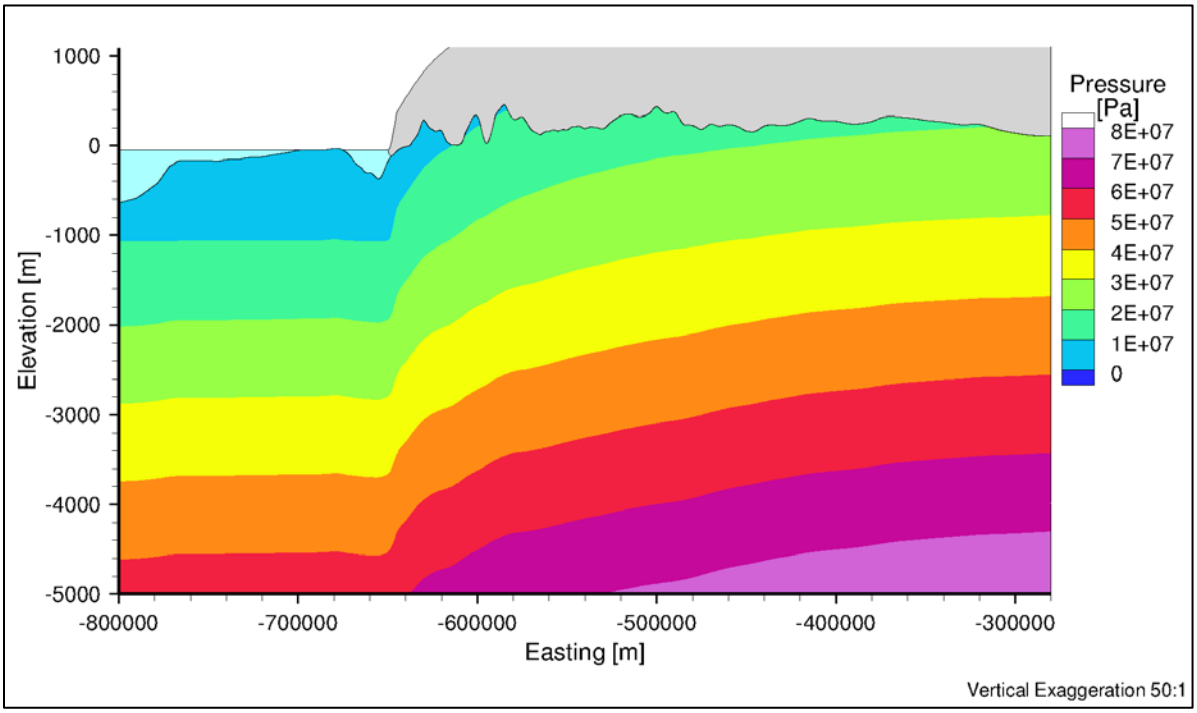

Figure B.3 West-East cross-section of pressure distribution for density-dependent flow with heat transport after 30,000 years

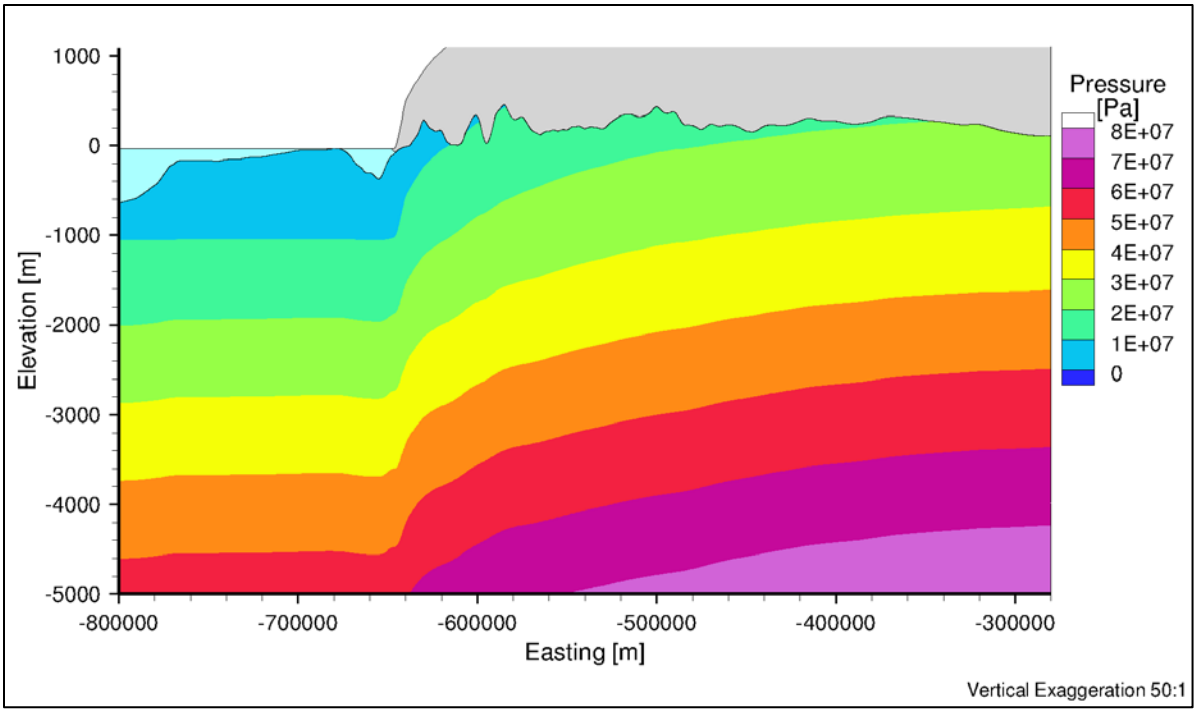

Figure B.4 West-East cross-section of pressure distribution for density-dependent flow with heat transport after 40,000 years

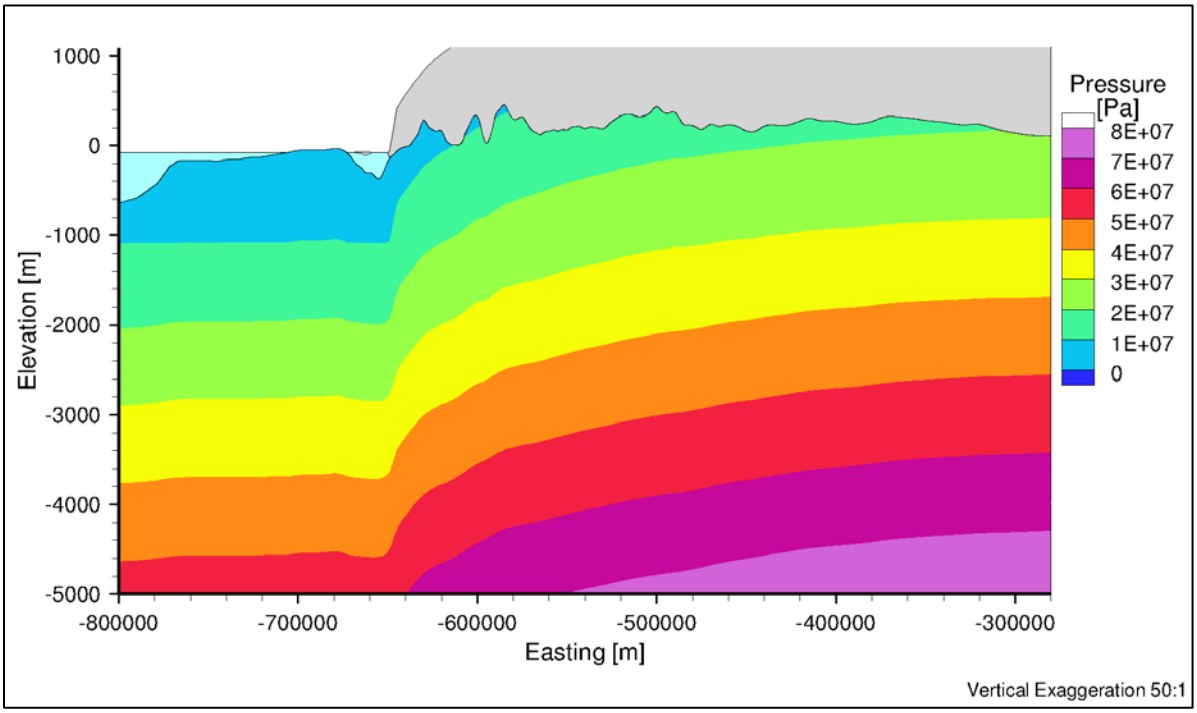

Figure B.5West-East cross-section of pressure distribution for density-dependent flow with heat transport after 50,000 years

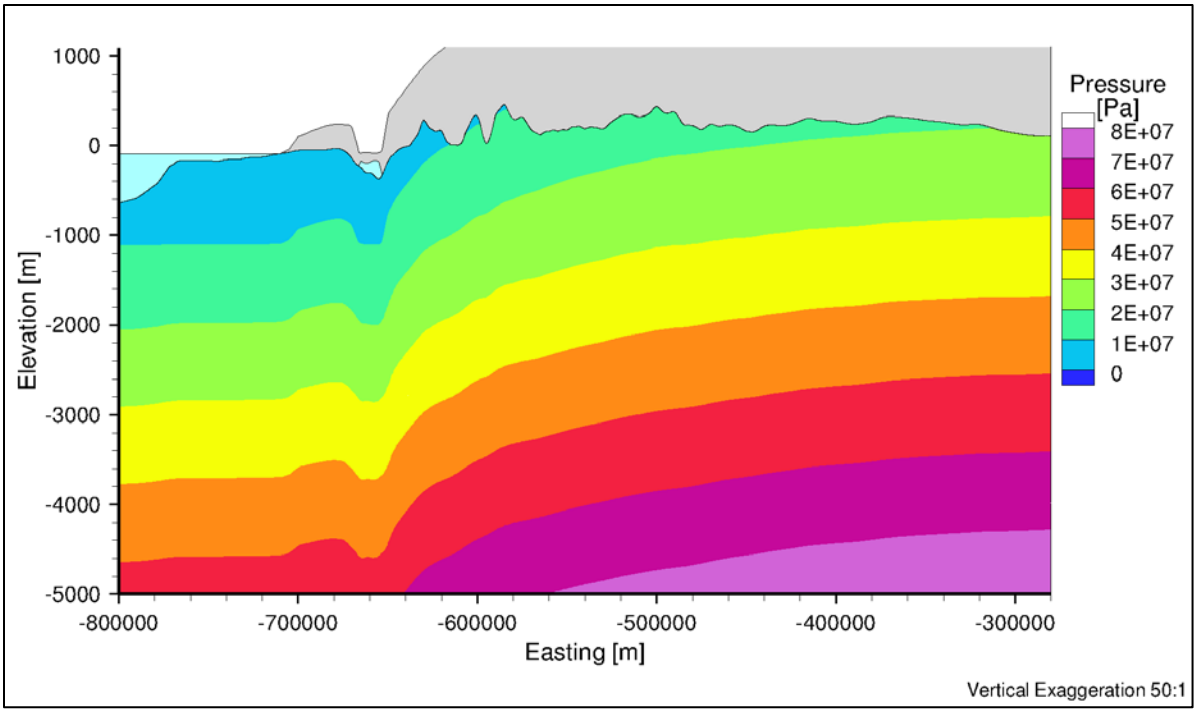

Figure B.6 West-East cross-section of pressure distribution for density-dependent flow with heat transport after 60,000 years

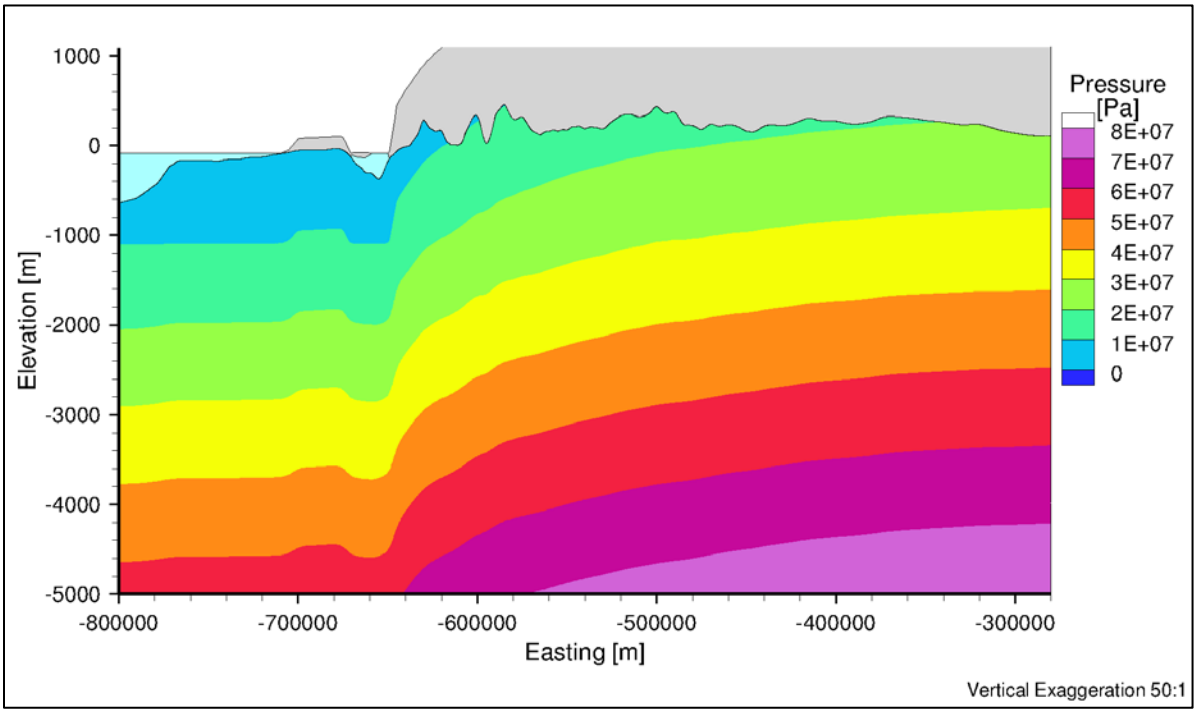

Figure B.7 West-East cross-section of pressure distribution for density-dependent flow with heat transport after 70,000 years

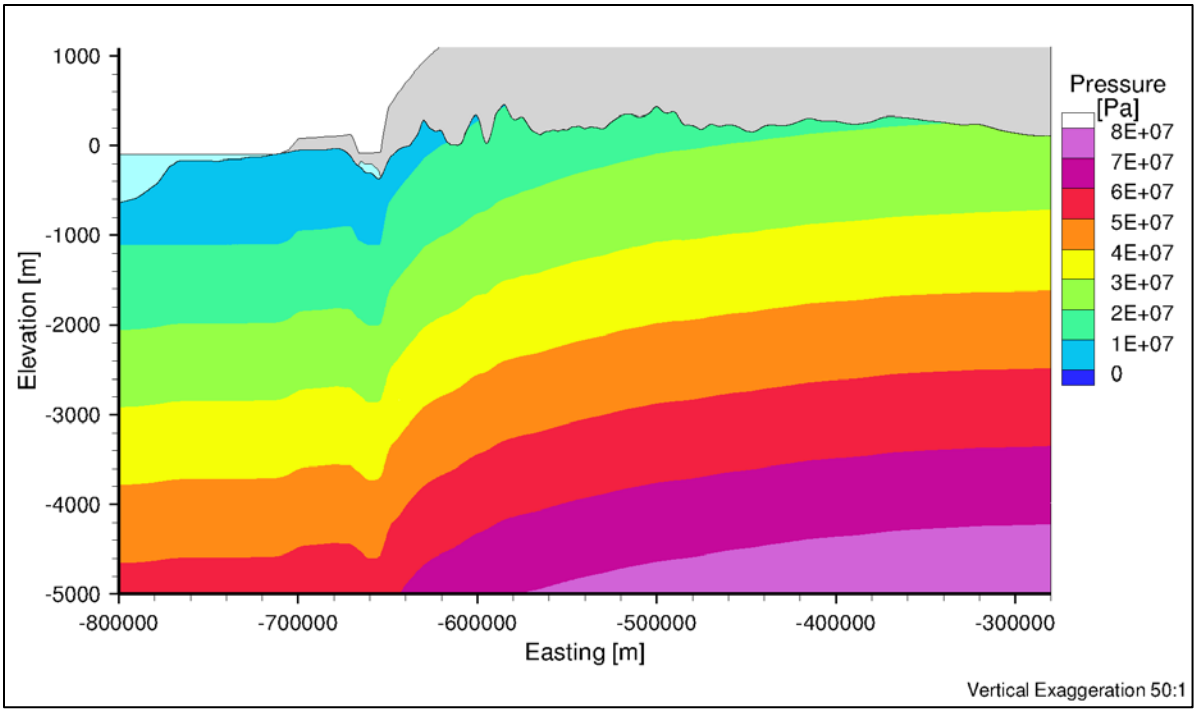

Figure B.8 West-East cross-section of pressure distribution for density-dependent flow with heat transport after 80,000 years

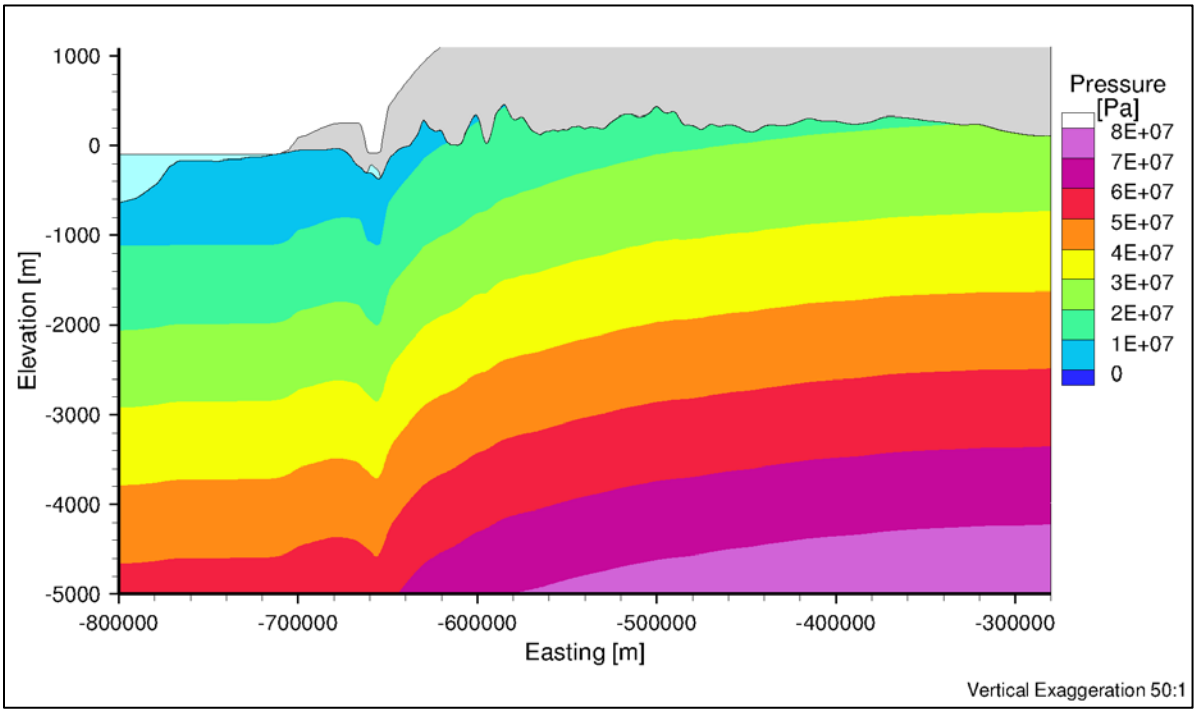

Figure B.9 West-East cross-section of pressure distribution for density-dependent flow with heat transport after 90,000 years

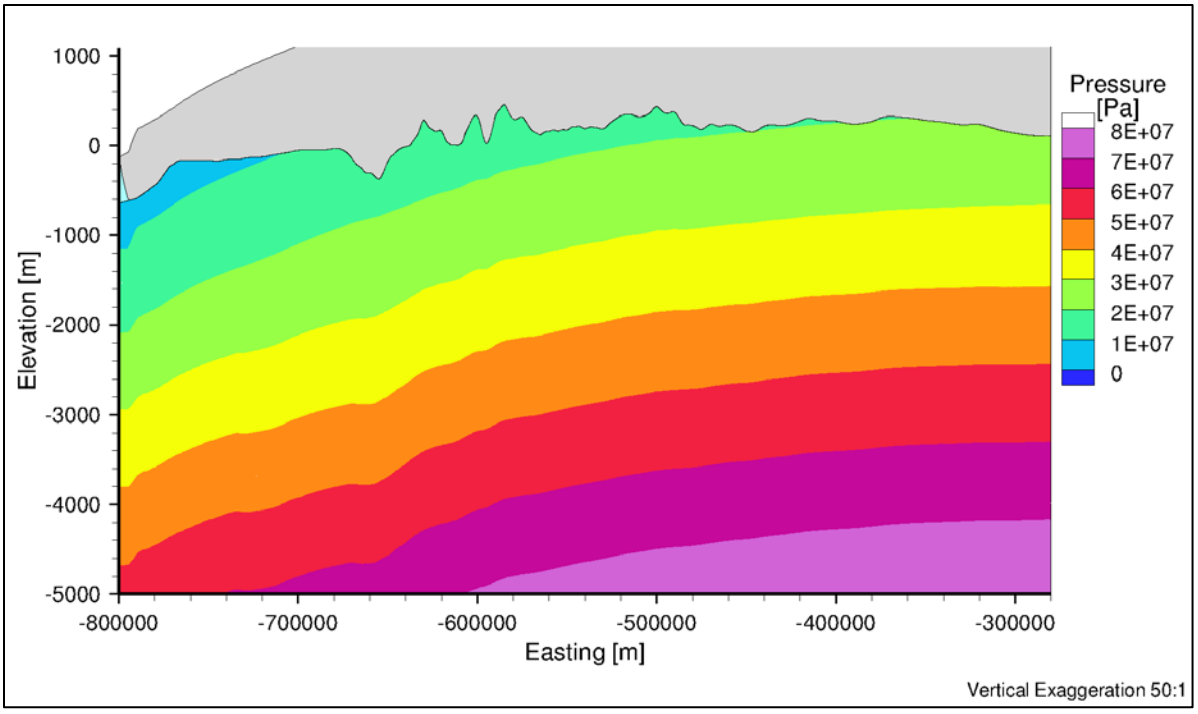

Figure B.10 West-East cross-section of pressure distribution for density-dependent flow with heat transport after 100,000 years

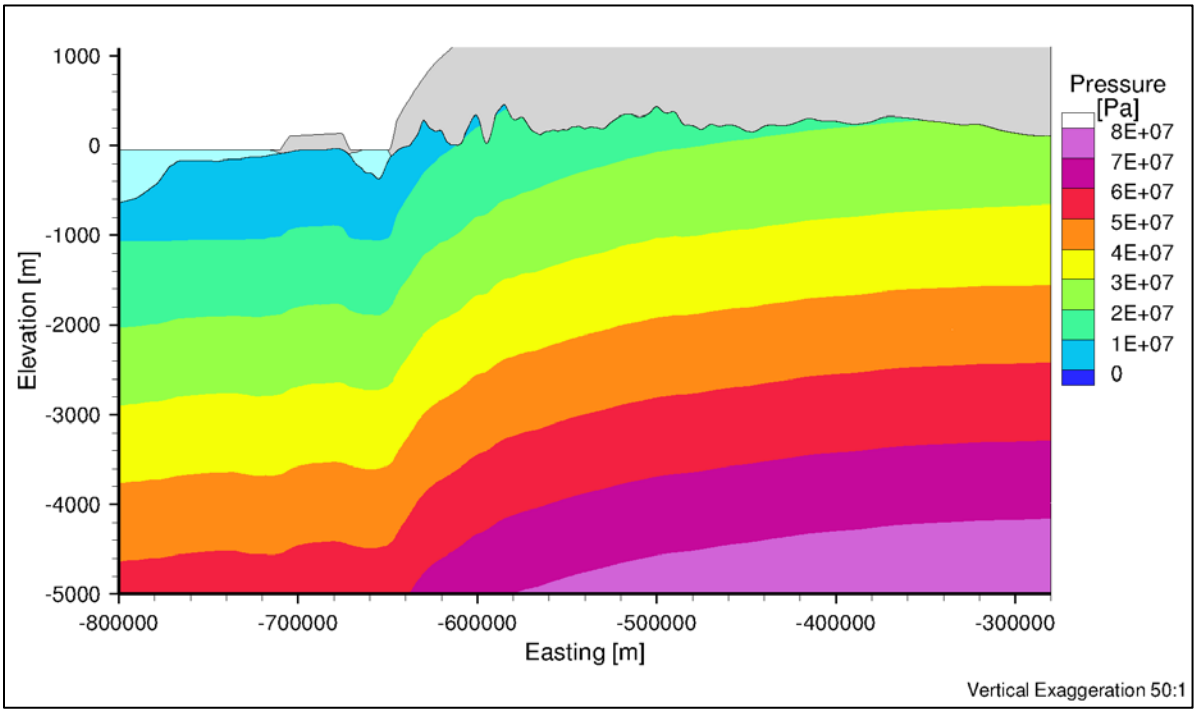

Figure B.11 West-East cross-section of pressure distribution for density-dependent flow with heat transport after 110,000 years

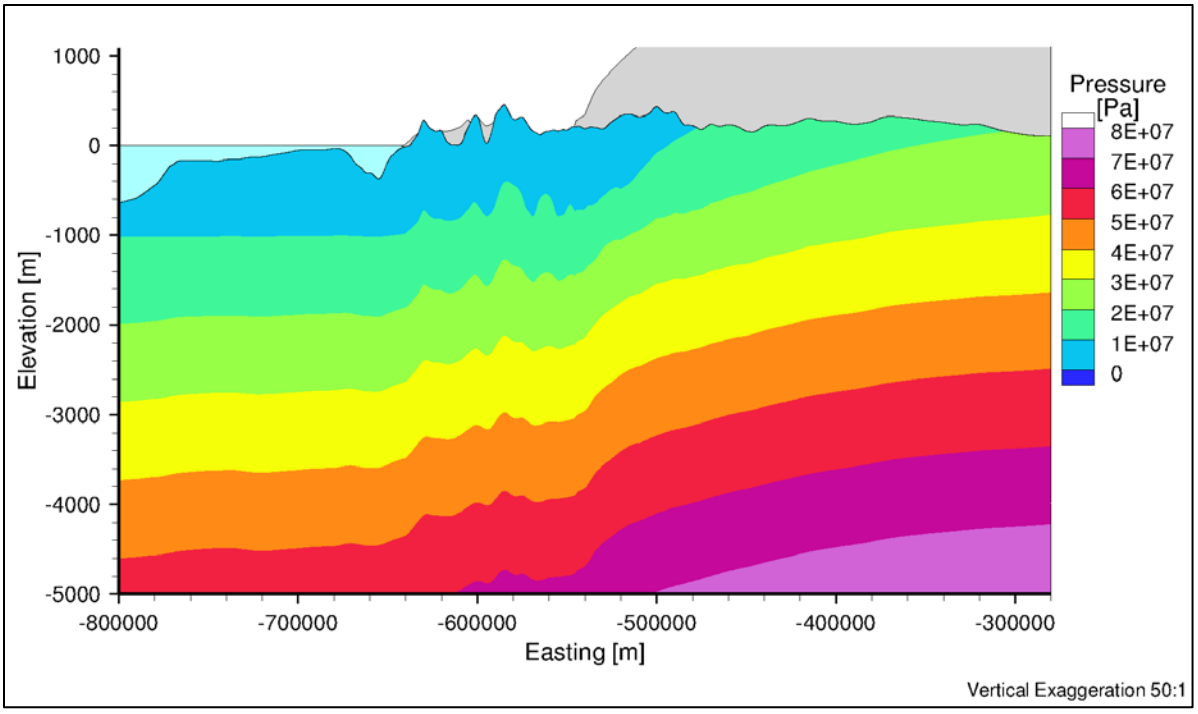

Figure B.12 West-East cross-section of pressure distribution for density-dependent flow with heat transport after 120,000 years

B.2 Velocity Magnitude Distribution for Density-Dependent Flow with Heat Transport

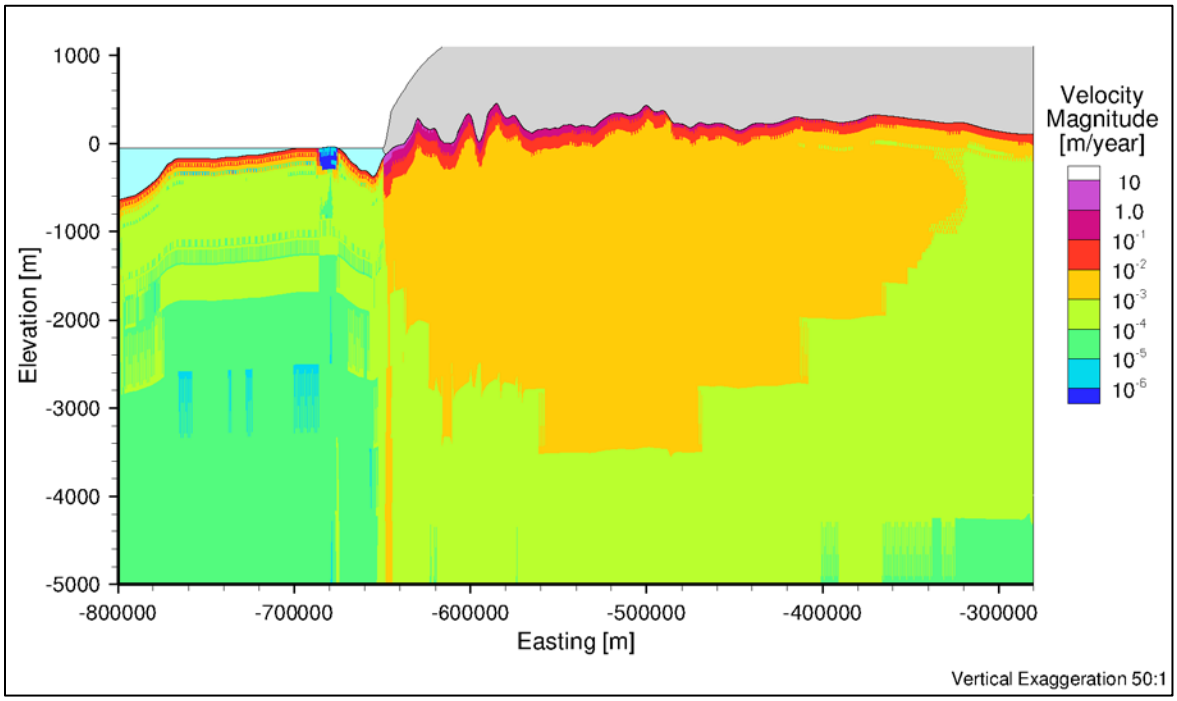

Figure B.13 West-East cross-section of velocity magnitude distribution for density-dependent flow with heat transport after 10,000 years

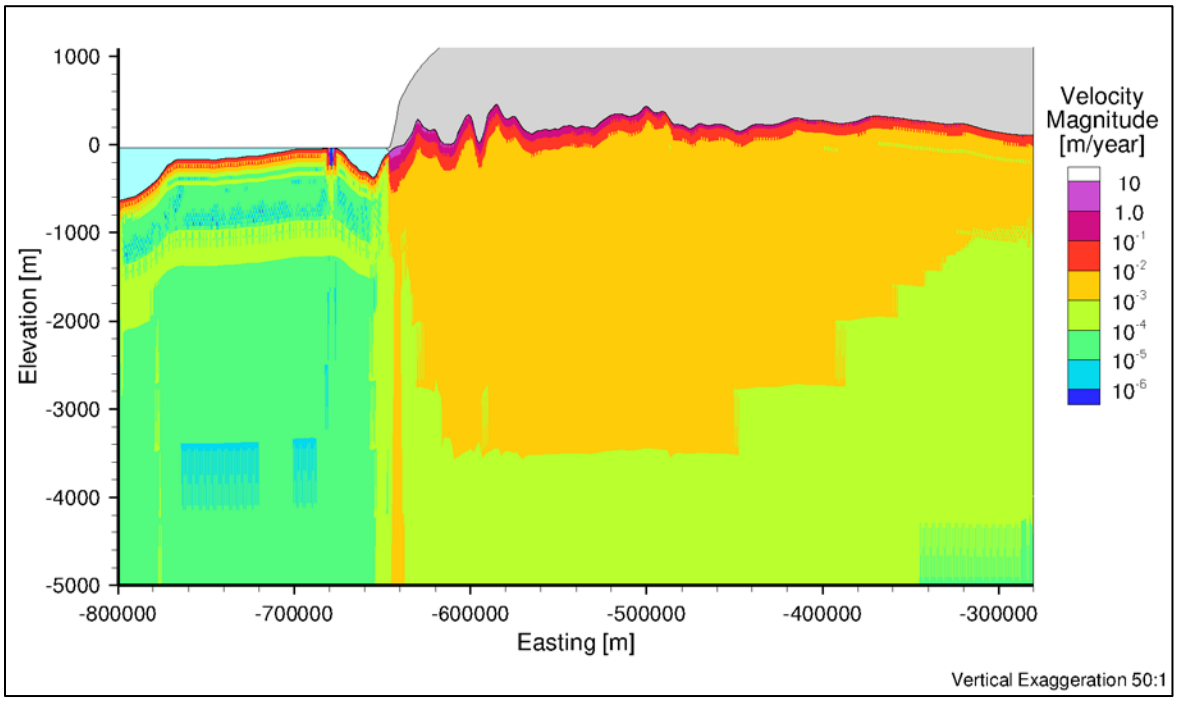

Figure B.14 West-East cross-section of velocity magnitude distribution for density-dependent flow with heat transport after 20,000 years

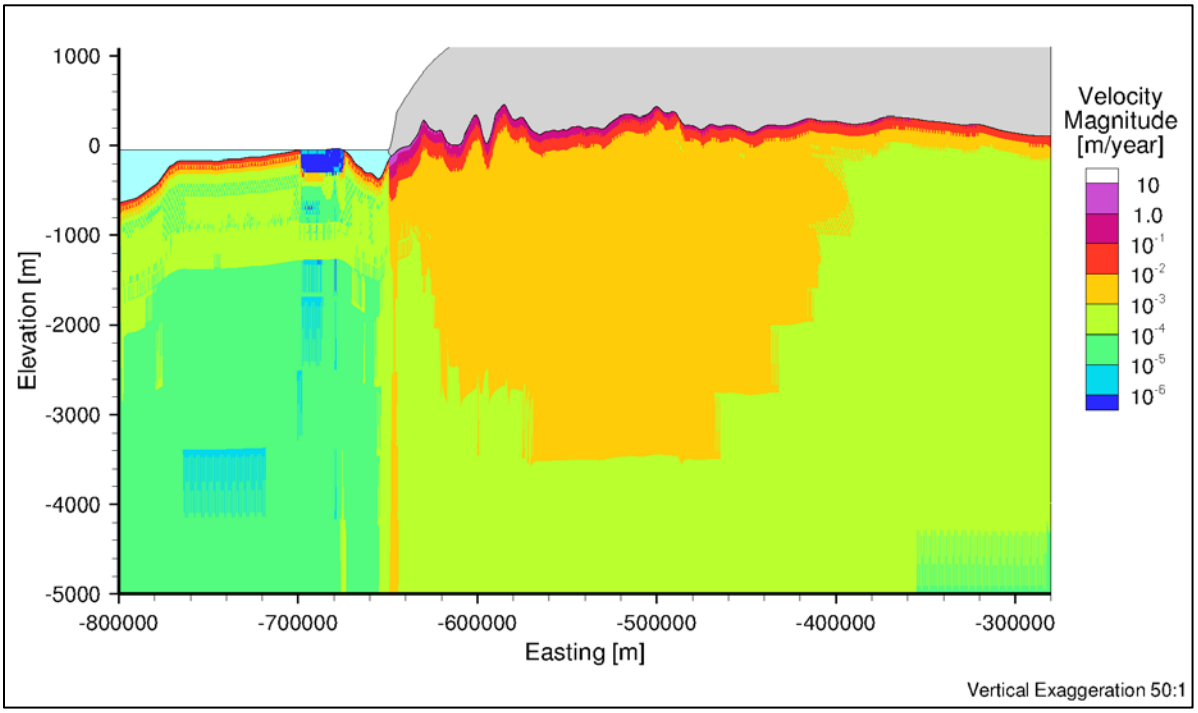

Figure B.15 West-East cross-section of velocity magnitude distribution for density-dependent flow with heat transport after 30,000 years

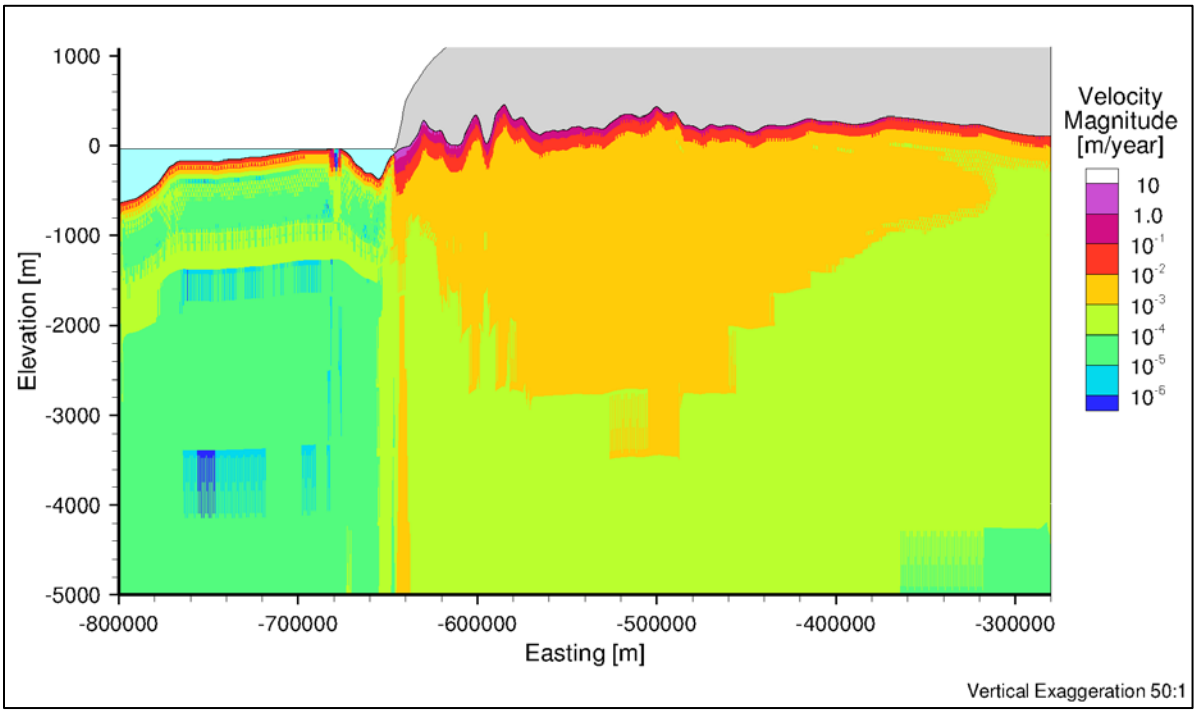

Figure B.16 West-East cross-section of velocity magnitude distribution for density-dependent flow with heat transport after 40,000 years

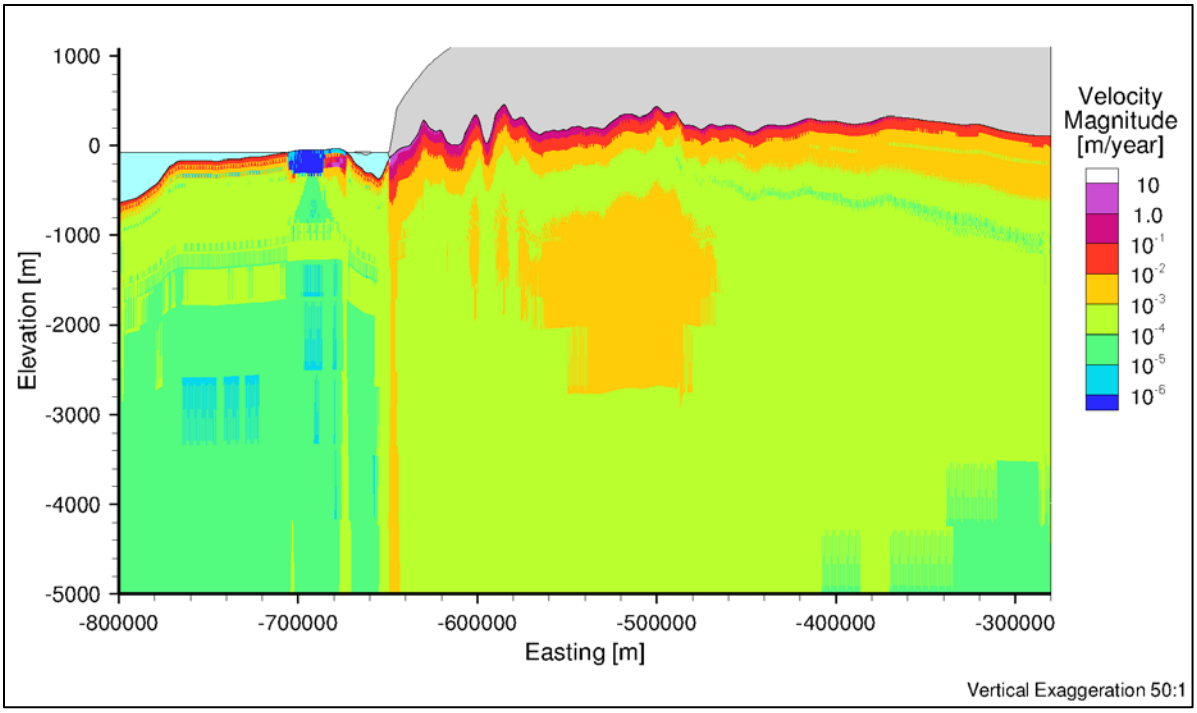

Figure B.17 West-East cross-section of velocity magnitude distribution for density-dependent flow with heat transport after 50,000 years

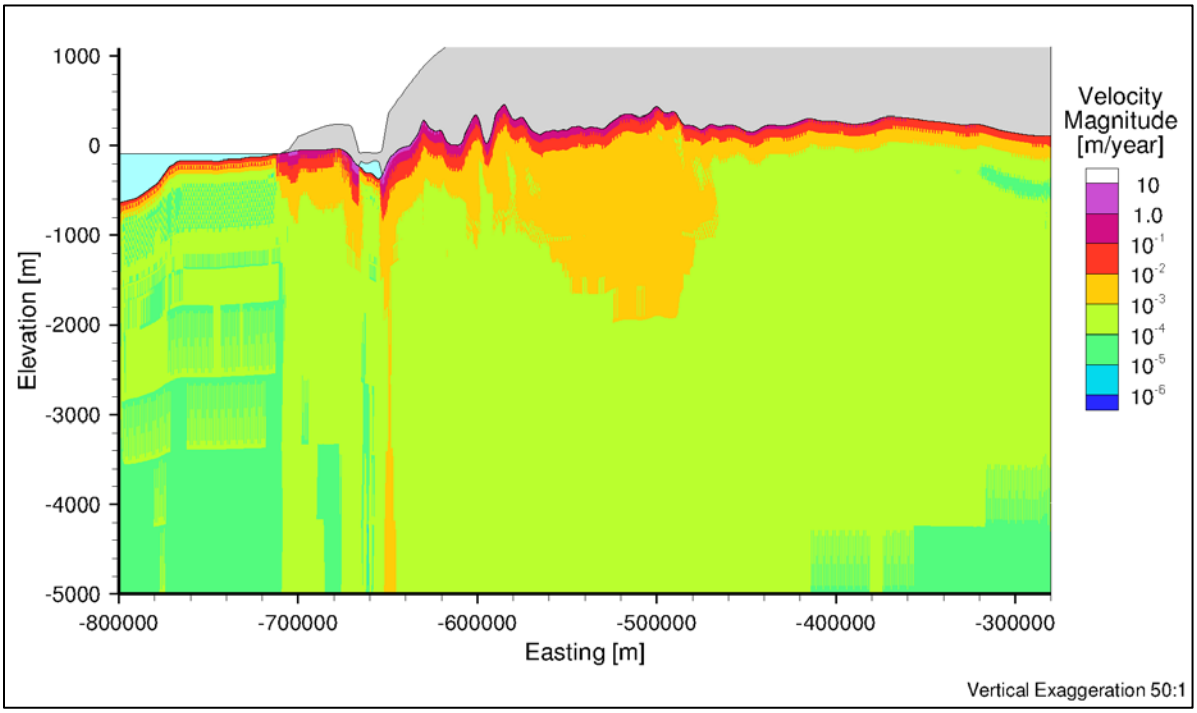

Figure B.18 West-East cross-section of velocity magnitude distribution for density-dependent flow with heat transport after 60,000 years

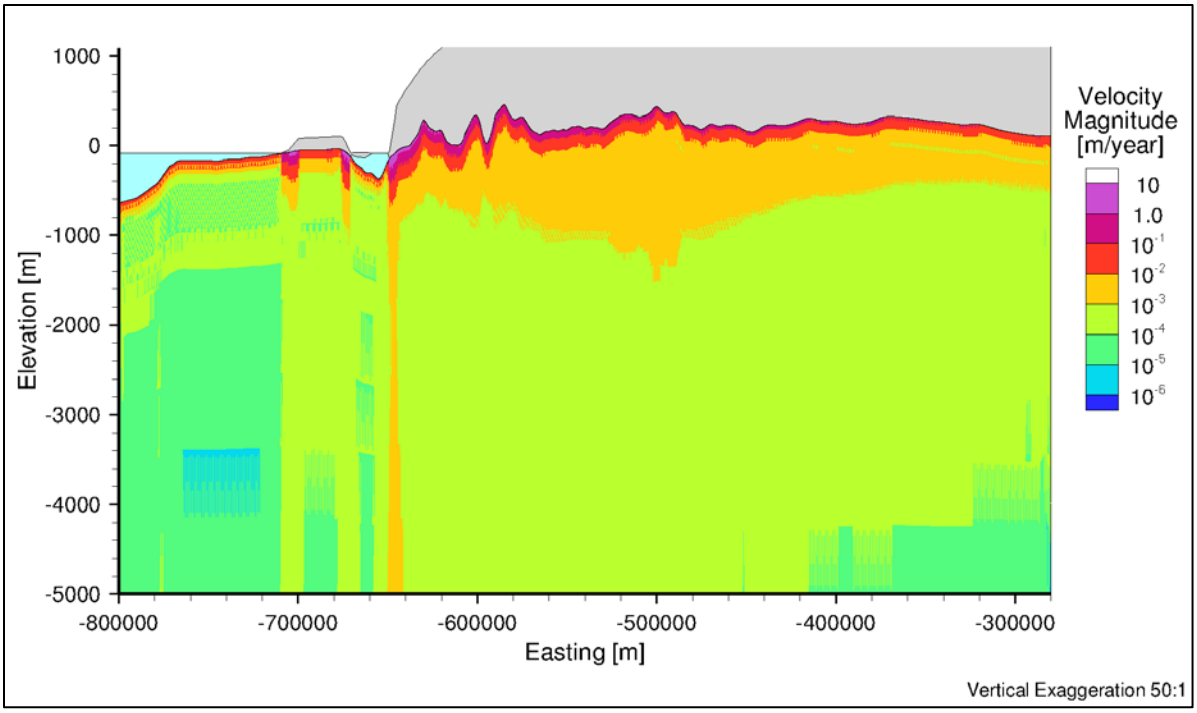

Figure B.19 West-East cross-section of velocity magnitude distribution for density-dependent flow with heat transport after 70,000 years

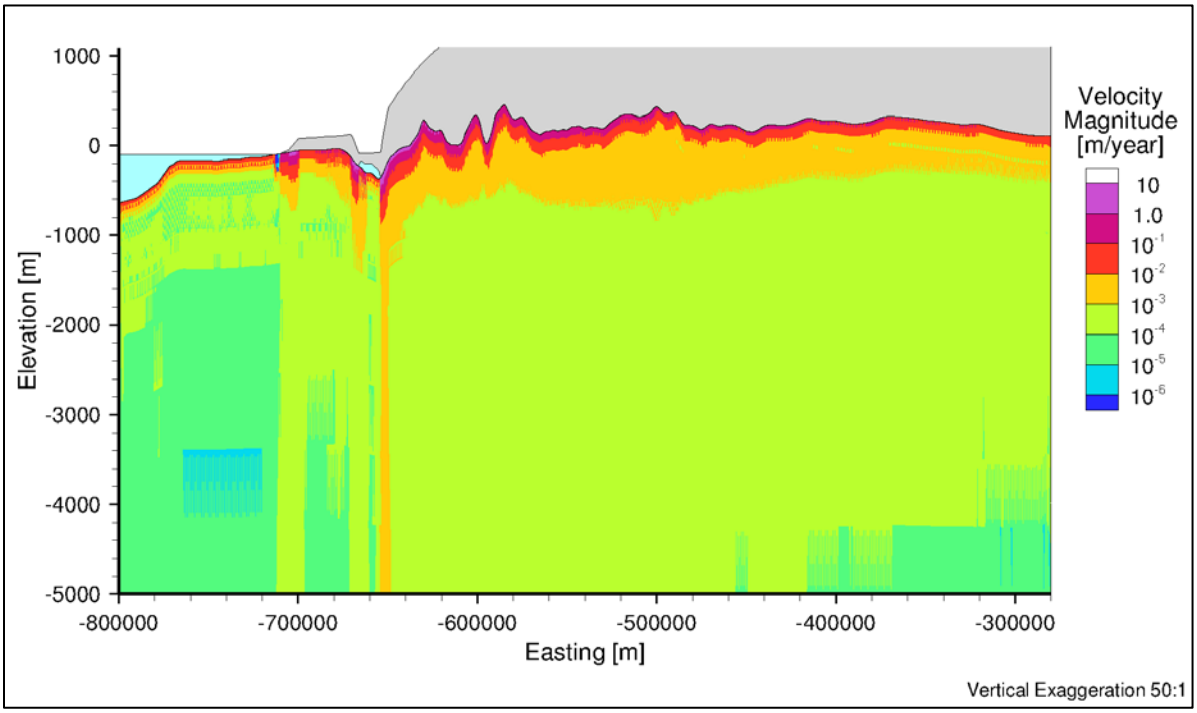

Figure B.20 West-East cross-section of velocity magnitude distribution for density-dependent flow with heat transport after 80,000 years

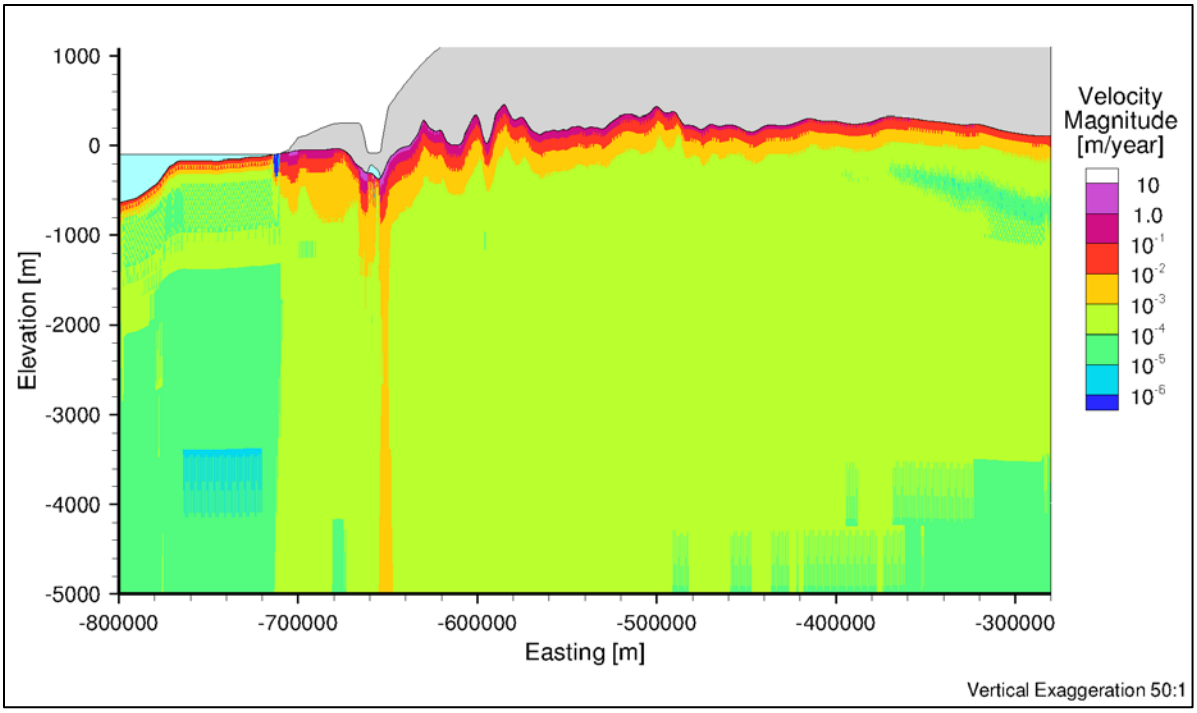

Figure B.21 West-East cross-section of velocity magnitude distribution for density-dependent flow with heat transport after 90,000 years

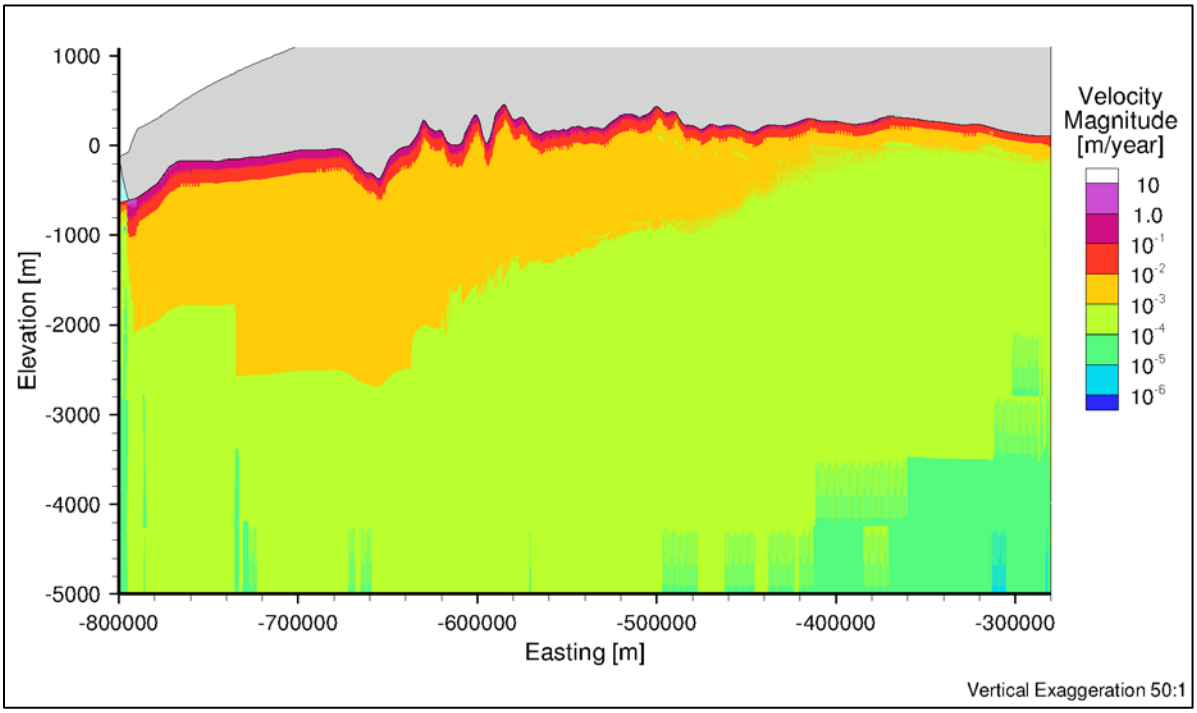

Figure B.22 West-East cross-section of velocity magnitude distribution for density-dependent flow with heat transport after 100,000 years

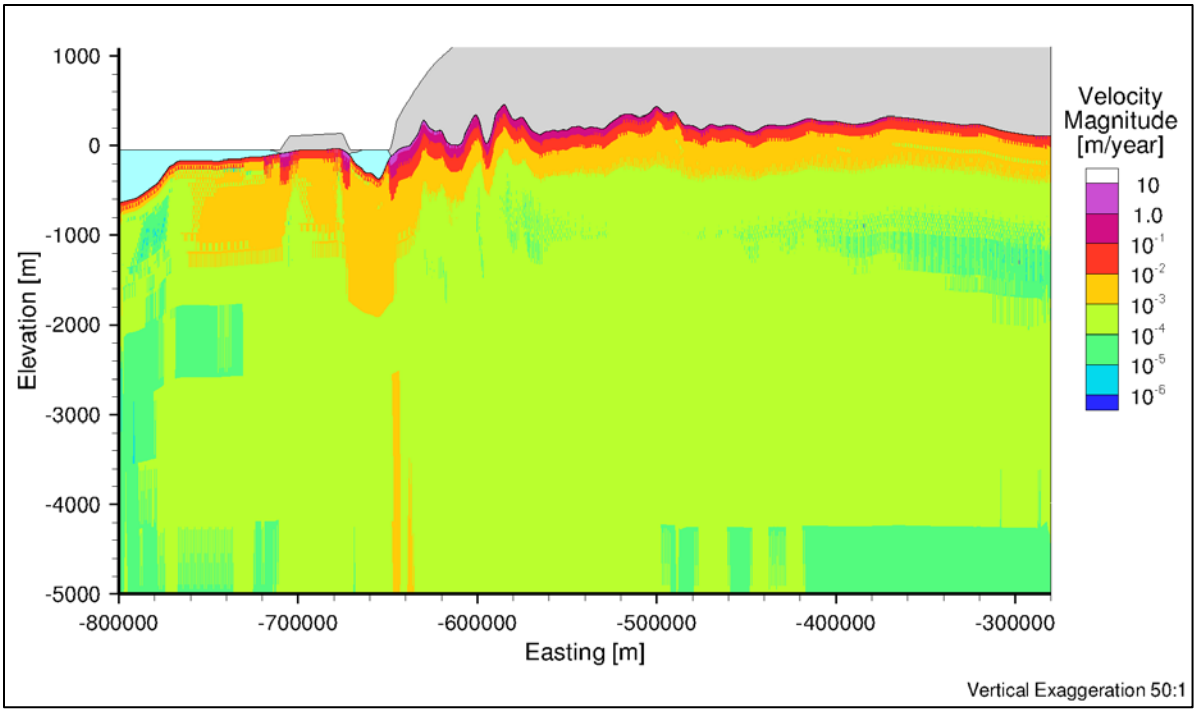

Figure B.23 West-East cross-section of velocity magnitude distribution for density-dependent flow with heat transport after 110,000 years

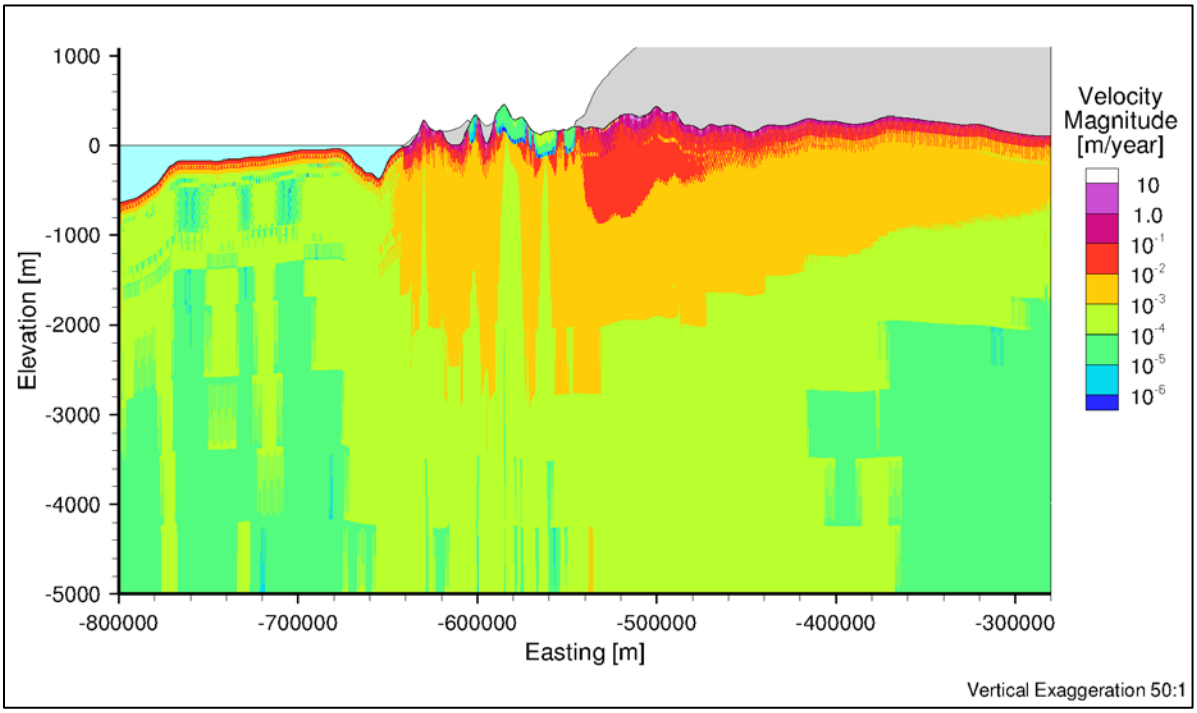

Figure B.24 West-East cross-section of velocity magnitude distribution for density-dependent flow with heat transport after 120,000 years

Appendix C – Greenland Analogue Project Analysis of Variably-Saturated Flow and Permafrost

Table of Contents

C.1 Freshwater Head Distributions for Variably-Saturated Flow without Permafrost

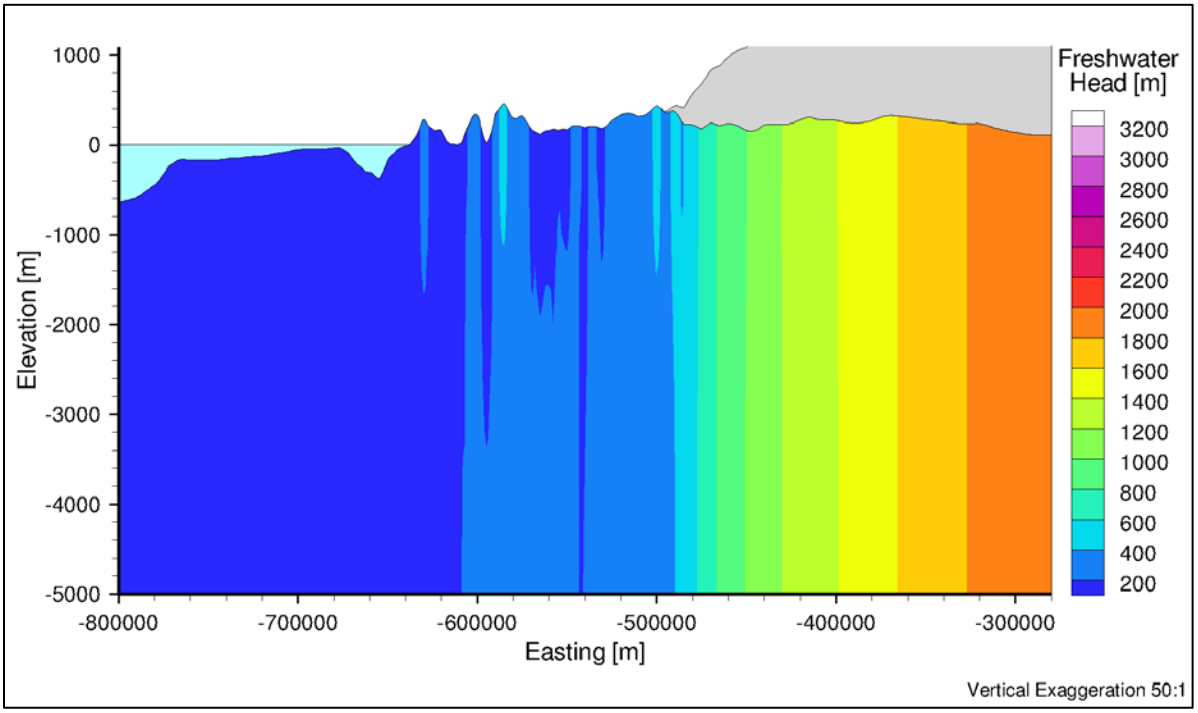

Figure C.1 West-East cross-section of freshwater head distribution for variably-saturated flow without permafrost after 200 years

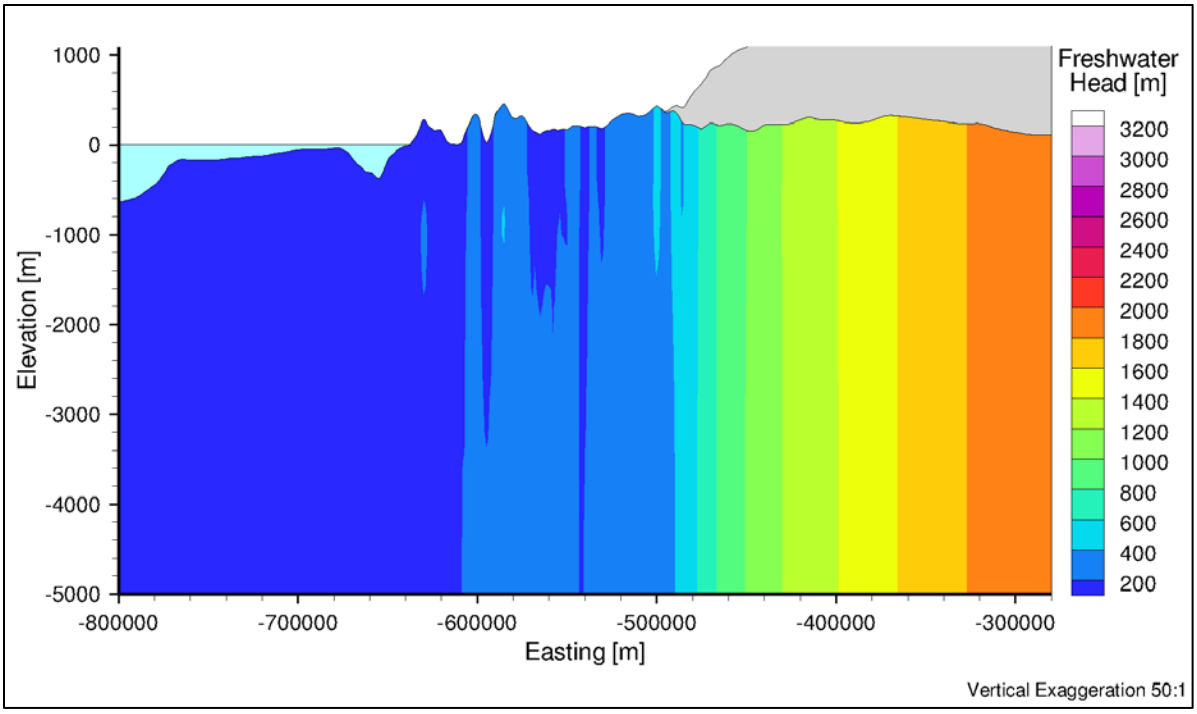

Figure C.2 West-East cross-section of freshwater head distribution for variably-saturated flow without permafrost after 400 years

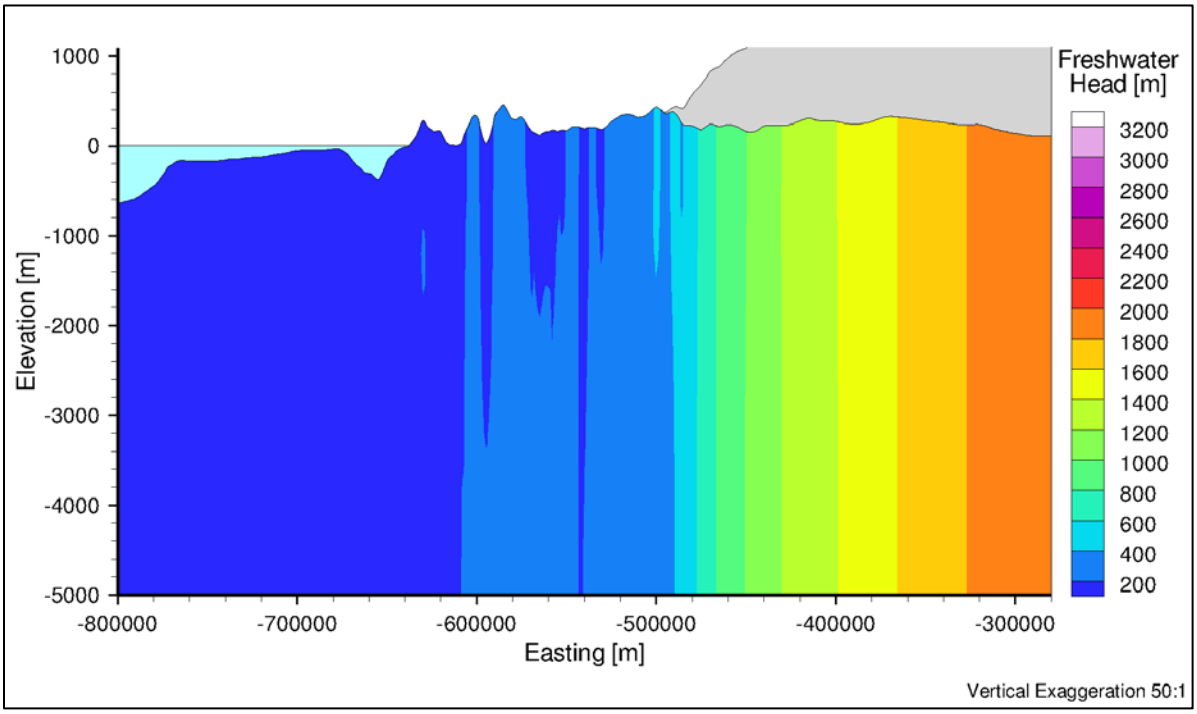

Figure C.3 West-East cross-section of freshwater head distribution for variably-saturated flow without permafrost after 600 years

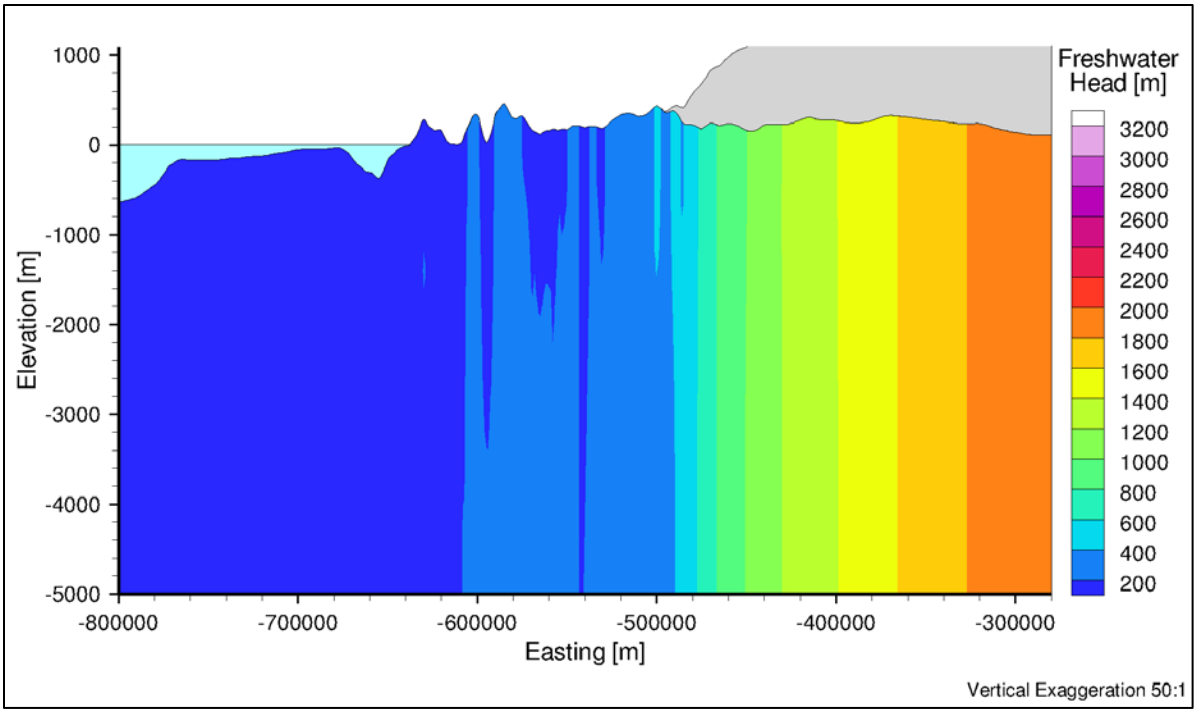

Figure C.4 West-East cross-section of freshwater head distribution for variably-saturated flow without permafrost after 800 years

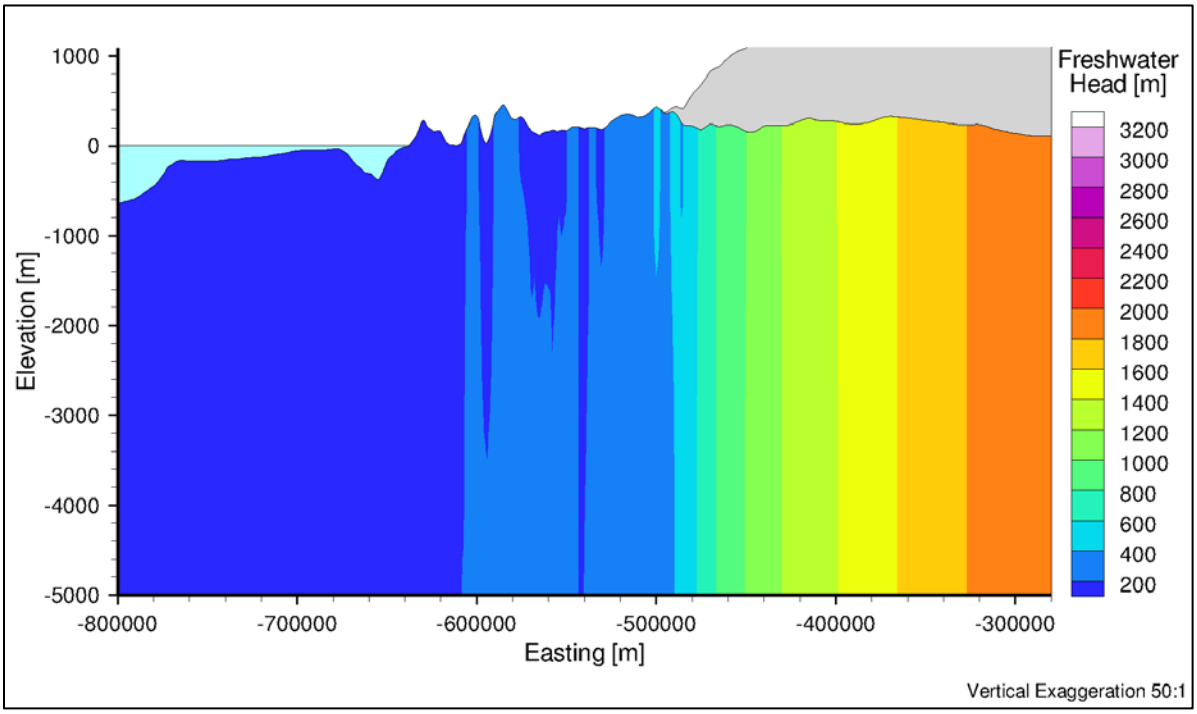

Figure C.5 West-East cross-section of freshwater head distribution for variably-saturated flow without permafrost after 1,000 years

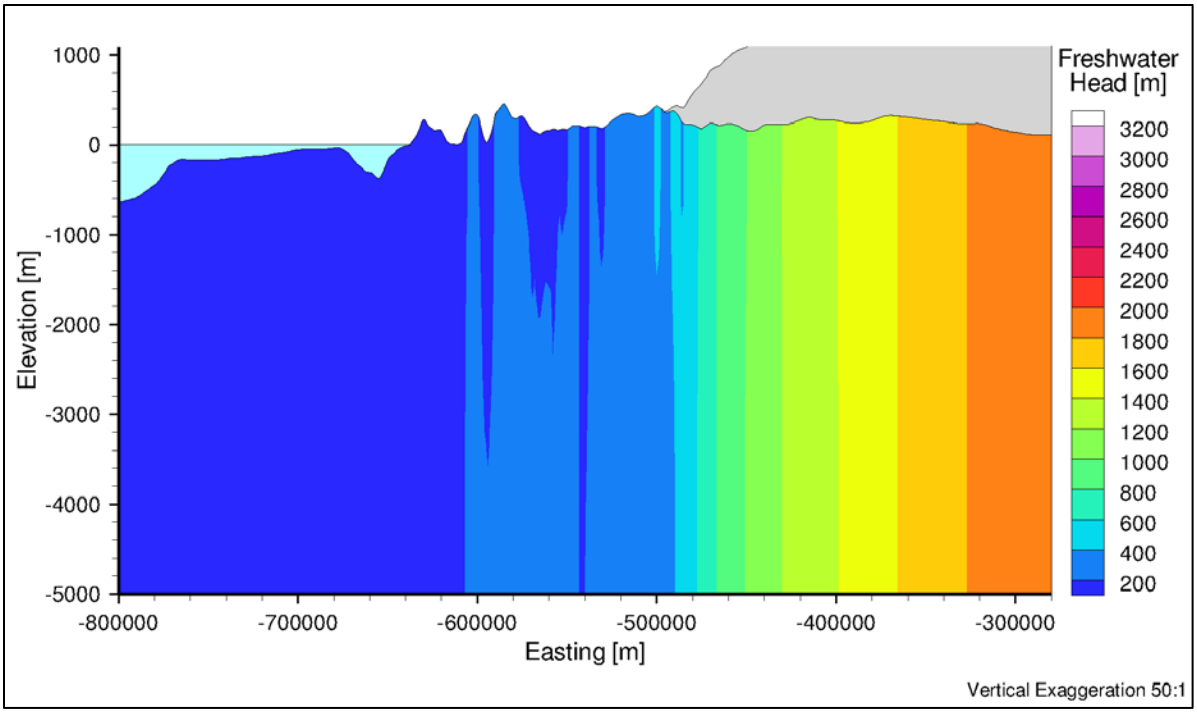

Figure C.6 West-East cross-section of freshwater head distribution for variably-saturated flow without permafrost after 1,200 years

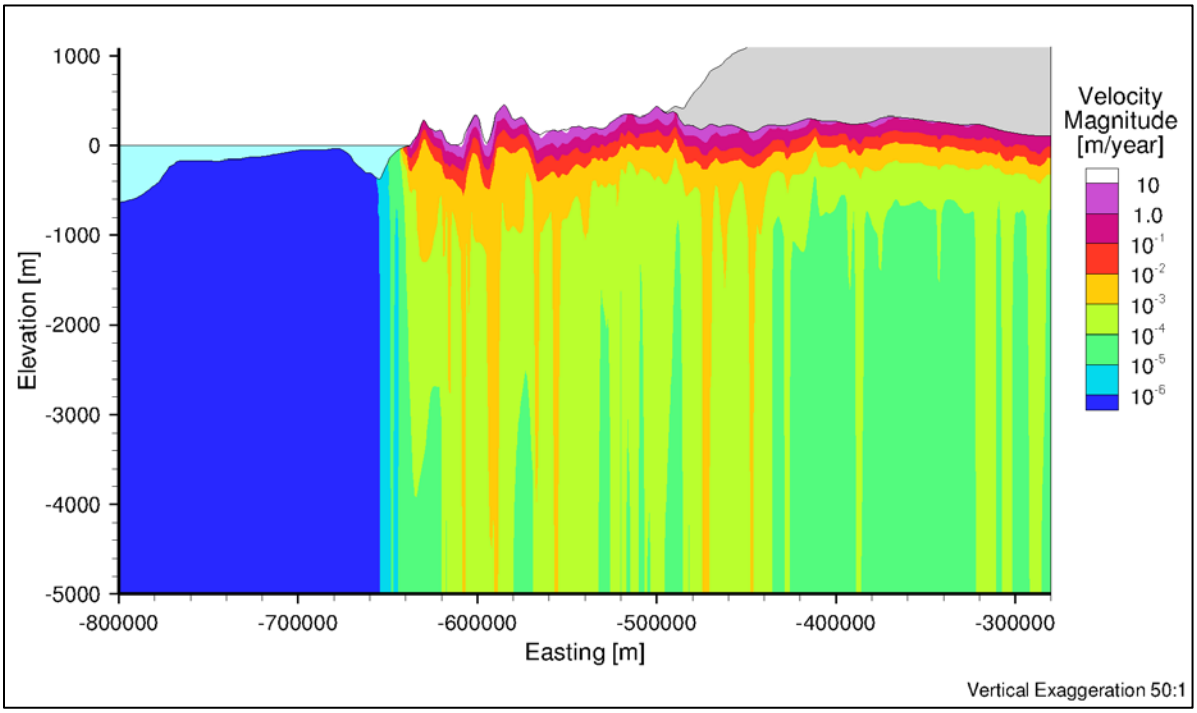

Figure C.7 West-East cross-section of freshwater head distribution for variably-saturated flow without permafrost after 1,400 years

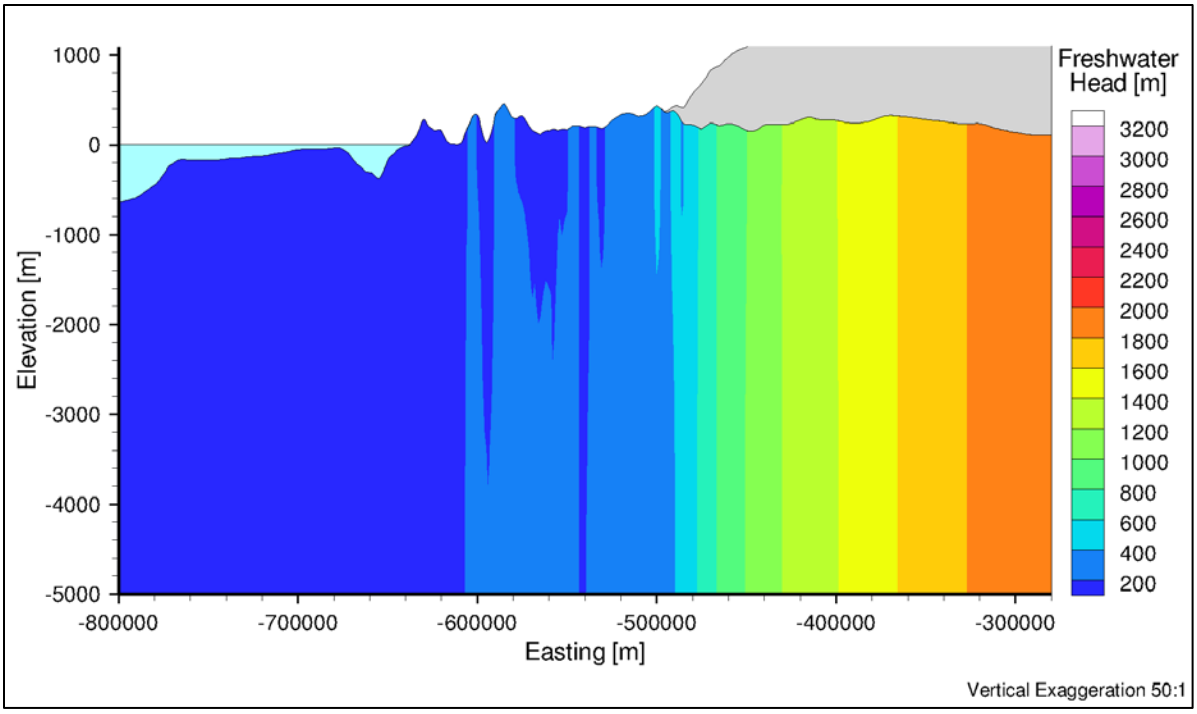

Figure C.8 West-East cross-section of freshwater head distribution for variably-saturated flow without permafrost after 1,600 years

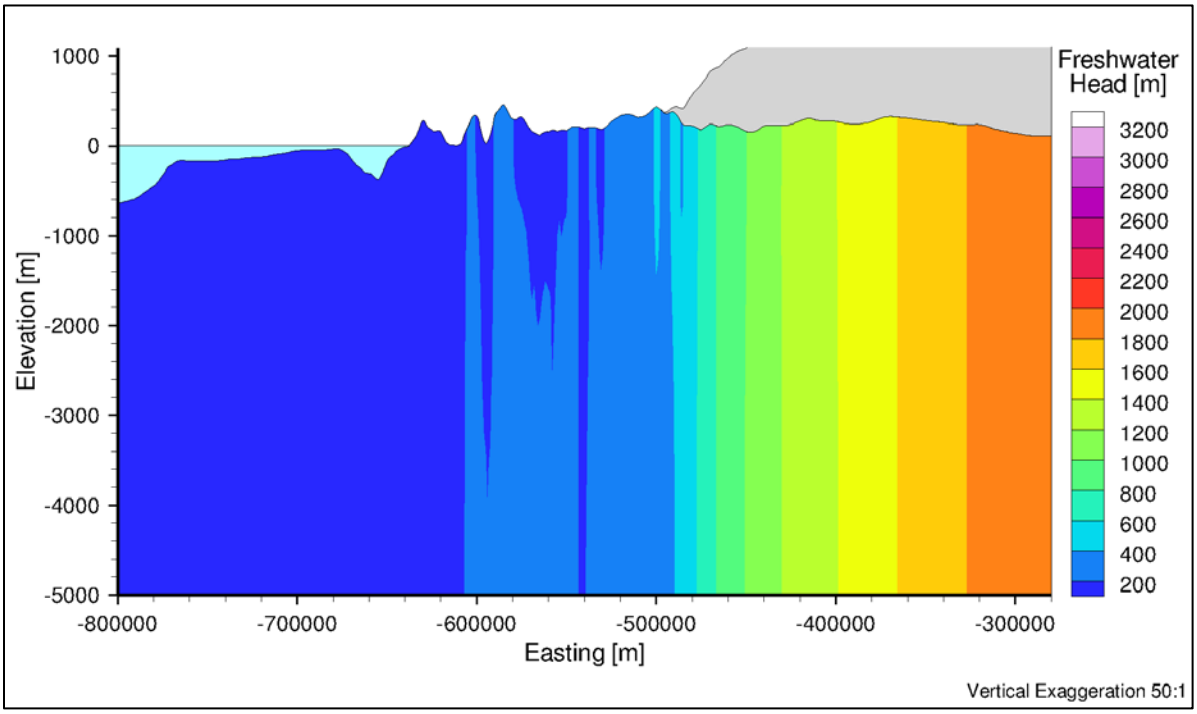

Figure C.9 West-East cross-section of freshwater head distribution for variably-saturated flow without permafrost after 1,800 years

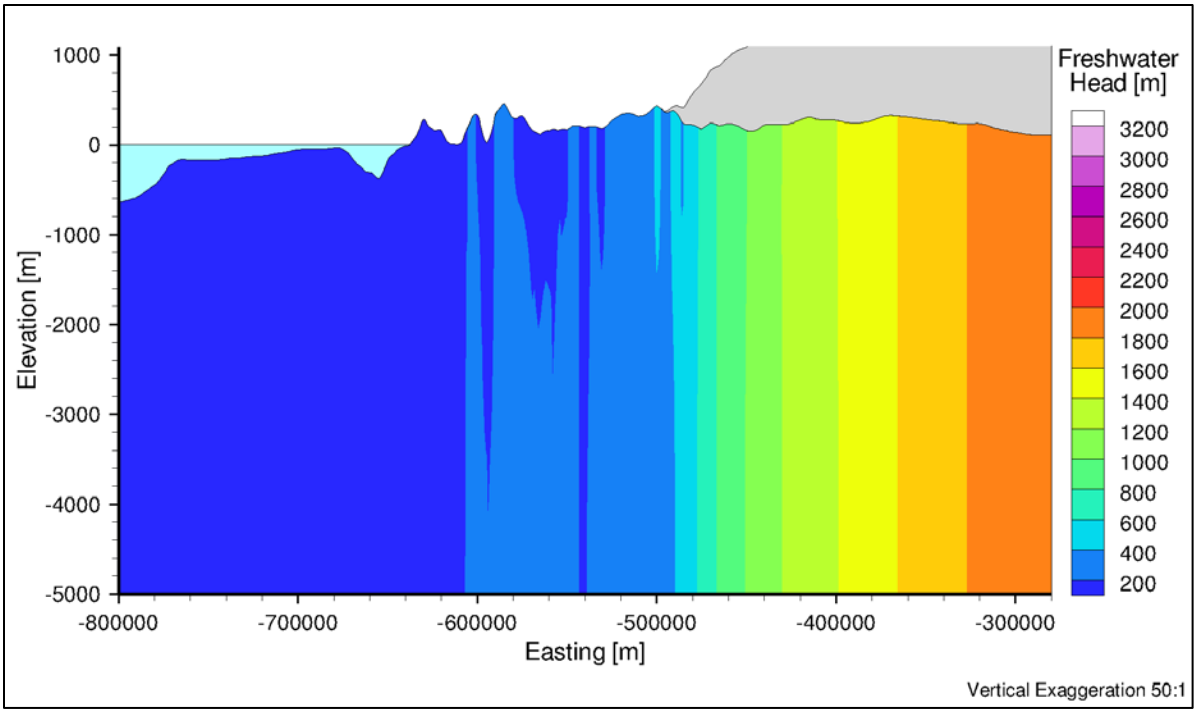

Figure C.10 West-East cross-section of freshwater head distribution for variably-saturated flow without permafrost after 2,000 years

C.2 Freshwater Head Distribution for Variably-Saturated Flow with Permafrost

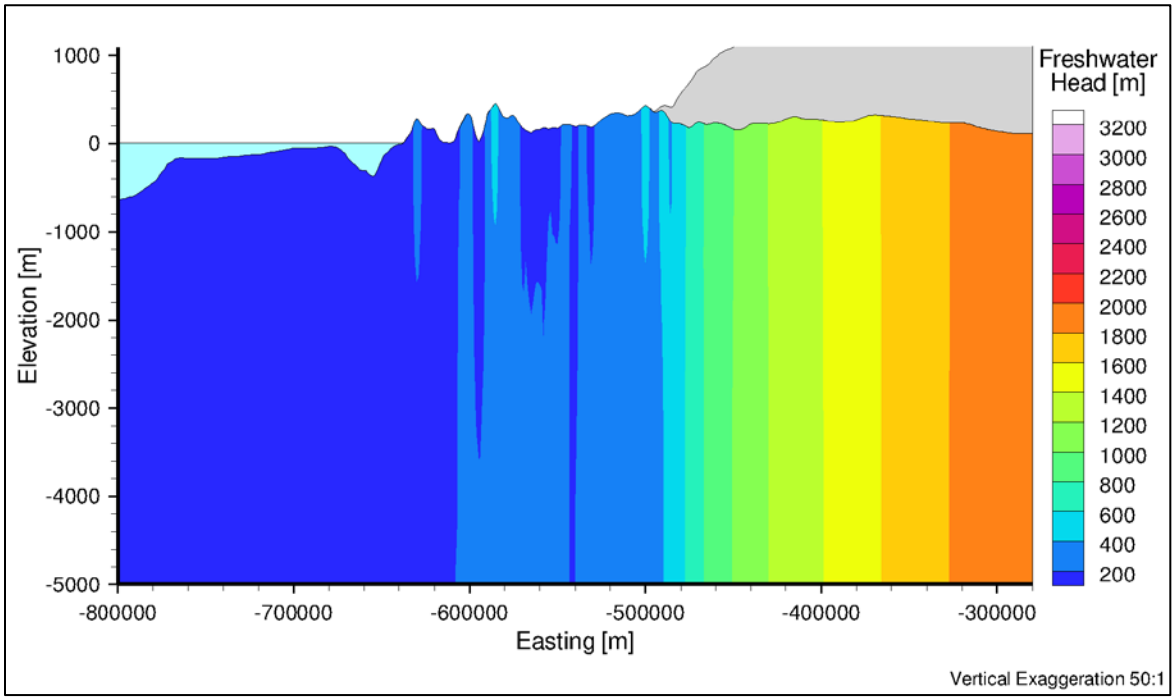

Figure C.11 West-East cross-section of freshwater head distribution for variably-saturated flow with permafrost after 2,000 years

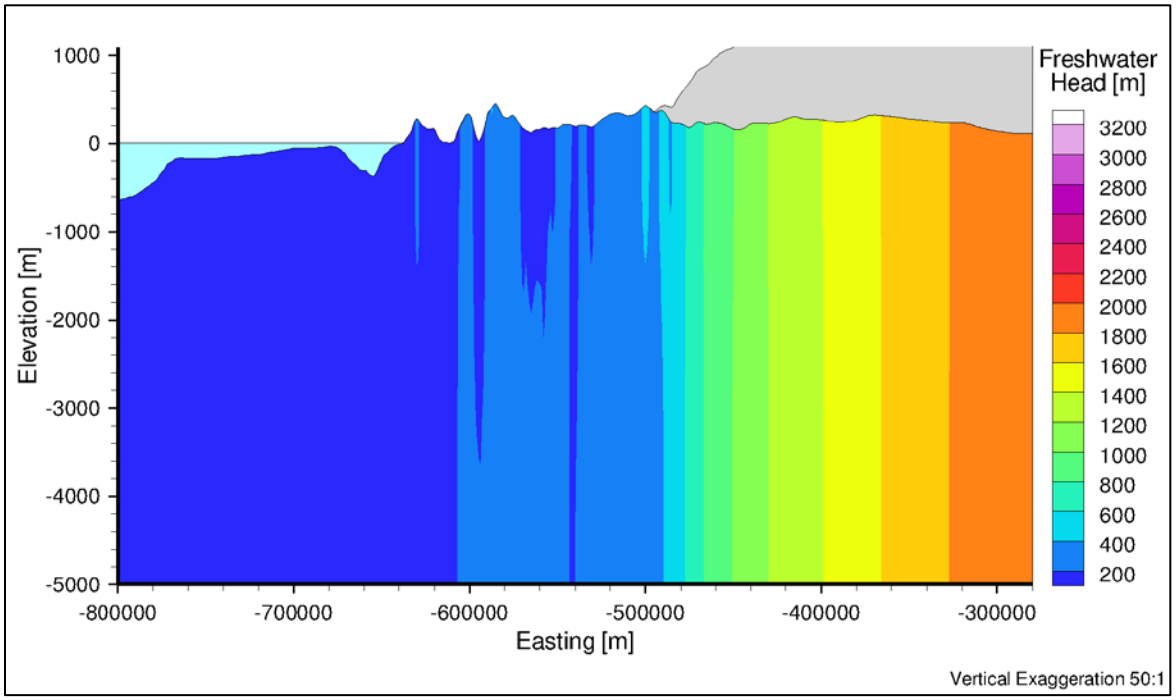

Figure C.12 West-East cross-section of freshwater head distribution for variably-saturated flow with permafrost after 4,000 years

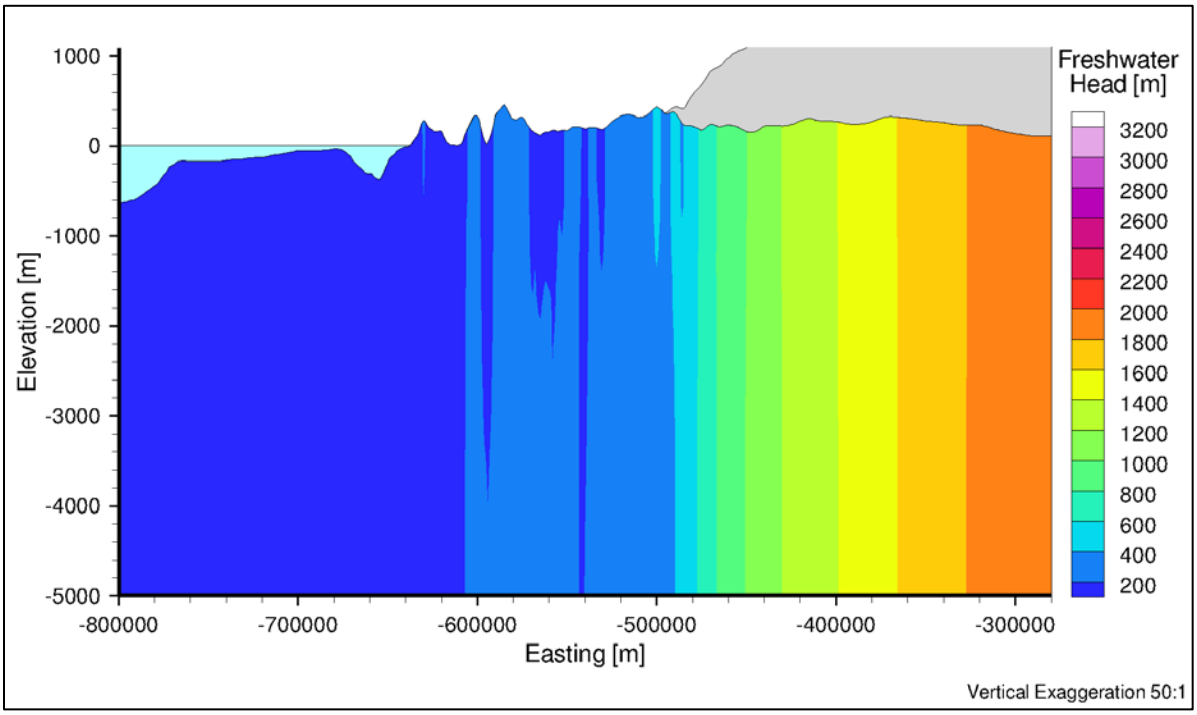

Figure C.13 West-East cross-section of freshwater head distribution for variably-saturated flow with permafrost after 6,000 years

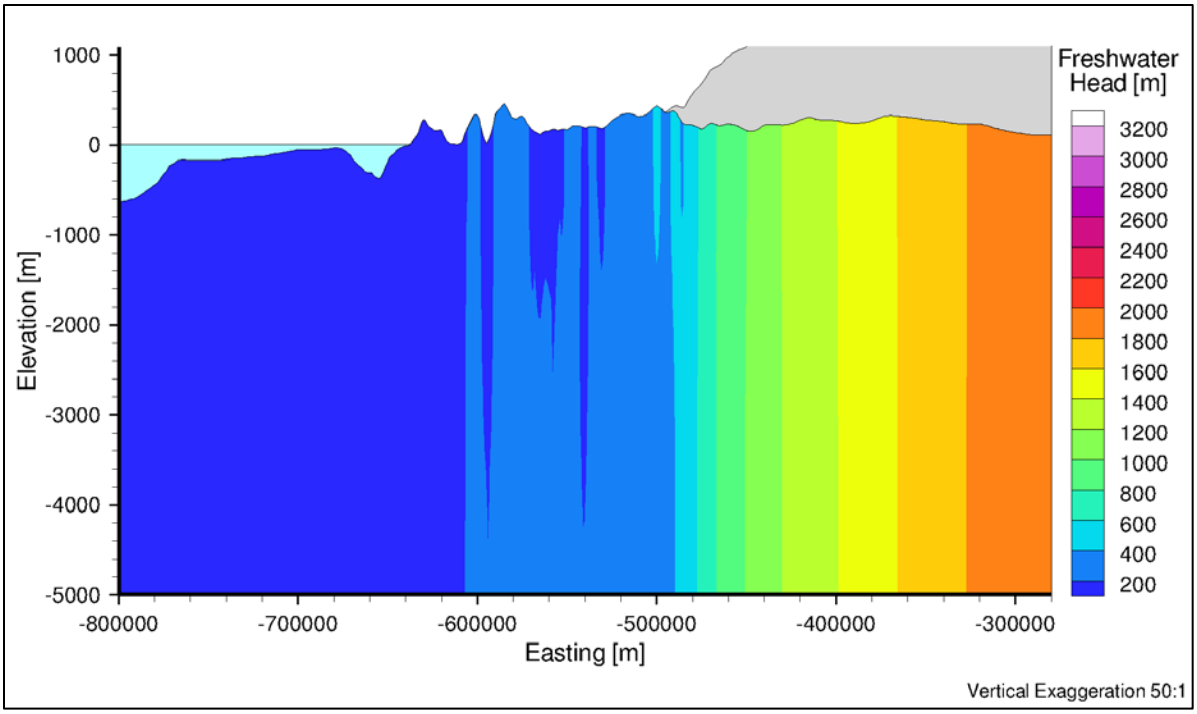

Figure C.14 West-East cross-section of freshwater head distribution for variably-saturated flow with permafrost after 8,000 years

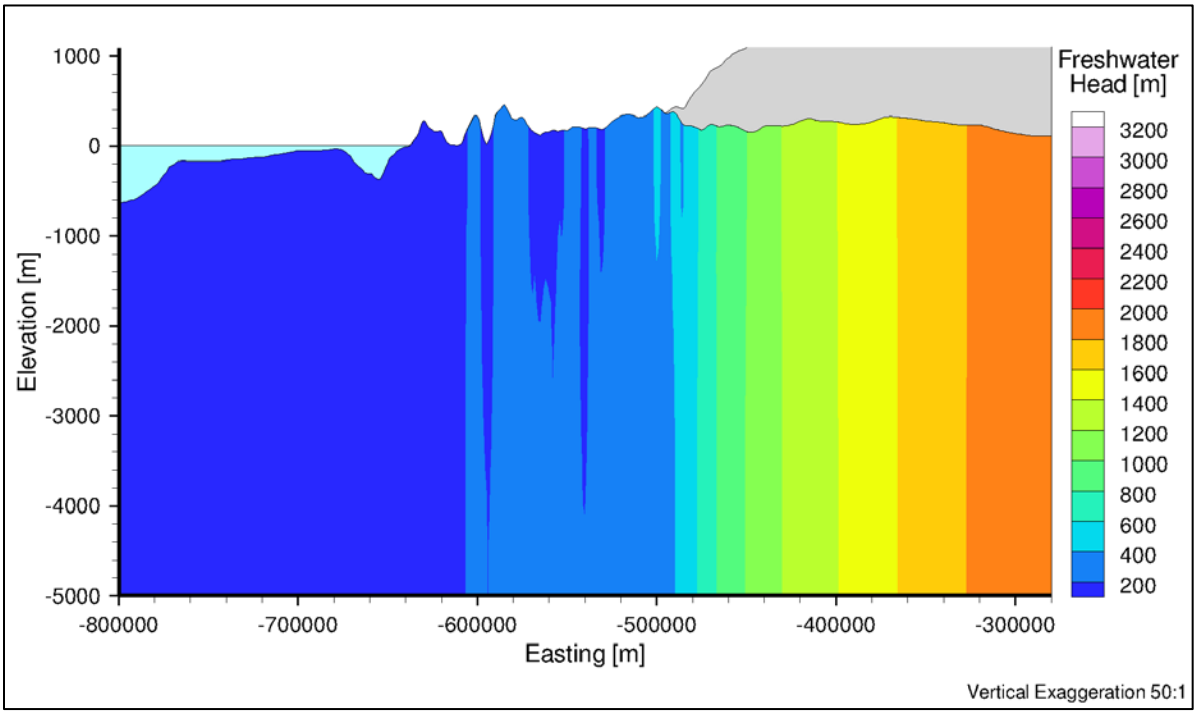

Figure C.15 West-East cross-section of freshwater head distribution for variably-saturated flow with permafrost after 10,000 years

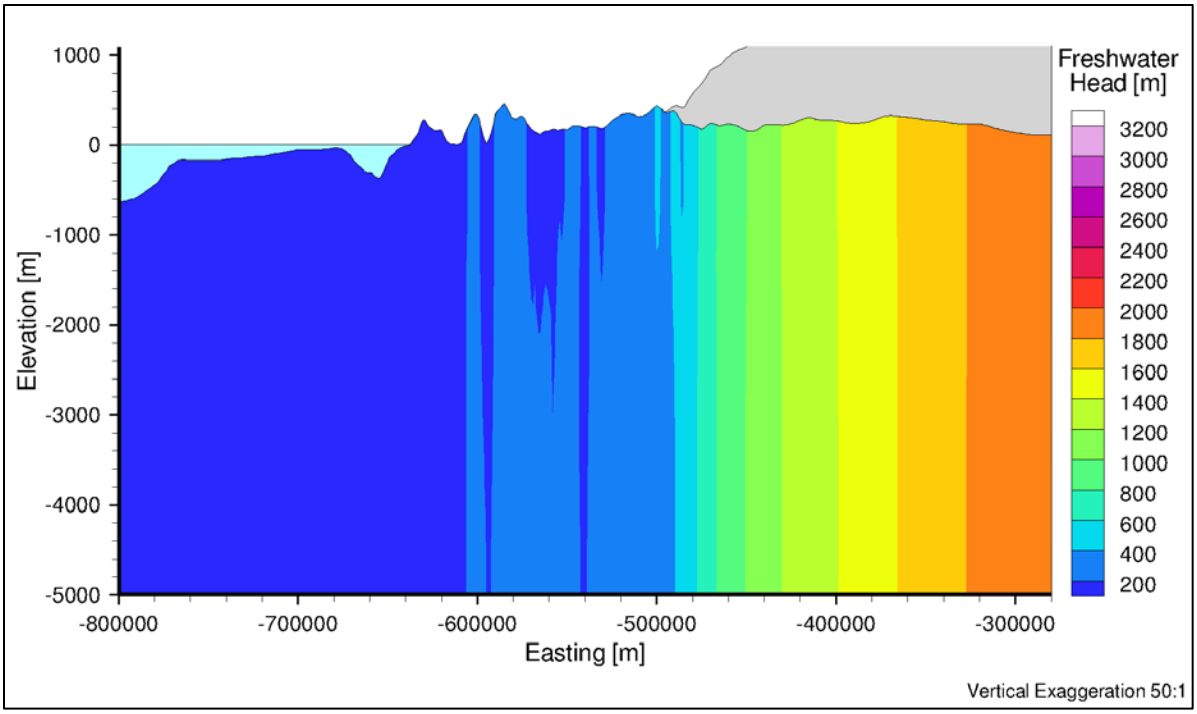

Figure C.16 West-East cross-section of freshwater head distribution for variably-saturated flow with permafrost after 20,000 years

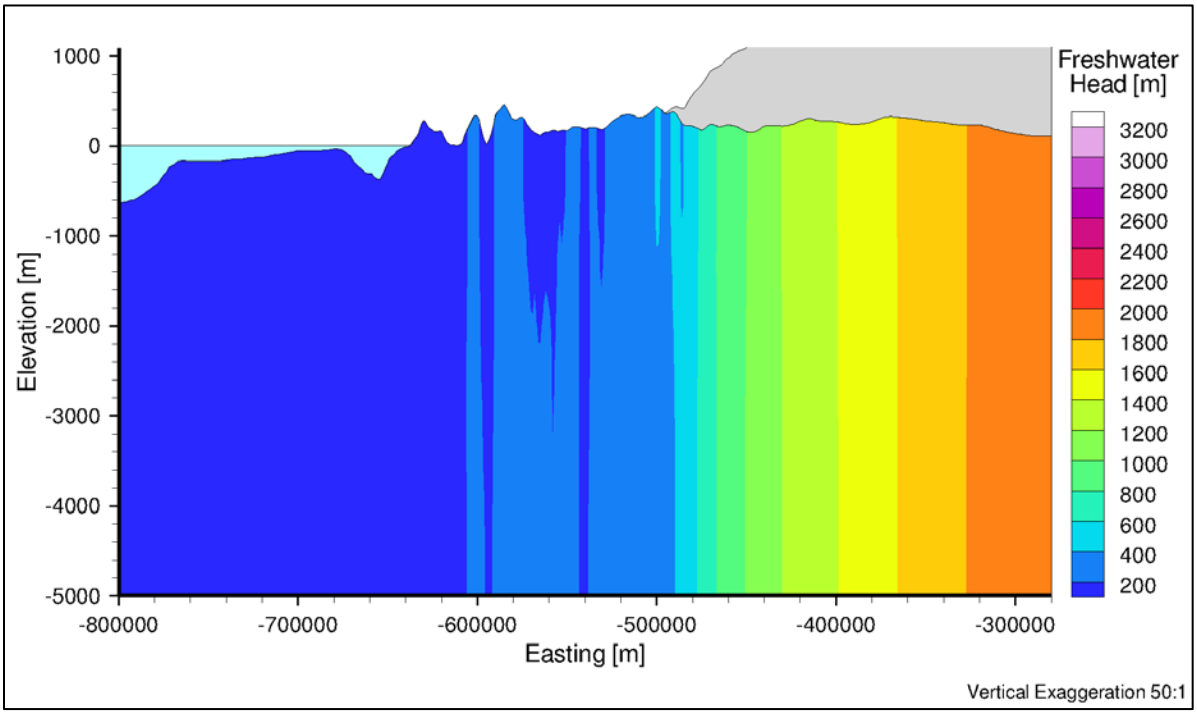

Figure C.17 West-East cross-section of freshwater head distribution for variably-saturated flow with permafrost after 30,000 years

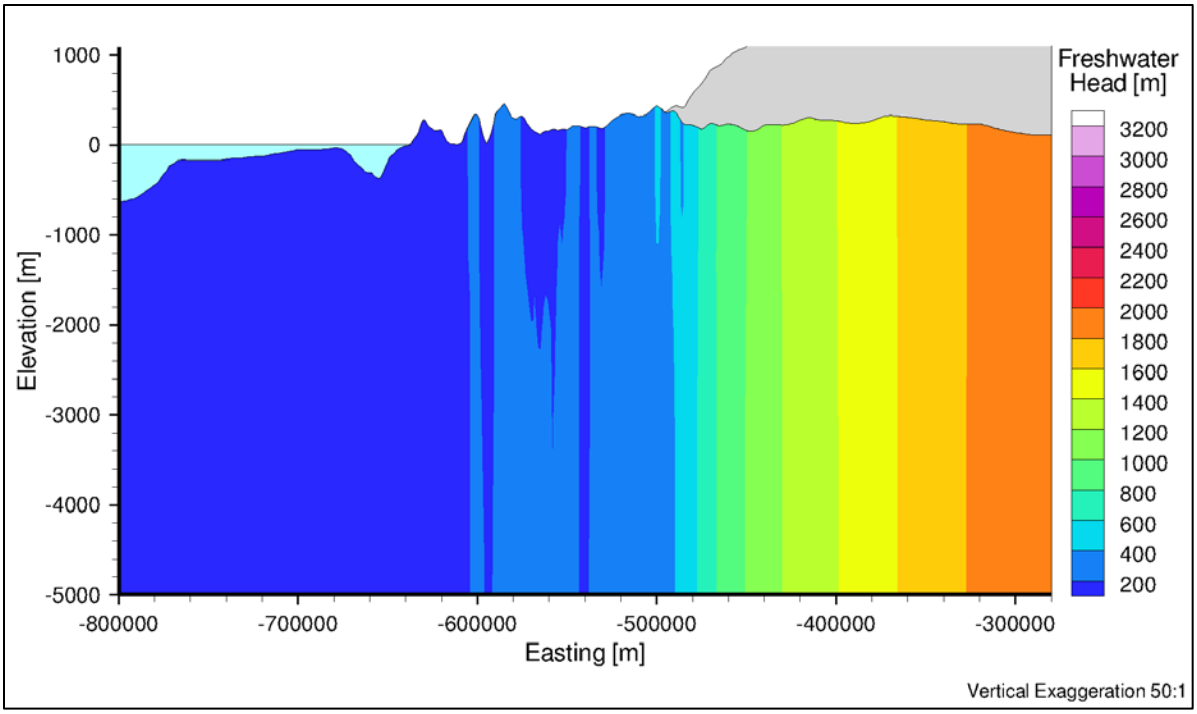

Figure C.18 West-East cross-section of freshwater head distribution for variably-saturated flow with permafrost after 40,000 years

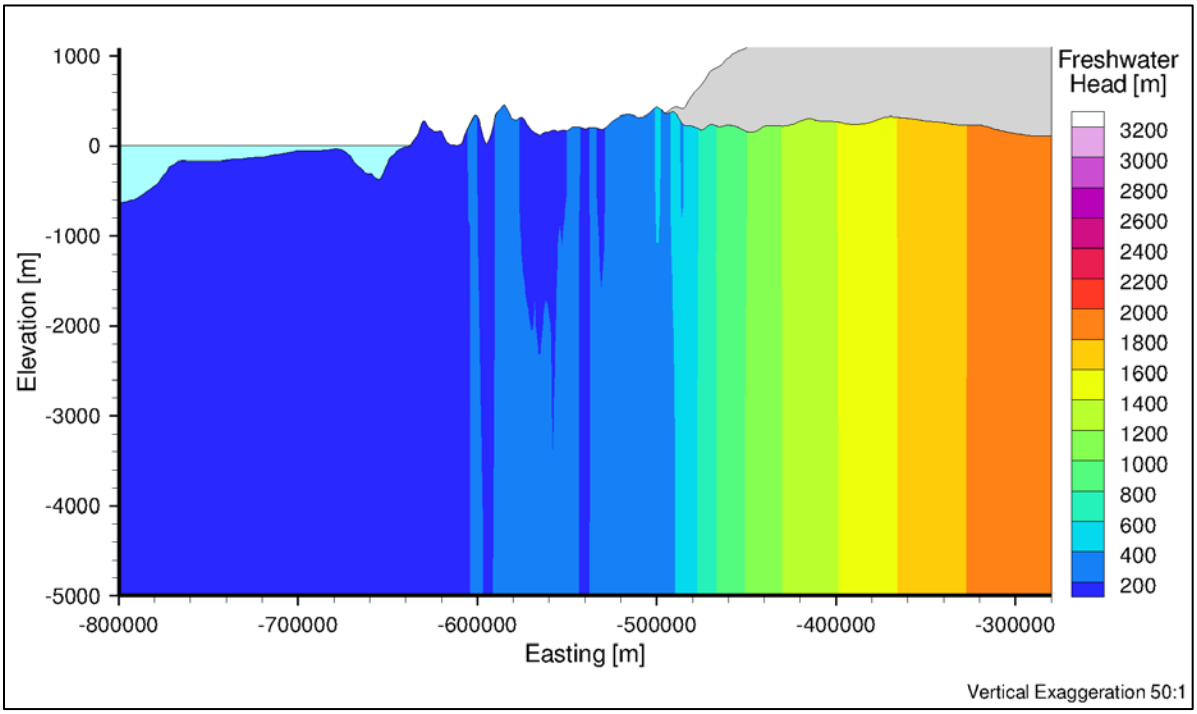

Figure C.19 West-East cross-section of freshwater head distribution for variably-saturated flow with permafrost after 50,000 years

C.3 Depth to Water Table for Variably-Saturated Flow without Permafrost

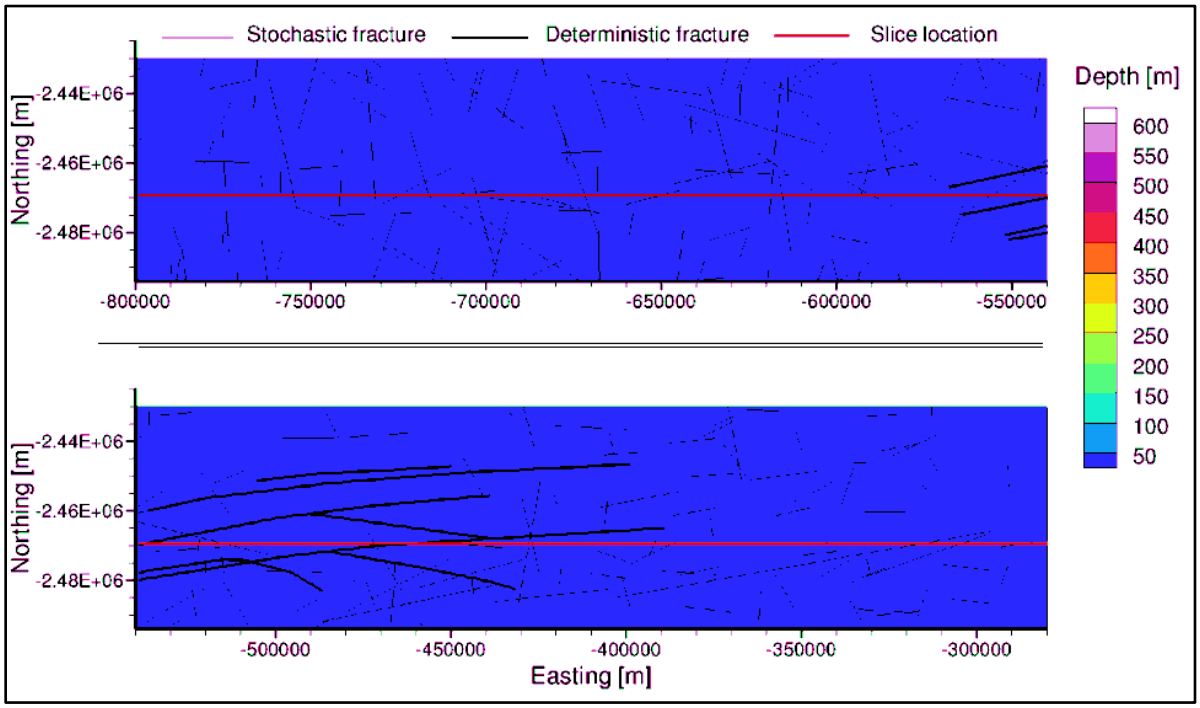

Figure C.20 Areal view of the depth to water table for variably-saturated flow without permafrost after 200 years

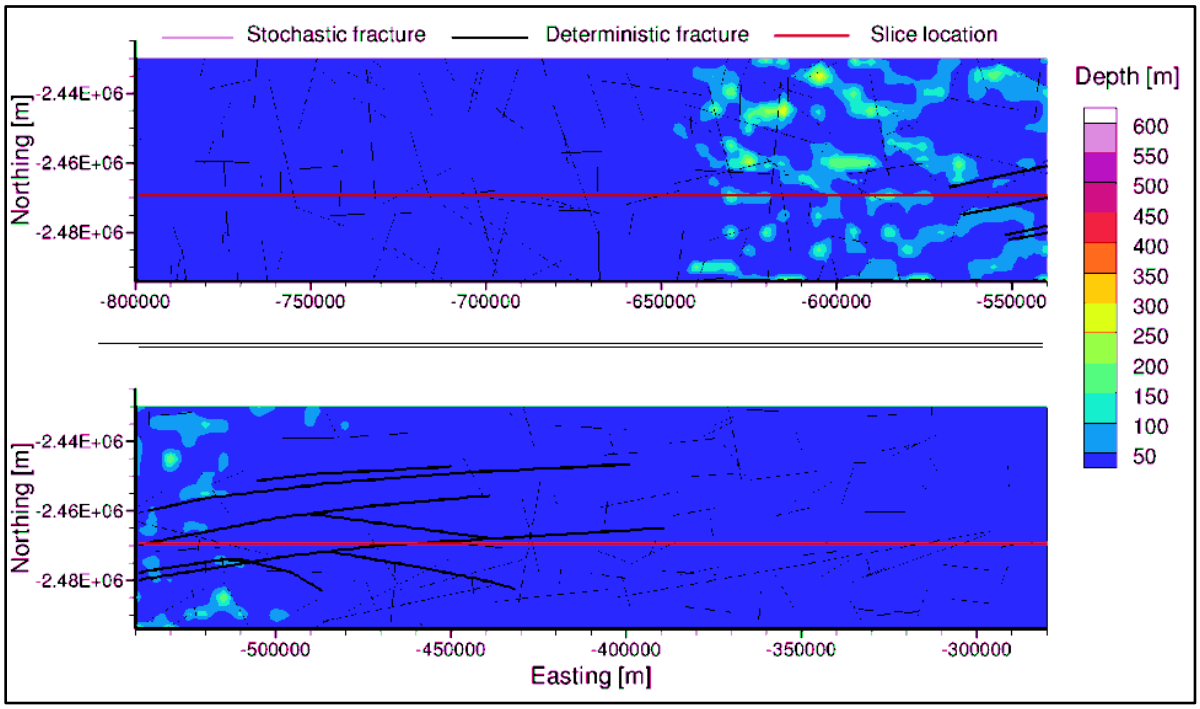

Figure C.21 Areal view of the depth to water table for variably-saturated flow without permafrost after 400 years

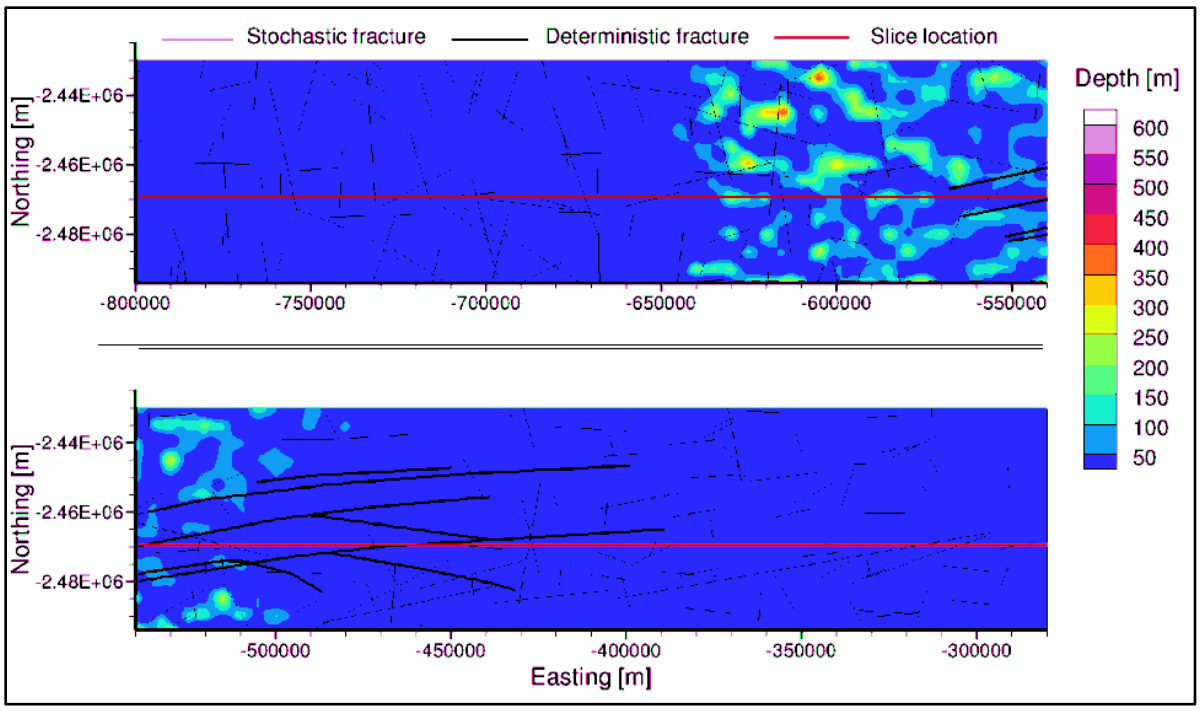

Figure C.22 Areal view of the depth to water table for variably-saturated flow without permafrost after 600 years

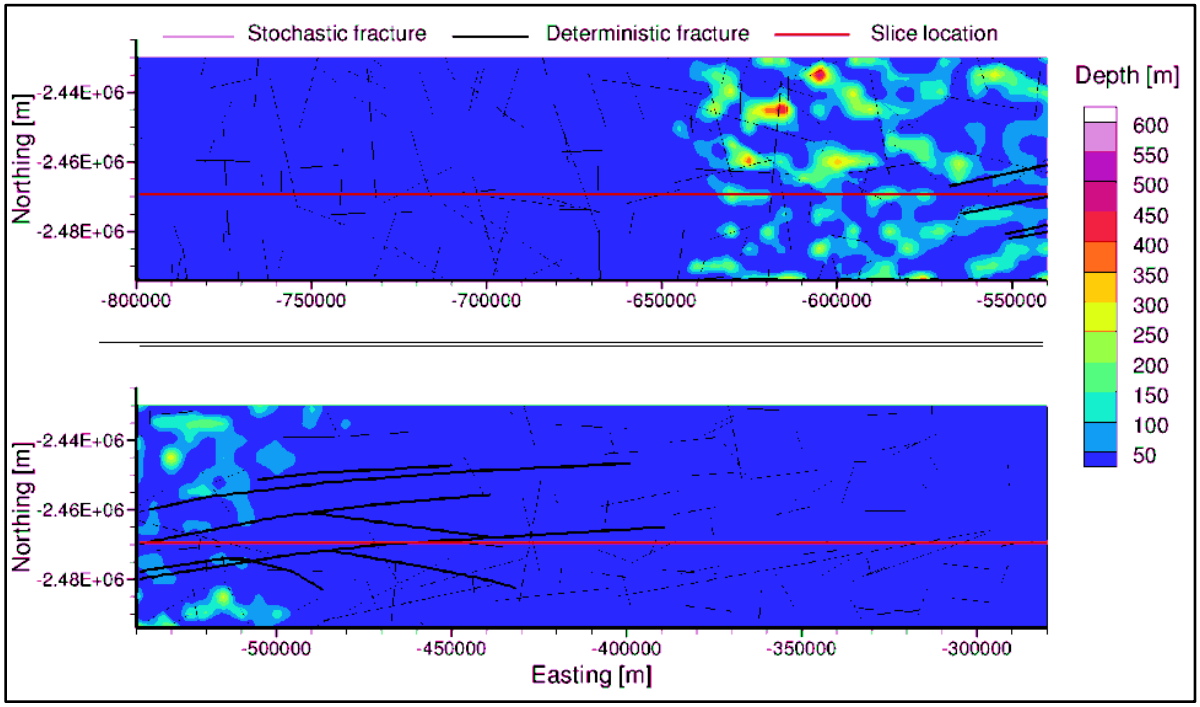

Figure C.23 Areal view of the depth to water table for variably-saturated flow without permafrost after 800 years

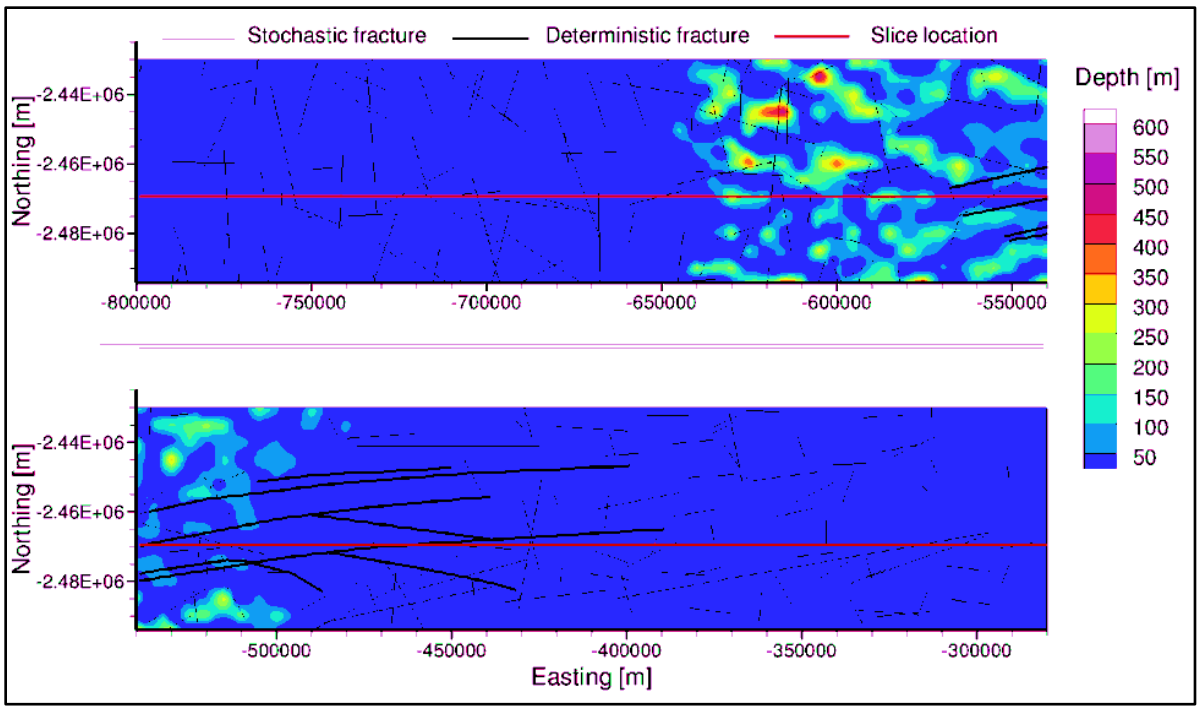

Figure C.24 Areal view of the depth to water table for variably-saturated flow without permafrost after 1,000 years

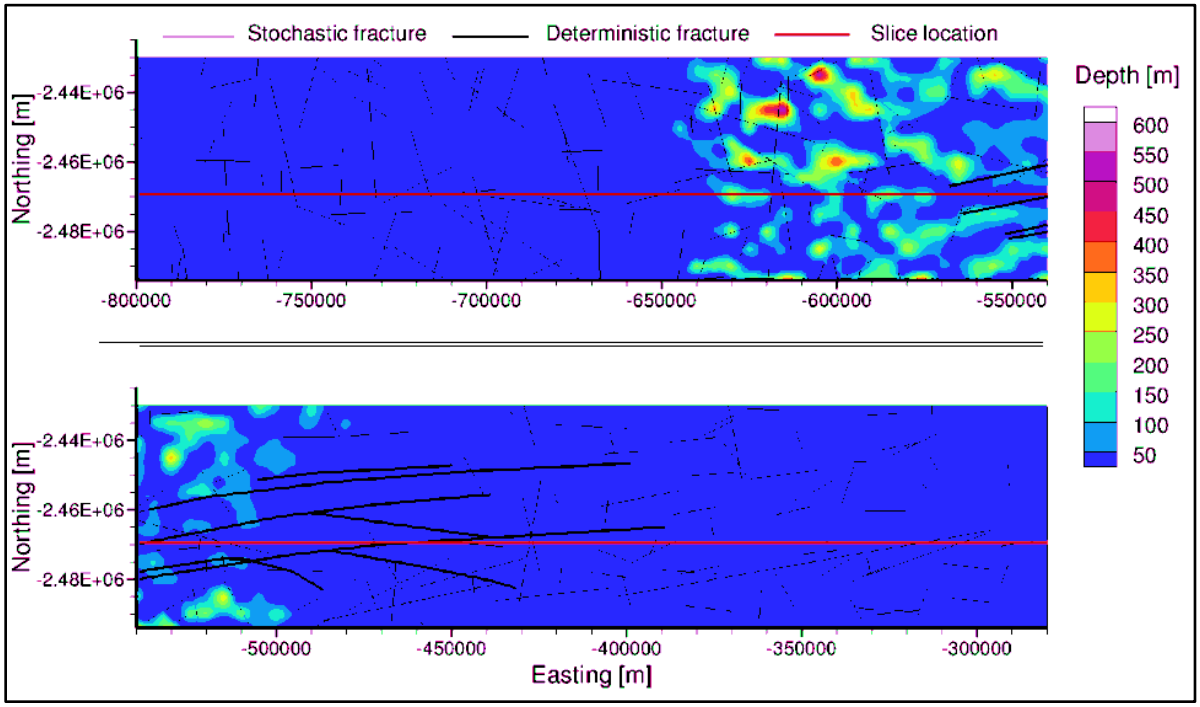

Figure C.25 Areal view of the depth to water table for variably-saturated flow without permafrost after 1,200 years

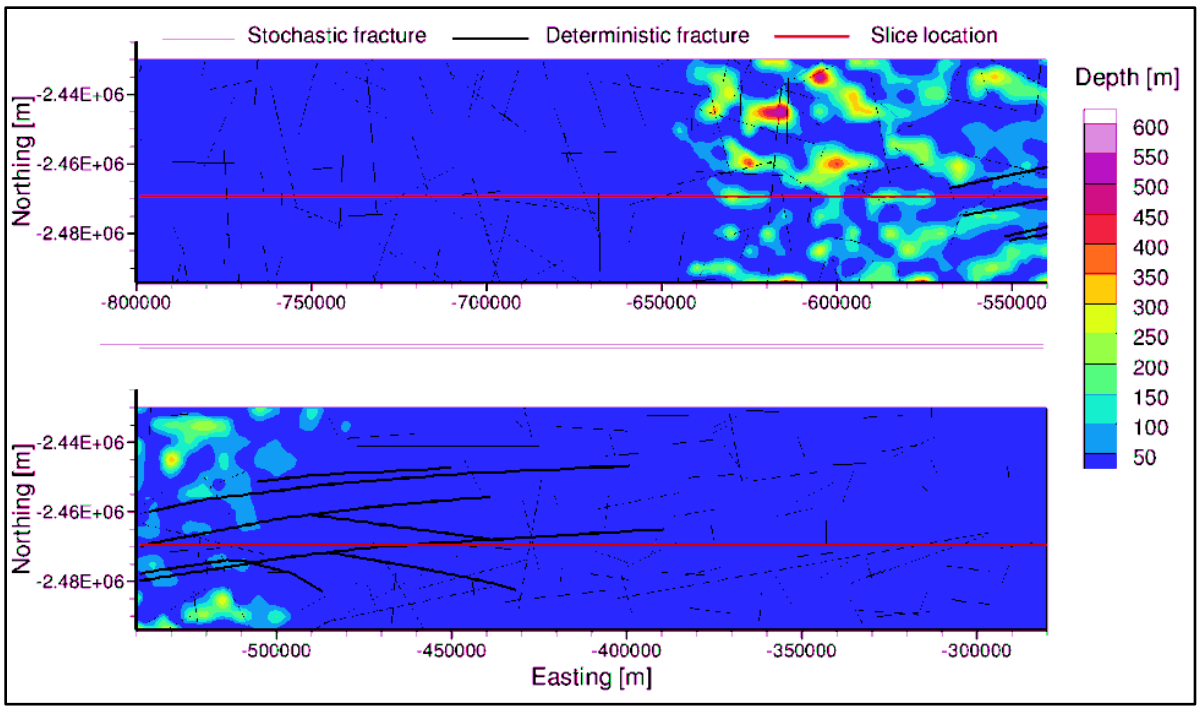

Figure C.26 Areal view of the depth to water table for variably-saturated flow without permafrost after 1,400 years

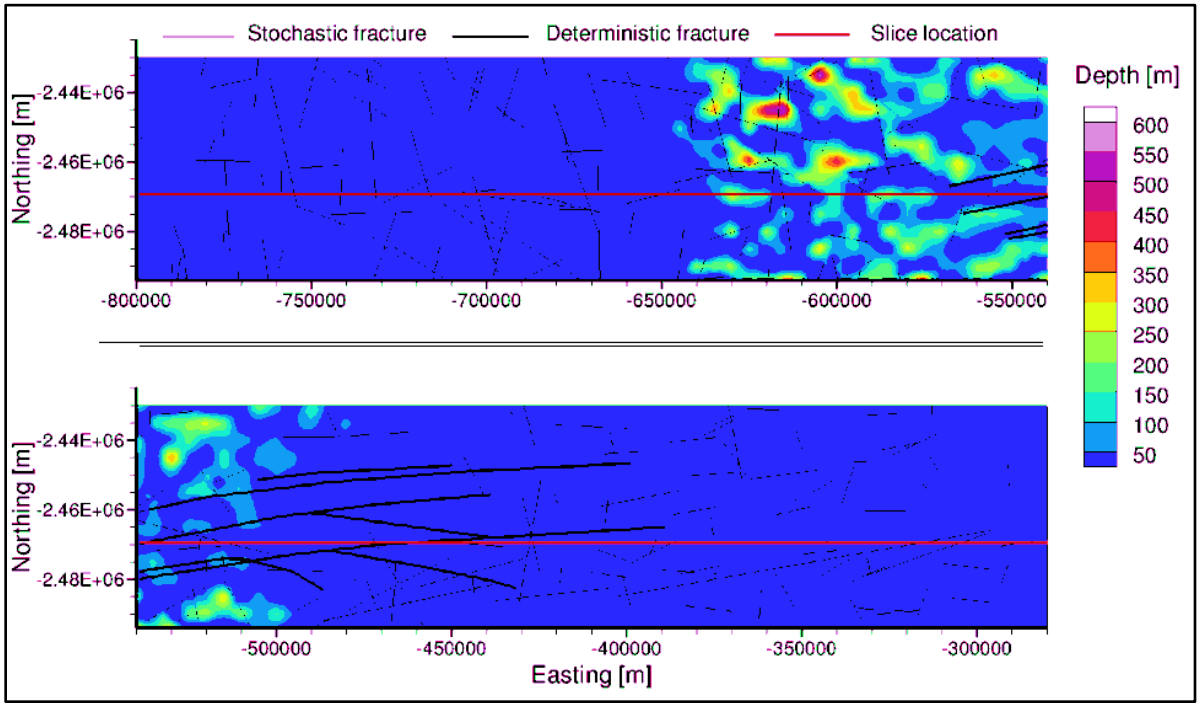

Figure C.27 Areal view of the depth to water table for variably-saturated flow without permafrost after 1,600 years

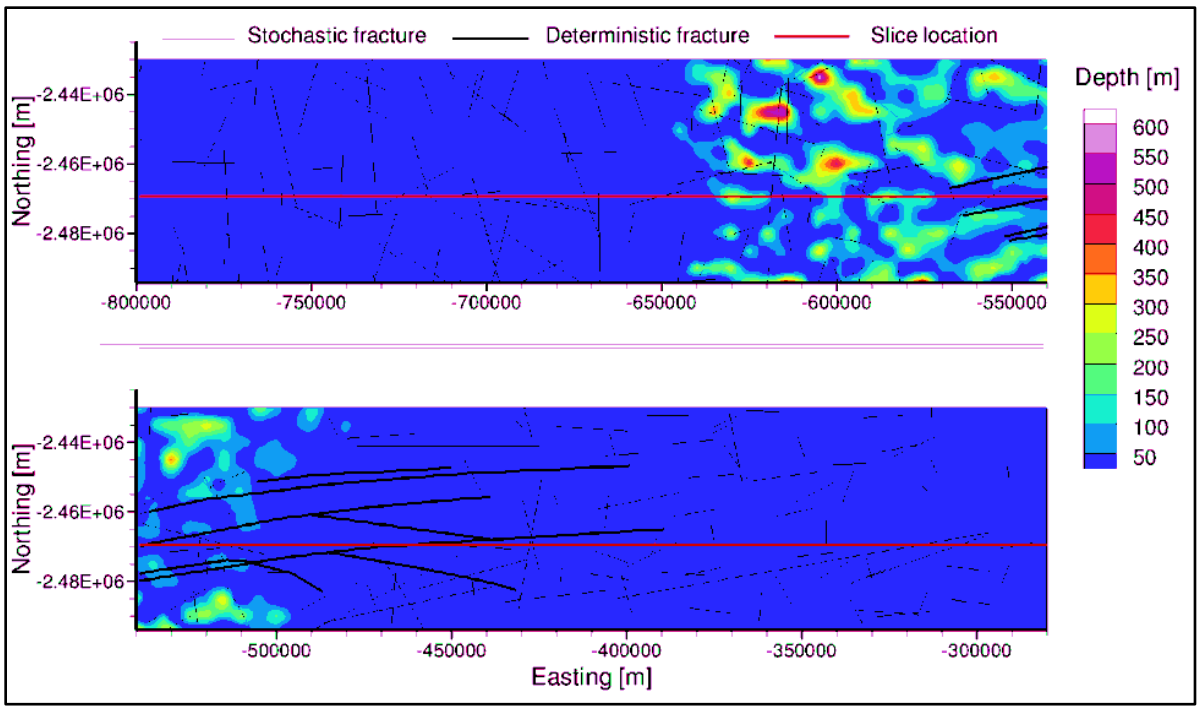

Figure C.28 Areal view of the depth to water table for variably-saturated flow without permafrost after 1,800 years

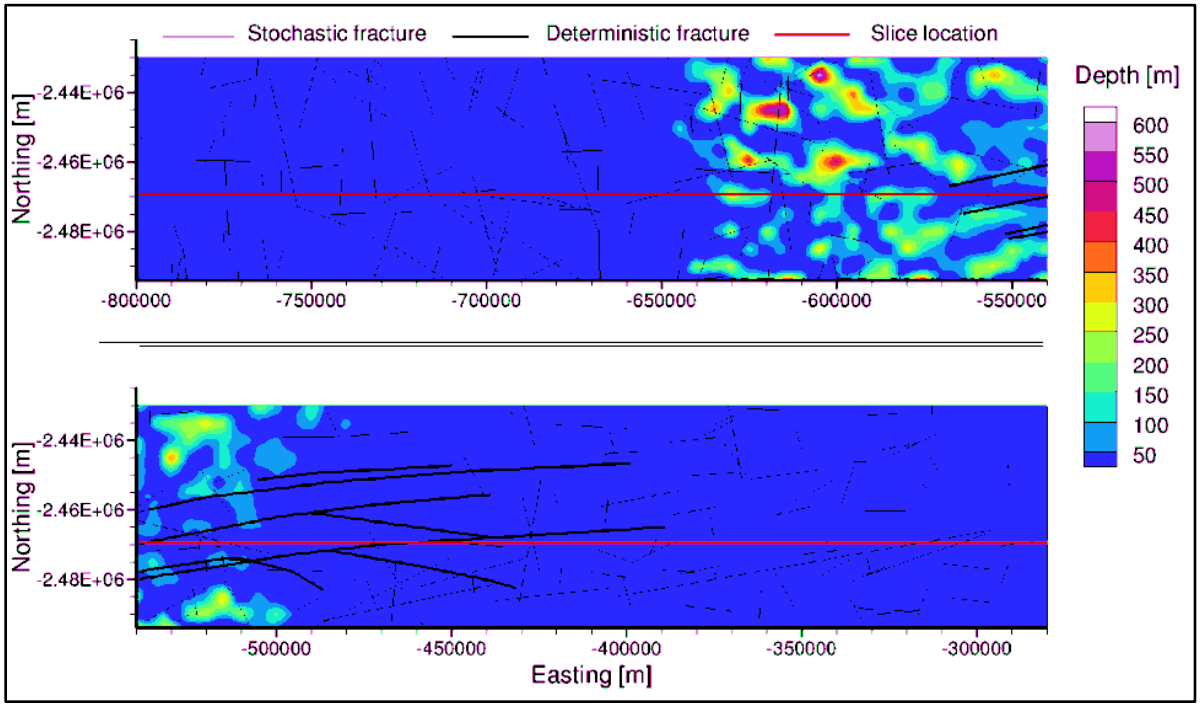

Figure C.29 Areal view of the depth to water table for variably-saturated flow without permafrost after 2,000 years

C.4 Depth to Water Table for Variably-Saturated Flow with Permafrost

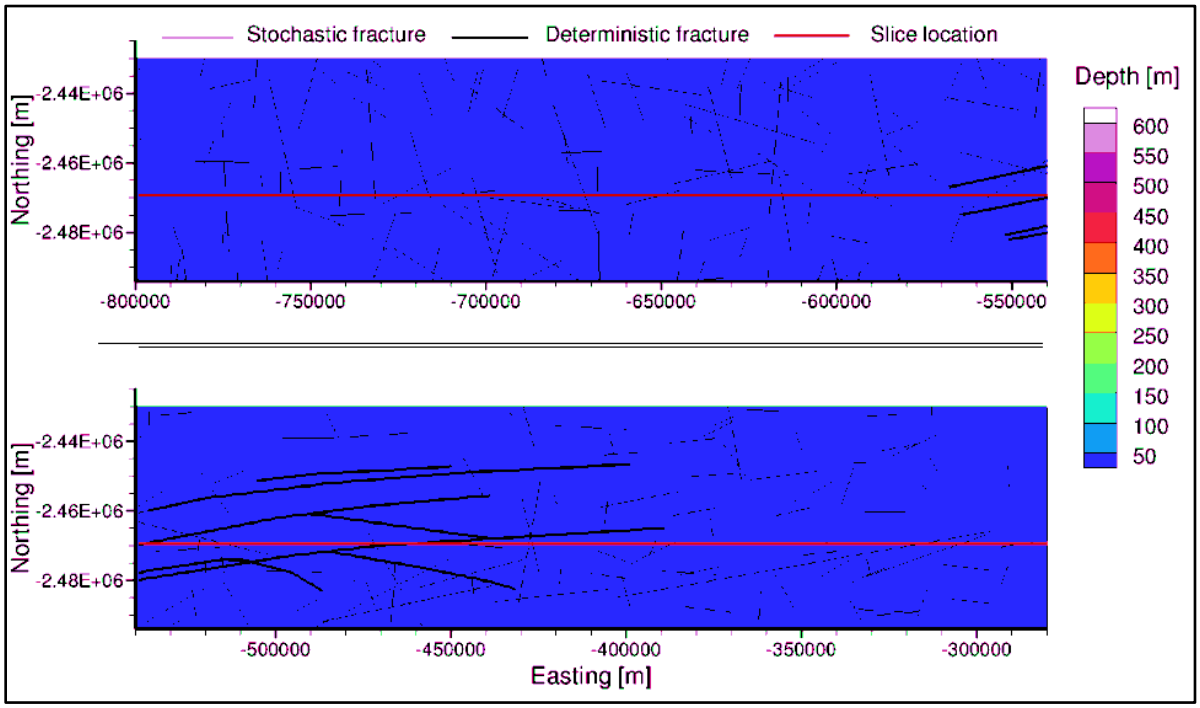

Figure C.30 Areal view of the depth to water table for variably-saturated flow with permafrost after 2,000 years

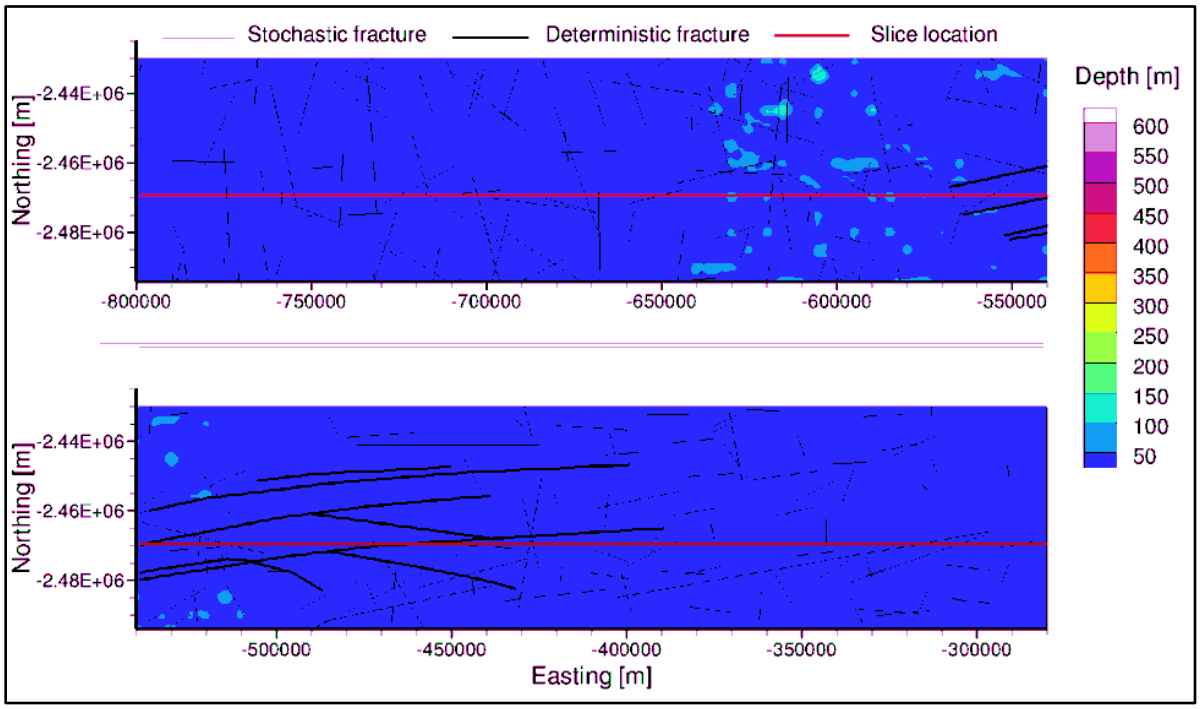

Figure C.31 Areal view of the depth to water table for variably-saturated flow with permafrost after 4,000 years

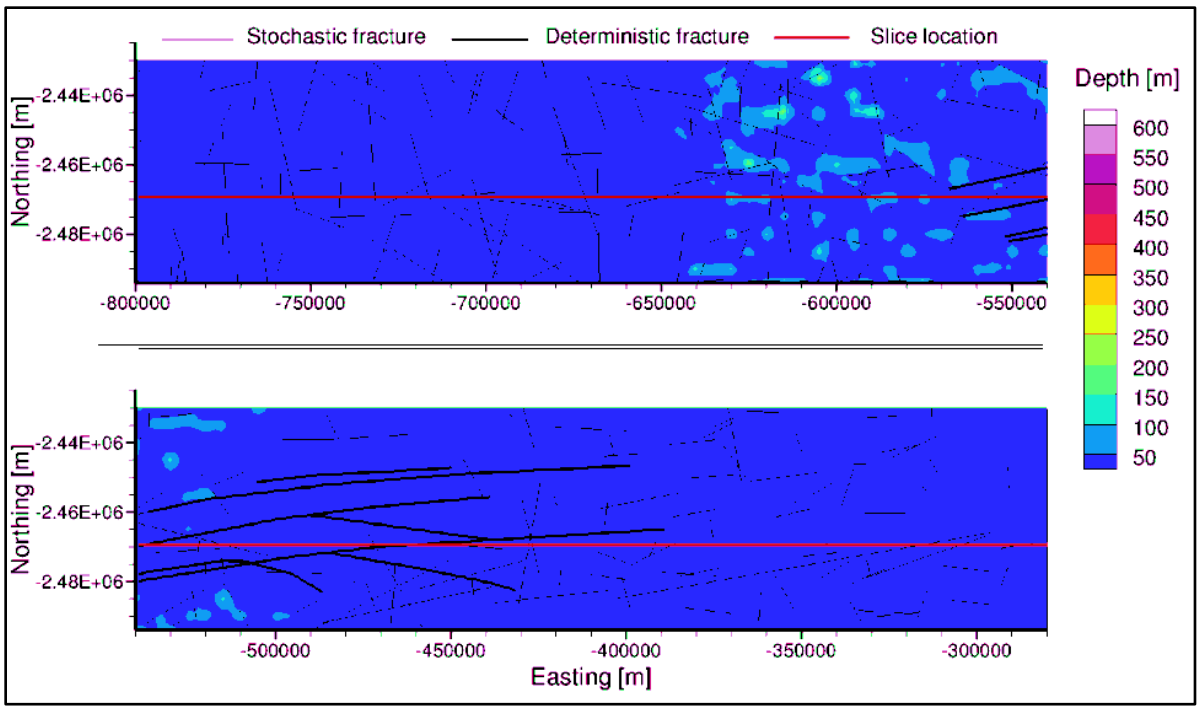

Figure C.32 Areal view of the depth to water table for variably-saturated flow with permafrost after 6,000 years

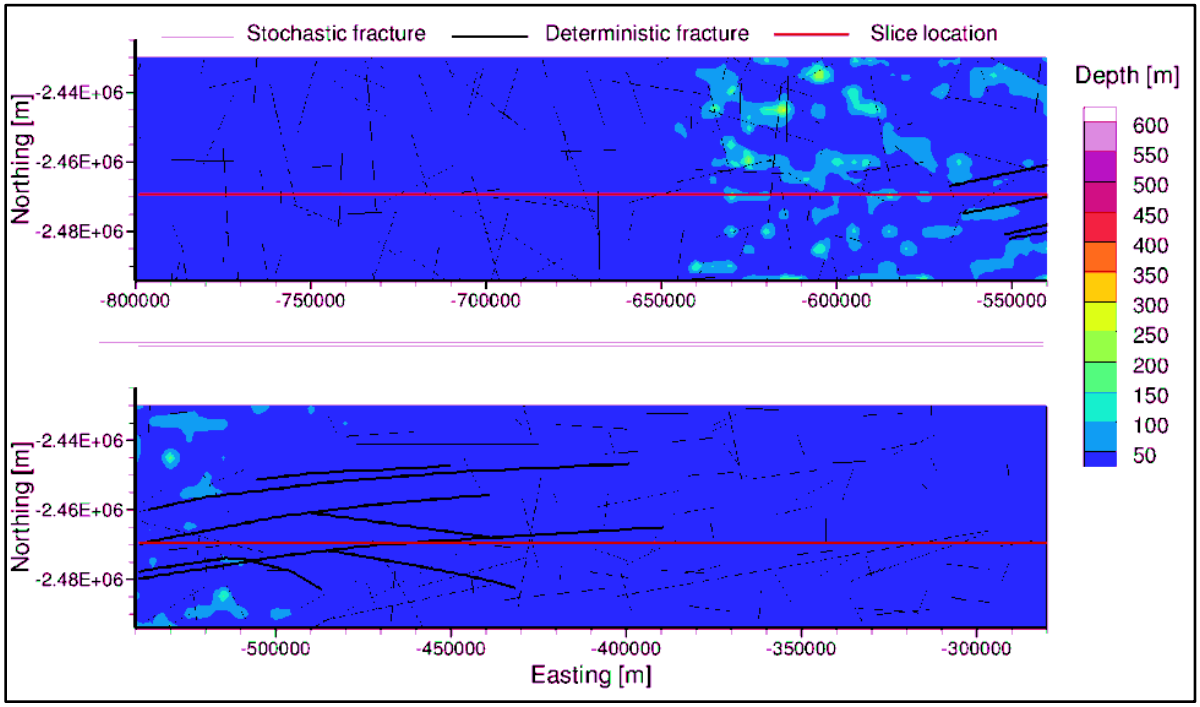

Figure C.33 Areal view of the depth to water table for variably-saturated flow with permafrost after 8,000 years

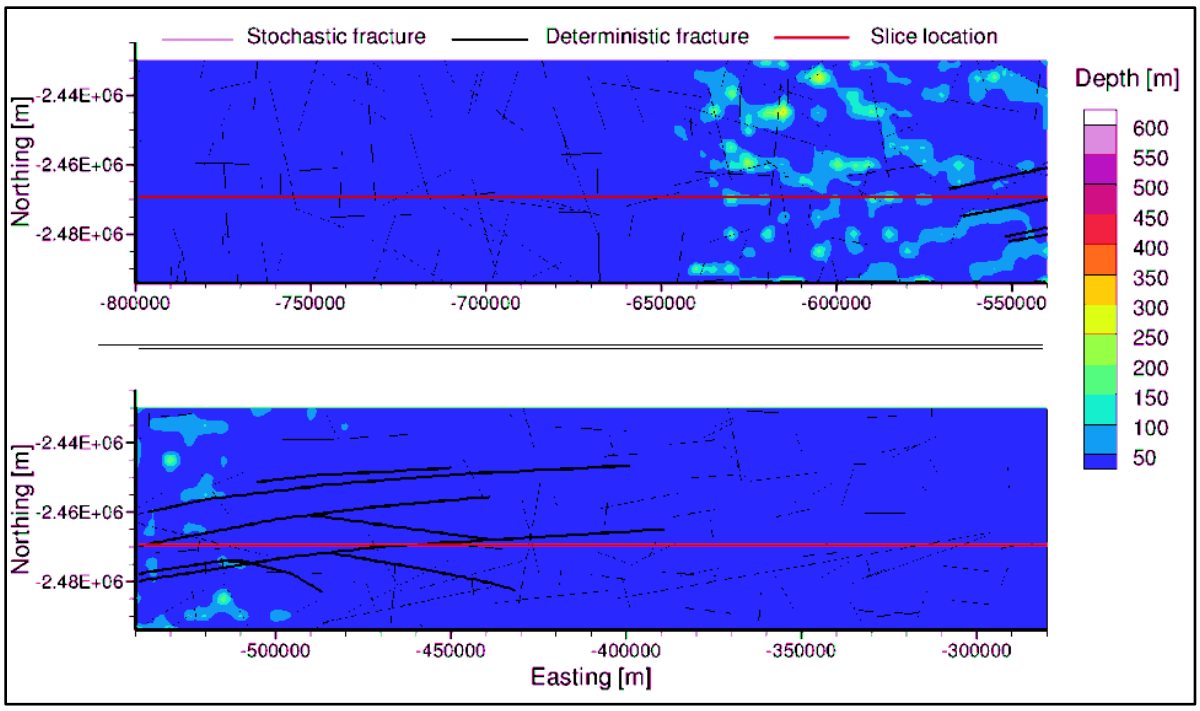

Figure C.34 Areal view of the depth to water table for variably-saturated flow with permafrost after 10,000 years

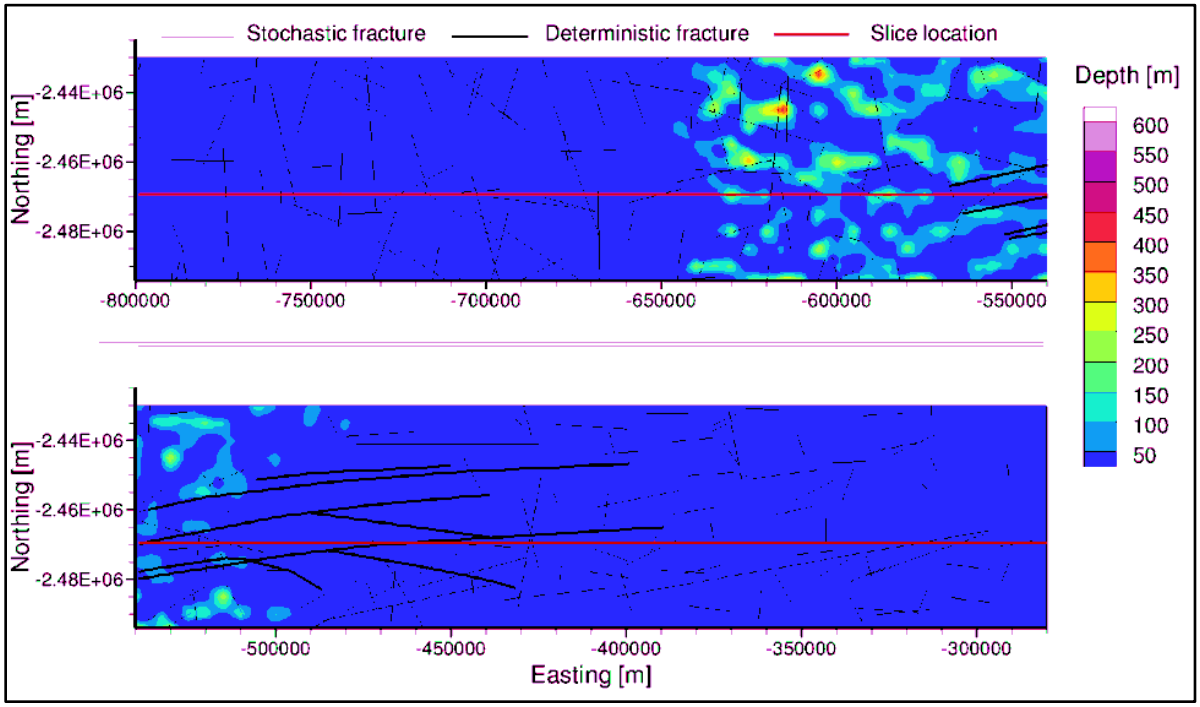

Figure C.35 Areal view of the depth to water table for variably-saturated flow with permafrost after 20,000 years

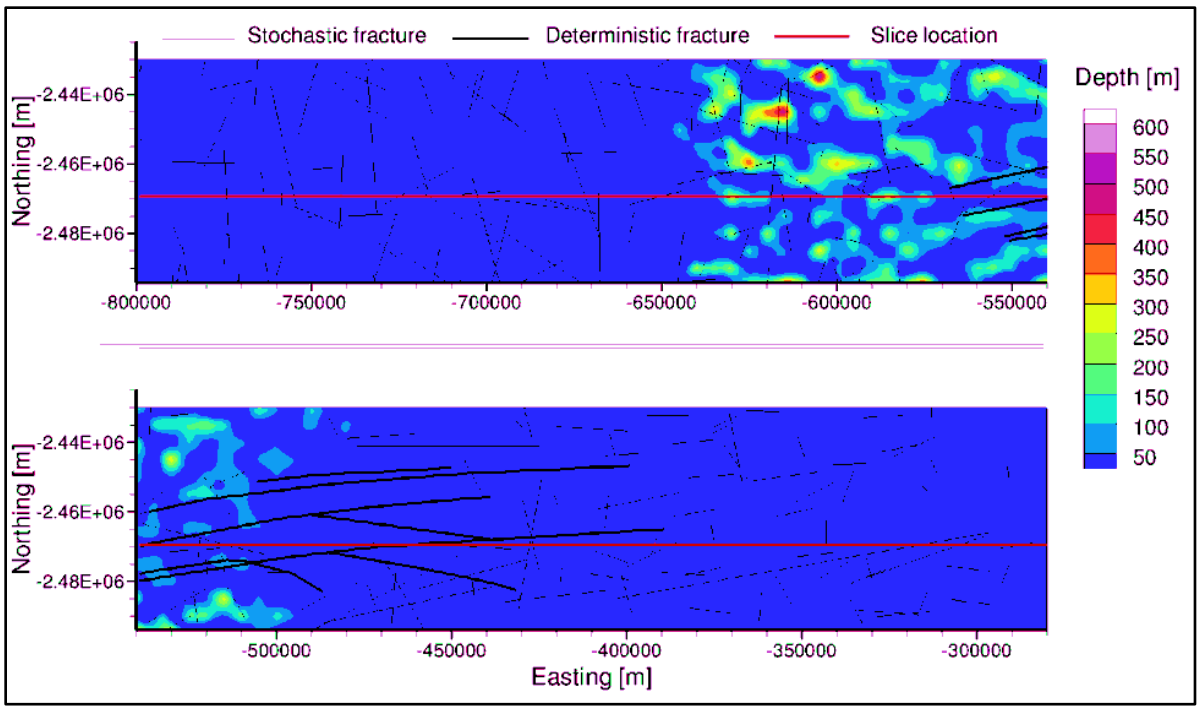

Figure C.36 Areal view of the depth to water table for variably-saturated flow with permafrost after 30,000 years

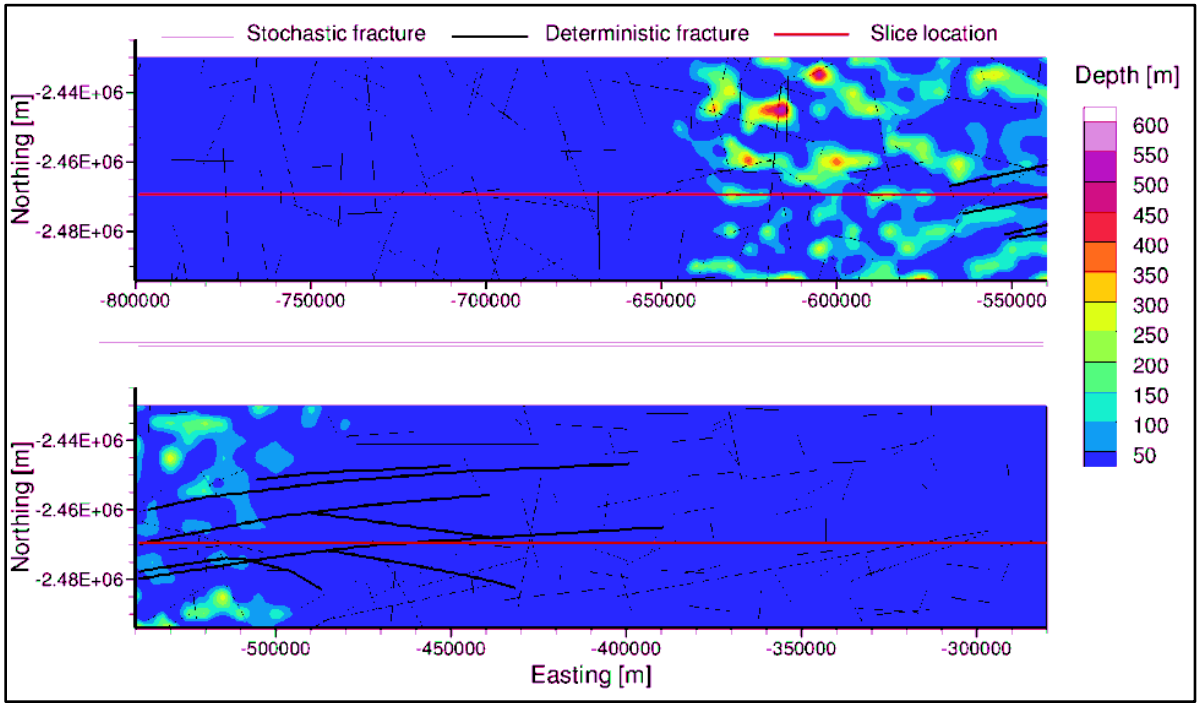

Figure C.37 Areal view of the depth to water table for variably-saturated flow with permafrost after 40,000 years

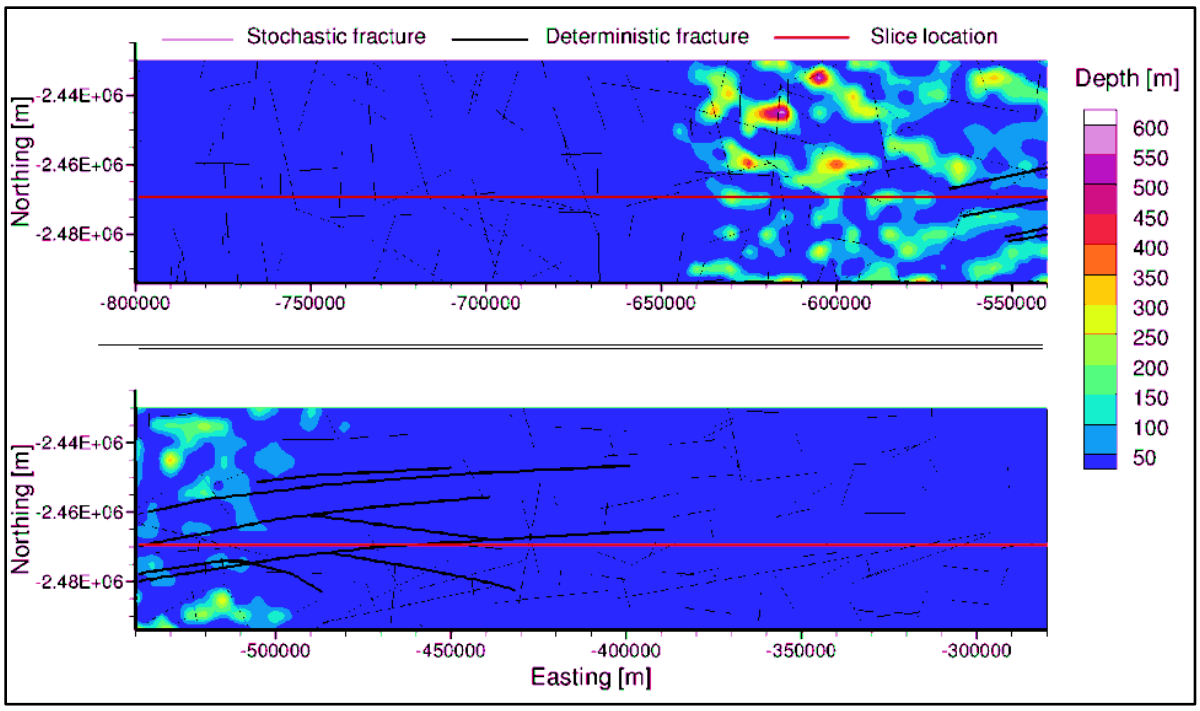

Figure C.38 Areal view of the depth to water table for variably-saturated flow with permafrost after 50,000 years

C.5 Depth to Water Table for Fully-Saturated Flow with Permafrost

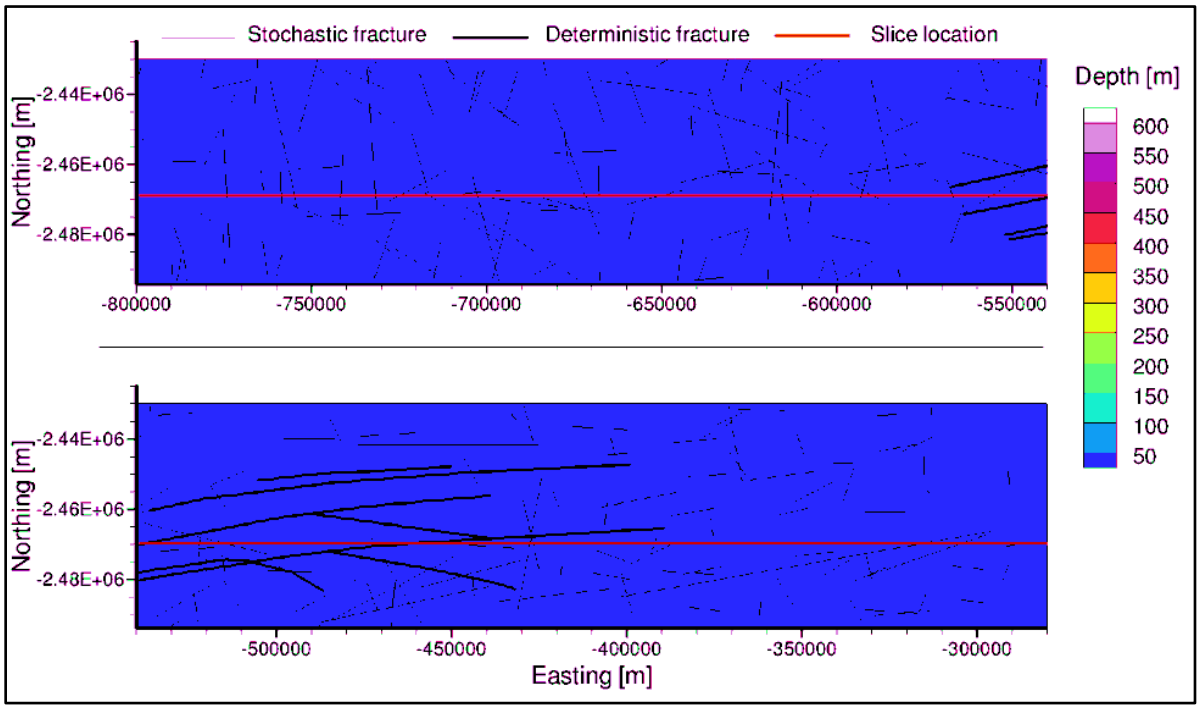

Figure C.39 Areal view of the depth to water table for saturated flow with permafrost after 2,000 years

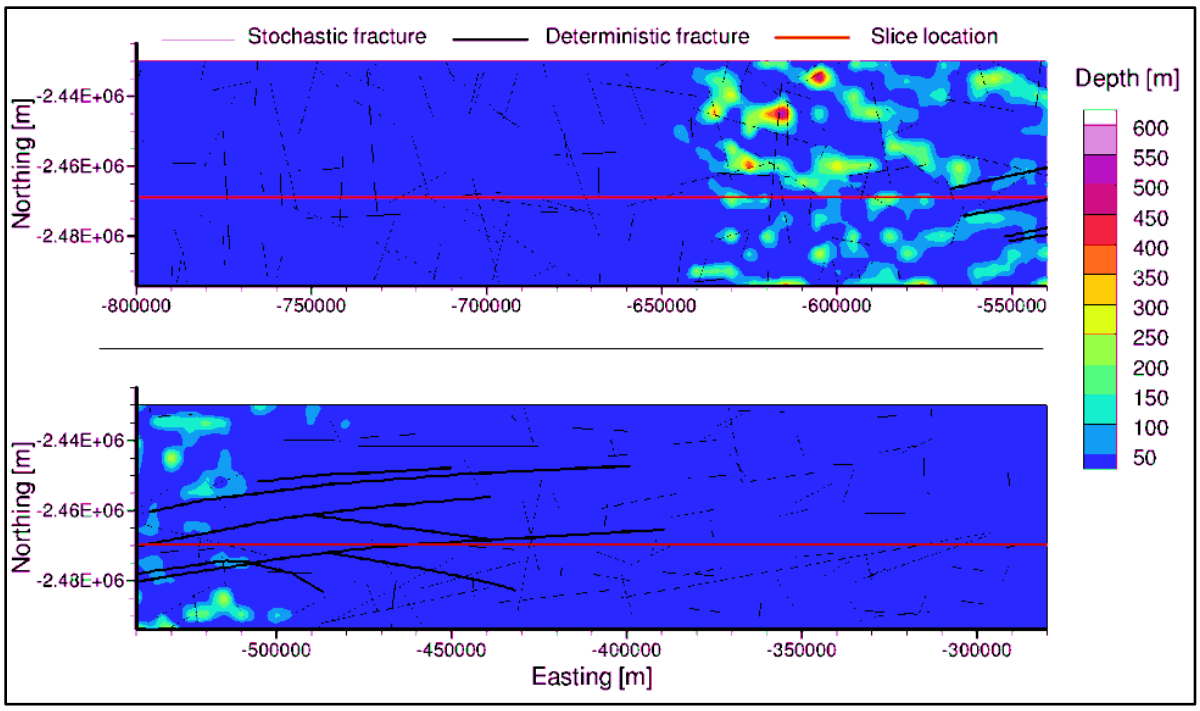

Figure C.40 Areal view of the depth to water table for saturated flow with permafrost after 4,000 years

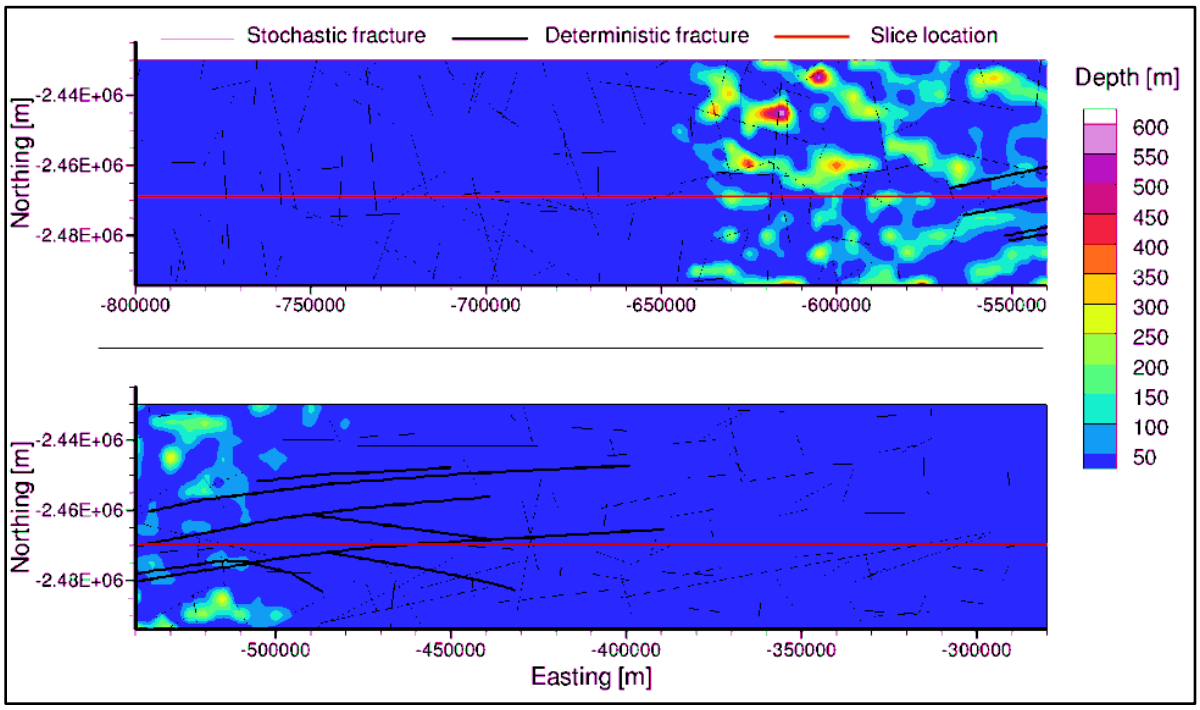

Figure C.41 Areal view of the depth to water table for saturated flow with permafrost after 6,000 years

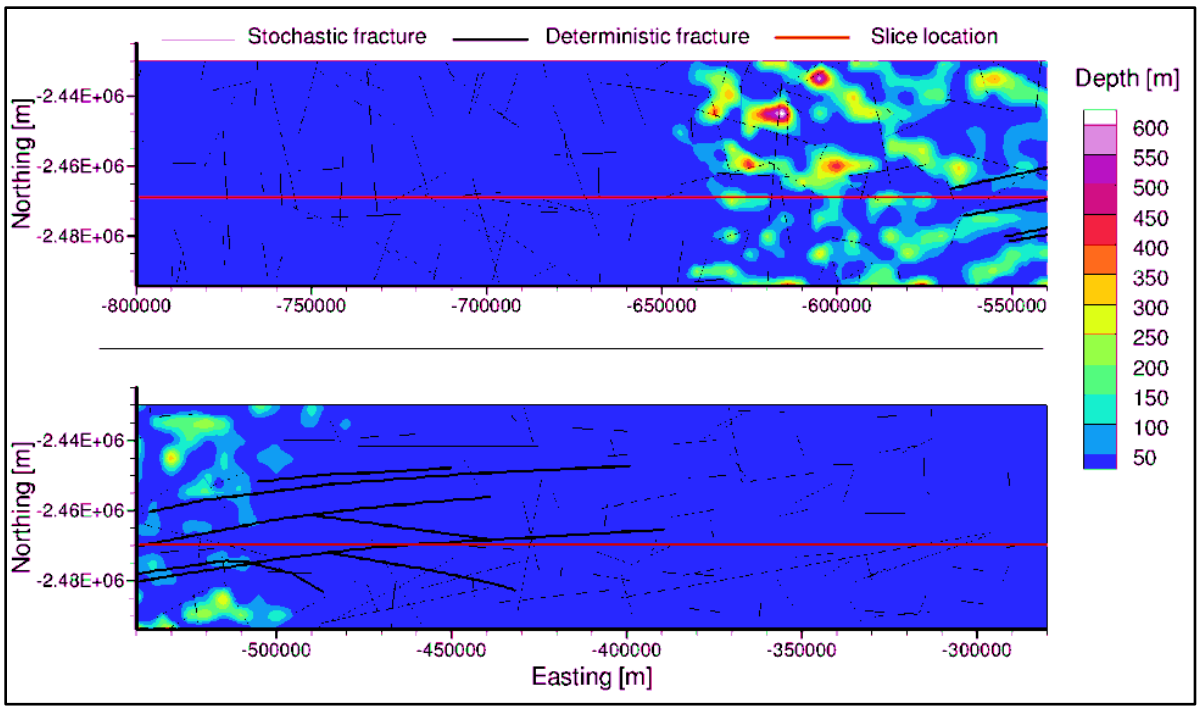

Figure C.42 Areal view of the depth to water table for saturated flow with permafrost after 8,000 years

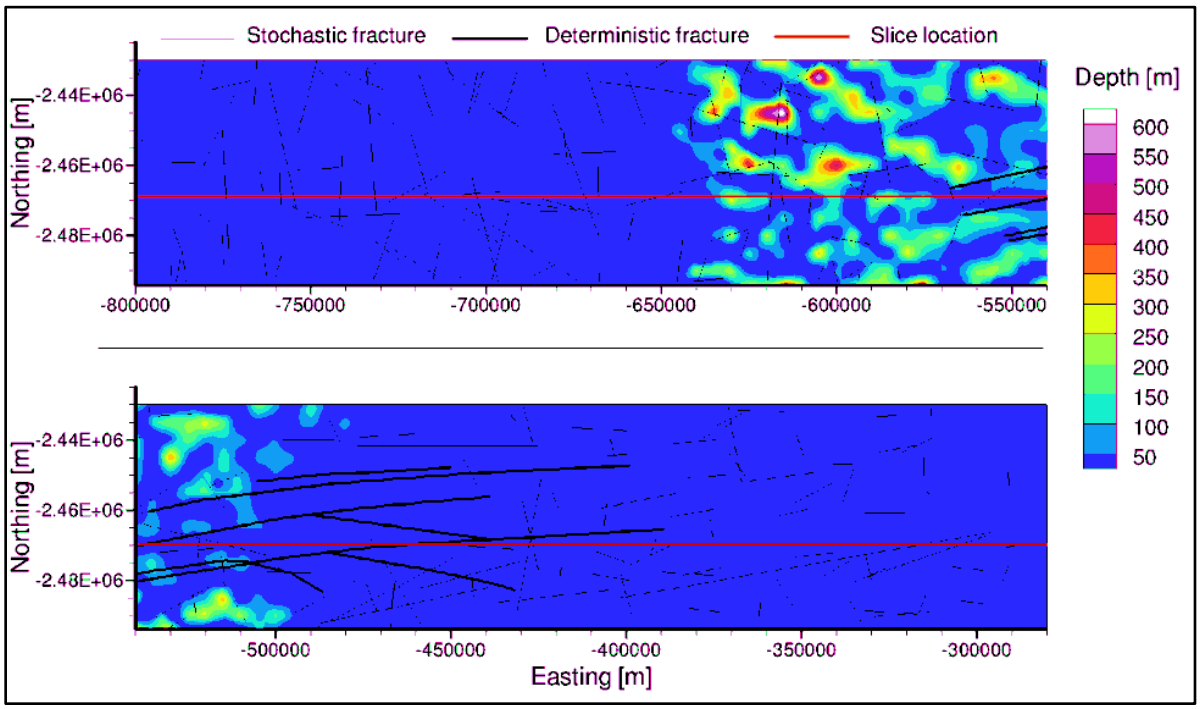

Figure C.43 Areal view of the depth to water table for saturated flow with permafrost after 10,000 years

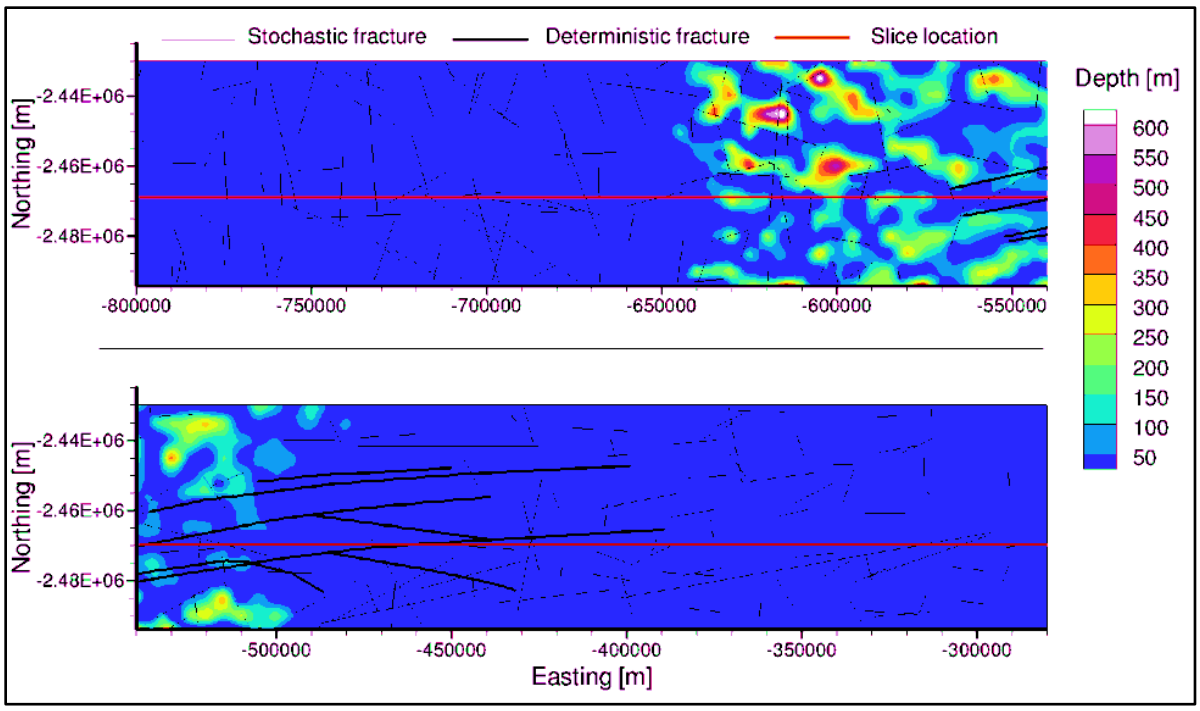

Figure C.44 Areal view of the depth to water table for saturated flow with permafrost after 20,000 years

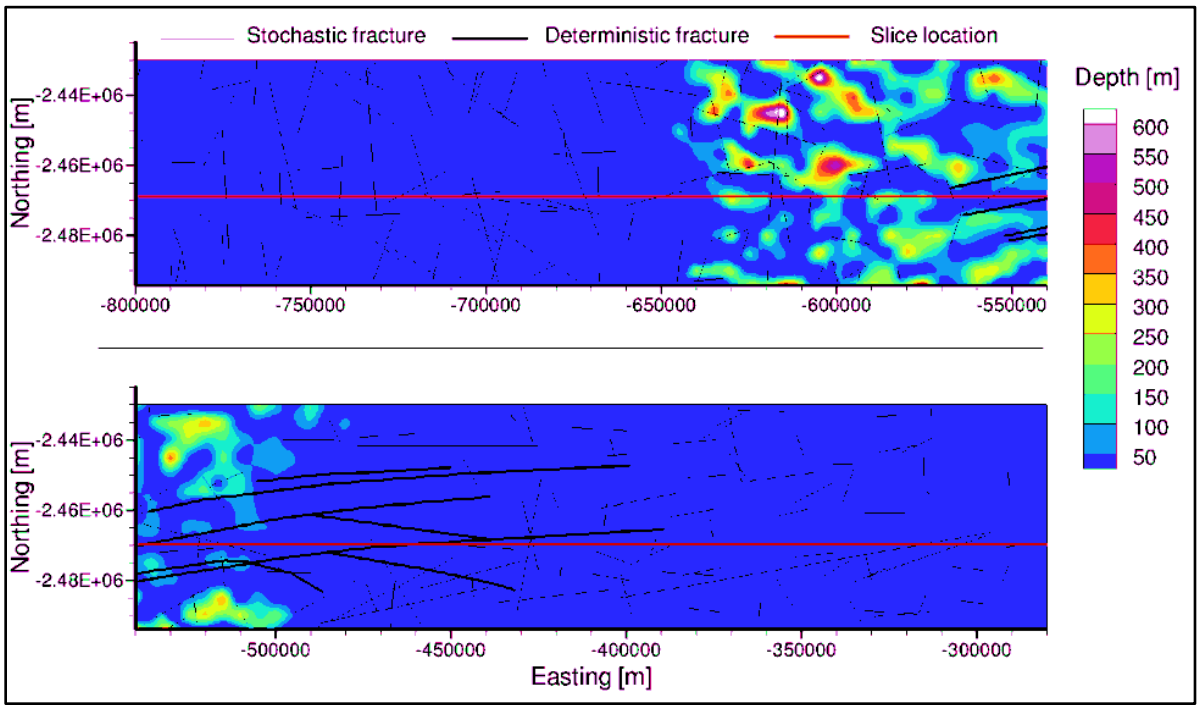

Figure C.45 Areal view of the depth to water table for saturated flow with permafrost after 30,000 years

C.6 Velocity Magnitude Distribution for Variably-Saturated Flow without Permafrost

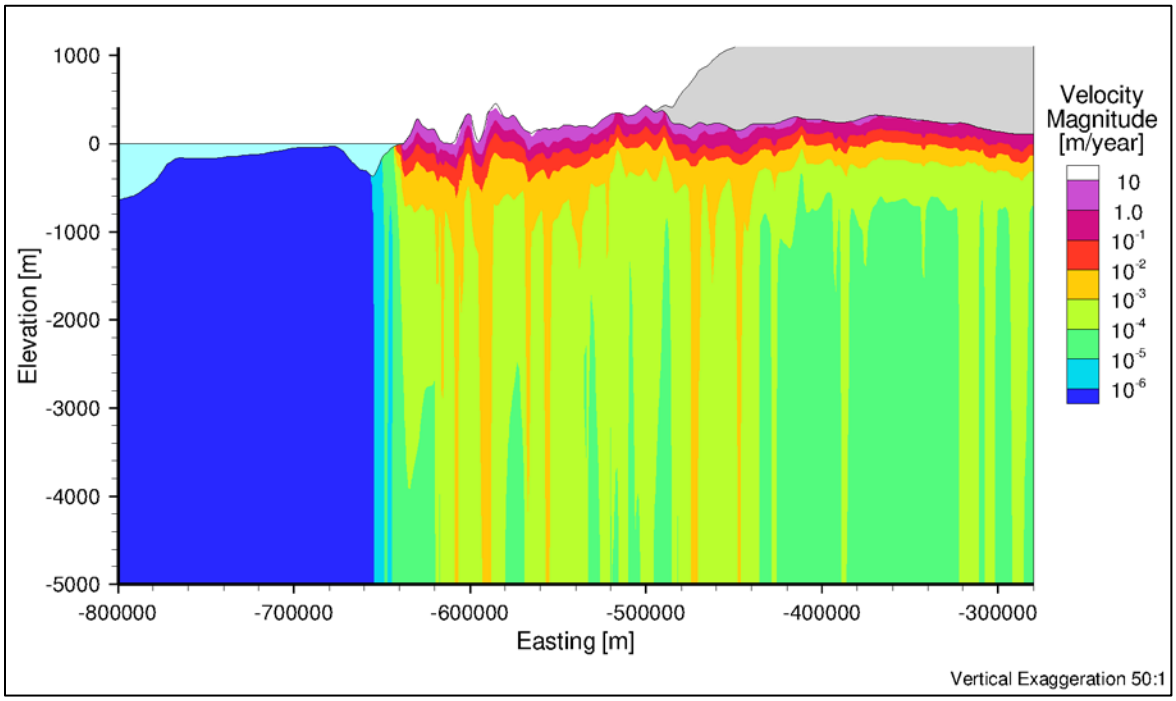

Figure C.46 West-East cross-section of velocity magnitude distribution for variably-saturated flow without permafrost after 200 years

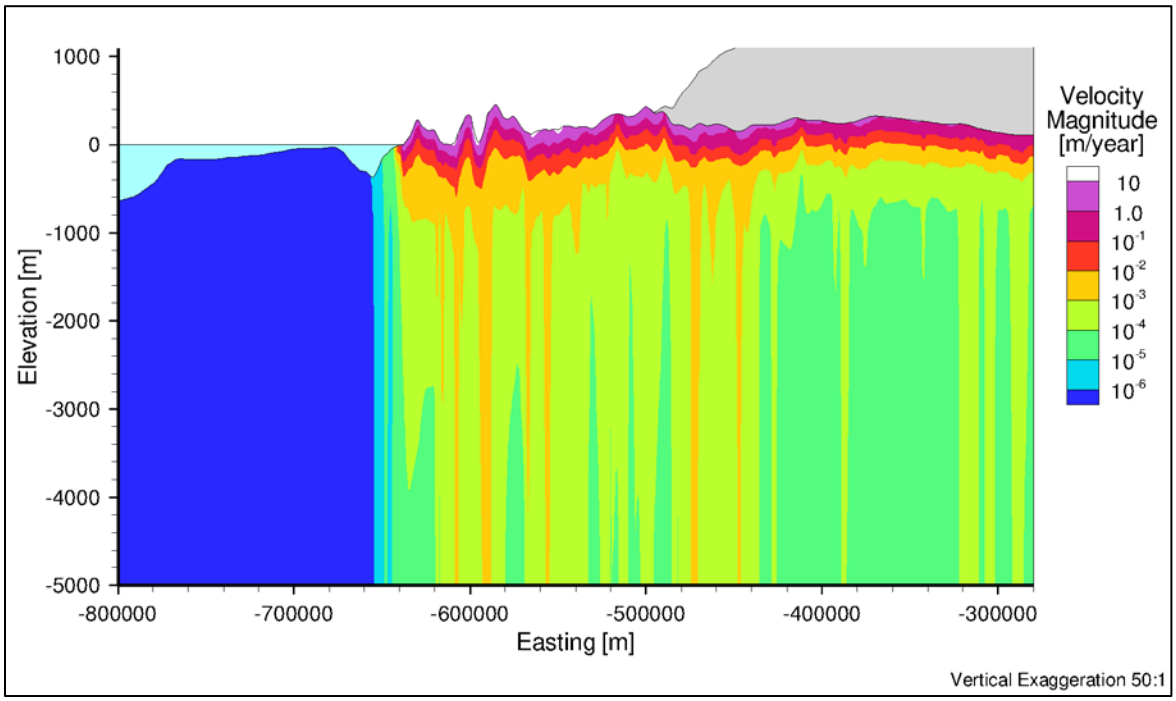

Figure C.47 West-East cross-section of velocity magnitude distribution for variably-saturated flow without permafrost after 400 years

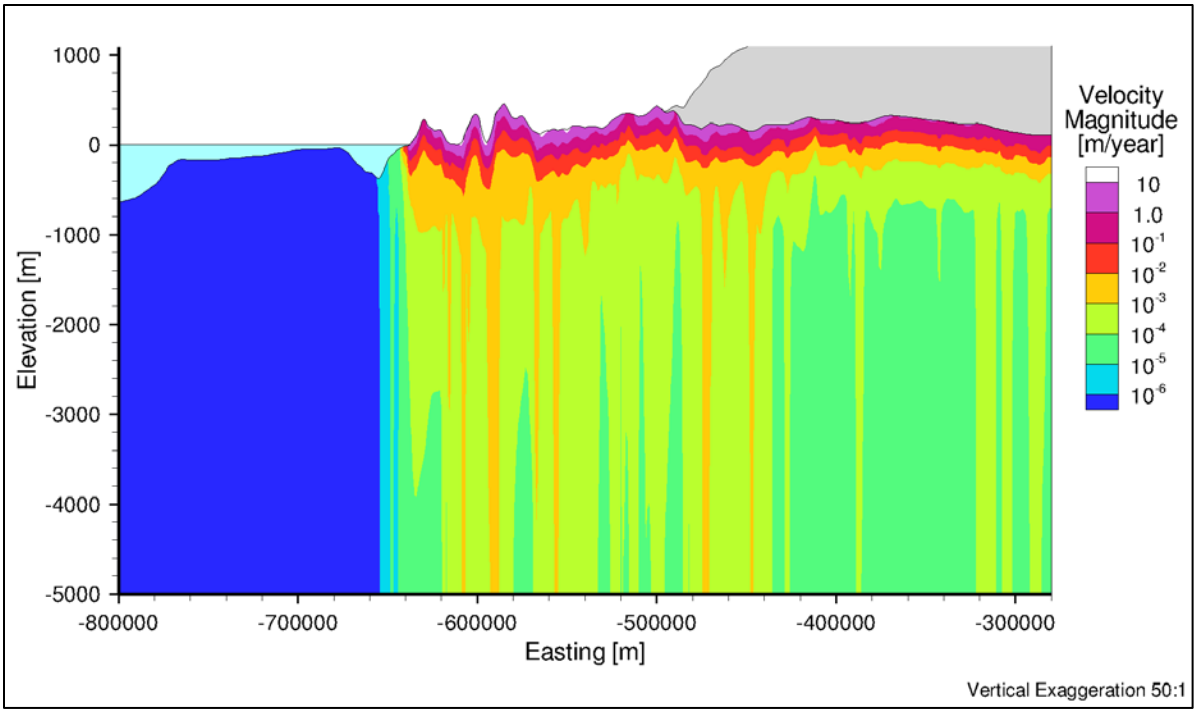

Figure C.48 West-East cross-section of velocity magnitude distribution for variably-saturated flow without permafrost after 600 years

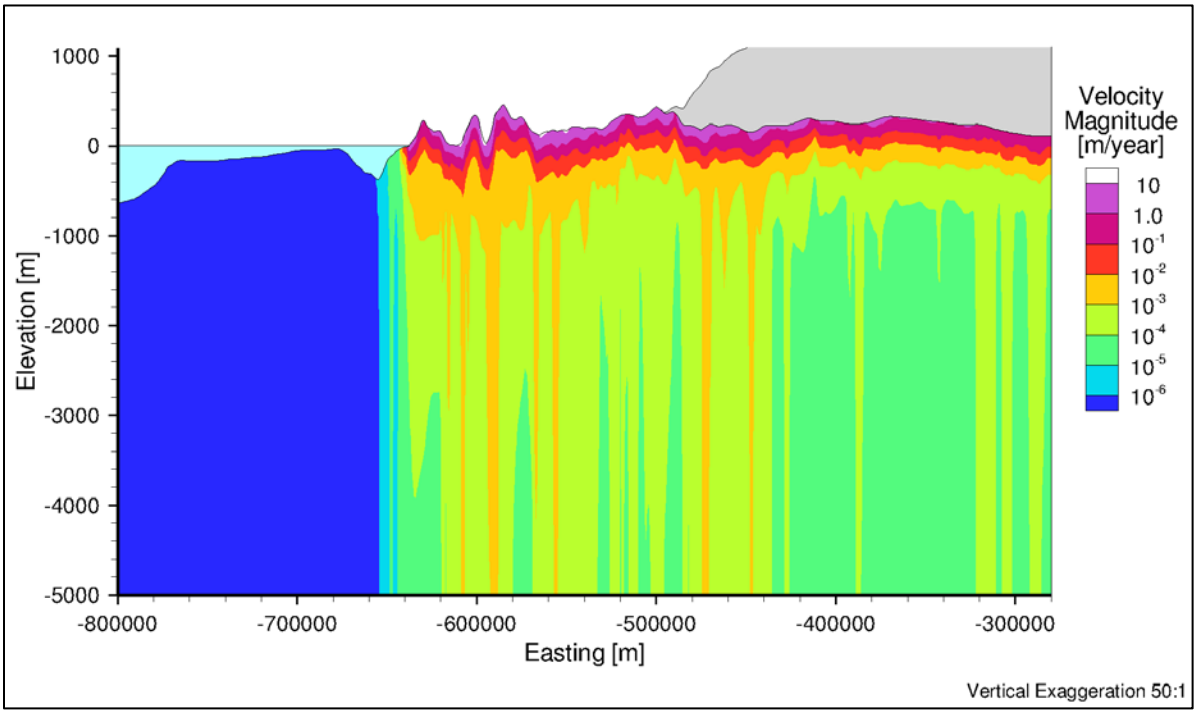

Figure C.49 West-East cross-section of velocity magnitude distribution for variably-saturated flow without permafrost after 800 years

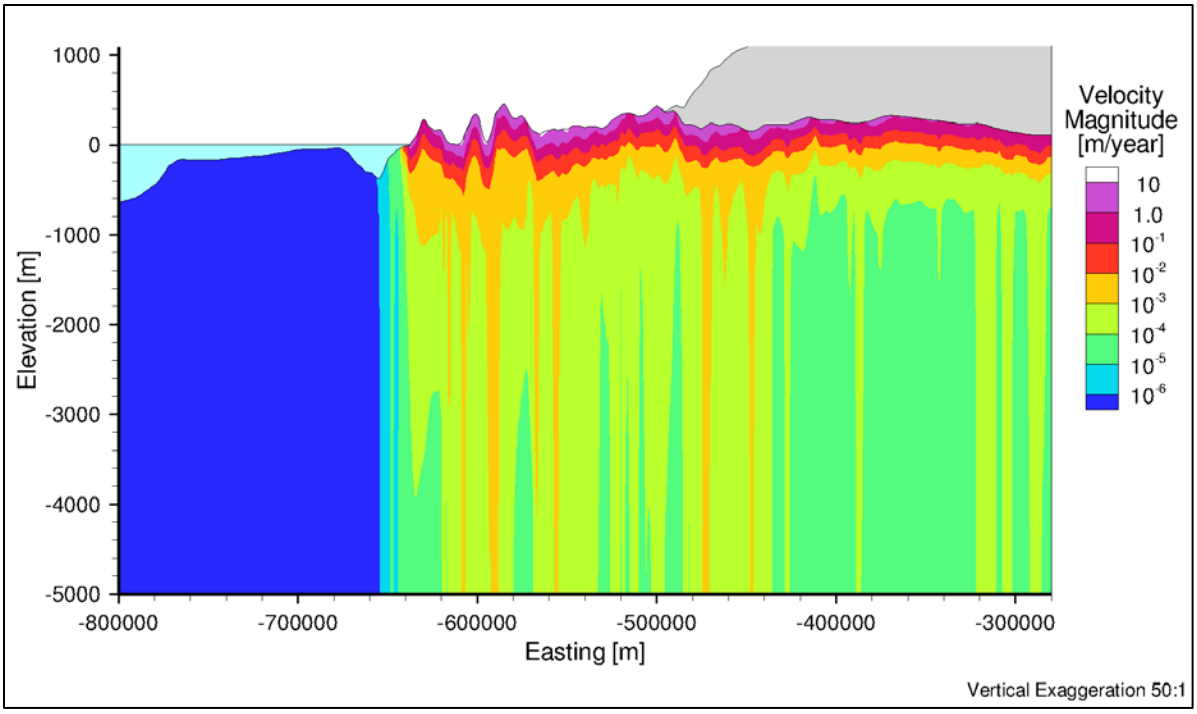

Figure C.50 West-East cross-section of velocity magnitude distribution for variably-saturated flow without permafrost after 1,000 years

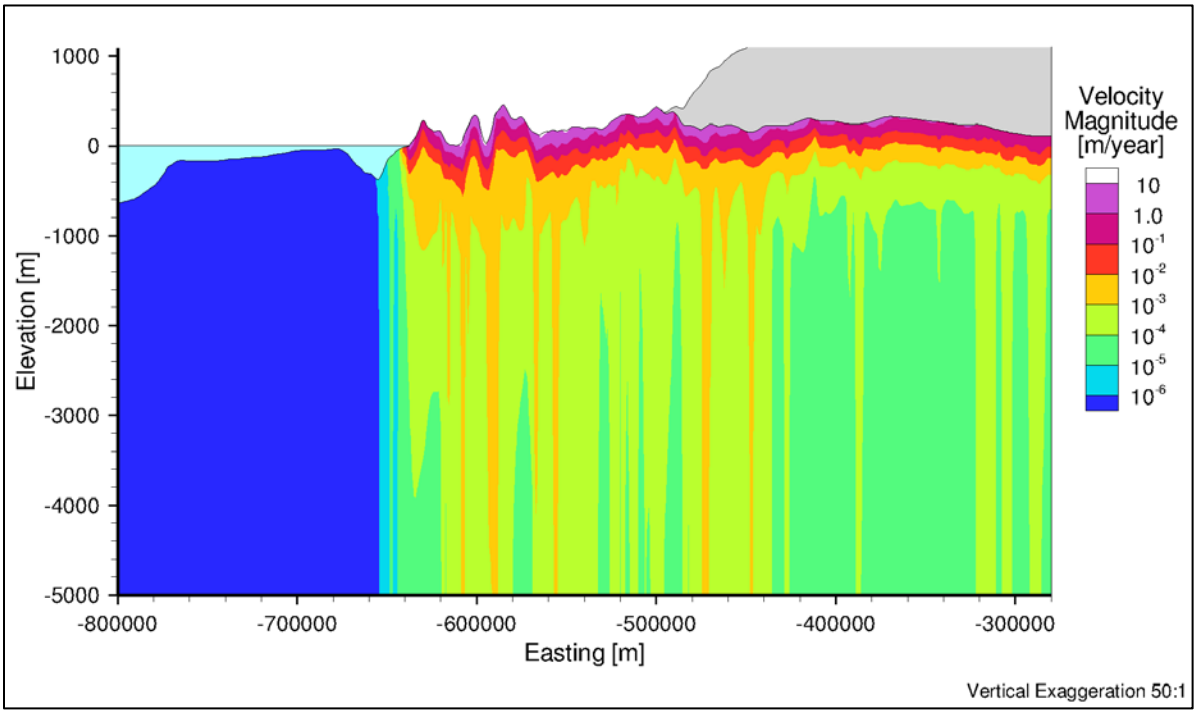

Figure C.51 West-East cross-section of freshwater head distribution for variably-saturated flow without permafrost after 1,200 years

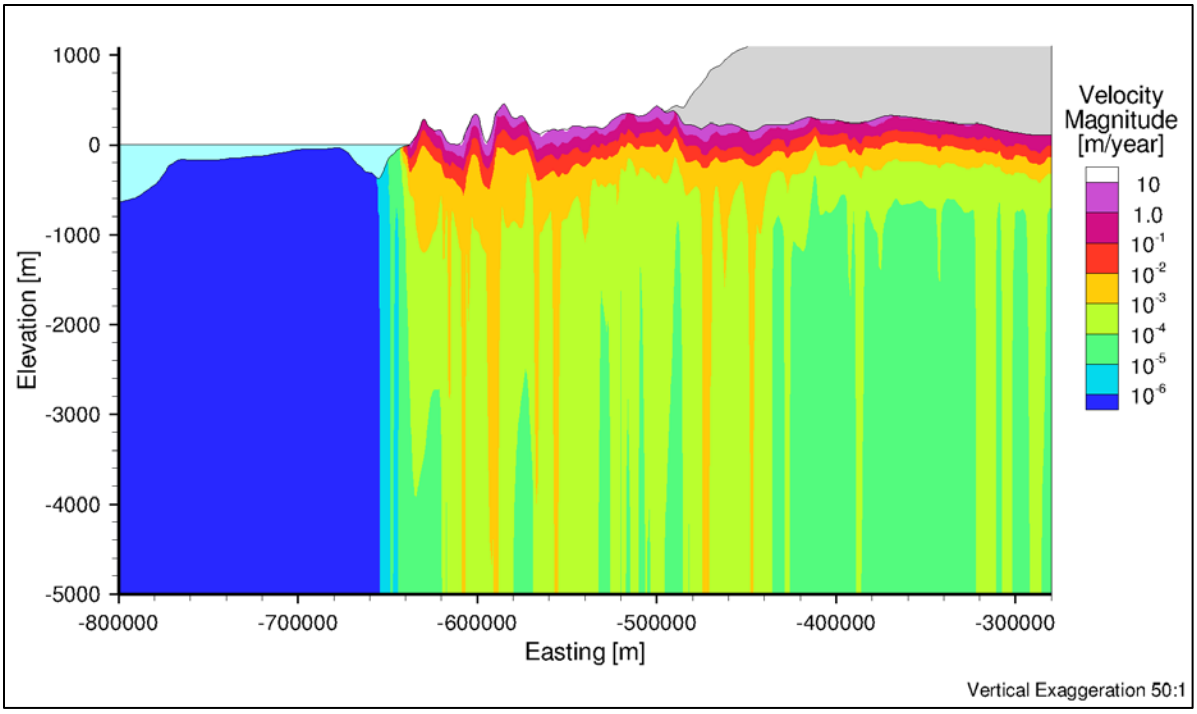

Figure C.52 West-East cross-section of velocity magnitude distribution for variably-saturated flow without permafrost after 1,400 years

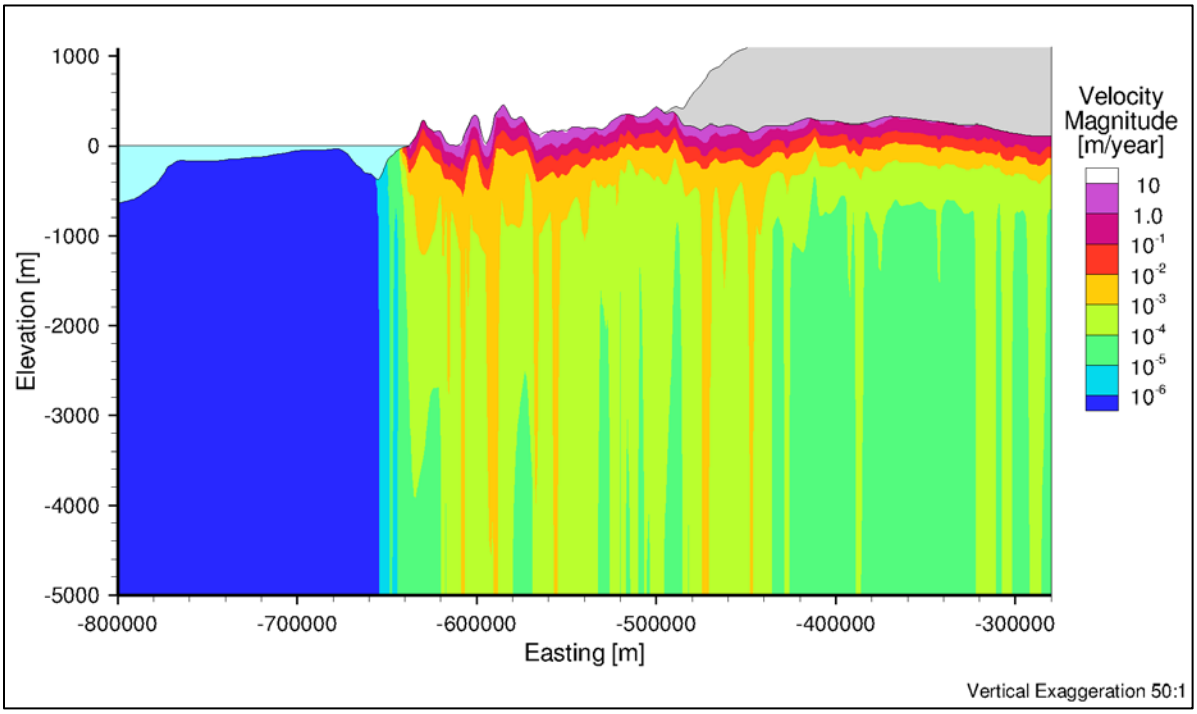

Figure C.53 West-East cross-section of velocity magnitude distribution for variably-saturated flow without permafrost after 1,600 years

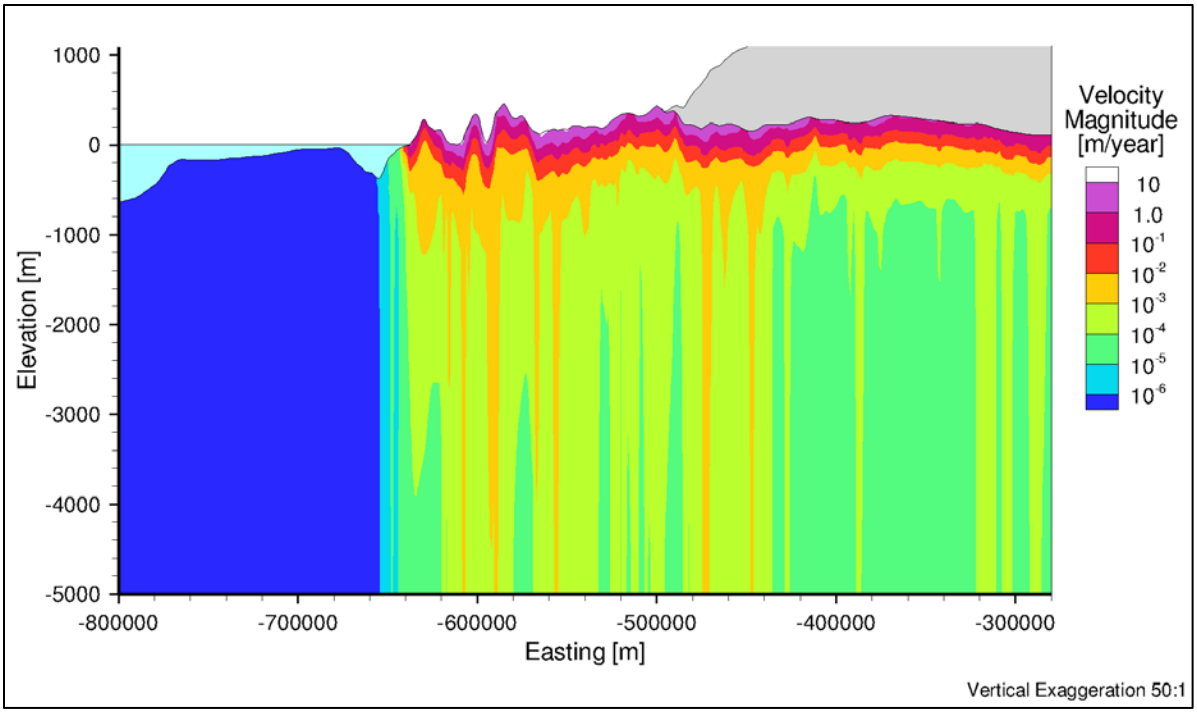

Figure C.54 West-East cross-section of velocity magnitude distribution for variably-saturated flow without permafrost after 1,800 years

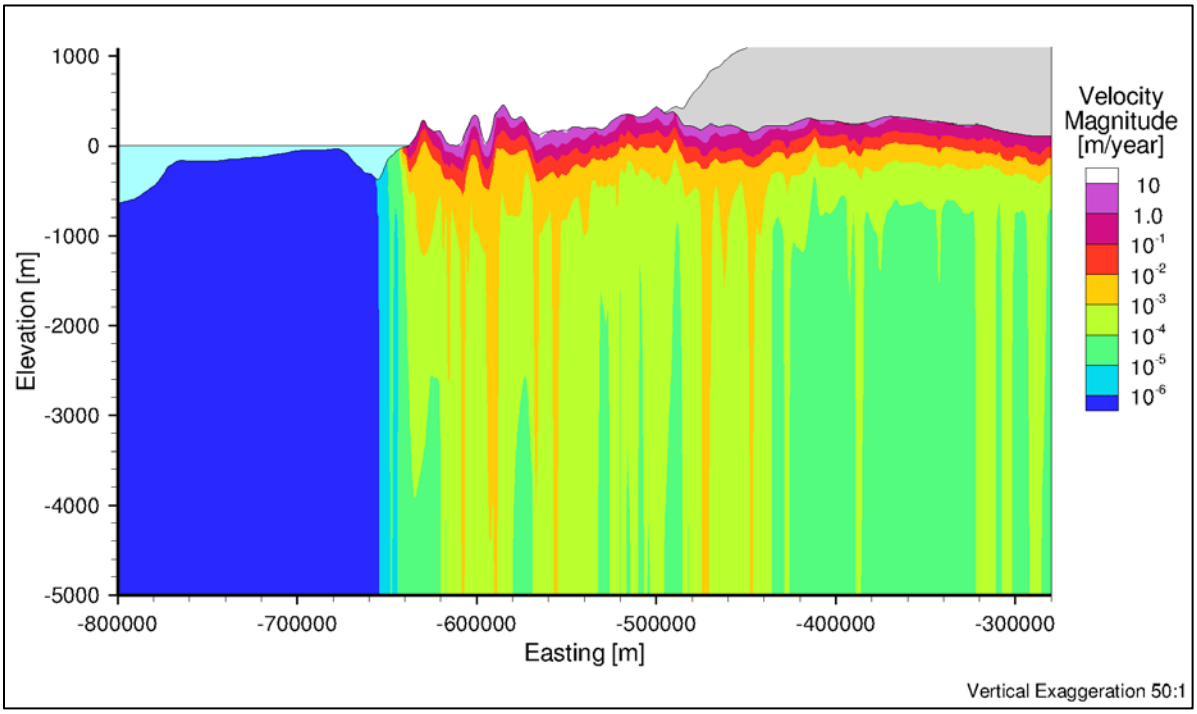

Figure C.55 West-East cross-section of velocity magnitude distribution for variably-saturated flow without permafrost after 2,000 years

C.7 Velocity Magnitude Distribution for Variably-Saturated Flow with Permafrost

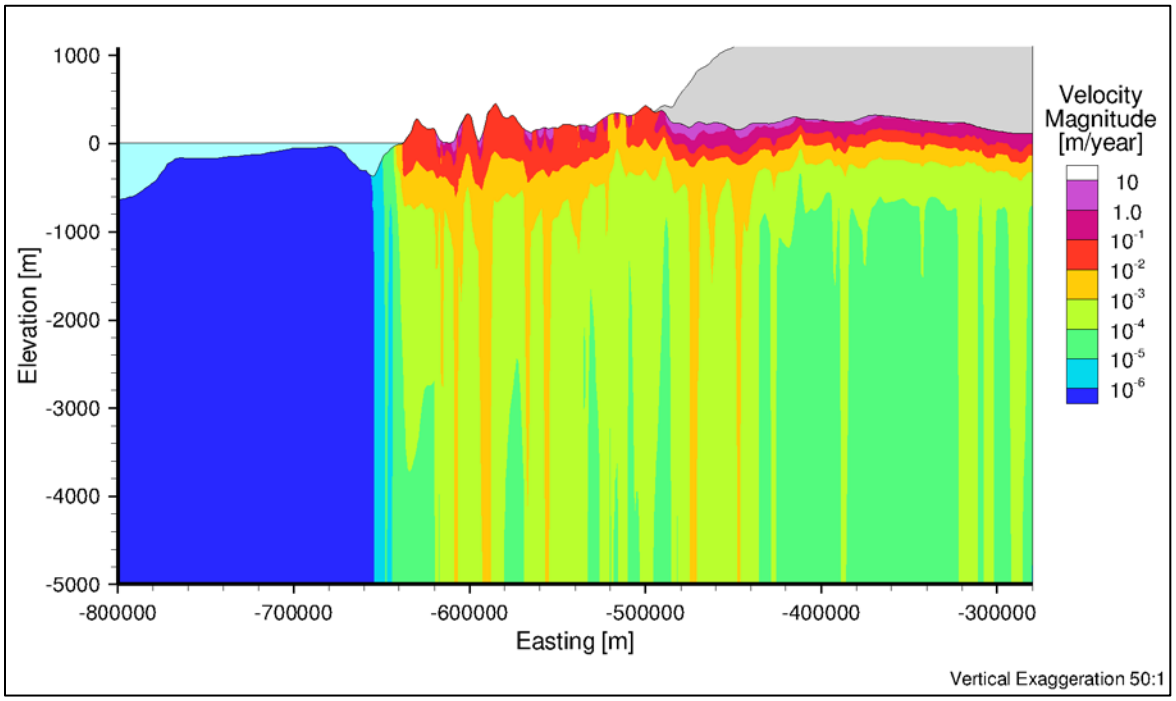

Figure C.56 West-East cross-section of velocity magnitude distribution for variably-saturated flow with permafrost after 2,000 years

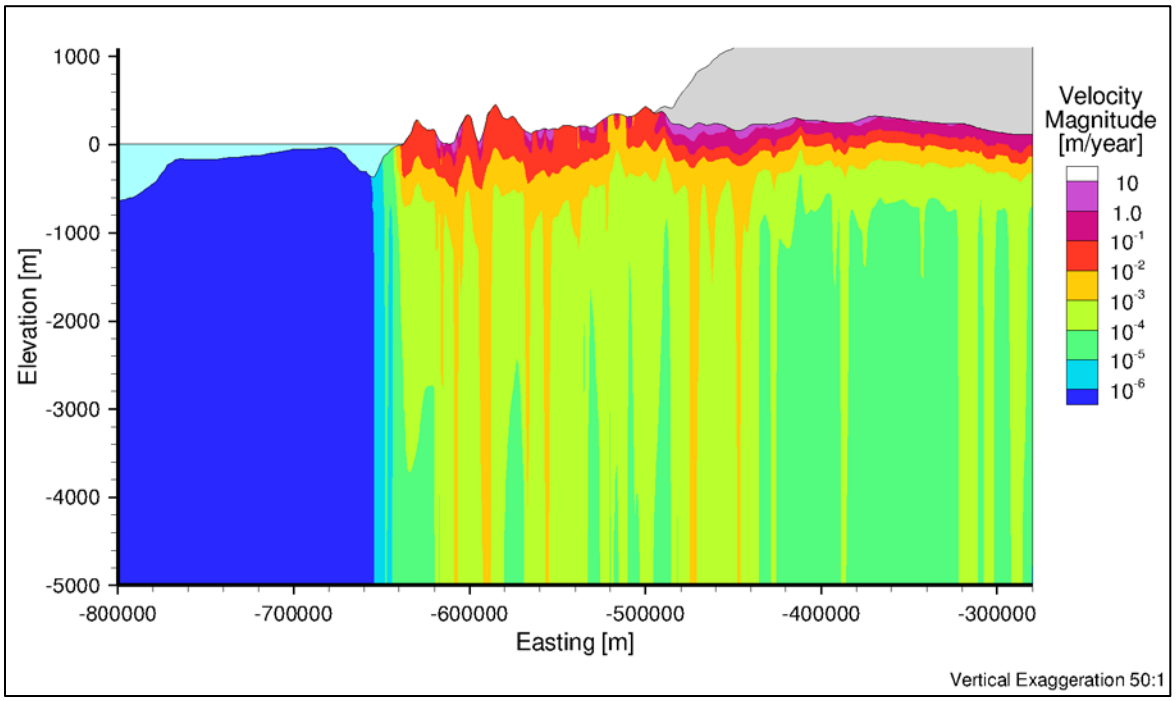

Figure C.57 West-East cross-section of velocity magnitude distribution for variably-saturated flow with permafrost after 4,000 years

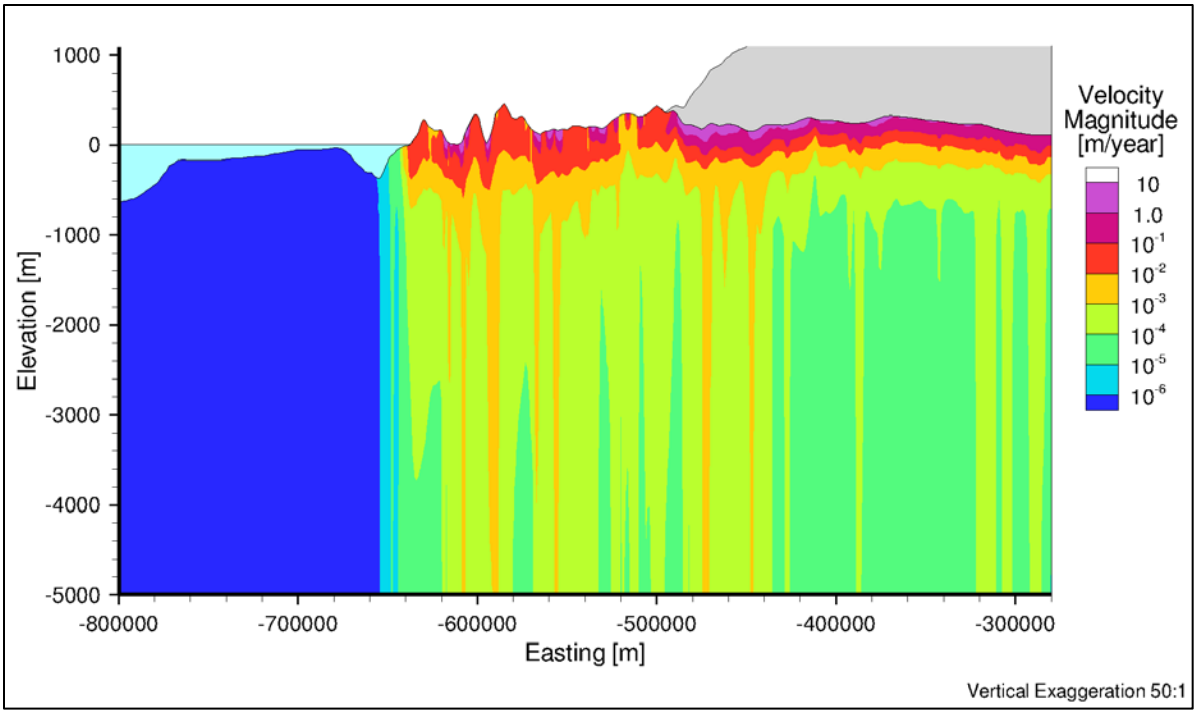

Figure C.58 West-East cross-section of velocity magnitude distribution for variably-saturated flow with permafrost after 6,000 years

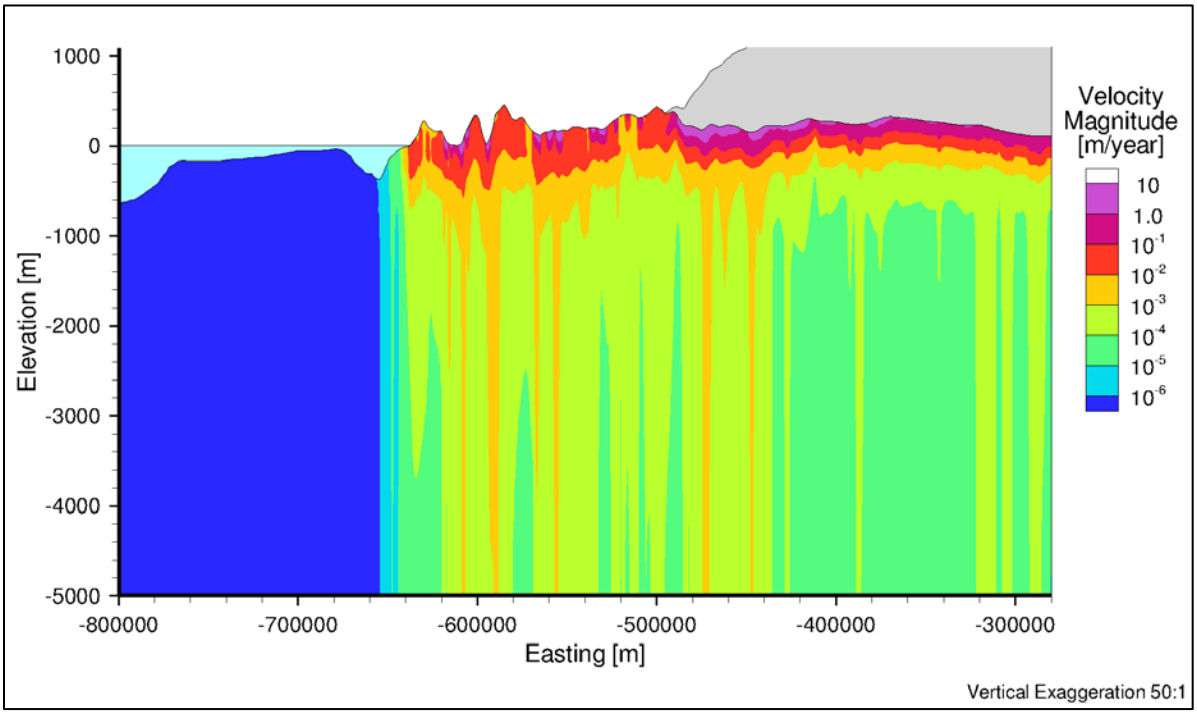

Figure C.59 West-East cross-section of velocity magnitude distribution for variably-saturated flow with permafrost after 8,000 years

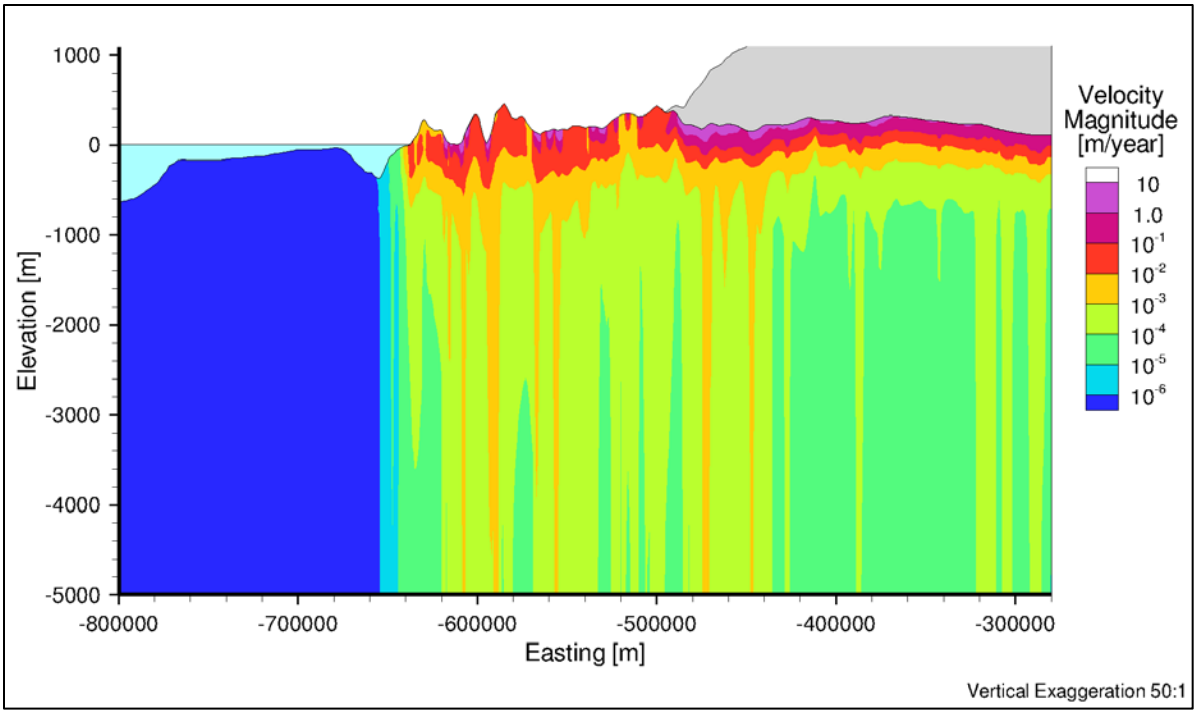

Figure C.60 West-East cross-section of velocity magnitude distribution for variably-saturated flow with permafrost after 10,000 years

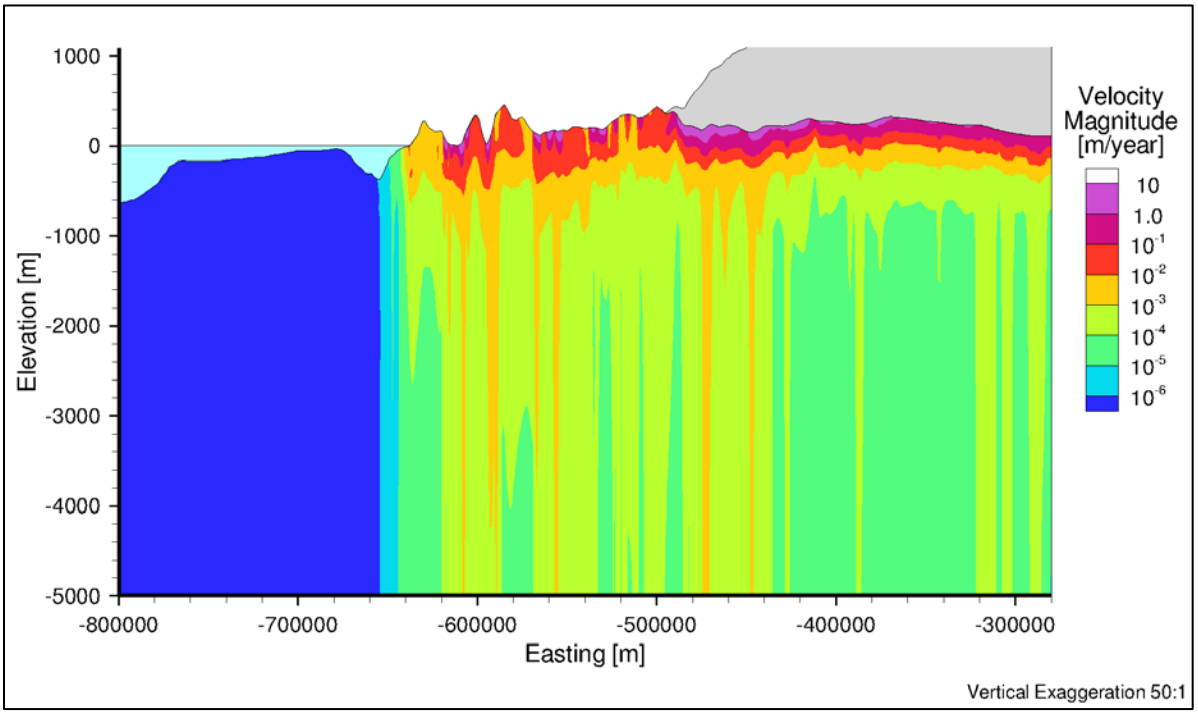

Figure C.61 West-East cross-section of freshwater head distribution for variably-saturated flow with permafrost after 20,000 years

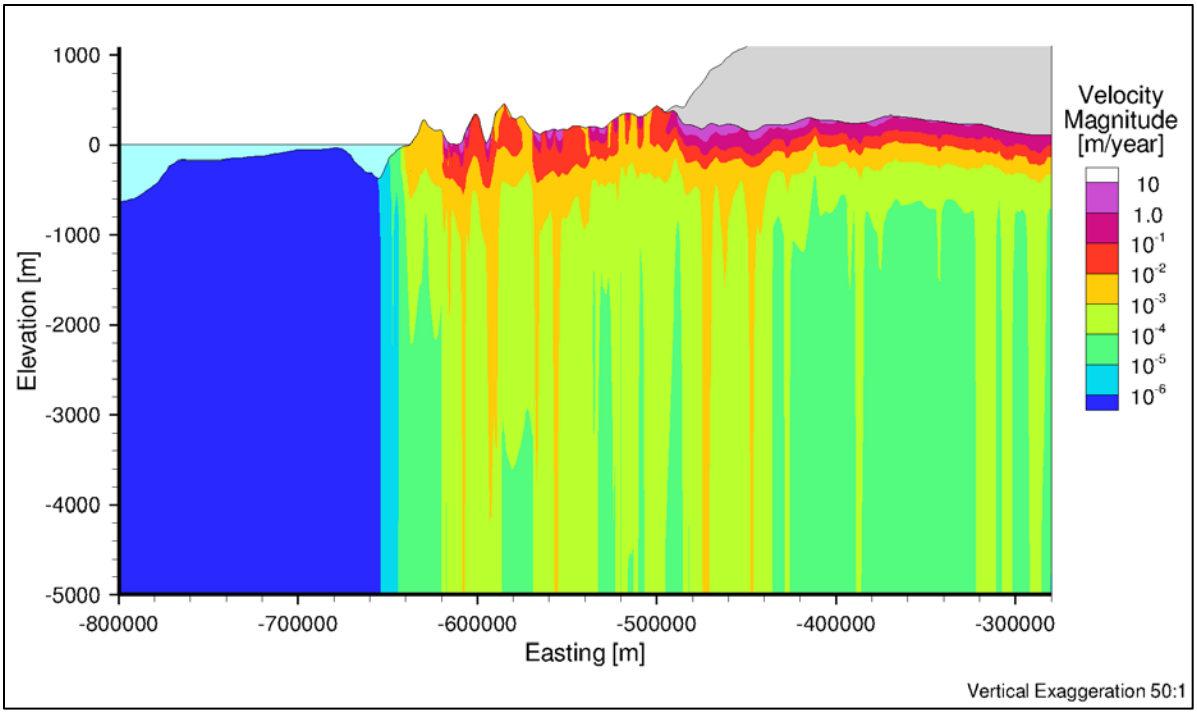

Figure C.62 West-East cross-section of velocity magnitude distribution for variably-saturated flow with permafrost after 30,000 years

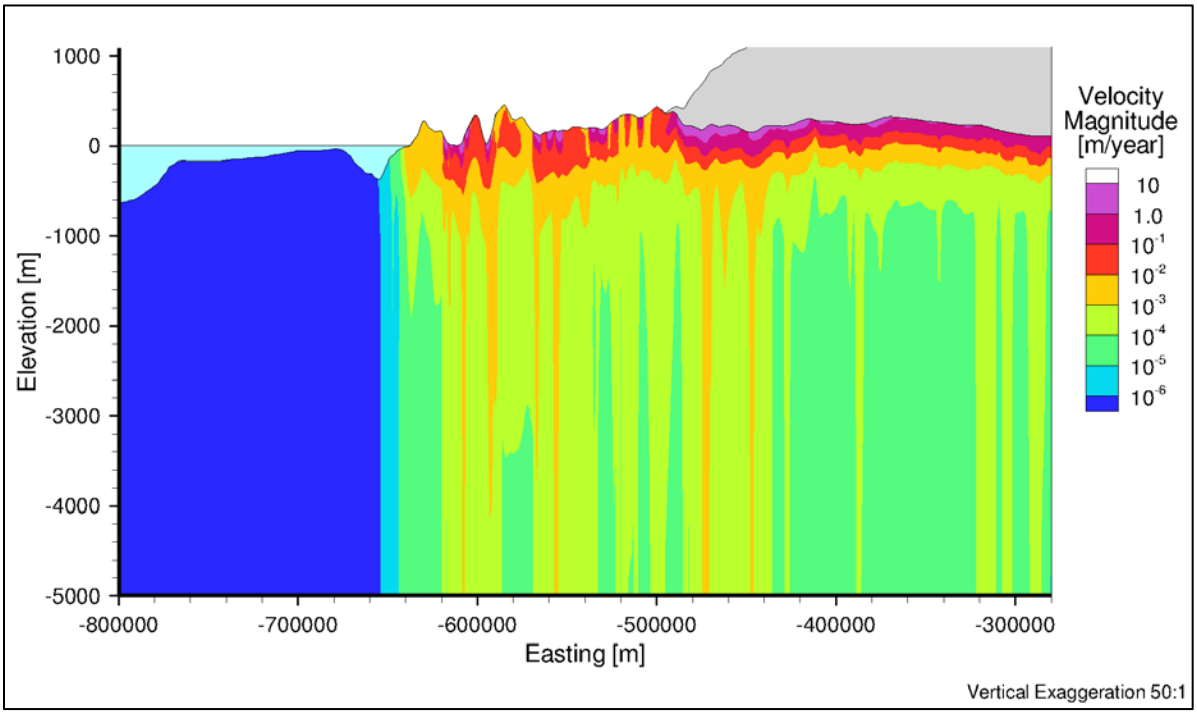

Figure C.63 West-East cross-section of velocity magnitude distribution for variably-saturated flow with permafrost after 40,000 years

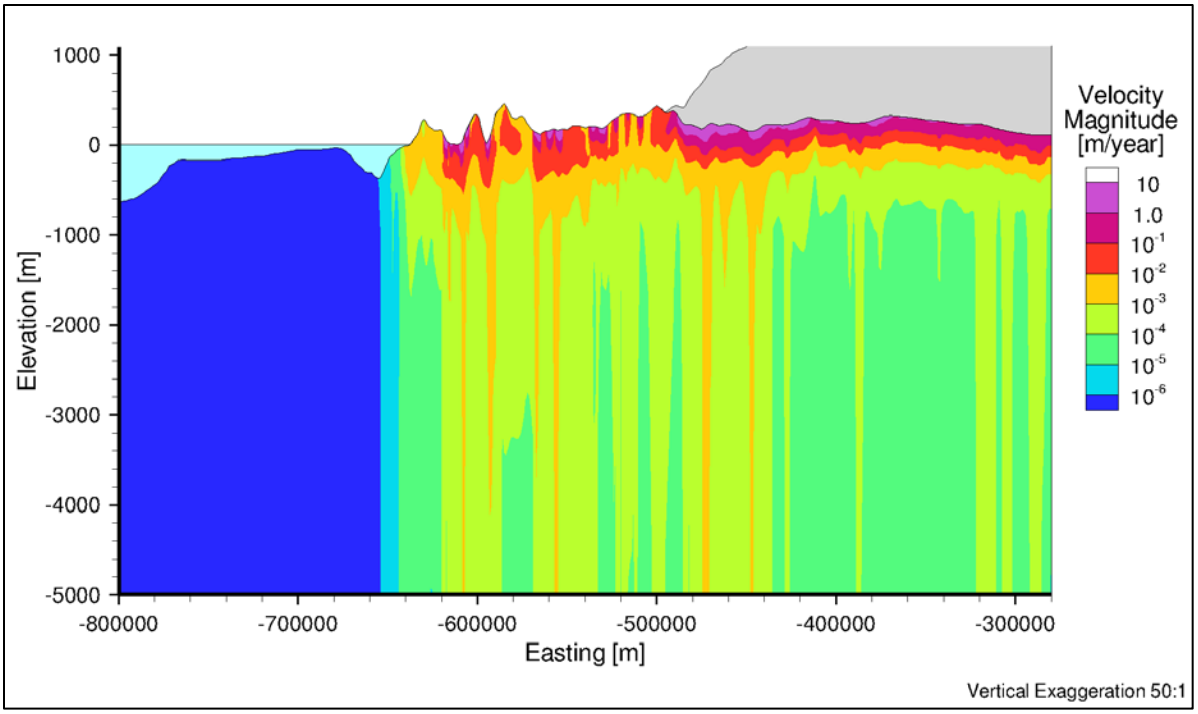

Figure C.64 West-East cross-section of velocity magnitude distribution for variably-saturated flow with permafrost after 50,000 years